Edited by
Peter Capper and
Peter Rudolph

Crystal Growth Technology

Related Titles

Scheel, H. J., Capper, P. (eds.)

Crystal Growth Technology

From Fundamentals and Simulation to Large-scale Production

2008
ISBN: 978-3-527-31762-2

Jackson, K. A.

Kinetic Processes

Crystal Growth, Diffusion, and Phase Transitions in Materials

Second, Completely Revised and Enlarged Edition
2010
ISBN: 978-3-527-32736-2

Dubois, J.-M., Belin-Ferré, E. (eds.)

Complex Metallic Alloys

Fundamentals and Applications

2010
ISBN: 978-3-527-32523-8

Kainer, K. U. (ed.)

Magnesium

8th International Conference on Magnesium Alloys and their Applications

2010
ISBN: 978-3-527-32732-4

Kumar, C. S. S. R. (ed.)

Mixed Metal Nanomaterials

2009
ISBN: 978-3-527-32153-7

Kumar, C. S. S. R. (ed.)

Nanostructured Oxides

2009
ISBN: 978-3-527-32152-0

Kumar, C. S. S. R. (ed.)

Metallic Nanomaterials

2009
ISBN: 978-3-527-32151-3

Levitin, V., Loskutov, S.

Strained Metallic Surfaces

Theory, Nanostructuring and Fatigue Strength

2009
ISBN: 978-3-527-32344-9

Herlach, D. M. (ed.)

Phase Transformations in Multi-component Melts

2009
ISBN: 978-3-527-31994-7

Köhler, M., Fritzsche, W.

Nanotechnology

An Introduction to Nanostructuring Techniques

2007
ISBN: 978-3-527-31871-1

Pfeiler, W. (ed.)

Alloy Physics

A Comprehensive Reference

2007
ISBN: 978-3-527-31321-1

Braga, D., Grepioni, F. (eds.)

Making Crystals by Design

Methods, Techniques and Applications

2007
ISBN: 978-3-527-31506-2

Edited by Peter Capper and Peter Rudolph

Crystal Growth Technology

Semiconductors and Dielectrics

WILEY-VCH Verlag GmbH & Co. KGaA

The Editors

Dr. Peter Capper
SELEX Galileo
1st Ave.
Millbrook Industrial Estate
Southampton SO15 0LG
United Kingdom

Prof. Dr. Peter Rudolph
Leibniz Institute for
Crystal Growth
Max-Born-Straße 2
12489 Berlin
Germany

All books published by Wiley-VCH are carefully produced. Nevertheless, authors, editors, and publisher do not warrant the information contained in these books, including this book, to be free of errors. Readers are advised to keep in mind that statements, data, illustrations, procedural details or other items may inadvertently be inaccurate.

Library of Congress Card No.: applied for

British Library Cataloguing-in-Publication Data
A catalogue record for this book is available from the British Library.

Bibliographic information published by the Deutsche Nationalbibliothek
The Deutsche Nationalbibliothek lists this publication in the Deutsche Nationalbibliografie; detailed bibliographic data are available on the Internet at <http://dnb.d-nb.de>.

© 2010 WILEY-VCH Verlag GmbH & Co. KGaA, Weinheim

All rights reserved (including those of translation into other languages). No part of this book may be reproduced in any form – by photoprinting, microfilm, or any other means – nor transmitted or translated into a machine language without written permission from the publishers. Registered names, trademarks, etc. used in this book, even when not specifically marked as such, are not to be considered unprotected by law.

Composition Toppan Best-set Premedia Limited

Printing and Binding betz-druck GmbH, Darmstadt

Cover Design Schulz Grafik.Design, Fußgönheim

Printed in the Federal Republic of Germany
Printed on acid-free paper

ISBN: 978-3-527-32593-1

Foreword

This volume deals with the technologies of the fabrication of important semiconducting and dielectric crystals, with their characterization, and with the machining of these bulk crystals. Thus, it will be of interest to all scientists, engineers and students who are engaged in this wide field of *crystal technology*. The largest fraction of industrial crystals consists of semiconductors such as silicon, gallium arsenide, indium phosphide, germanium, cadmium telluride and its solid solutions, and group-III nitrides. Another large fraction of dielectric crystals includes optical and scintillation crystals and crystals for the watch and jewelry industries.

The requirements with respect to structural perfection, homogeneity and yield are ever increasing, so that the crystal-producing industries are interested in the *optimum method* to fabricate quasiperfect crystals economically. For a specific crystal there are perhaps only one or two optimum growth methods, when taking into account all relevant factors like thermodynamics, amortization of equipment, building and infrastructure, labor and material costs, consumption of energy and cooling water, and increasingly important ecological aspects. Thereby, the advantages and problems of batch processes should be compared with a quasicontinuous Czochralski (CCZ) process, an example of which is discussed in this book. Also, the many growth parameters have to be optimized and often compromised, like the *temperature gradient* at the growth interface, which should be low for high structural perfection and homogeneity, but as high as possible to remove the latent heat and to achieve economic high growth rates.

Another growth parameter is *convection* that was long regarded as harmful by causing inhomogeneities (striations). Thus, great efforts were spent to reduce convection by microgravity (Skylab, Spacelab, etc.) or by damping magnetic fields. But then it was theoretically and experimentally demonstrated that forced convection of nearly isothermal melt fractions does not cause striations. Now, forced convection has become more widespread as it has the additional advantage to reduce the diffusion boundary layer in front of the growing crystal and thus increases the stable growth rate of inclusion-free crystals. Even alternating flow directions and flow velocities like reciprocal stirring in growth from aqueous solutions, or accelerated crucible rotation (ACRT) or the small mixed-melt volume in the CCZ process in growth from high-temperature melts can be optimized to yield striation-free crystals. In this connection it will be interesting to see whether

Crystal Growth Technology. Semiconductors and Dielectrics. Edited by P. Capper and P. Rudolph
Copyright © 2010 WILEY-VCH Verlag GmbH & Co. KGaA, Weinheim
ISBN: 978-3-527-32593-1

vibrations or magnetic stirring, as proposed in this volume, will find wide application, despite some obvious problems.

Modeling of crystal growth processes has become increasingly important as – with progress in computers and software – it is approaching realistic time, dimension and energy scaling, including complex convection regimes for industrial crystal fabrication. Five reviews in the book deal with numerical process simulation, which will thus assist with establishing the optimum growth method and the optimum growth parameters.

Also, in the production of epitaxial layers (epilayers) and multilayers one would expect an optimum growth method although epitaxy from the vapor phase (like metal-organic chemical vapor deposition (MOCVD) and molecular beam epitaxy (MBE)) has become dominating, whereas *liquid-phase epitaxy* (LPE) is losing its dominating role. Since in LPE the free-energy difference between the mobile species and the solid is by several orders of magnitude lower than in epitaxy from the vapor phase, the corresponding low supersaturation in LPE allows a real layer-by-layer (Frank–Van der Merwe) growth mode. Thus, the fabrication of structurally quite perfect layers with extremely flat surfaces is possible in homoepitaxy and in heteroepitaxy when the misfit between substrate and layer is low. These advantages are exploited in LPE production of CdHgTe (CMT) and of magnetic garnet films as outlined in this book; LPE of GaN is also now in development.

Characterization of industrial crystals, layers and surfaces is well established and required to achieve optimum performance and yield. However, characterization is not often done for crystals used in solid-state physics research. *Sufficient characterization* is defined as analysis of all those structural and chemical aspects of the sample that have or may have an influence on the specific measurement, because all crystals are different with respect to defects, impurities and inhomogeneities. Especially in physical measurements of high-temperature superconductors this was neglected so that many measurements are not reproducible.

Optimization is required for all aspects of crystal technology, also for *crystal machining*. Optimized sawing of crystals increases the yield of crystal and wafers and reduces the lapping and polishing/etching efforts. The development of novel crystal machining processes is essential and is covered in this volume.

Crystal technology has been and continues to be a key element in the development of micro- and optoelectronics and thus of computers, communications, and widespread electronics. With the forthcoming *energy crisis*, and the related climate–CO_2 problem, advances in crystal technology will become even more important and an essential factor for the future of mankind. Contributions of crystal technology will be crucial for saving energy, in energy transport, in renewable energy, and possibly also for the future hope of inertial fusion energy; the required crystal development of which is discussed in this book. Enormous amounts of energy can be saved with improved wide-bandgap devices based on GaN and SiC to be applied in all kinds of illumination (LEDs) and in high-power/high-temperature electronics. In renewable energy, photovoltaic cells based on III-V compounds with high efficiency ($\varepsilon > 35\%$) using concentrated sunlight will compete with the presently preferred silicon-based solar cells with a maximum ε of only 18%, thus requiring

large panel surface areas. *High-temperature superconductivity* (HTSC) could have an enormous role in energy saving and storage, in electric power transmission and in renewable energy, if its complex crystal- and material-technology problems could be solved, a chance missed in the hectic 20 years after the discovery of HTSC that were dominated by nonreproducible HTSC physics.

Despite its importance crystal technology is faced with the problem that *no targeted education exists of crystal-technology scientists and engineers*. So far, crystal-producing companies have had to hire chemists, material scientists, or physicists and provide them with extended education and training. One would wish that soon some technical universities would establish a multidisciplinary curriculum followed by special courses of all aspects of crystal technology and practical training in companies in order to produce crystal-technology scientists and engineers. This book will assist students and lecturers in this task, besides being useful for the exchange of experiences of current crystal-growth experts.

Beatenberg, Switzerland, February 2010 *Hans J. Scheel*

Contents

Foreword *V*
Preface *XVII*
List of Contributors *XIX*

Part I Basic Concepts in Crystal Growth Technology *1*

1 Thermodynamic Modeling of Crystal-Growth Processes *3*
Eberhard Buhrig, Manfred Jurisch, Jürgen Korb, and Olf Pätzold
1.1 Introduction *3*
1.2 General Approach of Thermodynamic Modeling *4*
1.2.1 Basics *4*
1.2.1.1 State Variables for the Description of Equilibrium Conditions *4*
1.2.1.2 The *ChemSage* Software Package *5*
1.3 Crystal Growth in the System Si–C–O–Ar (Example 1) *6*
1.3.1 Selection of Species *7*
1.3.2 Test Calculation, Check of Consistency *7*
1.3.3 Calculation of Gibbs Free Energy for Selected Reactions *8*
1.3.4 Minimization of Gibbs Free Energy of Complex Systems *9*
1.3.5 The Thermodynamic-Technological Model of the Edge-Defined Film-Fed Growth of Silicon *10*
1.4 Crystal Growth of Carbon-Doped GaAs (Example 2) *15*
1.4.1 Components and Species in the System *16*
1.4.2 Results *17*
1.4.3 Extended Model *19*
1.5 Summary and Conclusions *22*
Acknowledgments *23*
References *23*

2 Modeling of Vapor-Phase Growth of SiC and AlN Bulk Crystals *25*
Roman A. Talalaev, Alexander S. Segal, Eugene V. Yakovlev, and Andrey N. Vorob'ev
2.1 Introduction *25*

Crystal Growth Technology. Semiconductors and Dielectrics. Edited by P. Capper and P. Rudolph
Copyright © 2010 WILEY-VCH Verlag GmbH & Co. KGaA, Weinheim
ISBN: 978-3-527-32593-1

2.2 Model Description *28*
2.2.1 Quasi-Thermodynamic Model of AlN and AlGaN HVPE *29*
2.2.2 Modeling of Gas-Phase Nucleation in SiC CVD and HTCVD *30*
2.3 Results and Discussions *31*
2.3.1 GaN, AlN, and AlGaN HVPE *31*
2.3.2 SiC HTCVD *35*
2.4 Conclusions *38*
References *39*

3 Advanced Technologies of Crystal Growth from Melt Using Vibrational Influence *41*
Evgeny V. Zharikov
3.1 Introduction *41*
3.2 Axial Vibrational Control in Crystal Growth *42*
3.3 AVC-Assisted Czochralski Method *49*
3.4 AVC-Assisted Bridgman Method *54*
3.5 AVC-Assisted Floating Zone Method *58*
3.6 Conclusions *59*
Acknowledgments *60*
References *60*

Part II Semiconductors *65*

4 Numerical Analysis of Selected Processes in Directional Solidification of Silicon for Photovoltaics *67*
Koichi Kakimoto
4.1 Introduction *67*
4.2 Directional Solidification Method *67*
4.3 Crystallization Process *68*
4.4 Impurity Incorporation in Crystals *71*
4.5 Summary *74*
Acknowledgment *74*
References *74*

5 Characterization and Control of Defects in VCz GaAs Crystals Grown without B_2O_3 Encapsulant *75*
Frank M. Kiessling
5.1 Introduction *75*
5.2 Retrospection *76*
5.3 Crystal Growth without B_2O_3 Encapsulant *77*
5.4 Inclusions, Precipitates and Dislocations *80*
5.5 Residual Impurities and Special Defect Studies *83*
5.6 Electrical and Optical Properties in SI GaAs *84*
5.7 Boron in SC GaAs *89*

5.8 Outlook on TMF-VCz *91*
5.9 Conclusions *94*
Acknowledgments *95*
References *95*

6 The Growth of Semiconductor Crystals (Ge, GaAs) by the Combined Heater Magnet Technology *101*
Peter Rudolph, Matthias Czupalla, Christiane Frank-Rotsch, Frank-Michael Kiessling and Bernd Lux
6.1 Introduction *101*
6.2 Selected Fundamentals *102*
6.2.1 Convection-Driven Forces *102*
6.2.2 The Features of Traveling Magnetic Fields *104*
6.3 TMF Generation in Heater-Magnet Modules *106*
6.4 The HMM Design *107*
6.5 Numerical Modeling *109*
6.6 Dummy Measurements *111*
6.7 Growth Results under TMF *112*
6.7.1 LEC of GaAs *112*
6.7.2 VGF of Ge *114*
6.8 Conclusions and Outlook *118*
Acknowledgment *118*
References *119*

7 Manufacturing of Bulk AlN Substrates *121*
Oleg V. Avdeev, Tatiana Yu. Chemekova, Heikki Helava, Yuri N. Makarov, Evgenii N. Mokhov, Sergei S. Nagalyuk, M.G. Ramm, Alexander S. Segal, and Alexander I. Zhmakin
7.1 Introduction *121*
7.1.1 Substrates for Group III Nitride Devices *121*
7.1.2 Growth of Bulk Group III Nitride Crystals *123*
7.1.3 Sublimation Growth of AlN Crystals *125*
7.2 Modeling *126*
7.3 Experiment *129*
7.3.1 Pregrowth Processing *129*
7.3.2 Seeding and Initial Growth *131*
7.3.3 Growth of Bulk AlN Crystals *131*
7.4 Results and Discussion *131*
7.5 Conclusions *133*
Acknowledgments *133*
References *133*

8 Interactions of Dislocations During Epitaxial Growth of SiC and GaN *137*
Jochen Friedrich, Birgit Kallinger, Patrick Berwian, Elke Meissner
8.1 Introduction *137*

8.2 Classification, Nomenclature and Characterization of Dislocations in SiC and GaN *138*
8.3 Conversion of Basal Plane Dislocations During SiC Epitaxy *141*
8.3.1 Experimental Strategies for Obtaining High Conversion Rates *141*
8.3.2 Driving Force for BPD Conversion *143*
8.4 Reduction of Dislocations During Homoepitaxy of GaN *144*
8.4.1 Objectives and Techniques *144*
8.4.2 Driving Force for Dislocation Reduction *145*
8.5 Conclusions *148*
Acknowledgment *148*
References *148*

9 Low-Temperature Growth of Ternary III-V Semiconductor Crystals from Antimonide-Based Quaternary Melts *151*
Partha.S. Dutta
9.1 Introduction *151*
9.2 Crystal Growth from Quaternary Melts *152*
9.3 Advantages of Quaternary Melts *152*
9.4 Synthesis and Bulk Crystal Growth *154*
9.4.1 Growth from $Ga_{1-x}In_xAs_{1-y}Sb_y$ Melt *158*
9.4.1.1 Growth of $Ga_{1-x}In_xAs$ *158*
9.4.1.2 Growth of $GaAs_{1-y}Sb_y$ *161*
9.4.2 Growth from $Ga_{1-x}In_xP_{1-y}Sb_y$ Melt *161*
9.4.2.1 Growth of $Ga_{1-x}In_xP$ *161*
9.4.3 Growth from $Al_{1-x}Ga_xAs_{1-y}Sb_y$ Melt *163*
9.4.3.1 Growth of $Al_{1-x}Ga_xAs$ *163*
9.4.3.2 Growth of $AlAs_{1-y}Sb_y$ *164*
9.4.4 Growth from $Al_{1-x}In_xAs_{1-y}Sb_y$ Melt *164*
9.4.4.1 Growth of $Al_{1-x}In_xAs$ *165*
9.4.4.2 Growth of $AlAs_{1-y}Sb_y$ *165*
9.4.5 Growth from $Al_{1-x}In_xP_{1-y}Sb_y$ Melt *165*
9.4.5.1 Growth of $Al_{1-x}In_xP$ *166*
9.4.6 Growth from $Al_{1-x}Ga_xP_{1-y}Sb_y$ Melt *166*
9.4.6.1 Growth of $Al_{1-x}Ga_xP$ *166*
9.4.7 Growth from $Al_{1-x-y}Ga_xIn_ySb$ Melt *167*
9.4.7.1 Growth of $Al_{1-x}Ga_xSb$ *168*
9.4.8 Growth from $InP_{1-x-y}As_xSb_y$ Melt *168*
9.4.8.1 Growth of $InP_{1-y}As_y$ *168*
9.4.9 Growth from $GaP_{1-x-y}As_xSb_y$ Melt *169*
9.4.9.1 Growth of $GaP_{1-y}As_y$ *169*
9.4.10 Growth from $AlP_{1-x-y}As_xSb_y$ Melt *170*
9.4.10.1 Growth of $AlP_{1-y}As_y$ *170*
9.5 Conclusion *171*
References *172*

10 Mercury Cadmium Telluride (MCT) Growth Technology Using ACRT and LPE *175*
Peter Capper
10.1 Introduction *175*
10.2 Bridgman/ACRT Growth of MCT *177*
10.2.1 Introduction *177*
10.2.2 Processing *178*
10.2.3 Accelerated Crucible Rotation Technique (ACRT) *178*
10.2.3.1 Introduction *178*
10.2.3.2 High-*x* Material *179*
10.2.4 Summary *182*
10.3 Liquid Phase Epitaxy of MCT *184*
10.3.1 Introduction *184*
10.3.2 Growth *185*
10.3.3 Summary *191*
References *192*

11 The Use of a Platinum Tube as an Ampoule Support in the Bridgman Growth of Bulk CZT Crystals *195*
Narayanasamy Vijayan, Verónica Carcelén, and Ernesto Diéguez
11.1 Introduction *195*
11.2 The Importance of the Solid/Liquid Interface *197*
11.3 Approaches for Crystal Growth Using Ampoule Support *199*
11.4 Results and Discussions *201*
11.5 Conclusions *208*
Acknowledgments *209*
References *209*

Part III Dielectrics *211*

12 Modeling and Optimization of Oxide Crystal Growth *213*
Svetlana E. Demina, Vladimir V. Kalaev, Alexander T. Kuliev, Kirill M. Mazaev, and Alexander I. Zhmakin
12.1 Introduction *213*
12.2 Radiative Heat Transfer (RHT) *214*
12.3 Numerical Model *217*
12.4 Results and Discussion *218*
12.4.1 Sapphire *219*
12.4.2 Yttrium Aluminum Garnet *219*
12.4.3 Bismuth Germanate (BGO) *222*
12.5 Conclusions *225*
Acknowledgments *225*
References *225*

13 Advanced Material Development for Inertial Fusion Energy (IFE) *229*
Kathleen Schaffers, Andrew J. Bayramian, Joseph A. Menapace, Gregory T. Rogowski, Thomas F. Soules, Christopher A. Stolz, Steve B. Sutton, John B. Tassano, Peter A. Thelin, Christopher A. Ebbers, John A. Caird, Christopher P.J. Barty, Mark A. Randles, Charles Porter, Yiting Fei, and Bruce H.T. Chai
13.1 Introduction *229*
13.2 Production of Nd:phosphate Laser Glass and KDP Frequency-Conversion Crystals *233*
13.2.1 Nd : phosphate Laser Glass *233*
13.2.2 KDP Frequency-Conversion Crystals *235*
13.3 Yb : S-FAP Crystals *235*
13.3.1 Crystal Growth *237*
13.3.2 Modeling *238*
13.3.3 Slab Fabrication *239*
13.4 YCOB Crystals *241*
13.4.1 YCOB Crystal Growth and Fabrication *242*
13.5 Advanced Material Concepts for Power-Plant Designs *243*
13.6 Summary *246*
References *246*

14 Magneto-Optic Garnet Sensor Films: Preparation, Characterization, Application *249*
Peter Görnert, Andreas Lorenz, Morris Lindner, and Hendryk Richert
14.1 Introduction *249*
14.2 Bi-Substituted Garnets *249*
14.3 LPE Deposition and Topological Film Properties *251*
14.4 Magnetic and Magneto-Optic Film Properties *253*
14.4.1 Magnetic Properties *253*
14.4.2 Magneto-Optic Properties *254*
14.4.3 Reproducibility *260*
14.5 Applications *260*
14.5.1 Images of Magnetic Field Distributions *261*
14.5.2 Quantitative Determination of Magnetic Fields *264*
14.6 Conclusions *264*
Acknowledgments *265*
References *265*

15 Growth Technology and Laser Properties of Yb-Doped Sesquioxides *267*
Rigo Peters, Klaus Petermann, and Günter Huber
15.1 Introduction *267*
15.2 Structure and Physical Properties *267*
15.3 Crystal Growth *269*
15.3.1 Growth Methods with Crucibles *269*
15.3.2 Heat-Exchanger Method *270*

15.3.2.1 Crucible *270*
15.3.2.2 Atmosphere *271*
15.3.2.3 Setup *272*
15.3.2.4 Growth Procedure *273*
15.3.2.5 Results *274*
15.4 Spectroscopic Characterization *276*
15.5 Laser Experiments *279*
15.6 Summary and Outlook *280*
Acknowledgment *280*
References *281*

16 Continuous Growth of Alkali-Halides: Physics and Technology *283*
Oleg Sidletskiy
16.1 Modern Requirements to Large Alkali-Halide Crystals *283*
16.2 Conditions of Steady-State Crystallization in Conventional Melt-Growth Methods and in Their Modifications *284*
16.2.1 Conventional Methods *284*
16.2.2 Melt-Feeding Methods *285*
16.2.3 Growth-Process Control *286*
16.3 Macrodefect Formation in AHC *287*
16.4 Dynamics of Thermal Conditions during Continuous Growth *290*
16.5 Advanced Growth-Control Algorithms *292*
16.6 Summary *295*
Acknowledgements *296*
References *296*

17 Trends in Scintillation Crystals *299*
Alexander V. Gektin
17.1 Introduction *299*
17.2 Novel Scintillation Materials *300*
17.3 Scintillation Detectors for Image Visualization and Growth Techniques for Scintillation Crystals *302*
17.4 High Spatial Resolution Scintillation Detectors *305*
17.5 Conclusions *310*
References *312*

Part IV Crystal Machining *313*

18 Crystal Machining Using Atmospheric Pressure Plasma *315*
Yasuhisa Sano, Kazuya Yamamura, and Kazuto Yamauchi
18.1 Introduction *315*
18.2 Plasma Chemical Vaporization Machining (PCVM) *315*
18.2.1 General Description of PCVM *315*
18.2.2 Machining of SiC by PCVM *316*
18.2.3 Beveling of SiC Wafer *317*

18.2.3.1 Background *317*
18.2.3.2 Apparatus and Experimental Method *317*
18.2.3.3 Results and Discussion *318*
18.2.3.4 Summary of Beveling of SiC Wafer *320*
18.2.4 Thinning of SiC Wafer *320*
18.2.4.1 Background *320*
18.2.4.2 Sample Preparation and Experimental Conditions *320*
18.2.4.3 Results and Discussion *320*
18.2.4.4 Summary of Thinning of SiC Wafer *322*
18.3 Numerically Controlled Sacrificial Oxidation *322*
18.3.1 Basic Concepts *322*
18.3.2 Basic Experiments *323*
18.3.2.1 Experimental Apparatus *323*
18.3.2.2 Oxidation Mark *323*
18.3.2.3 Oxidation Rate *324*
18.3.2.4 Surface Roughness *324*
18.3.2.5 Summary of the Basic Experiments *326*
18.3.3 Improving Thickness Uniformity of SOI *326*
18.3.3.1 Background *326*
18.3.3.2 Procedure for Uniformizing *327*
18.3.3.3 Uniformizing of 300 mm SOI *327*
18.3.3.4 Summary of Improving Thickness Uniformity of SOI *328*
18.4 Conclusions *328*
References *329*

Index *331*

Preface

This book deals with the technologies of crystal growth, crystal characterization and crystal machining. As such it will be of interest to all scientists, engineers and students who are engaged in this wide field of technology. High-quality crystals form the basis of many industries, including telecommunications, information technology, energy technology (both energy saving and renewable energy), lasers, and a wide variety of detectors of various parts of the electromagnetic spectrum.

Of the approximately 30 000 tons of bulk crystals produced annually the largest fraction consists of semiconductors such as silicon, gallium arsenide, indium phosphides, germanium, group-III nitrides, cadmium telluride and cadmium mercury telluride. Other large fractions include optical and scintillator crystals and crystals for the laser, watch and jewellery industries.

For most applications these crystals must be machined, i.e. sliced, lapped, polished, etched or surface treated in various ways. These processes are critical to the economic use of these crystals as they are a strong driver of yields of usable material. Improvements are always sought in these various areas for a particular crystal.

This book contains 18 selected reviews from the "Fourth International Workshop on Crystal Growth Technology" organized in Beatenberg, Switzerland by Hans Scheel between 18–25 May, 2008. The first in the series "First International School on Crystal Growth Technology" was also in Beatenberg between 5–14, September 1998, the second in the series was held between August 24–29, 2000 in Mount Zao Resort, Japan and the third was held in Beatenberg, Switzerland between 10–18 September, 2005. The first workshop generated a book of 29 selected reviews that was published in 2003 by Wiley, UK entitled "Crystal Growth Technology" edited by Hans J. Scheel and Tsuguo Fukuda, while the third generated a book of 19 selected reviews that was published in 2008 by Wiley-VCH, Germany entitled "Crystal Growth Technology" edited by Hans J. Scheel and Peter Capper.

Part 1 covers general aspects of crystal-growth technology, including thermodynamics, modelling of vapor growth, and the influence of vibration on growth. Part 2 discusses the growth of several compound semiconductors in more detail. These include gallium arsenide, aluminum nitride, silicon carbide, III-V ternaries, cadmium mercury telluride and cadmium zinc telluride. Part 3 covers the growth and applications of a range of dielectric crystals, including oxides and sesquioxides,

Crystal Growth Technology. Semiconductors and Dielectrics. Edited by P. Capper and P. Rudolph
Copyright © 2010 WILEY-VCH Verlag GmbH & Co. KGaA, Weinheim
ISBN: 978-3-527-32593-1

halides, and garnets for a wide range of applications. The final section of the book, Part 4, contains just one chapter on the current situation in crystal machining using plasmas.

The editors would like to thank all the contributors for their valuable reviews and the sponsors of IWCGT-4. Furthermore, the editors gratefully acknowledge the patience and hard work of the following at Wiley-VCH: Eva-Stina Riihiäki, Martin Graf, Maike Petersen and Hans-Jochen Schmitt.

The editors hope that the book will contribute to the scientific development of crystal-growth technologies and the education of future generations of crystal-growth engineers and scientists.

Southampton, UK and Berlin, Germany *Peter Capper and Peter Rudolph*

List of Contributors

Oleg V. Avdeev
Nitride Crystals Inc.
10404 Patterson Ave., S. 108
Richmond, VA 23238
USA

C.P.J. Barty
Lawrence Livermore National Laboratory
PO Box 808
Livermore, CA 94551
USA

A.J. Bayramian
Lawrence Livermore National Laboratory
PO Box 808
Livermore, CA 94551
USA

Patrick Berwian
Fraunhofer Institute of Integrated Systems and Device Technology (IISB)
Department of Crystal Growth
Schottkystraße 10
91058 Erlangen
Germany

Eberhard Buhrig
Freiberger Compound Materials GmbH
Crystal Growth and Basic Research
Am Junger Löwe Schacht 5
Freiberg 09599
Germany
Institut für NE-Metallurgie und Reinststoffe
TU Bergakademie Freiberg, Leipziger Straße 34
Freiberg 09599
Germany

J.A. Caird
Lawrence Livermore National Laboratory
PO Box 808
Livermore, CA 94551
USA

Peter Capper
Selex Galileo Infrared Ltd
1st Avenue, Millbrook Industrial Estate
Southampton SO15 0LG
UK

Crystal Growth Technology. Semiconductors and Dielectrics. Edited by P. Capper and P. Rudolph
Copyright © 2010 WILEY-VCH Verlag GmbH & Co. KGaA, Weinheim
ISBN: 978-3-527-32593-1

V. Carcelén
Universidad Autónoma de Madrid
Laboratorio de Crecimiento de Cristales, Dpto. Física de Materiales
Facultad de Ciencias
Madrid 28049
Spain

B.H.T. Chai
Crystal Photonics, Inc.
5525 Sanford Lane
Sanford, FL 32773
USA

Tatiana Yu. Chemekova
Nitride Crystals Inc.
10404 Patterson Ave., S. 108
Richmond, VA 23238
USA

Matthias Czupalla
Leibniz Institute for Crystal Growth (IKZ)
Max-Born-Straße 2
12489 Berlin
Germany

Svetlana E. Demina
STR Group Ltd.
Engels av. 27, P.O. Box 89
194156, St.-Petersburg
Russia

Ernesto Diéguez
Universidad Autónoma de Madrid
Laboratorio de Crecimiento de Cristales, Dpto. Física de Materiales
Facultad de Ciencias
Madrid 28049
Spain
Universidad Autónoma de Madrid
Crystal Growth Laboratory (CGL)
Materials Physics Department.
Madrid 28049
Spain

Partha.S. Dutta
Rensselaer Polytechnic Institute
Department of Electrical, Computer, and Systems Engineering
Troy, NY 12180
USA

C.A. Ebbers
Lawrence Livermore National Laboratory
PO Box 808
Livermore, CA 94551
USA

Y. Fei
Crystal Photonics, Inc.
5525 Sanford Lane
Sanford, FL 32773
USA

Christiane Frank-Rotsch
Leibniz Institute for Crystal Growth (IKZ)
Max-Born-Straße 2
12489 Berlin
Germany

Jochen Friedrich
Fraunhofer Institute of Integrated Systems and Device Technology (IISB)
Department of Crystal Growth
Schottkystraße 10
91058 Erlangen
Germany

Alexander V. Gektin
Institute of Scintillation Materials
Department of Crystal Growth Technology
60 Lenin Ave
61001 Kharkov
Ukraine

Peter Görnert
Innovent e.V.
Pruessingstraße 27B
07745 Jena
Germany

Heikki Helava
Nitride Crystals Inc.
10404 Patterson Ave., S. 108
Richmond, VA 23238
USA

G. Huber
University of Hamburg
Institute of Laser-Physics
Luruper Chaussee 149
22761 Hamburg
Germany

Manfred Jurisch
Institut für NE-Metallurgie und Reinststoffe
TU Bergakademie Freiberg, Leipziger Straße 34
Freiberg 09599
Germany

Koichi Kakimoto
Kyushu University
Research Institute for Applied Mechanics
6-1, Kasuga-Koen
Kasuga 816-8580
Japan

Vladimir V. Kalaev
STR Group Ltd.
Engels av. 27, P.O. Box 89
194156, St.-Petersburg
Russia

Birgit Kallinger
Fraunhofer Institute of Integrated Systems and Device Technology (IISB)
Department of Crystal Growth
Schottkystraße 10
91058 Erlangen
Germany

Frank M. Kiessling
Leibniz-Institut für Kristallzüchtung
Max-Born-Straße 2
12489 Berlin
Germany

Frank-Michael Kiessling
Leibniz Institute for Crystal Growth (IKZ)
Max-Born-Straße 2
12489 Berlin
Germany

Jürgen Korb
Institut für NE-Metallurgie und Reinststoffe
TU Bergakademie Freiberg, Leipziger Straße 34
Freiberg 09599
Germany

Alexander T. Kuliev
STR Group Ltd.
Engels av. 27, P.O. Box 89
194156, St.-Petersburg
Russia

Morris Lindner
Innovent e.V.
Pruessingstraße 27B
07745 Jena
Germany

Andreas Lorenz
Innovent e.V.
Pruessingstraße 27B
07745 Jena
Germany

Bernd Lux
Leibniz Institute for Crystal Growth (IKZ)
Max-Born-Straße 2
12489 Berlin
Germany

Yuri N. Makarov
Nitride Crystals Inc.
10404 Patterson Ave., S. 108
Richmond, VA 23238
USA

Kirill M. Mazaev
STR Group Ltd.
Engels av. 27, P.O. Box 89
194156, St.-Petersburg
Russia

Elke Meissner
Fraunhofer Institute of Integrated Systems and Device Technology (IISB)
Department of Crystal Growth
Schottkystraße 10
91058 Erlangen
Germany

J.A. Menapace
Lawrence Livermore National Laboratory
PO Box 808
Livermore, CA 94551
USA

Evgenii N. Mokhov
Nitride Crystals Inc.
10404 Patterson Ave., S. 108
Richmond, VA 23238
USA

Sergei S. Nagalyuk
Nitride Crystals Inc.
10404 Patterson Ave., S. 108
Richmond, VA 23238
USA

Olf Pätzold
Institut für NE-Metallurgie und Reinststoffe
TU Bergakademie Freiberg, Leipziger Straße 34
Freiberg 09599
Germany

Klaus Petermann
University of Hamburg
Institute of Laser-Physics
Luruper Chaussee 149
22761 Hamburg
Germany

R. Peters
University of Hamburg
Institute of Laser-Physics
Luruper Chaussee 149
22761 Hamburg
Germany

C. Porter
Northrop Grumman/Synoptics
1201 Continental Blvd.
Charlotte, NC 28273
USA

Mark G. Ramm
Nitride Crystals Inc.
10404 Patterson Ave., S. 108
Richmond, VA 23238
USA

M.A. Randles
Northrop Grumman/Synoptics
1201 Continental Blvd.
Charlotte, NC 28273
USA

Hendryk Richert
Innovent e.V.
Pruessingstraße 27B
07745 Jena
Germany

G.T. Rogowski
Lawrence Livermore National
Laboratory
PO Box 808
Livermore, CA 94551
USA

Peter Rudolph
Leibniz Institute for Crystal Growth
(IKZ)
Max-Born-Straße 2
12489 Berlin
Germany

Yasuhisa Sano
Osaka University
Graduate School of Engineering
Department of Precision Science and
Technology
2-1 Yamadaoka, Suita
Osaka 565-0871
Japan

Kathleen Schaffers
Lawrence Livermore National
Laboratory
PO Box 808
Livermore, CA 94551
USA

Alexander S. Segal
Nitride Crystals Inc.
10404 Patterson Ave., S. 108
Richmond, VA 23238
USA
STR Group Ltd
P.O. Box 89
194156, St.Petersburg
Russia

Oleg Sidletskiy
Institute for Scintillation Materials
Department of Crystal Growth
Technology
NAS of Ukraine, 60 Lenin Ave.
61001 Kharkiv
Ukraine

T.F. Soules
Lawrence Livermore National
Laboratory
PO Box 808
Livermore, CA 94551
USA

C.A. Stolz
Lawrence Livermore National
Laboratory
PO Box 808
Livermore, CA 94551
USA

S.B. Sutton
Lawrence Livermore National
Laboratory
PO Box 808
Livermore, CA 94551
USA

Roman A. Talalaev
STR Group Ltd
P.O. Box 89
194156, St.Petersburg
Russia

J.B. Tassano
Lawrence Livermore National
Laboratory
PO Box 808
Livermore, CA 94551
USA

P.A. Thelin
Lawrence Livermore National Laboratory
PO Box 808
Livermore, CA 94551
USA

N. Vijayan
Universidad Autónoma de Madrid
Laboratorio de Crecimiento de Cristales, Dpto. Física de Materiales
Facultad de Ciencias
Madrid 28049
Spain
National Physical Laboratory
New Delhi 110 012
India

Andrey N. Vorob'ev
STR Group Ltd
P.O. Box 89
194156, St.Petersburg
Russia

Eugene V. Yakovlev
STR Group Ltd
P.O. Box 89
194156, St.Petersburg
Russia

Kazuya Yamamura
Osaka University
Graduate School of Engineering
Research Center for Ultra-Precision Science and Technology
2-1 Yamadaoka, Suita
Osaka 565-0871
Japan

Kazuto Yamauchi
Osaka University
Graduate School of Engineering
Department of Precision Science and Technology
2-1 Yamadaoka, Suita
Osaka 565-0871
Japan
Osaka University
Graduate School of Engineering
Research Center for Ultra-Precision Science and Technology
2-1 Yamadaoka, Suita
Osaka 565-0871
Japan

Evgeny V. Zharikov
D. Mendeleyev University of Chemical Technology of Russia
Miusskaya Sq., 9
Moscow, 125047
Russia
General Physics Institute of Russian Academy of Sciences
Vavilov St., 38
Moscow, 119991
Russia

Alexander I. Zhmakin
Russian Academy of Sciences
A.F. Ioffe Physical Technical Institute
Polytechnicheskaya 26
194021, St. Petersburg
Russia

Part I
Basic Concepts in Crystal Growth Technology

Crystal Growth Technology. Semiconductors and Dielectrics. Edited by P. Capper and P. Rudolph
Copyright © 2010 WILEY-VCH Verlag GmbH & Co. KGaA, Weinheim
ISBN: 978-3-527-32593-1

1
Thermodynamic Modeling of Crystal-Growth Processes

Eberhard Buhrig, Manfred Jurisch, Jürgen Korb, and Olf Pätzold

1.1
Introduction

Single-crystal growth from the melt is a very complex process that can be described, analyzed and controlled by various models. Relevant models [1–9] focus on:

- temperature distribution in melt, growing crystal and growth equipment, convective flow in the melt, stress/strain field in the growing crystal including the formation of defects like dislocations;
- temperature-dependent defect inventory of the crystal;
- behavior of melt/crystal interface and atomic growth mechanisms;
- thermochemical reactions in the growth chamber.

This chapter shows current possibilities and limitations of thermodynamic/thermochemical modeling in bulk single-crystal growth. In view of the highly complex subject matter the choice of the examples makes no claim to be complete, but shall consider very different modeling applications.

The fundamentals of thermodynamics/thermochemistry in crystal-growth processes have been described by Jacobs [5] in a very comprehensive way and are assumed to be known as a basis for the following.

The complex software package *ChemSage* and its successor *FactSage* [10] that are based on a minimization of the Gibbs free reaction energy are used for the thermodynamic calculations. This software offers solutions for the entire procedure from data gathering up to process simulation. To avoid confusion with other definitions and to facilitate our own activities the *ChemSage* nomenclature is used in this chapter [11].

It should, however, be mentioned that there are also available other program packages with similar capabilities, for example, Thermo-Calc [12] or HSC Chemistry [13]. As the general approach of thermodynamic modeling does not depend on the software the application of *ChemSage/FactSage* is not compulsory.

Crystal Growth Technology. Semiconductors and Dielectrics. Edited by P. Capper and P. Rudolph
Copyright © 2010 WILEY-VCH Verlag GmbH & Co. KGaA, Weinheim
ISBN: 978-3-527-32593-1

Thermodynamic/thermochemical models are simplified versions of the real processes, that is, they may only reproduce aspects included in the model. The resulting limitations have to be taken into consideration for any interpretation of results. In particular, it should be emphasized that thermodynamic models only describe thermodynamic equilibrium conditions and do not include reaction kinetics.

1.2 General Approach of Thermodynamic Modeling

1.2.1 Basics

Thermodynamic modeling is a highly efficient tool that may be used to describe, develop, optimize and control crystal-growth technologies. It has, however, also the following shortcomings and limitations:

- only equilibrium conditions can be described that very seldom occur under conditions of practical relevance;
- a complete data set of all relevant species is necessary for a comprehensive description of the respective thermodynamic system;
- a highly efficient software is required for calculations.

Therefore, thermodynamic modeling is mainly applied to make statements of trend.

1.2.1.1 State Variables for the Description of Equilibrium Conditions

Thermochemical and *thermodynamic* modeling are regarded as synonyms with *thermodynamic* modeling being the preferred term in this chapter.

Thermodynamics defines thermodynamic state variables that are both independent influencing parameters and measures at the same time. The most important state variables are given in Table 1.1.

Table 1.1 State variables.

Temperature	***T***	**In K or °C**
Volume	*V*	In m^3, l, dm^3
Amount	*n*	In mole
Concentration	*c*,*x*	Mole fraction
Pressure	*P*	In bar
Partial pressure	*p*	For ideal systems
Fugacity	*f*	For real systems
Surface	*O*	In m^2 /mole, relevant for very small particles
Energy	*E*	In J (magnetic, mechanical, electromagnetic, etc.)

Reactions between the components of a thermodynamic system can be characterized by thermodynamic state functions (thermodynamic potentials) depending on state variables. The most important state function in thermodynamic modeling is the Gibbs free energy (G) that defines

- the equilibrium state of a system;
- the capacity for doing chemical work;
- the chemical potential of substances;
- the direction of chemical reactions;
- the magnitude of the driving force for chemical reactions.

The Gibbs free energy is given by

$$G = H - T \cdot S \tag{1.1}$$

with H, enthalpy, T, temperature and S, entropy.

It can be split into several terms:

$$G = G^{\mathrm{ref}} + G^{\mathrm{id}} + G^{\mathrm{ex}} \tag{1.2}$$

with the following meanings:

- G^{ref}, reference values of pure substances at $T = 298.5\,\mathrm{K}$ and $P = 1$ bar taken from databases;
- G^{id}, Gibbs free energy of an ideal system in dependence on state variables;
- G^{ex}, deviation from ideal behavior in a mixed system.

For the excess Gibbs free energy G^{ex} the model of a sub-regular solution according to Redlich–Kister–Muggianu [14] is used in this chapter. It is valid for binary i–j interactions in multi-component systems.

$$G_{ij}^{\mathrm{ex}} = x_i x_j \Sigma_{\mathrm{v}} L_{ij}^{(v)} (x_i - x_j)^{(v)} \tag{1.3}$$

$L^{(v)}$, interaction parameter
x, concentration

If necessary, a fourth member, the so-called *constrained power operator*, can be added to Equation 1.2 by which additional influencing parameters like magnetic or electric fields, electrolytic potentials as well as time-dependent aspects of single reactions may be integrated into the model [15].

1.2.1.2 The *ChemSage* Software Package

The commercial *ChemSage* software package has been developed by Gesellschaft für Technische Thermodynamik und -physik GmbH [16]. This package allows for the complete thermodynamic modeling of complex crystal-growth processes. A schematic overview of the ChemSage family is given in Figure 1.1.

The actual thermodynamic calculations for all program members take place in the central module (solver), the Gibbs free energy minimizer. This module is not accessible to users.

ChemApp [17] is a freely accessible programming platform which allows for programming of peripheral applications and online connection to external programs of global models, for example, crystal-growth processes.

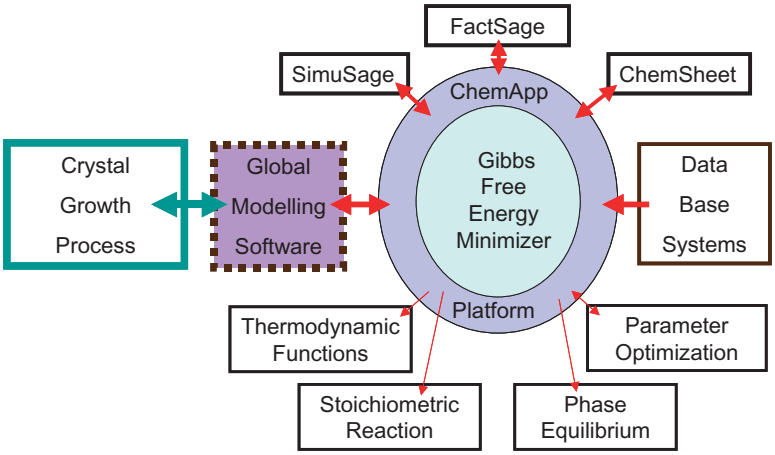

Figure 1.1 The *ChemSage* family.

In the following, the *FactSage* program is preferentially used. With this program it is possible to realize numerical calculations, graphical representations and input/output procedures, as well. *FactSage* also allows for connections with international database systems by which the standard values of the Gibbs free energy can be obtained for all relevant species of the investigated system.

In addition, the following modules belong to the *ChemSage* family:

- *SimuSage*, a software for interactive simulation of processes;
- *ChemSheet*, a software for handling input/output operations including all functions of the *Excel* software. Even externally programmed processes like diffusion or other time-dependent procedures can be integrated by *ChemSheet*.

Furthermore, the *ChemSage* family comprises an effective module for optimization of thermodynamic data by which missing initial data can be added or adjusted. Finally, a thermodynamic model of a reactor is available that allows for simulations of pseudo-3D and time-dependent processes.

In the following, there are given some examples for the calculation of realistic thermodynamic functions of single-species and stoichiometric reactions as well as calculations of many-component, many-phase equilibria.

The first example will be considered in detail in order to demonstrate the single steps of thermodynamic modeling, whereas the remaining ones are illustrated in an abbreviated form, as the general approach is always the same.

1.3 Crystal Growth in the System Si–C–O–Ar (Example 1)

The first step of modeling is the detailed formulation of the task and the selection of the components relevant for the system.

In the following, a special aspect of thermal silicon technology will be shown. The system components are Si, C, O and Ar chosen because of their practical relevance:

- metallurgical silicon can be obtained from silicon oxides and carbon containing components in an electrical arc furnace (Si–O–C);
- silicon single crystals of electronic purity are grown under vacuum or in an Ar atmosphere by the Czochralski method from fused silica crucibles supported by graphite containers;
- silicon single crystals can also be grown by the floating zone technique under vacuum or argon protective gas;
- silicon sheets are produced by the EFG (edge-defined film-fed growth) process using graphite crucibles and graphite shapers;
- ingot casting of silicon for solar cell production.

In any case, the quality of silicon is mainly determined by carbon and oxygen impurities.

1.3.1 Selection of Species

As a rule, there are different and sometimes contradictory data for a given number of components of existing species and their modifications in international databases or publications. For this reason, a constrictive selection has to be made as the next step (Table 1.2).

1.3.2 Test Calculation, Check of Consistency

The next steps are test calculations and check of data consistency. As an example, the calculated Gibbs free energies for 1 mole of the stoichometric condensed phases of the system at 1413.85 °C and 1 bar are compiled in Table 1.3. Despite

Table 1.2 Species in the Si–C–O system under Ar as a possible protective gas.

Stoichiometric, condensed phases	**C, SiO_2, SiC**
Solid solution phase	Si(s) containing O and C
Liquid solution phase	Si(l) containing O, C
Gas phase	Containing SiO_2, SiC, Ar, SiO, CO, Si, Si_2C, Si_2, Si_3, CO2, Si_2O_2, SiC_2, O, O_2, C_2O, C(with a cut-off pressure of 2×10^{-16} bar)

Table 1.3 Gibbs free energy of selected condensed phases (original print).

Constituent	Heat capacity	Enthalpy	Entropy	Gibbs energy
	J K^{-1}	J	J K^{-1}	J
1 mol of Si (l)	2.719 60E + 01	8.625 02E + 04	9.156 88E + 01	−6.822 64E + 04
1 mol of Si (s)	2.922 24E + 01	3.604 22E + 04	6.179 75E + 01	−6.821 02E + 04
1 mol of SiC (s)	5.202 17E + 01	−7.501 57E + 03	9.016 19E + 01	−1.596 05E + 05
1 mol of SiO_2 (s)	7.367 27E + 01	−8.138 03E + 05	1.55 336E + 02	−1.075 85E + 06
				Original print

T = 1413.849 870 51 °C, P = 1.000 00E + 00 bar.

the different molecular weights the numerical values of the Gibbs free energies allow the following statements to be made:

- the Gibbs free energy of solid and liquid silicon are equal, that is, Si(l) and Si(s) are in thermodynamic equilibrium at a temperature of 1414.85 °C, defining the crystallization/melting temperature characteristic for the data set,
- the Gibbs free energies of SiO_2 and SiC are more negative than *G* for Si(l) and Si(s), that is, a reaction including silicon is impossible as long as free carbon or oxygen exist in the system,
- SiO_2 has a more negative Gibbs free energy compared with SiC, that is, oxygen suppresses carbon in silicon carbon compounds (at the given temperature).

In this way, the existence of all species of the model system can be roughly assessed as a function of temperature and pressure. The actual stability of species can, however, only be defined by a thermodynamic equilibrium calculation of the complete system or of single chemical reactions (see next item).

1.3.3 Calculation of Gibbs Free Energy for Selected Reactions

At high temperatures, permanent reactions take place between the individual species and phases of the model system. Therefore, dynamic equilibria will be calculated the status of which depends on temperature and concentration of species/components. As an example, the adjustment of the dynamic equilibrium for the single reaction of oxygen containing liquid silicon and gaseous SiO will be considered. The reaction scheme is displayed in Figure 1.2.

The temperature of 1414 °C just above the melting point of silicon (see Table 1.3) has been chosen. Using *FactSage* a negative Gibbs free energy of the reaction dG is obtained, that is, gaseous SiO is spontaneously formed. From the equilibrium constant describing the ratio of the oxygen activity in liquid silicon to the

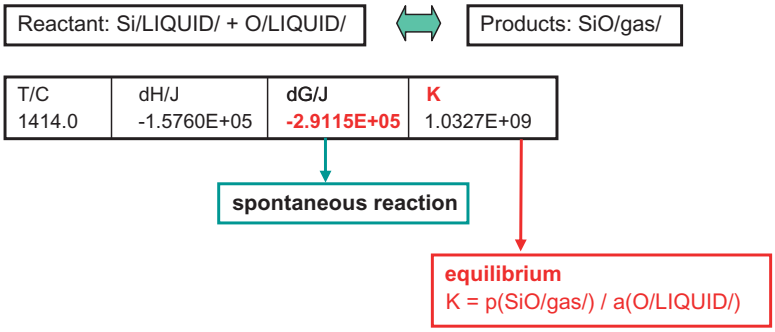

Figure 1.2 Reaction of liquid silicon with SiO.

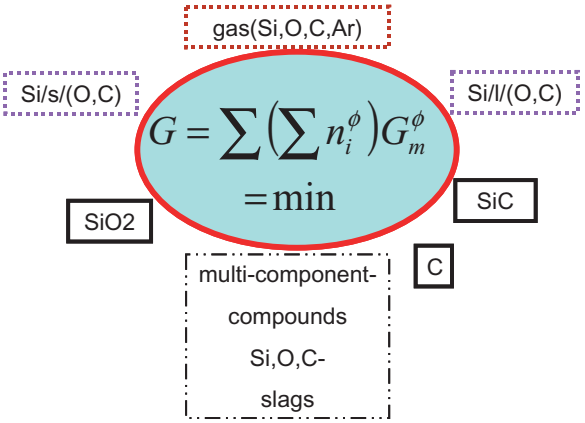

Figure 1.3 Principles of G minimization in the model system Si–C–O–Ar, G_m^{Φ}, molar integral Gibbs free energy of phase Φ, n_i^{Φ}, mole number of the constituents i of phase Φ.

activity of SiO in the gas phase it follows that there always exists a SiO partial pressure over oxygen-containing silicon.

1.3.4 Minimization of Gibbs Free Energy of Complex Systems

The calculation of Gibbs free energies of single components as well as the calculation of dG values for single reactions in a complex system is incomplete in the sense that in a multi-component system all species react with each other and an equilibrium state will occur. For the calculation of such a complex equilibrium a minimization of the Gibbs free energies of the entire system is necessary with consideration of concentrations, activities and partial pressures of all species in all phases. This procedure is schematically depicted for the model system Si–C–O–Ar in Figure 1.3. Slags have not been considered in these calculations.

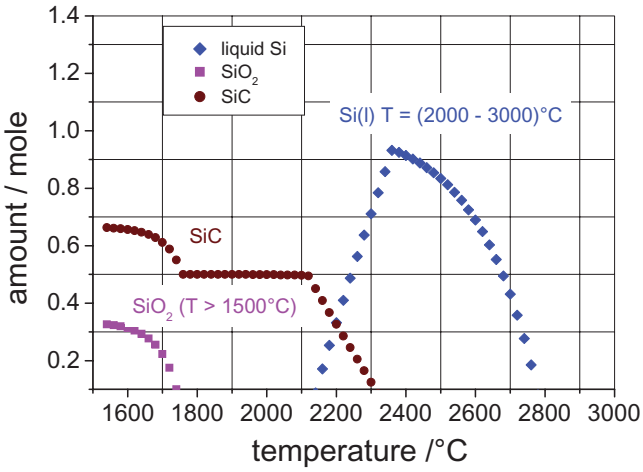

Figure 1.4 Condensed phases in the high-temperature reactor.

The question to be answered next is: What are the conditions for the production of elementary silicon in a high-temperature reactor? The high-temperature reactor for the production of metallurgical silicon could be an electrical arc furnace. One of the reactions that take place is:

$$SiO_2 + 2C \leftrightarrow Si + 2CO \tag{1.4}$$

The results of the calculations are graphically represented in Figure 1.4. The temperature-dependent coexistence of the condensed phases are given. Elemental silicon does not exist below 2100 °C, instead there are SiO_2, SiC or C. At temperatures above 2100 °C elemental liquid silicon is formed. The amount of silicon increases up to a maximum at a certain temperature. The following decrease of the amount of liquid silicon is caused by the increasing evaporation of silicon, that is, the transition into the gas phase. This is evident from Figure 1.5 representing the partial pressures of different species in the gas phase.

These calculations provide a first approximation of the conditions for the carbochemical production of silicon. A refined and more realistic thermodynamic description of the process requires the application of the above-mentioned reactor model. This has been demonstrated by Hack in [11].

1.3.5 The Thermodynamic-Technological Model of the Edge-Defined Film-Fed Growth of Silicon

In the above-discussed example the reactor is regarded as a black box without geometrical constraints. As an example of a geometrically structured thermodynamic-technological model the production of thin silicon ribbons by edge-defined

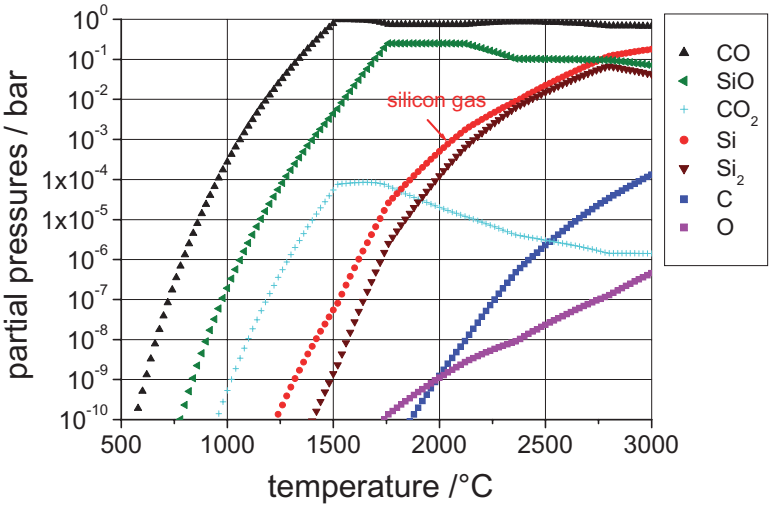

Figure 1.5 Partial pressures of species.

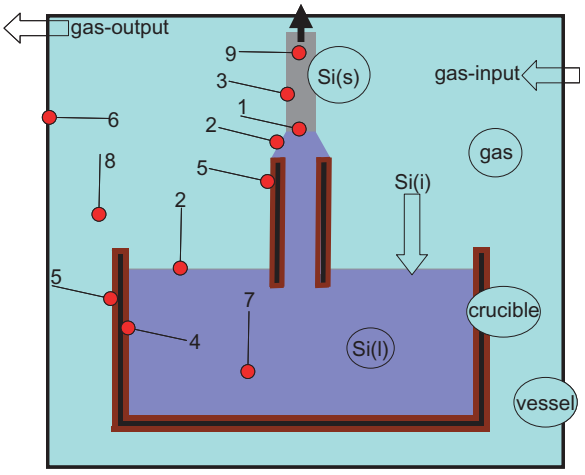

Figure 1.6 Technological model of Si-EFG.

film-fed growth (EFG) [18] is considered. A schematic cross-section of a EFG reactor is shown in Figure 1.6. It is not the real reactor, but provides the basis for a description of possible chemical reactions.

The process is performed in a closed reactor filled by an argon protective gas of about 1 bar. The crucible consists of graphite and is continuously charged with granulated silicon. The silicon ribbon is formed by a graphite shaper and is continuously drawn upwards at a certain rate. As the silicon granules are covered by SiO_2, oxygen is incorporated in the charge as an impurity. A second source of

oxygen impurity is the flushing with argon protective gas. Therefore, an accumulation of oxygen impurities will take place in the course of the process.

- Again, Si–C–O–Ar are the components of the systems. The species and phases are the same as given in Table 1.2. Inside the melt there are different temperatures: the highest at the graphite crucible (4), the lowest at the phase boundary between liquid and solid silicon (1). Without going into detail the thermodynamic calculations show the following:
- at position (1) in Figure 1.6 crystallization takes place characterized by the corresponding distribution coefficients of oxygen, carbon and other impurities:

$$k = \frac{\mathrm{Si(s)(O,C)}}{\mathrm{Si(l)(O,C)}}; \tag{1.5}$$

- at position (2) reactions between oxygen and carbon with the liquid silicon occur and the vessel is filled by reaction products;
- reactions between the gas atmosphere and solid silicon take place at positions (3), where either SiO_2 or SiC are formed depending on the chemical condition in the gas phase;
- at position (4) a reaction between the graphite crucible and liquid silicon is indicated, leading to a more or less closed SiC layer and an incorporation of carbon into liquid silicon;
- the outer surface of the graphite crucible (5) is likewise covered by SiO_2 or SiC due to O- and C-containing species in the gas atmosphere;
- condensation of SiO_2 and SiC, but also of Si (6) take place at the cold container wall;
- position (7) indicates a possible homogeneous precipitation in liquid silicon caused by a temperature and/or concentration supersaturation;
- the possible formation of solid or liquid particles in the gas phase is marked at (8);
- the possible precipitation in solid silicon during cooling down of the ribbon is indicated at (9).

At all positions mentioned above it is possible to optimize the process or to analyze negative effects.

In the following some results of the calculations are described.

As a first example, the evaporation of Si species from a Si melt at a temperature of 1414 °C in a reactor filled with argon at 1 bar is considered (Figure 1.7). The model describes the start of the process after melting of solid silicon. The calculation has been performed in such a way that an increasing amount of silicon was injected in a given volume. Three Si containing species are formed: Si, Si_2 and Si_3. The dominating species is Si, the amounts of Si_2 and Si_3 are lower by two orders of magnitude. By varying the Si amount (x-axis) equilibrium pressures between

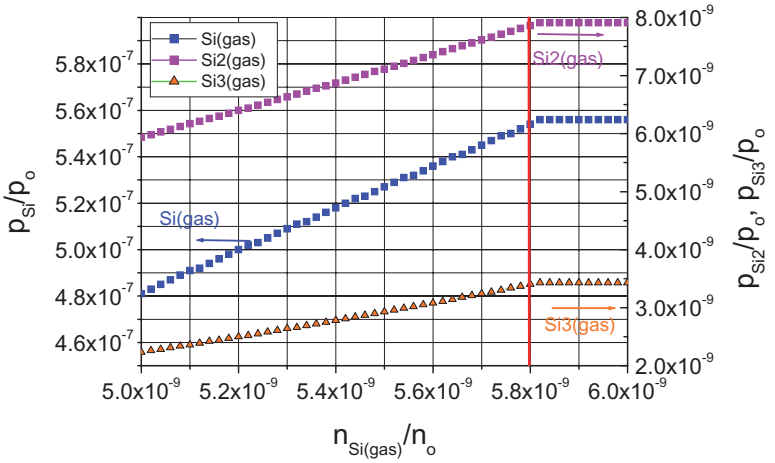

Figure 1.7 Evaporation of Si species into an Ar-filled reactor (p_o, reference pressure, n_o, reference amount).

Si, Si_2 and Si_3 species and the melt are reached at a value of 5.8 E–09 (vertical line in Figure 1.7). At this point, the gas phase is saturated by all of the Si containing species. A further increase of the total amount of silicon in the gas phase, for example, by an input of gaseous Si would result in a condensation of species and in an increase of the amount of liquid silicon.

The rate of equilibrium establishment is determined by the kinetics of evaporation/condensation as well as diffusion and convection in the system.

The next calculation deals with the influence of carbon in the crystallizer. The initial state of the system (1414 °C, 1 bar) is characterized by liquid and solid silicon in mixed phases and the Ar gas phase containing Si, Si_2, Si_3, C, C_2, C_3, SiC and SiC_2 as dominant species in the gas phase. The liquid and solid silicon contain carbon as the main constituent.

The addition of carbon can be realized in the *ChemSage* program by injecting carbon into the gas phase, by feeding of C-containing silicon or by dissolution of a carbon source (e.g., graphite from the internals). As can be seen from Figure 1.8, the C content of liquid and solid silicon increases with increasing C injection, at first without generation of a new phase. At the same time the carbon content of the mixed gas phase, that is, is the partial pressures of corresponding species increase (not displayed in Figure 1.8 for the sake of clarity). Each carbon content in liquid silicon corresponds to an equilibrium C content in solid silicon as well as in the gas phase.

At a critical amount of carbon (1.1×10^{-8} mole in the model) solid carbon carbide, SiC, is formed as a new phase. A further increase of the amount of carbon does not change the carbon content in the liquid and solid silicon as well as in the gas phase, but the amount of SiC will increase. The SiC forms a layer on the surface of liquid or solid silicon or precipitates in the volume of the phases.

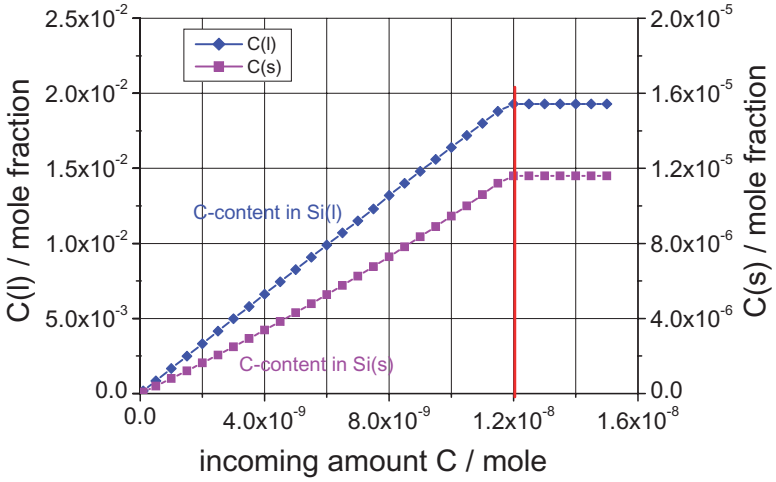

Figure 1.8 C injection in the system.

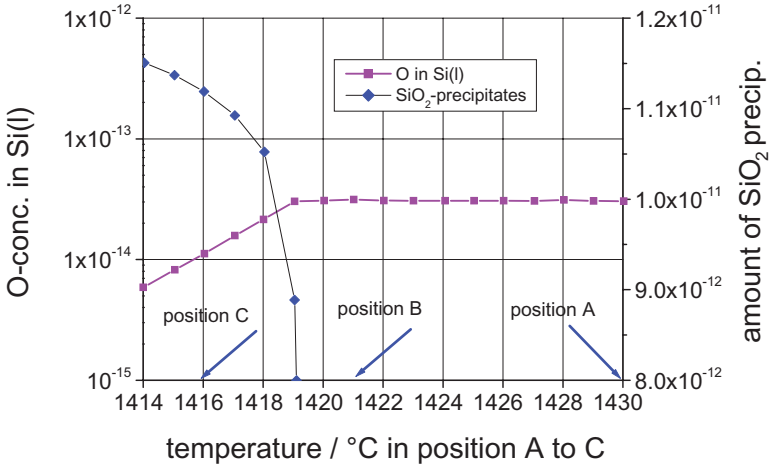

Figure 1.9 Oxygen content of liquid silicon in dependence of temperature. The data applied for the calculations were taken from SGTE pure substances database, version 2007.

In the next example the homogeneous reaction between oxygen and liquid silicon is considered as a function of temperature (Figure 1.9).

A confined region of the thermodynamic system (e.g., a chemically insulated region without phase boundaries) shall be contaminated by an oxygen-containing gas phase or oxygen loaded silicon at a temperature of 1430 °C ("position A" in Figure 1.9). We assume that this insulated region will be transported without material exchange with the surroundings to a region of lower temperature, for

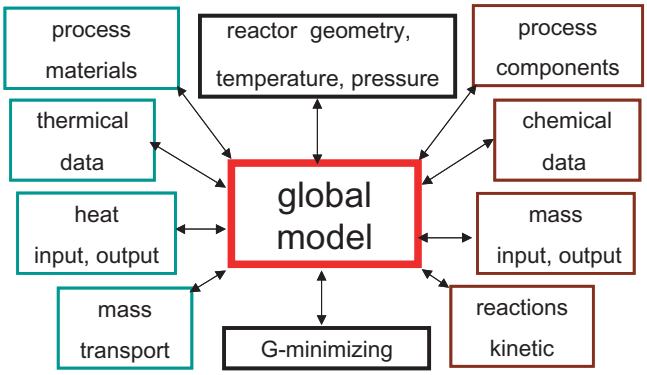

Figure 1.10 Global model of crystallization.

example, in the direction of the melting temperature of 1414 °C ("position C" in Figure 1.9). At first, during the transition to lower temperature the content of oxygen in the melt does not change. At the temperature marked by B in Figure 1.9 precipitation of SiO_2 starts assuming that no supersaturation is necessary. The amount of precipitated SiO_2 increases with further decreasing temperature reaching a maximum at the crystallization temperature of silicon ("position C" in Figure 1.9). The precipitates are possibly incorporated into the growing Si crystal. They can be the reason for the formation of structural defects up to the transition to polycrystalline growth. The formation of SiO_2 precipitates can only be suppressed by a reduction of oxygen content in liquid silicon below the solubility limit. An accumulation of SiO_2 precipitates is possible especially in the capillary region of the EFG crystallizer.

The above-discussed 3 examples supply qualitative statements only. To get quantitative results precise technological parameters like amounts, concentrations, volumes, etc., have to be used.

Nevertheless, to ensure that results will be feasible and more realistic, thermodynamic equilibrium calculations have to be supplemented by a global model of the process. This global model should combine the precise process parameters with the thermodynamics and kinetics of the process as well as with the transport of heat and mass in the system. Such a global model is outlined in Figure 1.10.

Solutions for components of the model are already available. The integration of these components into a global model is, however, a task for the future.

1.4
Crystal Growth of Carbon-Doped GaAs (Example 2)

A thermodynamic-technological model of SI (semi-insulating) GaAs growth has to consider:

a) the chemical reactions between the GaAs input, the construction elements and the auxiliary materials (boron oxide, crucible and impurities in the growth system);

b) the inventory of defects in the GaAs crystal which depends on the "freezing process" of defects after crystallization and determines the application-oriented properties.

SI behavior of GaAs (e.g., [19]) occurs if the condition $N_{EL2} > [C]-(N_{\Sigma SD} - N_{\Sigma SA}) > 0$ is fulfilled. N_{EL2} and [C] are the EL2 content and the concentration of intentionally doped carbon, respectively, and $(N_{\Sigma SD} - N_{\Sigma SA}) \approx 10^{14}\,cm^{-3}$ is the concentration of impurities acting as shallow acceptors (SA) and shallow donors (SD). EL2 is an intrinsic mid-gap double donor, most probably a single arsenic antisite atom As_{Ga} [20] controlled by the composition in the homogeneity range of GaAs. If the content of residual impurities can be considered to be low, the carrier concentration, and thus the electrical resistivity of SI GaAs is determined by the carbon concentration.

As a first approach, a thermodynamic analysis of the complex reaction system has been performed to establish a control procedure for carbon during LEC (liquid encapsulated Czochralski) growth or VGF (vertical gradient freeze) growth of SI GaAs. The reaction system comprises the gas atmosphere, the boron oxide encapsulant, solid and liquid GaAs, the pBN crucible and the graphite heaters. Again, transport of reactants in the fluid and solid phases is neglected. A fast reaction kinetics at phase boundaries is assumed. The temperature of the system is held at the congruent melting point of GaAs (1509.42 K).

The technological model presumes that

- the phases in the system (GaAs, B_2O_3, BN, gas) participate at the adjustment of the equilibrium with their entire volumes;
- the boron oxide coverage avoids a direct transition of elemental arsenic gas bubbles from the GaAs melt to the gas phase;
- the graphite heater does not influence the thermodynamics of the system;
- the pressure of the protective N_2 gas varies between 2 and 80 bar.

1.4.1 Components and Species in the System

The system contains the components Ga, As, B, C, O, H, Ar or N. The species considered in the calculations are summarized in Table 1.4.

The gas phase is considered as an ideal mixture of components and species. The liquid phases are regarded as sub-regular solutions according to the above mentioned Redlich–Kister–Muggianu model [14] with interaction coefficients between the main components and impurities and between the impurities. The interaction coefficients were deduced and/or approximated by adjusted thermodynamically relevant experimental data like phase diagrams. Details are given in [21]. An ideal behavior of dissolved impurities/dopants like C, N, B, O, etc., in solid GaAs is assumed as a first approximation (see below).

Table 1.4 Species and phases in the Ga, As, B, C, O, H, Ar or N system.

Stoichiometric phase	**BN**
Solid solution phase	GaAs(s) containing C, O, B, N and H
Liquid solution phase	GaAs(l) containing C, O, B, N and H as mixed phase with variable As/Ga-ratio
Liquid solution phase	B_2O_3(l) containing As_2O_3, As_2O_5, Ga_2O, GaO, Ga_2O_3, CO, CO_2, HBO_2
Gas phase	N_2, H_2, Ga_2O, H_2O, BHO_2, GaOH, AsH, Ga, CO, AsN, B_2O_3 und GaH (ranked according to the partial pressure with a cut-off pressure of 1×10^{-15} bar)

Graphite in the system requires separate consideration. If graphite is present the carbon activity under thermodynamic equilibrium conditions will be $a_C = 1$ because a Boudouard-type and other reactions are possible at the graphite heater. This would result in the saturation concentration of carbon in all phases of the system. However, GaAs single crystals grown in a graphite-containing system exhibit variable concentrations of carbon. Therefore, it is assumed that the local separation of the graphite heater and the GaAs melt and the low transport rate of carbon-containing species in liquid boron oxide are the reason for this discrepancy. As a consequence, graphite has to be excluded from the system in the case of thermodynamic equilibrium calculations of carbon incorporation.

1.4.2 Results

As pointed out by Oates and Wenzl [22] the results of the calculations can be best visualized as so-called *predominance area diagrams* as mainly redox equilibria are of importance. In the *predominance area diagram* the stability region of the GaAs melt is represented in the presence of the boron oxide encapsulant at the GaAs melting temperature of 1509.42 K in a plot of log(a_C) over log ($p_{O2)}$ with a_C and p_{O2} being the activity of carbon and the oxygen partial pressure, respectively (Figure 1.11). On the right-hand side of the diagram the scale of carbon concentration in the melt is given using the known activity coefficient of carbon in GaAs melt. The stability region of GaAs melt/liquid boron oxide that is essential for crystal growth is bounded by the dissociation of boron oxide at lower and the oxidation of Ga in the GaAs melt at higher oxygen chemical potentials. The upper boundary of the stability region is given by the solubility limit of carbon in liquid GaAs ($a_C = 1$). If the chemical potentials of the control species carbon and oxygen in this stability region are fixed, no degrees of freedom will be left in the system.

The chemical potentials of carbon and oxygen can be controlled by the partial pressures of CO and N_2 Nitrogen reacts with the boron oxide encapsulant forming solid boron nitride and oxygen [23]. Taking into account the possible N_2 pressure

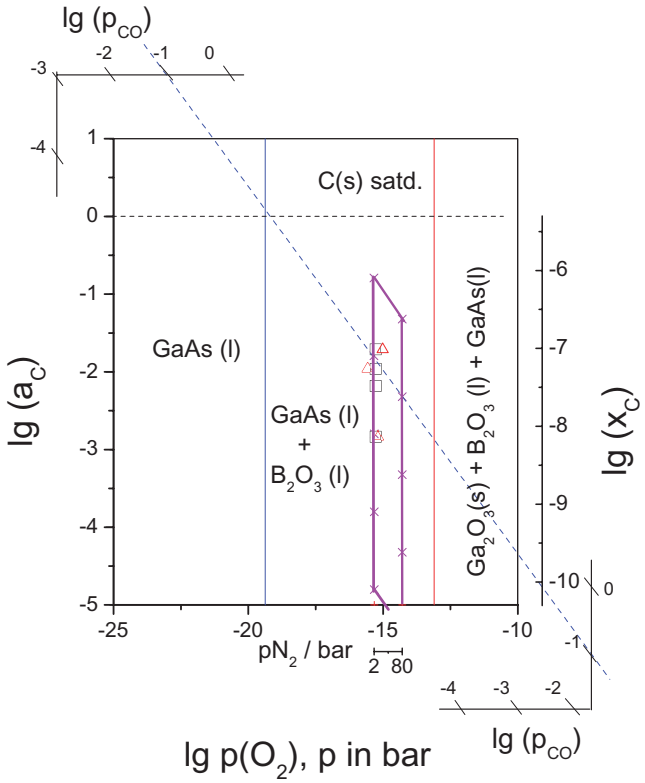

Figure 1.11 Predominance area diagram for LEC growth assuming oxygen control by nitrogen reaction with boron oxide.

in the growth equipment only a part of the stability region of GaAs(l)/B_2O_3(l) can be used for crystal growth. This working area under the assumption that the N_2 pressure varies between 2 and 80 bar is marked. The dotted line in Figure 1.11 indicates a constant CO partial pressure. It is obvious that it is not sufficient to keep the CO partial pressure constant to define the carbon content in the GaAs melt. The oxygen chemical potential must be kept constant, too. This sometimes has been ignored in the past.

A distribution coefficient $k_C = 2$ is used for the estimation of the carbon concentration in solid GaAs from the calculated C content in the melt. Likewise, the concentrations of B, O, N, H in solid GaAs are calculated by means of the corresponding distribution coefficients.

The data points in Figure 1.11 indicate experimental results observed in VGF growth at different CO partial pressures and constant oxygen potentials. They were obtained from measurements of carbon concentration in GaAs single crystals using the above distribution coefficient.

Table 1.5 Species of the SUBS model of solid GaAs.

Ga-sublattice	As-sublattice	3rd sublattice	4th sublattice
Ga_1	As_2	As_3	Va_4<0>
As_1<0>	O_2<0>	Va_3<0>	e
As_1<+>	O_2<–>		h
Va_1<0>	O_2<+>		
Va_1<3–>	C_2<–>		
Si_1<+>			
Zn_1<–>			
B_1			

Based on the results of the thermodynamic analysis a more sophisticated model has been developed by Eichler *et al*. [24] taking into account transport in the fluid phases.

1.4.3 Extended Model

For a more realistic description of solid GaAs a sublattice model (SUBS) has been developed [27] and included into ChemSage. It is based on the SCPBE model (species chemical potential–bond energy model) introduced by [25, 26] and avoids the assumption of a stoichiometric solid GaAs.

The SUBS model of crystalline GaAs consists of 4 sublattices: the Ga and As sublattice and a sublattice of interstitial atoms and one occupied by electrons and holes. In the nomenclature of ChemSage the Ga sublattice contains: Ga_1, As_1<0>, As_1<+>, Va_1<0>, Va_1<3–>, Si_1<+>, Zn_1<–> and B_1, that is, arsenic antisites, Ga vacancies, Si, Zn and B atoms. They can exist in different charge states that are given in angle brackets. The constituents of the other sublattices are summarized in Table 1.5. Vacancies in the As sublattice are not considered. The interstitial sublattice contains arsenic and vacancies, only. In agreement with the crystallographic structure of GaAs, the Ga and the As sublattice have the same number of lattice sites. The defects considered in the model reflect current knowledge, but other defects can be included too, if necessary.

The positions of the localized states in the bandgap are displayed in Table 1.6 defining the midgap energy as the reference energy. E_g is the temperature-dependent energy gap. The negative U behavior of oxygen in the arsenic sublattice could not be considered in the model. Instead, it has been described by two neighboring levels resulting in the known effective level at $E_c - 0.36\,\text{eV}$. A Fermi-level effect has not been considered.

The minimization of the Gibbs free energy for the calculation of the equilibrium concentrations of the species has been carried out under the conditions that the number of sublattice sites is constant and charge neutrality is fulfilled. The

Table 1.6 Localized states (relating to the middle of the bandgap E_g).

Defect	Level in the bandgap J/mol	Level in the bandgap eV
As_1<+/0>	4000	0.041
C_2<–/0>	$-E_g/2$	$-E_g/2$
O_2<+/0>	34000	0.35
O_2<0/–>	35000	0.36
Va_1<0/3–>	–60000	–0.62
Zn_1<0/–>	$-E_g/2$	$-E_g/2$
Si_1<+/0>	$+E_g/2$	$+E_g/2$

chemical potentials of the sublattice species have been calculated using the SCPBE model that supplies expressions for mixing enthalpies (interaction between the defect and the Ga and As atom, respectively) and mixing entropy. Standard species chemical potentials for charged species are derived from standard species chemical potentials for neutral species and the defect levels in reference to midgap. For the threefold-occupied vacancy in the Ga sublattice it is written for example, $\mu^0_{\mathrm{Va\_1<3->}} = \mu^0_{\mathrm{Va\_1<0>}} + E<0/3->$ with E<0/3–> being the electronic transition level given in Table 1.6. The interactions between the defects in different charge states were not considered. As there shall be modeled the influence of carbon doping on resistivity of semi-insulating GaAs, the positions of the shallow defects are set to $+/- E_g/2$ without substantial error. Further details can be found in [27].

To account for the decreasing mobility of lattice species with decreasing temperature a freezing temperature is introduced. An adjustment of thermodynamic equilibrium is possible up to this freezing temperature, only. Below this temperature lattice defects are frozen, that is, the sum over the different charge states of a single defect is constant. But charge reloading is possible. The freezing temperature is dependent on the cooling conditions of solid GaAs.

This model has been used for the calculation of the homogeneity range of solid GaAs (without impurities). The result is shown in Figure 1.12. The thermodynamic data of the As antisite have been adjusted so that its concentration is roughly in agreement with the measured EL2 concentration in solid GaAs at room temperature. A constant pressure of 1 bar has been assumed.

For the native defects included in the model (Table 1.5) the calculated homogeneity range is bounded by the stoichiometric composition at lower temperatures and is extended to the arsenic-rich side. A retrograde solidus is observed. It describes the experimental result that arsenic precipitates can be formed during cooling to room temperature, depending on the starting composition of the melt and the resulting solid GaAs. The maximum solid solubility is found to be about 1180 °C, the corresponding As concentration of off-stoichiometric GaAs remains unsure because an experimental verification is not yet possible due to the insufficient accuracy of available analytical methods.

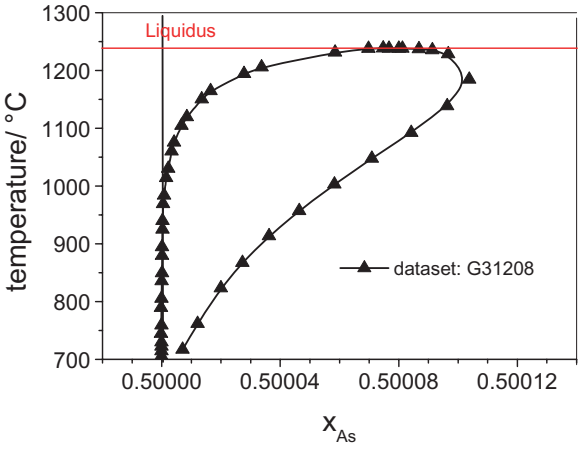

Figure 1.12 Homogeneity range of GaAs.

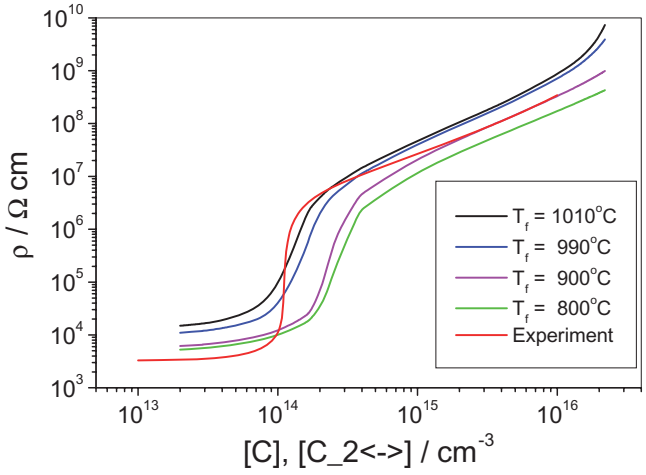

Figure 1.13 Room-temperature electrical resistivity of GaAs in dependence on C concentration for different freezing temperatures.

It should be mentioned that a slightly larger homogeneity range and a lower temperature of maximum solubility is obtained if the assumption p = 1 bar is replaced by the actual As pressure at the three-phase equilibrium GaAs(s)-GaAs(l)-As vapor.

In a second example of the application of the SUBS model the electrical resistivity of GaAs at room temperature is calculated in dependence on carbon doping (Figure 1.13). For this purpose, the calculated carrier concentrations at room

temperature and their known mobilities are used. A constant As_1<+/0> (EL2)-concentration and an effective shallow donor concentration ($N_{\Sigma SD} - N_{\Sigma Sa}$) $\approx 10^{14}\,cm^{-3}$ are assumed. The freezing temperature varies between 800 °C and 1010 °C. Experimental results are included into the graph for comparison.

The electrical resistivity increases linearly with the carbon concentration at [C] > $2 \times 10^{14}\,cm^{-3}$. In this region the above-given condition for semi-insulating behavior is met. The Fermi level is pinned at the deep As_1<+/0> (EL2) donor. At about C_2<−/0> = [C] ≈ $1 \times 10^{14}\,cm^{-3}$ resistivity drops to a level of about $5 \times 10^{3}\,\Omega cm$. In this medium-resistivity region the carbon donor is compensated by the medium-deep oxygen donor, that is, the Fermi level is pinned at the effective level of oxygen. The EL2 concentration does not influence the electrical behavior.

As can be seen in Figure 1.13 resistivity is highly influenced by the freezing temperature. It decreases with decreasing freezing temperature. This is mainly caused by the decrease of the As_1<+/0> (EL2) concentration due to a transition of arsenic into the interstitial sublattice As_3. Furthermore, the calculations show an increase of the Ga vacancy concentration Va_1<0/3–> with increasing freezing temperature.

The Fermi-level effect on the thermodynamic data of defects in GaAs and its influence on the electrical behavior has been thoroughly studied in [28].

The Chemsage software package with the implementation of the SUBS model is a suitable tool for a chemical control of the GaAs crystal-growth process and for the understanding of the defect inventory of crystals and their physical properties.

1.5 Summary and Conclusions

Concept development and application of thermodynamic models comprise the following:

- definition of project and determination of the relevant components of the chemical system;
- selection of an appropriate thermodynamic software package;
- formulation of a thermodynamic-technological model, that is, description of phases and species to be included in the system and extraction of the required data from databases;
- test calculations with the option to modify the initial data and the boundary conditions of the model;
- calculation of the Gibbs free energies of separate phases, species and constituents;
- calculation of the Gibbs free energies for selected reactions;
- calculation of the multi-component system by minimization of the Gibbs free energy of the entire system;

- linking of the thermodynamic model with models describing reaction kinetics, mass and heat transport, etc.;
- verification and adjustment of the model;
- The modeling effort and the degree of approximation to reality will increase with the above steps;
- The applied *ChemSage* software package and the considered examples should demonstrate the possibilities and limitations of thermodynamic modeling of crystallization and crystal-growth processes.

In detail, there have been considered:

- the production of metallurgical silicon;
- reactions important for the silicon EFG process;
- carbon doping during GaAs single-crystal growth.

The results show that there are available thermodynamic software packages. However, comprehensive modeling of all aspects of crystal growth is still a vision.

Acknowledgments

The authors would like to thank P. Rudolph and U. Wunderwald for helpful discussions and critical reading of the manuscript. In addition, special thanks are expressed to A. Seidl, B. Weinert, and J. Friedrich. Eberhard Buhrig: I dedicate the part of the work formulated by me to my wife Renate†.

This work has been partly financed by BMBF 01–BM 631/2 and Freiberger Compound Materials GmbH.

References

1 Rosenberger, F. (1979) Fundamentals of Crystal Growth I, Springer, Berlin/Heidelberg/New York.
2 Wilke, K.-T. (1988) Kristallzüchtung (ed. J. Bohm), VEB Deutscher Verlag der Wissen-schaft, Berlin.
3 Müller, G., and Friedrich, J. (2004) *J. Cryst. Growth*, **266**, 1–19.
4 Hurle, D.T.J. (1999) A comprehensive thermodynamic analysis of native point defect and dopant solubilities in Gallium Arsenide. *J. Appl. Phys.*, **85** (10), 6957–7023.
5 Jacobs, K. (2008) Crystal Growth Technology (eds H.J. Scheel and P. Capper), Wiley-VCH Verlag GmbH, Weinheim.
6 Bohm, J. (1995) Realstruktur von Kristallen, E. Schweitzerbart'sche Verlagsbuchhandlung, Stuttgart.
7 Hein, K., and Buhrig, E. (1983) Kristallization aus Schmelzen, VEB Deutscher Verlag für Grundstoffindustrie, Leipzig.
8 Roewer, G., and Buhrig, E. (2007) 50 Jahre Halbleitermaterialien in der Region Freiberg, ZS für Freunde und Förderer der technischen Universität Freiberg.
9 Kuchar, L., and Drapala, J. (2008) Metallurgy of Pure Metals, Cambridge International Science Publishing.
10 Eriksson, G., and Hack, K. (1990) ChemSage – a computer program for the

calculation of complex chemical equilibria. *Metall. Trans. B*, **21B**, 1013–1023.
11 Hack, K. (1996) The SGTE Casebook, Materials Modelling Series, The Institute of Materials, ISBN: 0 901716 74X.
12 Thermo www.thermocalc.com (accessed 07-130N-2010).
13 HSC www.hsc-chemistry.net (accessed 07-130N-2010).
14 Redlich, O., and Kister, A.T. (1948) *Ind. Eng. Chem.*, **40**, 345. Muggianu, Y.M., Gambino, M., and Bros, J.P. (1975) *J. Chem. Phys.*, **72**, 83.
15 Koukkari, P., Pajarre, R., and Hack, K. (2007) *Int. J. Mater. Res.*, **98**, 926–934.
16 GTT http://gttserv.lth.rwth-aachen.de/~cg/ (accessed 07-130N-2010).
17 Petersen, S., and Hack, K. (2007) *Int. J. Mater. Res.*, **98**, 935–945.
18 Rudolph, P. (1982) Profilzüchtung von Einkristallen, Akademie-Verlag, Berlin.
19 Rudolph, P., and Jurisch, M. (1999) *J. Cryst. Growth*, **198/199**, 325–335.
20 Wirbeleit, F. (1998) The atomic structure of point defects in semiconductors by improved EPR/ENDOR data analysis, PhD thesis, Technical University Mining Academy, Freiberg.
21 Korb, J., Flade, T., Jurisch, M., Köhler, A., Reinhold, T., and Weinert, B. (1999) *J. Cryst. Growth*, **198/19**, 343–348.
22 Oates, W.A., and Wenzl, H. (1998) *J. Cryst. Growth*, **191**, 303–312.
23 Emori, H., Terashima, K., Orito, F., Kikuta, T., and Fukuda, T. (1984) Semi-Insulating III–V Materials, Kahnee-ta (eds D.C. Look and J.S. Blakemore), Shiva, Nantwich, p. 111.
24 Eichler, S., Seidl, A., Börner, F., Kretzer, U., and Weinert, B. (2003) *J. Cryst. Growth*, **247**, 69–76.
25 Oates, W.A., and Wenzl, H. (1992) *CALPHAD*, **16**, 73.
26 Oates, W.A., and Wenzl, H. (1993) *CALPHAD*, **17**, 35.
27 Oates, W.A., Eriksson, G., and Wenzl, H. (1995) Thermodynamic modelling of solid gallium arsenide. *J. Alloy. Compd.*, **220**, 48–52.
28 Kretzer, U. (2007) Punktdefekte und elektrische Kompensation in Galliumarsenid-Einkristallen, PhD thesis, Technische Universität Chemnitz.

2
Modeling of Vapor-Phase Growth of SiC and AlN Bulk Crystals

Roman A. Talalaev, Alexander S. Segal, Eugene V. Yakovlev, and Andrey N. Vorob'ev

2.1
Introduction

Due to the unique physical properties, silicon carbide (SiC) and aluminum nitride (AlN) are now considered as most promising materials to produce high-power high-frequency electronic devices and short-wavelength optoelectronic devices with superior characteristics. Wide-band-gap, high breakdown field, and high heat conductivity provide benefits of SiC for the production of high-voltage Schottky diodes and high electron mobility transistors (HEMTs) with extremely fast switching and temperature-independent behavior. The superiority of AlN is largely related to its still wider band-gap, transparency in the UV range, and small mismatches of thermal expansion coefficients and lattice constants with respect to gallium nitride (GaN). These properties make AlN most prospective material for ultraviolet (UV) optoelectronic applications, including UV LEDs, UV active units of "white" LEDs, and so forth.

Despite the obvious benefits, mass production of the SiC- and AlN-based devices is still hindered by the lack of suitable high-quality substrates. Conventional silicon, sapphire, and gallium arsenide substrates exhibit quite large mismatches of physical properties with respect to SiC and AlN, which results in excessive defect generation in the overlying device heterostructures and eventually limits the device lifetime and performance. The best substrates for the SiC- and AlN-based epitaxial layers should be made from the same materials.

Currently, SiC and AlN substrates are produced by post-growth processing of the bulk single crystals grown with physical vapor transport (PVT) technology. As applied to SiC, PVT technology now allows production of up to 4-inch diameter micropipe-free substrates with a low dislocation density (see, for example, [1] for details). AlN substrates made using PVT are only now moving into commercial production. 2-inch diameter AlN substrates with about 40 mm diameter single-crystal core and 5 mm thick polycrystalline periphery were demonstrated in Ref. [2]. Totally single-crystal high-quality 1-inch diameter AlN substrates were presented in Ref. [3].

Crystal Growth Technology. Semiconductors and Dielectrics. Edited by P. Capper and P. Rudolph
Copyright © 2010 WILEY-VCH Verlag GmbH & Co. KGaA, Weinheim
ISBN: 978-3-527-32593-1

Despite the impressive progress, PVT growth of SiC and AlN bulk crystals still remains a poorly controllable and expensive technology. As the bulk crystals are grown in PVT in tightly closed crucibles, there are few technological parameters to control the process. Besides, due to a very high growth temperature (2200–2400 °C), many component parts of the growth systems degrade during one run, which results in low stability of the growth conditions and the need to replace them after each run. Because of these negative features, alternative approaches to the production of SiC and AlN substrates have lately attracted much interest. Among these approaches, high-temperature chemical vapor deposition (HTCVD) of SiC and hydride vapor phase epitaxy (HVPE) of AlN are now considered as most promising technologies.

HVPE was initially developed to grow GaN epitaxial layers (see, for example, Ref. [4]). Further progress of the technology (Ref. [5]) showed that it was capable of producing high-quality GaN thick quasi-bulk epitaxial layers on the commercially available sapphire or SiC substrates. Typically, GaN HVPE provides the crystal growth rates of 50–100 μm/h, however, due to the high reproducibility and controllability of the technology, the growth rate can be controllably increased up to ~1000 μm/h (www.tdii.com, Ref. [6]). Such high growth rates in combination with the well-known effect of reducing the dislocation density with the crystal layer thickness makes GaN HVPE a very attractive technology to grow long GaN boules. Many efforts have lately been made to develop such technology. Probably, the most recent achievement in this area was exhibited in Ref. [7], where 52-mm diameter and 5.8-mm thick GaN single-crystal boules with the dislocation density of 1.2×10^6–$5.1 \times 10^6\,cm^{-2}$ were grown with HVPE.

Considerable progress in growth of GaN epitaxial layers and bulk single crystals with HVPE has initiated the extension of this technology to AlN. Besides, compatibility of AlN HVPE with GaN HVPE gives rise to growth of AlGaN alloy within a single technological process. Normally, AlN HVPE provides growth rates of several tens of micrometers per hour (for example, 57 μm/h in Ref. [8], 60–85 μm/h in Ref. [9]). Probably, the highest AlN growth rate of 122 μm/h was reported in Ref. [10], though the authors note that the crystal quality deteriorates at such high growth rates. Currently, HVPE is largely used to produce so-called AlN templates, that is AlN epitaxial layers with the characteristic thickness of 1–83 μm grown on commercial sapphire or SiC substrates (see Refs. [9, 11]). Simultaneously, the technology is successfully used to grow quasi-bulk epitaxial layers with a thickness of up to 1 mm to produce free-standing AlN wafers (Ref. [8]), which suggests that HVPE has a good potential for growth of AlN bulk single crystals. Note that there are few papers on HVPE of AlGaN alloy and they all report on growth of rather thin epitaxial layers. So, HVPE growth of 0.1–2-μm thick AlGaN epitaxial layers reported in Ref. [12]. Much thicker AlGaN epitaxial layers (1.3–35 μm) were grown at a rate of around 30 μm/h in Ref. [13]. Anyway, HVPE is not used currently to grow AlGaN bulk crystals.

HTCVD is considered as a very promising technique to grow bulk SiC. It allows such advantages as a better control of species transport resulting in an optimal silicon-to-carbon ratio near the wafer; the use of high-purity gas sources providing

minimal doping level; reducing strain and dislocation level through the optimization of temperature gradient near the wafer, and so on.

The successful application of SiC HTCVD and AlN HVPE to growth of bulk single crystals depends on a number of factors and, to analyze them as taken together, modeling analysis and optimization of the processes are strongly desirable.

To date, theoretical analysis of AlN and AlN/AlGaN HVPE is far behind the practical needs and there are only few papers in this area. Let us note, first, Ref. [14] where an original kinetic model of gas-phase and surface chemistry is coupled with two-dimensional model of transport processes to give a rather detailed description of AlN HVPE in a hot-wall axisymmetrical vertical reactor. Here, poorly known gas-phase and surface kinetics in the $AlCl_3$–NH_3 system is largely analyzed relying on the analogy with the much better studied BCl_3–NH_3 system. However, due to the lack of information on the kinetic mechanisms and parameters, the authors fit a number of reaction rate constants to provide good agreement of their own computed and experimental data, which reduces the reliability of their results. Besides, the model is not directly extended to the description of AlGaN HVPE.

Quite another approach to theoretical analysis of AlN and AlGaN HVPE was suggested in Refs [15, 16]. Here, the authors omit a detailed description of kinetic mechanisms and transport processes but use some "integral" thermodynamic consideration. Within this approach, they consider the initial vapor composition and some "final" vapor composition that is assumed to be in equilibrium with the deposited AlN or AlGaN. Such an approach proved rather productive and allowed qualitative conclusions and even some quantitative estimates on the crystal growth rate and alloy composition to be made. In particular, it describes the experimental fact of dominant Al incorporation into AlGaN alloy by a small addition of H_2 to the N_2 carrier gas.

The approach to modeling of SiC HTCVD and AlN, GaN, and AlGaN HVPE that combines the advantages of the reduced thermodynamic consideration and detailed description of transport processes was suggested in [17–19]. Within this approach, surface kinetics at the reactive interfaces is described within a so-called quasi-thermodynamic model that is rather close to the model developed in [15, 16] but is embodied as local boundary conditions for the species transport equations.

As applied to HVPE, the quasi-thermodynamic approach was initially developed for GaN in Ref [18] and then extended to AlN and AlGaN in Ref. [19]. In Ref. [18], the model of GaN HVPE was reliably validated using a wide range of experimental data and then is applied to detailed three-dimensional modeling and optimization of the process in a hot-wall horizontal reactor. In Ref. [19], the major focus was made on the difference in mechanisms of AlN and GaN HVPE and on related regularities of the Al and Ga incorporation into AlGaN alloy. It was found that AlN grows under essentially nonequilibrium conditions while GaN grows under near-equilibrium conditions. The effect is related, in particular, to the dominant growth of AlN and GaN from aluminum trichloride ($AlCl_3$) and gallium

monochloride (GaCl), respectively. Relative contents of different group-III chlorides in the vapor are important to understand these effects, and an additional benefit of the quasi-thermodynamic approach as applied to HVPE is that it provides a detailed description of HCl conversion into different group-III chlorides in the metal sources.

Gas-phase chemistry is one of the essential aspects that should be accounted for in a model of SiC CVD and HTCVD processes. Normally, silane (SiH_4) and propane (C_3H_8) are used as precursors highly diluted by hydrogen carrier gas. The temperature strongly influences the pathways of thermal decomposition of these precursors, producing different gaseous products involved in SiC growth. There is a large body of information on SiH_4 and C_3H_8 chemical transformation in the literature [20–22]. The most detailed data on the gas-phase reaction rates are collected in Ref. [21]. In this paper, pyrolysis of the reactants is simulated by 83 elementary reactions and by about 30 decomposition products. It should be noted that most of the species have very low concentrations and do not influence Si and C atom transport to the growing surface. As for the bulk HTCVD of SiC, the following species can be selected: C_2H_4, C_2H_2, SiH, Si, Si_2C, and SiC_2. Their contribution to the SiC growth is most essential.

To achieve high growth rates, significant flow rates of the precursors should be used. In this case, silicon vapor is supersaturated and, hence, its spontaneous condensation is possible under certain operating conditions. The gas-phase nucleation depends on the silane flow rate and results in losses of silicon and in a considerable decrease in the growth rate. Besides, the gas-to-particle conversion of silicon influences the Si/C ratio and, consequently, affects the properties of the growing SiC epilayer. Normally, growth conditions should be chosen in such a way as to avoid the silicon condensation.

In this chapter, we discuss the approach to modeling of SiC HTCVD and AlN, GaN, and AlGaN HVPE and present the latest results in this area. Concerning HVPE, the major focus is made on the concentrations of different group-III chlorides in the vapor, analysis of the rate-limiting species, and the related differences in the mechanisms of AlN and GaN growth. With respect to SiC HTCVD, the possibility to minimize material losses due to parasitic deposition and formation of particles in the gas phase is discussed. Special attention is given to the growth of bulk SiC and AlN crystals with high rates.

2.2 Model Description

As discussed above, the GaN growth rate as well as the AlGaN layer composition are largely controlled by the surface chemical mechanisms. On the other hand, gas-phase chemical reactions, giving rise eventually to the production of Si-containing particles, are essential during SiC CVD. Thus, the surface chemistry model is discussed with reference to AlN and AlGaN HVPE, whereas the approach to the modeling of particle generation is described for the SiC CVD process.

2.2.1
Quasi-Thermodynamic Model of AlN and AlGaN HVPE

A comprehensive description of heat transfer, multicomponent species diffusion, and gas-flow dynamics is provided by solving the full set of conventional heat conduction, radiation transfer, diffusion, and Navier–Stokes equations. A specific feature of the developed approach is given by the quasi-thermodynamic model of surface kinetics. Within this model, the interface species fluxes at all the reactive interfaces are described by the extended Hertz–Knudsen equations

$$J_i = \alpha_i \beta_i \left(P_i^{w} - P_i^{e}\right) \tag{2.1}$$

where α_i are the sticking probabilities, $\beta_i = (2\pi\mu_i RT)^{1/2}$ are the Hertz–Knudsen factors, μ_i are the molar masses, R is the gas constant, T is the temperature, P_i^{w} are the partial pressures at the interface, P_i^{e} are the quasi-equilibrium pressures representing multicomponent analogs of a one-component saturated vapor pressure, and subscript i stands for all the gaseous species.

Quasi-equilibrium pressures P_i^{e} satisfy the mass-action low equations for the surface reactions. The interface species fluxes J_i satisfy stoichiometric relationships indicating the fact that chemical elements are incorporated into the crystal proportional to their total interface fluxes. Eventually, the quasi-thermodynamic model of surface kinetics is implemented as complex boundary conditions for the species transport equations and thus is incorporated into the general description of transport processes.

As applied to AlN, GaN, and AlGaN HVPE, the quasi-thermodynamic model is first applied to the description HCl conversion into metal chlorides in the metal sources. Here, the model does not assume *a priori* that HCl reacts with the metals to produce either mono- or trichlorides but allows three reactions of the metal chlorides formation to proceed in parallel

$$\mathrm{HCl} + \mathrm{Me(s/l)} \rightarrow \mathrm{MeCl} + (1/2)\mathrm{H_2} \tag{2.2}$$

$$2\mathrm{HCl} + \mathrm{Me(s/l)} \rightarrow \mathrm{MeCl_2} + \mathrm{H_2} \tag{2.3}$$

$$3\mathrm{HCl} + \mathrm{Me(s/l)} \rightarrow \mathrm{MeCl_3} + (3/2)\mathrm{H_2} \tag{2.4}$$

where, Me is either solid Al or liquid Ga. Correspondingly, AlN and GaN may grow from all the metal chlorides and ammonia, following the reactions

$$\mathrm{MeCl} + \mathrm{NH_3} \rightarrow \mathrm{MeN(s)} + \mathrm{HCl} + \mathrm{H_2} \tag{2.5}$$

$$\mathrm{MeCl_2} + \mathrm{NH_3} \rightarrow \mathrm{MeN(s)} + 2\mathrm{HCl} + (1/2)\mathrm{H_2} \tag{2.6}$$

$$\mathrm{MeCl_3} + \mathrm{NH_3} \rightarrow \mathrm{MeN(s)} + 3\mathrm{HCl} \tag{2.7}$$

Let us make some remarks on the quasi-thermodynamic model of AlN, GaN, and AlGaN HVPE.

1) Surface kinetic limitations in GaN HVPE are known to begin at a growth temperature of 900–950 °C or somewhat lower [6]. Similar literature data for

AlN HVPE are rather limited and contradictory (see, for example, Refs. [10, 23]). The transition temperature between the transport-limited and kinetically limited growth conditions varies in the range of 950–1100 °C and higher, though all the papers note a minor decrease of the growth rate due to the surface kinetic limitations (normally, an order of magnitude in the temperature range of 200–400 °C). Simultaneously, there is a trend to perform the growth under the transport-limited conditions via raising the growth temperature (in Ref. [9], for example, the growth temperature is above 1200 °C). In this situation, we neglect the kinetic limitations at the crystal surfaces and assume all the species sticking probabilities, except for N_2, to be unity.

2) Generally, if $AlCl_3$ and NH_3 meet each other at an insufficiently high temperature, adducts of $AlCl_3$-$n$$NH_3$ type may appear due to gas-phase reactions to produce small suspended particles. In elaborated processes, however, the effects of gas-phase chemistry are minimized and normally do not manifest themselves, for which reason they are not considered in our model.

3) Literature data on the NH_3 decomposition on the AlN and GaN surfaces are also rather limited and contradictory. Earlier, we showed that the best agreement of the computed and experimental data in modeling of GaN HVPE is achieved under the assumption of negligible NH_3 decomposition (Ref. [18]). Test computations have shown that this assumption can be extended to AlN HVPE. Within the quasi-thermodynamic model, this corresponds to a near-zero N_2 sticking probability, in which case N_2 does not participate in the surface chemistry but serves as an inert carrier gas.

2.2.2 Modeling of Gas-Phase Nucleation in SiC CVD and HTCVD

A key feature of the processes considered is homogeneous nucleation of silicon. Estimations show that under the operating conditions for SiC CVD reactor, the drop size is a few orders of magnitude less than the mean free path of molecules in the vapor. Therefore, clusters can be considered as a pseudo-gas of heavy particles with a size-independent growth rate. Since the gas flow is slow, a steady-state size distribution of nuclei becomes achievable. The approach suggested in [17] is then suited to simulate the gas-phase condensation of silicon with equations for the first three moments of the size-distribution function

$$\vec{\nabla}\cdot\left(\vec{\mathbf{V}}_c\Omega_n\right) = r_*^n I + n\dot{r}\Omega_{n-1};\ n = 0, 1, 2 \tag{2.8}$$

where $\vec{\mathbf{V}}_c$ is the transport velocity of the particle pseudo-gas, r_* is the critical nucleus radius, I is the formation rate of critical-sized nuclei, $\dot{r}$ is the rate of mass exchange between the clusters and the gas phase defined by the Hertz–Knudsen equation. The nucleation rate (I) is given by the Becker–Döring theory, r^* is the critical nucleus radius.

Transport of clusters is described by their continuity equation

$$\vec{\nabla}\cdot\left(\rho_{Si}^{c}\vec{V}_{c}\right)=\dot{W}^{c} \tag{2.9}$$

where

$$\dot{W}^{c}=\frac{4}{3}\pi\rho_{Si}^{0}\left(r_{*}^{3}I+3r_{*}^{2}\Omega_{2}\right) \tag{2.10}$$

The expression (2.10) is introduced into the gaseous Si transport equation to provide the consumption/generation of silicon due to homogeneous nucleation/evaporation of clusters where ρ_{Si}^{0} is the liquid phase density.

2.3 Results and Discussions

2.3.1 GaN, AlN, and AlGaN HVPE

The developed model of AlN and GaN HVPE was validated using the available literature experimental data on the crystal growth rate as a function of different technological parameters (Refs [18, 19]). Some results of this validation are presented in Figure 2.1.

Figure 2.1a shows the computed AlN growth rate vs. NH_3 flow rate in comparison with the data of Ref. [23] (here, the growth temperature is 1200 °C, the total pressure is 10 hPa, the $AlCl_3$ flow rate is 1.33 sccm, and the carrier N_2 and H_2 flow

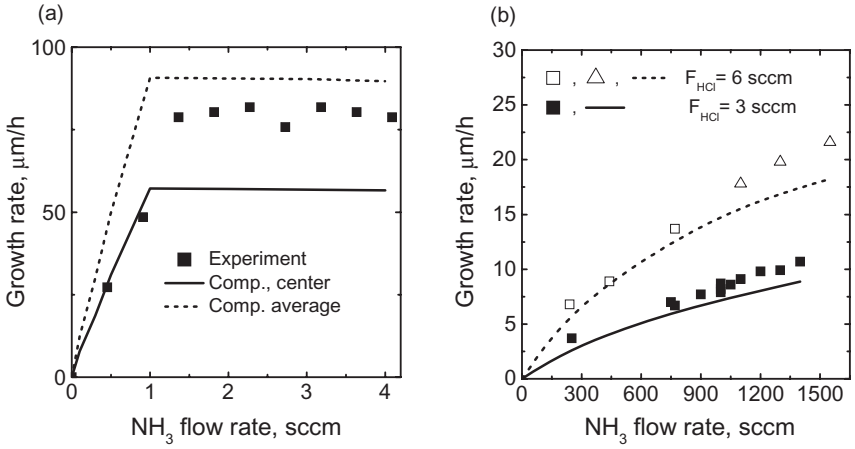

Figure 2.1 (a) computed AlN growth rate at the substrate center (solid line) and averaged over the substrate surface (dash line) vs. NH_3 flow rate in comparison with the experimental data of Ref. [23]; (b) GaN growth rate vs. NH_3 flow rate at two HCl flow rates – comparison of the computed (solid and dash lines) and experimental (squares and triangles) data (Ref. [18]).

rates are 100 sccm each). The computed dependence is presented by two lines corresponding to the AlN growth rate at the substrate center (solid line) and to that averaged over all the substrate surface (dash line). The two lines are seen to restrict an area that contains the experimental points. The difference between the two lines is attributed to some center-to-edge increase of the AlN growth rate due to some thinning of the diffusion boundary layer near the edge. Anyway, both the computed and experimental data exhibit a sharp common boundary between the linear and saturated regions corresponding to the NH_3- and $AlCl_3$-limited growth conditions. It is essential that a similar dependence of the GaN growth rate on the NH_3 flow rate exhibits no such sharp boundary between the two regimes, which is clearly seen from Figure 2.1b (here, the growth temperature is 1050 °C, the total pressure is atmospheric, the carrier H_2 flow rate is 1500 sccm, the carrier N_2 flow rate is 1550 sccm or 1650 sccm, and the HCl flow rate through the Ga metal source is 3 or 6 sccm, see the experimental data of [18]).

The quasi-thermodynamic model allows making clear the treatment of the difference in the dependencies of the AlN and GaN growth rates on the NH_3 flow rate. This treatment is based on two facts.

First, HCl dominantly converts into aluminum trichloride ($AlCl_3$) in the Al metal source, following reaction (2.4), but into gallium monochloride (GaCl) in the Ga metal source, following reaction (2.2). Figure 2.2 shows computed 2D distributions of the AlCl (a) and $AlCl_3$ (b) molar fractions in the system for AlGaN HVPE described in [13]. It is seen that $AlCl_3$ dominants over AlCl by a factor of ~20 at the Al source temperature of 550 °C, and this factor sharply increases at a lower temperature. Simultaneously, GaCl dominates over $GaCl_3$ by several orders of magnitude in a wide range of the Ga source temperature (see, for example, [18]). Thus, AlN dominantly grows from $AlCl_3$ and NH_3, following reaction (2.7), while GaN – from GaCl and NH_3, following reaction (2.5). Then, AlN growth following reaction (2.7) occurs under essentially nonequilibrium conditions, while GaN

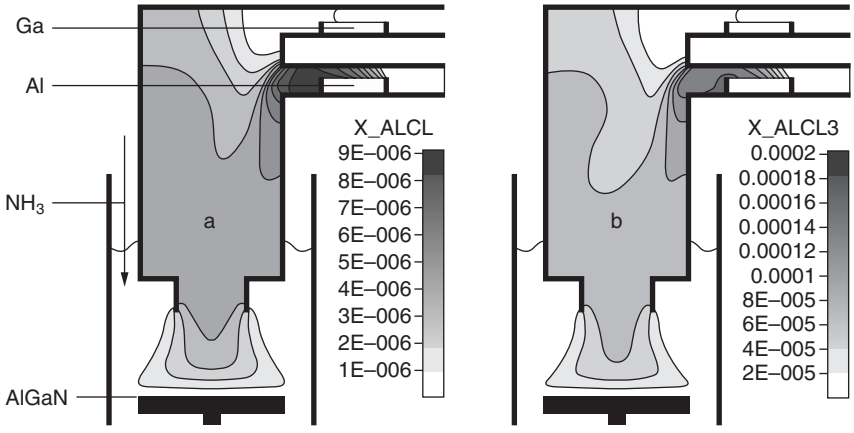

Figure 2.2 Distribution of the AlCl (a) and $AlCl_3$ (b) molar fractions in the system for AlGaN HVPE presented in Ref. [13].

growth following reaction (2.5) occurs under near-equilibrium conditions. Within the quasi-thermodynamic model, this corresponds to the fact that, due to the particular thermodynamic properties of the species involved in reactions (2.7) and (2.5) for AlN and GaN, respectively, the equilibrium constant K_{R6} for reaction (2.7) proves negligibly small while the equilibrium constant K_{R4} for reaction (2.5) is close to unity.

The smallness of the equilibrium constant K_{R6} results in the fact that the mass-action law equation for reaction (2.7) for AlN can be approximately written as $P^e_{AlCl3}P^e_{NH3} \sim 0$, so that either the $AlCl_3$ or NH_3 quasi-equilibrium pressure proves close to zero. Which of the two quasi-equilibrium pressures is close to zero depends on which of the two species is deficient at the reactor inlet. In such a situation, the AlN growth rate linearly depends on the flow rate of the deficient species (NH_3 at the linear region and $AlCl_3$ at the saturated region of the plots in Figure 2.1a) but is insensitive to those of the other species. On the contrary, the GaN growth rate proves sensitive to the flow rates of all the species involved in reaction (2.5) for GaN.

The revealed difference in growth of AlN and GaN enables clear treatments to be given to many experimental regularities of AlN, GaN, and AlGaN HVPE. For example, it simply explains the experimental fact of dominant Al incorporation into AlGaN alloy on small addition of H_2 in N_2 carrier gas. Figure 2.3 displays the computed dependencies of the AlN molar fraction in AlGaN on the Al content in group-III vapor for pure carrier N_2 (solid line) and in 10% addition of H_2 (dash line) in comparison with the data of Ref. [13] (here, the growth temperature is 1100 °C, the Ga and Al source temperatures are 850 °C and 550 °C, respectively, the total pressure is atmospheric, the group-III partial pressure is 3×10^{-4} atm, and the NH_3 partial pressure is 0.015 atm). Good agreement of the computed and

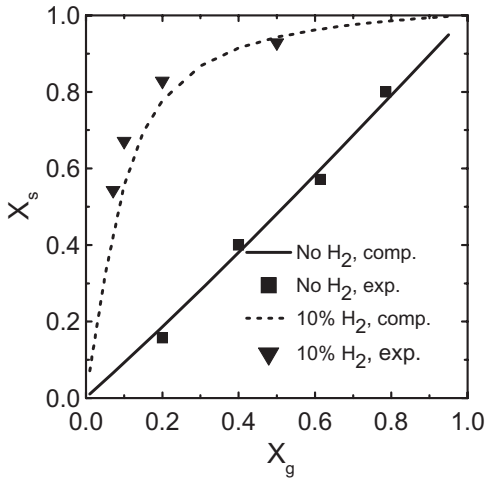

Figure 2.3 Computed AlN molar fraction in AlGaN vs. Al content in group-III vapor for pure carrier N_2 (solid line) and in 10% addition of H_2 (dashed line) in comparison with experimental data of Ref. [13].

experimental data is observed for the two carrier gases, regardless of the linear or sharp superlinear behavior of the dependencies. Small addition of H_2 to N_2 carrier gas sharply slows down reaction (2.5) that provides incorporation of Ga into the alloy but affects in no way reaction (2.7) that is responsible for the Al incorporation. This treatment is rather similar to that given in the original paper [13], however, our modeling analysis allows making some extended conclusions. Namely, it predicts that the Al content in the alloy is also sensitive to the flow rates of HCl and NH_3. Though these species are involved in both the growth reactions (2.7) for AlN and (2.5) for GaN, the effect is provided here by the above-discussed differences in the reaction equilibrium constants K_{R6} and K_{R4}.

The different features of AlN and GaN HVPE also lead to different strategies in raising their growth rates to grow bulk crystals. In the case of AlN, when the growth rate depends on the concentration of the limiting species only (normally, $AlCl_3$), one should raise the concentration of this species. In the case of GaN, when the growth rate depends on the concentration of all the species involved in reaction (2.5) for GaN, it is better to minimize the concentrations of the reaction products (HCl and H_2) and to raise the concentration of the reactive precursors (GaCl and NH_3). Simultaneously, the concentrations of the precursors affect the GaN growth rate in different ways. Figure 2.4 shows the computed dependencies of the GaN growth rate on V/III ratio at a fixed total partial pressure of the precursors. It is seen from the figure that the maximum growth rate is reached at the equal contents of the precursors in the vapor, that is, at V/III ~ 1. Note, however, that this analysis says nothing about the crystal quality. It is well known from various experimental data that good GaN crystal quality is provided at V/III ratio of several dozens, at least at V/III > 10. Figure 2.4 illustrates the fact that the combination of sufficiently high crystal growth rate (>400 μm/h) and good crystal quality (V/

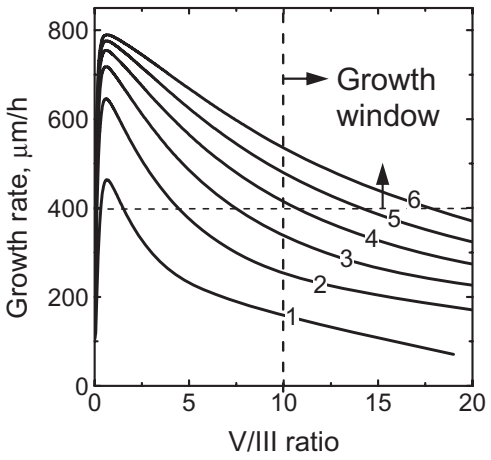

Figure 2.4 Computed GaN growth rate vs. V/III ratio at different dilution of the reactive precursors by neutral carrier gas (lines 1–6 correspond to the N_2 molar fraction of 0.9, 0.8, 0.7, 0.6, 0.5, and 0.4).

III > 10) is possible at relatively low dilution of the precursors by neutral carrier gas (nitrogen molar fraction in the gaseous mixture below 0.6) – see "growth window" in the figure. The requirement of a high V/III ratio also restricts raising the limiting $AlCl_3$ in AlN HVPE.

2.3.2 SiC HTCVD

An HTCVD method to grow SiC crystals with high rates may be to use silicon tetrachloride ($SiCl_4$) and propane (C_3H_8) as precursors supplied separately and diluted by argon and hydrogen, respectively [24]. The process is carried out in a vertical reactor with the susceptor located on the top. The following process conditions were used in the experiments and specified in the computations: the total pressure is 200 Torr, the growth temperature is 2000 °C, Ar and H_2 flow rates are 3 slm, the flow rates of precursors are varied in a wide range.

Typically, the process simulation predicts a recirculation zone near the wafer edge (as shown in Figure 2.5, left). However, its influence on the uniformity of temperature distribution in the growth region appears to be negligible (see Figure 2.5, right). Propane decomposes completely in the gas phase, so that acetylene (C_2H_2) becomes the main C-containing by-product. Note that a significant graphite etching at the outlet of reactor injectors provides an additional supply of acetylene. Similarly, $SiCl_4$ is irreversibly transformed into $SiCl_2$ and SiCl. Thus, C_2H_2, $SiCl_2$ and SiCl are the main species contributing to SiC growth. In addition, a large percentage of hydrogen chloride results from $SiCl_4$ decomposition. To get an insight into the process, computations were performed at various flow rates of precursors. The growth rate dependence on C_3H_8 flow rate is demonstrated in Figure 2.6. It follows from the modeling results that a nonzero growth rate can be expected at zero propane flow rate. This is associated with the additional production of carbon due to the graphite etching. Figure 2.7 illustrates the growth rate as a function of $SiCl_4$ flow rate. Our computations show saturation in the growth

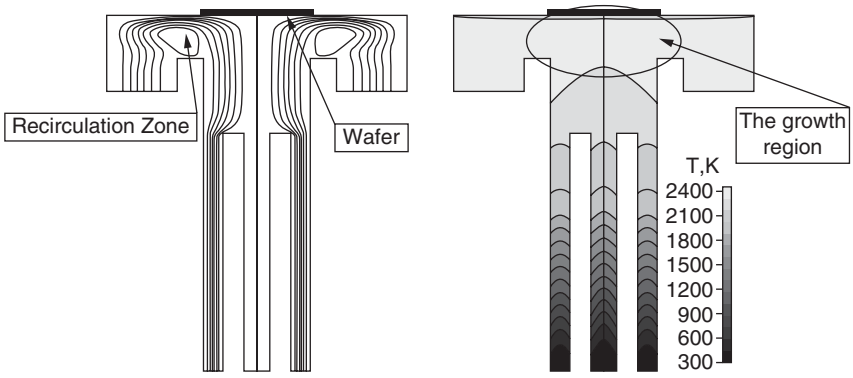

Figure 2.5 Flow patterns (left) and temperature distribution (right) in the SiC HTCVD reactor.

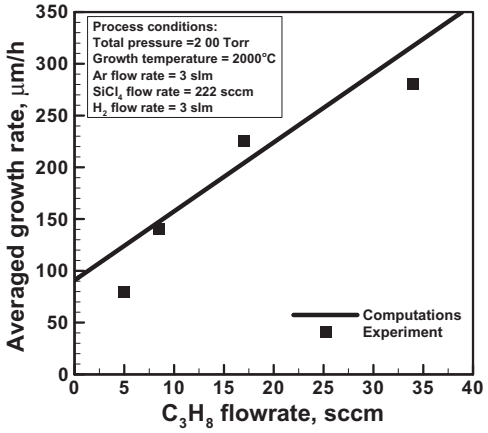

Figure 2.6 Growth rate as a function of the C_3H_8 flow rate. Experimental data from [24].

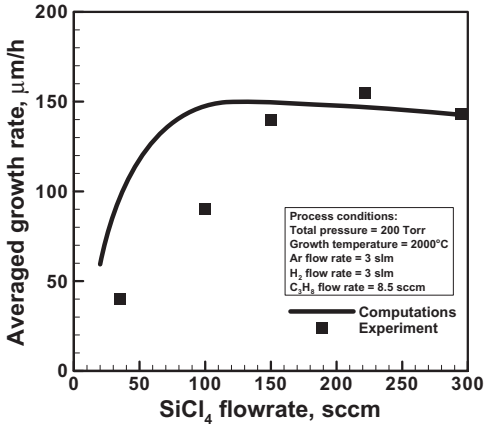

Figure 2.7 Growth rate as a function of the $SiCl_4$ flow rate. Experimental data from [23].

rate at the Si/C ratio close to unity. Nevertheless, the saturation in experiment [24] is reached at somewhat higher values of the Si/C ratio.

In summary, computational analysis of SiC HTCVD from silicon tetrachloride ($SiCl_4$) and propane (C_3H_8) precursors shows that the process conditions considered provide complete precursor decomposition in the growth chamber. On the other hand, as follows from a comparative analysis, parasitic deposits at the reactor walls and inlet unit influence negligibly the growth rate for the reactor geometry and temperature distributions. As a result, a high growth rate of 100–300 μm/h and maximal yield are expected due to minimal precursor losses.

The conventional precursors employed in CVD-reactors for growing monocrystalline silicon carbide are silane (SiH_4) and propane (C_3H_8) highly diluted by a carrier gas. A novel reactor, schematically presented in Figure 2.8 together with the flow patterns, was suggested in [25]. SiC crystal is grown simultaneously on two

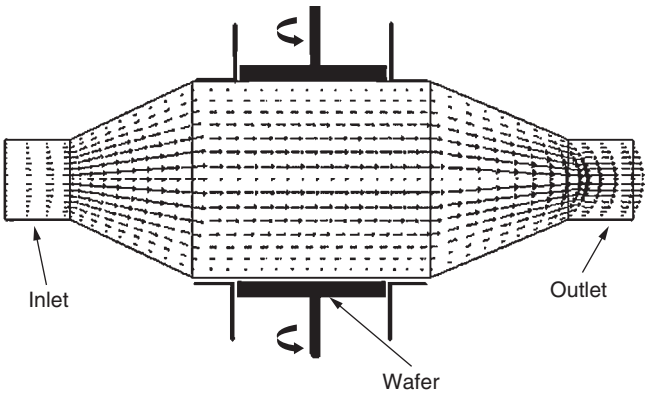

Figure 2.8 Schematic view and flow patterns in the HTCVD reactor from [25].

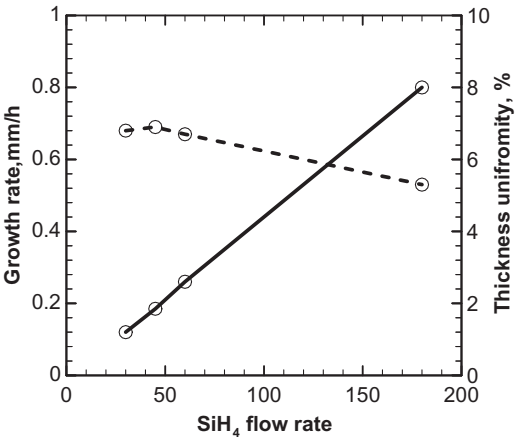

Figure 2.9 Growth rate and thickness uniformity versus SiH_4 flow rate, predicted by modeling.

substrates located opposite each other on the upper and lower walls of the chamber. In this case, most of the vapor-phase silicon carbide is deposited on the substrates. The object of the method is to provide a reactor for growing bulk silicon carbide single crystal of a high quality required to produce semiconductor devices, while providing low production costs and a high output to ensure industrial application.

The reactor design optimization along with the selection of operating parameters providing high growth rates and good thickness uniformity has been performed using simulations. A good uniformity of typical temperature distribution is predicted along the reactor height, providing the complete decomposition of precursors into such Si- and C-containing by-products as SiH, Si, C_2H_4, and C_2H_2. As one can see from the velocity vectors, there are no stagnation and recirculation zones for typical operating conditions.

Modeling analysis has shown that the mean growth rate increases linearly with the silane flow rate (see Figure 2.9). This is due to the fact that under the optimized

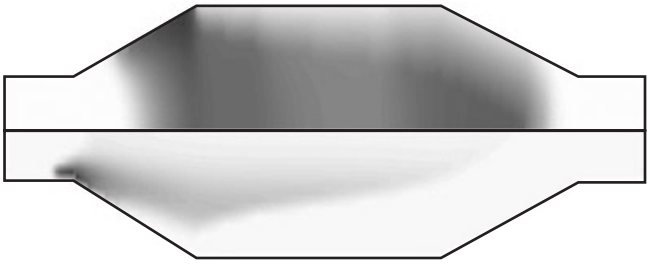

Figure 2.10 Computed distributions of the Si vapor concentration (upper part of the figure) and Si cluster density (upper part of the figure) for the HTCVD reactor from [25].

conditions there is practically no depletion of the gas mixture in silicon due to the gas-phase nucleation. Silicon clusters are formed in a cold zone near the inlet and completely evaporate at high temperature in the growth zone. This result is illustrated by the distributions of the Si vapor concentration and Si particle density, presented in Figure 2.10 for the central cross-section of the reactor.

The wafer rotation provides the efficient smoothing of the growth rate distribution. The growth rate of about 0.8 mm/h is predicted at the total pressure of 200 mbar, wafer temperature of 2200 °C, and Ar flow rate of 1.2 slm.

2.4 Conclusions

Application of the quasi-thermodynamic model to the analysis of AlN, GaN, and AlGaN HVPE has revealed considerable differences in the growth of AlN and GaN. First, HCl dominantly converts into aluminum trichloride ($AlCl_3$) in the metal Al source but into gallium monochloride (GaC) in the metal Ga source. Then, AlN grows largely following reaction $AlCl_3 + NH_3 \rightarrow AlN(s) + 3HCl$ under essentially nonequilibrium conditions, while GaN – following reaction $GaCl + NH_3 \rightarrow GaN(s) + HCl + H_2$ under near-equilibrium conditions. As a result, the AlN growth rate is sensitive only to the flow rate of the limiting species (normally, $AlCl_3$), while the GaN growth rate is sensitive to the flow rates of all the species involved in the latter reaction. The differences in AlN and GaN HVPE results in sensitivity of the AlGaN alloy composition to H_2, HCl and NH_3 flow rates and eventually determine different strategies of raising the AlN and GaN growth rates to grow bulk crystals.

Reactor-scale modeling of the SiC HTCVD process allows a reasonable reproduction of the experimentally measured growth rate as a function of the major operating parameters. From the model predictions, one can conclude that the use of a properly designed reactor and optimized growth conditions, high growth rates of about 1 mm/h with reasonable uniformity can be achieved. This suggests that modeling can be successfully used for elaborating the SiC HTCVD process, providing low production costs and a high output to ensure industrial application.

References

1 www.cree.com/products/pdf/MAT-CATALOG.pdf.
2 Makarov, Y.N., Avdeev, O.V., Barash, I.S., Bazarevskiy, D.S., Chemekova, T.Y., Mokhov, E.N., Nagalyuk, S.S., Roenkov, A.D., Segal, A.S., Vodakov, Y.A., Ramm, M.G., Davis, S., Huminic, G., and Helava, H. (2008) *J. Cryst. Growth*, **310**, 881.
3 Raghothamachar, B., Dudley, M., Rojo, J.C., Morgan, K., and Schowalter, L.J. (2003) *J. Cryst. Growth*, **250**, 244.
4 Molnar, R.J., Götz, W., Romano, L.T., and Johnson, N.M. (1997) *J. Cryst. Growth*, **178**, 147.
5 Zhang, W., and Meyer, B.K. (2003) *Phys. Status Solidi*, **0**, 1571.
6 Seifert, W., Fitzl, G., and Butter, E. (1981) *J. Cryst. Growth*, **52**, 257.
7 Fujito, K., Kubo, S.H., Nagaoka, H., Mochizuki, T., Namita, H., and Nagao, S. (2009) *J. Cryst. Growth*, **311**, 3011–3014.
8 Nikolaev, A., Nikitina, I., Zubrilov, A., Mynbaeva, M., Melnik, Y., and Dmitriev, V. (2000) *Mater. Res. Soc. Symp. Proc.*, **595**, W6.5.1.
9 Nagashima, T., Harada, M., Yanagi, H., Fukuyama, H., Kumagai, Y., Koukitu, A., and Takada, K. (2007) *J. Cryst. Growth*, **305**, 355.
10 Kumagai, Y., Yamane, T., and Koukitu, A. (2005) *J. Cryst. Growth*, **281**, 62.
11 Kovalenkov, O., Soukhoveev, V., Ivantsov, V., Usikov, A., and Dmitriev, V. (2005) *J. Cryst. Growth*, **281**, 87.
12 Mastro, M.A., Tsvetkov, D., Soukhoveev, V., Usikov, A., Dmitriev, V., Luo, B., Ren, F., Baik, K.H., and Pearton, S.J. (2003) *Solid State Electron.*, **47**, 1075.
13 Koukitu, A., Satoh, F., Yamane, T., Murakami, H., and Kumagai, Y. (2007) *J. Cryst. Growth*, **305**, 335.
14 Dollet, A., Casaux, Y., Chaix, G., and Dupuy, C. (2002) Thin Solid Films, **406**, 1.
15 Kumagai, Y., Takemoto, K., Kikuchi, J., Hasegawa, T., Murakami, H., and Koukitu, A. (2006) *Phys. Status Solidi B*, **243**, 1431.
16 Murakami, H., Kikuchi, J., Kumagai, Y., and Koukitu, A. (2006) *Phys. Status Solidi C*, **3**, 1457.
17 Vorob'ev, A.N., Karpov, S.Y., Bogdanov, M.V., Komissarov, A.E., Bord, O.V., Zhmakin, A.I., and Makarov, Y.N. (2002) *Comput. Mater. Sci.*, **24**, 520.
18 Segal, A.S., Kondratyev, A.V., Karpov, S.Y., Martin, D., Wagner, V., and Ilegems, M. (2004) *J. Cryst. Growth*, **270**, 384.
19 Segal, A.S., Bazarevskiy, D.S., Bogdanov, M.V., and Yakovlev, E.V. (2009) *Phys. Status Solidi*, **6** (**S2**), S329–S332.
20 Stinespring, C.D., and Wormhoudt, J.C. (1988) *J. Cryst. Growth*, **87**, 481.
21 Allendorf, M.D., and Kee, R.J. (1991) *J. Electrochem. Soc.*, **138** (**3**), 841.
22 Pons, M., Meziere, J., Di Cioccio, L., Blanquet, E., Ferret, P., Dedulle, J.-M., Baillet, F., Pernot, E., Anikin, M., Madar, R., and Billon, T. (2004) *J. Phys. Condens. Matter*, **16**, S1579.
23 Armas, B., de Icaza Herrera, M., and Sibieude, F. (2000) *Surf. Coat. Technol.*, **123**, 199.
24 Nigam, S., Chung, H.J., Polyakov, A.Y., Fanton, M.A., Weiland, B.E., Snyder, D.W., and Skowronski, M. (2005) *J. Cryst. Growth*, **284**, 112.
25 Makarov, Y.N. (2000) CVD Method of and Reactor for Silicon Carbide Monocrystal Growth. Patent International Publication Number WO 00/43577, 27 July 2000.

3
Advanced Technologies of Crystal Growth from Melt Using Vibrational Influence

Evgeny V. Zharikov

3.1
Introduction

The crystallization process is a complex versatile multiscale phenomenon. There is a large spectrum of different length scales in crystal growth starting with atomic-scale processes and finishing with macroscale elements of crystal growth. The difference in length scales covers 10 orders of magnitude, over which crystal-growth phenomena take place. It is important to stress that most of them, including oscillations of atoms on microscale, fine flows in boundary layer on mesoscale and characteristic oscillation, resonance features of growth system on the macroscale are vibration sensitive. The situation becomes even more complicated due to a great variety of different time scales in crystal-growth process. The time scales range from subsecond values up to many hours, and they appear as the rapid variations of the melt flow, intermediate solidification rates or slow transient phenomena of the thermal environment.

In crystal growth from the melt one of the most serious problem is a problem of convection control. Convective flows in nonuniformly heated inhomogeneous fluids significantly affect on many aspects of the growth processes producing a number of undesirable defects including nonuniform distribution of components and dopants, unstable shape of the interface, growth striations, inclusions, bubbles, etc. Control of convective transport of heat and constituent components appear to be an efficient way of improvement of the quality of single crystals.

In recent years there have been a number of efforts to develop an efficient technology of melt crystal growth either by damping of irregular natural convection by putting into the melt motionless baffles [1], rotating rings [2], etc., or by creation of forced convection using rotation of crystal (or both crystal and crucible) [3, 4] and low-energy external force fields including magnetic fields (static [steady] and dynamic [nonsteady] with a number of varieties like longitudinal, transverse, rotating RMF, pulsating PMF, and traveling magnetic field TMF) [5–8]; as well as electrical fields [9–12]; rotating thermal fields [13]; centrifugal forces [14, 15]; submerged heaters [16, 17]; and various vibrational techniques, such as accelerated crucible rotation technique, ACRT [18, 19], its variation called angular vibrational

Crystal Growth Technology. Semiconductors and Dielectrics. Edited by P. Capper and P. Rudolph
Copyright © 2010 WILEY-VCH Verlag GmbH & Co. KGaA, Weinheim
ISBN: 978-3-527-32593-1

technique, AVT [20], coupled vibrational stirring CVS [21, 22], ultrasonic influence [23, 24], etc.

There are several review papers discussing low-energy methods (see, for instance [6, 25–27]). All of the proposed methods of creation of forced convection and damping of irregular buoyancy convection allow control of the heat–mass transfer in the melt and improvement in the quality of grown crystals to a different extent. Among them the most widely used and the better investigated today are RMF, ACRT and ultrasound techniques.

At the same time the variety of different methods used as well as the length of their list itself together with regular appearance of new variants is direct evidence that all the proposed methods do not meet completely the requirements of growing of high-quality crystals. The criticism of most of particular methods could easily be found in the literature (see, for instance [6, 22, 28, 29]). Practically, there is no method that would not be criticized either because of its limitations or weak features and disadvantages.

3.2 Axial Vibrational Control in Crystal Growth

In addition to previously discussed low-energy methods there is one more specific vibrational technique, namely axial vibrational control, AVC, which use the applying of axial low frequency and small amplitude vibration to the growth system [30, 31].

A large variety of different kinds of vibrations exists. Gershuni and Lubimov [32] distinguish the following types: (i) progressive (linear, circular, noncircular etc.); (ii) rotational, (circular and noncircular); (iii) swinging; (iv) total volume vibrations and/or submerged body vibrations; (v) harmonic and nonharmonic; (vi) low- and high-frequency vibration. It should be noted that a number of authors who discuss the use of vibrations in crystal growth, consider them as the different variants of "vibrational technique" and often they do not make any distinction between their types. However, the different kinds of vibration (for instance, ACRT, CVS, AVC, ultrasound, etc.) demonstrate a significant difference in mechanisms and large variety of forced convection flows.

We consider here only progressive (translational) vertical vibrations induced either by the crystal itself or by special solid body (baffle). Using the different variants of the AVC technique in crystal growth from the melt is the subject of the present chapter.

Many authors point out that crystallization is periodic, oscillatory ("rhythmic") process [33–36]. Numerous supporting facts are gathered in metallurgy and mineralogy [37, 38]. Various publications studied the different kinds of related growth striations that were attributed to crystal rotation, thermal asymmetry in the system, etc. It was demonstrated that the microscopic growth rate exhibited a periodic variation and differed from the macroscopic growth rate by as much as a factor of 10 [39]. Other studies suggest that the oscillatory growth striation ("zoning") in

some cases could not be caused by external reasons but was generated by complex kinetics at the crystal/melt interface (e.g., [40–42]). The physical origin of the instability, although it varies for different systems, is normally believed to associate with the competition of interfacial kinetics and chemical transportation, and nonlinear boundary conditions are sometimes required [42].

Various mechanisms were proposed. Some authors explain the phenomenon of oscillatory crystallization based on the concept of a jump in constitutional supercooling (see, for instance [43]), the anomalous nonmonotone dependence of growth rate upon temperature [34, 35, 44], the kinetic transition from the steady-state regime of continuous crystallization to a self-oscillating one [45, 46], the alternate switching of the crystal surface between smooth and rough states that results in a drastic change in the growth velocity [42, 47, 48], etc. Others [49, 50] introduce the idea of clusters (or nanoclusters) into this process by blocking the growth interface and further their reconstructing and growth of crystal by attachment of the nanoclusters. The authors of Refs [51–53] consider that formation of stratified structures (oscillatory zoning) is not random and describe it in the framework of the concept of deterministic chaos. The quantitative description of the character of oscillatory zoning pattern in crystals can be performed by nonisotropic self-affine fractal geometry [54, 55]. The fractal dimension of the pattern is a quantitative measure of the nonrandomness of the striation and emphasizes the need to develop a model for crystal growth with the requirement that the model predict an oscillatory zoning pattern with the same fractal characteristics as the observed pattern.

Discussion on the nature and mechanisms of oscillatory crystallization started in the 1950s still did not finished and no single opinion exists up to now. However, it should be recognized that among the action of various external fields the oscillatory (vibrational) impact should most closely correspond to the fundamental nature of crystallization and it would be the most efficient way to influence the crystal-growth process. Moreover, there is a point of view [56] that fabrication of highly uniform crystals needs in insertion of external oscillation into a growth system that make the process steady state.

The history of studies of vibrational influence on crystal growth from liquid phase starts from the mid-1950s. The first paper was published by Vitovskii in 1955 [57] where he used low-frequency vibration of the crystal during growth from solution. Vitovskii demonstrated a 4-fold increase growth rate under vibration with 50 Hz frequency and amplitudes in the range 0.1–0.5 mm. Since then, many authors have studied the influence of vibration on the growth of crystals from the melt and solution (see the detailed list of references in our review papers [58, 59]). The influence of vibrations on the character of the crystallization and the crystal properties was demonstrated. Experimental data on various aspects of vibrational influence on growth behavior and crystal properties have been obtained. The vibration affects on nucleation velocity and rate of crystal growth [57, 60, 61], the shape of a freely growing crystal [62, 63], the incorporation of impurities [64–66], local inhomogeneity [67], and the dislocation density in a crystal [68] were all determined. The effects found occur to a different extent for a wide region of intensities

and frequencies of vibration. The influence of vibrations on crystal growth in the ultrasonic (from tens of kHz to several MHz), acoustic (usually tens to hundreds of Hz), and even subsonic ranges (from 0.5 to 5 Hz) has been investigated. The displacement amplitudes are usually confined to several micrometers for ultrasound [69] and reach 10–25 mm in experiments on the influence of infrasound [70, 71].

However, those studies of axial low-frequency vibration were nonsystematic and odd: each author published usually no more than one or two papers. This situation is quite natural and explicable since the mechanisms were unknown and really efficient use of axial vibration in crystal growth was very difficult to perform. A series of mechanisms has been proposed to explain the effect of low-frequency vibration on crystal growth. These include the destruction of the diffusion layer [67], the motion of dislocation loops under vibrational influence [63], fluidization of the semiordered near-surface layer [72], modulation of the growth rate during crystal vibration caused by temperature oscillations near the crystallization front [73, 74], and intensification of heat and mass transfer in the sonic field [75, 76].

At the same time a number of observed effects (see below), which take place during crystal growth under low-frequency vibrations of small amplitude, cannot be explained in terms of these mechanisms. As will be shown below, the effects of vibrational influence can be understood in terms of complex vibrational induced flow both in the bulk and on surface of liquid that significantly modify the heat and mass transfer and vary the kinetics and rate of crystal growth.

It was found [30, 31] that a solid body in the liquid subjected to vibration with low frequency (tens of Hz) and small amplitude (tens to hundreds of micrometers) produces the closed stationary flows in the form of a vortex near their sharp edges perpendicular to the direction of vibration (Figure 3.1). This was demonstrated experimentally by physical modeling on transparent liquids (water–glycerin mixtures) and also by numerical simulation. Only after discovery of this phenomenon did it became easy to interpret the facts and explain the effects occurring via the vibrational influence on crystal growth from a liquid phase.

The primary numerical modeling of this phenomenon was carried out in Refs [77, 78]. It was supposed that the body with a dihedral rectangular edge executed linear harmonic vibrations in a stationary infinite liquid. The direction of vibration is perpendicular to one of the facets of the body, whereas its amplitude is to a large extent smaller than the size of the body. The numerical solution of the Navier–Stokes equations was executed in approximation to a viscous incompressible liquid by a splitting scheme [79]. The solution reveals the existence of a stationary average flow characterized by two areas of circulation with opposite direction of motion (Figure 3.1). Computation shows that the sizes of circulation increase both with the rise of the amplitude, the frequency of vibrations, and with the viscosity of the liquid. For example, at an amplitude of 0.1 mm, a frequency of 30 Hz and a kinematic viscosity of 0.1 $cm^2 s^{-1}$ the average diameter of circulation can reach 40 mm. These primary flows induce the formation of intensive secondary flows in the bulk liquid that can drastically change the hydrodynamic situation in a growth system.

As is shown on Figure 3.1, the flow near vibrating edges develops in the form of vortex tubes. The physical nature of this phenomenon encloses the formation

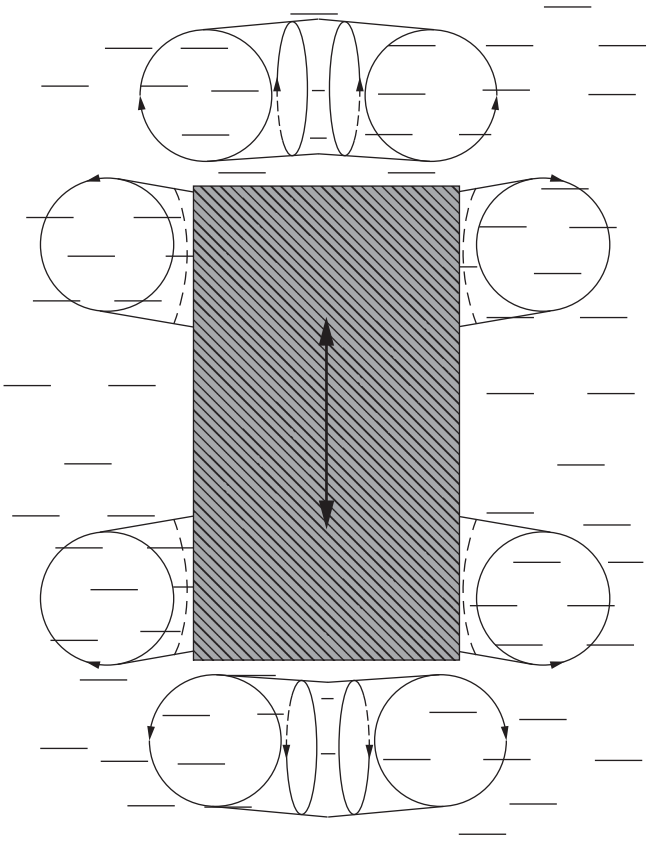

Figure 3.1 Circular motion of a liquid near a cylinder subjected to low-frequency and small-amplitude axial vibration.

of a nonstationary boundary layer near the body surface and its periodic break-off, which causes the stationary movement in the liquid.

Vibrational convection arising from the applying of vibrations (with low-frequency and small-scale amplitude) to the body with sharp edges is a specific type of stationary flow in the fluid. It differs from known fluid flow that is evident from a comparison with acoustic flows [80] and Schlichting flow [81]. In fact, certain important effects of vibrational convection cannot be adequately described based on known solutions of the boundary-layer problem that are applied to vibrations normal to the axis of a cylinder submerged in a liquid as well as vibrations of a sphere or body with a Chaplygin profile [82]. A correlation between the scales and structure of steady-state fluid flows, on the one hand, and the amplitude–frequency characteristics of vibrations, on the other hand, show this [58].

The phenomenon of vibrational convection cannot be explained by the theory of acoustic flow because the characteristic dimension of the vortices in such flows is similar to or greater than the wavelength of the sound [80]. In contrast, the typical wavelengths for the vibrations under study are about 10 m, whereas the

characteristic dimensions of the vortex, as a rule, are three orders of magnitude less. Steady-state convective flows generated by vibration occur at considerably lower amplitudes than Schlichting flow [58]. The appearance of small-scale vortices near the sharp edge of the vibrating body is a significant difference from ordinary flows within the boundary layer. The authors of Ref [83] called this specific new flow "anti-Schlichting" flow, and they noted that the latter flow could convert into regular Schlichting flow when the sharp edges of a vibrating body will change to round edges. In addition, the specific character of vibrational convection is corroborated in the case of a Czochralski configuration by complex surface flow [84] arising together with the bulk flow distinguishes vibrational convection from other known flows.

The influence of low-frequency vibrations on a liquid is substantially different from that of ultrasound. Low-frequency vibrations induce a controlled large-scale melt flow that can make the temperature and composition near the growth front homogeneous due to additional stirring. In contrast, the ultrasound possesses higher energy capacity compared to low-frequency vibrations and its nonlinear effects are much more pronounced. The special features of ultrasound are formation of acoustic flow, radiation pressure, cavitation, and production of the traveling or standing waves assisted with release of heat [85]. Especially harmful are cavitation effects leading to damage and dispersion of crystal and standing waves producing stratification (antinodes) in the liquid and strong striation in the grown crystals [24, 85, 86].

The technique of applying vibration with low-frequency and small amplitude called axial vibrational control (AVC) is realized either by vibration of growing crystal or by oscillation of special submerged body, which is located near the crystal/melt interface and oscillates inducing vibrational convection flows. AVC can easily be adapted to many methods of crystal growth from a fluid medium (melt or solution) [31]. Application of AVC to different techniques of crystal growth from melt shown on Figure 3.2. By now it was realized in Czochralski, top-seeded solution growth (TSSG), vertical Bridgman and floating zone methods that will be discussed below in more detail. The most comprehensive work has been done for AVC-assisted Bridgman (AVC-BR) and Czochralski (AVC-CZ) techniques, and major attention in the chapter is paid to these two important melt growth methods assisted with controlled vibrational influence.

In the experiments electromechanical vibrating converters were used as a vibration source. They could produce vibration with amplitudes up to 1.5 mm and frequencies between 0 and 500 Hz. In the experimental studies vibrations with frequencies up to 80 Hz and amplitude from 50 to 500 μm were applied. Physical modeling of heat and mass transfer was carried out on water–glycerine mixtures; in model crystallization experiments $NaNO_3$ was used, as it possesses a transparent melt with suitable physical properties. The "light-knife" system and computer processing of photographs were used to investigate the melt motion in the experiments.

Mathematical modeling was performed on the basis of unsteady 2D Navier–Stokes–Boussinesq equations for incompressible fluid. The finite element method and both computer codes ASTRA [87] and FLUENT 6.4 software [88] were used

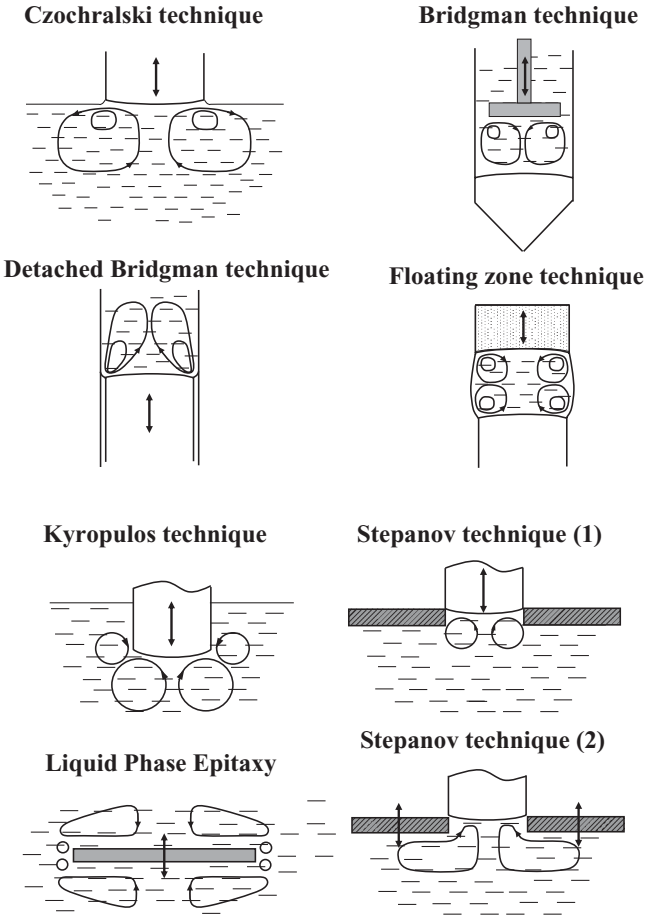

Figure 3.2 Use of axial-vibrational control in different techniques of melt crystal growth.

for calculations. In the mathematical model the following assumptions were used: the applied vibrations are assumed to be of small amplitude, therefore the vibrator displacements are negligible, and the velocity of the vibrator is predefined as a harmonic function

$$v = A\omega \cdot \sin(\omega t),$$

where A, vibration amplitude, ω, vibration frequency.

Convective and diffusive terms were approximated symmetrically, for stabilization the additional dissipative diffusion terms were added to each convection–diffusion equation.

The vibrating baffle forces the melt flow, which is the superposition of two-component flows of different time scale and different nature. The first one is the instantaneous vibrational convective melt flow, which is controlled by the vibrator

frequency. This flow cannot normally be detected visually in experiments at rather high vibrator frequencies f=10–100 Hz. The second flow is the averaged vibrational flow (AVF), which has significantly reduced velocities and becomes quasistationary with time. This flow can be observed as particle tracks in the experiments with transparent liquids. It is not gravity sensitive and exists also in the case of microgravity and under isothermal conditions. Under nonisothermal conditions when the vibrational flow and thermal convection flow (TCF) are present simultaneously, the integrated flow, which is the superposition of AVF and TCF flows appear.

In numerical simulation the calculated instantaneous flows were averaged in time to evaluate averaged vibrational flow. The calculations were made using the time-step value so that its value was 1/100–1/10 of one period of vibrations (depending on the frequency of vibrations). In all cases, the results of calculations correspond to the time when the averaged vibrational flow becomes quasistationary.

For comparison of the various vibration regimes the vibrational Reynolds number was used:

$$\mathrm{Re}_v = \frac{2\pi \cdot f \cdot A \cdot R}{\nu}.$$

Here,

f, vibration frequency;
A, vibration amplitude;
ν, kinematic viscosity;
R, vibrating body radius.

Consideration of fluctuation effects in directional crystallization shows [89] that after a single disturbance at the growth interface the steady-state composition is reached within a time:

$$t \approx 2\delta^2/D,$$

where δ is boundary layer thickness, and D is diffusion coefficient.

Taking typical values $\delta = 10^{-4}$ m and $D = 10^{-8}\,\mathrm{m^2\,s^{-1}}$, we obtain a time of the order of 1 s. This means that the solutal transient of the growing interface is quite slow, and the interface acts as a "low-pass filter" (Ref. [90]) preventing the influence of growth-rate perturbations or temperature oscillations with certain frequencies. The frequency limit from the above estimation is about 1 Hz. The same value can also be obtained from the analysis presented in Ref. [91]. According to estimates in Ref. [92] the critical value could be about 10 Hz. Below this limit (a few Hz) any fluctuations are dangerous. On the contrary, higher-frequency perturbations including typical for AVC values should be damped.

The influence of low-frequency and small-amplitude axial vibration on crystal growth from a liquid phase is not confined by formation of bulk flows shown in Figures 3.1 and 3.2. Some new important effects of vibration were discovered during other studies (see Refs [58, 59, 88, 93]). They will be discussing in the following sections. Although the effects were observed in the case of particular vibration-assisted growth configurations, there are reasons to believe that these effects have a common character.

3.3
AVC-Assisted Czochralski Method

In the Czochralski configuration the crystal itself plays a role of vibrating body, which contacts the surface of melt and produces intensive vibrational flows in the bulk melt. The photo of a typical flow pattern in a transparent model liquid under axial vibration is shown in Figure 3.3. In this particular case the distilled water ($\nu = 0.01\,\mathrm{cm}^2/\mathrm{s}$) used as a model liquid in a crucible with diameter $D = 74\,\mathrm{mm}$. The lower end of the vibrating model crystal (with $d = 25\,\mathrm{mm}$) located at 1 mm below the surface of liquid.

Experimental studies of interaction between vibrational and thermal convections showed that vibration efficiently suppressing the natural convection flows [31]. The direction of melt motion in vibrational vortices is opposite to that of thermal convection. Along with an increase of the vibrational Reynolds number the vortices of vibrational convection spread to the crucible wall, occupying more and more space. Finally, the whole volume of crucible becomes occupied only by vibrational flow without any thermal convection.

The simultaneous interplay of the vibration, thermal convection and rotation (the case of opposite rotations of the crystal and the crucible) was investigated by primary studies of numerical calculations in Ref. [94]. It was shown that interaction of these three factors leads to the appearance of a complex structured flow. The parameters for calculations were chosen the following: $A = 100\,\mu\mathrm{m}$, $f = 50\,\mathrm{Hz}$,

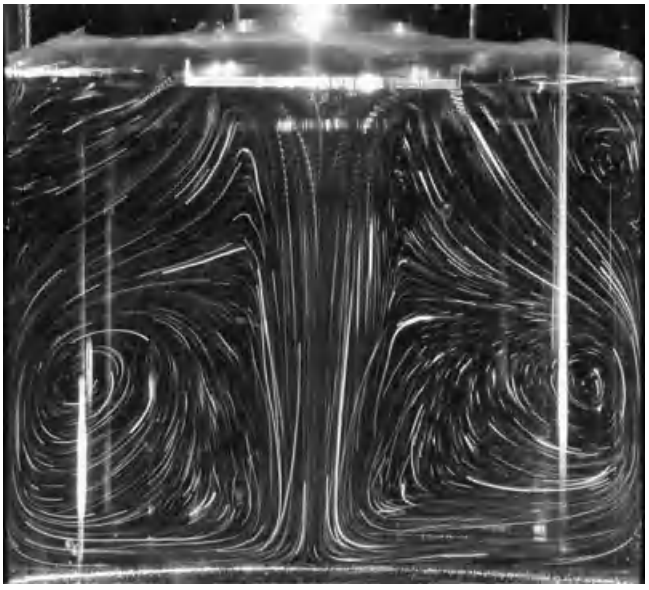

Figure 3.3 Flow pattern in AVC-assisted Czochralski ($D = 74\,\mathrm{mm}$; $d = 25\,\mathrm{mm}$; $H/D = 0.9$; $h = -1\,\mathrm{mm}$; $\mathrm{Re}_v = 2563$).

$Re_{crystal} = -500$, $Re_{crucible} = 500$, Gr = 214610, Pr = 5.43. The full melt volume could conditionally be divided into two domains by the line, which connects the lateral side of the crystal and the bottom corner of the crucible. The flow structure in the external domain is formed by the thermal convection. In the internal domain the flow structure is formed by both the vibration and rotation. Conflict between the vibration and the rotation takes place. The preliminary results from Ref. [94] suggest that this fight could lead to the homogeneity alterations of the temperature field. Further parametric investigation of this triple interaction is necessary to obtain the authentic view of these complex phenomenon.

AVC gives efficient suppression of the temperature oscillations at the interface [95] and control of both the composition and dopant segregation/distribution in the crystal [96]. In particular, it produces the smoothing of compositional fluctuations in doped crystals, and provides the leveling of both dopant concentration and nonstoichiometry along and across the crystal [96, 97]. Experiments on AVC-assisted high-temperature Czochralski growth of yttrium-scandium-gallium garnet doped by erbium and chromium ions, Er,Cr:YSGG (melting point 1910 °C), showed [97] the noticeable weakening of striation. Figure 3.4 demonstrates the fluctuations of the Er concentration obtained by microprobe analysis in a grown crystal both without vibration and under vibrational influence (f = 50 Hz, A = 40 μm). Instead of nonoptimized vibrational parameters one can see that the amplitude of concentration fluctuations (swing) reduces under vibration by about a factor of two. Another effect of vibration that is clearly seen from this graph is a notable decrease of the average Er concentration (from about 30.4 at.% to 29.9

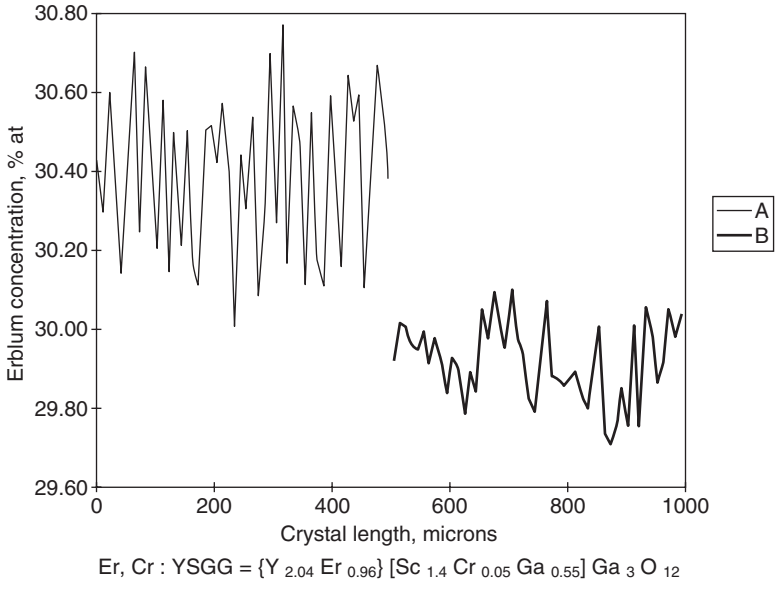

Figure 3.4 Smoothing of compositional fluctuations under crystal vibration: (a) no vibration; (b) vibration with frequency f = 50 Hz and amplitude A = 40 μm.

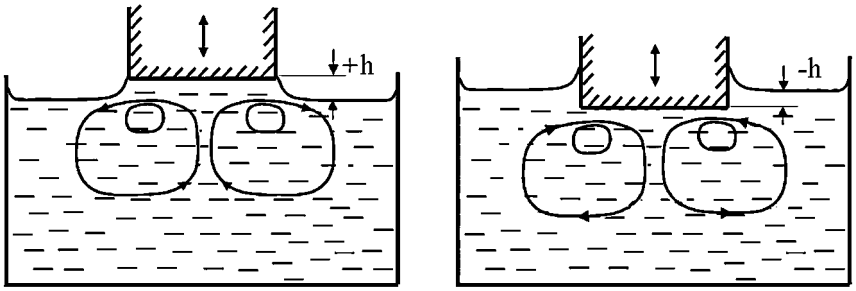

Figure 3.5 Effect of crystal penetration on bulk flow pattern in AVC-CZ.

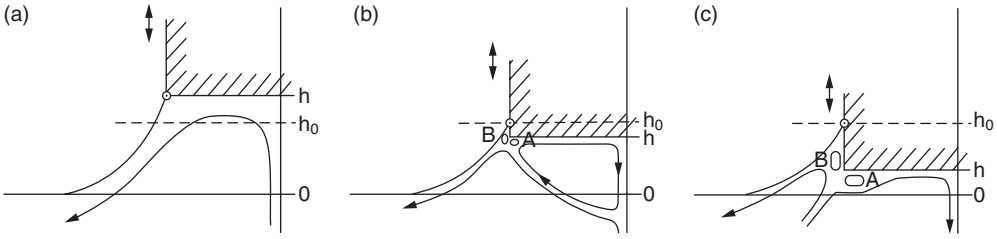

Figure 3.6 Mechanism of change of flow direction under the crystal in AVC-CZ. *h*, penetration depth of crystal regarding position of free surface of liquid (h_0).

at.%). This is due to the influence of low-frequency vibration on the segregation processes during crystal growth, resulting in the change of distribution coefficients of components in the presence of vibration compared to "nonvibrating" crystal.

Bulk flow under the growing crystal could be significantly changed by the position of crystallization front regarding free surface of liquid. A schematic sketch (Figure 3.5) shows that along with penetration of crystal into a liquid the direction of bulk flow alters to the opposite one. Figure 3.6 explains the cause of this. When a vibrating solid/liquid interface is located above the free surface of liquid (Figure 3.6a) we observe the normal direction of vibrational convection flow ("anti-Schlichting" flow) under the crystal. However, when the interface shifts below the free surface (Figure 3.6b) a couple of new primary vortices (rotating in the same direction as the former flow) appear in the meniscus. This results in formation of secondary flow, which occupies all the space under the crystal. The further penetration of crystal into a liquid (Figure 3.6c) leads to growth of primary vortices and a corresponding realignment of the secondary flow. The detailed investigation of this phenomenon in dependence on *h* and Re_v values was performed in Refs [59, 98].

Intensive axial low-frequency vibration applied to a vibrating body in Czochralski configuration produces not only bulk flow, but also complex surface flow (Figure 3.7). It is polyharmonic motion that includes two different but closely related flows [84]. The first of these is a standing surface wave that expands from the vibrating

Figure 3.7 Surface flow induced by low-frequency axial vibration (distilled water, vibration with $f = 30\,\text{Hz}$, $A = 300\,\mu\text{m}$, $\text{Re}_v = 1117$).

crystal to the crucible wall. The other type of flow superimposed on this wave appears as large vortices, similar to cells, the dimension of which is several times greater than the length of the surface wave. The surface vortices could be involved in a slow motion around crucible axis in a ring gap between a vibrating crystal and a crucible wall. Additional effect produces the crucible rotation, which creates a shearing perturbation. It leads to a reduction of a number of surface vortices by their association into pairs [98]. The wavelengths, number of vibrational vortices, and velocity of motion of the liquid in them are controlled by the vibration parameters. For instance, in the case presented on Figure 3.7 the number of surface vortices is 8 and the velocity of surface flow $V = 2.2\,\text{cm/s}$.

The numerical calculations of interaction between the low-frequency vibration ($A = 100\,\mu\text{m}$, $f = 50\,\text{Hz}$) and the Marangoni convection (Mn = 500) showed [94] that the vibration weakens the influence of the thermocapillary Marangoni convection in Czochralski crystal growth. The vibration makes the temperature distribution at the free surface more homogeneous. This decreases the temperature gradient along the melt surface and reduces the Marangoni convection intensity. So, the phenomenon of complex surface flow formation gives a unique opportunity to control/compensate undesirable surface flows caused by both thermocapillary and thermoconcentration Marangoni convections [84].

Recently, a new scheme of AVC introduction in the Czochralski configuration has been proposed [88]. In fact, it is a kind of combination of Czochralski and AVC-assisted Bridgman methods. According to this scheme (Figure 3.8) the forced flows in the melt are generated by axial oscillations of a disk submerged under the crystal. The experiments were performed on model water–glycerin mixtures with viscosities from 1 to 100 cP and by crystal growth from an optically transparent $NaNO_3$ melt ($\eta = 2.25\,\text{cP}$ at $T_{\text{melt}} = 580\,\text{K}$). It was found that this new scheme can produce stable symmetric vibrational bulk flows within the entire range of viscosities during overheating of the crucible walls in relation to the growth interface up to 60 K. According to the results of physical model experiments proved by

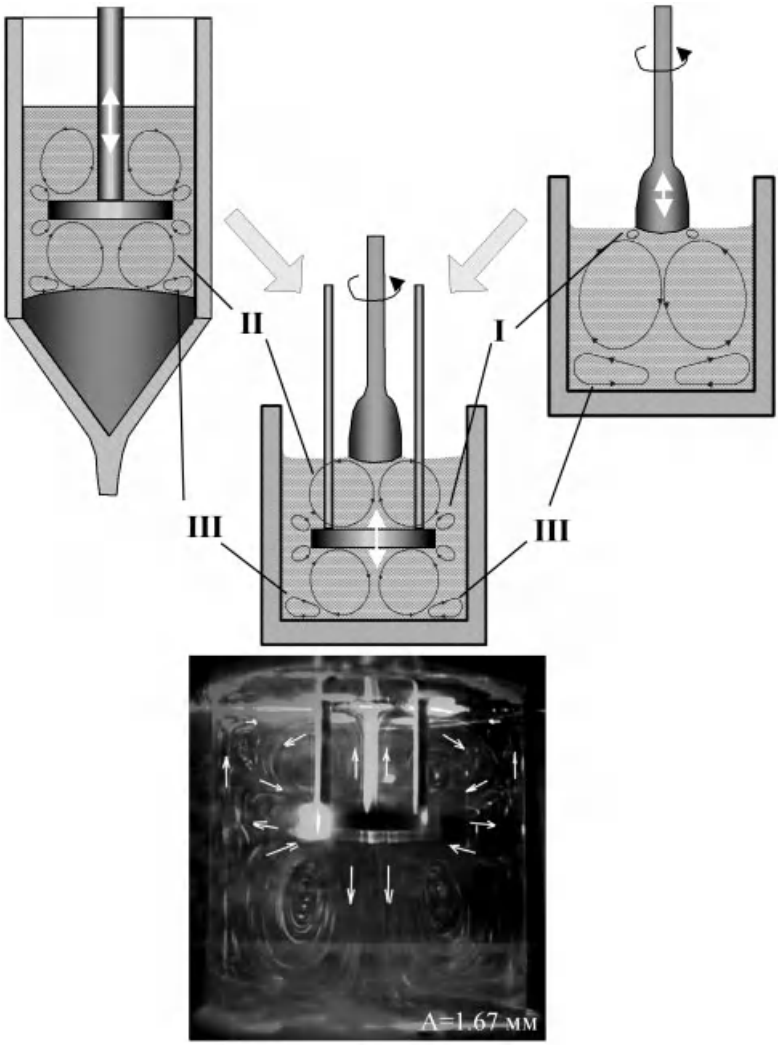

Figure 3.8 Scheme of insertion of axial vibration into a melt by submerged vibrating disk and photo of flow pattern in model experiment (distilled water, vibration with $f = 50$ Hz, $A = 1.67$ mm). Numbers indicate primary (I), secondary (II), and ternary (III) bulk flows.

numerical simulation results obtained with the use of Fluent 6.4 software, the application of the new version of the AVC-CZ technique provides temperature leveling over the full melt volume. For this configuration it was also shown that dislocation density could be the same in "vibrational" $NaNO_3$ crystals grown at growth rates four times larger compared to crystals fabricated by a regular Czochralski process without vibration. Another impressive result was found by studies of the Raman spectra of the grown single crystals. It was found [88] that AVC

influences the vibrational and rotational modes of NO_3^- groups at Na atoms in the $NaNO_3$ structure, reducing the half-width and intensity ratio of characteristic Raman peaks that confirms the refinement of structure perfection of single crystals.

Up to now, the AVC-assisted crystal growth by the Czochralski method has been realized for $NaNO_3$ and some complex oxides with garnet structure, in particular, Er,Cr:YSGG discussed above. In addition, the authors of Ref. [99] reported a successful growth of $BaTiO_3$ and $K(Ta_{1-x}Nb_x)O_3$ with composition $0.30 < x < 1$ using the AVC technique with a vibration frequency of 50 Hz and an amplitude of 0.5 mm by the TSSG method. They considered these vibration parameters as optimal growth conditions to produce striation-free $K(Ta_{1-x}Nb_x)O_3$ samples.

3.4 AVC-Assisted Bridgman Method

The problem of effective control of heat–mass transfer is essentially important for vertical Bridgman growth configuration due to its low efficiency of heat-mass transport. It makes the use of external force fields in a Bridgman process very desirable and promising. As experiments have shown, closed-ampoule translational vibration under isothermal conditions does not result in any flow. The liquid in this case behaves as a rigid body. Buoyancy driven vibroconvective motion occurs when oscillatory displacement of a container wall induces the acceleration of a container wall relative to the inner fluid. The vibrations of an ampoule with a free surface can produce rather intensive flows. However, these currents are limited by the surface and cannot exert much influence directly on the crystallization front.

In the presence of an axial temperature gradient when the fluid density is nonuniform, fluid motion may ensue. However, the magnitude of this motion depends on the orientation of the vibrational direction with respect to the local density gradients. In Ref. [100] the angle between the direction of vibration and the ampoule has been studied for translational vibrations in the presence of an axial temperature gradient. It was shown that axial vibration of the ampoule is the least efficient and the maximum observed effect corresponds to an angle of 90 degrees.

There are several papers that discuss low-frequency vibration axially applied to the ampoule in vertical Bridgman growth [101–104]. It is not surprising that no notable effect of vibration on microstructure, compositional profile, interface shape, etc. was found [101, 102] for such a configuration of experiment. Nevertheless, the investigation of crystal quality performed in a recent paper [104] has shown that low-frequency axial vibration applied even to a growth ampoule can produce a perceptible effect. This paper was devoted to growth of $Bi_{12}SiO_{20}$ crystals by vertical Bridgman under 50-Hz ampoule vibration with amplitudes within the 50–100 μm range. Extension of the short-wavelength spectral absorption edge was observed and a corresponding squeeze of X-ray rocking curves in a certain range of vibration amplitudes that is evidence for improvement of crystal perfection.

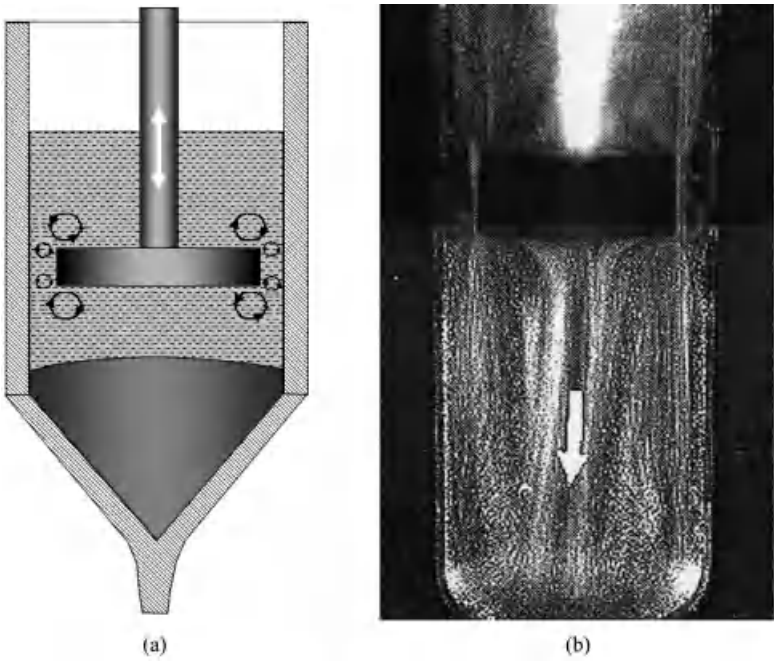

Figure 3.9 AVC-assisted Bridgman technique: (a) insertion of axial vibration; (b) the flow pattern.

A significantly more efficient influence, compared to ampoule vibration, is produced by the insertion of a submerged body, which locates near the crystal/melt interface and oscillates in the melt (Figure 3.9) with a frequency of tens Hz and an amplitude of tens to hundreds micrometers, inducing macroscopic vibrational convection flows. Disks appear to be the simplest way to introduce vibrations that result in controllable axially symmetric flow.

The experiments performed in Ref. [105] showed that insertion of a motionless baffle into an ampoule with $NaNO_3$ melt resulted in retardation of heat transfer and prevented heat exchange between the upper and lower parts of melt in the ampoule. It also led to a change of flow pattern of the natural convection (Figures 3.10a and b). In the absence of vibration, the crystal/melt interface is slightly convex to the melt. Switching on the vibration resulted in formation of a vibrating flow near the disk (Figure 3.10c). Flow from a vibrator body down to a crystal causes a displacement of the crystal/melt interface and deflects it toward the crystal. Manipulation of the amplitude–frequency input can be used to obtain a practically flat crystal/melt interface (Figure 3.10d). The flow strength grew with increase in vibration amplitude and resulted in considerable ordering at $Re_v = 1290$ [105]. Very large amplitudes cause unstable flows with no axial symmetry that prevailed over the entire volume.

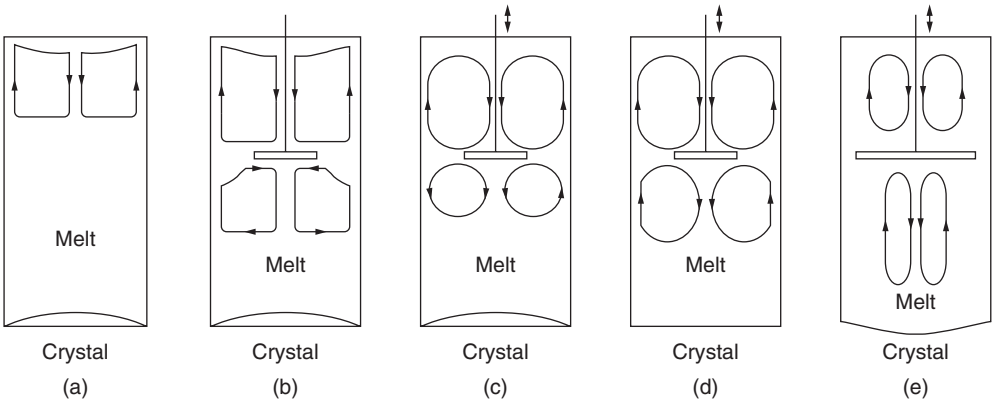

Figure 3.10 Flow patterns in $NaNO_3$ melt ($\nu = 1.47 \times 10^{-2}\,cm^2\,s^{-1}$) in Bridgman configuration. (a) free melt; (b) melt with motionless vibrating body, $S_k = 2.33$; (c) vibration $f = 50\,Hz$, $A = 200\,\mu m$, $Re_v = 684$, $S_k = 2.33$; (d) $f = 66\,Hz$, $A = 300\,\mu m$, $Re_v = 1354$, $S_k = 2.33$; (e) $f = 50\,Hz$, $A = 300\,\mu m$, $Re_v = 1026$, $S_k = 2.33$; (f) $f = 50\,Hz$, $A = 300\,\mu m$, $Re_v = 1026$, $S_k = 0.96$.

Changing the diameter of the vibrating baffle considerably altered the flow pattern in the melt. The normalized difference between the cross-sectional area of the ampoule and the cross-sectional area of the vibrator is used as a geometrical parameter and is

$$S_k = \frac{D^2}{d^2} - 1.$$

Here,

D, internal diameter of ampoule;
d, diameter of vibrating body.

For S_k equal to 2.33, the introduction of the (nonvibrating) baffle into the melt resulted in two separate, but similar, flow structures in the top and bottom parts of the ampoule. Under vibration, the pre-existing flow structure is retained, but it increased in intensity with increasing vibration amplitude. In the area close to the crystallization front there is a practically isothermal and motionless layer of melt. The thickness of this layer decreased with increasing vibration amplitude.

In the system with S_k equal to 0.96, and all other conditions the same, the increase of the disk size has a pronounced effect on the flow structure (Figure 3.10e). The flow intensity sharply increases. At $Re_v = 1300$, in contrast to the previous case, axial symmetry is lost. Furthermore, the flow reached the crystal surface. This results in a deflection of the crystal/melt interface toward the crystal (Figure 3.10e).

AVC-assisted crystal growth by the Bridgman method has been realized for both low melting point and high melting point dielectric and semiconductor materials [106–109]. In particular, AVC-BR technique was adapted for growth of $NaNO_3$, AbBr, AgBrCl, PbTe, and CdTe crystals and the corresponding equipment for

crystal growth was fabricated including an AVC-assisted computer-controlled transparent furnace for growth of low melting point compounds [106] and a high-temperature sealed furnace for crystallization of decomposing materials [107].

It was shown that crystal growth under axial vibration results in substantial increase of growth rate (from 2 mm/h to 10 mm/h for $NaNO_3$ crystals) without loss of crystal quality [108]. The solid/liquid growth interface shape and position have been measured as a function of vibrational parameters. The interface could be controlled very finely from slightly convex to concave. Other measurements include growth rates, dopant (Ag) concentration profiles and dislocation density as a function of forced convection parameters [88, 108]. The reason for the significant decrease of dislocation density and substantial enhancement of the growth rate along with maintenance of crystal quality could be the influence of the vibrational force on heat and mass transfer at the interface as well as its influence on precrystallization phenomena that stimulate the destruction of clusters in the liquid at the boundary layer due to insertion of additional energy.

It was demonstrated [108] that the AVC technique produces an effective distribution coefficient that approaches the equilibrium value. In fact, the growth process needs the deviation from equilibrium. Usually, this deviation is realized by a temperature gradient or chemical potential gradient at the solid/liquid interface. Insertion of vibration gives us the additional force, which makes possible the decrease in chemical potential gradient. In this case, the system under vibration could be far from equilibrium conditions while the chemical potentials of the components in the vapor, melt and crystal can be very close to the equilibrium ("nonvibrational") values.

The measurements showed [108] that for a "nonvibrating" $NaNO_3$ crystal K_{eff} (Ag) = 0.88, while for the crystal grown at f = 50 Hz and A = 200 μm the K_{eff} (Ag) = 0.78, which is close to the equilibrium value K_0(Ag) = 0.76. So, by varying the vibration parameters one can govern the effective distribution coefficient and, practically, control the impurity distribution in the growing crystal.

This result showing the increase of the average degree of segregation due to oscillational impact on the growth interface does not support the conclusions of theory [92] that predicting the opposite situation, that is, the shift of the effective distribution coefficient toward unity in the presence of growth-rate fluctuations (temperature fluctuations) in the melt. The possible reason for this contradiction is the versatile effects of low-frequency small-amplitude vibrations on crystal growth. In contrast to the temperature fluctuations the vibrations result not only in the interface oscillation but also drastically change the temperature distribution and decrease the thickness of boundary layers (see below). An additional reason for the contradiction could be the fact that theory [92] does not take into account the role of latent heat of solidification, which has a huge effect on the oscillation velocity and the time constant of heat transfer [110].

Numerical modeling of the process discovered other new interesting effects of vibration [87, 93, 94]. AVC can vary the value of the temperature gradient at the interface that has the critical importance for improvement of growth technologies because it allows the kinetics and rate of crystal growth to be varied. In particular,

vibration can decrease the thickness of the boundary layer and enhance the gradients of temperature at the interface [87, 93]. It intensifies the heat–mass transfer in the growth process and increases the growth rate. On the other hand, the change of hydrodynamic situation and temperature conditions near the interface gives the possibility to control the shape of crystallization front. The interface can be controlled very finely from convex to concave one.

The boundary layers thickness depends on the amplitude, the frequency and, also on the Prandtl number of the melt. The calculations indicate that for small values of Prandtl number Pr = 0.01 that are typical for semiconductors, the use of frequency $f = 50\,\text{Hz}$ and amplitude $A = 100\,\mu\text{m}$ is not suitable due to low viscosity and high thermal conductivity of melts. In this case, the influence of vibrations on the temperature boundary layer thickness is rather weak. This influence in melts with small Prandtl numbers will be essential with increasing amplitude and the frequency of vibration (with increase of vibrational Reynolds number Re_v).

The calculations [93] also show that along with an increase of vibration frequency of the baffle from $f = 10\,\text{Hz}$ to $f = 100\,\text{Hz}$ the intensity of the averaged vibrational flow also grows, while its direction could change from clockwise to anticlockwise due to exchange of momentum between vortices. This gives us one more tool to govern the heat and mass transfer during crystal growth.

3.5 AVC-Assisted Floating Zone Method

Several authors have investigated the use of axial vibration in the floating zone method [111–115]. Experimental studies were performed in Refs [111–113]. The controlled vibration induces a flow that streams away from the vibrating end wall along the zone surface, returning through the bulk [111]. Vibration effectively minimizes detrimental thermocapillary convection in a float zone due to the opposite flow direction. In Ref. [116] was found that for a low-viscosity liquid, the streaming pattern changes sign when the oscillation is adjusted from one side of a resonant peak to the other. This allows for more flexibility in the application of the streaming to counteract thermocapillary convection, during crystal growth in a float zone.

The authors of Ref. [112] showed that vibration with frequency $f = 65\,\text{Hz}$ and amplitude $A = 80\,\mu\text{m}$ reduces both the zone length and the temperature fluctuation in $NaNO_3$ melt as well as making the growth interface flatter compared to the nonvibrating growth process. Vibration at 5 kHz with an amplitude of 0.1 μm during silicon growth under terrestrial conditions [113] also produced an influence on the heat transport and on the interface curvature. In the case of eutectic solidification of $NaNO_3$-$Ba(NO_3)_2$ [111, 117], a flattening of the interface, that is, a reduction of radial temperature gradients was observed, as well as a change in the eutectic microstructure upon application of the vibration. Temperature measure-

ments in the zone [111] verify that vibration essentially eliminates radial temperature gradients ahead of the growth interface.

The numerical simulation of fluid flow and heat transfer in crystal growth by floating zone subjected to axial vibration was performed for the case of silicon [114]. In calculations, the vibration amplitude was varied in the range of 3 to 4.5 μm and the vibration frequency lay in the interval of 2 to 4.5 kHz. It was shown that both under zero gravity and 1-g conditions, in spite of a higher-frequency range the vibrations led to a significant suppression of thermocapillary flow near the crystal/melt interface and a flattening of the crystallization front. Although the vibration of only one of the rods reduces the intensity of the thermocapillary flows it could counterbalance it completely. For that, both rods have to be vibrated. Numerical simulation of flows and heat and mass transfer in the liquid zone subjected to high-frequency synchronous vibrations of the crystal and the feed rod was carried out in Ref. [118].

In Ref. [115] the ampoule zone melting assisted by vibration with the frequency ranging from 0.1 to 100 Hz was considered. As a model system the 2-cm GaAs in a quartz ampoule was using for the calculations. Also, for this case it was confirmed that the axial vibrations are effective for the control of melt flows and the growth interface.

3.6 Conclusions

In conclusion, axial vibrational control is a powerful method to govern the heat and mass transfer and growth kinetics during crystallization from liquid phase. The introduction of low-frequency (tens to hundreds of Hz) and small-amplitude (up to hundreds of μm) axial vibration into a liquid phase allows the growth of high-quality crystals with high growth rates, providing control of stoichiometry and dopant distribution. An important advantage of the AVC method compared to other ways of creation of forced convection is connected with the fact that the most significant impact on crystal growth occurs in the vicinity of the solid/liquid interface.

Besides the obvious advantages such as precise control of heat and mass transfer in the melt and creation of the necessary temperature conditions at the interface and its shape, the AVC method also suppresses the temperature oscillation at the interface, manipulates the impurity insertion and its distribution both radially and longitudinally. In contrary to the frequently used magnetic field, the AVC technique can be applied to nonelectroconducting melts and liquids with high Prandtl numbers that is important for the development of the technology of various dielectric materials.

Using axial vibration it is possible to vary the thickness of boundary layers at the solid/liquid interface. This is of principal importance for improvement of crystal-growth technologies due to the possibility to use the vibrations to control

the temperature gradients at the solid/liquid interface, that is, to control the kinetics and rate of crystal growth.

The flow formation is governed by variation of the vibrational Reynolds number and also by specific parameters like the edge sharpness of the vibrating crystal or baffle, and ring gap between the ampoule and the vibrating body (in vertical Bridgman), and the penetration depth of the vibrating crystal (in Czochralski configuration). The phenomena of reversing the direction of the vibrational flow is also considered and explained. Interaction of vibrational and natural convections as well as their interplay with rotation of the crystal and crucible was discussed.

The AVC technique was adapted for growth of both low melting point and high melting point dielectric and semiconductor materials by four important crystal growth methods: Czochralski, TSSG, Bridgman and floating zone techniques.

In general, the AVC method is promising for use not only in crystal growth, but in many other liquid-phase technologies: displacement of liquid-phase products in chemical reactors; stirring of fluids, suspensions, fabrication of gradient materials, etc.

Acknowledgments

The author is indebted to the many coworkers who contributed to the work described in this chapter. I gratefully thank my colleagues and students from the General Physics Inst. of Russian Acad. Sci. (L.N. Prikhod'ko, N.R. Storozhev, A.Z. Myaldun), the Inst. of Problems in Mechanics RAS (A.I. Fedyushkin, A.I. Prostomolotov, N.A. Verezub), Mendeleev Univ. (I.Kh. Avetisov, E.M. Koltsova, V.A. Kostikov, A.N. Kovalenko, A.P. Sadovskii and A.Yu. Zinoviev).

I am also grateful to Prof. P. Rudolph for a critical reading of this chapter and valuable advice.

References

1 Whiffin, P.A.C., Brice, J.C., *et al.* (1971) *J. Cryst. Growth*, **10**, 91–96.

2 Scheel, H.J. (2003) *Crystal Growth Technology* (eds H.J. Scheel and T. Fukuda), John Wiley & Sons, Ltd, Chichester, pp. 69–91.

3 Carruthers, J.R., and Nassau, K. (1968) *J. Appl. Phys.*, **39**, 5205–5214.

4 Brandle, C.D. (1977) *J. Cryst. Growth*, **42**, 400–404.

5 Hurle, D.T.J., and Series, R.W. (1994) Use of a magnetic field in melt growth, in *Handbook of Crystal Growth*, vol. 2a (ed. D.T.J. Hurle), North-Holland, Amsterdam, pp. 259–286.

6 Von Ammon, W., Gelfgat, Yu., Gorbunov, L., Muehlbauer, A., Muiznieks, A., Makarov, Y., Virbulis, J., and Mueller, G. (2005) Proc. Joint 15th Riga and 6th Pamir Intern. Conf. Fundamental and Applied M H D, Riga, Jurmala, Latvia, June 27–July 1, 2005, pp. 41–54.

7 Dold, P., and Benz, K.W. (1999) *Progr. Cryst. Growth Charac. Mater.*, **38**, 7–38.

8 Rudolph, P. (2008) *J. Cryst. Growth*, **310**, 1298–1306.

9 Pfann, W.G., and Wagner, R.S. (1962) *Trans. Met. Soc. AIME*, **224**, 1139–1146.

10 Nassau, K., Levinstein, H.J., and Loiacono, G.M. (1966) *J. Phys. Chem. Solids*, **27**, 989–996.

11 Walsh, F.C., and Herron, M.E. (1991) *J. Phys. D: Appl. Phys.*, **24**, 217–225.

12 Budevski, E., Staikov, G., and Lorenz, W.J. (2000) *Electrochim. Acta*, **45**, 2559–2574.

13 Kokh, A.E., and Kononova, N.G. (2000) *Solid State Electron.*, **44**, 819–824.

14 Rodot, H., Regel, L.L., Sarafanov, G.V., Hamidi, H., Videskii, I.V., and Turtchaninov, A.M. (1986) *J. Cryst. Growth*, **79**, 77–83.

15 Friedrich, J., Baumgartl, J., Leister, H.-J., and Mueller, G. (1996) *J. Cryst. Growth*, **167**, 45–63.

16 Ostrogorsky, A.G., Mosel, F., and Schmidt, M.T. (1991) *J. Cryst. Growth*, **110**, 950–954.

17 Golyshev, V.D., and Gonik, M.A. (1991) *Cryst. Prop. Prep.*, **36–38**, 623–630.

18 Scheel, H.J., and Schulz-Dubois, E.O. (1971) *J. Cryst. Growth*, **8**, 304–306.

19 Capper, P. (2008) *Crystal Growth Technology* (eds H.J. Scheel and P. Capper), Wiley-VCH Verlag GmbH, Weinheim, Germany, pp. 283–306.

20 Yu, W.C., Chen, Z.B., Hue, W.T., Roux, B., Lyubimova, T.P., and Lan, C.W. (2004) *J. Cryst. Growth*, **271**, 474–480.

21 Lu, Y.C., Wolf, M.F., Elwell, D., and Feigelson, R.S. (1987) *J. Cryst. Growth*, **82**, 589–597.

22 Zawilski, K.T., Custodio, M.C.C., DeMattei, R.C., and Feigelson, R.S. (2005) *J. Cryst. Growth*, **282**, 236–250.

23 Kapustin, A.P. (1962) *Influence of Ultrasound on Crystallization Kinetics*, Acad. Sci. USSR, Moscow (in Russian).

24 Kozhemyakin, G.N. (2003) *J. Cryst. Growth*, **257**, 237–244.

25 Dost, S., and Okano, Y. (eds) (2007) *Crystal Growth under Applied Fields*, Transworld Research Network, Kerala, India.

26 Rudolph, P., and Kakimoto, K. (2009) *MRS Bull.*, **34**, 251–258.

27 Barmin, I.V., Senchenkov, A.S., Avetisov, I.Ch., and Zharikov, E.V. (2005) *J. Cryst. Growth*, **275**, e1487–e1493.

28 Yeckel, A., and Derby, J.J. (2000) *J. Cryst. Growth*, **209**, 734–750.

29 Lan, C.W. (2005) *J. Cryst. Growth*, **274**, 379–386.

30 Zharikov, E.V., Prihod'ko, L.V., and Storozhev, N.R. (1989) The phenomenon of formation of steady-state fluid flow under solid body vibration. Preprint No. 18, General Phys. Inst. Acad. Sci. USSR, Moscow, pp. 1–10 (in Russian).

31 Zharikov, E.V., Prihod'ko, L.V., and Storozhev, N.R. (1990) *J. Cryst. Growth*, **99**, 910–914.

32 Gershuni, G.Z., and Lubimov, D.V. (1998) *Thermal Vibrational Convection*, John Willey & Sons, Ltd, New York.

33 Shubnikov, A.V. (1947) *Origin of Crystals*, Izd. AN SSSR, Moscow (in Russian).

34 Dugua, J., and Simon, B. (1978) *J. Cryst. Growth*, **44**, 280–286.

35 Chernov, A.A. (1980) *Modern Crystallography, Vol. III Origin of Crystals*, Nauka, Moscow, pp. 7–232 (in Russian).

36 Cherepanova, V.K., Cherepanov, A.N., Sharapov, V.N., and Plaksin, S.I. (2009) *Geochem. Int.*, **47**, 454–462.

37 Eldarkhanov, A.S. (1996) *Crystallization Processes in Field of Elastic Waves*, Metallurgia, Moscow (in Russian).

38 Shore, M., and Fowler, A.D. (1996) *Can. Mineral.*, **34**, 1111–1126.

39 Witt, A.F., and Gatos, H.C. (1968) *J. Electrochem. Soc.*, **115**, 70–75.

40 Haase, C.S., Chadam, J., Feinn, D., and Ortoleva, P. (1980) *Science*, **209**, 272–274.

41 Wang, Y., and Merino, E. (1995) *Am. J. Sci.*, **295**, 49–77.

42 Wang, M., Yin, X.B., Vekilov, P.G., Peng, R.W., and Ming, N.B. (1999) *Phys. Rev. E*, **60**, 1901–1905.

43 Landau, A.I. (1958) *Fizika tverdogo tela*, **6**, 148 (in Russian).

44 Kibalczyc, W., and Kolasinski, W. (1977) *Zesz Nauk Politech Lodz.*, **271**, 51–62 (in Polish).

45 Geilikman, M.B., and Temkin, D.E. (1982) *JETF Lett.*, **36**, 292–295.

46 Yanukyan, E.G. (2004) *Oscillatory Processes of Crystallization and Dissolution of Polydispersive Particle Systems*, Rostizdat, Rostov on Don (in Russian).

47 Sibley, D.F., Vogel, T.A., Walker, B.M., and Byerly, G. (1976) *Am. J. Sci.*, **276**, 275–284.

48 Tsune, A., and Toramaru, A. (2007) *Am. Mineral.*, **92**, 1071–1079.

49 Ubbelhode, A.R. (1965) *Melting and Crystal Structure*, Clarendon Press, Oxford.

50 Mirzade, F.Kh. (2006) *J. Phys. D: Appl. Phys.*, **39**, 1437–1441.

51 Fedorov, P.P., and Meleshina, V.A. (1999) *Doklady*, **364**, 498–502 (in Russian).

52 Perugini, D., Poli, G., and Valentini, L. (2005) *Contrib. Mineral. Petrol.*, **149**, 482–497.

53 Amelin, K.S., Shtukenberg, A.G., Punin, Yu.O., and Smetannikova, O.G. (2007) *Crystallogenesis and Mineralogy*, Izd. SPbGU, Saint Petersburg, 225–227 (in Russian).

54 Halden, N., and Hawthorne, F.C. (1993) *Am. Mineral.*, **78**, 1113–1116.

55 Holten, T., Jamtveit, B., Meakin, P., Cortini, M., Blundy, J., and Austrheim, H. (1997) *Am. Mineral.*, **82**, 596–606.

56 Fedorov, P.P. (2005) *Russian J. Inorg. Chem.*, **50**, 1933–1941.

57 Vitovskii, B.V. (1955) Increasing the growth rate of crystal by oscillations of sonic frequency. Proc. Inst. Crystallography Acad. Sci. USSR, vol. 11, pp. 221–222 (in Russian).

58 Zharikov, E.V., Prikhod'ko, L.V., and Storozhev, N.R. (1993) *Growth of Crystals*, vol. 19 (eds E.I. Givargizov and S.A. Grinberg), Consultants Bureau, New York, pp. 71–81.

59 Myal'dun, A.Z., Prostomolotov, A.I., Tolochko, N.K., Verezub, N.A., and Zharikov, E.V. (2002) *Growth of Crystals*, vol. **21** (eds E.I. Givargizov and A.M. Melnikova), Kluwer Academic Publishers, New York, pp. 181–196.

60 Danilov, V.I. (1956) *Structure and Crystallization of a Liquid*, Izd. Acad. Sci. USSR, Kiev (in Russian).

61 Borshchevskii, A.S., and Tretyakov, D.N. (1959) *Fiz. Tverd. Tela*, **1**, 1483–1485 (in Russian).

62 Kh, S., and Bagdasarov (1959) *Application of Ultrasound in Industry*, Mashgiz, Moscow (in Russian).

63 Langanecker, B., and Fransen, W.H. (1962) *Philos. Mag.*, **7**, 2079–2085.

64 Witt, A.F., and Gatos, H.C. (1967) *J. Electrochem. Soc.*, **114**, 413–414.

65 Arakelyan, V.S., and Avetisyan, A.G. (1988) *Kristallografiya*, **33**, 1239–1243 (in Russian).

66 Hayakawa, Y., Nagura, M., and Kumagawa, W. (1988) *Semicond. Sci. Technol.*, 372–376.

67 Nikitina, G.V., Romanenko, V.N., and Tuchkevich, V.S. (1962) *Crystallization and Phase Transitions*, Izd. Acad. Sci. USSR, Minsk, pp. 379–385 (in Russian).

68 Klubovich, V.V., Kashevich, I.F., Mikhnevich, V.V., and Tolochko, N.K. (1984) *Kristallografiya*, **29**, 822–823 (in Russian).

69 Agranat, B.A., Dubrovin, M.N., and Khavskii, N.N. (1976) *Akust. Zh.*, **22**, 141–142 (in Russian).

70 Petrov, T.G. (1960) Method of growing single crystals, USSR Pat. No. 136,057 (in Russian).

71 Ship, V., and Vanichek, V. (1962) *Growth of Crystals*, vol. **3** (eds A.V. Shubnikov and N.N. Sheftal), Consultants Bureau, New York, pp. 191–195.

72 Klubovich, V.V., Tolochko, N.K., and Kashevich, I.F. (1985) *Izv. Akad. Nauk BSSR, Ser. Fiz.-Mat. Nauk*, **6**, 42–47 (in Russian).

73 Wheeler, A.A. (1982) *J. Cryst. Growth*, **56**, 67–76.

74 Manucharyan, S.M., and Nalbandyan, H.G. (1982) *Cryst. Res. Technol.*, **17**, 295–298.

75 Walker, C.T., and Adams, C.E. (1959) *J. Acoust. Soc. Am.*, **31**, 813–814.

76 Arkhangelskii, M.E. (1967) *Usp. Fiziol. Nauk*, **92**, 181–206 (in Russian).

77 Zharikov, E.V., Prikhod'ko, L.V., and Storozhev, N.R. (1989) *Cryst. Res. Technol.*, **24**, 761–765.

78 Avdonin, N.A., Zharikov, E.V., Kalis, Kh.E., and Storozhev, N.R. (1989) Analysis of secondary fluid flows nearby vibrating surface. Preprint of General Physics Inst., No. 90, pp. 1–18.

79 Belotserkovskii, O.M. (1984) *Numerical Modeling in Continuous Media Mechanics*, Nauka, Moscow.

80 Nyborg, W.L. (1965) Acoustic streaming, in *Physical Acoustics*, vol. IIB (ed. W.P. Mason), Academic Press, New York, pp. 265–331.

81 Schlichting, G. (1979) *Boundary-Layer Theory*, 7th edn, McGraw-Hill, New York.

82 Sorokodum, E.D. (1973) *Akust. zh.*, **19**, 767–772 (in Russian).

83 Lyubimov, D.V., Lyubimova, T.P., Meradji, S., and Roux, B. (1997) *J. Cryst. Growth*, **180**, 648–659.

84 Verezub, N.A., Zharikov, E.V., Myaldun, A.Z., and Prostomolotov, A.I. (1996) *Doklady Acad. Sci.*, **350**, 474–477.

85 Agranat, B.A., Dubrovin, M.N., Khavskii, N.N., and Eskin, G.I. (1987) *Principles of Physics and Techniques of Ultrasound*, Vysh. Shkola, Moscow (in Russian).

86 Bagdasarov, Kh.S. (1958) *Kristallografiya*, **3**, 110–112 (in Russian).

87 Fedyushkin, A.I., Bourago, N.G., Polezhaev, V.I., and Zharikov, E.V. (2001) *Proc. VII Russian Symp. Mechanics of Microgravity*, IPM RAS, Moscow, pp. 365–392 (in Russian).

88 Avetisov, I.Ch., Zharikov, E.V., Zinovjev, A.Yu., and Sadovski, A.P. (2009) *Dokl. Phys.*, **54**, 410–412.

89 Rosenberger, F. (1979) *Fundamentals of Crystal Growth I. Macroscopic Equilibrium and Transport Concepts*, Springer-Verlag, Berlin, Heidelberg, New-York.

90 Hurle, D.T.J., and Rudolph, P. (2004) *J. Cryst. Growth*, **264**, 550–564.

91 Haddad, F.Z., Garandet, J.P., Henry, D., and Ben Hadid, H. (1999) *J. Cryst. Growth*, **204**, 213–223.

92 Hurle, D.T.J., and Jakeman, E. (1969) *J. Cryst. Growth*, **5**, 227–232.

93 Fedyushkin, A., Bourago, N., Polezhaev, V., and Zharikov, E. (2005) *J. Cryst. Growth*, **275**, e1557–e1563.

94 Fedyushkin, A.I., and Bourago, N.G. (2001) Proc. 2nd Pan Pacific Basin Workshop on Microgravity Sciences, Pasadena, USA, paper CG-1072.

95 Verezub, N.A., Zharikov, E.V., Myaldun, A.Z., and Prostomolotov, A.I. (1996) *Crystallogr. Rep.*, **41**, 335–342.

96 Fedyushkin, A.I., Bourago, N.G., Polezhaev, V.I., and Zharikov, E.V. (2001) Proc. 2nd Pan Pacific Basin Workshop on Microgravity Sciences, 2001, Pasadena, USA, paper CG-1065.

97 Verezub, N.A., Zharikov, E.V., Kalitin, S.P., Lavrishchev, S.V., Myaldun, A.Z., Papin, Yu.M., and Prostomolotov, A.I. (1996) *Crystallogr. Rep.*, **41**, 1056–1060.

98 Verezub, N.A., Zharikov, E.V., Myaldun, A.Z., Prostomolotov, A.I., and Tolochko, N.K. (1996) *Crystallogr. Rep.*, **41**, 151–157.

99 Hesse, H., and Pankrath, R. (1993) Conf. Photorefractive Materials, Effects, and Devices, Kiev, Ukraine, Technical Digest, p. 192. Pankrath, R., Doeppner, K., Kuper, C., and Hesse, H. (1995) XI-th Intern. Conf. Cryst. Growth, Hague, The Netherlands, Abstracts, p. 131; http://www.sfb225.uos.de/bericht2000/ba01.pdf

100 Fedoseyev, A.I., and Alexander, J.I.D. (2000) *J. Cryst. Growth*, **211**, 34–42.

101 Caram, R., Banan, M., and Wilcox, W.R. (1991) *J. Cryst. Growth*, **114**, 249–254.

102 Yuan, W., Banan, M., Regel, L.L., and Wilcox, W.R. (1995) *J. Cryst. Growth*, **151**, 235–242.

103 Fengouan, W., Shiyu, C., Deping, H., and Bingbo, W. (1994) *J. Mater. Sci.*, **29**, 3997–4000.

104 Zhang, Y., Liu, Y., Jiang, W., Pan, X.H., Jin, W.Q., Ai, F., and Wang, H.C. (2009) *Cryst. Res. Technol.*, 248–252.

105 Zharikov, E.V., Myaldun, A.Z., Prostomolotov, A.I., Skorenko, A.V., and Verezub, N.A. (2000) *Vibrational Effects in Fluid Dynamics* (eds G.Z. Gershuni and I. Alexander), Perm State Univ., Perm, pp. 1–10.

106 Avetisov, Kh., Zharikov, E.V., Zinov'ev, A.Yu., and Mel'kov, A.Yu. (2004) *Instrum. Exp. Tech.*, **47**, 554–561.

107 Avetisov, Kh., Mel'kov, A.Yu., Zinov'ev, A.Yu., and Zharikov, E.V. (2005) *Crystallogr. Rep.*, **50** (Suppl. 1), S124–S129.

108 Avetissov, I.Ch., Zinovjev, A.Yu., Romanenkov, M.V., Romanenkova, L.V., and Zharikov, E.V. (2005) New Achievements in Materials Science. Proc. II France–Russia Seminar, Moscow, 10–12 November, 2005, pp. 48–51.

109 Korsakov, A.S., Zhukova, L.V., Zharikov, E.V., Vrublevsky, D.S., and Korsakov, V.S. (2010) *Tsvet. Metal.*, **1**, 69–72 (in Russian).

110 Stelian, C., Duffar, T., Santailler, J.-L., and Nicoara, I. (2002) *J. Cryst. Growth*, **237–239**, 1701–1706.

111 Shen, X.F., Anilkumar, A.V., Grugel, R.N., and Wang, T.G. (1996) *J. Cryst. Growth*, **165**, 438–446.

112 Verezub, N.A., Myaldun, A.Z., and Prostomolotov, A.I. (1997) Heat and Mass Transfer and growth of single crystals and thin film structures. Proc. 2nd Russian Symp., Obninsk, 22–24 Sept., 1997, pp. 110–118 (in Russian).

113 Dold, P., Benz, K.W., Croell, A., Roux, B., Lyubimov, D., Lyubimova, T., and Scuridin, R. (2001) *Acta Astronaut.*, **48**, 639–646.

114 Lyubimova, T.P., Scuridin, R.V., Croell, A., and Dold, P. (2003) *Cryst. Res. Technol.*, **38**, 635–653.

115 Lan, C.W. (2000) *Int. J. Heat Mass Transfer*, **43**, 1987–1997.

116 Anilkumar, A.V., Lee, C.P., and Wang, T.G. (1996) *Phys. Fluids*, **8**, 03234–03246.

117 Grugel, R.N., Shen, X.F., Anilkumar, A.V., and Wang, T.G. (1994) *J. Cryst. Growth*, **142**, 209–214.

118 Lyubimov, D.V., Lyubimova, T.P., and Roux, B. (1997) *Int. J. Heat Mass Transfer*, **40**, 4031–4042.

Part II
Semiconductors

Crystal Growth Technology. Semiconductors and Dielectrics. Edited by P. Capper and P. Rudolph
Copyright © 2010 WILEY-VCH Verlag GmbH & Co. KGaA, Weinheim
ISBN: 978-3-527-32593-1

4
Numerical Analysis of Selected Processes in Directional Solidification of Silicon for Photovoltaics

Koichi Kakimoto

4.1
Introduction

This chapter introduces crystallization process of multicrystalline silicon by using a directional solidification method. Numerical analysis that includes convective, conductive and radiative heat transfers in the furnace is also introduced. Moreover, a model of impurity segregation is included in this chapter.

4.2
Directional Solidification Method

Multicrystalline silicon (MC-Si) is in great demand for photovoltaics to solve the current greenhouse gases problem [1]. The directional solidification method is one of the key methods for large-scale production of MC-Si in highly efficient solar cells. The maximum efficiency of the crystalline solar cells was about 18%, while the use of commercially available wafers typically results in solar cell efficiency of about 16% in industrial solar cell processes. There are many problems that must be solved to achieve high conversion efficiency of solar cells. MC-Si has many dislocations and grain boundaries that are introduced during the solidification and/or cooling process. Moreover, MC-Si crystals are grown in a crucible, which degrades the purity of the crystals due to attachment to the crucible wall. Such defects and impurities can reduce the conversion efficiency of solar cells. Therefore, we should control the distributions of dislocations, grain boundaries and impurities during the solidification and/or cooling process. In recent studies, quasi-single crystal or multicrystalline with large grain size have been grown by using modified directional solidification methods [2, 3].

The directional solidification process has several merits, as follows. Square-shaped crystalline silicon can be grown by using a square-shaped crucible. When round-shaped crystals grown by the Czochralski method are used as raw materials for square-shaped solar cells, a large amount of waste of silicon materials is inevitably produced. Therefore, the unidirectional solidification process has a merit concerning the feedstock problem.

Crystal Growth Technology. Semiconductors and Dielectrics. Edited by P. Capper and P. Rudolph
Copyright © 2010 WILEY-VCH Verlag GmbH & Co. KGaA, Weinheim
ISBN: 978-3-527-32593-1

4.3 Crystallization Process

Optimization of the crystallization process is a key issue to obtain solar cells with high efficiency. Control of crystallization velocity of MC-Si, especially the cooling rate, solid/liquid interface shape and impurity distributions, is important for obtaining solar cells with high conversion efficiency. The crystallization process is complicated since heat- and mass-transfer systems in a furnace is highly nonlinear and time dependent. Due to the development of computer technology and computation techniques, numerical simulation has become a powerful tool for optimization of the directional solidification process and crystal-growth process [4–12]. Since a furnace for the directional solidification is a nonlinear conjugated thermal system, transient simulation with global modeling is an essential tool for improvement of the directional solidification process from melting to cooling processes through the solidification process. The global model includes processes of radiative, conductive and convective heat and mass transfer in a furnace. Therefore, we can quantitatively estimate the distributions of temperature in a furnace, the velocity of the melt, and the distributions of impurities. The author has developed a transient code with a global model for the directional solidification process. By using the code, the author carried out calculations to study distributions of temperature and impurities such as iron, carbon, oxygen, nitrogen and nitride in a silicon ingot during the directional solidification process [13–15].

The dimensions of a small unidirectional solidification furnace for producing MC-Si are shown are Figure 4.1. The grid of the entire furnace for computation is shown in the right part of Figure 4.1. In order to establish a discrete system for numerical simulation using the finite-difference method, the domains of all components in a furnace for the unidirectional solidification are subdivided into a number of block regions, for example, as shown in the left part of Figure 4.1, in which subdivision resulted in a total of 13 blocks. Each of these blocks is then discretized by a structured grid as shown in the right part of Figure 4.1.

In order to fit to the moving interface as a function of time, the grid cells in the melt and solidified ingot are stretched, and the grid points are moved upward as well. Two heaters marked by numbers 12 and 13 can be recognized in the furnace. The following major assumptions are used in the present model: (i) the geometry of the furnace configuration is axisymmetric, (ii) radiative transfer is modeled as diffuse-gray surface radiation, (iii) melt flow in the crucible is laminar and incompressible, and (iv) the effect of gas flow in the furnace is negligible. Conductive heat transfer in all solid components, radiative heat exchange between all diffusive surfaces in the unidirectional solidification furnace, and the Navier–Stokes equations for the melt flow in the crucible are coupled. Then, they are solved iteratively in a transient way. The time histories of heater power, fraction solidified and growth velocity during a unidirectional solidification process are shown in Figure 4.2 [16]. Variation of heater power as a function of time was imposed as a process parameter during the growth process.

The diameter of the inside wall of the crucible and the height of the solidified ingot are 100 mm. We carried out a transient global calculation for a fast-cooling

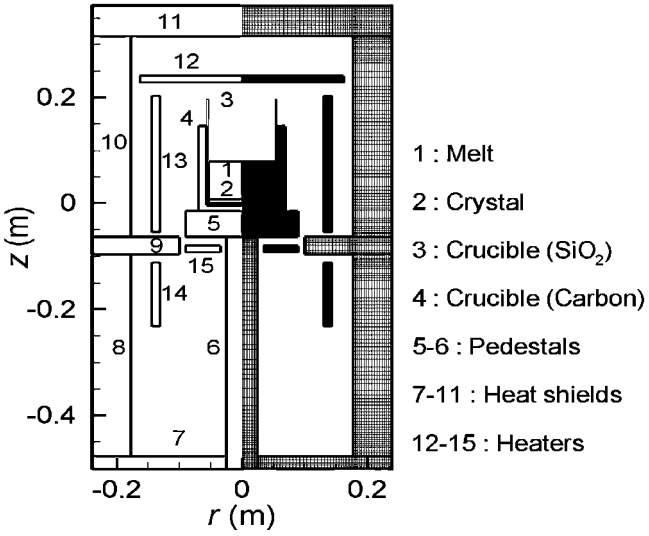

Figure 4.1 Configuration and computation grid of a directional solidification furnace [14].

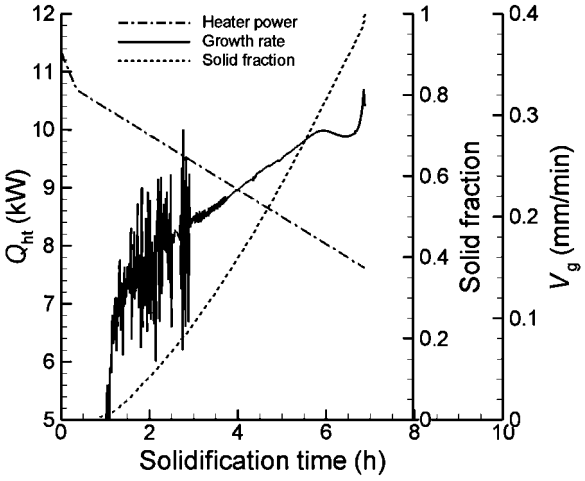

Figure 4.2 Heater power, fraction solidified and solidification rate as a function of time during solidification process.

solidification process in which the cooling rate is 0.42 kW/h for the first 1.8 h and 0.084 kW/h thereafter. The initial heater power was fixed at 13.9 kW. Duration of the solidification process is 8.1 h. The average solidification rate is about 0.21 mm/min.

The impurity distribution in the silicon melts and solidified silicon ingot was solved on the basis of calculated results of the thermal field and melt flow in a crucible. Impurity segregation at the solid/liquid interface was also taken into account. The solid/liquid interface shape was obtained by a dynamic interface tracking method. The global iterative procedure is described in Ref. [16].

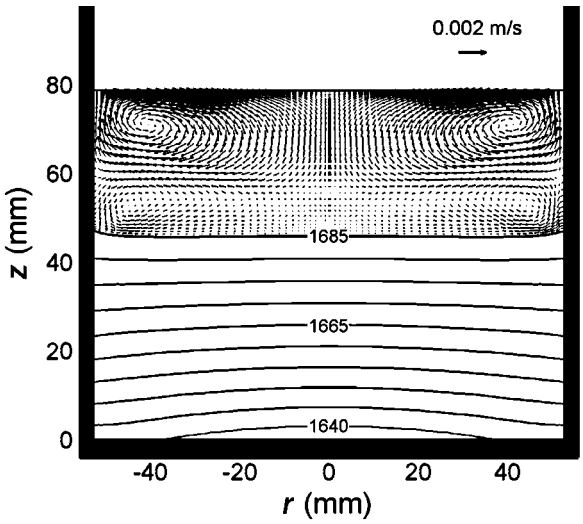

Figure 4.3 Flow velocity of the melt and temperature distributions during solidification of the ingot.

The velocity vectors in the melt and temperature distribution in the solidified ingot when half of the volume of melt has been solidified are shown in Figure 4.3. Two pairs of vortices were formed in the melt. The flow velocity of the melt is of the order of several mm/s, which is almost one order of magnitude smaller than that of Czochralski crystal growth. The solid/liquid interface is concave to the crystal in this case since the diameter of the crucible was smaller than that of a commercially used crucible. The present calculation revealed that the temperature gradient in the solid, which is 10 K/cm, is about one third to one fourth of the values in the Czochralski crystal growth system. The growth rate of the unidirectional solidification process is about one third to one fifth of that of the Czochralski growth system. Therefore, we can discuss the distribution of point defects in both single crystals and MC-Si based on Voronkov's theory that is expressed by the ratio between growth velocity and temperature gradient in a growing crystal (V/G) [17].

The heater power was decreased at a constant rate until 400 min and then kept constant until 460 min during the solidification process. Then, a fast cooling rate was imposed during the cooling process after the completion of solidification. Solidification was started after 100 min from the initial stage of the process, which corresponds to the time when the heater power started to be decreased. The growth rate was increased during the period of decrease in heater power and it was decreased when the heater power was kept constant. The time response of the imposed heater power to the growth rate was calculated to be about twenty minutes. The fraction solidified was gradually increased and finally became constant. The whole process was completed in about six hours.

The concentration taking into account segregation of impurity was expressed by Equation 4.1 at the solid/liquid interface:

$$D_m \frac{\partial C_m}{\partial n} + V_g C_m (1 - k_0) = D_s \frac{\partial C_s}{\partial n} \tag{4.1}$$

where C_m, C_s, and V_g are the impurity concentrations of the melt and solid and the growth velocity, respectively. D_m and $\boldsymbol{D}_s$ show diffusion constants of the impurity in the melt and the crystal, respectively. n is the growth direction (normal to the interface) and k is the equilibrium segregation coefficient.

4.4 Impurity Incorporation in Crystals

There are several deleterious impurities in MC-Si, including carbon, oxygen, nitrogen and iron that degrade conversion efficiency. Carbon is one of the major impurities in silicon feedstock. It will precipitate to form SiC particles in a directional solidification process when the concentration of carbon exceeds its solubility limit in silicon. It has been experimentally proved that the dislocation density is a function of carbon concentration in MC-Si [18]. The SiC precipitates can cause severe ohmic shunts in solar cells [5] and result in nucleation of new grains in MC-Si. Both carbon and SiC precipitates in MC-Si can greatly reduce the conversion efficiency of solar cells.

We focused on the modeling formation of SiC particles that are precipitated in the molten silicon and then incorporated into the solidified ingot [19]. The carbon precipitation in the solid is neglected due to the small diffusion constant in a solid in this study. Figure 4.4 shows a phase diagram between silicon and carbon in the melt. The diagram shows how SiC particle precipitation forms in Si-melt in the carbon-rich domain [20], in which the solubility limit of carbon in Si-melt $C_L(T)$ is approximated by a polynomial function. With the molten silicon being solidified and the solidification interface moving upward in the crucible during the solidification process, the carbon concentration in the melt increases due to the small segregation coefficient of carbon in silicon.

If the carbon concentration exceeds the local solubility limit in the melt, excessive carbon precipitates and the following chemical reaction occurs:

$$\mathrm{Si} + \mathrm{C} \rightarrow \mathrm{SiC} \tag{4.2}$$

Carbon as a substitutional atom is reduced and the same amount of SiC particles is generated in the melt. The formation rate of SiC particles and the destruction rate of substitutional carbon are equal and proportional to the supersaturation degree of substitutional carbon and the speed of the chemical reaction (4.2):

$$G_{SiC} = -G_C = \alpha(C_C - C_L(T)) \quad \text{when } C_C > C_L(T) \tag{4.3}$$

$$G_{SiC} = -G_C = 0 \quad \text{when } C_C \le C_L(T) \tag{4.4}$$

where C_{SiC} and G_C are the formation rates of SiC particles and substitutional carbon, respectively. The reaction velocity coefficient α is a factor correlating the particle formation rate and the chemical reaction rate in (4.2). The value of the

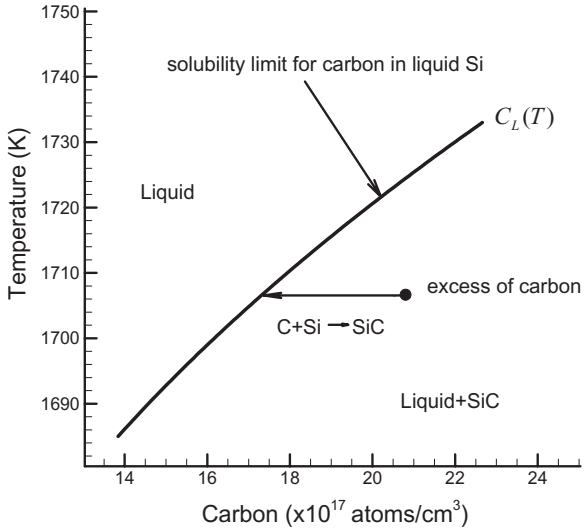

Figure 4.4 Schematic of SiC particle precipitation with the Si–C phase diagram in the C-rich domain.

coefficient was set to 100 cm/s which was defined our group. With these assumptions, the governing equations for the concentrations of substitutional carbon and SiC particles in the melt can be written as follows:

$$\frac{\partial C_C}{\partial t} + \mathbf{V} \cdot \nabla C_C = \nabla \cdot (D_C \nabla C_C) + G_C \quad \text{for substitutional carbon} \tag{4.5}$$

$$\frac{\partial C_{SiC}}{\partial t} + \mathbf{V} \cdot \nabla C_{SiC} = G_{SiC} \quad \text{for SiC particles} \tag{4.6}$$

The zero mass flux condition is applied at the crucible walls and the top of the melt for both impurities. The segregation coefficient of carbon in silicon was set to 0.07.

Figures 4.5a and b show the substitutional carbon and SiC particle distributions, respectively, in a cross-section of the solidified ingot. The SiC particles are clustered at the center-top region of the ingot, where the concentration of substitutional carbon is almost constant. This distribution pattern is due to the solid/liquid interface shape, which is concave to the solid side throughout the solidification process. The obtained concentration distributions of substitutional carbon and SiC particle along the center axis of the solidified ingot are compared in Figure 4.4 with the carbon concentration in silicon feedstock ranging from $1.26 \times 10^{16}\, atoms/cm^3$ (equivalent to 0.1 ppmw) to $6.30 \times 10^{17}\, atoms/cm^3$ (equivalent to 5.0 ppmw). When C_0 is $1.26 \times 10^{16}\, atoms/cm^3$, no SiC particles is precipitated in the ingot and there is only a very thin layer at the top rich of substitutional carbon. When C_0 increases higher than $1.26 \times 10^{17}\, atoms/cm^3$, the content of SiC particles increases significantly in magnitude as well as in space in the solidified ingot. It is thus necessary to control the carbon concentration in silicon feedstock less than $1.26 \times 10^{17}\, atoms/cm^3$ which is equal to 1.0 ppmw.

Removal of heavy metals from the ingot is a key issue to realize solar cells with high efficiency. Iron is one of the most important heavy metals. Figure 4.6 shows the

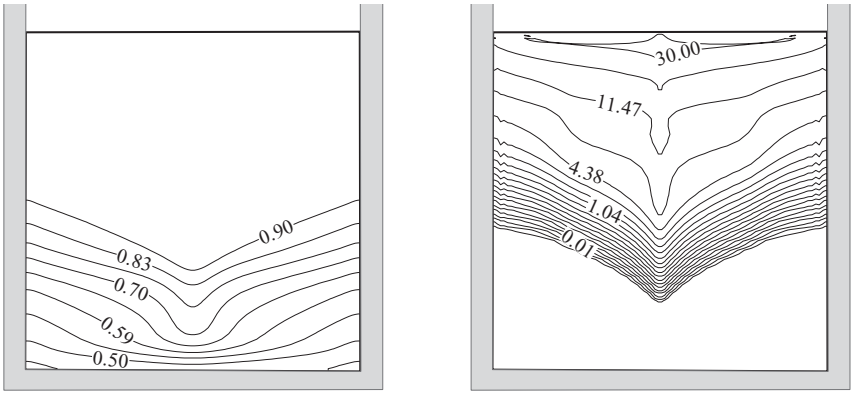

Figure 4.5 Substitutional carbon and SiC particle distributions in a cross-plane of the ingot solidified in a fast-cooling process. $C_0 = 6.3 \times 10^{17}$ atoms/cm^3. Contour lines are plotted in exponential distribution. The unit of concentration is 10^{17} atoms/cm^3. (a) substitutional carbon; (b) SiC particles.

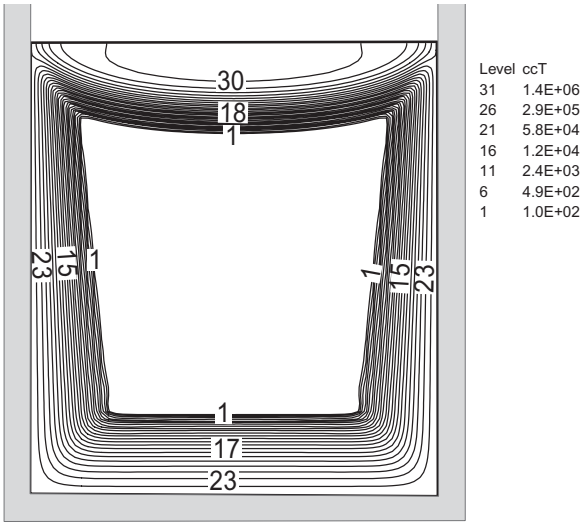

Figure 4.6 The distribution of iron concentration in a solidified silicon ingot.

distribution of iron concentration in a solidified silicon ingot that had been cooled for one hour during the cooling process. Areas with high iron concentration were formed at the top of the melt. This is due to the segregation phenomenon of iron, by which iron is segregated from the melt to the solid. Therefore, such areas with high concentration of iron were formed at the end of solidification. Moreover, areas with a high concentration of iron were formed close to the crucible walls. Such areas were formed by diffusion, which occurred during and after the solidification process. This is based on the small activation energy of iron diffusion in the solid silicon.

4.5 Summary

The unidirectional solidification method has both merits and demerits. Controlling the process is a key issue for achieving a solidification process that can produce solar cells with high conversion efficiency. We can neglect the reaction of Si_3N_4 in gas phase since vapor pressure of the gas is small. Numerical modeling is important for realizing such a process with optimization.

Acknowledgment

This work was partly supported by New Energy and Industrial Technology Development Organization. This work was also supported by a Grand-in-Aid for Scientific Research (B) 14350010 and a Grant-in-Aid for the creation of innovation through business-academy-public sector cooperation from the Japanese Ministry of Education, Science, Sports and Culture.

References

1 Franke, D., Rettelbach, T., Habler, C., Koch, W., and Müller, A. (2002) *Sol. Energy Mater. Sol. Cells*, **72**, 83.
2 Fujiwara, K., Pan, W.G., Usami, N., Sawada, K., Tokairin, M., Nose, Y., Nomura, A., Shishido, T., and Nakajima, K. (2006) *Acta Mater.*, **54**, 3191–3197.
3 Stoddard, N., Wu, B., Maisano, L., Russel, R., Creager, J., Clark, R., and Ferrandez, J.M. (2008) *18th Workshop on Crystalline Silicon Solar Cells and Modules: Materials and Processes* (ed. B.L. Sopori), Vail, National Renewable Energy Laboratory, pp. 7–14.
4 Ghosh, M., Bahr, J., and Muller, A. (2004) Proc. 19th European Photovoltaic Sol. Energy Conf., 7–11, June, 2004, Paris, 560–563.
5 Vizman, D., Eichler, S., Friedrich, J., and Müller, G. (2004) *J. Cryst. Growth*, **266**, 396.
6 Krauze, A., Muiznieks, A., Muhlbauer, A., Wetzel, Th., and Ammon, W.V. (2004) *J. Cryst. Growth*, **262**, 157.
7 Liu, L.J., and Kakimoto, K. (2005) *Cryst. Res. Technol.*, **40**, 347.
8 Kakimoto, K., and Liu, L.J. (2003) *Cryst. Res. Technol.*, **38**, 716.
9 Derby, J.J., and Brown, R.A. (1986) *J. Cryst. Growth*, **74**, 605.
10 Dupret, F., Nicodeme, P., Ryckmans, Y., Wouters, P., and Crochet, M.J. (1990) *Int. J. Heat Mass Transfer*, **33**, 1849.
11 Li, M., Li, Y., Imaishi, N., and Tsukada, T. (2002) *J. Cryst. Growth*, **234**, 32.
12 Kalaev, V.V., Evstratov, I.Yu., and Makarov, Yu.N. (2003) *J. Cryst. Growth*, **249**, 87.
13 Liu, L.J., and Kakimoto, K. (2005) *Int. J. Heat Mass Transfer*, **48**, 4492–4497.
14 Liu, L.J., Nakano, S., and Kakimoto, K. (2005) *J. Cryst. Growth*, **282**, 49–59.
15 Liu, L.J., and Kakimoto, K. (2005) *Int. J. Heat Mass Transfer*, **48**, 481–4491.
16 Liu, L.J., Nakano, S., and Kakimoto, K. (2006) *J. Cryst. Growth*, **292**, 515–518.
17 Voronkov, V. (1982) *J. Cryst. Growth*, **56**, 625.
18 Arafune, K., Ohishi, E., Sai, H., Ohshita, Y., and Yamaguchi, M. (2007) *J. Crystal Growth*, **308**, 5.
19 Liu, L.J., Nakano, S., and Kakimoto, K. (2008) *J. Cryst. Growth*, **310**, 2192–2197.
20 Laux, H., Ladam, Y., Tang, K., and Meese, E.A. (2006) Proceedings 21st EUPVSEC, Sept. 4–8, 2006, Dresden, Germany.

5
Characterization and Control of Defects in VCz GaAs Crystals Grown without B_2O_3 Encapsulant

Frank M. Kiessling

5.1
Introduction

Liquid-encapsulated Czochralski (LEC) and vertical gradient freeze (VGF) are standard technologies to grow large semiconducting (SC) and semi-insulating (SI) GaAs crystals [1, 2]. LEC crystals are grown with a liquid B_2O_3 layer on top of the melt surface, which prevents in combination with the inert gas counter-pressure, the loss of the volatile component arsenic and can getter impurities from the melt. It is used as a chemical communicator between the vapor and liquid phases to control the oxygen and carbon potential in the melt. However, boron is the predominant impurity in the melt, it incorporates in the crystal, and it affects the electrical properties of the material [3, 4].

Crystals are grown from slightly As-rich melts simply because the congruent melting point deviates from the stoichiometric composition towards the As-rich side, but this growth also has essential disadvantages. One of the most serious consequences is the condensation of arsenic excess atoms in precipitates during postsolidification cooling due to retrograde solubility [5]. The presence of such second-phase particles is undesired, because it may markedly affect the surface polishing process of wafer and also device properties. A drastic reduction in density and size of the arsenic precipitates, or better their complete avoidance, is sought. Ingot annealing allows the dissolution of these As-precipitates but does not change the Ga/As ratio in the solid.

In principle, the excess of arsenic in the solid can be reduced, if the crystals are grown from Ga-rich melts. In order to avoid a continuous change in melt composition during growth, the melt composition has to be controlled at all growth stages. This can be accomplished by an adjustable partial vapor pressure of the volatile component, but in LEC growth, the cover layer prevents the direct contact with the melt. Growth from uncovered melt with an additional As source in a hot-wall-type chamber would be a possibility to control the melt composition *in situ*. Therefore, a modified vapor-pressure controlled Czochralski (VCz) growth technique without boron oxide encapsulation has been developed in a standard Czochralski puller at the Leibniz Institute for Crystal Growth in Berlin (IKZ). Attempts to grow

Crystal Growth Technology. Semiconductors and Dielectrics. Edited by P. Capper and P. Rudolph
Copyright © 2010 WILEY-VCH Verlag GmbH & Co. KGaA, Weinheim
ISBN: 978-3-527-32593-1

GaAs by the Czochralski technique go back to the 1950s and will be overviewed in section 5.2.

There are some more advantages of growth from uncovered GaAs melts. The absence of the B_2O_3 cover eliminates boron contamination in the crystals. It is known that the impact of boron increases as the melt becomes more Ga-rich [6]. Furthermore, LEC growth of heavily Si-doped crystals is even worse and quite impracticable. Scum is formed on the melt surface that may induce serious growth problems like twinning [7]. Simultaneously, boron incorporation increases due to a reaction of silicon with boron oxide [8, 9]. Lately, so-called area counts are being focused upon, which affect the quality of wafer. These are second-phase particles of different origin due to the use of the B_2O_3 [10].

So far, almost all defect studies on GaAs have been performed on boron-contaminated material. In order to improve the electrical properties of the material, their defect distribution must be controlled during the crystal-growth process regarding impurities, dopant concentration and composition. These deviation from stoichiometry in the solid are strictly related to the melt compositions. By applying the VCz method and removing the cover layer, the melt composition can be adjusted during the whole growth process by *in situ* control of the partial arsenic vapor pressure. In order to justify, whether a technological transfer of the VCz technique to production might be useful, first at all, the properties of boron-reduced VCz GaAs crystals have to be revealed and compared with those grown conventionally.

5.2 Retrospection

The attempts to grow GaAs without liquid encapsulant by the Czochralski technique are not new. Back in the 1950s Gremmelmaier [11] described a hot-wall equipment consisting of a gas-tight fused silica container. The inner walls were kept sufficiently hot to prevent condensation of arsenic and to maintain a constant arsenic partial pressure in order to avoid dissociation from the melt. The seed and crucible were moved by a magnetic levitation system without any mechanical leads. Steinemann and Zimmerli [12] developed this type of apparatus and grew the first undoped dislocation-free GaAs single crystals up to ~15 mm in diameter. However, the magnetically coupled pulling rod gave unstable movements and was difficult to use. Richards [13], Tanenbaum [14], Mullin *et al.* [15] and, Leung and Allred [16] proposed various systems with liquid seals (molten metals, B_2O_3) and with mechanical lead-throughs. Since the B_2O_3 is not in direct contact with the melt, the contamination from the boron oxide was limited. In the 1960s, hot-wall-type Czochralski technologies to pull GaAs crystals were developed at Texas Instruments Incorporated, offering solutions for gas-tight lead-throughs [17, 18]. Moulin *et al.* [19] grew GaAs single crystal up to 25 mm in diameter, also using a fused silica ampoule with a rotating liquid B_2O_3 seal. The main impurity in their crystals was silicon at a level of 2 ppm. In 1965, Baldwin *et al.* [20] were the first, who described a separately heated As source placed at the container bottom in a hot-

wall Czochralski (HWC) chamber. A syringe puller, consisting of a ceramic pull rod, has been used and it was reported that the arsenic loss was tolerable. In 1984, Tomizawa *et al.* [21] proposed an advanced HWC apparatus named As-pressure controlled Czochralski method. Their 2-inch diameter GaAs crystals were grown in a low temperature gradient of 10 K cm^{-1} inherent to the hot-wall system. The mean etch pit density (EPD) was as low as 2×10^3 cm^{-2}. The hot-wall chamber was still made of fused silica and the unintentionally doped GaAs crystals showed an n-type conductivity of 5×10^{16} cm^{-3} due to silicon contamination. Later, Tomizawa *et al.* [22, 23] controlled the melt composition very precisely *in situ* and obtained 3-inch diameter semi-insulating GaAs single crystals. Nizhizawa [24] mentioned that gallium seems to be the best sealant in respect to the leak-tightness. Not many activities on HWC-type growth without B_2O_3 encapsulation were reported in the 1990s [25–27]. In the last few years, the uncovered Czochralski growth of GaAs crystals was rediscovered on an improved construction level [28].

5.3
Crystal Growth without B_2O_3 Encapsulant

Compared to the quasi-hermitically closed HWC system, the semi-open design features of the vapor-pressure controlled Czochralski systems used at the IKZ enable dynamic control of gas streams. The VCz technique combines an inner hot-wall chamber and a standalone heated As source. Figure 5.1 shows the

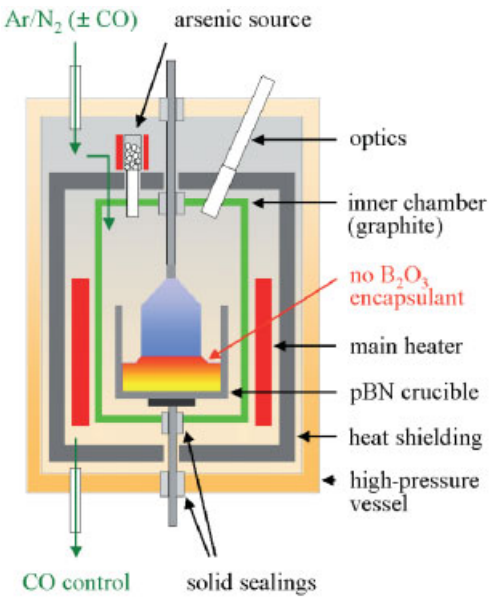

Figure 5.1 Principle sketch of the uncovered VCz GaAs crystal growth method.

schematic drawing of the applied growth principle. The main design feature is an inner chamber made purposely of graphite to solve the known problem of unintentional silicon contamination from hot walls made of fused silica. The inner chamber shields the growing crystal as well as its surrounding hot gas from the water-cooled walls of the outer high-pressure vessel. All sites of the inner chamber wall are kept at temperatures higher than that of the As source. In order to obtain a boron-free environment, solid sealings are used for lead-throughs [29]. Small diffusive losses of arsenic are compensated and decomposition of the melt is controlled *in situ* by a separately temperature-controlled arsenic source [30]. Their temperature can widely be varied within the range of 540–650 °C depending on the exact construction and, corresponds to an arsenic pressure between 0.02 and 0.21 MPa.

Since the As partial vapor pressure controls the melt composition, this relation has to be determined experimentally. The composition can easily be determined via separation of the liquid gallium from the residual last-to-freeze crucible charge. Mole fractions $\gamma = N_{As}/(N_{Ga} + N_{As})$ of the liquid phase $Ga_{1-\gamma}As_{\gamma}$ from $\gamma \approx 0.450$ to 0.500 within an error of ±0.005 could be estimated from volumes, which were at least twice as much as that of the grown crystals.

Global numerical simulations of the temperature and heat distribution were applied to optimize the growth process. The thermal shielding and the B_2O_3-free melt surface provide significantly reduced temperature gradients at the growing interface of about 3–5 K cm^{-1} and 17–23 K cm^{-1} in the radial and axial directions, respectively [31], which differ markedly from LEC and even VCz designs used with B_2O_3 encapsulation. Morphological instabilities at the solid/liquid interface [32] may arise due to growth conditions, which are defined by a relatively low axial temperature gradient and an enrichment of Ga in the diffusion boundary layer adjacent to the crystallization front. In dependence on the melt composition, the crystals have to be pulled at growth velocities of 3–5 mm h^{-1} to avoid constitutional supercooling [33], while the seed and crucible rotate contrariwise at rates of 6 and −25 rpm, respectively. The crucible should be moved upwards during growth to ensure a fixed position of the melt level with respect to the heater.

Since the diameter control of VCz GaAs crystals grown from uncovered melts is challenging, due again to the system inherent low temperature gradients, the growth process has to be optimized carefully [34]. Then, 2- and 3-inch diameter GaAs single crystals with nearly constant diameter can be grown. Figure 5.2a shows such a twin-free SI GaAs crystal grown from a Ga-rich melt with $\gamma \approx 0.46$. For analyses of striations, that is, of the morphology of the growing interface, a longitudinal slice was cut parallel to the growth axis along the <100> direction and etched by diluted Sirtl with light. Figure 5.2b illustrates the slightly convex shapes of striations with undesired concave parts at the rim, reflecting the difficulties in optimizing the thermal growth conditions. Figure 5.2c depicts a twin-free single crystal also grown from a Ga-rich melt. The diameter was intentionally changed to verify the stability of the growth regime. This experiment disproves the view that twin-free crystals cannot be grown from Ga-rich melts [16, 35, 36]. All crystals tend to grow with considerably developed facets showing the two-fold symmetry

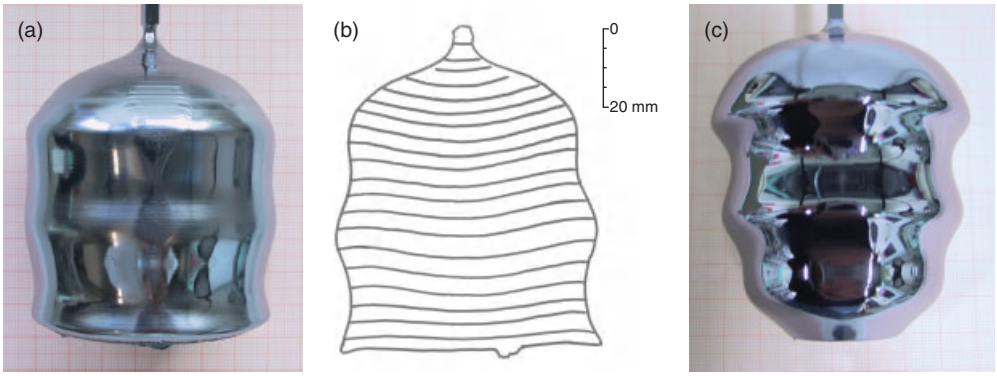

Figure 5.2 Images of: (a) a twin-free GaAs single crystal grown in diameter controlled mode; (b) striations revealed on a DSL-photoetched longitudinal cut sample and; (c) a twin-free GaAs single crystal grown with intentional diameter changes to prove diameter-dependent twinning probabilities.

of the [001] direction in the zincblende structure and a typical mirror-like surface, which evidences growth within low radial temperature gradients and in thermodynamic equilibrium.

Since the SI behavior of GaAs material is caused by compensation of the native defect EL2 by residual acceptors, a precondition to grow SI GaAs is the control of the shallow acceptor carbon. The carbon incorporation into the melt can mainly be attributed to the high CO fugacity in the gas phase. CO gas is released by the reaction of residual water with graphite according to $C + H_2O \leftrightarrow CO + H_2$ and due to the Boudouard equilibrium $CO_2 + C \leftrightarrow 2CO$. Besides a possible direct absorption of carbon species by the uncovered GaAs melt surface, unbounded carbon can also be produced by the reactions $CO + 2Ga \leftrightarrow C + Ga_2O$ and $3CO + 2Ga \leftrightarrow 3C + Ga_2O_3$ at the liquid/vapor interface.

The nonconservative VCz setup enables *in situ* control of the CO fugacity via gas-stream adjustments. Without controlling the CO content in the process gas, carbon concentrations in the crystal are typically measured as $2–5 \times 10^{16}\,cm^{-3}$, while an *in situ* adjusted CO partial pressure of 7–70 mbar results in carbon concentrations of $9 \times 10^{14}\,cm^{-3}$ to $4 \times 10^{16}\,cm^{-3}$, respectively. The carbon content measured axially in different crystals was evaluated from local vibrational mode (LVM) absorptions at 80 K. Although it was not clear until recently, whether a B_2O_3 layer is necessary to control the carbon concentration in the melt, the curves of Figure 5.3 demonstrate that the carbon concentration purposely varied can easily be adjusted at any stage of the crystal-growth process.

Low-n-type SC GaAs crystals can be grown using fused silica crucibles and high-n-type semiconducting material by the usual Si-doping method. Growing without boron oxide, the known reaction of silicon with the encapsulant can be avoided, resulting in a low boron impurity content [37]. In order to compare defect populations of n-type SC VCz crystals with those published for boron-contaminated

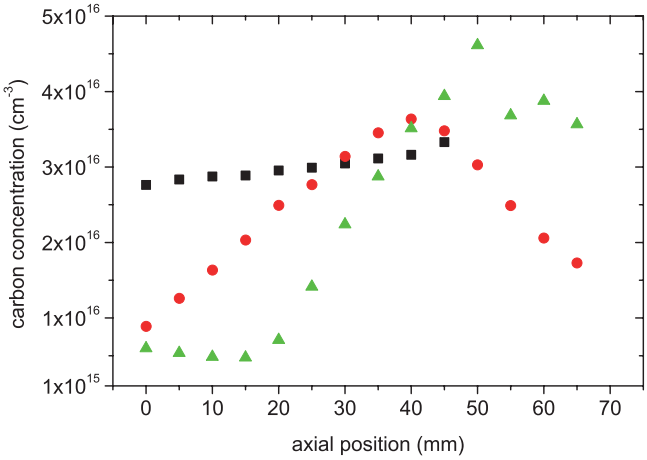

Figure 5.3 Carbon concentration in dependence on the axial position.

Table 5.1 Growth features of SI and SC GaAs crystals

Material type	Crucible	B_2O_3	Mole fraction (melt)	Carbon control	Silicon doping
Semi-insulating	pBN	No	0.45–0.50	Yes	No
	pBN	Yes	~0.50	Yes	No
Semiconducting	SiO_2/pBN	No	~0.50	No	Yes
	pBN	Yes	~0.50	No	Yes

as-grown LEC samples, the crystals have only been grown from stoichiometric melts. In contrast, semi-insulating GaAs crystals were grown from different melt compositions (Table 5.1). To ensure that the conditions (time and temperature) for defects to migrate after solidification were comparable, all crystals were cooled down at first to 900 K at a rate of 25 K h^{-1} and then at 50 K h^{-1} to room temperature. This temperature regime takes into account results obtained from investigations on point defect mobilities. According to Lagowski *et al.* [38], critical postsolidification defect interaction takes place at least above a temperature of about 1050 K, while Jurisch and Wenzl [39] discussed a freeze-in temperature of mobile As-interstitials of about 1250 K and Frigeri *et al.* [40] specified a temperature range of about 950 to 1350 K for solid-state transitions.

5.4 Inclusions, Precipitates and Dislocations

During postsolidification cooling, the excess arsenic condenses in second-phase particles, due to its retrograde solubility in the GaAs matrix, and on dislocations.

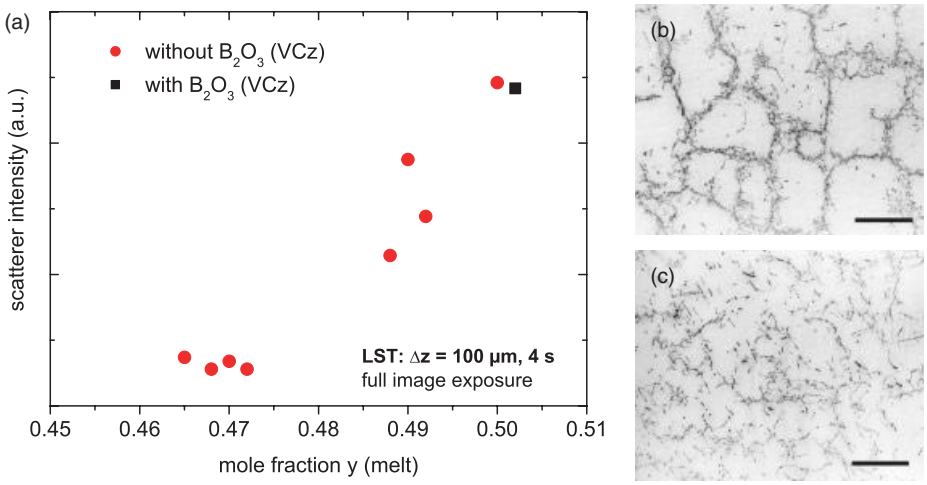

Figure 5.4 (a) Scatterer intensities from precipitates in crystals grown without B_2O_3 in dependence on melt composition $Ga_{1-y}As_y$. Squared symbol represents a measurement on a conventional VCz crystal grown with B_2O_3; (b, c) Negative images of laser scattering tomographs showing As-decorated dislocation structures of two crystals grown from melts with (b) $y \sim 0.50$ and (c) $y \sim 0.47$. For all measurements identical LST conditions were used. The markers equal 1 mm.

Infrared (IR) laser scattering tomography (LST) [41] is used to investigate arsenic precipitates [42]. One can see from LST measurements plotted in Figure 5.4a that the scatterer intensities from precipitates in GaAs crystals only depend on the off-stoichiometry and decrease significantly with increasing Ga fraction in the melt. For comparison, the scatterer value of a conventional VCz crystal grown with B_2O_3 encapsulant and with the same thermal history is added. Simultaneously, the decoration degree on dislocation drops (Figures 5.4b and c). Surprisingly, this type of scatterer could not be ascertained by LST in crystals grown from melts with just a mole fraction of $y \approx 0.45$. Similar results were published by Fornari *et al.* [43] on Si-doped LEC GaAs crystals grown from Ga-rich melts of $y \approx 0.43$. A drastic reduction in density and size of As precipitates down to $3 \times 10^6\,cm^{-3}$ and 40 nm, respectively, was reported. Usually, the density of precipitates in LEC crystals grown from As-rich melts has been determined as 10^8–$10^9\,cm^{-3}$ and their sizes to 50–200 nm [5, 40, 44–46]. Obviously, melt compositions $Ga_{1-y}As_y$ less than or around a mole fraction of $y \approx 0.45$ yield near-stoichiometric crystals without essential precipitation, which is in good agreement with the value predicted by Hurle [47].

The crystal composition or the deviation from stoichiometry in the solid $Ga_{1-x}As_x$ is governed by the solidification conditions at the solid/liquid interface and reflects the concentration of native defects, residual impurities and dopants in both sublattices. The deviation from stoichiometry δ is correlated to the mole fraction x as $\delta = 1 - 2x$ and is defined as:

$$\delta = [Ga_{As}] + 1/2[Ga_i] + 1/2[V_{As}] + 1/2[X_{As}] - [As_{Ga}] - 1/2[As_i] - 1/2[V_{Ga}] - 1/2[X_{Ga}] \quad (5.1)$$

with (V, vacancies; I, interstitials, antisites) the native defects and X the extrinsic defects in each sublattice (As and Ga). It has to be mentioned that there was a long-lasting discussion about the extension and temperature dependence of the solid solubility range (see, for example, [48, 49]). This is due to the fact that the chemical and physical methods, available to determine δ in GaAs, are not precise enough. The latest thermodynamic calculations confirm experimental results of the homogeneity range, which seems to be completely located on the As-rich side [50, 51]. To the best of our knowledge no contrary experimental evidences are known. This implies that only As-rich, or at least stoichiometric, GaAs material exists, when grown from Ga-rich melts of $\gamma \geq 0.45$.

The more Ga excess in the melt the more complicated the growth process becomes in the VCz configuration. The growth from such Ga-rich melts drastically increases the incorporation probability of Ga-rich inclusions. Their diameters are of some hundred micrometers, that is three orders of magnitude larger than that of precipitates, and their composition can be identified in a scanning electron microscope by energy-dispersive X-ray analysis (EDX). Already Wenzl *et al.* [48] mentioned the appearance of Ga inclusions with diameters of about 200 µm in crystals grown by HWC at As source temperatures below 600 °C and pulling rates of 8 mm h^{-1}. It has to be noted in this context that it is important to distinguish between precipitation and inclusion genesis. Precipitation is due to retrograde solubility of point defects, in this case As interstitials, while inclusions are originated by melt-solution droplet capture at the growing solid/liquid interface, for example, in case of a Ga-enriched diffusion boundary layer adjacent to the crystallization front. Such inclusion incorporation should be avoided. When they are incorporated in the crystal, due to an overcritical v/G ratio at the crystallization front, where v is the growth velocity (different from the pulling velocity) and G is the temperature gradient at the liquid interface, they follow the propagating interface, that is, they move towards higher temperature by the traveling-solvent mechanism [52]. In general, growth in low-temperature gradients leads to morphological instabilities [33] but growth velocities less than the critical one allow inclusion-free GaAs material to be obtained. Since the growth rate is diffusion limited, the characteristics of the diffusion boundary layer can be changed to improve growth conditions, for example, by reducing the layer thickness. Nonsteady magnetic fields [53, 54] can be applied to stabilize the growth process, to improve crystal quality and to increase yield. The application of traveling magnetic fields in the VCz setup will be discussed in section 5.8.

Besides fewer As precipitates, the crystals tend to show lower dislocation densities. Using molten KOH etching, an improved radial homogeneity of its distribution due to the absence of boron oxide encapsulation is found. The etch pit density distribution is typical for all crystals grown and cooled in low-temperature gradients (VCz [28] and HWC [22, 25]). Also, the effects of melt composition and, hence of crystal composition, on dislocation density have been well known for a long

time. In the mid-1960s, Brice and King [55] grew horizontal Bridgman GaAs crystals under different arsenic pressure and also from melts with an excess of gallium. They reported that the EPD decreases with decreasing deviation from stoichiometry in agreement with results obtained on boron-reduced VCz GaAs crystals nowadays. The dislocation structure of VCz GaAs crystals shows typical cellular patterning, which can already be dissolved in crystals grown from a Ga-rich melt of $\gamma \approx 0.45$. A lower concentration of intrinsic point defects reduces dislocation climbing, resulting in a decreasing mean EPD with increasing Ga fraction of the melt down to $\sim 5 \times 10^3\,cm^{-2}$ [56, 57]. Comparing EPDs from sample to sample, one has to keep in mind that the free-carrier concentrations have to be similar, since the dislocation density is affected by the Fermi energy [58].

5.5 Residual Impurities and Special Defect Studies

The VCz GaAs crystals have been grown from presynthesised high-purity material [59] commercially available. The most important, but also expected effect is the strong reduction of the boron and oxygen concentration in the GaAs crystals. The boron content measured by electron probe microanalysis in undoped VCz GaAs is reduced by at least one order and in highly Si-doped VCz GaAs by more than two orders of magnitude compared to the concentration in crystals grown with B_2O_3 encapsulation [31, 32]. Independently, whether B_2O_3 is applied or not, the residual levels of metals are $<3 \times 10^{14}\,cm^{-3}$, while the concentration of zinc is less than $10^{15}\,cm^{-3}$. In all crystals grown without B_2O_3 encapsulant, neither other evident impurity concentrations of residual electrically active defects have been found, nor could oxygen defects and related complexes be detected by LVM analysis. In all these samples, H-related complexes can be ascertained, even though their content is smaller by a factor of 10 to 100 compared to crystals grown with encapsulation. It has to be pointed out that all contamination sources have to be eliminated prior to growth of GaAs crystal from uncovered melts, like sulfur, which might be released from the inner graphite assemblies.

A prerequisite to study the electrical and optical material properties is the reduction of the residual impurity concentration. Generally, the properties of GaAs crystals reviewed, for example, in [60] have been obtained from boron-contaminated material. By contrast, only very few studies could be done on boron-reduced GaAs, even though the role of boron and its interaction with intrinsic and extrinsic point defects depending on melt composition and doping has always been of interest [6, 61–64]. The boron-dependent properties of SI and SC GaAs crystals grown without B_2O_3 encapsulant are reported in the following sections, while for the sake of completeness some fundamental studies should briefly be mentioned. Fundamental studies on the nature of vacancies in p-type GaAs [37, 65–67] are still under discussion, while for example, the identification of the Z-H complex as (N-H-V_{Ga}) [68] is revealed. Since it was experimentally impossible to distinguish whether the origin of Z was oxygen or nitrogen, B_2O_3-free growth was required to tackle this

problem. An increased pressure of nitrogen in a LEC setup would increase the nitrogen concentration in the melt and unfortunately the oxygen concentration also released from the B_2O_3. However, the growth from uncovered melts offers some limitations for fundamental studies too, for example, the investigation of oxygen-related defects like EL3 [69].

5.6 Electrical and Optical Properties in SI GaAs

Semi-insulating bulk GaAs is today obtained from a near-stoichiometric melt by the balance in concentrations of the carbon acceptor and the deep level defect EL2 (As_{Ga}), as long as the residual impurity concentration is kept low. The characteristics of the intrinsic point defect As_{Ga} under the influence of electrically active dopants is still under investigation [40, 70, 71]. Growing SI GaAs from Ga-rich melts with controlled carbon concentration would be of high interest to reduce the concentration of the omnipresent As precipitates. However, when changing the melt composition from stoichiometric to Ga-rich, it was found that the conductivity type in LEC GaAs changed from SI to p-type at a critical melt composition caused by an additionally formed double acceptor and a reduction in concentration of the EL2 defect [47, 72, 73]. From the data in Figure 5.5, one can see that the concentration of the midgap donor EL2 decreases very gradually with increasing Ga fraction in the melt. In contrast to the results published by Holmes *et al.* [72], not only the $EL2^0$ concentration was ascertained by near-IR absorption analysis, but also the $EL2^+$ concentration using deep-level transient spectroscopy (DLTS). The latter depends on the net concentration of shallow acceptors. Since the additionally formed acceptor concentration observed only in boron-contaminated GaAs

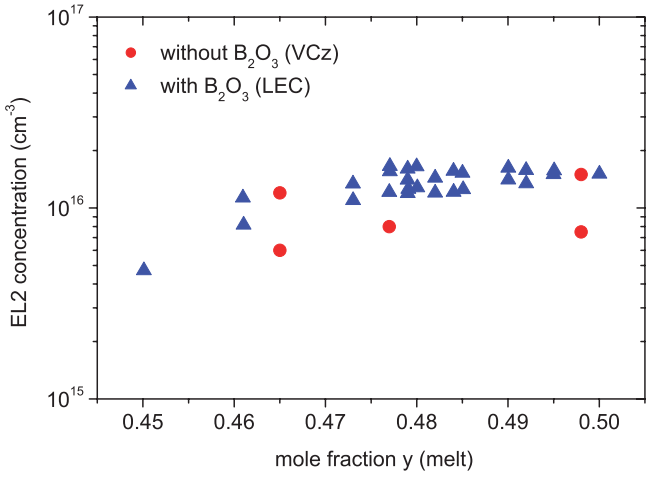

Figure 5.5 Dependence of the EL2 concentration on melt composition. LEC data are taken from [73].

crystals increases with decreasing mole fraction of the melt, the EL2 gets fully ionized at a critical melt composition and charge state transitions alter the detectable concentration of $EL2^0$.

The double acceptor responsible for this state transition has energy levels at 78 meV and at 203 meV above the valence band and as already mentioned, its concentration increases with increasing Ga fraction of the melt. The corresponding luminescence bands at 1.316 eV and at 1.441 eV have controversially been attributed either to the Ga antisite (Ga_{As}) [74–77] or to boron on an As lattice site (B_{As}) [78–81]. Since boron is present in LEC and VGF growth, a conclusive assignment was impossible. Kiessling *et al.* [82] investigated the properties of crystals grown from Ga-rich melts with and without boron oxide encapsulation. In all cathodoluminescence (CL) spectra of their samples (Figure 5.6) grown without B_2O_3, neither the luminescence at 1.316 eV nor at 1.441 eV were found, which would indicate the presence of Ga antisites, nor could any other optical transitions towards longer wavelength be detected. In order to get conclusive data, the intensities of the $^{11}B_{As}$ LVM at 601 cm^{-1} and of the $^{11}B_{Ga}$ LVM at 517.3 cm^{-1} at 7 K, respectively, were measured. A significant concentration of $B_{As}^{-/2-}$ and B_{Ga}^{0} could be detected in the corresponding boron-contaminated sample, while boron-reduced samples do not show these intensities at all. Thus, the double acceptor is rather B_{As}-related than caused by Ga_{As}, which has dramatic consequences on the material properties.

The electrical properties were obtained from Hall effect and conductivity measurements at room temperature. Figure 5.7 shows the resistivity and carrier mobility of as-grown SI VCz GaAs grown without boron oxide encapsulation in the carbon-controlled growth regime in dependence on the melt composition, demonstrating that SI GaAs can even be grown from Ga-rich melts with a mole fraction of $y \sim 0.46$. The resistivities are similar to those obtained from measurement on as-grown LEC GaAs material [83]. For comparison, typical electrical values from as-grown SI VCz samples grown with B_2O_3 from near-stoichiometric melts [84] at the IKZ are added. Their variations in resistivity and electron mobility are caused by different carbon concentrations [2]. The type of conductivity changes in the LEC samples from n-type to p-type at about $y \sim 0.47$, while that of the boron-reduced GaAs crystals does not. Simultaneously, the electron mobility decreases with increasing Ga content in the melt from about 6500 cm^2/V s at a mole fraction of $y \sim 0.50$ to ~300 cm^2/V s at $y \sim 0.47$, likely caused by an increasing concentration of the shallow acceptor B_{As}. In contrast, the electron mobility of the boron-reduced GaAs samples increases with decreasing mole fraction of the melt, which indicates a reduced number of scattering centers.

In semi-insulating GaAs crystals, scattering at residual ionized impurities dominates at elevated temperatures. Neutral impurities, like B_{Ga}^{0}, do not act as strong scattering centers and thus will have less influence on the mobility. Phonon scattering competing with ionized impurity scattering should not depend on the residual doping of the sample. Thus, comparing boron-contaminated GaAs material with the boron-reduced one, the main difference consists in the boron contamination, where a part is B_{As} acting as charged scatterer. The mobility μ is inversely proportional to the concentration of ionized impurities according to

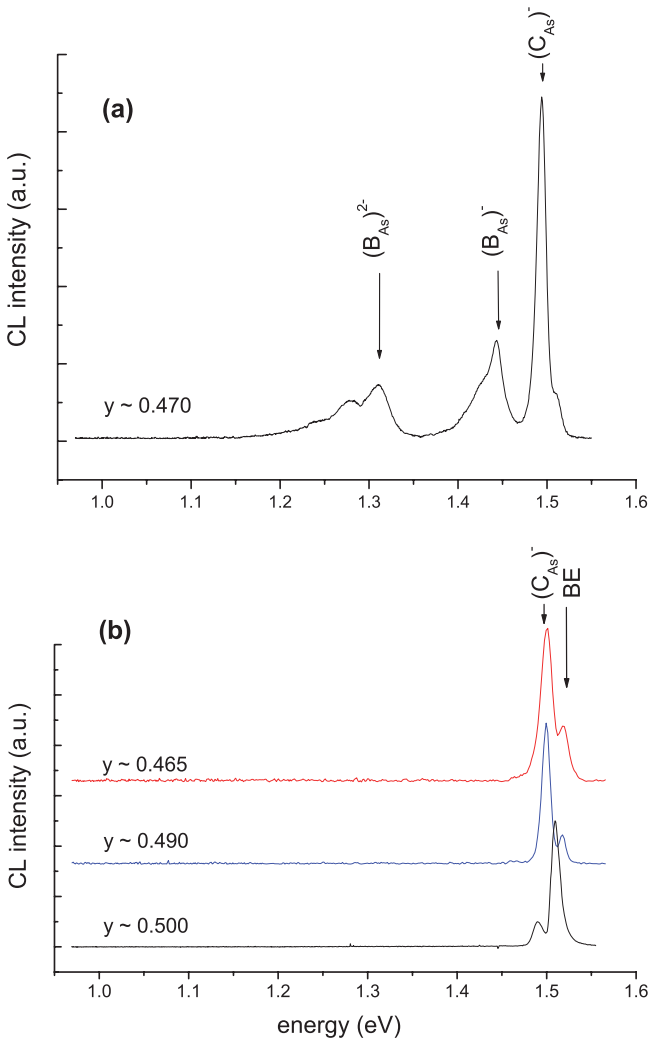

Figure 5.6 CL intensities measured at 15 keV, 1 nA, 7 K of the 1.316/1.441 eV B_{As}–related luminescences in undoped GaAs crystals grown from various Ga-rich melts. The luminescence bands at 1.493 eV reflect different carbon concentrations in samples (a) grown with B_2O_3 and (b) grown without B_2O_3.

$$\mu \sim 1/n_i Z^2 \tag{5.2}$$

with n_i the concentration of the ionized impurities and Z the charge state [85]. Although this explains the decrease in mobility in boron-containing material, it does not explain the increasing mobilities in boron-free samples. However, the dependence on the mole fraction of the melt suggests a reduced concentration of native defects, for example, EL2 (see Figure 5.5), which act as additional scattering

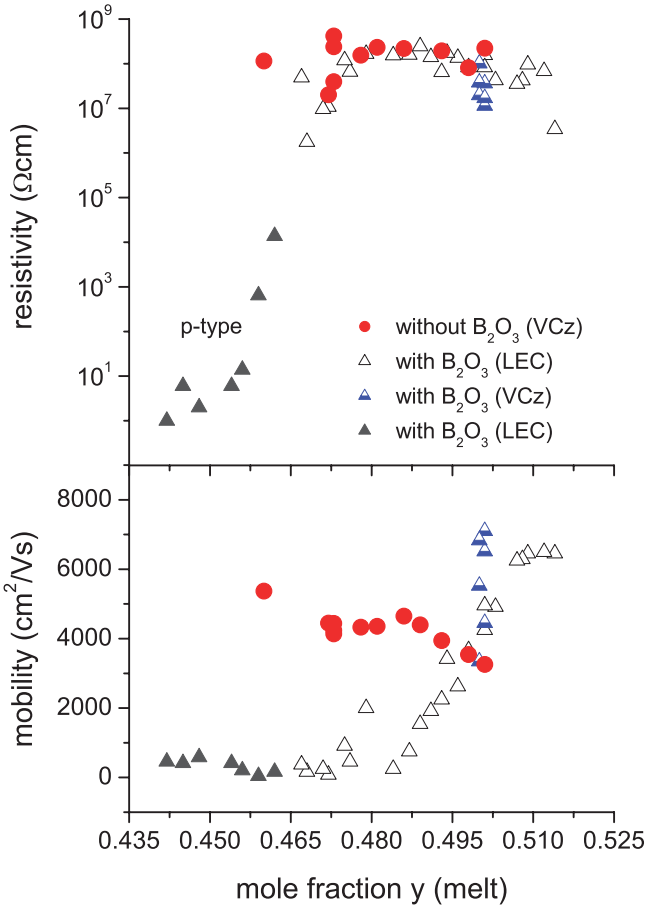

Figure 5.7 Resistivity and carrier mobility in dependence on melt composition of as-grown boron-reduced SI VCz GaAs samples compared to undoped as-grown LEC and VCz material grown with B_2O_3. Filled triangles indicate p-type conductivity of LEC material.

centers [86]. Since the absorption coefficient α is also dependent on the mobility according to

$$\alpha \sim n_i \lambda^2 / n(\lambda)\mu \tag{5.3}$$

with $n(\lambda)$ the wavelength, λ, -dependent refractive index, reduced near band edge absorption can be expected. The curves of Figure 5.8 show that the absorption coefficient of boron-reduced VCz GaAs crystals grown from Ga-rich melts is much lower compared to boron-contaminated standard VCz samples grown from a slightly As-rich melt with B_2O_3. The near-infrared optical absorption measurements were performed on SI GaAs with sample thicknesses of 5 mm in the photon energy interval of 0.6–1.5 eV. The measurement temperature was chosen as 300 K

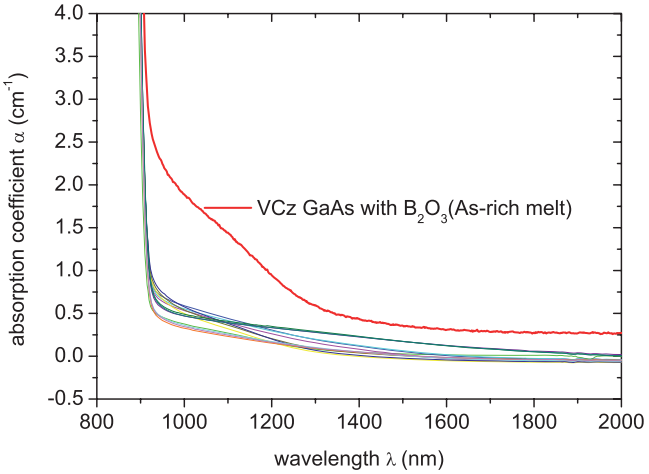

Figure 5.8 Wavelength-dependent absorption coefficient of as-grown VCz material grown with B_2O_3 compared to those of as-grown boron-reduced VCz GaAs samples.

in order to demonstrate device operating properties like for example, for IR immersion optics at the particular Nd:YAG laser wavelength of 1064 nm. At this wavelength $EL2^0$ dominates the absorption [87]. Depending on melt composition and carbon concentration, the concentration of the EL2 in the neutral state typically determined in boron-reduced SI VCz GaAs material ranges from $2–9 \times 10^{15}\,cm^{-3}$. Absorption coefficients as low as $\alpha = 0.26\,cm^{-1}$ at 1064 nm [88] have been ascertained in semi-insulating and low carbon doped p-type VCz GaAs crystals grown from Ga-rich melts with 46 at% As and $EL2^0$ concentration of $2 \times 10^{15}\,cm^{-3}$ and can probably be lowered by postgrowth heat treatments. Recently, the new material quality was also demonstrated on such a p-type as-grown GaAs sample with a carrier concentration of $5.4 \times 10^{11}\,cm^{-3}$ and with an absorption value of only $1.4\%\,cm^{-1}$ at a wavelength of 2.25 µm [89] showing no dependence inside the crystal on the pump power up to 250 mW.

In summary of this section one has to assess that in contrast to previous assumptions, semi-insulating material can be obtained from Ga-rich melts of mole fractions $\gamma < 0.475$ with negligible charged B_{As} scatterers when grown in a boron-free environment. More typical characteristics of these crystals are:

a) fewer arsenic precipitates;
b) no B_2O_3- or bubble-related area counts;
c) low dislocation densities;
d) reduced EL2 concentration;

compared to LEC, VGF or VCz GaAs crystals grown from slightly As-rich melts under boron oxide encapsulation. The reduced dislocation density might also result in improved EL2 uniformity [90]. Incidentally, due to the growth technique the concentration of oxygen-related defects like for example, EL3 cannot increase

with decreasing As fraction of the melt as normally observed under B_2O_3-covered melt growth conditions.

5.7 Boron in SC GaAs

When semi-conducting GaAs crystals are grown from Si-doped melts covered by B_2O_3, silicon reacts chemically with the encapsulant, resulting in significant higher boron incorporation in the crystal. The boron and silicon on As lattice sites (B_{As}, Si_{As}) act as acceptors and the silicon on Ga lattice sites (Si_{Ga}) as donor. Isolated vacancies form (donor–V_{Ga}) complexes due to Coulomb interaction and their concentration relates to the intensity of luminescence bands at 0.95 eV and 1.15 eV. Our latest studies show that in contradiction to the results published so far [91–95], the 0.95 eV band has to be assigned to the $(V_{Ga}Si_{Ga})^{2-}$ and the 1.15 eV transition to the $(Si_{Ga}V_{Ga}Si_{Ga})^{-}$ complex. Detailed arguments will be published elsewhere [96].

Studies of the influence of boron on vacancy concentrations show that boron decreases the concentration of Ga vacancies (V_{Ga}) [6, 67], while their total density increases with Si doping, both illustrated in Figure 5.9. The densities of negatively charged vacancies can be obtained from positron annihilation lifetime spectroscopy (PALS) measurements [99], while electrical properties can be deduced from Hall effect measurements at room temperature. The V_{Ga} concentration in boron-reduced and highly boron-contaminated SC GaAs samples increases with increasing electron concentration, that is, Si doping. The V_{Ga} concentration in the former

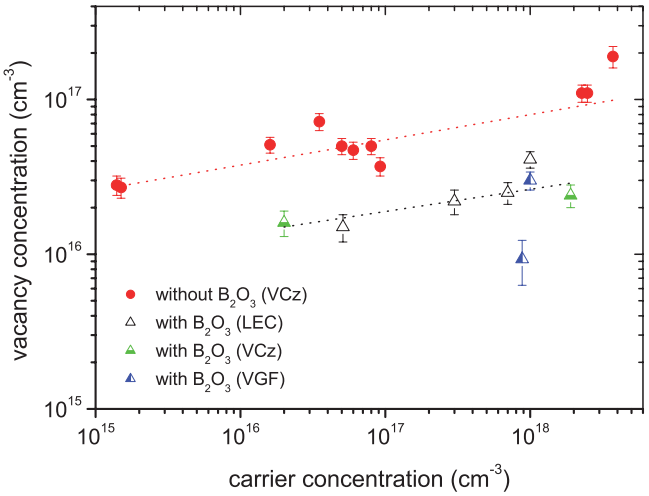

Figure 5.9 Vacancy concentrations obtained from PALS at 300 K are plotted in dependence on the carrier concentration in highly boron-contaminated Si-doped GaAs samples compared to boron-reduced VCz GaAs : Si material. LEC and VGF data are taken from [97] and [98], respectively.

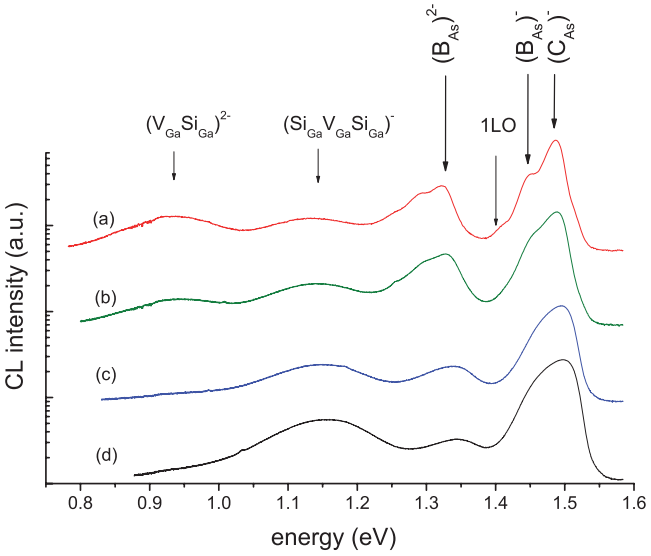

Figure 5.10 CL spectra (20 keV, 10 nA) of Si-doped boron-contaminated VGF GaAs samples ($\gamma \sim 0.50$, with B_2O_3) of different doping levels. Measured carrier concentration: (a) $2.0 \times 10^{17}\,cm^{-3}$, (b) $4.1 \times 10^{17}\,cm^{-3}$, (c) $8.6 \times 10^{17}\,cm^{-3}$ and (d) $1.35 \times 10^{18}\,cm^{-3}$.

is always higher by a factor of about 3 at similar electron concentrations and compensates for the missing $B_{As}^{-/2-}$. This can be explained by the fact that V_{Ga}^{3-} has the lowest formation energy of all native defects in Si-doped GaAs, when the Fermi level is close to the conduction band [100].

Semiconducting VCz GaAs crystals grown at IKZ have drastic lower boron concentrations, which results in the formation of additional autocompensating (donor–V_{Ga}) complexes. Figures 5.10 and 5.11 show CL spectra of a series of highly boron-contaminated Si-doped VGF GaAs and boron-reduced VCz samples, respectively, all grown from near-stoichiometric melts ($\gamma \sim 0.50$). The CL spectra were obtained from measurements performed at 7 K [82]. In both figures, two dominant bands at 0.95 eV and 1.15 eV are present attributed to autocompensating (donor–V_{Ga}) complexes. The band at 0.95 eV decreases with increasing Si doping, while the band at 1.15 eV increases. Beyond an electron concentration of about $1 \times 10^{18}\,cm^{-3}$ the former vanishes completely. In Figure 5.11, the boron-related transition at 1.316 eV (see Figure 5.6) cannot be detected, reflecting again the low boron concentration in boron-reduced VCz GaAs crystals. In contrast, both transitions (1.316 eV/1.441 eV) clearly arise in the VGF samples (Figure 5.10), which proves that boron is incorporated on an As substitutional site in Si-doped GaAs, even though the crystals were grown from stoichiometric melts. This indicates that B_{As} has a comparatively low formation energy and seems to be an efficient compensating defect in n-doped material, when the Fermi level moves toward the conduction band [101]. As the donor concentration increases, the 1.441 eV transition can no longer be resolved. Besides the increasing Si_{Ga} donor concentration,

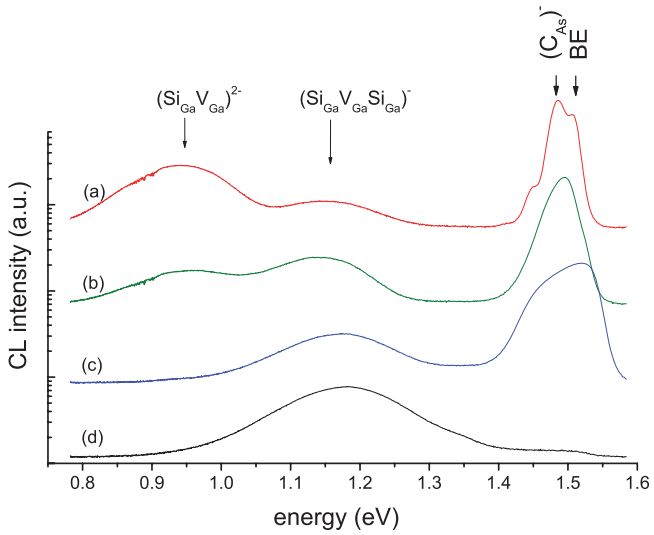

Figure 5.11 CL spectra (20 keV, 10 nA) of VCz GaAs:Si samples ($\gamma \sim 0.50$, without B_2O_3) with different Si concentrations. Measured carrier concentration: (a) $9 \times 10^{16}\,cm^{-3}$; (b) $5.9 \times 10^{17}\,cm^{-3}$; (c) $2.48 \times 10^{18}\,cm^{-3}$; and (d) $3.73 \times 10^{18}\,cm^{-3}$.

the broadening of the band edge luminescence could also be ascribed to an increasing concentration of the compensating Si^{-}_{As} acceptor at 1.485 eV [102, 103].

In n-type GaAs the mobility decreases with increasing Si doping. Even though a significant difference in samples with low and high boron contamination cannot be observed, a tendency of higher mobilities in boron-reduced GaAs crystals may be inferred [82]. These slightly higher mobilities could be a result of the reduced boron, which is a highly efficient scattering center in boron-compensated GaAs, according to Walukiewicz *et al.* [104].

In conclusion, the main difference of VCz grown GaAs without boron oxide encapsulation to commercially available SC GaAs crystals is the different defect distribution, which finally does not change the properties significantly.

5.8 Outlook on TMF-VCz

The application of magnetic fields in melt growth processes offers the possibility to control melt convection. It is expected that this affects the solid/liquid interface, temperature fluctuations of the melt and the incorporation of dopants and impurities in the crystal. Therefore, a (traveling magnetic field) TMF-VCz growth technology without boron oxide encapsulant has been developed for a Czochralski puller LPA Mark 3 at the IKZ, especially in order to improve growth stability at the Ga-enriched interface during growth of near-stoichiometric GaAs crystals

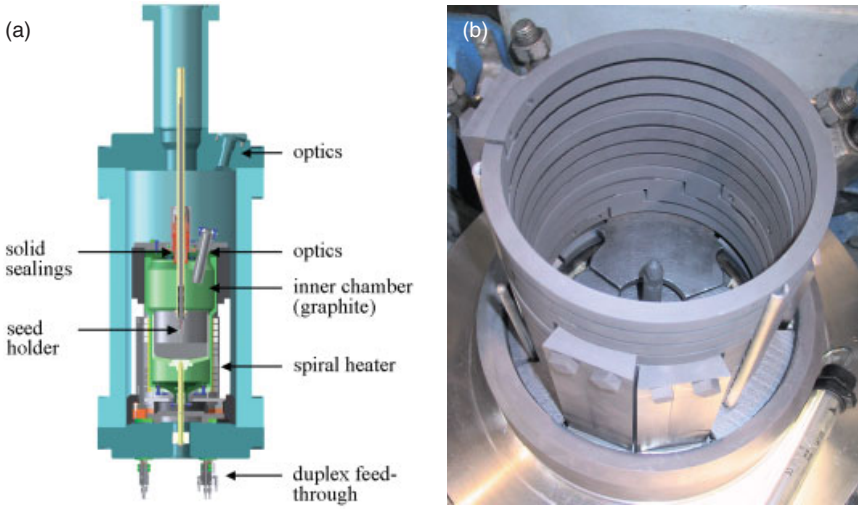

Figure 5.12 (a) drawing of TMF-VCz design with internal magnet-heater; (b) image of the used magnet-heater in the LPA Mark 3 at IKZ.

from Ga-rich melts. Within the framework of the KRIST$\widetilde{MAG}^{®}$ project [53, 105, 106] an inner magnet-heater for coupled generation of temperature- and time-dependent magnetic fields has been developed. The magnet-heater and special duplex feedthroughs replace the conventional used equipment (Figures 5.12a and b). At the same time, as the temperature is controlled as usual, the characteristics of the magnetic field can be adjusted via frequency f, phase shift φ of the alternating current (AC) and by changing the amplitude via the AC/DC (D-direct) ratio. More details are described in the chapter of Rudolph *et al.* [54] of this book.

Visual observations of floating particles placed on top of the melt are an excellent way to prove whether the magnetic field has an impact on the melt flow. Since the boron oxide encapsulation layer is omitted, an unrestricted flow of the melt surface can be visualized. In contrast to the conventional mode without magnetic field, controllable melt flow patterns as functions of the magnetic field parameters are obtained and show that the melt flow can be directed toward the crucible wall against the Marangoni convection-driven forces. By just changing the direction of the TMF, the melt flow direction can be reversed. Even vortex flows can be obtained, when the Lorentz forces are increased [107]. Numerical calculations of the Lorentz force density distribution show that the buoyancy-driven convection with maximum forces of about $300\,\mathrm{N\,m^{-3}}$ in the TMF-VCz configuration can be completely suppressed. With such a traveling magnetic field an additional powerful parameter field to control melt flow directions and velocities is established.

Kimura *et al.* using (steady magnetic) M-LEC [108] investigated material properties in dependence on pulling rate under the influence of magnetic fields and proposed that high speed pulling followed by ingot annealing might be a good

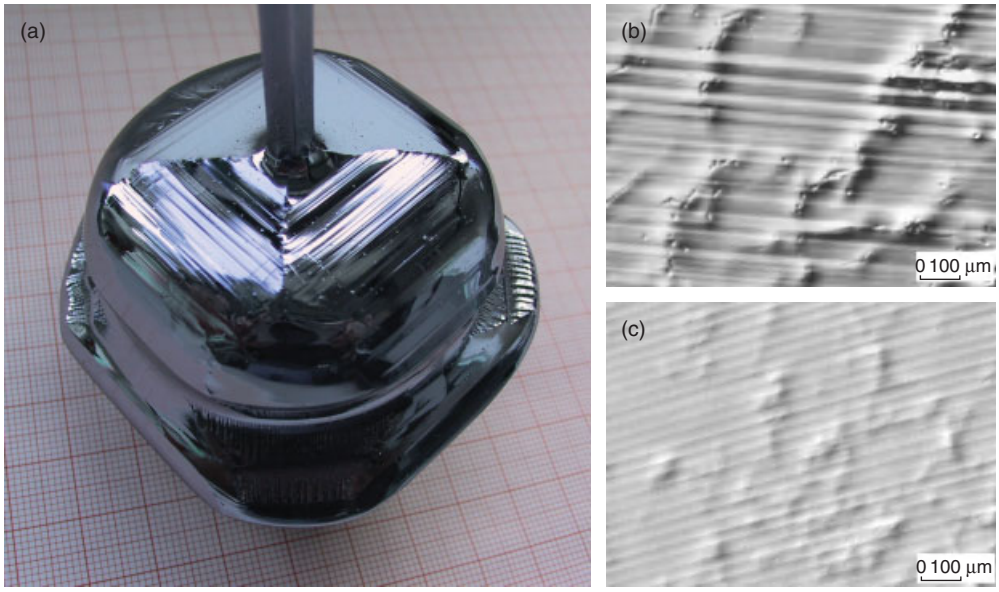

Figure 5.13 Images of: (a) as-grown GaAs crystal pulled from Ga-rich melt by the TMF-VCz method without boron oxide encapsulant ($f = 400$ Hz, $\varphi = 110°$); (b) typical striations fluctuating in amplitude and interspaces in a VCz crystal grown without traveling magnetic field; (c) reduced striation intensities and uniform distances of about 20 ± 2 µm revealed on a longitudinal cut of a TMF-VCz crystal.

production technology. Our TMF-VCz growth experiments showed that the traveling magnetic field has a strong influence on the growth conditions. In order to verify the influence of TMFs, global numerical simulations of the temperature field [109] in the melt and striation analysis on longitudinal {100} cuts of GaAs crystals have been performed (Figure 5.13a [110]). Significant differences between crystals grown without (Figure 5.13b) and under the induced forces of different traveling magnetic fields are found. Markedly reduced striation amplitudes and uniform interspaces were observed (Figure 5.13c). Independent of the applied TMF typical striation interspaces of about 20 ± 2 µm can be found in the cylindrical parts of the crystals. Thermal striations in interspaces of ~3 µm caused by rotation in an asymmetric thermal field could not been revealed. An enhanced temperature stability at the solid/liquid interface, which reduces growth-rate variations, seems to cause this improved uniformity [111–113]. And indeed in accordance with our calculations, Nakajima *et al.* [114] reported negligibly small temperature fluctuations in the melt under the influence of magnetic fields compared with those obtained during conventional LEC growth due to thermal convection.

Mean dislocation densities of 1×10^4 cm^{-2} of enhanced uniformity were deduced on as-grown TMF-VCz GaAs wafer. The first results on the homogeneity of electrical and optical properties indicate that the traveling magnetic field seems to influence defect distributions, but not that dramatically, as reported by Terashima

et al. [115–117]. Their GaAs crystals have been grown in a vertical magnetic field applied LEC apparatus (a superconducting magnetic field generator was placed outside a high-pressure puller). The effects of magnetic fields on residual impurity concentrations in the crystal were reported, which might be mainly caused by the boron oxide layer. The carbon and boron concentration changed depending on the applied magnetic field strength.

In contrast to their M-LEC technique, B_2O_3-related impurity problems cannot occur in the newly developed TMF-VCz growth. Systematic studies on TMF-VCz growth have to be done in order to optimize the process, to investigate and control the material properties. Several results on mostly process-related numerical simulations have already been published [118–122]. Currently, TMF-VCz GaAs crystal growth from Ga-rich melts seems to be a promising technology.

5.9 Conclusions

A new quality of semi-insulating GaAs material is obtained, when the crystals are grown from Ga-rich melts $\gamma < 0.475$ by the VCz or TMF-VCz method without boron oxide encapsulation. Melt composition and carbon concentration can be controlled *in situ* in order to grow GaAs crystals with well-defined electrical and optical material properties. All crystals solidified in As-rich composition in accordance with the latest calculations of the solid solubility range. The conductivity type changes from SI to p-type at a critical melt composition attributed to an additionally formed double acceptor are not found, because the responsible acceptors are B_{As}-related rather than caused by Ga antisites. The very low near-band edge absorption coefficient in SI GaAs crystals strongly depends on the gradually decreasing EL2 concentration with increasing Ga fraction in the melt, its ionization degree and the markedly reduced boron concentration. The significantly reduced As precipitate concentration is yet another key benefit of these as-grown SI GaAs crystals grown from uncovered Ga-rich melts.

Studies on semi-conducting GaAs crystals clearly demonstrate the influence of boron on intrinsic point defects. The V_{Ga} concentration is inversely proportional to the B_{As} concentration and about 3 times higher in boron-reduced GaAs crystals than in similar standard crystals. The intensities of optical transitions at 0.95 eV and at ~1.15 eV are assigned to the $(V_{Ga}Si_{Ga})^{2-}$ and to the $(Si_{Ga}V_{Ga}Si_{Ga})^{-}$ complex, respectively. The band at 0.95 eV decreases with increasing Si doping, while the band at 1.15 eV increases. All these features do not change the semiconducting material properties significantly. From recent results, a transfer of the rather complicated VCz technique to production does not seem to offer advantages.

Experiments have shown that a traveling magnetic field influences the melt flows tremendously, even in low aspect ratio configurations, and can be additionally used to control the growth process and hopefully, to homogenize defect distributions. Striation patterns revealed on TMF-VCz GaAs crystals already showed an improved homogeneity in striation intensities and interspaces.

Even though twin- and inclusion-free SI GaAs crystals can successfully be grown from Ga-rich melts in boron-free environment, pulling them with growth velocities less than the critical one, the VCz growth technique is still sophisticated in respect to the whole process control. The relatively high complexity of the equipment and low pulling rates, responsible for longer process times, offer just a transfer of the VCz or TMF-VCz technology of SI GaAs crystals for special applications to limited-lot production.

Acknowledgments

The author is very grateful to Dr. M. Albrecht and Dr. K. Irmscher of the Leibniz Institute of Crystal Growth, to Prof. R. Krause-Rehberg of the Martin Luther University Halle-Wittenberg and to Prof. W. Ulrici of the Paul Drude Institute for Solid State Electronics for their contributions. He is thankful to the director of the IKZ, Prof. R. Fornari, and to Prof. P. Rudolph for their continuous support. The work was co-financed by the Deutsche Forschungsgemeinschaft under contract numbers RU 505/10-1, 10-2 and 10-3 and partially done within the KRIST$\widetilde{MAG}^{®}$ project co-financed by the European Regional Development Fund (EFRE), Zukunftsfonds Berlin within the Technology Foundation Berlin (TSB) and Zukunftsagentur Brandenburg.

References

1 Rudolph, P., and Jurisch, M. (2003) *Crystal Growth Technology* (eds H.J. Scheel and T. Fukuda), John Wiley & Sons, Ltd, Chichester, p. 293.
2 Jurisch, M., Börner, F., Bünger, Th., Eichler, St., Flade, T., Kretzer, U., Köhler, A., Stenzenberger, J., and Weinert, B. (2005) *J. Cryst. Growth*, **275**, 283–291.
3 Orito, F., Kawabata, S., Yamada, Y., and Okada, Y. (1988) *J. Appl. Phys.*, **63**, 2691–2693.
4 Okada, Y., and Orito, F. (1988) *Appl. Phys. Lett.*, **52**, 582–583.
5 Oda, O., Yamamoto, H., Seiwa, M., Kano, G., Inoue, T., Mori, M., Shimakura, H., and Oyake, M. (1992) *Semicond. Sci. Technol.*, **7**, A215–A223.
6 Osaka, J., Hyuga, F., Kobayashi, T., Yamada, Y., and Orito, F. (1987) *Appl. Phys. Lett.*, **50**, 191–193.
7 Cockayne, B., MacEwan, W.R., Hope, D.A.O., Harris, I.R., and Smith, N.A. (1988) *J. Cryst. Growth*, **87**, 6–12.
8 Orito, F., Fujii, K., and Okada, Y. (1990) *J. Appl. Phys.*, **68**, 5696–5699.
9 Hashio, K., Sawada, S., Tatsumi, M., Fujita, K., and Akai, S. (1997) *J. Cryst. Growth*, **173**, 33–41.
10 Eichler, S., Fliegel, W., Jurisch, M., Köhler, A., Naumann, M., and Rockoff, A. (2008) *J. Cryst. Growth*, **310**, 1410–1417.
11 Gremmelmaier, R. (1956) *Z. Naturforsch.*, **11a**, 511–513.
12 Steinemann, A., and Zimmerli, U. (1967) *Crystal Growth* (ed. H.S. Peiser), Pergamon Press, Oxford, p. 81.
13 Richards, J.L. (1957) *J. Sci. Instrum.*, **34**, 289–290.
14 Tanenbaum, M. (1959) *Semiconductors* (ed. N.B. Hannay), Reinhold, New York.
15 Mullin, J.B., MacEwan, W.R., Holliday, C.H., and Webb, A.E.V. (1972) *J. Cryst. Growth*, **13/14**, 629–634.
16 Leung, P.C., and Allred, W.P. (1973) *J. Cryst. Growth*, **19**, 356–358.

17 Texas Instruments Inc. (1964) Patent description GB000001074248A.

18 Morton, E.J. (1961) Patent description DE000001519914A.

19 Moulin, M., Faure, M., and Bichon, G. (1974) *J. Cryst. Growth*, **24–25**, 376–379.

20 Baldwin, E.M.N., Brice, J.C., and Millet, E.J. (1965) *J. Sci. Instrum.*, **42**, 883–884.

21 Tomizawa, K., Sassa, K., Shimanuki, Y., and Nishizawa, J. (1984) *J. Electrochem. Soc.*, **131**, 2394–2397.

22 Tomizawa, K., Sassa, K., Shimanuki, Y., and Nishizawa, J. (1987) Proceedings, 14th Int. Symp. on GaAs and Related Compounds, Heraklion, Inst. Phys. Conf. Ser., IOP, Bristol, vol. 91, pp. 435–438.

23 Tomizawa, K., Sassa, K., Shimanuki, Y., and Nishizawa, J. (1987) *Defects and Problems of Semiconductors* (eds J. Chikawa, K. Sumino, and K. Navada), KTK Scientific Publishers, Tokyo, pp. 25–36.

24 Nishizawa, J. (1990) *J. Cryst. Growth*, **99**, 1–8.

25 Nishizawa, J., and Oyama, Y. (1994) *Mater. Sci. Eng. R*, **12**, 273–426.

26 Dahlen, A., Fattah, A., Wenzl, H., Wiedemann, B., and Winnaker, A. (1995) Abstracts, ICCG-XI, The Hague, June 18–23, 1995, p. 337.

27 Oates, W.A., and Wenzl, H. (1998) *J. Cryst. Growth*, **191**, 303–312.

28 Neubert, M., and Rudolph, P. (2001) *Prog. Cryst. Growth Charact. Mater.*, **43**, 119–185.

29 Trompa, K., Neubert, M., Rudolph, P., Krause, P., Seifert, M., Jurisch, M., and Prause, J. (1996) Patent description DE000019604027C1.

30 Rudolph, P., and Kiessling, F.-M. (2006) *J. Cryst. Growth*, **292**, 532–537.

31 Kiessling, F.-M., Bondarenko, V., Frank-Rotsch, Ch., Neubert, M., Rudolph, P., and Ulrici, W. (2002) Abstract Book. ACCGE-14, Seattle, August 4–9, 2002, p. 92.

32 Hurle, D.T.J., and Rudolph, P. (2004) *J. Cryst. Growth*, **264**, 550–564.

33 Kiessling, F.-M., Rudolph, P., Neubert, M., Juda, U., Naumann, M., and Ulrici, W. (2004) *J. Cryst. Growth*, **269**, 218–228.

34 Frank-Rotsch, Ch., Neubert, M., Kießling, F.-M., and Lange, R.-P. (2004) Patent description DE102004020656A1.

35 Tower, J.P., Tobin, R., Pearah, P.J., and Ware, R.W. (1991) *J. Cryst. Growth*, **114**, 665–675.

36 Hurle, D.T.J. (1995) *J. Cryst. Growth*, **147**, 239–250.

37 Kiessling, F.-M., Neubert, M., Rudolph, P., and Ulrici, W. (2003) *Mater. Sci. Semicond. Proc.*, **6**, 303–306.

38 Lagowski, J., Gatos, H.C., Parsey, J.M., Wada, K., Kaminska, M., and Walukiewicz, W. (1982) *Appl. Phys. Lett.*, **40**, 342–344.

39 Jurisch, M., and Wenzl, H. (2002) Workshop, German Ass. of Crystal Growth (DGKK) on Simulations in Crystal Growth, Memmelsdorf, October, 2002.

40 Frigeri, C., Weyher, J.L., and Alt, H.Ch. (1993) *Phys. Status Solidi A*, **138**, 657–663.

41 Steinegger, T., Naumann, M., Jurisch, M., and Donecker, J. (2001) *Mater. Sci. Eng. B*, **80**, 215–219.

42 Weyher, J.L., Frigeri, C., Zanotti, L., Alt, H.Ch., van der Wel, P., and Gall, P. (1992) 7th Conf. Semi-Insulating III-V Materials, Ixtapa, Mexico, Chapter 3, p. 97.

43 Fornari, R., Frigeri, C., and Gleichmann, R. (1989) *J. Electron. Mater.*, **18**, 185–189.

44 Cullis, A.G., Augustus, P.D., and Stirland, D.J. (1980) *J. Appl. Phys.*, **51**, 2556–2560.

45 Schlossmacher, P., Urban, K., and Rüfer, H. (1992) *J. Appl. Phys.*, **71**, 620–629.

46 Weyher, J.L., Schober, T., Sonnenberg, K., and Franzosi, P. (1998) *Mater. Sci. Eng. B*, **55**, 79–85.

47 Hurle, D.T. (1999) *J. Appl. Phys.*, **85**, 6957–7022.

48 Wenzl, H., Oates, W.A., and Mika, K. (1997) *Handbook of Crystal Growth*, vol. **1** (ed. D.T.J. Hurle), Elsevier, North-Holland, Amsterdam, p. 103.

49 Rudolph, P. (2003) *Cryst. Res. Technol.*, **38**, 542–554.

50 Dreyer, W., and Duderstadt, F. (2008) *Proc. R. Soc. Lond. Ser. A Math. Phys. Eng. Sci.*, **464**, 2693–2720.

51 Eichler, S., Börner, F., Bünger, T., Jurisch, M., Köhler, A., Kretzer, U., Scheffer-Czygan, M., Weinert, B., and Flade, T. (2008) *Crystal Growth Technology* (eds H.J. Scheel and P. Capper), Wiley-VCH Verlag GmbH, Weinheim, p. 231.

52 Pfann, W.G (1966) *Zone Melting*, John Wiley & Sons, Inc., New York.

53 Rudolph, P. (2008) *J. Cryst. Growth*, **310**, 1298–1306.

54 Rudolph, P., Czupalla, M., Frank-Rotsch, Ch., Kiessling, F.-M., and Lux, B. (2010) *Crystal Growth Technology* (eds P. Capper and P. Rudolph), Wiley-VCH Verlag GmbH, Weinheim, p. 701.

55 Brice, J.C., and King, G.D. (1966) *Nature*, **209**, 1346.

56 Rudolph, P., Frank-Rotsch, Ch., Juda, U., and Kiessling, F.-M. (2005) *Mater. Sci. Eng. A*, **400–401**, 170–174.

57 Rudolph, P. (2005) *Cryst. Res. Technol.*, **40**, 7–20.

58 Lagowski, J., Gatos, H.C., Aoyama, T., and Lin, D.G. (1984) *Appl. Phys. Lett.*, **45**, 680–682.

59 Immenroth, H., Lambert, U., and Tomzig, E. (1994) *J. Cryst. Growth*, **142**, 37–48.

60 Blakemore, J.S. (1982) *J. Appl. Phys.*, **53**, R123–R181.

61 Elliot, K.R. (1984) *Appl. Phys. Lett.*, **55**, 3856–3858.

62 Kikuta, T., and Ishida, K. (1986) *Inst. Phys. Conf. Ser.*, **83**, 45.

63 Okubo, S., Otoki, Y., Watanabe, M., and Kuma, S. (1993) *Jpn. J. Appl. Phys.*, **32**, 1898–1901.

64 Mucchino, C., Görög, T., Zanotti, L., Mignoni, G., and Catellani, A. (1996) *Mater. Sci. Forum*, **203**, 7–12.

65 Mih, R., Gronsky, R., Dahlen, A., Howell, R.H., and Sterne, P.A. (1995) *Mater. Res. Soc. Symp. Proc.*, **373**, 517–522.

66 Bondarenko, V. (2004) MLU Halle-Wittenberg, thesis.

67 Kiessling, F.-M., and Rudolph, P. (2008) *J. Phys. Chem. Solids*, **69**, 289–293.

68 Ulrici, W., Kiessling, F.-M., and Rudolph, P. (2004) *Phys. Status Solidi B*, **241**, 1281–1285.

69 Wohlrab, A., Gründig-Wendrock, B., Jurisch, M., Kiessling, F.-M., and Niklas, J.R. (2004) *Eur. Phys. J.- Appl. Phys.*, **27**, 223–226.

70 Kretzer, U., and Alt, H.Ch (2003) *Phys. Status Solidi C*, **0**, 845–849.

71 Alt, H.Ch., Gomeniuk, Y., and Kretzer, U. (2003) *Phys. Status Solidi B*, **235**, 58–62.

72 Holmes, D.E., Chen, R.T., Elliott, K.R., and Kirkpatrick, C.G. (1982) *Appl. Phys. Lett.*, **40**, 46–48.

73 Kozlova, J.P., Bowles, T.J., Eremin, V.K., Gavrin, V.N., Koshelev, O.G., Markov, A.V., Morozova, V.A., Polyakov, A.J., Verbitskaya, E.M., and Veretenkin, E.P. (2003) *Nucl. Instrum. Methods Phys. Res. A*, **512**, 1–7.

74 Elliott, K.R., Holmes, D.E., Chen, R.T., and Kirkpatrick, C.G. (1982) *Appl. Phys. Lett.*, **40**, 898–901.

75 Yu, P.W., Mitchel, W.C., Mier, M.G., Li, S.S., and Wang, W.L. (1982) *Appl. Phys. Lett.*, **41**, 532–534.

76 Shanabrook, B.V., Moore, W.J., and Bishop, S.G. (1986) *J. Appl. Phys.*, **59**, 2535–2537.

77 Bugajski, M., Ko, K.H., Lagowski, J., and Gatos, H.C. (1989) *J. Appl. Phys.*, **65**, 596–599.

78 Ta, L.B., Hobgood, H.M., and Thomas, R.N. (1982) *Appl. Phys. Lett.*, **41**, 1091–1093.

79 Woodhead, J., Newman, R.C., Grant, I., Rumsby, D., and Ware, R.M. (1983) *J. Phys. C: Solid State Phys.*, **16**, 5523–5533.

80 Addinall, R., and Newman, R.C. (1992) *Semicond. Sci. Technol.*, **7**, 1005–1007.

81 Newman, R.C., Davidson, B.R., Adinall, R., Murray, R., Emmert, J.W., Wagner, J., Götz, W., Roos, G., and Pensl, G. (1994) *Mater. Sci. Forum*, **143–147**, 229–234.

82 Kiessling, F.-M., Albrecht, M., Irmscher, K., Krause-Rehberg, R., Ulrici, W., and Rudolph, P. (2008) *J. Cryst. Growth*, **310**, 1418–1423.

83 Ta, L.B., Hobgood, H.M., Rohatgi, A., and Thomas, R.N. (1982) *J. Appl. Phys.*, **53**, 5771–5775.

84 Neubert, M. (2002) BMbf report 01 Bm 501/A0.

85 Balkanski, M., and Wallis, R.F. (2000) *Semiconductor Physics and Applications*, Oxford University Press, New York, p. 169.

86 Silverberg, P., Omling, P., and Samuelson, L. (1988) *Appl. Phys. Lett.*, **52**, 1689–1691.

87 Tüzemen, S., Brozel, M.R., and Breivik, L. (1992) *J. Electron. Mat.*, **21**, 389–394.

88 Kiessling, F.-M., Albrecht, M., Irmscher, K., Roßberg, M., Rudolph, P., Ulrici, W., and Fornari, R. (2009) Abstract Book. 15th Semiconducting and Insulating Materials Conf., Vilnius, June 15–19, 2009.

89 Alexandrovski, A., Fejer, M., Markosyan, A., and Route, R. (2009) Proceedings, SPIE Photonics West, San Jose, January 24–29, 2009.

90 Weber, E.R., Ennen, H., Kaufmann, U., Windscheif, J., Schneider, J., and Wosinski, T. (1982) *J. Appl. Phys.*, **53**, 6140–6143.

91 Queisser, H.J. (1966) *J. Appl. Phys.*, **37**, 2909–2910.

92 Sauncy, T., Palsule, C.P., Holtz, M., and Gangopadhyay, S. (1996) *Phys. Rev. B*, **53**, 1900–1906.

93 Reshchikov, M.A., Gutkin, A.A., and Sedov, V.E. (1995) *Mater. Sci. Forum*, **196–201**, 237–242.

94 Lei, H., Leipner, H.S., Bondarenko, V., and Schreiber, J. (2003) *J. Phys.: Condens. Matter.*, **15**, 1–7.

95 Ky, N.H., and Reinhart, F.K. (1998) *J. Appl. Phys.*, **83**, 718–724.

96 Albrecht, M., Freysoldt, Ch., Irmscher, K., Kiessling, F.-M., and Neugebauer, J. (2010) *Phys. Rev. B*, to be published.

97 Gebauer, J. (2000) Thesis, Martin Luther University Halle-Wittenberg.

98 Bondarenko, V. (2004) Thesis, Martin Luther University Halle-Wittenberg.

99 Corbel, C., LeBerre, C., Saarinen, K., and Hautojarvi, P. (1997) *Mater. Sci. Eng.*, **B44**, 173–180.

100 Northrup, J.E., and Zhang, S.B. (1993) *Phys. Rev. B*, **47**, 6791–6794.

101 Kretzer, U., Börner, F., Bünger, T., and Eichler, S. (2007) *Phys. B: Condens. Matter.*, **401–402**, 246–249.

102 Ashen, D.J., Dean, P.J., Hurle, D.T.J., Mullin, J.B., White, A.M., and Greene, P.D. (1975) *J. Phys. Chem. Solids*, **36**, 1041–1053.

103 Pätzold, O., Gärtner, G., and Irmer, G. (2002) *Phys. Status Solidi B*, **232**, 314–322.

104 Walukiewicz, W., Lagowski, L., Jastrzebski, L., Lichtensteiger, M., and Gatos, H.C. (1979) *J. Appl. Phys.*, **50**, 899–908.

105 Ziem, M., Rudolph, P., and Lange, R.-P. (2007) Patent description DE102007020239A1.

106 Lange, R.-P., Jockel, D., Ziem, M., Rudolph, P., Kießling, F.-M., Frank-Rotsch, Ch., Czupalla, M., Nacke, B., and Kasjanow, H. (2007) Patent description DE102007028547A1.

107 Kießling, F.-M., Czupalla, M., Juda, U., Lange, P., Root, O., Ziem, M., Rudolph, P., Klein, O., and Lechner, Ch. (2008) Abstract Book. Annual Convention of German Ass. of Crystal Growth (DGKK), München, March 05–07, 2008.

108 Kimura, T., Obokata, T., and Fukuda, T. (1987) *J. Cryst. Growth*, **84**, 394–398.

109 Klein, O., Lechner, Ch., Druet, P.-E., Philip, P., Sprekels, J., Frank-Rotsch, Ch., Kießling, F.-M., Miller, W., Rehse, U., and Rudolph, P. (2008) *J. Cryst. Growth*, **310**, 1523–1532.

110 Rudolph, P. (2007/2008) IKZ Annual Report, pp. 66–70.

111 Kiessling, F.-M., Klein, O., Lechner, Ch., and Rudolph, P. (published).

112 Osaka, J., Kohda, H., Kobayashi, T., and Hoshikawa, K. (1984) *Jpn. J. Appl. Phys.*, **23**, L195–L197.

113 Kimura, T., Katsumata, T., Nakijama, M., and Fukuda, T. (1986) *J. Cryst. Growth*, **79**, 264–270.

114 Nakajima, M., Katsumata, T., Terashima, K., and Ispida, K. (1985) *Jpn. J. Appl. Phys.*, **24**, L65–L68.

115 Terashima, K., Orito, F., Katsumata, T., and Fukuda, T. (1984) *Jpn. J. Appl. Phys.*, **23**, L485–L487.

116 Terashima, K., Katsumata, T., Orito, F., and Fukuda, T. (1984) *Jpn. J. Appl. Phys.*, **23**, L302–L304.

117 Terashima, K., Katsumata, T., Orito, F., Kikuta, T., and Fukuda, T. (1983) *Jpn. J. Appl. Phys.*, **22**, L325–L327.

118 Kasjanow, H., Nacke, B., Eichler, St., Jockel, D., Frank-Rotsch, Ch., Lange, P., Kießling, F.-M., and Rudolph, P. (2008) *J. Cryst. Growth*, **310**, 1540–1545.

119 Rudolph, P., Frank-Rotsch, Ch., Lux, B., Jockel, D., Kiessling, F.-M., and Czupalla, M. (2008) *IEEE Catalog Nr.*

CFP08IIP-CDR, ISBN: 978-1-4244-2259-3, ISSN: 1092-8669.

120 Nacke, B., Kasjanow, H., Krauze, A., Muiznieks, A., Kiessling, F.-M., Rehse, U., and Rudolph, P. (2008) *Proceedings, 7th PAMIR International Conference on Fundamental and Applied MHD*, Presqu'lle de Giens, France, 2008, Vol. 1, pp. 643–648.

121 Rudolph, P., Frank-Rotsch, Ch., Kiessling, F.-M., Miller, W., Rehse, U., Klein, O., Lechner, Ch., Sprekels, J., Nacke, B., Kasjanow, H., Lange, P., Ziem, M., Lux, B., Czupalla, M., Root, O., Trautmann, V., and Bethin, G. (2008) Proceedings, International Scientific Colloquium MEP, pp. 79–84.

122 Klein, O., Druet, P.-E., Lechner, Ch., Philip, P., Sprekels, J., Frank-Rotsch, Ch., Kießling, F.-M., Miller, W., Rehse, U., and Rudolph, P. (2008) Proceedings, International Scientific Colloquium MEP, pp. 91–98.

6
The Growth of Semiconductor Crystals (Ge, GaAs) by the Combined Heater Magnet Technology

Peter Rudolph, Matthias Czupalla, Christiane Frank-Rotsch, Frank-Michael Kiessling and Bernd Lux

6.1
Introduction

Gallium arsenide (GaAs) with a melting point of 1238 °C is the leading semiconductor material for optoelectronics and high-frequency microelectronics. It is also used in radiation detectors and solar cells of high photovoltaic efficiency [1, 2]. Since the 1990s the industrial crystal growth capacity was increased markedly. During the last five years the production scale of GaAs wafers has been nearly doubled. As a result, the price of 4-inch wafers fell below $1, being about three orders of magnitude cheaper than InP substrates of the same diameter. This was first of all due to the efficient improvements of the crystal growth and wafer handling technologies. Today, two methods have been established for mass production, (i) the liquid encapsulated Czochralski (LEC) method for semiconducting (mostly Si-doped) optoelectronic material; and (ii) the vertical Bridgman (VB) or vertical gradient freeze (VGF) technique for semi-insulating (SI) wafers as the basis of high-frequency devices. Up to 6-inch crystals are produced by both LEC and VGF. Also, the growth of 8-inch diameter has already been tested successfully [3].

To increase the future crystal output per growth run, as the essential step towards further price reduction, both diameter and length enlargement and, consequently, an increase of the melt volume is required. This, however, proves to be the most problematic challenge because of the increasing intensity of buoyancy-driven convection leading to turbulent flows with violent nonstationary perturbations. They disturb the single-crystalline growth and give rise to compositional inhomogeneities. The use of stabilizing high crucible rotation rates fails when growing from very large melt masses. Therefore, the induction of a magnetic field into the melt proves to be the most promising measure to damp the convections and to control the interface shape. In particular, nonsteady fields became very popular because, in this case, the needed strength of the magnetic induction is much lower than for steady fields. In the present chapter, the first results of the LEC growth of GaAs crystals under traveling magnetic field (TMF) generated in a heater-magnet module (HMM) are summarized.

Crystal Growth Technology. Semiconductors and Dielectrics. Edited by P. Capper and P. Rudolph
Copyright © 2010 WILEY-VCH Verlag GmbH & Co. KGaA, Weinheim
ISBN: 978-3-527-32593-1

Germanium (Ge) is a popular model substance for crystal-growth studies from the melt due to its low melting point (937.4 °C) and resistance against oxygen. As is well known, Ge crystals are also of increasing appliance in high-resolution γ-ray spectroscopy, temperature sensors, and radiation detectors. Recently, the increasing interest in low-resistivity single-crystalline germanium for triple-junction solar cell production has been reported [4].

Ge was the first semiconductor grown by the Czochralski method [5] and is now a well-matured industrial technique for this material. However, during the last decade also VB and VGF have become of increasing interest [6–8] due to the reduced complexity, high diameter uniformity and lower power consumption. However, there are still three cardinal problems, (i) the concavity of the melt/solid interface due to the lower thermal conductivity compared to that of the melt; (ii) the contact situation at the container wall; and (iii) the increase in convection-driven thermal instabilities with increasing melt height. To master these objectives a slightly convex interface morphology and very high temperature stability, both being maintained constant during the entire growth process, prove to be most suitable measures. Even the application of TMF can help to achieve this aim very effectively. The results of Ge VGF growth within a combined inner HMM placed closely around the growth container demonstrate that such a technology is favored from the technical as well as economical point of view. Nearly flat and slightly convex interfaces leading to homogeneous parameter distributions can be achieved.

The combined heater-magnet technology was developed within the framework of the KRIST$\widetilde{MAG}^{®}$ project [9]. Amplitude, frequency and phase shift of the three-phase alternating current (AC) are all adjustable and combined with a DC component to control the dynamics of the crystallization process effectively. The induced TMF and its effect on the melt convection in LEC and VGF systems was analyzed by global 2.5 and 3D modeling with codes CrysMAS [10], NAVIER, WIAS-HiTNIHS [11] and CFX [12]. The induced Lorentz force density was measured by the weight responses of a dummy made of stainless steel when the traveling magnetic field of given amplitude, frequency and phase shift was switched on. A good agreement with the numerical calculations has been observed.

6.2 Selected Fundamentals

6.2.1 Convection-Driven Forces

When the heat flux in melt-growth systems is directed against or angular to the gravity vector, a thermally instable liquid phase is presented. This is typical in the case of Czochralski crucible when heated from below or from the side. It appears also in vertical gradient freeze containers due to the radial temperature differences. As a result, buoyancy-driven laminar or even turbulent convections appear that are responsible for harmful temperature fluctuations affecting the crystal-growth

stability and compositional homogeneity. Additionally, the melt convection vortices may cause undesirable deformations of the melt/solid interface shape leading to enhanced dislocation density.

The intensity of buoyancy convection can be estimated via the force density [13]

$$F_B = \rho\beta g\Delta T \tag{6.1}$$

with ρ the melt density, β the volume expansion coefficient, g the gravitational acceleration (= 9.81 m s^{-2}), and ΔT the characteristic temperature difference. For instance, in a GaAs melt with ρ = 5200 kg m^{-3} and $\beta = 1.8 \times 10^{-4}$ K^{-1} the value F_B amounts to ~460 N m^{-3} when the characteristic ΔT is 50 K. In a Ge melt under identical conditions F_B becomes about 300 N m^{-3} (ρ = 5510 kg m^{-3}, $\beta = 1.11 \times 10^{-4}$ K^{-1}). Note, the F_B values represent the reference for external forces to counteract such buoyancy-driven flux.

At first, the rotation of the melt crucible, such as in LEC method, proves to be an effective measure for temperature homogenization that stabilizes the heat and mass fluxes against undesirable temperature perturbations. In fact, the convective meridional flows can be suppressed by the rotational force density [13]

$$F_{rot} \approx \rho\omega^2 r \tag{6.2}$$

with $\omega = u_{rot}\, 2\pi$ (u_{rot}, rotation rate) the crucible angular frequency and r the radius. When comparing F_{rot} with the convection force density F_B in Equation 6.1 to be counteracted, crucible rotation rates u_{rot} above 10 rpm are already effective for GaAs melt when r is taken to be 0.075 m (6-inch crucible). However, the situation is markedly more complicated when larger temperature differences are present, as is typical for higher melts.

A stability analysis of the interplay between rotation rate and convection force in various melts was carried out by Rossby [14]. Comparing the thermal Rayleigh number

$$\mathrm{Ra}^T = g\beta\Delta T h^3 (\nu\kappa)^{-1} \tag{6.3}$$

with h, melt height, ν, kinematic viscosity, κ, thermal diffusivity (= $\lambda c_p^{-1}\rho^{-1}$, λ, heat conductivity, c_p, specific heat capacity) with the forced rotation-related Taylor number

$$\mathrm{Ta} = 4\omega^2 h^4 (\nu)^{-2} \tag{6.4}$$

one obtains material-independent boundary criteria between regions of stationary laminar, oscillating and nonstationary (turbulent) convection (Figure 6.1). As can be seen, the higher the melt column h the larger the crucible angular frequency ω should be selected to depress turbulent flows. In dependency on the material parameters such as thermal diffusivity and kinematic viscosity the stabilizing rotation rates can differ markedly. Whereas in the case of a silicon melt with heights in the range of 50–100 mm still practicable crucible rotations of $u_{rot} \approx$ 10 rpm can be used, the situation for GaAs proves to be much more critical. For example, at temperature difference of 10 K in melts of height h = 10 cm stabilizing rotation rates markedly larger than 20 rpm would be necessary (see Figure 6.1). This may

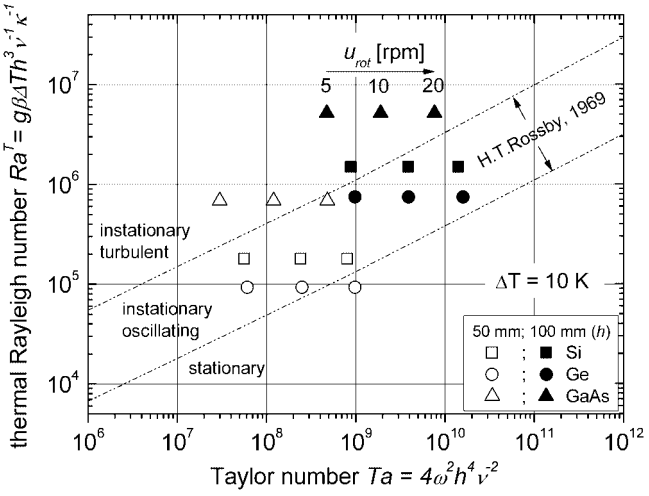

Figure 6.1 Thermal Rayleigh versus Taylor number responsible for the ratio between buoyancy-driven convection and rotation-driven flow in melts, respectively. The lines of Rossby criteria [14] show the transitions between stationary laminar, oscillating and nonstationary (turbulent) streaming modes. Some selected values of Si, GaAs and Ge for rotation rates u_{rot} = 5, 10, 20 rpm and melt heights h = 50, 100 mm at constant temperature difference ΔT = 10 K over melt height are inserted.

be technically difficult to realize, especially when big melt charges (up to 50 kg) in very large crucibles are used.

Usually, in VGF growth no rotation is used. Hence, for both LEC and VGF the application of another external stabilizing force such as a magnetic field becomes favorable.

6.2.2
The Features of Traveling Magnetic Fields

The application of magnetic fields as an external force for damping natural convection has been well known for a long time. One difference is between steady and nonsteady fields whereas both variants can be subdivided into many variants such as horizontal, vertical and cusp-shaped permanent fields or rotating, alternating and traveling variable fields (see Figure 6.1 in Ref. [9]).

A TMF is generated by means of applying out-of-phase AC to a number of coils that are arranged vertically one upon the other or of interleaved connected spirals. As a result, a meridional traveling Lorentz field is induced when an electrically conducting melt is applied inside. The field line direction (up- or downward and out- or inward in coil or spiral mode, respectively), frequency f, phase shift φ and amplitude I can be controlled very conveniently. The magnetic induction B can be described as a wave model consisting of axial and radial components $B = (B_z^2 + B_r^2)^{1/2}$ with wavelength $\lambda = 2\pi/k = nh$ (k, wave number, $n \geq 2$, number of coils/spirals, h, distance between coils/spirals).

Even the traveling magnetic fields show certain advantages in comparison with other field variants. First, an axisymmetric toroidal Lorentz force pattern is created. This manifests its effective counteracting property against buoyancy-driven convection generating mostly axisymmetric (toroidal) roll patterns. Secondly, a higher damping efficiency is obtained due to its proportionality with the field frequency. Finally, TMF proves to be most suitable to control the shape of the growing interface in VGF arrangements (see Ref. [15], for example).

Comparing the generated magnetic inductions of steady and nonsteady fields the higher damping efficiency of TMF is obvious. According to Equation 6.1 a magnetic force density of $F_m \approx 460\,\mathrm{N\,m^{-3}}$ is required to counteract the buoyancy-driven convection in a GaAs melt with a characteristic temperature difference of 50 K. The needed induction strength of a steady magnetic field B_{SMF} would be [9]

$$B_{SMF} \approx \sqrt{460/\sigma u} \approx 85\,\mathrm{mT} \tag{6.5}$$

with σ, electrical conductivity = $6.5 \times 10^5\,\mathrm{S\,m^{-1}}$, u, convection stream velocity $\approx 0.1\,\mathrm{m\,s^{-1}}$ [16]. In contrast, in the case of TMF an identical suppression force density $F_{TMF} \approx \sigma \pi f L B^2 = 460\,\mathrm{N\,m^{-3}}$ demands only an induction intensity of

$$B_{TMF} \approx \sqrt{460/\sigma \pi f L} \approx 5.5\,\mathrm{mT} \tag{6.6}$$

being more than one magnitude lower when a frequency of $f = 100\,\mathrm{Hz}$ and characteristic length of $L \equiv r = 0.075\,\mathrm{m}$ are assumed. Thus, much lower power consumption is required.

The penetration depth of a nonsteady magnetic field within the melt can be estimated by the skin thickness δ_s to be

$$\delta_s = (\pi \mu_o \mu_r \sigma f)^{-1/2} \tag{6.7}$$

where μ_o is the magnetic field constant ($= 12.566 \times 10^{-7}\,\mathrm{H\,m^{-1}}$) and $\mu_r \approx 1$ the relative permeability. Skin depths of $\delta_s \approx 20$–$2\,\mathrm{cm}$ appear in a GaAs melt when TMF frequencies in the range $f = 10$–$600\,\mathrm{Hz}$ are used, respectively.

Today, the research is concentrated on TMF application in VB and VGF arrangements for fundamental studies in metallic alloys [17], Ge [18, 19] and semiconducting compounds such as GaAs [8, 10, 20] and InP [15]. Concordantly, an effective controllability of the interface shape, significant reduction of thermal shear stress, and damping of compositional inhomogeneities (striations) were reported. Also, the Czochralski growth of silicon crystals under TMF is under investigation [21–23] and has proven to be favorable for convenient control of temperature distribution, interface shape, and oxygen incorporation with relatively low power consumption. However, one critical point of TMF is noteworthy. The field strength has to be adjusted for each given crystal-growth system with care since, otherwise, undesirable oscillating instabilities might appear [19, 24, 25]. The criterion is given by the TMF-related Taylor number of the melt [15]:

$$\mathrm{Ta}_{TMF} = \frac{\sigma \pi f r^3}{\rho \nu^2 k} B_{TMF}^2 \tag{6.8}$$

Schwesig *et al.* [15] found numerically that in a 2-inch InP melt within a TMF the critical Taylor number Ta^*_{TMF} is about 2×10^7 being almost independent of the

aspect ratio H/D (H, height, D, diameter). We observed a nearly identical result in a Ge melt (see Chapter 4).

6.3 TMF Generation in Heater-Magnet Modules

Usually, in the crystal-growth practice the coils for generation of any mode of magnetic field are positioned outside of the growth chamber [25, 26], which, in turn, causes the magnet to be designed for production of a much higher induction force than is actually needed for convection control. This allows compensation for the field losses due to the distance between the magnet and the crucible, with the obvious screening effects of chamber walls, heat shields, and heaters. As a result, only up to one order of magnitude lower flow density will reach the melt volume [11]. In general, external magnets are very expensive and energy-consuming because they must be designed thus to generate relatively high induction forces. Therefore, a significant economical effect can be achieved when the generator is placed as close as possible to the melt, as first proposed for a rotating magnetic field (RMF) in a Czochralski puller by Brückner and Schwerdtfeger [27]. The coil pairs were positioned separately around the heater. However, to overcome the problem of extensive heat-up caused by heat transfer from the melt a special cooler was placed between both heater and magnet. Obviously, the temperature limit of the inductor parts (155 °C for the insulation of windings) stopped further developments of such RMF variant especially for the industry.

Within the framework of KRIST$\widetilde{MAG}^{®}$ project (2005–2008) we developed inner heater-magnet modules (HMM) for coupled generation of temperature and translating magnetic fields adjusting to industrial crystal-growth equipments [28–30]. To obtain a suitable magnetic field and to control the crystallization process effectively the amplitude, frequency and phase shift of the three-phase current are all adjustable over wide ranges and are combined with a DC component. For the generation of vertically translating TMF the heater design must be changed completely, that is, from a conventional standard meandering "picket fence" to a hollow cylindrical body with an upwards-winding slit forming a single-layered spiral- or staircase-shaped current path (see Figure 6.3 in Ref. [9]). The path is subdivided into coil segments by contact points for the phase-shifted power supply in a delta or star connection.

To that end, a universal HMM controller system has been developed and performed. It contains a 6-pack integrated intelligent power system (SkiiP) impulse- and frequency-driven by an electronic control module. As a result, both a three-phase well-formed sine AC of desired frequency and phase shift for TMF generation and a DC component for controlling the melting and crystallization temperature are supplied to the heater-magnet. For our experiments the following parameter range was available: maximum power P = 40 kW, voltage V = 0–40 V, maximum current I = 330 A per coil section, frequency f = 10–600 Hz, and phase shift φ = 5–120 °. By means of such variables the generation of mag-

netic induction $B = 1–10\,\mathrm{mT}$ and Lorentz force densities F_m up to about $1000\,\mathrm{N\,m^{-3}}$ were possible.

The basic idea of combined heater-magnet in crystal growth is not new and goes back to the 1970s [31]. It was tested to produce rotating magnetic fields [32–34] and proposed for generation of steady [35] and longitudinally traveling fields [36, 37]. However, numerous technological issues had to be solved by the KRISTMAG® team to realize such a concept in crystal-growth equipments of industrial scale. For instance, asymmetry effects due to the passages between windings and electric supply lines have to be overcome [29]. Furthermore, the combination of jacket and bottom heater-magnet modules generating vertically and horizontally translating fields were designed [30]. In the following, we report the first growth experiments of GaAs and Ge crystals within HMMs in industrial LEC and VGF equipments, respectively.

6.4 The HMM Design

Figure 6.2 shows the HMM made of graphite for LEC growth of GaAs crystals that has been inserted in the industrial high-pressure puller "CI 358" from Cambridge Instruments Ltd. A special multicoil design was worked out [30] to generate

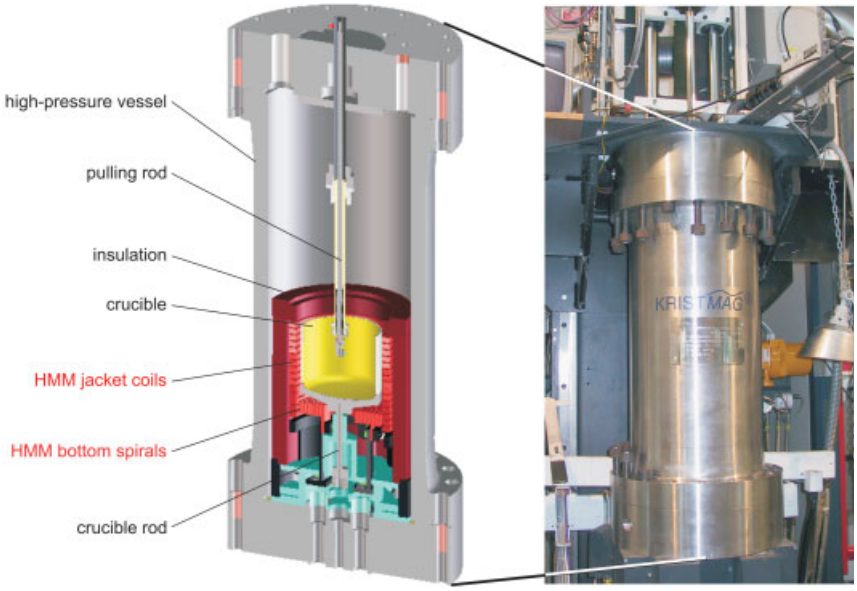

Figure 6.2 Schematic cross-section (left) and real vessel image (right) of the commercial LEC crystal puller "CI 358" with inserted HMM around the crucible consisting of three jacket coils and two bottom spirals generating heat and TMF simultaneously by supplying of out-of-phase AC.

simultaneously vertical and horizontal TMFs by jacket and bottom HMMs around the wall and under the bottom of the crucible, respectively. Such an arrangement proved to be the favored one for an optimal Lorentz field against buoyancy-driven temperature oscillations below the growing crystal (see Section 6.5).

Out-of-phase AC was delivered in a star connection to the HMM sections for simultaneous heating and magnetic field generation. Both jacket and bottom THM parameters could be varied in the traveling direction (down- or upwards in the jacket region, in- and outwards in the bottom region), frequency f, and phase angle φ. Generally, in our first experiments coincident f and φ values for both jacket and bottom HMMs have been applied. The coil sections were power- and temperature-controlled in order to hold the temperature field constant when various f/φ ratios were selected.

For the VGF growth of Ge crystals the standard jacket heater within the commercial equipment "Kronos" from Crystal Growing Systems GmbH was replaced by a graphite HMM subdivided into three coil segments connected by star-type wiring with a special power and controller system for delivering of both DC and AC with variable amplitude I, frequency f and phase shift φ. Bottom and top heaters, responsible for adjusting the axial temperature gradient, were used in an unmodified standard version. Special configurations of the power-supplying bars were constructed in order to minimize magnetic field asymmetries [12, 29]. Figure 6.3 shows the scheme of the applied VGF arrangement with HMM. The crystal-

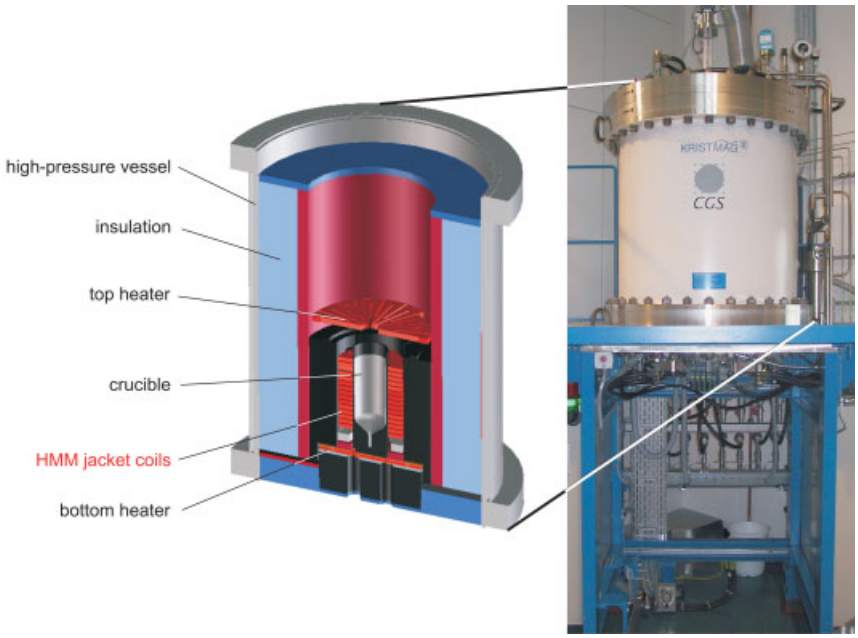

Figure 6.3 Schematic cross-section (left) and real vessel image of the commercial VGF equipment "Kronos" with inserted HMM around the crystallization container consisting of three jacket coils for simultaneous generation of heat by supplying DC and TMF by feeding AC.

lization process was provided by computer-controlled gradient propagation of the DC share.

6.5 Numerical Modeling

The global temperature distribution and electromagnetic field within the TMF LEC growth configuration for pulling of GaAs crystals (Figure 6.4) were modeled by the software CrysMAS, WIAS-HiTNIHS in combination with the code NAVIER [38] allowing computation of the melt flow under the influence of Lorentz forces. It has been found that two contrarily directed THM waves, independently generated within the jacket and bottom sections, may produce a favorable Lorentz force field that separates the weak flow under the growing crystal (Taylor–Proudman cells) from the intense nonsteady vortices in the crucible-wall region. As can be seen from Figure 6.4b for this the Lorentz force vectors must be directed diagonally from below the crucible periphery towards the crystal rim [16]. As a result, the temperature oscillation can be damped and shifted to less dangerous higher frequencies very effectively. Figure 6.5 compares the simulated temperature fluctuations obtained below the growing crystal without (a) and with TMF (b). The fluctuation amplitudes are reduced from 8 K to 2 K. Our experimental setup was selected in accordance with these numeric results. Note, a similar idea of flow regulation by separating the convection stream regions has been proposed by Scheel [39]. However, instead of use of a solid hollow cylinder around the crystal, being coaxially immersed in the melt in our case, a noncontaminating

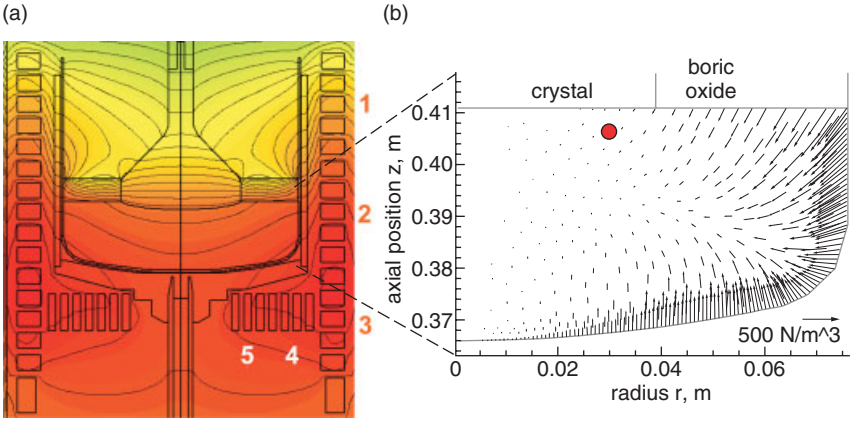

Figure 6.4 Simulated temperature field for the growth of GaAs within the LEC chamber showing the jacket coils 1–3 and bottom spirals 4–5 of the HMM (left) and distribution of Lorentz force density within GaAs melt at TMF directed downward in coils 1–3 and outward in spirals 4–5 with frequency $f = 300$ Hz and phase shift $\varphi = 70°$ [16]. The point under the growing crystal in (b) marks the location for monitoring of the temperature fluctuation (see Figure 6.5).

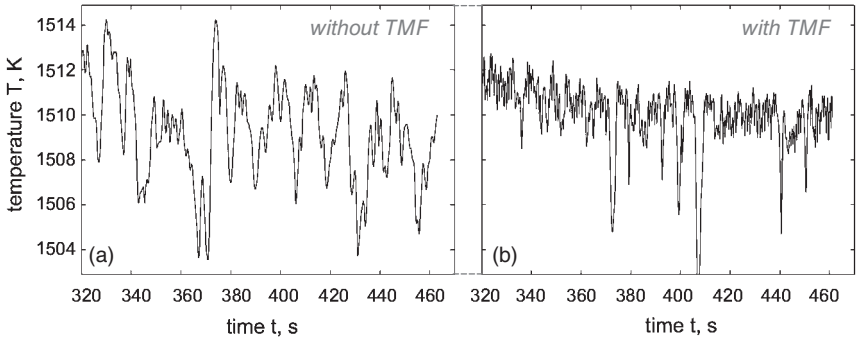

Figure 6.5 Temperature oscillations below the growing GaAs crystal in the monitor point marked in Figure 6.4b obtained by the local simulation of the used LEC configuration (see Figure 6.2) without (a) and with TMF configuration (b) as described in Figure 6.4 (adapted from Ref. [16]).

and programmable Lorentz "shade" is used. Of course, this can be realized by traveling-field combinations only, but not by unsymmetric static magnetic fields.

Different codes were used for the analysis of the VGF growth process [8, 10, 12]. First, possible 3D asymmetry effects generated by the electromagnetic field distribution using the HMM were analyzed by the commercial package ANSYS. Simulations of the melt flow were carried out with the commercial package CFX well adapting the interface to ANSYS. By using this combination, a simple transfer of the Lorentz force distribution data calculated with ANSYS into CFX was possible. It is noteworthy that the investigated effects of asymmetry require the use of the total system geometry without any simplifications by symmetry. Different connections to the three-phase power supply have been modeled considering the input of current or voltage with variable phases and frequencies [12]. An optimized bus bar configuration minimizing Lorentz-force asymmetries has been ascertained [29].

Then, the induced TMF and its effect on the melt convection and interface morphology were studied by global 3D modeling with the code CrysMAS [8, 10]. The optimization of the solid/liquid interface shape during the crystallization was carried out by means of snapshots of different growth positions. As a result, the interface morphology as function of the H/D aspect ratio was obtained (H, melt height, D, melt diameter). Additionally, the transition value of the TMF force from the steady-state situation to nonstationary melt flow was studied by 3D time-dependent simulations. The creation of the Lorentz force density was simulated for each coil segment in such a manner that the effective power could not exceed the power for generation of the heat requiring for the melting and crystallization process (in the range of 4–5 kW) that was obtained from the temperature field simulations and delivered by the DC share. For a slightly convex growing interface the TMF parameters of $I = 120$ A/coil segment, $f = 20$ Hz and $\varphi = 60°$ were found to be most suitable. The induced magnetic flux intensity of $B_0 \approx 2.5$ mT guaranteed a laminar flow regime with uniform isotherm courses and no quantifiable oscillation amplitudes (<0.05 K). Thus, a still stationary regime was obtained although

the Taylor number of $Ta_{TMF} \approx (2–3) \times 10^7$ approached the critical one. Compared to this at an induction of $B \approx 6\,mT$ and related $Ta_{TMF} \approx 10^8$, a markedly inhomogeneous fluctuating isotherm field with characteristic and dangerous low-frequency oscillation of 0.18 Hz was obtained [8].

For constant TMF parameters during the whole growth process the interface curvature does not remain constant and the convexity tends to increase with decreasing H/D ratio. Considering this fact for realistic growth processes the application of a time-dependent TMF program to satisfactorily adapt to each growth situation is required. In order to maintain a constant slightly convex interface curvature over the whole VGF process the total power must be gradually reduced from 4.5 to 4.0 kW and the TMF responsible AC share from 3.0 to 2.0 kW when a field frequency of $f = 20\,Hz$ and a phase shift of $\varphi = 60°$ are selected [8].

6.6 Dummy Measurements

The vertical component of the Lorentz force density F_{Lz} can be measured by the mass responses of a dummy made of stainless steel when the traveling magnetic field of given I, f and j is briefly switched on under room conditions (note the electrical conductivity of steel is $\sigma = 1.3 \times 10^6\,S\,m^{-1}$ being nearly identically with those of GaAs and Ge melts). For this, a hollow cylinder dummy of height and weight identical with the melt column was hung inside the HMM on a steel rod connected with the load cell of the high-precision balance system, as is used for crystal weighing during Czochralski growth. The weight response $F_w = \Delta m\, g$ can be converted into an axial Lorentz force intensity by the relation

$$F_{Lz} = \Delta m\, g\, V^{-1} \tag{6.9}$$

with g the gravitational acceleration and V the dummy volume. The results were compared with the numerical calculations. Figure 6.6 shows the results of dummy measurements within the HMMs in the LEC (a) and VGF (b) equipments. Whereas in LEC the F_{Lz} value was determined for a given crucible position as a function of the frequency and phase shift in downward-directed THM in the VGF case constant parameters $I = 180\,A$, $f = 500\,Hz$ and $\varphi = 70°$ were selected but F_{Lz} was measured along the whole HMM length by moving the dummy in 10-mm steps and changing the TMF direction. As can be seen, in both cases a good agreement with numeric calculations is obvious.

From Figure 6.6a it follows that the specific HMM configuration in the LEC puller consisting of 3 jacket coils and 2 bottom spirals allows the variation of value and direction of F_{Lz} by alternating f and φ without changing the TMF direction. Downward (–) and upward (+) directed F_{Lz} values between +120 and $-200\,N\,m^3$ have been registered. Note, these values denote the mean axial forces acting on the dummy but not referring to local values that can be markedly stronger even near the crucible wall (in the range of $600–800\,N\,m^{-3}$) as has been found by numerical simulations [11, 16, 40]. As follows from Equation 6.1 such mean force

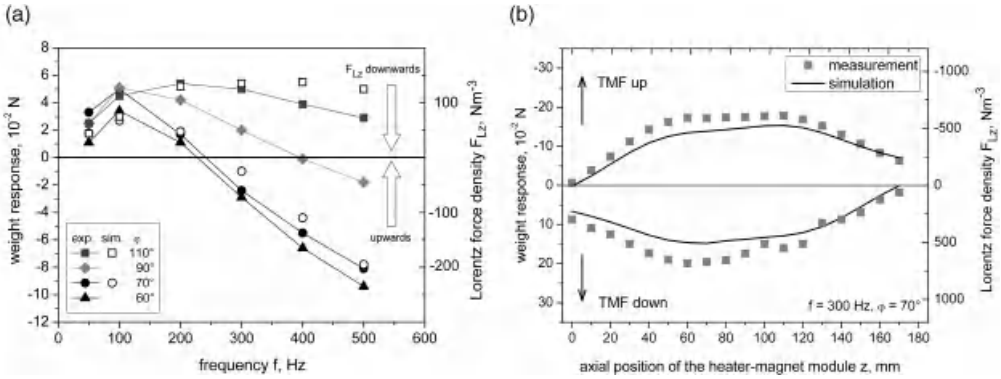

Figure 6.6 (a) weight response and related axial Lorentz force density F_{Lz} (left ordinate) against TMF frequency f and phase shift φ. (b) axial distribution of the measured and calculated mass response of the dummy within the heater-magnet module of the VGF equipment shown in Figure 6.3 (see also Ref. [10]) when an up- or downward TMF of I = 180A per coil segment, f = 300 Hz and φ = 70° was induced. The right ordinate shows the deduced averaged Lorentz force density.

density exceeds the buoyancy-driven convection force density $F_b \approx 460\,\mathrm{N\,cm^{-3}}$ when a temperature difference over the melt height of ΔT = 50 K is assumed. In general, one must select the ratio between frequency and phase shift very carefully. From Figure 6.6a it follows that in such a HMM arrangement the vertical Lorentz force density can be well balanced by the phase shift, as in the case of f = 400 Hz and φ = 90°, for example. We found by our numeric simulations that a sufficiently intense radial component $F_{Lz} > 500\,\mathrm{N\,m^{-3}}$ still remains.

In the TMF VGF arrangement maximum force density of $700\,\mathrm{N\,m^{-3}}$ has been deduced from the mass response when f = 500 Hz is applied (Figure 6.6b). This proves to be much more than required for damping of the convection-driven forces being usually in VGF containers less than $100\,\mathrm{N\,m^{-3}}$. In fact, a much lower frequency was selected experimentally to obtain an undercritical growth situation (see Section 6.2). Again, a good agreement between dummy measurements and numeric calculation was observed. Generally, a proper TMF-time program must be tuned in order to adapt the Lorentz force density and distribution to the changing convection pattern with decreasing melt height during the normal freezing process [8].

6.7 Growth Results under TMF

6.7.1 LEC of GaAs

Such experiments were provided first to test the feasibility of LEC growth within TMFs by applying a new design of combined heater-magnet. Undoped 3-inch

[001]-oriented GaAs crystals have been grown within the AC-provided HMM configuration presented in Figure 6.2. Up to now, more than twenty crystals were grown under different TMFs by varying the frequency and phase shift in the ranges $f = 50–400$ Hz and $\varphi = 5–90°$, respectively. The diameter stability, interface curvature, striation morphology, etch pit density (EPD), content of residual impurities, and electrical properties have been analyzed.

In Figure 6.7 some as-grown boules obtained under different f and φ values are presented. Relatively good diameter accuracy has been obtained, especially, when high field frequencies $f = 300–400$ Hz were selected. On the other hand, at low frequency, $f = 50$ Hz, the unfavorable concavity of the interface rim could be reduced most effectively. Figure 6.9a shows the melt/solid boundary morphology ascertained by diluted Sirtl with light (DSL) method on such a longitudinal crystal

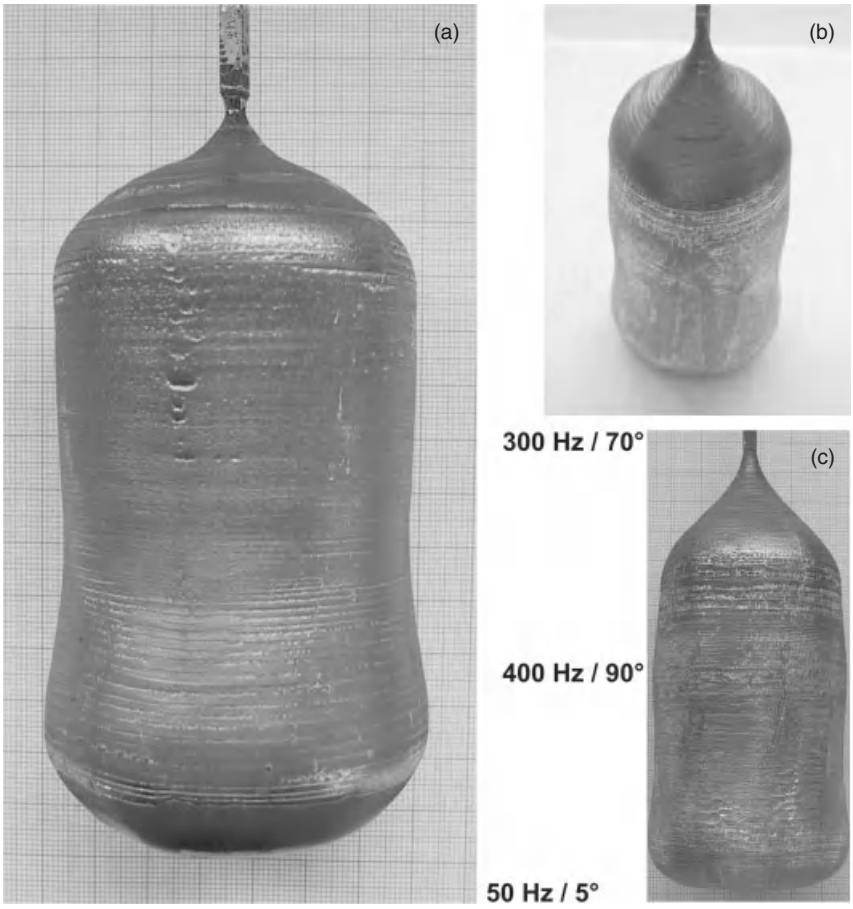

Figure 6.7 Images of as-grown GaAs crystals grown by TMF-LEC method within the HMM arrangement presented in Figure 6.2 at ratios of frequency and phase shift $f/\varphi = 50$ Hz/90° (a), 300 Hz/70° (b), and 400 Hz/90°.

cut. Of course, in the end the parameter optimization has to be found in combination with the best thermal conditions for each growth equipment and crystal diameter particularly.

The designed HMM configuration helps to damp temperature fluctuations under the growing crystal, especially when higher frequencies are used. Microscopic DSL etching of cuts parallel to the growth axis taken from crystals grown at $f = 300$ and $\varphi = 70°$ show very weak and uniform residual striation arrangements no longer correlating with sporadic buoyancy-driven convection [41] but with the strong periodicity of the crucible-crystal rotation ratio only (Figure 6.10a). This is in good accord with the numeric calculations shown in Figure 6.5 [11, 16].

Mean dislocation densities of ~$10^4\,cm^{-2}$ have been obtained. Minimum values of (4–5) × $10^3\,cm^{-2}$ at half radius along the radial <100>directions were observed in crystals grown at low TMF frequency. As a first approximation this agrees with the above-reported effect of interface flattening.

Low residual impurity concentrations in the range 10^{13}–$10^{14}\,cm^{-3}$ of the elements S, Zn, Fe, Cr and Cd have been measured by glow discharge mass spectrometry (GDMS). Surprisingly, markedly enhanced contents of oxygen and boron greater than $10^{18}\,cm^{-3}$ were detected. As a result, the substitutional carbon concentrations [C_{As}], measured by local vibrational mode (LVM) absorption at 300 K, became distinctly lower than $10^{16}\,cm^{-3}$ being related to the high oxygen content [42, 43] and having, apparently, nothing to do with TMF but is due to the activity contrariness of the chemical CO and O potentials in a LEC system [44]. At the present time we assume that TMF-induced high-speed vortices under the boric oxide encapsulant (see e.g., Ref. [16]) contribute essentially to the O and B release from it and their transport to the interface. However, more experimental facts are still required.

All as-grown crystals show semi-insulating behavior with specific electrical resistivities in the range of ρ = (2–4) × 10^8 Ω cm and free carrier concentrations of n_e = (3–6) × $10^6\,cm^{-3}$ measured by the van der Pauw method at 300 K. The ρ values correlate with the measured carbon concentrations in the range of C_{As} = (5–9) × $10^{15}\,cm^{-3}$, as is known from standard behavior of LEC crystals [44]. A typical as-grown single crystal pulled from freshly synthesized melt shows an electron mobility of μ_n = 5680 $cm^2/V\,s$ at ρ = 2.3 × 10^8 Ω cm, n_e = 4.8 × $10^6\,cm^{-3}$ and [C_{As}] = 9 × $10^{15}\,cm^{-3}$. Finally, relatively low $EL2^0$ concentrations in the range of (0.5–1.2) × $10^{16}\,cm^{-3}$ were ascertained by near-IR absorption when comparing with standard as-grown LEC material.

6.7.2 VGF of Ge

As is well known, favorable flat or slightly convex melt/solid interfaces cannot be achieved under conventional VGF growth conditions [8]. To demonstrate the feasibility in traveling magnetic fields <111>- and <100>-oriented Ge single crystals with diameter of 110 mm and weight up to 6 kg were grown in a HMM VGF

arrangement generating downward-directed Lorentz forces. More experimental details are reported in our former papers [8, 10].

For the investigation of the interface curvature by the striation technique the as-grown crystals were longitudinally cut along the <211> and <110> directions and then analyzed by etching and lateral photovoltage scanning (LPS) [45]. The etch pit density (EPD) was determined on polished {111} and {100} planes at room temperature by using the Sirtl and 1 HF : 2 HNO_3 : 4 CH_3COOH etchant, respectively. The conductivity type, specific electrical resistivity, carrier concentration, and mobility were ascertained by van der Pauw measurements at 300 K.

Figure 6.8 shows images of the body and shoulders of as-grown <111>- and <001>-oriented Ge single crystals obtained in a downward-traveling magnetic field of $f = 40$ Hz and $\varphi = 60°$. The three- and four-fold symmetries are well distinguishable due to shoulder faceting in case of <111>- (b) and <001>-orientation (c), respectively. The striation-revealed interface morphology in Figure 6.9b taken from a longitudinal cut of a Ge crystal grown under nearly optimum TMF conditions refers to flat and slightly convex interface shapes within the central region. A combined AC/DC programming of TMF and heating power according to the

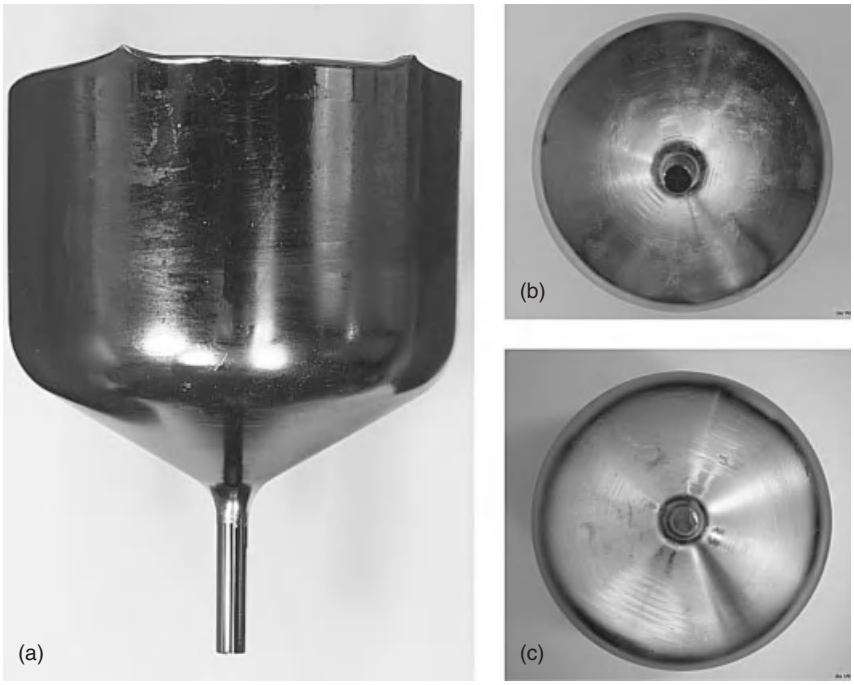

Figure 6.8 Images of as-grown body (a) and shoulders of <111>- (b) and <100>-oriented (c) Ge single crystals obtained in the HMM arrangement shown in Figure 6.3 at downward traveling magnetic field of $f = 40$ Hz and $\varphi = 60°$ (adapted from Ref. [8]).

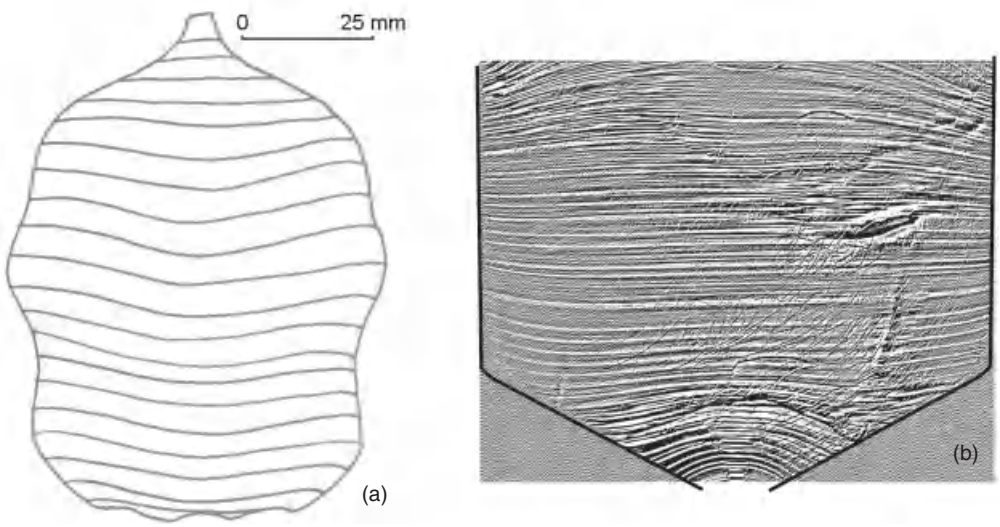

Figure 6.9 DSL-revealed interface morphologies of as-grown GaAs (a) and Ge crystals (b). The GaAs sample was obtained by TMF-LEC at f/φ ratio of 50 Hz/5°. The Ge crystal was crystallized by VGF in a downward-directed TMF at nearly optimum TMF conditions in order to achieve slightly convex interface (see also Ref. [8]).

numeric estimation [8] was applied to consider the decreasing aspect ratio of the melt during the crystallization process. A very sensitive TMF impact on the melt/solid interface morphology without changing the heating conditions has been observed [8].

Figure 6.10b presents a striation image of the microscopic scale taken from a crystal grown under nearly optimized TMF conditions. The inset shows distinct striations obtained when overcritical conditions with $Ta_{TMF} \approx 10^8$ were chosen. It has been found that the striation intensity (amplitude) reduces and the interspace increases with lowering magnetic induction. Therefore, our experimental results verify that convection-driven temperature fluctuations can be effectively damped by a well-adopted TMF. Comparable results have been reported by Lantzsch *et al.* [19] using, however, a more expensive TMF coil outside the growth chamber.

The EPD in crystals grown without TMF was in the range of $(0.8–5) \times 10^3\,cm^{-2}$. Often, dislocation bundles at the crystal edge were observed, obviously caused by the concave interface bending. Compared to that, a somewhat lower EPD of $(0.6–3) \times 10^3\,cm^{-2}$ was found when optimum TMF conditions for ensuring a stationary flow regime and slightly convex interface were adjusted. In <100>-oriented crystals the center was even free of dislocations. We found that independent of the magnetic field the pyrolytic BN container is responsible for dislocation generation at the crystal edge, in agreement with the observation of Schweizer *et al.* [46] in conventionally grown Ge crystals.

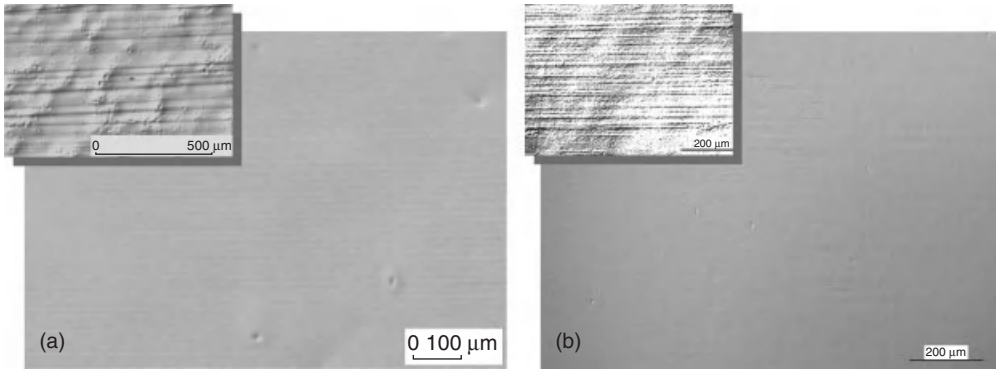

Figure 6.10 Microscopic striation analysis in slices cut parallel to the growth axis taken from TMF-LEC GaAs (a) and TMF-VGF Ge crystals (b) grown under optimum TMF conditions damping effectively the convection-driven temperature fluctuations. The respective insets show distinct striations obtained under nonoptimum TMF conditions.

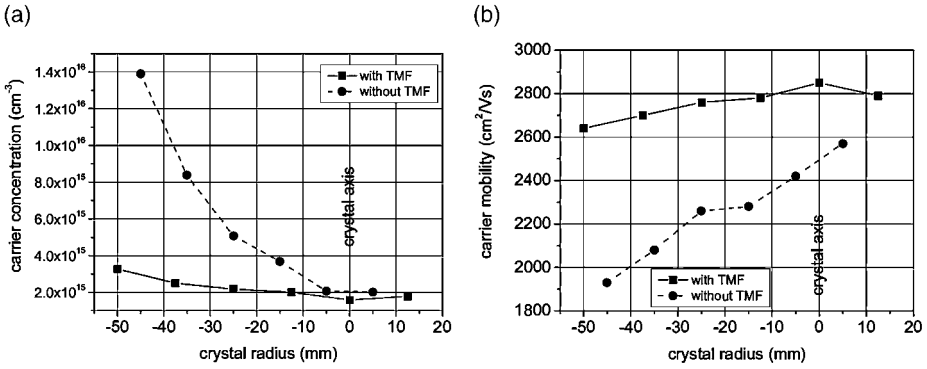

Figure 6.11 Radial distribution of carrier concentration (a) and carrier mobility (b) in as-grown 4-inch p-type VGF Ge single crystals grown in pBN crucibles without magnetic field (broken curves) and under nearly optimum TMF conditions (unbroken curves).

Figure 6.11 compares the hole concentration n_p and hole mobility μ_p of Ge crystals grown without and with TMF. In crystals grown under nearly optimized TMF conditions $n_p = (0.9–2.8) \times 10^{15}\,cm^{-3}$ and $\mu_p = 2500–2800\,cm^2\,V^{-1}\,s^{-1}$ have been ascertained. As follows from the radial distributions an improvement of the homogeneity takes place when TMF is applied. This is due to the flattening of the interface by a well-selected downward-traveling magnetic field. From our first results we can conclude that an optimal adjusted TMF is favorable for the structural and electrical qualities of as-grown VGF 4-inch Ge crystals.

6.8 Conclusions and Outlook

The first growth results of GaAs and Ge crystals by LEC and VGF in HMMs within the framework of the KRIST$\widetilde{MAG}^{®}$ project have been summarized. It was demonstrated that semi-insulating GaAs crystals can be successfully grown in a HMM design consisting of three jacket coils and two bottom spirals. Such a configuration allows adjustment of a stable melt flow situation, especially, at high TMF frequencies damping the harmful temperature fluctuations below the growing crystal. However, enhanced oxygen and boron concentrations are incorporated into the growing crystals, probably caused by the TMF-induced rapid flow vortices under the boric oxide encapsulant contributing essentially to the O and B release from it. At low field frequency (50 Hz) the unfavorable concavity of the peripheral interface region and, thus, the dislocation density can be reduced. The electrical crystal properties show standard as-grown behavior. At present, the experiments were provided first to test the feasibility of LEC growth within TMFs by applying new designs of combined heater-magnet. In the future, a more systematic experimental complex by using AC and DC combination is required to determine the explicit correlations between TMF and crystal qualities.

Ge single crystals were grown by VGF in a traveling magnetic field generated in an inner heater-magnet module producing heat by DC and TMF by AC simultaneously. It was found that the morphology of the growing melt/solid interface can be controlled by TMF very sensitively. A well-adjusted AC/DC relation, low frequencies in the range of $f = 20–50$ Hz and magnetic field programming, proved to be the most suitable conditions for ensuring a constant slightly convex crystallization front during the whole growth run. Improved structural and electrical crystal qualities have been obtained. Striations are minimized by effective damping of the convection-driven temperature fluctuations. Lowered EPD, high carrier mobility up to $\mu_p = 2800\,cm^2\,V^{-1}s^{-1}$ and markedly improved radial homogeneity of electrical parameters were measured in the as-grown crystals.

The results demonstrate that the KRIST$\widetilde{MAG}^{®}$ concept is very promising. The simultaneous TMF generation within the heater proves to be a helpful cost-reducing additional tool for sophisticated variation and optimization of the crystal pulling process.

Acknowledgment

The authors are indebted to the IKZ co-workers R.-P. Lange, O. Root, M. Ziem, U. Rehse, Dr. W. Miller, Dr. N. Dropka, Dr. U. Juda, Th. Wurche, M. Imming, K. Banse, Dr. A. Lüdge, Dr. K. Irmscher, M. Naumann, M. Pietsch, and the director of IKZ Prof. R. Fornari, also Prof. B. Nacke and Dr. H. Kasjanow from the Leibniz University of Hanover, Prof. J. Sprekels, Dr. O. Klein and Dr. Ch. Lechner from WIAS Berlin, V. Trautmann and his team from Steremat GmbH and G. Bethin and his team from Auteam GmbH.

The KRISTMAG® project was co-financed by the European Regional Developments Fund (EFRE), "Zukunftsfonds" Berlin and "Zukunftsagentur" of the State Brandenburg.

References

1 Kasap, S., and Capper, P. (2006) *Handbook of Electronic and Photonic Materials*, Springer, New York.
2 Oda, O. (2007) *Compound Semiconductor Bulk Materials and Characterizations*, World Scientific, Singapore.
3 Eichler, St., Börner, F., Bünger, Th., Jurisch, M., Köhler, A., Kretzer, U., Cheffer-Czygan, M., and Flade, T. (2008) *Crystal Growth Technology* (eds H.J. Scheel and P. Capper), Wiley-VCH Verlag GmbH, Weinheim, Chapter 9.
4 Umicore Team (2008) *Compound Semiconductor*, IOC Publishing Ltd., August 2008, 14, 17 and September 2008, 14, 7.
5 Teal, G.T., and Little, J.B. (1950) *Phys. Rev.*, **25**, 16.
6 Volz, M.P., Walker, J.S., Schweizer, M., Cobb, S.D., and Szofran, F.R. (2005) *J. Cryst. Growth*, **282**, 305–312.
7 Henager, C.H., Edwards, D.J., Schemer-Kohrn, A.L., Sundaram, S.K., Riley, B.J., and Bliss, M. (2008) *J. Cryst. Growth*, **311**, 10.
8 Frank-Rotsch, Ch., and Rudolph, P. (2009) *J. Cryst. Growth*. doi: 10.1016/j.jcrysgro.2009.01.139
9 Rudolph, P. (2008) *J. Cryst. Growth*, **310**, 1298.
10 Frank-Rotsch, Ch., Jockel, D., Ziem, M., and Rudolph, P. (2008) *J. Cryst. Growth*, **310**, 1505.
11 Klein, O., Druet, P.-E., Lechner, Ch., Philip, P., Sprekels, J., Frank-Rotsch, Ch., Kießling, F.-M., Miller, W., Rehse, U., and Rudolph, P. (2008) *J. Cryst. Growth*, **310**, 1523.
12 Kasjanow, H., Nacke, B., Eichler, St., Jockel, D., Frank-Rotsch, Ch., Lange, P., Kießling, F.-M., and Rudolph, P. (2008) *J. Cryst. Growth*, **310**, 1540.
13 Muiznieks, A., Krauze, A., and Nacke, B. (2007) *J. Cryst. Growth*, **303**, 211.
14 Rossby, H.T. (1969) *J. Fluid Mech.*, **36**, 309.
15 Schwesig, P., Hainke, M., Friedrich, J., and Mueller, G. (2004) *J. Cryst. Growth*, **266**, 224.
16 Klein, O., Lechner, C., Druet, P.-E., Philip, P., Sprekels, J., Frank-Rotsch, C., Kießling, F.-M., Miller, W., Rehse, U., and Rudolph, P. (2008) Proceedings of the International Scientific Colloquium "Modeling for Electromagnetic Processing" (MEP 08), Hanover, October 27–29, 2008, p. 91.
17 Galindo, V., Grants, I., Lantzsch, R., Pätzold, O., and Gerbeth, G. (2007) *J. Cryst. Growth*, **303**, 258.
18 Yesilyurt, S., Motakef, S., Grugel, R., and Mazuruk, K. (2004) *J. Cryst. Growth*, **263**, 80.
19 Lantzsch, R., Grants, I., Galindo, V., Pätzold, O., Gerbeth, G., Stelter, M., and Cröll, A. (2006) *Magnetohydrodynamics*, **42**, 445.
20 Lyubimova, T.P., Cröll, A., Dold, P., Khlybov, O.A., and Fayzrakhmanova, I.S. (2004) *J. Cryst. Growth*, **266**, 404.
21 Wetzel, Th (2001) *Fortschritt-Berichte VDI*, Reihe 9, Nr. **328**, 1.
22 Tomzig, E., Virbulis, J., Ammon, W., Gelfgat, Y., and Gorbunov, L. (2003) *Mat. Sci. Semicond. Proc.*, **5**, 347.
23 Krauze, A., Muiznieks, A., Mühlbauer, A., Wezel, Th., Gorbunoov, L., Pedchenko, A., and Virbulis, J. (2004) *J. Cryst. Growth*, **266**, 40.
24 Fischer, B., Friedrich, J., Kupfer, C., Vizman, D., and Müller, G. (1999) *Magnetohydrodynamic and Electroconducting Flows* (eds A. Alemany, P. Marty, and J.P. Thibault), Kluwer, Boston, p. 279.
25 Lantzsch, R., Grants, I., Pätzold, O., Stelter, M., and Gerbeth, G. (2008) *J. Cryst. Growth*, **310**, 1518.
26 Hurle, D.T.J., and Series, R.W. (1994) *Handbook of Crystal Growth*, vol. 2a (ed. D.T.J. Hurle), Elsevier, Amsterdam, Chapter 5.

27 Brückner, F.U., and Schwerdtfeger, K. (1994) *J. Cryst. Growth*, **139**, 351.
28 Ziem, M., Rudolph, P., and Lange, P. (2006) Patent description DE 10 2007 020 239.
29 Lange, P., Jockel, D., Ziem, M., Rudolph, P., Kießling, F., Frank-Rotsch, Ch., Czupalla, M., Nacke, B., and Kasjanow, H. (2007) Patent description DE 10 2007 028 547.
30 Frank-Rotsch, Ch., P.Rudolph, O., Klein, P., Lange, B., and Nacke (2007) Patent description DE 10 2007 028 548.
31 Fujimori, K., and Ayusawa, T. (1970) Patent description DE 2107646.
32 Hoshikawa, K., Kohda, H., Hirata, H., and Nakanishi, H. (1980) *Jpn. J. Appl. Phys.*, **19**, L33.
33 Hull, E.M. (1980) *IBM Tech. Discl. Bull.*, **23**, 2756.
34 Kim, K.M., Schwuttke, G.H., and Smetana, P. (1982) *IBM Tech. Discl. Bull.*, **25**, 2277.
35 Grimes, H.M., and Hariri, F.A. (1996) Patent description US 5,571,320.
36 von Ammon, W., Virbulis, J., Tomzig, E., Gelfgat, Y., and Gorbunov, L. (2001) Patent description DE 10102126.
37 Mühe, A., Altekrüger, B., and Vonhoff, A. (2003) Patent descriptions DE 10349339 and (2004) US 0087125.
38 Geiser, J., Klein, O., and Philip, P. (2007) *J. Cryst. Growth*, **303**, 352.
39 Scheel, H. (2006) *J. Cryst. Growth*, **287**, 214.
40 Frank-Rotsch, Ch. private communication.
41 Ozawa, S., Nakayama, H., Shiina, Y., Ohashi, E., and Kikuta, T. (1989) *Inst. Phys. Conf. Ser.*, **96**, 343.
42 Nishio, J., and Terashima, K. (1989) *J. Cryst. Growth*, **96**, 605.
43 Seifert, M., Neubert, M., Ulrici, W., Wiedemann, B., Donecker, J., Kluge, J., Wolf, E., Klinger, D., and Rudolph, P. (1996) *J. Cryst. Growth*, **158**, 409.
44 Jurisch, M., Börner, F., Bünger, Th., Eichler, St., Flade, T., Kretzer, U., Köhler, A., Stenzenberger, J., and Weinert, B. (2005) *J. Cryst. Growth*, **275**, 283.
45 Abrosimov, N.V., Lüdge, A., Riemann, H., and Schröder, W. (2002) *J. Cryst. Growth*, **237–239**, 356.
46 Schweizer, M., Volz, M.P., Cobb, S.D., Vujisic, L., Motakef, S., Szoke, J., and Szofran, F.R. (2002) *J. Cryst. Growth*, **237**, 161.

7
Manufacturing of Bulk AlN Substrates

Oleg V. Avdeev, Tatiana Yu. Chemekova, Heikki Helava, Yuri N. Makarov, Evgenii N. Mokhov, Sergei S. Nagalyuk, M.G. Ramm, Alexander S. Segal, and Alexander I. Zhmakin

7.1
Introduction

The unique properties of the group III-nitrides [1, 2] make them the best material for optoelectronic devices emitting light in the visible and UV spectral ranges, including sources for general illumination [3–7], and high-power/high-frequency electronic devices capable of operating at high temperatures and in harsh environment [8–11]. To fully exploit them in optoelectronics and communication technology, two problems are to be solved: (i) the difficulties of high-level p-doping and (ii) the lack of lattice and thermally matched substrates.

7.1.1
Substrates for Group III Nitride Devices

The requirements for a good substrate are: lattice and thermal expansion coefficient (TEC) matching, large size, affordable price; sometimes additional features are desirable, for example, cleavability for laser diodes or high electrical resistivity for field effect transistors (FETs). The best substrates for GaN-based devices are GaN and AlN. AlN ones are superior for structures with high Al content, for example, UV devices (AlN is transparent down to about 200 nm), FETs and both vertical and lateral Schottky and p-i-n diodes [12] (unintentionally doped [UID] AlN crystals are insulators[1)] in contrast to GaN ones that have a high background concentration of free electrons [13]), as well as for power devices due to high thermal conductivity.[2)] AlN crystals, possessing the highest surface and bulk acoustic wave

1) The concentration of residual oxygen is high for sublimation grown AlN, however, most of the oxygen is incorporated not as a substitutional shallow donor, but as impurity-forming complexes with point and extended defects located deep in the gap [13, 14].

2) The cooling of devices on AlN substrates could be effectively better than that on SiC substrates having higher thermal conductivity since the former do not require a buffer layer that is highly defective and thus presents considerable thermal resistance [15].

Crystal Growth Technology. Semiconductors and Dielectrics. Edited by P. Capper and P. Rudolph
Copyright © 2010 WILEY-VCH Verlag GmbH & Co. KGaA, Weinheim
ISBN: 978-3-527-32593-1

velocity known for piezoelectric materials and a large piezoelectric coupling coefficient, are also needed for the surface acoustic wave devices.

In the absence of native GaN or AlN substrates, a number of foreign ones are used in practice, leading to low quality of the grown epitaxial layers in terms of large threading dislocation density (DD), inversion domain boundaries, stacking faults, bowing of the structure, cracks. While high DD is acceptable for light-emitting diodes (LEDs), it is fatal for laser diodes and power transistors; even for the LEDs it reduces efficiency and is the main factor in device failure [16, 17].

The most important foreign substrates are sapphire and silicon carbide (6H-SiC or 4H-SiC).[3)] The former is inferior, leading to higher DD in structure; in addition, the insulating nature of sapphire restricts the device architecture, for example, an LED on sapphire requires on-one-side contacts, excluding vertical die design; a low refractive index of sapphire in comparison to III-nitrides also leads to waveguiding of light emitted in an LED that reduces the light extraction efficiency [16]. Still, over 80% of LEDs are fabricated on sapphire 2" substrates now [21] due to the low cost and availability. The drawback of SiC substrates is high cost and surface roughness on the scale of a few atomic bilayers leading to stacking-mismatch defects at the interface between SiC and III-nitride layers in the form of a 2H-polytype [16].

Reducing the high cost of SiC substrates, while conserving high thermal conductivity, is possible by mounting of a thin film of monocrystalline SiC onto polycrystalline SiC [22] that has a thermal conductivity lower than that of single crystal but close to it [23] and is produced by the low-cost process of SiC powder sintering [24]. Bonding a thin sapphire layer to polycrystalline AlN (P–AlN) retains the epitaxial template for the growth while improving the thermomechanical properties of substrate [25]. Another example of composite substrates is SiC semiconductor-on-insulator (SOI) structures that are low cost 3C-SiC (111) substrates fabricated by the conversion of silicon SOI by carbonization of the surface – reaction with propane and hydrogen at high temperatures [26].

Epitaxy of InGaN/GaN layers on foreign substrates with large lattice mismatch[4)] requires a preliminary growth of a buffer layer or multiple buffer layers [20, 32]. The buffer layer material for sapphire and SiC substrates is AlN; GaN, AlGaN, ZnO [33] or platinum nanocluster [34] is used for sapphire, while HfN buffer layers

3) The list of other substrates used for InGaN epitaxy includes GaAs, AlAs, GaP, ZnO, MgO, Mg(Zn) Fe_2O_4, $LiGaO_2$, $LiAlO_2$, SiO_2, $NdGaO_3$, $ScAlMgO_4$, ZrO_2 [18–20].

4) Lattice mismatch leads to misfit strain in grown layer that should be accommodated if the layer thickness exceeds a critical one (according to either the energy minimization theory of Frank–Van der Merwe or the force-balance theory of Matthews–Blakeslee) via the introduction of misfit dislocations, modulation of the free surface profile, composition modulation [27], microtwin formation [28] or interdiffusion between the layer and the substrate [29]. These mechanisms could be cooperative as well as competitive [30]. The critical thickness is the equilibrium entity, thus metastable metamorphic layers of higher thickness could exist at low temperatures: for example, recently an n-type AlGaN layer on the bulk AlN substrate with a thickness more than an order of magnitude greater than the critical value was reported [31].

are used for Mo substrates [35]. The large lattice (17%) and TEC (33%) mismatch between Si and GaN cannot be fully accommodated by an AlN buffer layer [36], still, involving additionally nitridation [37] or carbonization of the surface or SiC coating [18], some GaN devices grown on Si substrates such as HEMTs show acceptable performance. In MBE the best results (an order of magnitude decrease of the DD in GaN epilayers) are obtained when the growth is initiated by exposing the Si surface to NH_3 first [38]. Usually, the Si (111) surface is used, while an integration with Si microelectronics requires growth on Si (100).

Considerable efforts were directed to development of *templates* (foreign substrates with deposited thin nitrides layers) [20, 39] and *pseudo-bulk* or *free-standing* nitride substrates [40, 41] obtained by separation of thick nitride layers from the substrate after the growth (by laser-assisted lift-off [LLO] [40, 42] or by etching, e.g., in aqua regia for GaAs substrates) or during the growth on sapphire substrates with patterned GaN seeds by spontaneous self-separation [43]. Recently, Ashraf *et al*. [44] have used a number of characterization techniques (diffraction interference contrast optical microscopy, scanning electron microscopy, micro-Raman scattering, X-ray diffraction) to assess the quality of thick GaN layers grown by hydride vapor-phase epitaxy (HVPE) directly on sapphire (with optimal nucleation layer deposition at low temperatures and low pressures on the nitridated surface) and on the GaN/Al_2O_3 templates prepared by GTS-MOCVD process [45] (GTS stands for the gallium treatment step that is a long exposition of the substrate surface to TMGa at high temperature). The authors found that the layers did not significantly differ in the surface morphology and the structural quality, but the layers grown on the MOCVD templates suffered from cracking in a few cases, while no cracking occurred in the HVPE layers grown directly on sapphire.

The study of deep-UV emission of AlGaN quantum wells [46], AlGaN UV LEDs [47] and high electron mobility transistors (HEMTs) [48] grown on bulk AlN substrates prove the superiority of the latter, for example, the luminescence intensity of the QW grown on bulk AlN was higher than that of the QW grown on SiC by a factor of 28, the reverse breakdown voltage of the m-i-m structure on bulk AlN was an order of magnitude greater than that on free-standing GaN [12]. Substrates cut from the bulk crystals can have different orientation (polar, semipolar or nonpolar), enhancing the freedom of the device design [49–51].

7.1.2
Growth of Bulk Group III Nitride Crystals

Although the first AlN crystals were synthesized by Briegler and Gúther using the reaction between molten aluminum and nitrogen a century and a half ago [52], growth of bulk GaN, AlN and AlGaN crystals is difficult [53]; InN bulk crystals have not been demonstrated so far. These crystals could not be grown from the melt as most semiconductors not due to the high melting temperature itself, as sometimes stated, but due to the decomposition of the crystals occurring at much lower temperature resulting from the strong bonding of the nitrogen molecule and low free energy of the crystal [54]. The solubility of nitrogen in the Ga melt is

very low [55] and formation of the N_2 bubbles is possible in the supersaturated GaN liquid [54]. Nitrogen dissolution in metal melt could be increased by two orders of magnitude – as is well known in iron- and steelmaking – by dissolving nitrogen radicals instead of nitrogen itself, thus ammonia is preferable as an ambient gas [56].

Growth of centimeter-size GaN crystals was achieved at high temperatures and ultrahigh N_2 pressures that provide a sufficient concentration of nitrogen in the Ga melt (high nitrogen pressure solution growth – HNPSG) [57, 58]. The GaN crystals grown by this method have a very low DD of $10^2\,cm^{-2}$. HNPSG without intentional seeding produces needle-like AlN crystals [59]. Similar temperatures and pressures are used in the pressure-controlled solution growth (PCSG) [53].

The extreme parameters needed for HNPSG and PCSG are reduced in ammonothermal [60–62] and alkali metal flux methods [63–66].

The former is similar to the hydrothermal growth of quartz crystals with supercritical ammonia instead of water. No growth of GaN crystals is observed in pure Ga solution [60]. It is necessary, similar to other hydrothermal-type processes, to add either lithium as a transporting agent [60] or mineralizers such as NH_4X (where X = Cl, Br, I) [61, 62] or gallium triiodide with CuI or LiI [61]. In the first approach chemical reactions occur in the solution involving $LiGa(NH_2)_2$ and $LiNH_2$. Acidic mineralizers effectively increase the reaction rate by increasing the number of anions in the solution.

In the sodium flux method Na acts as a catalyst that releases electrons easily. It is speculated that nitrogen in N_2 molecules absorbed onto the Ga–Na melt surface receives electrons from Na, that weakens the N_2 bonds and causes dissociation of N_2 into two negatively charged radicals at much lower temperature and pressure [63]. The use of lithium instead of sodium is more promising since the ability of the former to fix nitrogen is higher and that allows one to achieve the growth of GaN single crystals under a pressure of 1–2 atm [66].

The sodium flux growth is performed in a closed [65] or in an open tube [63, 64]. In the former the only source of nitrogen is a solid precursor such as NaN_3 powder, thus the pressure decreases during the process as nitrogen is being consumed for GaN growth. In the latter, N_2 or its mixture with NH_3 serves as a nitrogen source and the pressure can be either kept constant or varied in time by a prescribed law [64]. NH_3 is superior to N_2, however, the size of GaN crystals grown in $NH_3 - N_2$ mixture is smaller than in pure N_2. CL spectra show that GaN crystals grown in the open system are of higher quality [67].

A new method called electrochemical solution growth (ESG) based on the transport of the nitrogen ion N^{3-} in the molten chloride salt is being developed now [68]; so far only millimeter-size GaN crystals were produced. Reaction between Ga and Li_3N under NH_3 atmosphere via formation of $LiNH_2$ is used to grow GaN crystals by T. Hirano *et al.* [69]. Advances in ammonothermal growth of GaN have been reviewed in [53, 70] of AlN crystals with potassium azide KN_3 as mineralizer – in [71], of AlN growth from Cu–Al–Ti–N solution in [72]. The solution growth in the near future will hardly be developed to the production scale due to the difficult control of the process and the low growth rate.

The alkali metal flux growth has been used in the liquid phase epitaxy (LPE) [56]. 3-μm thick MOCVD-GaN layers with the DD 1.3×10^6 were used to grow 500-μm crystals that were almost dislocation free. PL intensity of the LPE-GaN with Na flux and Ca–Na mixed flux was 47 and 86 times, respectively, greater than that of the seed crystal. LPE was also used to grow platelets of hexagonal or prismatic habit at ambient pressure with NH_3 as a nitrogen source; the growth anisotropy was found to be comparable to that in bulk Na flux growth and much smaller than in HNPSG [73].

7.1.3 Sublimation Growth of AlN Crystals

Sublimation growth (or physical vapor transport – PVT) of AlN is the most mature technology of bulk nitride crystal growth (sublimation is also used to grow AlN fibers [74]); sublimation growth of GaN crystals is less successful [75]. The overall reaction can be written as

$$(\mathrm{AlN})_{\mathrm{solid}} \xrightarrow[T_{\mathrm{growth}}+\Delta T]{\text{Sublimation}} \mathrm{Al}_{\mathrm{vapour}} + \frac{1}{2}\mathrm{N}_2 \xrightarrow[T_{\mathrm{growth}}]{\text{Deposition}} (\mathrm{AlN})_{\mathrm{solid}}$$

This method developed in 1976 [76] now provides growth rates up to 1 mm/h [77] and high crystal quality (the DD is lower than 1000 cm^2 and FWHM of the rocking curve is less than 10 arcsec in the best samples [78]). Either spontaneous nucleation (self-seeding growth) without any attempt to control the crystal orientation or intentional seeding (homoepitaxial [79] or heteroepitaxial [80, 81]) can be exploited. SiC substrates are often used [82, 83], other substrates – sapphire, tantalum carbide TaC and niobium carbide NbC – have also been tried [84]. Decomposition of SiC affects the growth morphology and could provoke growth of polycrystalline AlN [85]. Both crucible and source are usually cylindrical, however, conical crucible are used sometimes [76] as well as a central hole in the powder source to increase the source surface area [86].

High growth temperature and highly reactive Al vapor create a problem in selection of crucible material. Different crucibles have been tried including ones made from refractory transition metals (W, Ta, Nb, Zr) and graphite coated with SiC, NbC or TaC [52, 80] revealing their weak points: for example, a boron nitride growth environment results in highly anisotropic growth [52], coated graphite crucibles deteriorate at high temperatures, and carbon detrimentally influences the growth morphology as in pure C crucibles; crucibles made from nitrides or carbides suffer severe cracking. Among the most successful ones are crucibles made from transition metals and their carbides [80]. The duration of the growth process is limited by the degradation of crucible [86, 87] and of graphite insulation [88] as well as by continuous operation of the source that requires the temperature gradients within the source to be as low as possible [89, 90]. The growth temperature critically influences the crystal morphology [91]. The dislocations in the crystal can arise both during growth or after the growth in the course of the mechanical stress relaxation [89, 92]. The effect of substrate misorientation and buffer layers

on growth modes and defects in AlN sublimed onto 6H-SiC substrates were studied in Refs. [93, 94]; different growth modes were related to the low mobility of AlN adatoms on the crystal surface.

Currently, stable growth of 15–25 mm diameter and 10–20 mm long AlN single crystals has been achieved [78, 95–97]. Still, a number of problems such as improvement of the crystal seeding and stoichiometry, reduction of impurities, maintenance of stable conditions during the long growth remains. The present chapter reports advances in AlN sublimation growth and its modeling.

7.2 Modeling

As AlN sublimation growth is implemented in a tightly closed crucible under high-temperature, it is difficult to study and control *in situ*, thus the importance of computer modeling is evident [87, 89, 90].

Theoretical analysis of AlN PVT growth was probably first performed in [98]. In this paper, surface decomposition of low-reactive N_2 was noted as the rate-limiting stage of the AlN evaporation/growth kinetic mechanism. A 1D model of the process was developed, no transport effects being taken into account. In contrast, most of later studies assumed the AlN growth rate to be limited by the species transport [99–101] and the AlN growth rate was found using the Hertz–Knudsen equation for the interface Al fluxes at the AlN surfaces. These papers neither clarified the boundaries of the kinetically and transport-limited approximations, nor accounted for mass exchange between the crucible and the ambient through small gaps that may essentially affect the process. Besides, they do not consider evolution of the AlN crystal and source and corresponding gradual change of the growth conditions. The evolution effects are also important as they determine the crystallization front shape that, in turn, affects distributions of dislocations and other defects in the crystal (a slightly convex crystallization front is preferable). A model of AlN sublimation growth that does not rely on the kinetically or transport limited approximations and describes all the above effects within a single approach was developed in [102–104] where one-dimensional stationary model was considered. Here, we extend it to the 2D axisymmetrical case and consider the process in evolution.

The model of AlN sublimation growth is based on a conventional description of heat and radiation transfer, gas-flow dynamics, and species diffusion in the growth system coupled with reduced quasi-thermodynamic description of surface kinetics at the AlN surfaces. The latter was earlier applied to modeling of other growth techniques (see, for example, [105] and references therein). As applied to AlN sublimation growth, it utilizes the extended Hertz–Knudsen relationships for two reactive gaseous species, Al and N_2

$$J_i = \alpha_i(T)\beta_i(T)\left(P_i^{w} - P_i^{e}\right)$$

Here, J_i are the interface molar fluxes, $\alpha_i(T)$ are the temperature-dependent sticking probabilities, T is the temperature, $\beta_i(T) = (2\pi\mu_i RT)^{-1/2}$ are the Hertz–Knudsen

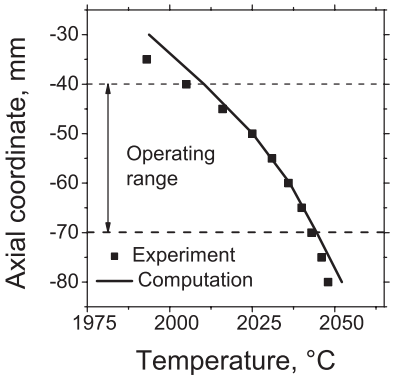

Figure 7.1 Temperature at the center of the crucible lid vs. crucible coordinate at the vertical axis, computed (solid line) and pyrometrically measured (points).

collision factors, μ_i are the molar masses, R is the gas constant, P_i^w are the species partial pressures at the interface, P_i^e are the quasi-equilibrium (thermodynamic) species pressures, and subscript i indicates a particular species (Al or N_2). The Al sticking probability is assumed to be unity due to its high reactivity. In contrast, the N_2 sticking probability is very low. In [103], it was fitted as a function of temperature using data of [106] on the AlN evaporation in vacuum (more recent data of [107] confirmed the derived approximation). The pressures P_i^e satisfy the mass-action law equation $\left(P_{Al}^e\right)^2 P_{N_2}^e = K(T)$, where $K(T)$ is the equilibrium constant for the surface reaction $2Al + N_2 \Leftrightarrow 2AlN(s)$. The model was validated in [104] by comparison with the experimental data on the AlN growth rate as a function of the temperature and the pressure; it is implemented as the software package Virtual Reactor™ [108, 109]. Figure 7.1 illustrates the high accuracy of temperature prediction.

The ambient pressure strongly affects the growth, which is largely related to the idea of critical pressure. In equilibrium, $J_i = 0$, $P_i^e = P_i^w$, and the two species partial pressures can be found from the system of two equations: $\left(P_{Al}^w\right)^2 P_{N_2}^w = K(T)$, $P_{Al}^w + P_{N_2}^w = P$, where P is the total pressure in the crucible. Analysis shows that if $P > P^*(T) = 3/2[2K(T)]^{1/3}$ (critical pressure) then the system has two solutions corresponding to the Al-rich and N-rich vapor, if $P = P^*(T)$ then there is the unique solution corresponding to the stoichiometric vapor, and if $P < P^*(T)$ there is no solution. The latter means that in a hermetically closed crucible the equilibrium pressure is always higher than the critical pressure. In a nonhermetic crucible, the equilibrium is impossible if the ambient pressure is so low that the related pressure inside the crucible is lower than the critical pressure. In this case, both the AlN source and seed evaporate, with the Al/N_2 vapor coming out from the crucible to the ambient (Figure 7.2).

Mass exchange between the crucible and the ambient occurs through a narrow ring gap between the crucible side wall and the lid. The internal and external pressures are close to each other at a sufficiently high external pressure but considerably deviate as it decreases, depending on the gap hydraulic resistance ζ that is

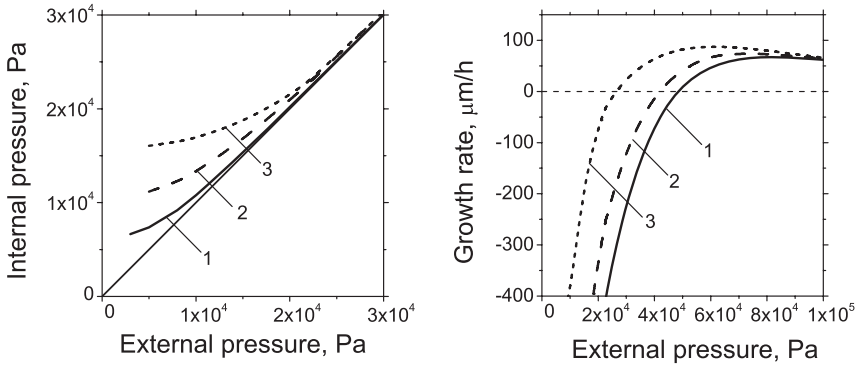

Figure 7.2 Pressure inside the crucible (left) and AlN crystal growth rate (right) vs. ambient pressure at different gaps between the side crucible wall and the lid: 1, gap length λ is 1 mm, gap thickness δ is 100 μm, 2, λ = 1 mm, δ = 50 μm, 3, λ = 10 mm, δ = 100 μm.

proportional to the gap length and inversely proportional to the third power of the gap thickness. Al and N_2 evaporate from the AlN source and then either deposit on the AlN crystal or escape from the crucible. The ratio of the deposited and escaped material depends on the external pressure and on ζ. Figure 7.2 shows the computed dependencies of the AlN growth rate at the crystal center. As the external pressure decreases, a higher fraction of the material escapes from the crucible and the growth rate decreases. At a sufficiently low ambient pressure P_a^0, the crystal begins evaporating, with all vapors coming out from the crucible through the gap (negative growth rates). The value P_a^0 decreases with the gap hydraulic resistance (at a sufficiently high ζ, the crystal does not evaporate at an arbitrary small ambient pressure). The local AlN evaporation/growth rate is determined by the local supersaturation, both for the source and seed. The local interface flux on an AlN surface can be approximated as

$$J \approx \frac{\left(P_{Al}^{w}\right)^2 P_{N_2}^{w} \Big/ K(T) - 1}{4 \Big/ \left[3\beta_{Al}(T) P_{Al}^{w}\right] + 1 \Big/ \left[3\alpha_{N_2}\beta_{N_2}(T) P_{N_2}^{w}\right]}$$

Here, the quantity in the numerator is the local supersaturation that represents the driving force for the local AlN evaporation/growth, while the denominator corresponds to the local kinetic resistance. The distribution of the supersaturation over the crystal surface determines its evolution (Figure 7.3). Note that the absolute values of supersaturation are rather small due to the smallness of the relative temperature difference between the source and seed.

The higher the local supersaturation, the faster the crystal grows there. At the very periphery, supersaturation is negative due to the species exchange between the crucible and the ambient through the ring gap (here, the vapor is enriched by N_2 and depleted in Al) and the crystal evaporates here, taking a fungi shape; the vapor escapes from the crucible through the gap (the last right streamline is directed to the gap). Computational results are in good agreement with the

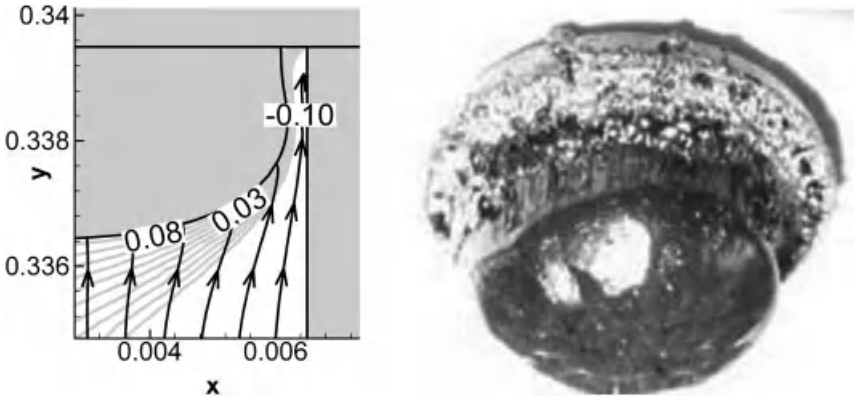

Figure 7.3 Computed shape of AlN boule in 20 h of growth (left) in comparison with the observed shape (right). Black lines with arrows are the streamlines, gray lines are the supersaturation isolines, numbers at the crystal surface are the local supersaturation values.

observed crystal shapes. Using this model, we have optimized the growth conditions and crucible design, which eventually favored the growth of 2" diameter and up to 10 mm long AlN boules with a slightly convex shape providing a low defect content in the crystal.

7.3 Experiment

Before our own AlN seeds became available, we used SiC seeds and two-stage technology to exploit the best features of different crucibles by avoiding interaction of W with Si and C that form easily melted eutectics and by limiting the incorporation of Si and C in C-rich environment: (i) seeding and initial growth of 2–3 mm long AlN crystals on SiC seeds in TaC crucibles in graphite equipment and (ii) growth of bulk AlN crystals on the AlN seeds in tungsten crucibles and equipment.

Another kind of two-stage procedure was reported by Sitar *et al.* [91] who used vaporization of Al (use of a metal vapor source is called the *direct synthesis method* by Nishino *et al.* [110]) at the first and AlN powder at higher temperature at the second stage; two-stage growth was also used by Dalmau *et al.* [111] with stages differing in the growth temperature and, thus, growth rate.

7.3.1 Pregrowth Processing

Preparation of crucibles includes annealing of W ones to remove the adsorbed impurities and precarbonization of Ta (Figure 7.4). The crucibles are remarkably

Figure 7.4 Ta crucible completely covered with a layer of TaC–Ta_2C ceramics that is converted into TaCN during the growth to prevent the formation of easily melted eutectics (Ta–Si and Ta–Al) [112].

thermally and chemically stable and can endure over 3000 (1000) h of cumulative AlN growth in graphite (tungsten) equipment.

The presence of oxygen is detrimental in AlN growth due to the formation of oxynitrides and enhanced formation of stacking faults [87]. Oxygen has a negligible effect on the growth rate itself, but can provoke at low temperature (e.g., during the heating of the system) generation of Al_2O_3 inclusions [113] that, in turn, causes surface roughness [114]. The addition of hydrogen to the nitrogen during growth is beneficial [103]; alternatively, sources could be processed to reduce the oxygen content. High-purity AlN sources were prepared from commercially available AlN powders either by annealing in the N_2 atmosphere or by sublimation-recrystallization, producing, respectively, dense porous or polycrystalline AlN source. The content of impurities in the AlN samples was studied at Kansas State University using glow discharge mass spectrometry (GDMS). Sublimation-recrystallization was found to be superior and accepted as a standard technique. SiC seeds are cut from 6H SiC bulk crystals as 0.5 mm thick round plates of different diameters (15–50 mm). The SiC seeds are mechanically lapped and mounted onto the crucible lid using C-based glue.

To test the technique of lateral overgrowth of AlN crystals on small-diameter AlN seeds, we have also prepared AlN seeds from the previously grown AlN bulk single crystals as 0.5-mm thick and 15–18-mm diameter round plates. These seeds are similarly mechanically processed and mounted onto the crucible lid with AlN-based glue.

7.3.2
Seeding and Initial Growth

Use of SiC seeds in precarbonized Ta crucibles in graphite RF-heated furnaces is necessarily accompanied by the diffusion of Si and to a lesser degree of C into AlN. This process, along with the lattice and TEC mismatch, results in generation of defects at the SiC–AlN interface, such as micropipes inherited from SiC, dislocations, cracks, and others. Experiments show, however, that the growth of a 2–3-mm thick AlN layer leads to healing of these defects and eventually results in rather high crystal quality; the crystal surface has a distinct stepwise structure. X-ray diffractometry and topography of the grown AlN layers show FWHMs of the rocking curves in a ω-scan to lie in the range of 60–120 arcsec. At the same time, the *c*-parameter of the crystal lattice is found to vary between 4.984–4.988 Å, which suggests that the AlN layers contain high levels of impurities (the reference value of the *c*-parameter for pure AlN is 4.982 Å). X-ray microanalysis with an SEM CamScan MX2500S shows 5–6% wt of Si and 1% wt of C in the AlN layers. The concentration of other impurities is less than 100 ppm. It is known that the typical temperature of AlN growth on SiC seeds is lower by 200–300 °C than that on AlN seeds [115]. Analysis of the three-phase thermodynamic equilibrium in the system Al/N/Si/C(vapor)-AlN(solid)-SiC(solid) allows the gaseous species that may be responsible for the more intensive AlN growth on SiC to be found. Calculation of equilibrium partial pressures of the most volatile species in this system (more than 30 gaseous species were considered) showed that there are two "cross" volatile species (AlNC and Si_2N) that may intensify AlN growth on SiC.

7.3.3
Growth of Bulk AlN Crystals

The 2–3-mm thick AlN layers are mounted on the crucible lid. AlN bulk crystals 10–20 mm long are grown in W crucibles in W resistively heated furnace [96], the growth temperature was varied in the range of 2050–2250 °C, the N_2 pressure was varied in the range of 0.5–1 atm, and the AlN growth rate was of 50–150 μm/h. Long AlN crystals grow for several tens of hours and often in several runs.

7.4
Results and Discussion

Currently, the technology provides stable reproducible growth of 15–20 mm diameter and 10–15 mm long AlN single crystals. Post-growth processing includes calibration, slicing into plates, mechanical lapping-polishing, finishing chemical-mechanical polishing (CMP) performed at NOVASiC (this operation is known [116] to remove the subsurface damage due to the mechanical polishing that extends up to 4000 Å below the surface [13], and characterization. X-ray diffractometry of the AlN substrates gives FWHMs of the rocking curves in ω-scan of about 2–5 arcmin. Data of X-ray analysis are presented in [96]. The resistivity was

studied at Penn State University using a contactless resistivity mapping system, COREMA. Measurements showed that the resistivities are generally lower than 10^5 Ohm cm that is the lower limit of the COREMA. These values are much lower than the reference resistivity of undoped semi-insulating AlN (10^{11}–10^{13} Ohm cm). We associate this result with the effect of residual impurities (primarily Si) that still remain in the AlN bulk crystals grown on the SiC seeds. Repeated use of the initial AlN layer separated from "primary" crystal [117] results in high-purity material with resistivity in the range of 3×10^9–3×10^1 Ohm cm, which is rather close to the reference values.

Measurements of transmittance spectrum of the substrates (the sample thickness was 400 μm) in the UV range performed at Georgia Institute of Technology and at Helava Systems Inc. have shown that most of the crystals have average transmittance of 50–60% and demonstrate sharp cut-off between 250 nM and 320 nM.

The surface roughness of the substrate is characterized by RMS of the epi-side about 0.2–0.3 nm and RMS of the back side 1–2 nm.

The surface acoustic wave velocity of bulk AlN crystals was measured at different frequencies and extrapolated to zero frequency, yielding the value of ~5750 m/s.

The best characterization of the substrate quality is through the quality of the epitaxial structure grown on it. The epitaxial structures were studied using transmittance and reflectance optical microscopy, high-resolution XRD diffraction, cross-polarization. For example, the cathodoluminescence spectrum of the MOCVD grown AlGaN layer has a FWHM of about 10 nm.

Currently, the technology has been "scaled" to the growth of 2" AlN single crystals (Figure 7.5).

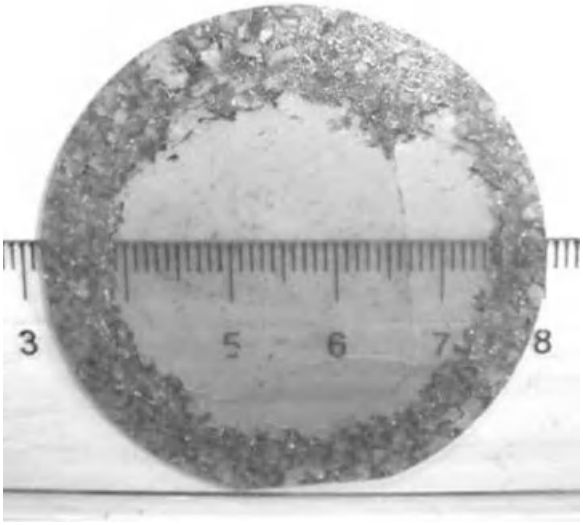

Figure 7.5 Transversal slice of 2-inch diameter 10 mm long bulk AlN crystal having a single-crystal core of about 40 mm diameter and a polycrystalline rim. No cracks are present in the single-crystal core.

7.5 Conclusions

The technology of sublimation growth of AlN bulk crystals has been developed that currently provides stable growth of 15–20-mm diameter and 10–15 mm long AlN single crystals. Repeated growth of a bulk AlN crystal on the initial AlN layer after separation of the first crystal results in a sharp increase of resistivity almost up to the reference value for pure AlN. The technology is scalable to grow large-diameter AlN bulk crystals. A 2-inch diameter and 10 mm long AlN crystal with 40 mm diameter single-crystal core without visible cracks has been demonstrated.

Acknowledgments

The authors thank J.H. Edgar from Kansas State University, T. Bogart from Penn State University, D. Yoo from Georgia Institute of Technology for characterization of the crystals and M.V. Bogdanov, S.Yu. Karpov, A.V. Kulik, and M.S. Ramm from Soft-Impact, Ltd. for useful discussions.

References

1 Edgar, J.H. *et al.* (ed.) (1999) *Properties, Processing and Applications of GaN and Related Semiconductors*, INSPEC, The IEE, London.
2 Jain, S.C., *et al.* (2000) *J. Appl. Phys.*, **87**, 965.
3 Liu, Y.S. (2009) *III-Nitride Devices and Nanoengineering* (ed. Z.C. Feng), World Scientific Publishing Company, London, pp. 1–20.
4 Nakamura, S., Fasol, G., and Pearton, S. (2000) *The Blue Laser Diode*, 2nd edn, Springer, New York.
5 Schubert, F.E. (2006) *Light-Emitting Diodes*, 2nd edn, CUP.
6 Taguchi, T. (2003) *J. Light Vis. Env.*, **27**, 131.
7 Zukauskas, A., Shur, M.S., and Gaska, R. (2002) *Introduction to Solid State Lighting*, John Wiley & Sons, Inc., New York.
8 Bennett, H.S., *et al.* (2004) *IEEE Circ. Dev. Mag.*, Nov./Dec., 38–51.
9 Morkoc, H. (1998) *Wide Band Gap Nitrides and Devices*, Springer, Berlin.
10 Pearton, S.J., *et al.* (2000) *Mater. Sci. Eng.*, **30**, 55.
11 Skierbiszewski, C. (2005) *Acta Phys. Polon.*, **108**, 635.
12 Luo, B., *et al.* (2002) *Solid State Electron.*, **46**, 573.
13 Freitas, J.A. (2005) *J. Ceram. Process. Res.*, **6**, 209.
14 Slack, G.A., *et al.* (2002) *J. Cryst. Growth*, **246**, 287.
15 Schowalter, L.J., *et al.* (2004) *IPAP Conf. Series*, **4**, 38.
16 Karpov, S.Yu. (2009) *III-Nitride Devices and Nanoengineering* (ed. Z.C. Feng), World Scientific Publishing Company, London, pp. 367–398.
17 Roycroft, B., *et al.* (2004) *Opt. Exp.*, **12**, 736.
18 Kukushkin, S.A., *et al.* (2008) *Rev. Adv. Mater. Sci.*, **17**, 1.
19 Liu, L., and Edgar, J.H. (2002) *Mater. Sci. Eng.*, **2R37**, 61.
20 Miskys, C.R., *et al.* (2003) *Phys. Status Solidi C*, **0**, 1627.
21 Russel, P. (2006) Proc. CS MANTECH Conf., Vancouver, pp. 231–232.
22 Pecz, B., *et al.* (2008) *Microscopy of Semiconducting Materials 2007* (eds A.G.

Cullis and P.A. Midgley), Springer, Berlin, pp. 53–56.
23 Franko, A., and Shanafield, D.J. (2004) *Ceramica*, **50**, 247.
24 Medraj, M., *et al.* (2005) *J. Mater. Process. Technol.*, **161**, 415.
25 Pinnington, T., *et al.* (2008) *J. Cryst. Growth*, **310**, 2514.
26 Steckl, A.J., *et al.* (1997) *J. Electron. Mater.*, **26**, 217.
27 Seol, D.J., *et al.* (2003) *Acta Mater.*, **51**, 5173.
28 Rojas, T.C., *et al* (1998) *Thin Solid Films*, **317**, 270.
29 Lim, Y.S., *et al.* (2000) *Appl. Phys. Lett.*, **77**, 4157.
30 Hull, R., *et al.* (2002) *J. Phys.: Condens. Matter*, **14**, 12829.
31 Maeffes *et al.* (2009) *phys. stat. sol. (a)*, **206**, 1153.
32 Xi, Y.A., *et al.* (2006) *Appl. Phys. Lett*, **89**, 103106.
33 Ougazzaden, A., *et al.* (2008) *J. Cryst. Growth*, **310**, 944.
34 Oh, T.S., *et al.* (2009) *J. Cryst. Growth*, **311**, 2655–2658, Avail. online 13 March.
35 Okamoto, K., *et al.* (2009) *J. Cryst. Growth*, **311**, 1311.
36 Lin, G.Q., *et al.* (2008) *Chin. Phys. Lett.*, **25**, 4097.
37 Yamabe, N., *et al.* (2009) *J. Cryst. Growth*, **311**, 3049–3053, Avail. online 20 January.
38 Le Louarn, A., *et al.* (2009) *J. Cryst. Growth*, **311**, 3278–3284, Avail. online 9 April.
39 Gautier, S., *et al.* (2008) *J. Cryst. Growth*, **310**, 4927.
40 Lee, H.Y., Lee, C., and Lee, K. (2004) *IPAP Conf. Series*, **4**, 25.
41 Nikolaev, A., *et al.* (2000) *MRS Internet J. Nitride Semicond. Res.*, **5S1**, W6.5.
42 Paskova, T., *et al.* (2004) *IPAP Conf. Series*, **4**, 14.
43 Tomita, K., *et al.* (2004) *IPAP Conf. Series*, **4**, 28.
44 Ashraf, H., *et al.* (2008) *J. Cryst. Growth*, **310**, 3957.
45 Grzegorczyk, A.P., *et al.* (2005) *J. Cryst. Growth*, **283**, 72.
46 Gaska, R., *et al.* (2002) *Appl. Phys. Lett.*, **81**, 4658.
47 Xi, Y.A., *et al.* (2006) Proc. L. Eastman Conf. High Performance Devices, Cornell Univ., p. 54.
48 Hu, X., *et al.* (2003) *Appl. Phys. Lett.*, **82**, 1299.
49 Mymrin, V.F., *et al.* (2005) *J. Cryst. Growth*, **281**, 115.
50 Schowalter, L.J., *et al.* (2006) *Phys. Status Solidi A*, **203**, 1667.
51 Stutzmann, M., *et al.* (2001) *Phys. Status Solidi B*, **228**, 505.
52 Dalmau, R., and Sitar, Z. (2005) *Encyclopedia of Materials: Science and Technology*, Elsevier, pp. 1–9.
53 Denis, A., *et al.* (2006) *Mater. Sci. Eng.*, **R50**, 167.
54 Krukowski, S. (1997) *Diamond Relat. Mater.*, **6**, 1515.
55 Nord, J., *et al.* (2003) *J. Phys.: Condens Matter*, **15**, 5649.
56 Kawahara, M., *et al.* (2005) *J. Ceram. Process. Res.*, **6**, 146.
57 Grzegory, I. (2001) *J. Phys.: Condens. Matter*, **13**, 6875.
58 Porowski, S., and Grzegory, I. (1997) *J. Cryst. Growth*, **178**, 174.
59 Bockowski, M. (2001) *Cryst. Res. Technol.*, **36**, 771.
60 Lan, Y.C., *et al.* (2000) *Mater. Res. Bull.*, **35**, 2325.
61 Purdy, A.P., *et al.* (2003) *J. Cryst. Growth*, **252**, 136.
62 Yoshikawa, A., *et al.* (2004) *J. Cryst. Growth*, **260**, 67.
63 Aoki, M., *et al.* (2002) *J. Cryst. Growth*, **246**, 133.
64 Onda, M., *et al.* (2002) *J. Cryst. Growth*, **237–239**, 2112.
65 Yamane, H., *et al.* (2000) *Mater. Lett.*, **42**, 66.
66 Song, Y., *et al.* (2003) *J. Cryst. Growth*, **247**, 275.
67 Aoki, M., *et al.* (2000) *J. Cryst. Growth*, **218**, 7.
68 Waldrip, K., Atcitty, S., and Boyes, J. (2008) Ann. DOE Peer Review Meeting, Washington.
69 Hirano, T., *et al.* (2009) *J. Cryst. Growth*, **311**, 3040–3043, Avail. online 20 January.
70 Ehrentraut, D., and Fukuda, T. (2008) *Frontiers in Materials Research* (eds Y. Fujikawa *et al.*), Springer, Berlin.
71 Adekore, B.T., *et al.* (2006) *J. Electron. Mater.*, **35**, 1104.
72 Yonemura, M., *et al.* (2005) *J. Mater. Sci. Mater. Electron.*, **16**, 197.
73 Meissner, E., *et al.* (2004) *IPAP Conf. Series*, **4**, 46.

74 Bao, H.Q., *et al.* (2009) *Appl. Phys. A*, **94**, 173.
75 Kallinger, B., *et al.* (2008) *Cryst. Res. Technol.*, **43**, 14.
76 Slack, G.A., and McNelly, T.F. (1977) *J. Cryst. Growth*, **34**, 263.
77 Rojo, J.C., *et al.* (2002) *Mater. Res. Soc. Symp. Proc.*, **722**, K1.1.1.
78 Raghothamachar, B., *et al.* (2003) *J. Cryst. Growth*, **250**, 244.
79 Hartmann, C., *et al.* (2008) *J. Cryst. Growth*, **310**, 930.
80 Lu, P. (2006) PhD Thesis, Kansas State Univ..
81 Miyanaga, M., *et al.* (2006) *SEI Tech. Rev.*, **63**, 22.
82 Lu, P., *et al.* (2008) *J. Cryst. Growth*, **310**, 2464.
83 Mokhov, E.N., *et al.* (2003) *Mater. Sci. Forum*, 433–436.**979**.
84 Lee, R.G. (2007) MS Thesis, Texas Tech University.
85 Noveski, V., *et al.* (2004) *MRS Internet J. Nitride Semicond. Res.*, **9**, 2.
86 Wang, X., Cai, D., and Zhang, H. (2006) AIAA Paper, 2006–3270.
87 de Almeida, V.F., and Rojo, J.C. (2002) Oak Ridge Nat. Lab., Tech. Rep. ORNL/TM-2002/64, pp. 1–32.
88 Cai, D., *et al.* (2006) AIAA Paper, 2006–3825.
89 Bogdanov, M.V., *et al.* (2003) *Cryst. Res. Technol.*, **38**, 237.
90 Bogdanov, M.V., *et al.* (2004) *Cent. Eur. J. Phys.*, **2**, 183.
91 Sitar, Z., *et al.* (2004) *IPAP Conf. Series*, **4**, 41.
92 Klapper, H. (2010) *Springer Handbook of Crystal Growth* (eds G. Dhanaraj *et al.*), Springer, Berlin.
93 Liu, L., *et al.* (2001) *MRS Internet J. Nitride Semicond. Res.*, **6**, 7.
94 Yakimova, R., *et al.* (2005) *J. Cryst. Growth*, **281**, 81.
95 Chemekova, T.Yu., *et al.* (2007) *Phys. Status Solidi C*, **4**, 2281.
96 Mokhov, E.N., *et al.* (2005) *J. Cryst. Growth*, **281**, 93.
97 Zhuang, D., *et al.* (2006) *J. Cryst. Growth*, **287**, 349.
98 Dryburgh, P.M. (1992) *J. Cryst. Growth*, **125**, 65.
99 Liu, L., and Edgar, J.H. (2000) *J. Cryst. Growth*, **220**, 243.
100 Noveski, V., *et al.* (2004) *J. Cryst. Growth*, **266**, 369.
101 Wu, B., *et al.* (2004) *J. Cryst. Growth*, **266**, 303.
102 Karpov, S.Yu., *et al.* (1999) *Phys. Status Solidi A*, **176**, 435.
103 Karpov, S.Yu., *et al.* (2001) *Phys. Status Solidi A*, **188**, 763.
104 Segal, A.S., *et al.* (2000) *J. Cryst. Growth*, **211**, 68.
105 Segal, A.S., *et al.* (2004) *J. Cryst. Growth*, **270**, 384.
106 Dreger, L.H., *et al.* (1962) *J. Phys. Chem.*, **66**, 1556.
107 Fan, Z.Y., and Newman, N. (2001) *Mater. Sci. Eng. B*, **87**, 244.
108 STR (2003) http://www.str-soft.com/products/Virtual_Reactor/ (accessed 22 March 2010).
109 Bogdanov, M.V., *et al.* (2001) *Mater. Sci. Forum*, **353–356**, **57**.
110 Nishino, K., *et al.* (2002) *J. Cryst. Growth*, **237–239**, **922**.
111 Dalmau, R., *et al.* (2005) *J. Cryst. Growth*, **281**, 68.
112 Vodakov, Yu.A., *et al.* (2003) US Patent 6,547,87.
113 Karpov, S.Yu., *et al.* (2003) *Phys. Status Solidi (c)*, **0**, 1989.
114 Kazan, M., *et al.* (2006) *J. Cryst. Growth*, **290**, 44.
115 Epelbaum, B., *et al.* (2002) *Mater. Sci. Form*, **389–393**, 1445.
116 Chen, X.F., *et al.* (2008) *Cryst. Res. Technol.*, **43**, 651.
117 Helava, H., *et al.* (2008) *Phys. Status Solidi C*, **5**, 1612.

8
Interactions of Dislocations During Epitaxial Growth of SiC and GaN

Jochen Friedrich, Birgit Kallinger, Patrick Berwian, Elke Meissner

8.1
Introduction

The market for compound semiconductor substrates including SiC and GaN will double its volume from approximately 600 million US$ in 2005 to approximately 1.2 billion US$ in 2012 according to a recent survey [1]. However, the produced area of all compound semiconductor wafers is still less than 1% of the area of the silicon wafers produced for microelectronic applications [1]. Among others one contribution to the dominance of silicon is the fact that silicon crystals can be grown dislocation free due to the necking procedure invented by Dash [2].

On the other hand, in 4H-SiC and GaN, which are forecasted to have the strongest growth rates within the compound semiconductor market, the current dislocation density is typically between 10^4–$10^5\,cm^{-2}$ for 4H-SiC and even 10^5–$10^9\,cm^{-2}$ for GaN. The presence of a special type of dislocations – the so-called micropipes (MP) which are known to be hollow-core screw dislocations [3] – has dominated the poor material quality of SiC over the last two decades and hindered the commercialization of 4H-SiC devices. In the 1990s the MP density was still several hundred cm^{-2} in SiC substrates. Around the year 2000 the MP density dropped below $100\,cm^{-2}$ in production grade 4H-SiC substrates with 3" diameter [4]. This was an important milestone for the market introduction of commercially produced Schottky diodes in 2001 [5]. Since this breakthrough the MP density has dropped further . Intense research was carried out to develop and utilize different techniques for the MP reduction [6–11]. Due to the large progress that has been achieved over recent years 4H-SiC wafers with 100 mm diameter and a MP density of zero cm^{-2} [12] are commercially available today. Therefore, it is believed that MPs will not be the showstopper for the further commercialization of SiC devices in the future.

As the MP densities are sufficiently low for device production, other dislocation-related defects came into focus to be limiting the performance and reliability of SiC devices. The future exploitation of SiC power electronic devices will be influenced by whether it is possible to minimize the formation of such dislocation-related defects. Therefore, this article will address especially the behavior of basal

Crystal Growth Technology. Semiconductors and Dielectrics. Edited by P. Capper and P. Rudolph
Copyright © 2010 WILEY-VCH Verlag GmbH & Co. KGaA, Weinheim
ISBN: 978-3-527-32593-1

plane dislocations during homoepitaxial growth of 4H-SiC that are believed to be responsible for the degradation of bipolar SiC power devices [13].

At the moment, GaN layers grown heteroepitaxially on sapphire or SiC substrates are mainly commercialized in the form of blue and white LEDs. This is due to the fact that the performance of those devices is not significantly influenced by the dislocation content of the material. On the other hand, for blue GaN laser diodes or high-power LEDs the dislocations do have a remarkable impact and dislocation densities below $10^6\,cm^2$ are required. Several procedures are investigated and used during device fabrication to reduce the dislocation content. The underlying physical mechanisms of the behavior of the reduction mechanisms of dislocations in GaN will be compared in the second part of this chapter to the dislocation reactions found during epitaxial growth of SiC.

8.2 Classification, Nomenclature and Characterization of Dislocations in SiC and GaN

In general, dislocations are classified according to their Burgers vector b and their line vector l, the angle ζ between b and l, and their glide plane that is spanned by b and l. If the Burgers vector b is perpendicular to the dislocation line l ($\zeta(l,b) = 90°$), the dislocation is called an edge dislocation. If the Burgers vector b is parallel to the dislocation line l ($\zeta(l,b) = 0°$), the dislocation is termed a screw dislocation. For a mixed-type dislocation the angle $\zeta(l,b)$ is between $0 < \zeta < 90°$.

Both 4H-SiC and GaN have a hexagonal crystal lattice with wurtzite structure. For both materials, typically wafers and epitaxial layers with (0001) surfaces are used. In this case, dislocations that propagate in the <0001> growth direction during epitaxy are called "threading dislocations", whereas dislocations with a line parallel to the (0001) surface are named "basal plane dislocations". It is important to note that in 4H-SiC both threading dislocations as well as dislocations within the basal plane can easily penetrate from the substrate into the epitaxial layer during epitaxial processing because the (0001) Si-face substrate typically has an off-orientation of 4° or 8° towards <11–20>. The usage of off-oriented substrates is mandatory for SiC. The off-orientation enhances the polytype reproduction in the epilayer by step-flow growth mode [13, 14]. In the case of GaN, the off-orientation is typically 0.2° or less relative to the (0001) plane (Ga-face), and is thus much smaller than in SiC. This means that only threading dislocations and not dislocations moving in the basal plane will proceed from the substrate into the active area of the device.

Although in both materials the dislocations are of the same type due to the same crystal structure, a different nomenclature has evolved historically for the dislocations in SiC and GaN. Their classification and nomenclature is compiled in Figure 8.1. In 4H-SiC the most important types of dislocations are named threading screw dislocations (TSD), threading edge dislocations (TED), and basal plane dislocations (BPD). In GaN the dislocation are typically called c-type, mixed type, or a-type dislocations regardless of their propagation direction.

Burgers vector	$b = <0001>$ (c-direction)	$b = \frac{1}{3} <11\bar{2}0>$ (a-direction)	$b = \frac{1}{3} <11\bar{2}3>$ (r-direction)
Visualization	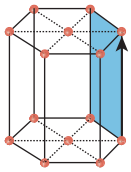	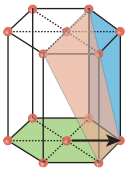	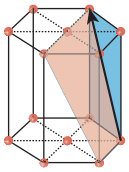
Possible glide planes	$\{1\bar{1}00\}$	$\{0001\}, \{1\bar{1}00\}, \{1\bar{1}0n\}$	$\{1\bar{1}00\}, \{1\bar{1}0n\}$
Nomenclature in 4H-SiC and 6H-SiC	Threading Screw Dislocations (TSD, ζ=0°)	Threading Edge Dislocations (TED, ζ=90°) on $\{1\bar{1}00\}$ Basal Plane Dislocations (BPD) on $\{0001\}$	Not observed in SiC
Nomenclature in GaN	c-type dislocations	a-type dislocations	a+c type dislocations or mixed type dislocations

Figure 8.1 Comparison of the nomenclature for some dislocations in wurtzite materials GaN and SiC. Dislocations with Burgers vector b = <0001> (*c*-direction) that propagate along their line vector l in the *c*-direction are called threading screw dislocations (TSD) in 4H-SiC and c-type dislocations in GaN. A-type dislocations are named all dislocations in GaN with Burgers vector b = 1/3 <11–20> (*a*-direction) independent of the glide plane. In 4H-SiC the dislocations with Burgers vector b = 1/3 <11–20> are further classified into threading edge dislocations (TED) which propagate along the *c*-direction (line vector l = <0001>) and basal plane dislocations (BPD) propagating within the basal plane (l lies in the *a*- or *m*-direction). In GaN, dislocations with Burgers vector b = 1/3 <11–23> that are either in the prismatic or pyramidal glide plane are called mixed or (a + c)-type dislocations. This type of dislocations is so far not reported to appear in SiC.

In order to characterize and count the dislocation density at the surface of SiC and GaN samples, the most frequently used method is defect selective etching (DSE). DSE gives an etch pit at the penetration point of the dislocation at the wafer surface, because the etching rate in the vicinity of the dislocation is increased in comparison to the surrounding matrix due to the distorted crystal lattice [15–18]. The morphology and the size of the etch pit are characteristic for the type of dislocation, its Burgers vector and depend on the doping level of the considered material and also strongly on the etching conditions (etchant, temperature, time, illumination, etc.). Under optimized etching conditions all different types of dislocations are revealed on the wafer and the dislocation density can be determined as etch pit density (EPD).

The most frequently used procedure of DSE is to etch 4H-SiC in molten KOH at around 500 °C for 5–10 min and GaN in the eutectic mixture of a KOH – NaOH

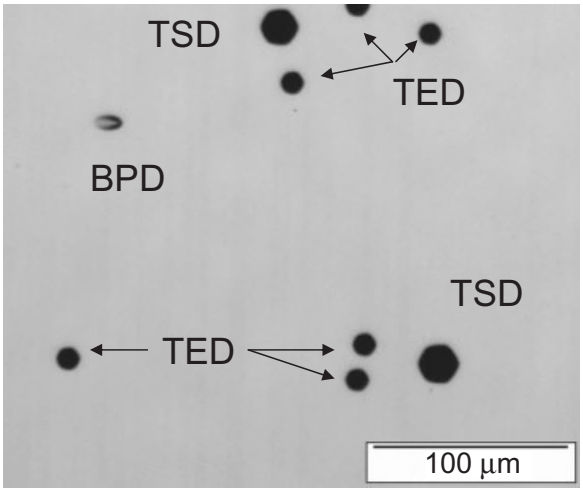

Figure 8.2 Typical etch patterns on a 4° off-axis 4H-SiC sample ($n \sim 10^{15}\,cm^{-3}$) after defect selective etching in molten KOH at 500 °C for several minutes. The oval-shaped pit corresponds to a BPD, small roundish or hexagonally shaped etch pits to TED and large hexagonal etch pits to TSD.

melt at around 400–450 °C for 2–5 min. In general, one can distinguish in both materials between small, medium and large hexagonally shaped etch pits after DSE. In addition, oval-shaped etch pits are visible in 4H-SiC samples. Figure 8.2 illustrates such typical etch pits generated after DSE on SiC samples. A survey of the current status of DSE of SiC and GaN can be found in [15].

DSE is a very simple and efficient method to quantitatively determine the dislocation density. However, it is an indirect method. It requires that complementary direct methods for the determination of dislocations' Burgers and line vectors are applied in order to prove that all different types of dislocations are really visible as characteristic etch pits on the etched sample. Such direct methods are for example transmission electron microscopy (TEM) as well as X-ray topography (XRT). In both methods, a dislocation gives a contrast on the micrograph, which depends on the type of the dislocation and the applied diffraction conditions [19, 20].

For an analysis of dislocations by TEM the dislocation density in the material must be high enough ($>10^8\,cm^{-2}$) in order to detect them with high probability. XRT is well suited for better material quality, that is, for a dislocation density $<10^5\,cm^{-2}$, so that each single dislocation can be identified in the XRT image. Therefore, TEM analysis is typically used for GaN to determine the type of dislocation at etch pits generated by DSE due to the large number of dislocations present in GaN epitaxial layers [17]. In the case of 4H-SiC the correlation of etch pits with the type of dislocations is usually done by XRT measurements due to the smaller total number of dislocations. A recent study confirms that in n-type 4H-SiC the small and large etch pits can be attributed to TEDs and TSDs [18] at least for samples with $n \sim 10^{15}$–$10^{17}\,cm^{-3}$ and that the oval-shaped etch pits represent BPDs independent of the n-doping level (see also Figure 8.2). For highly n-type 4H-SiC

the direct correlation of the size of the etch pit to TED and TSD is not absolutely clear so far [18].

8.3
Conversion of Basal Plane Dislocations During SiC Epitaxy

8.3.1
Experimental Strategies for Obtaining High Conversion Rates

Basal plane dislocations (BPD) are considered to be detrimental for the reliability of bipolar devices for blocking voltages >2 kV. Here, BPDs can trigger the formation and expansion of stacking faults during device operation that finally result in significant changes of the device characteristics [14]. The usage of off-oriented substrates allows that BPDs in the substrate can easily penetrate into the epitaxial layers during homoepitaxial processing. As a consequence, they are present in the active volume of the devices. This is illustrated in Figure 8.3.

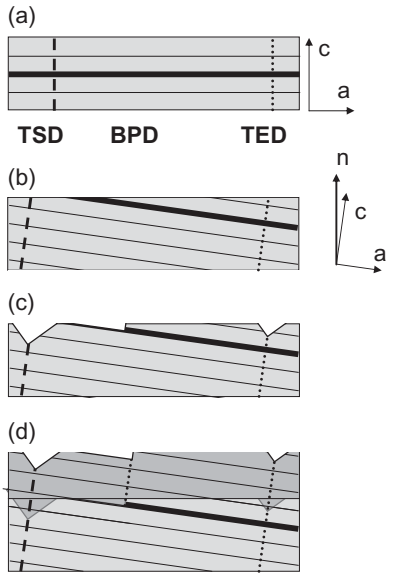

Figure 8.3 Illustration of the propagation direction of different dislocation types (BPD bold solid line, TED dotted line, TSD dashed line) in 4H-SiC. (a) On-axis substrate: TSD and TED will proceed parallel to the growth direction, BPD are perpendicular to the growth direction and will not propagate into the epitaxial layer; (b) Off-axis substrate: the dislocation lines of TSD and TED are slightly tilted to the surface, BPD can penetrate to the surface; (c) On a defect selectively etched off-axis substrate the oval-shaped, shallow etch pits at the penetration point of BPDs reveal locally on-axis conditions, the deep etch pits of TEDs and TSDs have a hexagonal shape; (d) During epitaxial growth on the etched substrate TEDs and TSDs will keep their propagation direction, whereas the BPDs become unstable and convert to TEDs.

The 4H-SiC substrates typically exhibit a BPD density in the range of 10^3 to $10^4\,cm^{-2}$ [21]. So far, the origin for the formation of the BPDs during bulk crystal sublimation growth is not well investigated and also no strategies are undertaken to avoid them. Therefore, it is necessary to identify measures for BPD reduction during homoepitaxy. Fortunately, a large fraction of the BPDs are more or less automatically converted into threading edge dislocations (TED) during epitaxial processing [21–24]. It is important to note that by this mechanism the total dislocation density in the epitaxial layer is not reduced compared to the initial dislocation density of the substrate, only the number of BPDs is decreased, but at the same time the number of TEDs is increased. Nevertheless, the remaining BPD density is typically $10^2\,cm^{-2}$ after a standard epitaxial growth run [21]. This is considered to be still too high for reliable device operation.

It is known from the literature [21–24] that the conversion rate from BPDs into TEDs during epitaxy depends, among other parameters on the off-axis angle, Si- or C-face of the {0001} 4H-SiC substrate, substrate preparation such as KOH etching and epitaxial growth parameters like C/Si ratio and growth rate. In particular, the approach to etch the substrates in molten KOH prior to epitaxial growth seems to be very efficient in order to achieve BPD free 4H-SiC layers [23]. This patented procedure consists of 4 steps: (i) KOH etching of the off-axis substrate; (ii) conversion of BPDs into TEDs during growth of a thick (50-μm) epitaxial layer; (iii) planarization down to 5 μm of the epitaxial layer thickness; (iv) growth of the final epitaxial layer for the device. These steps are explained in the following in more detail:

The etch pits generated on the substrate after step 1 (KOH etching) favor the conversion of the BPDs to TEDs at the beginning of step 2 (growth of thick layer) because the oval-shaped etch pits generate locally an on-axis surface on which the BPDs are unstable [14]. However, due to the etch pits generated on the substrate prior to epitaxy, the as-grown surface exhibits deep depressions and the grown layer cannot be used for device processing. Therefore, it is necessary to planarize the surface. This planarization step requires the growth of a relatively thick BPD free epitaxial layer (step 2) which is repolished (step 3) to get a plane, BPD-free, and subsurface-damage-free surface that serves as the starting point for the deposition of the final active layer (step 4). In summary, it can be stated that this procedure [23] allows BPD-free SiC layers to be obtained, but it is a time-consuming and very expensive procedure.

Alternative ways are currently under investigation for complete BPD conversion at less effort. It has been shown in [21] that several single modifications of the epitaxial growth process are less effective than the KOH etching procedure in order to enhance the conversion efficiency from BPDs into TEDs. These measures include various pretreatments of the substrate as well as the variation of a single epitaxial growth parameter. However, it is also reported in [21, 25] that by applying a combination of well-suited epitaxial parameters conversion ratios can be achieved that are comparable to KOH etching results (see Figure 8.4). Under such optimized growth conditions the BPD density can be reduced from 10^3–10^4 BPD/cm^2 in the substrate down to less than 3 BPD/cm^2 in the epitaxial layer. This excellent

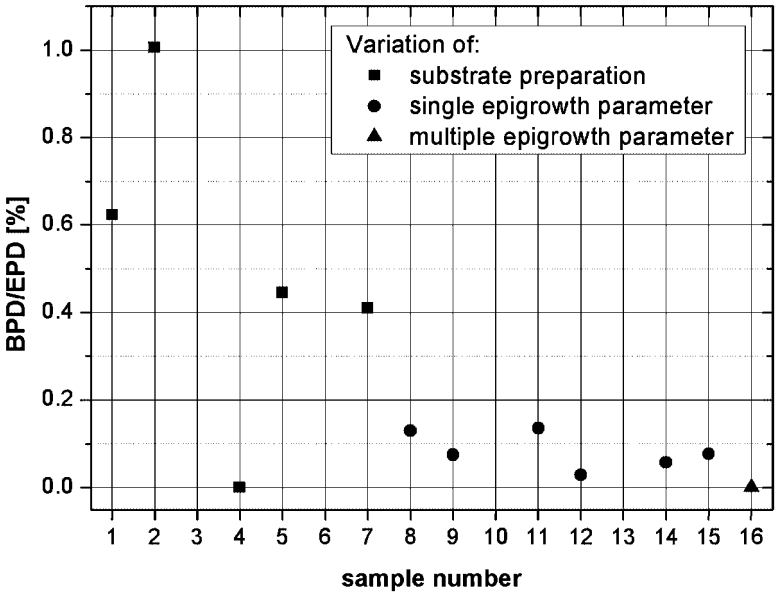

Figure 8.4 Ratio of BPD density to the etch pit density (EPD) in the epilayer (%) for different samples. All BPDs of the substrate are converted to TEDs in the epitaxial layer in case of epitaxial growth on a KOH etched substrate (sample 4) and an epitaxial layer deposited on an epi-ready substrate applying a certain combination of epi-growth parameters (sample 16). For more details see [13].

conversion ratio has been proven by XRT measurements carried out on the same sample before and after the epitaxial growth run [18]. As stated above, such low BPD values are thought to be an important prerequisite for manufacturing reliable bipolar 4H-SiC devices in the future.

8.3.2 Driving Force for BPD Conversion

The underlying mechanism that forces the BPD to convert to TED during SiC epitaxy is the tendency of the dislocation to minimize its elastic energy W. The elastic energy W of dislocations per unit of grown layer thickness is proportional to the line energy of the dislocation E and to the angle γ between the dislocation line l and the growth normal [26, 27].

$$W = \frac{E}{\cos\gamma} \tag{8.1}$$

As the line energies E of BPDs and TEDs were found to be almost equal [24], the elastic energy during growth W can be mainly influenced by the length of the dislocation line l, which depends on the angle γ of the dislocation line to the normal n of the growing surface [26, 27] (see also Figure 8.5). From this rough

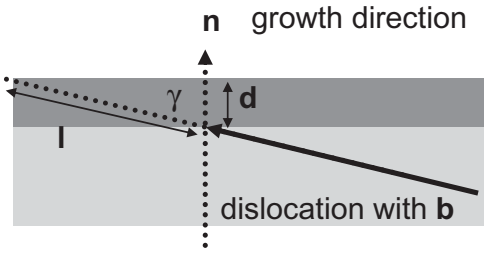

Figure 8.5 The dislocation with Burgers vector *b* propagates along its dislocation line *l*. The angle γ is the angle between the dislocation line *l* to the normal *n* of the growth direction. The effective length of the dislocation *d* along the growth direction is $d = l \cos \gamma$.

energetic consideration it follows that even without etching the energy of the TEDs $W_{TED} \sim 1/\cos 8°$ is smaller than the energy of the BPDs $W_{BPD} \sim 1/\cos 82°$ in case of an 8° off-oriented SiC substrate. Therefore, a fraction of the BPDs will convert into TEDs during a standard epitaxial process (see Figure 8.3).

This conversion ratio can be increased for a given off-oriented SiC substrate by the KOH etching procedure, because a quasi-on-axis surface is generated locally in the vicinity of the BPD [14]. The consequence is that γ becomes 90° for the BPD on an etched substrate. Thus, the elastic energy of the BPD $W_{BPD} \sim 1/\cos 90°$ is much higher than the corresponding value of the TED $W_{TED} \sim 1/\cos 0°$ and the conversion efficiency is much higher than for unetched substrates.

From this simple consideration it can be concluded that one has to modify the surface morphology of the growing interface during epitaxial processing in such a way that the elastic energy *W* becomes minimum. This modification can be achieved either by the *ex-situ* etching procedure [23] or by an adjustment of the epitaxial growth parameters to influence the step geometry in the desired way [25].

8.4 Reduction of Dislocations During Homoepitaxy of GaN

8.4.1 Objectives and Techniques

The principle of minimization of the elastic energy of dislocations in the vicinity of a grown crystal surface is not only actively used in SiC to obtain BPD-free material, but it is also an important basis to influence the propagation of dislocations during epitaxial growth of GaN layers. Thereby, the goal of influencing the dislocations in GaN is different in comparison to SiC. In GaN the main goal is a real reduction of the total number of (threading) dislocations rather than a conversion of one type of dislocations into another type, as it is the case in SiC. The real reduction of the overall dislocation density is necessary because the number of dislocations in GaN layers is typically 3–5 orders of magnitude higher

than in SiC and is harmful for the lifetime and performance of GaN-based devices [28, 29].

In GaN, basal plane dislocations are less important for device operation as compared to SiC because the epitaxial growth of GaN layers usually takes place on almost on-axis (0001)-oriented surfaces and the BPDs can not propagate into the active device layers. The strategy for a real dislocation reduction in GaN consists of three measures: (i) prevent threading dislocations from proceeding in the *c*-direction; (ii) enhance the probability of recombination and annihilation of dislocations; and (iii) force the remaining threading dislocations to continue to proceed mainly in the basal plane during epitaxial growth, that is, perpendicular to the [0001] growth direction.

Well-established epitaxial methods that can achieve the objectives 1 to 3 are the techniques epitaxial lateral overgrowth (ELO) [30], dislocation elimination by inverse pyramids (DEEP) [31], or the utilization of SiN_x interlayers [32]. Common to all these methods is that the growth surface is patterned in a way that growth pyramids with side facets having a steep angle relative to the (0001)-surface can form locally during epitaxial growth. An alternative way to form such facets is solution growth of GaN layers on MOCVD GaN seed layers. By using the Na-flux method [33, 34], the high-pressure solution growth method (HPSG) [35, 36] or the low-pressure solution growth method (LPSG) [37–39] three-dimensional growth islands with side facets are formed *in situ* during the initial growth stage and a reduction of the dislocation density is observed. Even in a conventional, but optimized MOCVD process such growth conditions can be realized [40].

8.4.2
Driving Force for Dislocation Reduction

The occurrence of three-dimensional growth islands with distinguished side facets is an important feature of efficient dislocation reduction procedures. The underlying reduction mechanism was investigated in detail by using transmission electron microscopy (TEM) and additional theoretical considerations [38].

In the vicinity of such a facet the dislocation can minimize its energy when the dislocation line l can bend from the original threading *c*-direction towards the normal of the side facet by the bending angle β [26, 27, 38] (see Figure 8.6). This energy corresponds to the energy W defined in Equation 8.1. The condition that $W = E/\cos\gamma$ will be minimum is fulfilled for a certain bending angle β. β depends on the dislocation type (E is a function of Burgers vector, dislocation line l, and the glide plane), and also on the facet angle α [38]. The bending angle of the dislocation β as well as the facet angle α can be easily correlated to the angle γ used in Equation 8.1 for the angle between the dislocation line l and the normal of the growing interface. Simple geometrical considerations as sketched in Figure 8.6 give $\gamma = \alpha - \beta$.

The facet angle α depends on the growth conditions and applied epitaxial techniques. It was found by TEM analyses that during the initial growth stage shallow side facets with $\alpha = 32°$ ({1–103}) and with $\alpha = 25°$ ({1–104}) are the most frequent

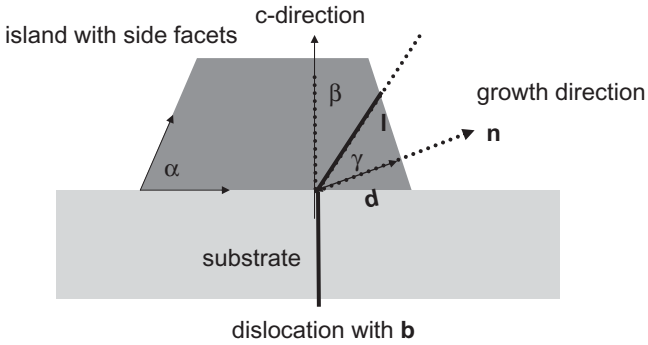

Figure 8.6 During the initial stage, islands with side facets are formed on a *c*-oriented substrate. The angle α is the angle of the side facet relative to the *c*-direction. The dislocation with Burgers vector *b* propagates in the substrate along its dislocation line *l* that is assumed for simplicity to be parallel to the *c*-direction. Due to the presence of the side facet the dislocation will bend towards the normal *n* of the side facet. The bending angle β is defined as the angle between the *c*-direction and the bent dislocation line *l*. The angle γ is the angle between the bent dislocation line *l* to the normal *n* of the growth direction. The effective length of the dislocation d along the growth direction is $d = l \cos \gamma$. The relation for the bending angle β, the angle γ and the facet angle α holds: $90° = \beta + \gamma + (90° - \alpha)$.

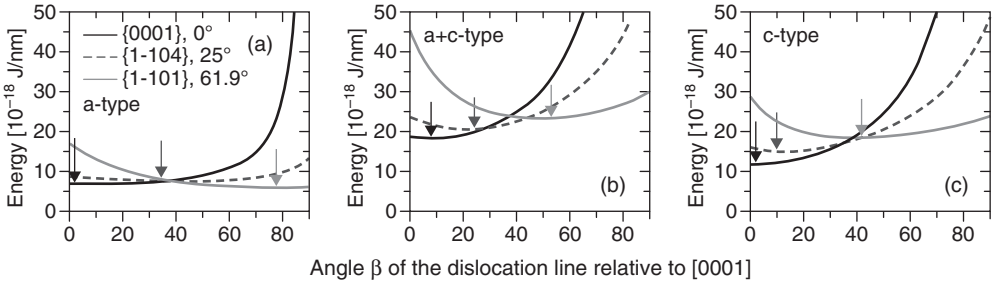

Figure 8.7 Line energy of a dislocation (normalized) as a function of the facet angle and the bending angle relative to the *c*-direction for the three typical dislocation types in GaN. (a) a-type Burgers vector, (b) (a + c)-type Burgers vector, (c) c-type Burgers vector. The minima of the respective curves are marked by arrows, indicating the theoretically expected bending angle β for the side facets taken into account in the present calculations.

in LPSG samples grown from Ga- and Ge-containing solutions [38, 39]. Steeper facets can be achieved for example by adding Si to the solution in the LPSG process [41], respectively, to the gas atmosphere during MOCVD growth [42]. ELO samples exhibit typically {1–101}, {11–22} side facets with an angle $\alpha > 45°$ [43].

Theoretical considerations that were confirmed by corresponding experimental observations show that an energy gain caused by the bending of dislocations is larger the steeper the side facets [38] (see also Figure 8.7). Furthermore, it is

obvious from Figure 8.7 that the bending angle β increases also with increasing facet angle α [38].

Therefore, for solution growth techniques with shallow facets ($\alpha < 32°$) the energy gain is not very pronounced when the dislocation bends. In particular, c-type dislocations are energetically already in a favorable situation. Furthermore, the bending angle β would be relatively small ($\beta < 45°$) and will therefore not remove the dislocation relative to the epitaxial surface.

For ELO techniques with steeper facets ($\alpha > 45°$) the energy gain becomes larger when the dislocations bend from the *c*-direction towards the normal of the facets. This driving force is much larger for all types of dislocations including c-type, compared to a case with shallow facets. For such steep facets occurring during ELO the bending angle β can be even 90°. A bend by $\beta = 90°$ into the basal plane removes completely the dislocation from the further growing layer because it becomes perpendicular to the macroscopic growth direction.

But, smaller bending angles $\beta < 90°$ can be beneficial as well, due to the fact that any change in line direction will increase the probability that during further growth the dislocations can come close enough and can either annihilate (two dislocations removed) or recombine (one dislocation removed). However, the smaller the bending angle β is the longer the growth of the islands with side facets has to be maintained in order to reach the necessary critical interaction distance for the dislocations. From such simple considerations it is also obvious that the reduction mechanism by bending of dislocations and further reactions only works if the initial dislocation density is high. The smaller the dislocation density the larger the distance becomes between the dislocations and the smaller the probability is that dislocations can meet and react based on the bending mechanism.

By using this bending mechanism, for example, solution-grown GaN layers grown on MOCVD seed layers (with an initial dislocation density of 10^9–$10^{10}\,cm^{-2}$) can typically achieve dislocation density values of 10^7–$10^8\,cm^{-2}$. Multiple layer growth by a sequence of solution-growth experiments on one sample confirms that the bending mechanism becomes inefficient for an initial dislocation density of the seed layer of below $1 \times 10^6\,cm^{-2}$ [35]. Both the small facet angle resulting in only a small energy gain and the small bending angle are responsible for the fact that these methods still do not reach the reduction efficiency of patterning techniques like ELO and related techniques. The steep facets created by the patterning technique increase the recombination efficiency of bent dislocations as well as the probability that dislocations bend into the basal plane. As a result, a particular fraction of the wafer area of such GaN samples exhibits locally a dislocation density as low as 10^5–$10^6\,cm^{-2}$ that is an important perquisite for blue GaN laser diodes with lifetimes of >10 000 h [31]. However, other areas of those wafers are not usable.

Lower values of the dislocation densities are up to now only reported for free standing GaN platelets grown without a foreign substrate, thereby avoiding the formation of misfit dislocations. Examples are GaN substrates grown by the high-pressure solution growth (10^2–$10^3\,cm^{-2}$) [44], as well as by the ammonothermal method (10^3–$10^4\,cm^{-2}$) [45].

8.5 Conclusions

For many types of SiC and GaN devices a significant reduction of dislocation densities is mandatory from a technological point of view. As long as no bulk crystals are available with very low dislocation densities this can only be achieved by promoting dislocation reactions during epitaxy like bending and annihilation using the principle of energy minimization. This technique has been successful up to a certain degree. Unfortunately, the most effective techniques like ELO or DEEP are quite complicated and expensive. Some simpler strategies, like nucleation of islands during epitaxial growth, cannot reach dislocation densities sufficient for all types of devices. In the long run, when it comes to manufacturing higher performance devices there seems to be no way of circumventing the development of bulk substrate growth processes with lower dislocation densities.

Acknowledgment

The authors thank Georg Müller, Isabel Knoke, Stephan Hussy, and Sebastian Polster for their contributions. Part of the work was financially supported by the German Ministry of Education and Research (BMBF), the Bavarian Research Foundation (BFS) and by a PhD scholarship from the Fraunhofer Society.

References

1 Roussel, P. (2008) *A Comprehensive Survey on Material Usage and Markets for GaAs, InP, SiC, Sapphire and GaN*, Yole Developement.
2 Dash, W.C. (1960) Growth of silicon crystals free from dislocations. *J. Appl. Phys.*, **31**, 736.
3 Frank, F.C. (1951) Capillary equilibria of dislocated crystals. *Acta Cryst.*, **4**, 497–501.
4 Powell, A., Jenny, J., Müller, S., Hobgood, H., Tsvetkov, V., Lenoard, R., and Carter, C. (2006) Growth of SiC substrates. *Int. J. High Speed Electron. Syst.*, **16** (**3**), 751–777.
5 Zverev I., Treu M., Kapels H., Hellmund O., Rupp R., and Weiss J. (2001) SiC Schottky Rectifiers: Performance, Reliability and key application, Proceedings of the 9th European Conference on Power Electronics (EPE), Graz (2001).
6 Rupp, R., Treu, M., Türkes, P., Beermann, H., Scherg, T., Preis, H., and Cerva, H. (2005) Influence of overgrown micropipes in the active area of SiC Schottky diodes on long term reliability. *Mater. Sci. Forum*, **483–485**, 925–928.
7 Nakamura, D., Gunjishima, I., Yamaguchi, S., Ito, T., Okamoto, A., Kondo, H., Onda, S., and Takatori, K. (2004) Ultrahigh-quality silicon carbide single crystals. *Nature*, **430**, 1009–1012.
8 Rost, H.-J., Schmidbauer, M., Siche, D., and Fornari, R. (2006) Polarity- and orientation-related defect distribution in 4H-SiC single crystals. *J. Cryst. Growth*, **290**, 37–143.
9 Shiomi, H., Kinoshita, H., Furusho, T., Hayashi, T., Tajima, M., and Higashi, E. (2006) Crystal growth of micropipe free 4H–SiC on 4H–SiC {03–38} seed and high-purity semi-insulating 6H–SiC. *J. Cryst. Growth*, **292**, 188–191.
10 Li, J., Filip, O., Epelbaum, B.M., Xu, X., Bickermann, M., and Winnacker, A. (2007) Growth of 4H-SiC on rhombohedral (01–14) plane seeds. *J. Cryst. Growth*, **308**, 41–49.

11 Basceri, C., Khlebnikov, I., Khlebnikov, Y., Muzykov, P., Sharma, M., Stratiy, G., Silan, M., and Balkas, C. (2006) Growth of micropipe-free single crystal silicon carbide (SiC) ingots via physical vapor transport (PVT). *Mater. Sci. Forum*, **527–529**, 39–42.

12 Leonard, R.T., Khlebnikov, Y., Powell, A.R., Basceri, C., Brady, M.F., Khlebnikov, I., Jenny, J.R., Malta, D.P., Paisley, M.J., Tsvetkov, V.F., Zilli, R., Deyneka, E., Hobgood, H.M., Balakrishna, V., and Carter, C.H., Jr. (2009) 100 mm 4HN-SiC wafers with zero micropipe density. *Mater. Sci. Forum*, **600–603**, 7–10.

13 Ha, S., Skowronski, M., and Lendenmann, H. (2004) Nucleation sites of recombination-enhanced stacking fault formation in silicon carbide p-i-n diodes. *J. Appl. Phys.*, **96** (**1**), 393–398.

14 Zhang, Z., and Sudarshan, T.S. (2005) Basal plane dislocation-free epitaxy of silicon carbide. *Appl. Phys. Lett.*, **87**, 151913.

15 Zhuang, D., and Edgar, J.H. (2005) Wet etching of GaN, AlN, and SiC: a review. *Mater. Sci. Eng. R*, **48**, 1–46.

16 Sakwe, S.A., Müller, R., and Wellmann, P.J. (2006) Optimization of KOH etching parameters for quantitative defect recognition in n- and p-type doped SiC. *J. Cryst. Growth*, **289**, 520–526.

17 Knoke, I.Y., Berwian, P., Meissner, E., Friedrich, J., Strunk, H.P., and Müller, G. Defect selective etching of dislocations in LPSG-GaN. To be published.

18 Kallinger, B., Polster, S., Berwian, P., Friedrich, J., Danilewsky, A., Wehrhahn, A., and Weber, A.-D. Comparative study on the dislocation densities of 4H-SiC substrates and homoepitaxial layers using defect selective etching and synchrotron white beam X-ray topography. To be published.

19 Bowen, D.K., and Tanner, B.K. (1998) *High-Resolution X-Ray Diffractometry and Topography*, Taylor and Francis, London.

20 Williams, D.B., and Carter, C.B. (1996) *Transmission Electron Microscopy – A Textbook for Materials Science*, Springer, New York.

21 Kallinger, B., Thomas, B., and Friedrich, J. (2009) Influence of substrate preparation and epitaxial growth parameters on the dislocation densities in 4H-SiC epitaxial layers. *Mater. Sci. Forum*, **600–603**, 143–146.

22 Chen, W., and Capano, M.A. (2005) Growth and characterization of 4H-SiC epilayers on substrates with different off-cut angles. *J. Appl. Phys.*, **98**, 114907.

23 Sumakeris, J.J. (2003) Techniques for minimizing the basal plane dislocation density in SiC epilayers to reduce Vf drift in SiC bipolar power devices, U.S. Patent Application 20050064723, filed Sept. 22, 2003.

24 Ohno, T., Yamaguchi, H., Kuroda, S., Kojima, K., Suzuki, T., and Arai, K. (2004) Direct observation of dislocations propagated from 4H–SiC substrate to epitaxial layer by X-ray topography. *J. Cryst. Growth*, **260**, 209–216.

25 Kallinger, B., Thomas, B., Polster, S., Berwian, P., and Friedrich, J. (2010) Dislocation conversion and propagation during homoepitaxial growth of 4H-SiC, Materials Science Forum Vols. 645–648, p. 299–302.

26 Klapper, H. (1972) Elastische Energie und Vorzugsrichtungen geradliniger Versetzungen in aus der Lösung gewachsenen organischen Kristallen. *Phys. Status Solidi A*, **14**, 99–106.

27 Klapper, H., Fishman, Yu.M., and Lutsau, V.G. (1974) Elastic energy and line directions of grown-in dislocations in KDP crystals. *Phys. Status Solidi A*, **21**, 115–121.

28 Speck, J.S., and Rosner, S.J. (1999) The role of threading dislocations in the physical properties of GaN and its alloys. *Phys. B*, **273–274**, 24–32.

29 Mion, C., Muth, J.F., Preble, E.A., and Hanser, D. (2006) Thermal conductivity, dislocation density and GaN device design. *Superlatt. Microstruct.*, **40**, 338–342.

30 Gradecak, S., Wagner, V., Ilegems, V., Bobard, F., and Stadelmann, P. (2002) Microstructure of ELO-GaN layers grown by hydride vapor phase epitaxy. *Mater. Res. Soc. Symp. Proc.*, **693**, I3.23.

31 Motoki, K., Okahisa, T., Nakahata, S., Uematsu, K., Hitoshi, K., Matsumoto, N., Kumagai, Y., Koukitu, A., and Seki, H. (2002) Preparation of large GaN substrates. *Mater. Sci. Eng. B*, **93**, 123–130.

32 Kappers, M.J., Datta, R., Oliver, R.A., Rayment, F.D.G., Vickers, M.E., and Humphreys, C.J. (2007) Threading dislocation reduction in (0001) GaN thin films using SiNx interlayers. *J. Cryst. Growth*, **300**, 70–74.

33 Morishita, M., Kawamura, F., Kawahara, M., Yoshimura, M., Mori, Y., and Sasaki, T. (2004) The influences of supersaturation on LPE growth of GaN single crystals using the Na flux method. *J. Cryst. Growth*, **270**, 402–408.

34 Kawamura, F., Umeda, H., Kawahara, M., Yoshimura, M., Mori, Y., Sasaki, T., Okado, H., Arakawa, K., and Mori, H. (2006) Growth of a two-inch GaN single crystal substrate using the Na flux method. *Jpn. J. Appl. Phys.*, **45**, 1136–1138.

35 Grzegory, I., Bockowski, M., Lucznik, B., Krukowski, S., Wroblewski, M., and Porowski, S. (1996) Recent results in the crystal growth of GaN at high N2 pressure. *Internet J. Nitride Semicond. Res.*, **1**, 20.

36 Bockowski, M., Grzegory, I., Krukowski, S., Lucznik, B., Wroblewski, M., Kamler, G., Borysiuk, J., Kwiatkowski, P., Jasik, K., and Porowski, S. (2005) Gallium nitride growth on sapphire/GaN templates at high pressure and high temperatures. *J. Cryst. Growth*, **274**, 55–64.

37 Hussy, S., Meissner, E., Berwian, P., Friedrich, J., and Müller, G. (2008) Low pressure solution growth (LPSG) of GaN templates with diameters up to 3 inch. *J. Cryst. Growth*, **310**, 738–747.

38 Knoke, I.Y., Meissner, E., Friedrich, J., Strunk, H.P., and Müller, G. (2008) Model for the dislocation reduction mechanism during solution growth of GaN. *J. Cryst. Growth*, **310**, 3351–3357.

39 Hussy, S., Berwian, P., Meissner, E., Friedrich, J., and Müller, G. (2008) On the influence of solution density on the formation of macroscopic defects in the liquid phase epitaxy of GaN. *J. Cryst. Growth*, **311**, 62–65.

40 Lang, T., Odnoblyudov, M., Bougrov, V., Suihkonen, S., Sopanen, M., and Lipsanen, H. (2006) Morphology optimization of MOCVD-grown GaN nucleation layers by the multistep technique. *J. Cryst. Growth*, **292**, 26–32.

41 Meissner, E., Birkmann, B., Hussy, S., Sun, G., Friedrich, J., and Müller, G. (2005) Characterisation of GaN crystals and epilayers grown from a solution at room pressure. *Phys. Status Solidi C*, **2**, 2040–2043.

42 Benzarti, Z., Halidou, I., Tottereau, O., Boufaden, T., and El Jani, B. (2002) Silicon effect on GaN surface morphology. *Microelectron. J.*, **33**, 995–998.

43 Gibart, P. (2004) Metal organic vapour phase epitaxy of GaN and lateral overgrowth. *Rep. Prog. Phys.*, **67**, 667–715.

44 Grzegory, I. (2001) High pressure growth of bulk GaN from solutions in gallium. *J. Phys.: Condens. Matter*, **13**, 6875–6892.

45 Dwilinski, R., Doradzinski, R., Garczynski, J., Sierzputowski, L., Puchalski, A., Yagi, K., and Kanbara, Y. (2008) Flat lattice of truly bulk ammonothermal GaN, Oral presentaion at Joint 5th Int. Conf. on Solid State Crystals & 8th Polish Conf. on Crystal Growth, Zakopane, Poland.

9
Low-Temperature Growth of Ternary III-V Semiconductor Crystals from Antimonide-Based Quaternary Melts

Partha.S. Dutta

9.1
Introduction

III-V compound semiconductors are being used for a multitude of electronic and optoelectronic applications [1]. These compounds are also turning out to be promising candidates for emerging technologies such as in terahertz, nonlinear optics, electro-optics, infrared sensing, and thermophotovoltaics [2–23]. Most of the current applications are being accomplished by the limited choice of binary compounds (such as GaAs, GaSb, InP, GaP, InAs, InSb) that are readily available from commercial vendors. The binary compounds provide few discrete lattice constants and bandgaps. The availability of compounds with any bandgap and any lattice parameter would certainly expand the scope of III-V semiconductors for new applications as well as help improve the performances of existing devices that are being fabricated using binary substrates. By using ternary compounds, one can tune the lattice parameter or the bandgap energy of the material by choosing appropriate chemical compositions [24, 25]. In spite of four decades of research on ternary semiconductor materials ([26–28] and references therein), substrates are still not readily available from commercial vendors in large scale. The inherent problems in growing ternary crystals from melts and potential solutions, have been described in detail in this author's recent article [28]. Much of the ternary crystal-growth research and development to-date has been focused on low-bandgap compounds, GaInAs and GaInSb (see extensive references in [28], [29–36]). The growth of larger bandgap ternaries of phosphides and arsenides is still in its early stages and requires additional innovations in melt chemistries to enable high-quality substrates to be obtained. This chapter presents a new pathway for growing high vapor pressure ternary compounds (GaInP, GaAsP, AlGaP, etc.) at low growth temperatures (1000–1100 °C) using quaternary melts containing binary antimonides. The focus of this chapter will be on the melt composition and growth temperature necessary to grow ternary crystals of any desirable alloy composition. Crystal-growth configurations and parameters such as melt replenishment and mixing that are generic to ternary crystal growth [28, 37] will not be discussed here.

Crystal Growth Technology. Semiconductors and Dielectrics. Edited by P. Capper and P. Rudolph
Copyright © 2010 WILEY-VCH Verlag GmbH & Co. KGaA, Weinheim
ISBN: 978-3-527-32593-1

9.2 Crystal Growth from Quaternary Melts

Based on thermodynamic calculations and analysis of the solid phase formation from multicomponent III-V melts, it was predicted that quaternary melts could produce binary, ternary or quaternary compounds depending on the melt temperature and the melt composition [38, 39]. Using $Ga_{1-x}In_xAs_ySb_{1-y}$ melts, the growth of $Ga_{1-x}In_xAs$ crystals of limited compositions and $Ga_{1-x}In_xAs$ thin films has been demonstrated [38, 40–43]. The usage of quaternary melt enables the growth of ternary crystals at lower temperatures compared to that possible using pseudobinary phase diagrams (such as GaP–InP, GaAs–InAs, etc.) [41, 42, 44]. Moreover, for pseudobinary melts, there is a single melt composition and growth temperature corresponding to any solid composition. On the other hand, the quaternary melts have two degrees of freedom. It is possible to grow a specific alloy composition at various temperatures by choosing different melt compositions. For example, $Ga_{0.8}In_{0.2}As$ can be grown at any temperature in the range of 900 °C and 1100 °C using different $Ga_{1-x}In_xAs_ySb_{1-y}$ melt compositions. This extra degree of freedom requires extensive and careful understanding of the variation in the crystal composition during the growth at various growth temperatures. There is a wide range of temperature (for each alloy system) for which phase diagrams need to be generated (such as in references [45–47]) and experimentally verified. This could take several years since thermodynamic phase diagram calculations using a Gibbs free energy minimization software requires extensive and reliable materials database that are currently unavailable. Hence, significant fundamental experimental research efforts are necessary before this concept can be put into practice for large-scale crystal growth. In the absence of such information, this chapter presents a systematic and unified approach towards the practical development of bulk crystal-growth process of ternary III-V semiconductors from quaternary melts.

9.3 Advantages of Quaternary Melts

Quaternary melts provide numerous attractive features during crystal growth, especially for high melting point and high vapor pressure P- and As-based compounds. Bulk growth of ternary crystals containing Al–In–Ga–As–P is very difficult due to the high vapor pressures of P and As at the high growth temperatures dictated by the pseudobinary phase diagrams such as AlP–GaP, GaP–GaAs, GaAs–InAs, etc. [26, 48]. Special crystal-growth configurations are necessary for the synthesis and growth of these compounds [48–54]. For example, a stainless=steel=lined pressure vessel designed for 150–170 atmospheres and continuously operating at 60–70 atmospheres is necessary for InP growth. While binary crystals such as GaP and InP are routinely grown in the industry with established processes, ternary and quaternary crystals such as GaInP, GaAsP, etc. are difficult to

grow. This is due to the slow growth rates necessary for the ternary crystals and the need for melt mixing and replenishment during growth [28]. These requirements would make the crystal-growth equipments extremely complex and difficult to monitor during operation. Hence, lowering the growth temperature is desirable such that the vapor pressures of P and As can be easily handled.

Traditionally, low-temperature growth of ternary and quaternary compounds from Ga- and In-rich solutions have been implemented during liquid phase epitaxial (LPE) growth of thin films. This approach has been used for growing bulk crystals from low-temperature solutions [55]. However, there are several experimental difficulties such as: (i) very low solubility of compounds in the elemental solutions making solute feeding difficult to implement during ternary growth; (ii) extremely low growth rates necessary to obtain metallic inclusion-free crystals; (iii) oxide scum on the Ga and In solutions that can impede seeding during bulk crystal growth; (iv) inability to provide effective melt encapsulation during growth; and (v) sticking of metallic solutions to the crucible walls and crystals making it extremely difficult to extract Bridgman-grown crystals. Figure 9.1 shows a $Ga_{1-x}In_xP$ crystal grown from an indium-rich Ga–In–P solution. The crystal is embedded inside the left-over indium-rich solution. The indium stuck to the silica crucible can be seen. Such a crystal can be extracted only by chemical etching of the indium in nitric acid. This process is quite tedious and often damages the crystals to some extent. In addition, metallic inclusions at the surface of the crystals damage the saw blades and wires during wafer slicing.

The growth temperatures for ternary alloys from quaternary melts are higher compared to the ternary solutions (such as Ga–In–As), but significantly lower compared to the pseudobinary melts. There are several technical advantages in using the quaternary melt: (i) since the quaternary melts can be prepared from presynthesized binary compounds, it enables the usage of liquid encapsulations during the growth [56, 57]; (ii) sticking of the melt to the crucible and crystal is

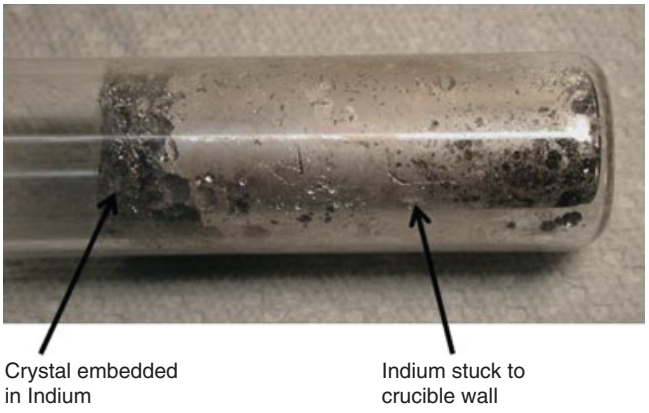

Figure 9.1 A $Ga_{1-x}In_xP$ crystal embedded inside the indium-rich growth solution. The indium stuck to the crucible wall can be seen.

not an issue; (iii) the solubility of binary compounds in significantly higher in quaternary melts, making solute feeding possible during ternary growth; (iv) crystal growth rates are significantly higher compared to solution growth; (v) seeding during a typical Bridgman growth becomes possible. In addition, due to lower growth temperature, the vapor pressure control for P- and As-based compounds becomes manageable. In fact, all crystals grown during this study were contained in sealed crucibles in furnaces without any external gas pressure or high-pressure vessel. Lower growth temperatures would also reduce native defects leading to improvements in the electrical and optical properties of the grown alloys. The opportunity to use a variety of melt compositions at different temperatures for the same crystal composition is extremely helpful for tuning the electrical and optical properties of the material. It must be mentioned that the ternary crystals grown from quaternary melts do contain residual amounts of the fourth element that can provide strain relaxation in the crystal and alloy hardening, thus improving the crystalline quality of the material. The effects of residual additive on the lattice parameter and the bandgap of ternary crystals are negligible.

Another interesting feature that has been observed during the growth of GaInAs thick layers on GaAs from GaInAsSb quaternary melt is the presence of a self-compositionally graded transition layer between a binary seed and the ternary crystal [41, 42]. The thickness of this graded region can be in the range of 10–100 μm depending on melt composition. Beyond the graded region, thick layers (~100 μm) of extremely uniform ternary compositions have been obtained. Typically, during solution growth (LPE), the composition of the layers changes within a few μm from the initial growth interface. This process can be used to grow ternary seeds of a desired composition starting from a binary seed and quaternary melt by the simple Bridgman or gradient freezing method without the need for any sophisticated grading procedures.

9.4 Synthesis and Bulk Crystal Growth

In this section, we will discuss the growth temperatures and quaternary melt compositions that are necessary for the growth of various ternary alloy systems.

The synthesis and growth experiments were carried out in sealed crucibles in the experimental configuration shown in Figure 9.2. Presynthesized binaries of InSb, GaSb, AlSb, InAs, GaAs, InP and GaP were used for our experiments. Due to their unavailability, AlAs and AlP were not used as starting materials. Silica (quartz) crucibles were used for the non-Al-based compounds. For Al-based compounds, alumina crucibles (long tubes closed on one end) were used to hold the melt. The alumina crucibles were placed inside silica crucibles and sealed under vacuum.

In general, the quaternary melts can be prepared using various combinations of binary constituents. For example, the $Ga_{1-x}In_xAs_{1-y}Sb_y$ quaternary melt can be synthesized from the four constituent binaries (GaAs, GaSb, InAs and InSb) such

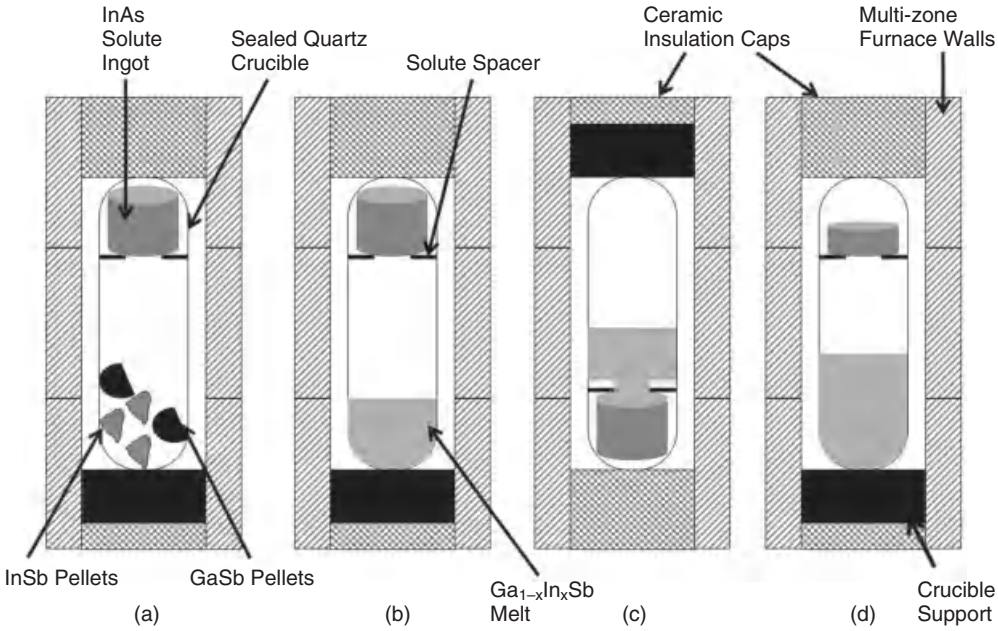

Figure 9.2 Schematic diagram of the quaternary melt preparation and ternary crystal growth from quaternary melt using vertical gradient freeze (VGF) method inside a sealed crucibles. The four stages are depicted for the growth of $Ga_{1-x}In_xAs$ crystal from $Ga_{1-x}In_xAs_{1-y}Sb_y$ melt: (a) at the beginning of the experiment, (b) after $Ga_{1-x}In_xSb$ solvent has been prepared, (c) during dissolution of InAs by $Ga_{1-x}In_xSb$ solvent to form a quaternary $Ga_{1-x}In_xAs_{1-y}Sb_y$ melt, and (d) during the directional solidification of the crystal.

as by: (i) melting GaSb and InAs together, (ii) dissolving GaAs in InSb, (iii) dissolving InAs in a GaSb–InSb melt, (iv) dissolving GaAs and InAs in InSb or GaSb. The final melt composition depends on the sequence in which the dissolution process is implemented using different binaries. For example, if the InAs is dissolved in InSb first, the solubility of GaSb or GaAs is lower than if the latter were dissolved in InSb first. However, if the binaries are mixed in exact quantities and heated to the liquidus temperature of quaternary alloy composition, the sequence of dissolution does not matter. For example, to prepare a $Ga_{0.1}In_{0.9}As_{0.5}Sb_{0.5}$ melt, one can either mix (i) 10 mole% GaAs, 50 mole% InSb and 40 mole% InAs or (ii) 10 mole% GaSb, 40 mole% InSb and 50 mole% InAs beyond its liquidus temperature. Due to inadequate experimental data for the liquidus temperature and composition for quaternary systems, it is important to design systematic pathways for the crystal-growth process as described below for various alloy systems.

To quantitatively understand the role of quaternary melt composition on the ternary crystal composition, we used a *two-step* melt-synthesis process in our experiments. In the first step, a pseudobinary melt comprising of at least one Sb-based binary (InSb, GaSb or AlSb) is prepared. Literature data for pseudobinary

phase diagrams are reasonably accurate and can be used for this step [26, 48]. Examples of synthesized melts would be $(GaSb)_{1-x} - (InSb)_x$, $(AlSb)_{1-x} - (InSb)_x$, $(InAs)_{1-y} - (InSb)_y$, etc. In the second step, the pseudobinary melt is used as a solvent to dissolve another high melting point binary compound to form a quaternary melt at an elevated temperature. The solute dissolution temperature (the same as the crystal-growth temperature in this study) was selected based on two considerations. First, there is a specific temperature for each alloy system beyond which the ternary phases are formed from the quaternary melt. Secondly, it is important to have substantial dissolution of the binaries at the growth temperature that will enable the precipitation of ternary alloys from the melt.

The 4 steps used in the melt synthesis and crystal growth are schematically shown in Figures 9.2a–d. An example of GaInAs crystal growth from GaInAsSb melt has been shown. After placing the binary compounds as shown in Figure 9.2a, the crucibles were evacuated to a vacuum level of approximately 10^{-6} Torr and sealed. The crucible was then placed inside a multizone furnace and heated to melt the Sb-based compounds first (the solvent) as depicted in Figure 9.2b. The furnace was further heated to a specific solute dissolution temperature and the solvent was brought into contact with the solute by tilting the furnace–crucible assembly as shown in Figure 9.2c. As the solvent dissolved the solute, a quaternary melt was prepared by rocking the melt back and forth across the crucible for an extended period of time (30 min to 2 h depending on melt volume). This ensured the homogenization of the quaternary melt and an equilibrium melt after complete dissolution of the solute in the solvent up to the solubility limit was obtained. During the melt-preparation process, the zones of the furnace were kept at the same temperature to avoid precipitation of the dissolved solute at other (cooler) locations of the crucible. It should be mentioned that for experiments involving Al-based compounds in alumina crucibles (open at one end), the furnace and crucible assembly in Figure 9.2c was only titled partially to bring the solvent and solute in contact. After the solute-dissolution step, the furnace was kept in a vertical position to separate the quaternary melt from the solute (Figure 9.2d). The temperature of quaternary melt was raised further by 10 °C to dissolve any undesirable precipitates present in the melt. After stabilizing the melt temperature for 2–3 h, crystal growth was initiated by directional cooling. Gradient freezing was implemented by slowly cooling the furnace zones at the bottom of the crucible. Directional solidification was carried out by cooling the entire melt. A typical cooling rate was in the range of 1–2 °C/h for the duration of the crystal growth followed by fast cooling of the grown crystal at a rate of 50 °C/h. In some experiments, a single-zone furnace was used during the synthesis and crystal growth using the vertical Bridgman configuration. In this case, the crucible was initially held in the uniform zone of the furnace during the dissolution and melt homogenization step. Thereafter, the crucible was slowly translated through the temperature gradient of the furnace to implement directional solidification. Typical growth rates were in the range of 0.1–0.5 mm/h. After the crystal growth, the first-to-freeze sections of the crystals were analyzed by preparing wafers. Compositional analyzes were carried out using electron microprobe X-ray analysis (EPMA). The

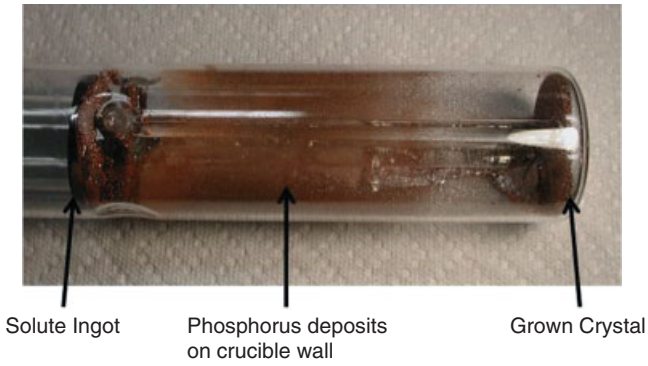

Figure 9.3 A sealed silica crucible used for $Ga_{1-x}In_xP$ growth from $Ga_{1-x}In_xP_{1-y}Sb_y$ melt.

bandgap of the grown wafers were evaluated by optical transmission or absorption measurements.

Due to the sticking of the melt droplets to the solute during the synthesis step, it is hard to accurately estimate the dissolution amounts of the solute in the solvent. Hence, the melt compositions are only approximately known. In this chapter, the exact composition of the solvent, the solute species and the experimental solute dissolution temperature have been presented along with the alloy composition in the first-to-freeze portion of the crystal (referred to as *crystal composition*) in Tables 9.1–9.10. These data makes it easy to further develop solute feeding strategies that are necessary for growing homogeneous ternary crystals. Figure 9.3 shows a typical sealed silica crucible used during the growth of $Ga_{1-x}In_xP$ from $Ga_{1-x}In_xP_{1-y}Sb_y$ melt. The solute ingot can be seen held at one end of the crucible with the grown crystal at the other end. Red phosphorus deposits can be seen on the walls of the crucible.

Based on the Al–In–Ga–P–As–Sb system, there are 18 possible ternary alloys (with $0 < x < 1$; $0 < y < 1$): $Al_{1-x}Ga_xP$, $Al_{1-x}In_xP$, $Al_{1-x}Ga_xAs$, $Al_{1-x}In_xAs$, $Al_{1-x}Ga_xSb$, $Al_{1-x}In_xSb$, $AlP_{1-y}As_y$, $AlP_{1-y}Sb_y$, $AlAs_{1-y}Sb_y$, $Ga_{1-x}In_xP$, $Ga_{1-x}In_xAs$, $Ga_{1-x}In_xSb$, $GaP_{1-y}As_y$, $GaAs_{1-y}Sb_y$, $GaP_{1-y}Sb_y$, $InP_{1-y}As_y$, $InAs_{1-y}Sb_y$, $InP_{1-y}Sb_y$. The quaternary melt systems containing Sb-based binary compounds that can be used for growing the above ternary alloys are (with $0 < x < 1$; $0 < y < 1$): $Ga_{1-x}In_xAs_{1-y}Sb_y$, $Ga_{1-x}In_xP_{1-y}Sb_y$, $Al_{1-x}Ga_xAs_{1-y}Sb_y$, $Al_{1-x}In_xAs_{1-y}Sb_y$, $Al_{1-x}In_xP_{1-y}Sb_y$, $Al_{1-x}Ga_xP_{1-y}Sb_y$, $Al_{1-x-y}Ga_xIn_ySb$, $InP_{1-x-y}As_xSb_y$, $GaP_{1-x-y}As_xSb_y$ and $AlP_{1-x-y}As_xSb_y$. It must be mentioned that the crystal compositions are not strictly ternary. For example, residual Sb content does show up in the $Ga_{1-x}In_xAs$ crystals grown from $Ga_{1-x}In_xAs_{1-y}Sb_y$ melts. But the level of Sb is less than 0.5 mole% and for all practical purposes, there is no effect of the residual Sb on the bandgap of the material. Isoelectronic dopants such as Sb can have effects on the electrical and optical properties of the semiconductors. However, this has not been studied yet in these crystals.

Of the 18 ternary alloys listed above, the ones containing both In and Sb, namely, $Al_{1-x}In_xSb$, $Ga_{1-x}In_xSb$, $InAs_{1-y}Sb_y$, $InP_{1-y}Sb_y$ are the lowest melting point phases

and hence do not preferentially precipitate from quaternary melts. For example, during the crystal growth from $Ga_{1-x}In_xAs_{1-y}Sb_y$ melt, the two higher melting points phases, $Ga_{1-x}In_xAs$ and $GaAs_{1-y}Sb_y$ preferentially precipitate out and form solids. The remaining phases $Ga_{1-x}In_xSb$ and $InAs_{1-y}Sb_y$ are formed only when either the melt has been completed depleted of As or Ga, respectively. The 4 alloy systems containing both In and Sb can be suitably grown using the pseudobinary melts: $(AlSb)_{1-x}-(InSb)_x$, $(GaSb)_{1-x}-(InSb)_x$, $(InAs)_{1-y}-(InSb)_y$ and $(InP)_{1-y}-(InSb)_y$. The effects of quaternary melt chemistries on the growth properties of these 4 alloys were not investigated in this study. In general, the presence of the 4th element in the melt (as an additive) can have an influence on the segregation coefficient of the other 3 elements, dopant incorporation properties in the solid (like defect and impurity compensation), lattice stress, etc. The remainder of this chapter will focus on 14 ternary alloy systems. The methodologies for solvent preparation, solute dissolution and directional solidification were the same for all the alloy systems (Figure 9.2). Henceforth, the role of solvent compositions, solute species and solute dissolution temperature on the crystal composition only will be discussed. The following subsections have been organized according to the quaternary melt systems used during growth.

9.4.1 Growth from $Ga_{1-x}In_xAs_{1-y}Sb_y$ Melt

There are three pseudobinary systems that were used as the solvent for preparing the quaternary $Ga_{1-x}In_xAs_{1-y}Sb_y$ melt (see Table 9.1). In the first case, $(GaSb)_{1-x}$ – $(InSb)_x$ melt was used as the solvent and InAs or GaAs as the solute. In the second case, $(InAs)_{1-y}$ – $(InSb)_y$ melt was used as the solvent and GaAs or GaSb as the solute. GaSb can be used as the solute only below 710 °C (melting point of GaSb). However, below 700 °C, no ternary compositions precipitated from the melt. The grown crystals exhibited quaternary $Ga_{1-x}In_xAs_{1-y}Sb_y$ compositions. In the third case, $(GaAs)_{1-y}$ – $(GaSb)_y$ melt was used as the solvent and InAs as the solute. The ternary alloys that can be successfully grown from this system are $Ga_{1-x}In_xAs$ and $GaAs_{1-y}Sb_y$.

9.4.1.1 Growth of $Ga_{1-x}In_xAs$

Using pseudobinary $(GaSb)_{1-x}$ – $(InSb)_x$ melt as the solvent at 900 °C and InAs or GaAs as the solute, a wide composition range of $Ga_{1-x}In_xAs$ solids can be obtained. Table 9.1 shows the first-to-freeze $Ga_{1-x}In_xAs$ compositions (referred to as *crystal composition*) as a function of solvent composition. The dissolution temperature had to be kept below the melting point of InAs (942 °C) to avoid melting of the solute and uncontrolled precipitation in the melt. When using GaAs as a solute, one can use higher dissolution/growth temperatures since GaAs melts at 1238 °C. However, in this study, the solute dissolution temperature was held constant for all experiments for the sake of comparison. For growth temperatures below 850 °C, the incorporation of Sb in the crystal increases with decreasing growth temperature, resulting in quaternary solid compositions. Due to this, the crystal-growth temperature for this study was kept above 850 °C. It is interesting to note from Table

Table 9.1 Solvent composition, solute species and solute dissolution temperature for $Ga_{1-x}In_xAs$ and $GaAs_{1-y}Sb_y$ growth from $Ga_{1-x}In_xAs_{1-y}Sb_y$ melt.

No.	Solvent composition	Solute species	Solute dissolution temperature (°C)	Crystal composition
1	$Ga_{0.1}In_{0.9}Sb$	InAs	900	$Ga_{0.17}In_{0.83}As$
2	$Ga_{0.2}In_{0.8}Sb$	InAs	900	$Ga_{0.42}In_{0.58}As$
3	$Ga_{0.3}In_{0.7}Sb$	InAs	900	$Ga_{0.84}In_{0.16}As$
4	$Ga_{0.5}In_{0.5}Sb$	InAs	900	$Ga_{0.96}In_{0.04}As$
5	$Ga_{0.2}In_{0.8}Sb$	GaAs	900	$Ga_{0.95}In_{0.05}As$
6	$Ga_{0.1}In_{0.9}Sb$	GaAs	900	$Ga_{0.93}In_{0.07}As$
7	$InAs_{0.9}Sb_{0.1}$	GaAs	950	$Ga_{0.32}In_{0.68}As$
8	$InAs_{0.8}Sb_{0.2}$	GaAs	950	$Ga_{0.48}In_{0.52}As$
9	$InAs_{0.5}Sb_{0.5}$	GaAs	950	$Ga_{0.76}In_{0.24}As$
10	$InAs_{0.1}Sb_{0.9}$	GaAs	950	$Ga_{0.88}In_{0.12}As$
11	$GaAs_{0.1}Sb_{0.9}$	InAs	900	$Ga_{0.99}In_{0.01}As$
12	$GaAs_{0.05}Sb_{0.95}$	InAs	900	$Ga_{0.98}In_{0.02}As$
13	$Ga_{0.4}In_{0.6}Sb$	InAs	730	$GaAs_{0.95}Sb_{0.05}$
14	$Ga_{0.7}In_{0.3}Sb$	InAs	730	$GaAs_{0.82}Sb_{0.18}$
15	$Ga_{0.8}In_{0.2}Sb$	InAs	730	$GaAs_{0.19}Sb_{0.81}$
16	$Ga_{0.9}In_{0.1}Sb$	InAs	730	$GaAs_{0.05}Sb_{0.95}$

9.1 that there is a significant difference in the solidified alloy composition depending on the choice of solute species (InAs or GaAs). For example, comparing experiments 1 and 6 or 2 and 5, it is clearly seen that though the solvent compositions were kept the same, the solute used for dissolution led to significantly different first-to-freeze solid compositions. Certainly the choice of InAs as a solute allows a better control on the solid compositions. Another interesting point to note by analyzing experiments 1–4 is that a wide composition range of $Ga_{1-x}In_xAs$ can be grown with solvent composition $x < 0.5$ in $Ga_{1-x}In_xSb$. Figure 9.4 shows a large-grain polycrystalline $Ga_{1-x}In_xAs$ grown from $Ga_{1-x}In_xAs_{1-y}Sb_y$ melt. No cracks or inclusions can be seen in the wafer.

Using pseudobinary $(InAs)_{1-y} - (InSb)_y$ melt as solvent at 950 °C, which is above the melting points of both binaries and GaAs as the solute, a wide range of $Ga_{1-x}In_xAs$ compositions can be grown (Table 9.1). Compared to the $Ga_{1-x}In_xSb$ solvent discussed above, the $InAs_{1-y}Sb_y$ solvent has a wider composition range for controlling the $Ga_{1-x}In_xAs$ solid compositions. Using pseudobinary $(GaAs)_{1-y} - (GaSb)_y$ melt as solvent at 900 °C (below the melting point of InAs) and InAs as a solute, the first-to-freeze compositions obtained is close to GaAs, irrespective of solvent composition (see Table 9.1). For the sake of comparison, the melt growth of $Ga_{1-x}In_xAs$ using pseudobinary GaAs–InAs mixture requires growth temperatures between 942 °C and 1238 °C, corresponding to the melting points of InAs and GaAs, respectively. In this study, growth across the entire GaAs–InAs composition range can be accomplished between 900 and 950 °C. Figure 9.5 shows the room-temperature transmission spectra of $Ga_{1-x}In_xAs$ polycrystalline substrates grown in different experiments described above. High optical transmission can

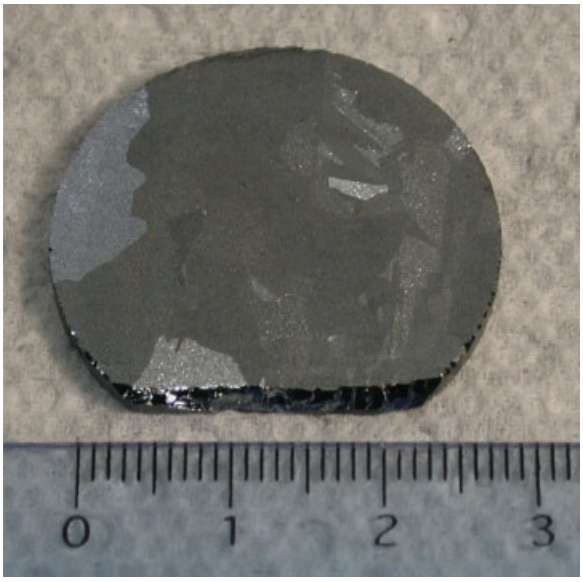

Figure 9.4 A polycrystalline $Ga_{1-x}In_xAs$ wafer extracted from the first-to-freeze section of an ingot grown from $Ga_{1-x}In_xAs_{1-y}Sb_y$ melt.

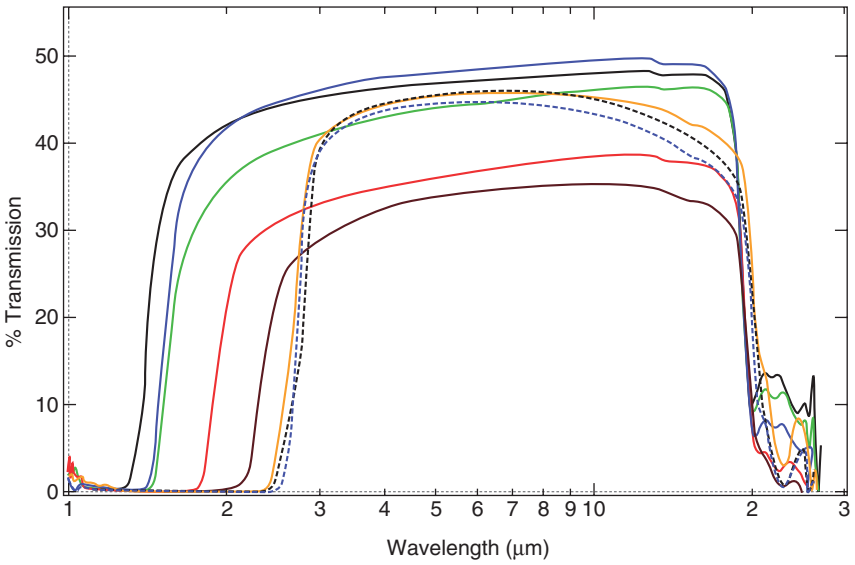

Figure 9.5 Room-temperature transmission spectra of $Ga_{1-x}In_xAs$ polycrystalline substrates grown in different experiments. The cut-off wavelengths are in the range of 1.3–2.6 μm, demonstrating the tunability of the alloy bandgap.

be seen for all samples. The bandgaps of the samples shown in Figure 9.5 are in the range of 0.47–0.95 eV.

9.4.1.2 Growth of $GaAs_{1-y}Sb_y$

For this alloy system, there exists a solid-solid miscibility gap for compositions in the range of $0.2 < y < 0.8$. These compositions are not stable and crystals grown exhibit a multiphase nature with poor crystalline and optical quality. For the compositions outside the above range, ternary $GaAs_{1-y}Sb_y$ can be grown only using $(GaSb)_{1-x} - (InSb)_x$ as the solvent and GaAs or InAs as the solute (see Table 9.1). The effect of GaAs or InAs (as a solute) on the grown compositions was not observed. This is primarily due to the very low solubility of both GaAs and InAs in the $Ga_{1-x}In_xSb$ melt at temperatures below 750 °C where the stable $GaAs_{1-y}Sb_y$ compositions form. Table 9.1 shows the first-to-freeze $GaAs_{1-y}Sb_y$ compositions as a function of solvent composition at 730 °C. It is interesting to note that $GaAs_{1-y}Sb_y$ alloy was obtained only for solvent compositions $x < 0.6$. For $x > 0.6$, either GaAs or quaternary $Ga_{1-x}In_xAs_{1-y}Sb_y$ alloy was obtained in the first-to-freeze solidified section of the crystal at this growth temperature.

9.4.2 Growth from $Ga_{1-x}In_xP_{1-y}Sb_y$ Melt

This quaternary melt system can be prepared using the four constituent binaries (GaP, GaSb, InP and InSb) similar to the manner described above for $Ga_{1-x}In_xAs_{1-y}Sb_y$. The only ternary alloy that can be successfully grown from this system is $Ga_{1-x}In_xP$, as presented below. The other system $GaP_{1-y}Sb_y$ has a severe miscibility gap and leads to two-phase regions with GaP embedded in a matrix of GaSb, $Ga_{1-x}In_xSb$ and $InP_{1-y}Sb_y$.

9.4.2.1 Growth of $Ga_{1-x}In_xP$

There are three pseudobinary systems that were used as the solvent for preparing the quaternary $Ga_{1-x}In_xP_{1-y}Sb_y$ melt (see Table 9.2). In the first case, $(GaSb)_{1-x} - (InSb)_x$ melt was used as the solvent and InP or GaP as the solute. In the second case, $(InP)_{1-y} - (InSb)_y$ melt was used as the solvent and GaP as the solute. In the third case, $(GaP)_{1-y} - (GaSb)_y$ melt was used as the solvent and InP as the solute. For all the experiments reported here, the solute dissolution temperature was kept at 1000 °C for three reasons: (i) for temperatures below 1000 °C, the solubility of InP or GaP in the above three solvents is poor; (ii) dissolution using InP solute can be implemented only below the melting point of InP (1060 °C); and (iii) beyond 1000 °C, the high vapor pressure of phosphorus becomes a challenge during melt growth in sealed crucibles, especially with larger melt volumes.

Using pseudobinary $(GaSb)_{1-x} - (InSb)_x$ melt as a solvent and InP or GaP as solute, ternary $Ga_{1-x}In_xP$ alloy spanning a wide composition range can be obtained (see Table 9.2). Comparing experiments 1 and 5 or 2 and 6, it is interesting to note the significant differences in crystal compositions by using GaP or InP as the solute. By using GaP as the solute, only compositions closer to GaP can be

Table 9.2 Solvent composition, solute species and solute dissolution temperature for $Ga_{1-x}In_xP$ growth from $Ga_{1-x}In_xP_{1-y}Sb_y$ melt.

No.	Solvent composition	Solute species	Solute dissolution temperature (°C)	Crystal composition
1	$Ga_{0.05}In_{0.95}Sb$	InP	1000	$Ga_{0.12}In_{0.88}P$
2	$Ga_{0.1}In_{0.9}Sb$	InP	1000	$Ga_{0.45}In_{0.55}P$
3	$Ga_{0.15}In_{0.85}Sb$	InP	1000	$Ga_{0.86}In_{0.14}P$
4	$Ga_{0.2}In_{0.8}Sb$	InP	1000	$Ga_{0.96}In_{0.04}P$
5	$Ga_{0.05}In_{0.95}Sb$	GaP	1000	$Ga_{0.94}In_{0.06}P$
6	$Ga_{0.1}In_{0.9}Sb$	GaP	1000	$Ga_{0.98}In_{0.02}P$
7	$InP_{0.7}Sb_{0.3}$	GaP	1000	$Ga_{0.11}In_{0.89}P$
8	$InP_{0.6}Sb_{0.4}$	GaP	1000	$Ga_{0.36}In_{0.64}P$
9	$InP_{0.4}Sb_{0.6}$	GaP	1000	$Ga_{0.79}In_{0.21}P$
10	$InP_{0.2}Sb_{0.8}$	GaP	1000	$Ga_{0.92}In_{0.08}P$
11	$GaP_{0.05}Sb_{0.95}$	InP	1000	GaP
12	$GaP_{0.02}Sb_{0.98}$	InP	1000	GaP

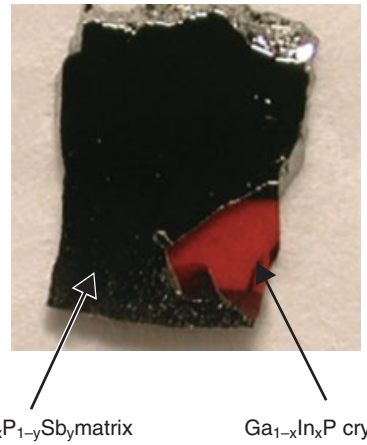

Figure 9.6 A polycrystalline $Ga_{1-x}In_xP$ crystal (red color) embedded inside a $Ga_{1-x}In_xP_{1-y}Sb_y$ solidified mass. The starting melt was prepared using InP, InSb and GaSb as the binary compounds.

obtained. Another interesting observation is the need for InSb-rich content of the solvent (experiments 1–4 with InP solute) to obtain a wide range of $Ga_{1-x}In_xP$ solid compositions. Figure 9.6 shows a polycrystalline $Ga_{1-x}In_xP$ ingot (red region) embedded inside a $Ga_{1-x}In_xP_{1-y}Sb_y$ solidified mass. This crystal was grown using $Ga_{1-x}In_xSb$ as the solvent and InP as the solute. Figure 9.7 shows the room-temperature absorption spectrum (curve c) of a $Ga_{1-x}In_xP$ polycrystalline substrate extracted from the grown ingot. For comparison, the absorption spectrum of pure GaP (curve a) is also shown in Figure 9.7.

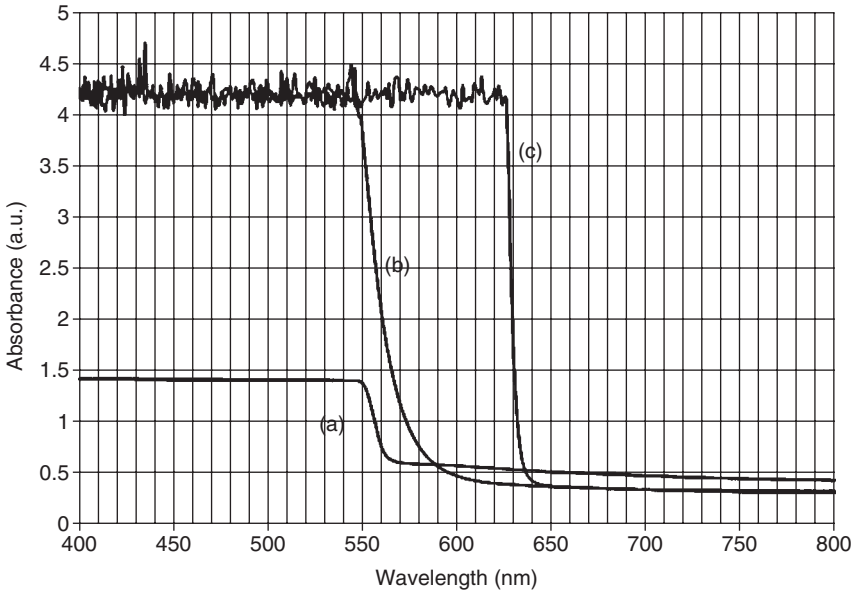

Figure 9.7 Room-temperature absorption spectra of (a) GaP, (b) $GaP_{1-y}As_y$ and (c) $Ga_{1-x}In_xP$ polycrystalline substrates grown in different experiments.

Using pseudobinary $(InP)_{1-y} - (InSb)_y$ melt as solvent and GaP as solute, ternary $Ga_{1-x}In_xP$ alloy compositions spanning a wide range can be obtained (Table 9.2). Compared to the $Ga_{1-x}In_xSb$ solvent discussed above, the $InP_{1-y}Sb_y$ solvent has a wider composition range for controlling the $Ga_{1-x}In_xP$ solid compositions. Using pseudobinary $(GaP)_{1-y} - (GaSb)_y$ melt as solvent and InP as solute, the first-to-freeze compositions obtained is close to GaP, irrespective of solvent composition (as shown in Table 9.2. For the sake of comparison, melt growth of $Ga_{1-x}In_xP$ using pseudobinary GaP–InP mixture requires growth temperatures between 1060 °C and 1480 °C, corresponding to the melting points of InP and GaP, respectively. In this study, $Ga_{1-x}In_xP$ growth across a wide composition range can be accomplished at 1000 °C.

9.4.3
Growth from $Al_{1-x}Ga_xAs_{1-y}Sb_y$ Melt

This quaternary melt system can be prepared using AlSb, GaAs and GaSb binary compounds. The ternary alloys that can be successfully grown from this system are $Al_{1-x}Ga_xAs$ and $AlAs_{1-y}Sb_y$. A limited number of studies has been performed using this quaternary melt system.

9.4.3.1 Growth of $Al_{1-x}Ga_xAs$

The quaternary $Al_{1-x}Ga_xAs_{1-y}Sb_y$ melt was prepared using the pseudobinary $(AlSb)_{1-x} - (GaSb)_x$ or $(GaAs)_{1-y} - (GaSb)_y$ as the solvent and GaAs or AlSb as the

Table 9.3 Solvent composition, solute species and solute dissolution temperature for $Al_{1-x}Ga_xAs$ and $AlAs_{1-y}Sb_y$ growth from $Al_{1-x}Ga_xAs_{1-y}Sb_y$ melt.

No.	Solvent composition	Solute species	Solute dissolution temperature (°C)	Crystal composition
1	$Al_{0.05}Ga_{0.95}Sb$	GaAs	1025	$Al_{0.85}Ga_{0.15}As$
2	$Al_{0.1}Ga_{0.9}Sb$	GaAs	1025	$Al_{0.95}Ga_{0.05}As$
3	$GaAs_{0.15}Sb_{0.85}$	AlSb	1025	$Al_{0.12}Ga_{0.88}As$
4	$GaAs_{0.05}Sb_{0.95}$	AlSb	1025	$Al_{0.87}Ga_{0.13}As$
5	$Al_{0.3}Ga_{0.7}Sb$	GaAs	1025	$AlAs_{0.86}Sb_{0.14}$
6	$Al_{0.6}Ga_{0.4}Sb$	GaAs	1025	$AlAs_{0.36}Sb_{0.64}$

solute, respectively (see Table 9.3). The solute dissolution temperature (1025 °C) was chosen to be below the melting point of AlSb (1065 °C). The solubility of GaAs and AlSb in these melts at 1025 °C is quite poor. Using $Al_{1-x}Ga_xSb$ as the solvent, only AlAs-rich compositions in $Al_{1-x}Ga_xAs$ solid can be obtained (see experiments 1 and 2). On the other hand, using $GaAs_{1-y}Sb_y$ solvent, a wide range of $Al_{1-x}Ga_xAs$ solid compositions is possible (experiments 3 and 4). For the sake of comparison, melt growth of $Al_{1-x}Ga_xAs$ using pseudobinary AlAs–GaAs mixture requires growth temperatures between 1238 °C and 1740 °C, corresponding to the melting points of GaAs and AlAs, respectively. In this limited study, growth across a wide composition range of this ternary compound appears feasible at 1025 °C. The first-to-freeze section of a typical polycrystalline $Al_{1-x}Ga_xAs$ ingot grown from $Al_{1-x}Ga_xAs_{1-y}Sb_y$ melt exhibited reddish-yellowish regions that are rich in AlAs.

9.4.3.2 Growth of $AlAs_{1-y}Sb_y$

For these experiments, the quaternary $Al_{1-x}Ga_xAs_{1-y}Sb_y$ melt was prepared using the pseudobinary $(AlSb)_{1-x} - (GaSb)_x$ as the solvent and GaAs as the solute (see Table 9.3). A wide range of ternary $AlAs_{1-y}Sb_y$ alloy compositions can be obtained for growth temperature of 1025 °C using this quaternary melt chemistry. For the sake of comparison, melt growth of $AlAs_{1-y}Sb_y$ using a pseudobinary AlAs–AlSb mixture would require growth temperatures in the range of 1065–1740 °C, corresponding to the melting points of AlSb and AlAs, respectively. Polycrystalline $AlAs_{1-y}Sb_y$ samples solidified from $Al_{1-x}Ga_xAs_{1-y}Sb_y$ melt tend to turn black when left in the laboratory environment or during substrate preparation using polishing slurries. Left to themselves, these wafers were found to disintegrate into a black powdery mass in a few months.

9.4.4 Growth from $Al_{1-x}In_xAs_{1-y}Sb_y$ Melt

This quaternary melt system was prepared using three binary compounds, AlSb, InAs and InSb. Two ternary alloys systems, $Al_{1-x}In_xAs$ and $AlAs_{1-y}Sb_y$ can be grown

Table 9.4 Solvent composition, solute species and solute dissolution temperature for $Al_{1-x}In_xAs$ and $AlAs_{1-y}Sb_y$ growth from $Al_{1-x}In_xAs_{1-y}Sb_y$ melt.

No.	Solvent composition	Solute species	Solute dissolution temperature (°C)	Crystal composition
1	$InAs_{0.95}Sb_{0.05}$	AlSb	1025	$Al_{0.45}In_{0.55}As$
2	$InAs_{0.9}Sb_{0.1}$	AlSb	1025	$Al_{0.68}In_{0.32}As$
3	$InAs_{0.5}Sb_{0.5}$	AlSb	1025	$Al_{0.81}In_{0.19}As$
4	$InAs_{0.2}Sb_{0.8}$	AlSb	1025	$Al_{0.92}In_{0.08}As$
5	$InAs_{0.05}Sb_{0.95}$	AlSb	1025	$AlAs_{0.96}Sb_{0.04}$
6	$InAs_{0.02}Sb_{0.98}$	AlSb	1025	$AlAs_{0.22}Sb_{0.78}$

from this melt. A limited number of studies has been performed using this quaternary melt system.

9.4.4.1 Growth of $Al_{1-x}In_xAs$

The quaternary $Al_{1-x}In_xAs_{1-y}Sb_y$ melt was prepared using the pseudobinary $(InAs)_{1-y} - (InSb)_y$ as the solvent and AlSb as the solute (see Table 9.4). A dissolution temperature of 1025 °C was chosen as in the previous set of experiments. At this temperature, very poor solubility of AlSb was seen. Nevertheless, as shown in Table 9.4, ternary $Al_{1-x}In_xAs$ alloy compositions spanning the composition range $0 < x < 0.5$ can be obtained using this quaternary melt chemistry. Comparing experiments 1–4 in Table 9.4, it is seen that the solvent composition needs to be altered significantly to obtain the above solid composition range. For the sake of comparison, melt growth of $Al_{1-x}In_xAs$ (for $0 < x < 0.5$) using pseudobinary AlAs–InAs mixture would require growth temperature in the range of 1100 and 1740 °C. As-grown polycrystalline $Al_{1-x}In_xAs$ thick substrate solidified from $Al_{1-x}In_xAs_{1-y}Sb_y$ melt shows yellowish regions with AlAs-rich compositions. These crystals were found to be relatively more stable than the $AlAs_{1-y}Sb_y$ ones.

9.4.4.2 Growth of $AlAs_{1-y}Sb_y$

Preliminary data on solvent composition for the growth of $AlAs_{1-y}Sb_y$ has been presented in Table 9.4. From initial experimental studies, it has been observed that the arsenic content in the melt needs to be controlled precisely. A wide range of $AlAs_{1-y}Sb_y$ compositions precipitated from the melt by slight variation in the solvent composition (see experiments 5 and 6 in Table 9.4).

9.4.5 Growth from $Al_{1-x}In_xP_{1-y}Sb_y$ Melt

This quaternary melt system was prepared using presynthesized AlSb, InP and InSb. The only ternary alloy that can be successfully grown from this melt is $Al_{1-x}In_xP$. The $AlP_{1-y}Sb_y$ has a severe miscibility gap and leads to two-phase regions with AlP embedded in a matrix of AlSb, $Al_{1-x}In_xSb$ and $InP_{1-y}Sb_y$.

Table 9.5 Solvent composition, solute species and solute dissolution temperature for $Al_{1-x}In_xP$ growth from $Al_{1-x}In_xP_{1-y}Sb_y$ melt.

No.	Solvent composition	Solute species	Solute dissolution temperature (°C)	Crystal composition
1	$Al_{0.05}In_{0.95}Sb$	InP	1000	AlP
2	$Al_{0.1}In_{0.9}Sb$	InP	1000	AlP
3	$InP_{0.5}Sb_{0.5}$	AlSb	1000	$Al_{0.15}In_{0.85}P$
4	$InP_{0.4}Sb_{0.6}$	AlSb	1000	$Al_{0.34}In_{0.66}P$
5	$InP_{0.2}Sb_{0.8}$	AlSb	1000	$Al_{0.88}In_{0.12}P$

9.4.5.1 Growth of $Al_{1-x}In_xP$

The quaternary $Al_{1-x}In_xP_{1-y}Sb_y$ melt was prepared using two methods. In the first method, the pseudobinary $(AlSb)_{1-x} - (InSb)_x$ was used as the solvent at 1000 °C and InP as the solute (see Table 9.5). However, irrespective of the solvent composition, precipitated crystallites of AlP only were obtained. For successful growth of $Al_{1-x}In_xP$ compositions, a second method was used to prepare the quaternary $Al_{1-x}In_xP_{1-y}Sb_y$ melt. In this case, the pseudobinary $(InP)_{1-y} - (InSb)_y$ was used as the solvent and AlSb as the solute (see Table 9.5). Ternary $Al_{1-x}In_xP$ alloy compositions spanning a wide composition range can be obtained using this quaternary melt chemistry (with $y > 0.5$). A solidified $Al_{1-x}In_xP$ polycrystalline mass appears as orange-red crystallites when grown from $Al_{1-x}In_xP_{1-y}Sb_y$ melt. For the sake of comparison, melt growth of $Al_{1-x}In_xP$ using pseudobinary AlP–InP mixture would require growth temperatures in the range of 1065 and beyond 2000 °C.

9.4.6 Growth from $Al_{1-x}Ga_xP_{1-y}Sb_y$ Melt

This quaternary melt system was prepared using presynthesized AlSb, GaP and GaSb. The only ternary alloy that can be successfully grown from this melt is $Al_{1-x}Ga_xP$. The $AlP_{1-y}Sb_y$ has a severe miscibility gap and leads to two-phase regions with AlP embedded in a matrix of AlSb, $Al_{1-x}Ga_xSb$ and $GaP_{1-y}Sb_y$.

9.4.6.1 Growth of $Al_{1-x}Ga_xP$

Due to the low solubility of GaP in GaSb around 1000 °C, it is preferable to use the pseudobinary $(AlSb)_{1-x} - (GaSb)_x$ as the solvent and GaP as the solute for the quaternary $Al_{1-x}Ga_xP_{1-y}Sb_y$ melt preparation (see Table 9.6). The solvent composition for $Al_{1-x}Ga_xP$ growth needs to be GaSb-rich. Ternary $Al_{1-x}Ga_xP$ alloy compositions in a wide range can be obtained for growth temperatures around 1000 °C using this quaternary melt chemistry. For the sake of comparison, melt growth of $Al_{1-x}Ga_xP$ using pseudobinary AlP–GaP mixture would require growth temperatures between 1480 and beyond 2000 °C, corresponding to the melting points of GaP and AlP, respectively. Figure 9.8 shows the first-to-freeze section of $Al_{1-x}Ga_xP$

Table 9.6 Solvent composition, solute species and solute dissolution temperature for $Al_{1-x}Ga_xP$ growth from $Al_{1-x}Ga_xP_{1-y}Sb_y$ melt.

No.	Solvent composition	Solute species	Solute dissolution temperature (°C)	Crystal composition
1	$Al_{0.05}Ga_{0.95}Sb$	GaP	1000	$Al_{0.22}Ga_{0.78}P$
2	$Al_{0.1}Ga_{0.9}Sb$	GaP	1000	$Al_{0.63}Ga_{0.37}P$
3	$Al_{0.15}Ga_{0.85}Sb$	GaP	1000	$Al_{0.93}Ga_{0.07}P$

Figure 9.8 The first-to-freeze section of $Al_{1-x}Ga_xP$ polycrystalline mass stuck to the bottom of a silica crucible grown from $Al_{1-x}Ga_xP_{1-y}Sb_y$ melt.

polycrystalline mass (orange-yellow crystallites) stuck to the bottom of a silica crucible grown from $Al_{1-x}Ga_xP_{1-y}Sb_y$ melt. Due to the high reactivity of AlSb with silica, these crystals should be grown in alumina crucibles. However, since the Al content in the solvent was low, silica crucibles was used in our initial experiments with limited success.

9.4.7
Growth from $Al_{1-x-y}Ga_xIn_ySb$ Melt

This quaternary melt system can be prepared using the three constituent binaries (AlSb, GaSb and InSb). Only limited studies have been conducted with this system due to its lower importance from the bulk crystal growth point of view. All three

Table 9.7 Solvent composition, solute species and solute dissolution temperature for $Al_{1-x}Ga_xSb$ growth from $Al_{1-x-y}Ga_xIn_ySb$ melt.

No.	Solvent composition	Solute species	Solute dissolution temperature (°C)	Crystal composition
1	$Al_{0.02}In_{0.98}Sb$	GaSb	675	$Al_{0.68}Ga_{0.32}Sb$
2	$Ga_{0.8}In_{0.2}Sb$	AlSb	750	$Al_{0.23}Ga_{0.77}Sb$
3	$Ga_{0.1}In_{0.9}Sb$	AlSb	750	$Al_{0.82}Ga_{0.18}Sb$

ternary systems $Al_{1-x}Ga_xSb$, $Ga_{1-x}In_xSb$ and $Al_{1-x}In_xSb$ can be easily grown from the pseudobinary melts $(AlSb)_{1-x} - (GaSb)_x$, $(GaSb)_{1-x} - (InSb)_x$, $(AlSb)_{1-x} - (InSb)_x$, respectively, without any vapor pressure issues. The only ternary system that can be grown from this quaternary melt is $Al_{1-x}Ga_xSb$.

9.4.7.1 Growth of $Al_{1-x}Ga_xSb$

The quaternary $Al_{1-x-y}Ga_xIn_ySb$ melt was prepared using two methods. In the first method, the pseudobinary $(AlSb)_{1-x} - (InSb)_x$ was used as the solvent and GaSb as the solute (see Table 9.7). The growth temperature in this case was kept below 700 °C to avoid melting of the GaSb solute. Due to the low solubility of AlSb in InSb at temperatures below 700 °C, this solvent is not preferred. In the second method, the pseudobinary $(GaSb)_{1-x} - (InSb)_x$ melt was used as the solvent and AlSb as the solute (see Table 9.7). Irrespective of the solvent used, the grown crystals exhibited $Al_{1-x}Ga_xSb$ compositions. It appears from limited studies that a wide range of $Al_{1-x}Ga_xSb$ compositions can be obtained at low growth temperatures around 750 °C using this quaternary melt chemistry. For the sake of comparison, melt growth of $Al_{1-x}Ga_xSb$ using pseudobinary AlSb–GaSb mixture would require growth temperatures between 710 and 1065 °C, corresponding to the melting points of GaSb and AlSb, respectively.

9.4.8 Growth from $InP_{1-x-y}As_xSb_y$ Melt

This quaternary melt system can be prepared using the three constituent binaries (InP, InAs and InSb). Preliminary studies have been conducted with this system. The only ternary system that can be grown from this quaternary melt is $InP_{1-y}As_y$.

9.4.8.1 Growth of $InP_{1-y}As_y$

The quaternary $InP_{1-x-y}As_xSb_y$ melt can be prepared by the pseudobinary $(InP)_{1-y} - (InSb)_y$ as the solvent and InAs as the solute. However, the solubility of InP in InSb is relatively poor compared to InAs in InSb. Hence, in our studies, we used the $(InAs)_{1-y} - (InSb)_y$ melt as the solvent and InP as the solute (see Table 9.8). It is possible to obtain $InP_{1-y}As_y$ crystals for a wide composition range using this melt at temperatures as low as 950 °C. For the sake of comparison, melt growth

Table 9.8 Solvent composition, solute species and solute dissolution temperature for $InP_{1-y}As_y$ growth from $InP_{1-x-y}As_xSb_y$ melt.

No.	Solvent composition	Solute species	Solute dissolution temperature (°C)	Crystal composition
1	$InAs_{0.9}Sb_{0.1}$	InP	950	$InP_{0.13}As_{0.87}$
2	$InAs_{0.5}Sb_{0.5}$	InP	950	$InP_{0.56}As_{0.44}$
3	$InAs_{0.1}Sb_{0.9}$	InP	950	$InP_{0.93}As_{0.07}$

Table 9.9 Solvent composition, solute species and solute dissolution temperature for $GaP_{1-y}As_y$ growth from $GaP_{1-x-y}As_xSb_y$ melt.

No.	Solvent composition	Solute species	Solute dissolution temperature (°C)	Crystal composition
1	$GaAs_{0.05}Sb_{0.95}$	GaP	1025	$GaP_{0.96}As_{0.04}$
2	$GaAs_{0.1}Sb_{0.9}$	GaP	1025	$GaP_{0.72}As_{0.28}$
3	$GaAs_{0.2}Sb_{0.8}$	GaP	1025	$GaP_{0.15}As_{0.85}$

of $InP_{1-y}As_y$ using pseudobinary InP–InAs mixture would require growth temperatures between 942 and 1062 °C, corresponding to the melting points of InAs and InP, respectively.

9.4.9
Growth from $GaP_{1-x-y}As_xSb_y$ Melt

This quaternary melt system can be prepared using the three constituent binaries (GaP, GaAs and GaSb). Limited studies have been conducted with this system. The ternary alloy that preferentially precipitates from this quaternary melt is $GaP_{1-y}As_y$.

9.4.9.1 Growth of $GaP_{1-y}As_y$

Due to the poor solubility of GaP in GaSb around 1000 °C, the quaternary $GaP_{1-x-y}As_ySb_y$ melt was prepared using the pseudobinary $(GaAs)_{1-y} - (GaSb)_y$ melt as the solvent and GaP as the solute (see Table 9.9). The grown crystals exhibited $GaP_{1-y}As_y$ compositions. It is possible to obtain ternary crystals with a wide composition range at growth temperatures as low as 1025 °C using this quaternary melt. For the sake of comparison, melt growth of $GaP_{1-y}As_y$ using pseudobinary GaP–GaAs mixture would require growth temperatures between 1238 and 1480 °C, corresponding to the melting points of GaAs and GaP, respectively. Figure 9.9 shows a section of a solidified $GaP_{1-y}As_y$ polycrystalline mass grown from $GaP_{1-x-y}As_xSb_y$ melt. Figure 9.7b shows the absorption spectrum of a sample

Figure 9.9 A section of a solidified $GaP_{1-\gamma}As_{\gamma}$ polycrystalline mass grown from $GaP_{1-x-\gamma}As_xSb_{\gamma}$ melt. Figure 9.7b shows the absorption spectrum of a sample extracted from this mass.

extracted from this mass. A sharp absorption edge is seen in the spectrum, clearly indicating the high optical quality of the grown sample.

9.4.10 Growth from $AlP_{1-x-\gamma}As_xSb_{\gamma}$ Melt

9.4.10.1 Growth of $AlP_{1-\gamma}As_{\gamma}$

In principle, this quaternary melt system can be prepared using the three constituent binaries (AlP, AlAs and AlSb). However, we experienced severe limitations during synthesis due to the absence of pure AlP and AlAs. Small crystallites of multiphase $AlAs_{1-\gamma}Sb_{\gamma}$ and $AlP_{1-\gamma}Sb_{\gamma}$ (from prior experiments) and AlSb were mixed to form the quaternary $AlP_{1-x-\gamma}As_{\gamma}Sb_{\gamma}$ melt at 1100 °C. For different experiments, the quantities of the two multiphase ternaries added to AlSb were varied (shown in absolute weight % in Table 9.10). Multiphase samples were obtained after the directional solidification. Analysis of the spatial composition of the sample revealed the formation of $AlP_{1-\gamma}As_{\gamma}$ randomly distributed in the matrix of AlSb, $AlAs_{1-\gamma}Sb_{\gamma}$ and $AlP_{1-\gamma}Sb_{\gamma}$. Table 9.10 shows the composition data for the random phases from these exploratory studies. An approximate correlation can be established in the final matrix composition with respect to quantities of the ternary species added to the melt. Solidified multiphase $AlP_{1-\gamma}As_{\gamma}/AlAs_{1-\gamma}Sb_{\gamma}/AlP_{1-\gamma}Sb_{\gamma}$

Table 9.10 Solvent composition, solute species and solute dissolution temperature for $AlP_{1-y}As_y$ multiphase growth from $AlP_{1-x-y}As_xSb_y$ melt.

No.	Solvent composition	Solute species (wt %)	Solute dissolution temperature (°C)	Multiphase compositions
1	AlSb	$AlP_{1-y}Sb_y$ (2) $AlAs_{1-y}Sb_y$ (1)	1100	$AlP_{0.66}As_{0.34}$ $AlAs_{0.2}Sb_{0.8}$ $AlP_{0.16}Sb_{0.84}$
2	AlSb	$AlP_{1-y}Sb_y$ (1) $AlAs_{1-y}Sb_y$ (1)	1100	$AlP_{0.2}As_{0.8}$ $AlAs_{0.63}Sb_{0.37}$ $AlP_{0.1}Sb_{0.9}$

polycrystalline mass grown from $AlP_{1-x-y}As_xSb_y$ melt exhibited randomly distributed regions of gray, orange and red crystallites.

9.5 Conclusion

The scope of technological applications using III-V bulk semiconductors is ever-increasing as and when high-quality substrates of different bandgaps are being made available. Currently, ternary polycrystalline substrates of low bandgap materials like GaInAs and GaInSb are available in small quantities for niche applications. The bottleneck in expanding this limited base of ternary substrates lies in the difficulties in redesigning the current crystal-growth infrastructure that exists for binary semiconductors. For ternary crystals, precise control of the melt composition and efficient melt mixing during growth is necessary. This poses significant difficulties during the growth of high vapor pressure and high melting point P- and As-based compounds. The combination of high temperatures and high pressures requires complex crystal-growth systems. Adding the melt mixing and melt replenishment features further add to the complexity of the design and operation of the crystal-growth systems. Lowering the growth temperature is certainly desirable to reduce this problem. This chapter presents a new fundamental approach for bulk ternary crystal growth from low-temperature quaternary antimonide-based melts. Intriguing observations of ternary alloy compositions precipitating out of quaternary melts have been made on a variety of alloy systems. While significant work is still needed for adopting this concept for large-scale bulk crystal growth, the current study demonstrates the feasibility of this crystal-growth process. The results presented here are based on exploratory studies on limited compositions in each alloy system. Nevertheless, this chapter provides a systematic approach towards developing large scale production of any specific alloy composition using Bridgman, gradient freeze or Czochralski techniques. The knowledge base generated using the melt preparation and crystal-growth processes described here is easy to translate to existing large-scale crystal-growth infrastructure. This would accelerate the development of different alloy composition crystals even in

the absence of precise phase diagrams. Issues such as continuous melt mixing, precise solute feeding, temperature controllability during and postgrowth phases are crucial for ternary crystal growth, as discussed in the literature. These topics were not discussed in detail here, but are absolutely necessary during crystal growth runs to obtain high-quality ternary crystals from quaternary melts. Of the 14 ternary alloy systems studied here, the $AlP_{1-y}Sb_y$ and $GaP_{1-y}Sb_y$ systems cannot be grown into a single ternary phase. AlP and GaP embedded in AlSb and GaSb, respectively were obtained. The $AlP_{1-y}As_y$ composition was difficult to control due to inadequate starting material compositions and availability. In general, the Al-rich compounds were found to be relatively unstable in air and moisture. Materials readily disintegrated during sample preparation such as by polishing slurries or by prolonged storage in the laboratory environment.

References

1 Holloway, P.H., and McGuire, G.E. (1995) *Handbook of Compound Semiconductors – Growth, Processing, Characterization, and Devices*, William Andrew Publishing/Noyes, Park Ridge, New Jersey.

2 Wei, J., Barnes, J., Guha, S., Gonzalez, L., Yeo, Y.K., Hengehold, R.L., and Rajagopalan, G. (2009) Electrical and optical characterization of melt grown bulk $InAs_{1-y}P_y$ crystals. Proc. of the 17th American Conference on Crystal Growth and Epitaxy, Wisconsin, p. 162.

3 Sengupta, S. (2009) Characterization of Terahertz Emission from High Resistivity Fe-doped Bulk GaInAs based Photoconducting Antennas excited at 800 nm, PhD Thesis, Rensselaer Polytechnic Institute, Troy, New York.

4 Ko, Y., Sengupta, S., Tomasulo, S., Dutta, P., and Wilke, I. (2008) *Phys. Rev. B*, **78**, 035201.

5 Lockhart, P., Han, P., Zhang, X.-C., and Dutta, P.S. (2008) *Appl. Phys. Lett.*, **92**, 011102.

6 Bhat, R., Dutta, P.S., and Guha, S. (2008) *J. Cryst. Growth*, **310**, 1910.

7 Ascazubi, R., Wilke, I., Kim, K.J., and Dutta, P.S. (2006) *Phys. Rev. B*, **74**, 075323.

8 Ascazubi, R. (2005) THz Emission Spectroscopy of Narrow Bandgap Semiconductors, PhD Thesis, Rensselaer Polytechnic Institute, Troy, New York.

9 Ascazubi, R., Shneider, C., Wilke, I., Pino, R., and Dutta, P.S. (2005) *Phys. Rev. B*, **72**, 045328.

10 Chandola, A., Kim, H.J., Guha, S., Gonzalez, L., Kumar, V., and Dutta, P.S. (2005) *J. Appl. Phys.*, **98**, 093103.

11 Chandola, A. (2005) Bulk Crystal Growth and Infrared Absorption Studies of GaInSb, PhD Thesis, Rensselaer Polytechnic Institute, Troy, New York.

12 Bhat, R. (2006) Bulk Crystal Growth and Infrared Absorption Studies of GaInAs, PhD Thesis, Rensselaer Polytechnic Institute, Troy, New York.

13 Ko, Y. (2007) Optical and Terahertz Emission Studies of GaInAs Bulk Crystals, PhD Thesis, Rensselaer Polytechnic Institute, Troy, New York.

14 Lockhart, P. (2007)Effects of Band Structure and Transport Properties on Terahertz Emission from III-V Semiconductors, PhD Thesis, Rensselaer Polytechnic Institute, Troy, New York.

15 Kim, H., Chandola, A., Guha, S., Gonzalez, L., Kumar, V., and Dutta, P.S. (2005) *J. Electron. Mater.*, **34** (**11**), 1391.

16 Refaat, T., Abedin, M.N., Bhagwat, V., Bhat, I.B., Dutta, P.S., and Singh, U.N. (2004) *Appl. Phys. Lett.*, **85** (**11**), 1874.

17 Pino, R., Ko, Y., Dutta, P.S., Guha, S., and Gonzalez, L.P. (2004) *J. Appl. Phys.*, **96** (**9**), 5349.

18 Rajagopalan, G., Reddy, N.S., Ehsani, H., Bhat, I.B., Dutta, P.S., Gutmann, R.J., Nichols, G., Charache, G.W., and

Sulima, O. (2003) *J. Electron. Mater.*, **32** (**11**), 1317.
19 Pino, R., Ko, Y., and Dutta, P.S. (2004) *J. Electron. Mater.*, **33** (**9**), 1012.
20 Chandola, A., Pino, R., and Dutta, P.S. (2005) *Semicond. Sci. Tech.*, **20**, 886.
21 Pino, R., Ko, Y., and Dutta, P.S. (2004) *Int. J. High Speed Electron. Syst.*, **14** (**3**), 658.
22 Pino, R., Ko, Y., and Dutta, P.S. (2004) *J. Appl. Phys.*, **96** (**2**), 1064.
23 Dutta, P.S., Borrego, J.M., Ehsani, H., Rajagopalan, G., Bhat, I.B., Gutmann, R.J., Nichols, G., and Baldasaro, P.F. (2002) GaSb and GaInSb thermophotovoltaic cells using diffused junction technology in bulk substrates. Proc. of the 5th Conference on Thermophotovoltaic Generation of Electricity, AIP Conference Proceedings, vol. 653, pp. 392–401.
24 Neuberger, M. (1972) III-V ternary semiconducting compounds-data tables, in *Handbook of Electronic Materials*, vol. 7, IFI/Plenum, New York, pp. 1–56.
25 Levinshtein, M., Rumyantsev, S., and Shur, M. (eds) (1999) *Handbook Series on Semiconductor Parameters, Vol. 2, Ternary and Quaternary III-V Compounds*, World Scientific Publishing Co., River Edge, New Jersey, pp. 1–152.
26 Bachmann, K.J., Thiel, F.A., and Schreiber, H., Jr. (1979) *Prog. Cryst. Growth Charact.*, **2**, 171.
27 Dutta, P.S. (2005) *J. Cryst. Growth*, **275**, 106.
28 Dutta, P.S. (2008) Crystal growth technology for ternary III-V semiconductor production by vertical bridgman and vertical gradient freezing methods with accelerated crucible rotation technique, in *Crystal Growth Technology* (eds H.J. Scheel and P. Capper), Wiley-VCH Verlag GmbH, Weinheim, Chapter 12, pp. 307–335.
29 Mitric, A., Duffar, T., Diaz-Guerra, C., Corregidor, V., Alves, L.C., Garnier, C., and Vian, G. (2006) *J. Cryst. Growth*, **287** (**2**), 224.
30 Garandet, J.P., Duffar, T., and Favier, J.J. (1990) *J. Cryst. Growth*, **106**, 426.
31 Duhanian, N., Duffar, T., Marin, C., Dieguez, E., Garandet, J.P., Dantan, P., and Guiffant, G. (2005) *J. Cryst. Growth*, **275**, 422.
32 Sen, S., and Lefever, R.A. (1978) *J. Cryst. Growth*, **43**, 526.
33 Yee, J.F., Lin, M.-C., Sarma, K., and Wilcox, W.R. (1975) *J. Cryst. Growth*, **30**, 185.
34 Okitsu, K., Hayakawa, Y., Yamaguchi, T., Hirata, A., Fujiwara, S., Okano, Y., Imaishi, N., Yoda, S., Oida, T., and Kumagawa, M. (1997) *Jpn. J. Appl. Phys.*, **36**, 3613.
35 Hayakawa, Y., Balakrishnan, K., Komatsu, H., Murakami, N., Nakamura, T., Koyama, T., Ozawa, T., Okano, Y., Miyazawa, M., Dost, S., Dao, L.H., and Kumagawa, M. (2002) *J. Cryst. Growth*, **237–239**, 1831.
36 Dutta, P.S., Kim, H.J., and Chandola, A. (2007) *Trans. Ind. Inst. Metals*, **60** (**2–3**), 155.
37 Dutta, P.S. (2005) "Method and Apparatus for Growth of Multi-Component Single Crystals", US Patent Application 20080203361 A1.
38 Dutta, P.S., and Miller, T.R. (2000) *J. Electron. Mater.*, **29**, 956.
39 Dutta, P.S., and Miller, T.R. (2003) "Multicomponent homogeneous alloys and method for making same", US 6613162 B1.
40 Marin, C., and Ostrogorsky, A.G. (2000) *J. Cryst. Growth*, **211**, 194.
41 Kumar, A. (2006) Growth of Thick Lattice Mis-matched layers of GaInAsSb on GaAs Substrates from Quaternary Melts, PhD Thesis, Rensselaer Polytechnic Institute, Troy, New York.
42 Kumar, A., and Dutta, P.S. (2008) *J. Cryst. Growth*, **310**, 1647.
43 Kumar, A., and Dutta, P.S. (2006) *Appl. Phys. Lett.*, **89**, 162101.
44 Gennett, A., and Dutta, P.S. (2009) Low temperature growth of Al-In-Ga-As-P crystals from Sb-rich melts. Proc. of the 17th American Conference on Crystal Growth and Epitaxy, Wisconsin, p. 163.
45 Ishida, K., Tokunaga, H., Ohtani, H., and Nishizawa, T. (1989) *J. Cryst. Growth*, **98**, 140.
46 Stringfellow, G.B. (1974) *J. Cryst. Growth*, **27**, 21.
47 Nakajima, K., Osamura, K., Yasuda, K., and Murakami, Y. (1977) *J. Cryst. Growth*, **41**, 87.
48 Willardson, R.K., and Goering, H.L. (1962) *Compound Semiconductors, Vol. 1*

Preparation of III-V Compounds, Reinhold Publishing Corporation, New York.

49 Gault, W.A., Monberg, E.M., and Clemens, J.E. (1986) *J. Cryst. Growth*, **74**, 491.

50 Grant, I.R. (2005) InP crystal growth, in *Bulk Crystal Growth of Electronic, Optical and Optoelectronic Materials* (ed. P. Capper), John Wiley & Sons, Ltd, Chichester, Chapter 4, pp. 121–147.

51 Brozel, M.R., and Grant, I.R. (2005) Growth of GaAs, in *Bulk Crystal Growth of Electronic, Optical and Optoelectronic Materials* (ed. P. Capper), John Wiley & Sons, Ltd, Chichester, Chapter 2, pp. 43–71.

52 Asahi, T., Kainosho, K., Kohiro, K., Noda, A., Sato, K., and Oda, O. (2003) Growth of III-V and II–VI single crystals by the vertical gradient-freeze method, in *Crystal Growth Technology* (eds H.J. Scheel and T. Fukuda), John Wiley & Sons, Ltd, Chichester, Chapter 15, pp. 323–348.

53 Kawase, T., Tatsumi, M., and Nishida, Y. (2003) Growth technology of III-V single crystals for production, in *Crystal Growth Technology* (eds H.J. Scheel and T. Fukuda), John John Wiley & Sons, Ltd, Chichester, Chapter 16, pp. 349–371.

54 Rudolph, P., and Jurisch, M. (2003) Fundamental and technological aspects of czochralski growth of high quality semi-insulating GaAs crystals, in *Crystal Growth Technology* (eds H.J. Scheel and T. Fukuda), John Wiley & Sons, Ltd, Chichester, Chapter 14, pp. 293–321.

55 Marshall, A.J., and Gillessen, K. (1977) *J. Cryst. Growth*, **41**, 93.

56 Duffar, T., Gourbil, J.M., Boiton, P., Dusserre, P., and Eustathopoulos, N. (1997) *J. Cryst. Growth*, **179**, 356.

57 Pino, R., Ko, Y., and Dutta, P.S. (2006) *J. Cryst. Growth*, **290**, 29.

10
Mercury Cadmium Telluride (MCT) Growth Technology Using ACRT and LPE

Peter Capper

10.1
Introduction

It is ~50 years now since the first development of the ternary compound mercury cadmium telluride (MCT) for infrared (IR) applications. In the early days of MCT production (1960s and 1970s) bulk growth techniques were the predominant ones. As time progressed into the 1980s and 1990s the various epitaxial techniques, particularly liquid phase epitaxy (LPE), metal-organic vapor phase epitaxy (MOVPE) and molecular beam epitaxy (MBE) took over the major role of MCT production, particularly for photovoltaic devices, due to their greater flexibility. Because of the sensitive nature of much of the research and development work associated with the material the history of MCT is one of most centers developing their own particular routes to its production, somewhat independently of their counterparts in other countries. MCT ($Cd_xHg_{1-x}Te$) is still the pre-eminent infrared material, and by varying the x value the material can be made to cover all the important infrared (IR) ranges of interest (i.e., 1–3, 3–5 and 8–14 μm).

There is an estimated 1.5$B pa. IR systems business worldwide, of which IR arrays account for perhaps $600 M pa. MCT is used in ~ half of these arrays, that is, ~$300 M pa, and it can be estimated that the materials element of this amounts to ~$30 M pa. This figure includes both bulk and epitaxial material, with ~$5 M and ~$25 M pa. values attaching, respectively, to the 2 areas. Currently, Selex Galileo probably accounts for over half of the bulk total.

MCT is the third most studied semiconductor after Si and GaAs and a great deal of work has been carried out on the various phase equilibria ([1, 2] contain reviews in this area). The liquidus and solidus lines in the pseudobinary HgTe-CdTe system are shown in Figure 10.1 [1]. The wide separation between the liquidus and solidus, leading to marked segregation between CdTe and HgTe, was instrumental in the development of all the bulk growth techniques applied to this system. In addition to the solidus–liquidus separation high Hg partial pressures are also influential both during growth and postgrowth heat treatments. A full appreciation of the $P_{(Hg)} - T$ diagram, shown in Figure 10.2, is therefore essential. Curves are the partial pressures of Hg along boundaries for solid solutions of

Crystal Growth Technology. Semiconductors and Dielectrics. Edited by P. Capper and P. Rudolph
Copyright © 2010 WILEY-VCH Verlag GmbH & Co. KGaA, Weinheim
ISBN: 978-3-527-32593-1

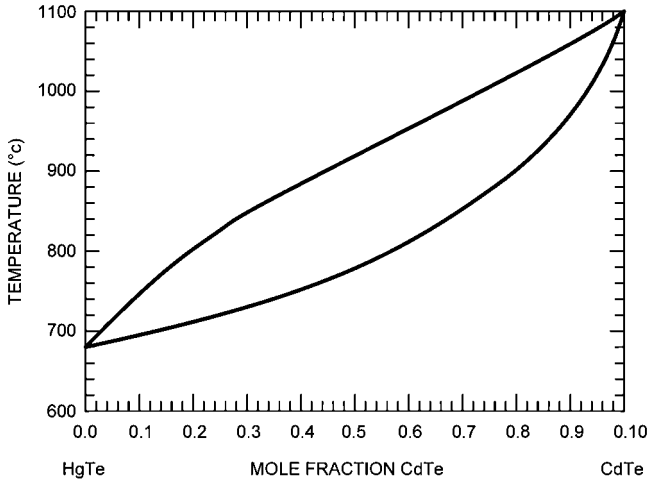

Figure 10.1 Pseudobinary phase diagram for HgTe-CdTe system (L = liquid, S = solid). (Reprinted from Yu and Brebrick [1], p. 56, copyright (1994) reproduced with permission from IEE.)

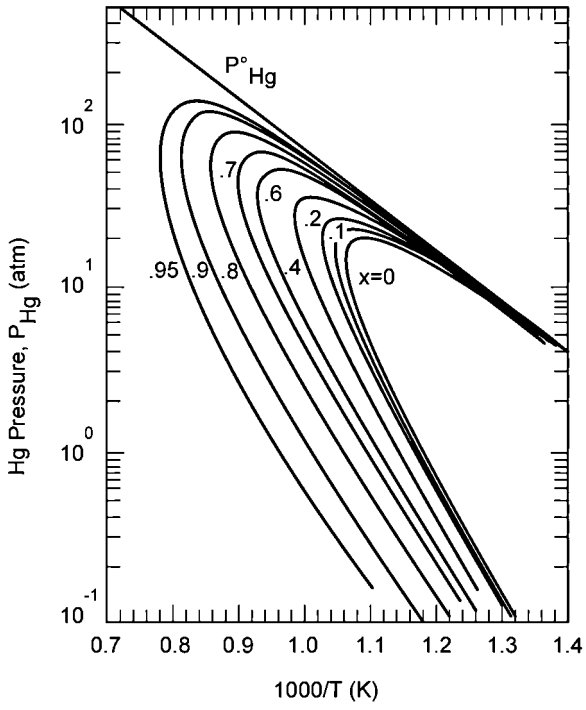

Figure 10.2 Pressure–temperature diagram for MCT. (Reprinted from Yu and Brebrick [1], p. 59, copyright (1994) reproduced with permission from IEE.)

composition x where the solid solution is in equilibrium with another condensed phase as well as the vapor phase.

This chapter is split into 2 main sections. The first deals with the bulk growth of MCT by the Bridgman process and the addition of the accelerated crucible rotation technique (ACRT) to the basic Bridgman process, concentrating on near-IR (short-wavelength) applications. Then, the growth and applications of MCT by Te-rich LPE will be discussed. The chapter does not emphasize growth fundamentals, rather it concentrates on the uses of ACRT and LPE as applied to MCT.

10.2
Bridgman/ACRT Growth of MCT

10.2.1
Introduction

Historically, the first technique used at Selex Galileo Infrared Ltd. was the Bridgman process. Later, the emphasis switched to the accelerated crucible rotation technique (ACRT), a modification of the Bridgman process. Reviews of bulk growth can be found in [3–5].

This section will focus on the technological aspects of the production of large bulk crystals, their assessment, and their use in photoconductive IR detectors and other IR optical applications. Bridgman growth takes place in simple 2-zone furnaces with the pure elements contained in thick-walled high-purity silica ampoules. The thick ampoule walls are needed to contain the high (up to ~70 atm) mercury vapor pressures within the ampoules. We have found it necessary to purify both the mercury and the tellurium on site before use to obtain the required electrical properties. The marked segregation of the matrix elements in standard Bridgman growth is both a disadvantage and an advantage. Its disadvantage is that the yield of material in terms of composition for the most commonly required regions is low. The advantage is that all regions of interest can be produced in the same crystal, to some extent. A further advantage is that segregation of impurities also occurs and this leads to low background donor levels in Bridgman material. The other main disadvantages of the standard Bridgman technique are that material is nonuniform in composition in the radial direction, as well as in the growth direction, resulting in low yields, and there are numerous grain and subgrain boundaries.

We have therefore developed an improved process based on the addition of ACRT. Here, ampoules are subjected to periodic acceleration/deceleration in their rotation, rather than constant rotation as in the Bridgman process. The major effect of this is to stir the melt during growth and produce flatter solid/liquid interfaces. This, in turn, improves the radial and axial compositional uniformity of the material, and reduces somewhat the grain and subgrain densities. An additional marked advantage of ACRT is that the improved radial compositional uniformity enables larger-diameter material to be produced (up from 13 mm to as

much as 70 mm in our case). Assessment of the material includes wavelength mapping of both radially cut slices and axially cut planks; the latter gives useful information on the shape and change in the solid/liquid interface as growth proceeds. Images taken with an IR camera, and a blackbody source, reveal features in slices, for example, cracks, inclusions of second phase (including Te on grain boundaries) and swirl patterns.

We are currently routinely growing 20-mm diameter, 200-mm long crystals of ~0.5 kg weight with excellent uniformity of composition and good electrical properties for first-generation photoconductive IR detectors requiring low carrier concentration n-type material. Compositions produced in these 20-mm diameter crystals range from $x \sim 0.88$ (~1.0 μm) through to $x = 0.0$ (i.e., HgTe), the latter in the tail ends of the crystals. Research is also progressing on larger-diameter crystals, with 40-, 50- and 70-mm crystals having been grown, the latter being the largest diameter crystal of MCT ever grown, to this author's knowledge.

10.2.2 Processing

Elemental Cd (unetched) plus in-house purified Hg and Te are loaded, within a nitrogen-purged glove box, into an etched, washed, heavy-wall (7 mm) silica ampoule (diameter 20–70 mm). A start composition of $x = 0.19$–0.8 is used and homogenization is by melting/rocking. Charges are then placed in a vertical grower (see Figure 10.3), remelted and then frozen slowly (0.5–0.25 mm h^{-1}) from one end in a vertical system to produce a large-grained ingot. Slow rotation about the vertical axis (standard Bridgman) is used to reduce radial temperature variations, or ACRT to stir the liquid and reduce radial temperature variations. Slices are cut from the resulting crystals using an abrasive slurry on a multiblade cutting machine. Slices are then assessed for wavelength, that is, x, uniformity with infrared transmission (IRT) measurements and for the electrical parameters by Hall effect measurements at 77 K, if detector material is the ultimate aim, or a MW IR camera system if material for optical applications is sought.

10.2.3 Accelerated Crucible Rotation Technique (ACRT)

10.2.3.1 Introduction

Limits on controlling melt mixing in the Bridgman process necessitated a means of stirring melts contained in sealed, pressurized ampoules. The ACRT of Scheel [6] was utilized as it increased the size of crystals, eliminated unwanted phases, and increased stable growth rates. The first reported use of ACRT in MCT Bridgman growth was given in [7]. These effects were developed and discussed in more detail in later papers, see [5, 8] for reviews. In essence, bidirectional rotation is used with maximum rotation rates governed by the ampoule diameter (e.g., 25 rpm for 20-mm and ~5 rpm for 50-mm diameter crystals, respectively) with short stop

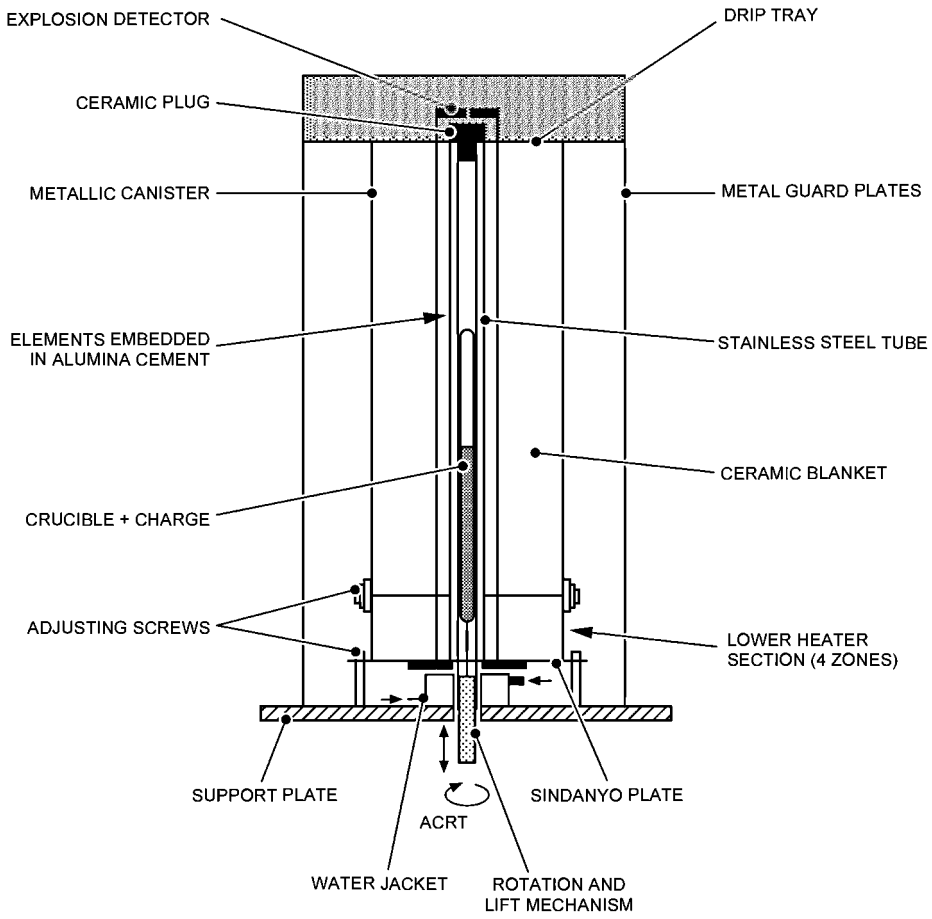

Figure 10.3 Bridgman/ACRT growth apparatus. (Reprinted from Capper *et al. J. Cryst. Growth* **46** (1979) p. 575, copyright (1979) reproduced with permission from Elsevier Science.)

and run times, for example, 1 s and 8 s. The main stirring mechanism is Ekman flow near the flat solid/liquid interface [9, 10].

10.2.3.2 **High-*x* Material**

This section focuses on the work undertaken to produce near-IR material, where higher starting x values are used. The assessment of the near-IR material has included wavelength mapping of both radially cut slices and axially cut planks. Images taken with an IR camera reveal features in slices, for example, cracks, inclusions of second phase (including Te on grain boundaries) and swirl patterns. This work is being undertaken to improve our basic understanding of the

properties of MCT in the near-IR region and to investigate the suitability of the material for use in various IR optical applications.

Figure 10.1 shows the pseudobinary phase diagram of the HgTe-CdTe system [1]. The wide separation between the liquidus and the solidus is actually a benefit when we are trying to produce higher x material. The initial goal was to produce material of $x \sim 0.88$, corresponding to ~1.0 μm cut-off wavelength. Figure 10.1 shows that this necessitates using starting x values of >0.6. Figure 10.2 shows the pressure–temperature phase diagram for various x values [1]. The region above the P^{o}_{Hg} line is essentially Hg vapor, with solid of the indicated x values existing in the loops on the lower right and liquid to the left of the loops. This clearly demonstrates how the maximum growth temperature and hence the Hg vapor pressure increases as x increases.

The loading procedure for these high-x crystals was as for the earlier crystals. We have had to develop the seal-off procedure to reduce the possibility of explosions due to the high pressures. This entailed ensuring that the wall thickness remained at the 7-mm value of the ampoule body and ensuring that there were no re-entrant angles in the seal-off area. By making the internal surface of the seal-off smooth we have greatly reduced the occurrence of explosions and have successfully grown at temperatures >950 °C, that is, some 130 °C above "standard" temperatures.

Start compositions of $x = 0.19$–0.8 have been used and the melts were homogenized by melting/rocking as for standard charges. The growth process remained essentially unchanged for these high-x crystals. Slices were cut (at >1 mm thickness) from the resulting crystals using a diamond peripheral-wheel cutting machine and then polished and assessed for x uniformity with infrared transmission (IRT) measurements and also using the mid-IR camera system.

Standard bidirectional rotation is still employed with rapid acceleration/deceleration (in 1–2 s). From considerations of the simple model [5] it was seen that maximum rotation rates for the 20-mm diameter crystals should be between 4 and 30 rpm. Also, for these crystals short run and stop times (8 and 1 s, respectively) were used as for standard crystals. To maximize the Ekman stirring, that is, increase the vertical and horizontal flow velocities, we chose to use 25 rpm as the maximum rate.

Figure 10.4 shows the FTIR map of a short-wavelength slice ($\lambda \sim 1.0$ μm) demonstrating excellent radial uniformity. The small nonuniform regions are associated with edge cracks in this slice; cracking is still a problem in these high-x crystals.

Another assessment tool that is used for these high-x crystals is that of IR imaging. By placing a blackbody on one side of the slice (polished on both sides to ~1 mm thickness) and a MW camera system (CEDIP) on the other, images can be taken that reveal IR-absorbing defects. (This camera system uses an OSPREY detector manufactured at Selex Galileo Infrared Ltd. from LPE material, see Figure 10.12). Figures 10.5–10.7 show wavelength uniformity plots, IR camera images (note the clear image for the 50-mm sample) and size details for the 40-, 50- and 70-mm diameter crystals, with that in Figure 10.7 being the largest MCT crystal

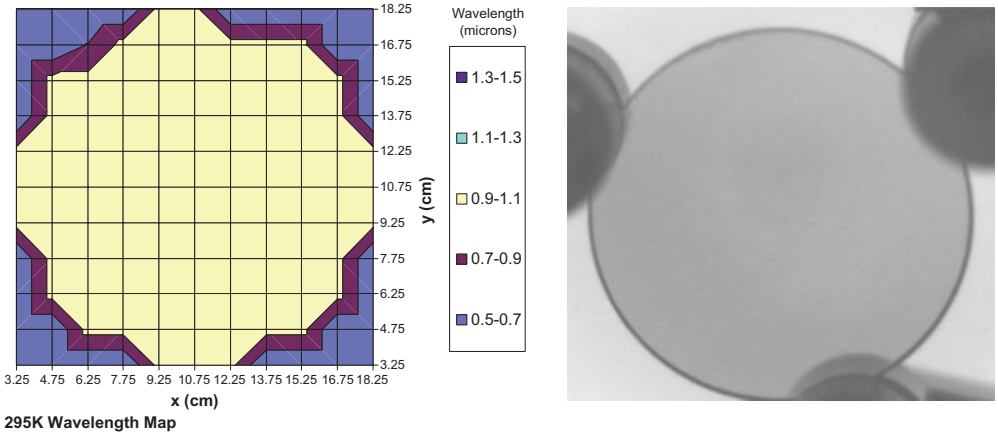

Figure 10.4 Wavelength uniformity plot and IR camera image for a 20-mm diameter high-*x* slice (courtesy of Selex Galileo Infrared Ltd).

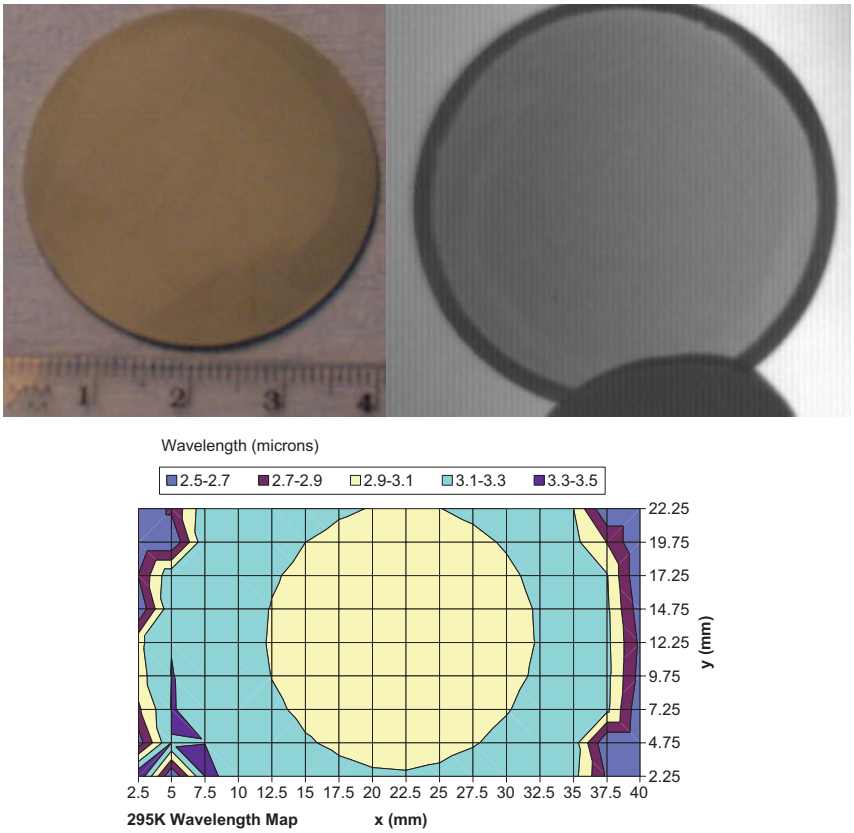

Figure 10.5 Wavelength uniformity plots, IR camera images and size details for the 40-mm diameter crystal (courtesy of Selex Galileo Infrared Ltd).

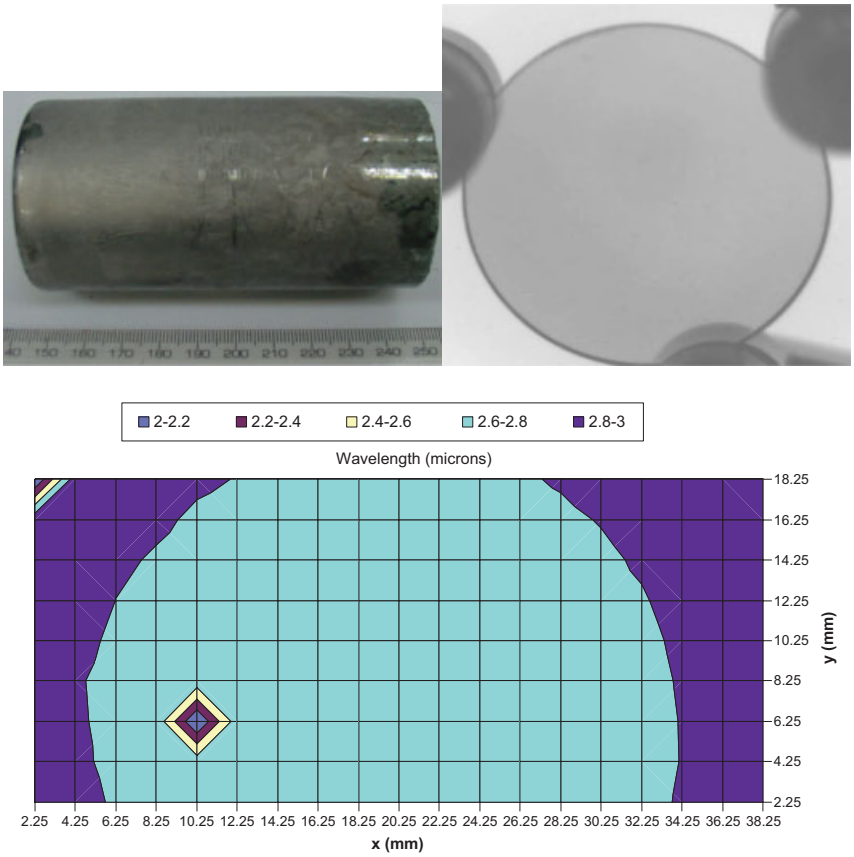

Figure 10.6 Wavelength uniformity plots, IR camera images and size details for the 50-mm diameter crystal (courtesy of Selex Galileo Infrared Ltd).

grown to date anywhere in the world, to this author's knowledge. Other techniques, such as magnetic/vibrational stirring have been attempted with MCT, with varying degrees of success [11–13]. A comparison of the radial uniformity of x (or wavelength) shows that ACRT produces the most uniform material of any given x value for all the melt stirring techniques used to date. It has been suggested [14] that ACRT may lead to striations in the material as the periodicity is of the order of minutes. In the preferred case of short cycle times, outlined above, Gray *et al.* [15] have confirmed the observations in our quenched crystals that no striations should be present.

10.2.4
Summary

In the Bridgman growth of MCT, a controlled increase in melt mixing produced by ACRT leads to an improvement in radial compositional variations and good axial uniformity, resulting in a factor of ten increase in overall material yield over

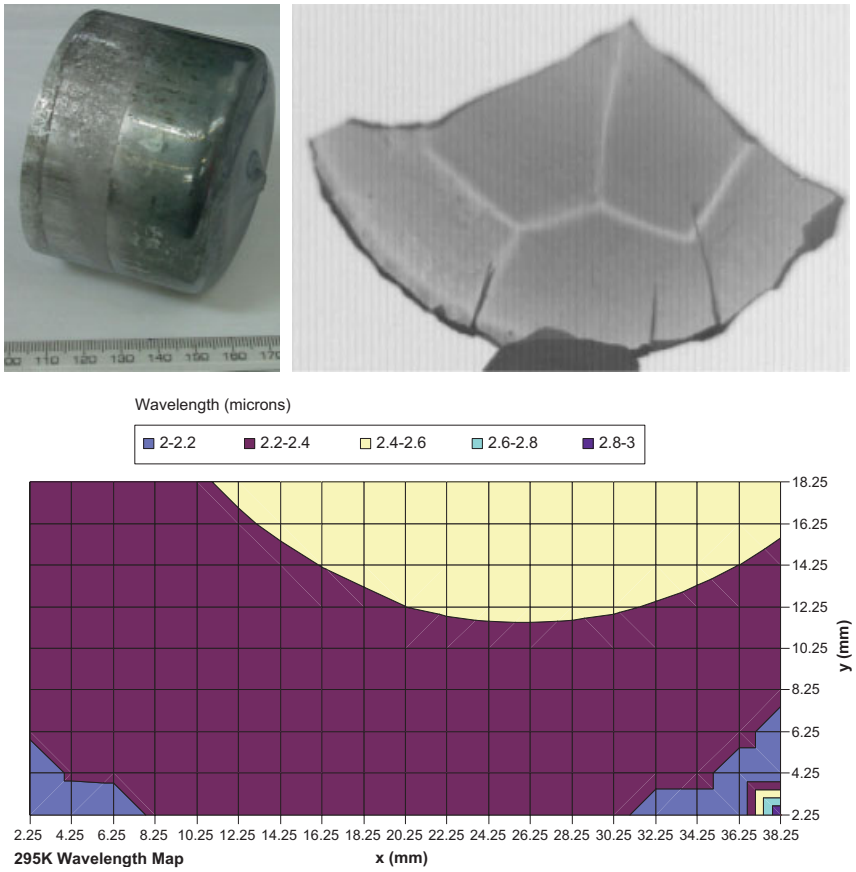

Figure 10.7 Wavelength uniformity plots, IR camera images and size details for the 70-mm diameter crystal (courtesy of Selex Galileo Infrared Ltd).

normal Bridgman growth. Large-diameter crystals (up to 70 mm) have been grown with a high degree of radial x uniformity by ACRT. Crystals of 20 mm diameter with a length of 200 mm weighing ~0.5 kg are now routinely produced. Electrical and chemical characterization shows that high-purity material is obtained and this allows the manufacture of a wide variety of high-performance photoconductive infrared detectors. We have shown that higher-x crystals can be grown, providing that the ampoule seal-off is improved to minimize the risk of ampoule explosions. Crystals with starting x values of up to ~0.8 and weights of ~2 kg have been grown at temperatures up to ~960 °C. Slices with x values up to ~0.88 (λ~ 1.0 μm) have been obtained from the tip regions of such crystals. These slices are highly uniform in x, indicating flat solid/liquid interfaces. Imaging of material with an IR camera has revealed no IR-absorbing defects in the first-to-freeze short-wavelength slices but cracks, second-phase inclusions and "swirl-like" patterns of varying contrast are revealed as growth proceeds, that is, as the wavelength increases.

10.3 Liquid Phase Epitaxy of MCT

10.3.1 Introduction

This section describes the growth of MCT by Te-rich liquid phase epitaxy (LPE). The section is an update of some of the material in this author's previous summary [16] with recent additions in the area of device applications, where there has been notable progress in the last few years. Baker [17] and Reine [18] have given recent summaries of infrared (IR) detector types made in MCT and this section draws on these two sources for some material.

While photoconductive IR arrays have mainly used bulk material [19] photovoltaic arrays mainly use epitaxial layers. Photovoltaic arrays have inherently low power consumption and can be easily connected to a silicon integrated circuit to produce a retina-like focal plane array. Such arrays are key for so-called 2nd-generation thermal imaging cameras. Photovoltaic devices tend to fall into two categories: long linear arrays of long-wavelength (8–12 μm) diodes and matrix arrays of medium wavelength (3–5 μm) diodes and short-wavelength diodes (1.5–3 μm). For long linear arrays, MCT is the sensor material of choice because the stringent sensitivity requirements of these systems demands a high quantum efficiency and near background limited infrared photodetector (BLIP)-limited performance detectors. MW detectors tend to use matrix arrays where the integration time can approach the frame time. The problem of point defects is considerably reduced in the medium waveband and large 2D arrays are more practical. The MW band thermal imaging market is concentrated on arrays using half-TV (320×256 or 384×288) or full-TV formats (640×480 or 640×512).

Several epitaxial growth techniques are in use today. Manufacturers will select a technique that suits their device technology and the type of detectors they are trying to make. For instance, high-performance LW arrays will call for the best possible crystal quality, whereas, large-area MW arrays can probably accept poorer material but must have large, uniform wafers. At the present time the best structural quality material is grown using LPE onto lattice-matched substrates of CdZnTe.

A crucial figure of merit, however, is the dislocation count that controls the number of defects in 2D arrays. Etch pit densities of $3–7 \times 10^4\,cm^{-2}$ are typically seen in the Te-rich sliding boat process, reproducing the substructure of the CdZnTe substrate [20]. The substrate defect level can be as low as mid-$10^3\,cm^{-2}$ in some Bridgman CdZnTe but this is not easy to reproduce. Device processing therefore must expect to cope with defect levels in the mid-$10^4\,cm^{-2}$ range for routine MCT epilayers and this will set the ultimate limit on the number of defects in MCT 2D arrays. LPE layers are grown using an isothermal supersaturation or programmed cooling technique or some combination. A detailed knowledge of the solid–liquid–vapor phase relation is essential to control the growth particularly in view of the high Hg pressure. Challenges include: the compositional uniformity through the

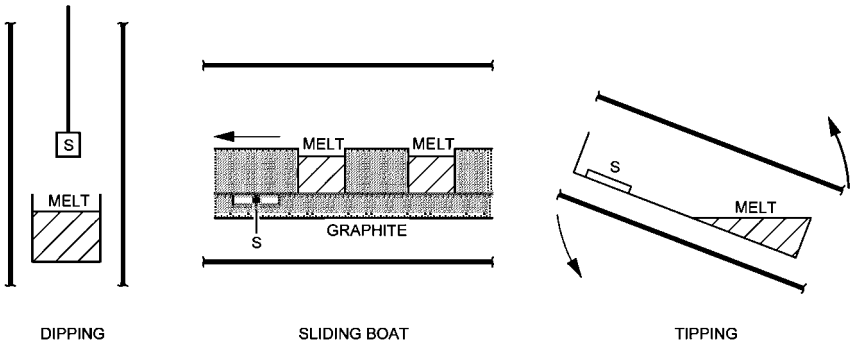

Figure 10.8 Schematic diagram of the three principal LPE growth techniques from Te-rich melts (Reprinted from [19] with kind permission of Springer Science + Bussiness Media).

layer, the surface morphology, the incorporation of dopants, the elimination of background impurities and the specifications for thickness, wavelength, etc.

Two different technical approaches are used: growth from a Hg-rich solution and growth from a Te-rich solution. Advantages of the Hg-rich route include: excellent surface morphology, a low liquidus temperature, which makes cap-layer growth more feasible and the ease of incorporation of dopants. Also, large melts can provide for very good compositional and thickness uniformity in large-area layers and give consistent growth characteristics over a long period of time. Growth from Te-rich solutions can use three techniques to bring the melt into contact with the substrate: dipping, tipping and sliding (see Figure 10.8). Sliding boats use small melt volumes and are very flexible for changing composition, thickness and doping and the remainder of this section concentrates on this method.

10.3.2 Growth

The pioneering work on the Te corner of the phase diagram of the Hg-Cd-Te system [21] and the associated LPE growth experiment [22] provided the necessary groundwork that led to several variations of open-tube LPE from Te solutions [23, 24]. It is difficult to prepare homogeneous, high-quality epitaxial layers even from Te-rich solutions, mainly because of the relatively high vapor pressure of Hg (~0.1 atm) at typical growth temperatures (~500 °C). The initial growth solution composition can be drastically changed during the growth cycle due to Hg being absorbed into or evaporated from the growth solution [25]. Unless provision is made during the growth process to keep the growth solution composition constant, MCT epilayers of uniform composition cannot be grown reproducibly. Several approaches have been adopted to overcome this problem.

Growth of MCT from tellurium-rich solutions was first used in the 1970s to grow layers as the required equipment was fairly simple and easy to implement. The quality, however, was poor due to microstructure, dislocations and low

substrate purity, mainly copper contamination [26–28]. The difficulties with substrates and the details of the MCT phase diagram were not well known in the early phases of the technology development and this gave problems in run-to-run composition reproducibility, and composition gradient control. It was not until Brebrick *et al.* [29] completed their phase diagram studies that accurate control of the composition was established. Composition uniformity and reproducibility was also complicated by the lack of good temperature control [30]. LPE growth from Te-rich melts is usually carried out in quartz crucibles when using the dipping or tipping techniques, mainly because quartz is available in very high purity, the melt does not interact with the quartz and it can be easily formed. Growth from the sliding boat, however, has been carried out in high-purity graphite boats also with great success [20, 26]. In [31] we showed data from laser source mass spectrometry of LPE layers that proved the absence of interface peaks of impurities that had been seen by other groups [32, 33] Layers yield low background n-type levels that support this view.

MCT growth from tellurium-rich solution solves a number of problems encountered with bulk crystal growth techniques. The most important being the reduction of the Hg vapor pressure over the liquid by almost two orders of magnitude at the growth temperature. Large-area layers can be grown with thicknesses up to ~150 μm reproducibly. Growth from Te-rich solutions uses three methods, dipping, tipping and sliding-boat technologies, and a comparison of the three techniques is shown in Table 10.1.

Dipping LPE reactors were initially very simple, utilizing small transparent gold-coated furnaces with melts of ~200 g allowing growth on ~5 cm^2 substrates. Current reactors are capable of growing in excess of 60 cm^2 per growth run and are kept at temperature for long periods, >6 months. Melts, on the other hand, last a very long time, >5 years. Westphal *et al.* [30] described a sensor-based reactor capable

Table 10.1 Comparison of three LPE growth techniques from Te-rich solutions.

Technique	Advantages	Disadvantages
Sliding boat	• Thickness control • Large area • Double layers	• Thick layers difficult to grow • Substrate thickness/ planarity control • High cost
Tipping	• Thickness control • Lowest investment for experimental investigation • Closed system/good P_{Hg} control	• High cost • Scale up
Dipping	• Thick layer growth • High throughput • Low cost • Large/flexible area	• Thin layer thickness control • Double layers

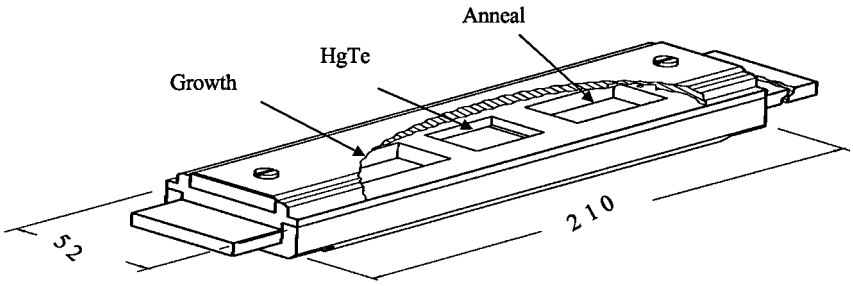

Figure 10.9 Schematic of Te-rich sliding-boat arrangement, dimensions in mm [35] (reproduced by permission of IoM Communications).

of growing MCT thick layers at relatively high production volumes and excellent reproducibility.

Sliding-boat LPE is the most widely used technique for compound semiconductor LPE in general. It normally consists of a graphite boat with a recess in the base for holding the substrate wafer and a movable block with wells that contain the LPE solution and that allows the solution to be brought into contact with the substrate and then wiped off after growth. Advantages of the technique are the efficient use of solution and the ease of growing multilayers. Disadvantages are the need for careful machining of the boat components in order to get efficient removal of the solution after growth and the need for precisely sized substrate wafers to fit into the recess in the boat. The sliding-boat growth process has several variants [23] but essentially, a polished substrate is placed in the well of a graphite slider and the Te-rich solution is placed in a well in the body of the graphite boat above the substrate and displaced horizontally from it (see Figure 10.9). Normally, a separate well contains the HgTe charge to provide the Hg vapor pressure needed during growth and during cool-down to control the stoichiometry. The boat is loaded into a silica tube that can be flushed with nitrogen/argon prior to the introduction of Pd-diffused H_2 for the growth phase. The temperature is increased to 10–20 °C above the relevant liquidus. A slow temperature ramp (2–3 °C h^{-1}) is initiated and when the temperature is close to the liquidus of the melt the substrate is slid under the melt and growth commences. After sufficient time has elapsed to grow the required thickness of MCT (typical growth rates are 9–10 μm h^{-1}) the substrate is withdrawn and the temperature is decreased to an annealing temperature before being reduced rapidly to room temperature [13]. Thicknesses of 25–30 μm are normally produced for loophole diode applications, see [17]. Capper *et al.* [31, 34] showed wavelength uniformity over a 2 × 3 cm LPE layer (see Figure 10.10 for more recent similar examples on 2 × 4 cm LW and MW layers).

The dislocation density of LPE MCT and its effects on device characteristics has received much attention [35, 36]. The dislocation density is dominated mainly by the dislocation of the underlying substrate as demonstrated by Yoshikawa [37]. For LPE material grown in a sliding-boat system, Baker *et al.* [20] showed this same variation of dislocation density with depth (typical values are 3–7 × 10^4 cm^{-2}) and the effect of dislocation density on diodes is discussed in [17].

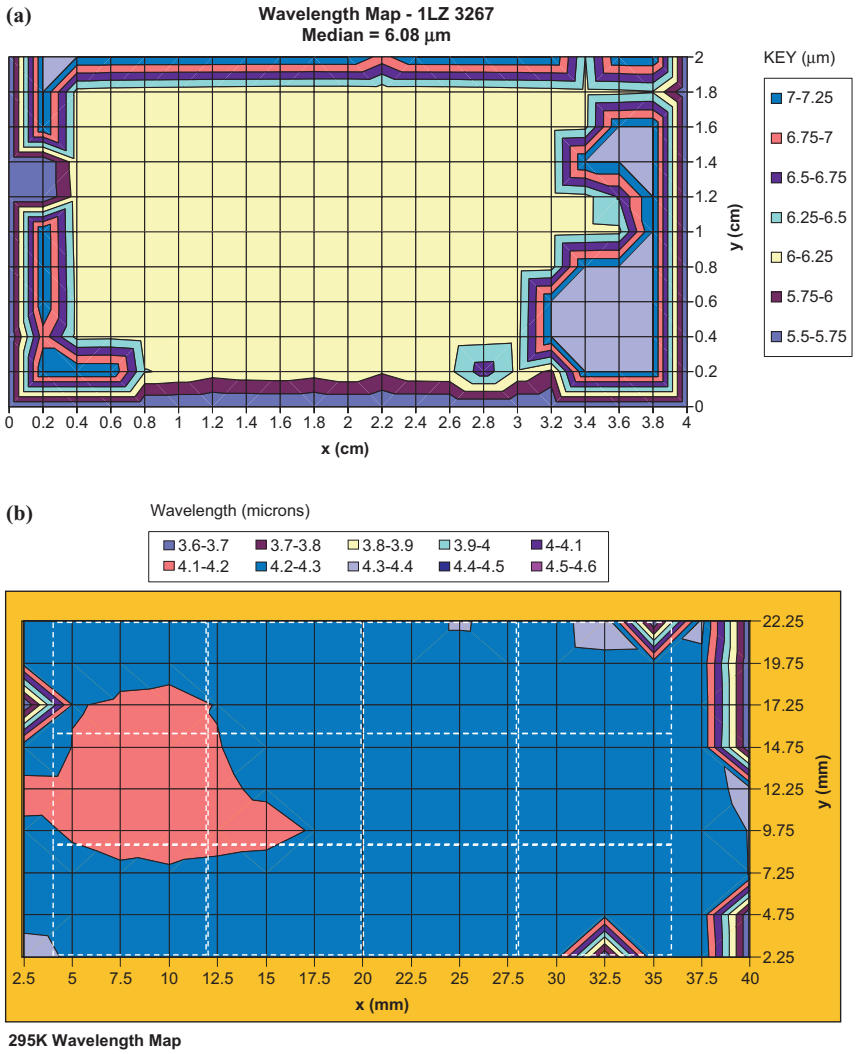

Figure 10.10 Wavelength uniformity plots of (a) LW and (b) MW 2 × 4 cm LPE layers from Te-rich sliding-boat growth (courtesy of Selex Galileo Infrared Ltd).

The process flow of the via-hole device using LPE material is illustrated in Figure 10.11 [20, 38]. Using ion beam milling, the MCT is eroded away in the holes until the contact pads are exposed. The holes are then backfilled with a conductor, to form the bridge between the walls of the hole and the underlying metal pad. The junction is formed around the hole during the ion beam milling process. A p-side contact is applied around the array. Figure 10.11 shows a photomicrograph of one corner of the hybrid illustrating the membrane-like nature of the MCT on the silicon.

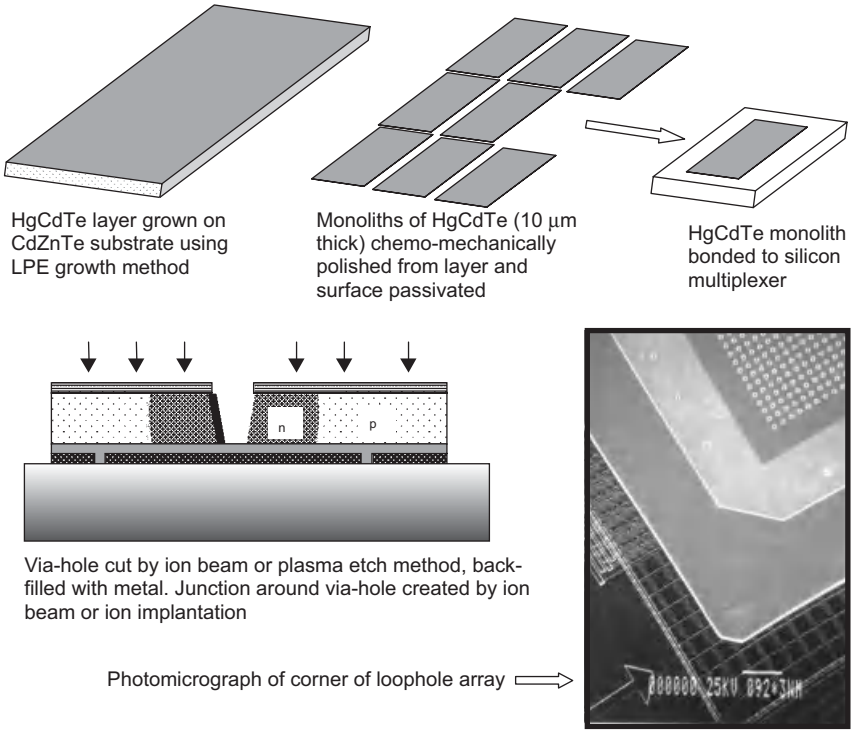
HgCdTe layer grown on CdZnTe substrate using LPE growth method
Monoliths of HgCdTe (10 μm thick) chemo-mechanically polished from layer and surface passivated
HgCdTe monolith bonded to silicon multiplexer
n
p
Via-hole cut by ion beam or plasma etch method, back-filled with metal. Junction around via-hole created by ion beam or ion implantation
Photomicrograph of corner of loophole array

Figure 10.11 Processing of MCT arrays using LPE material and loophole technology [17] (reproduced with kind permission of Springer Science + Bussiness Media).

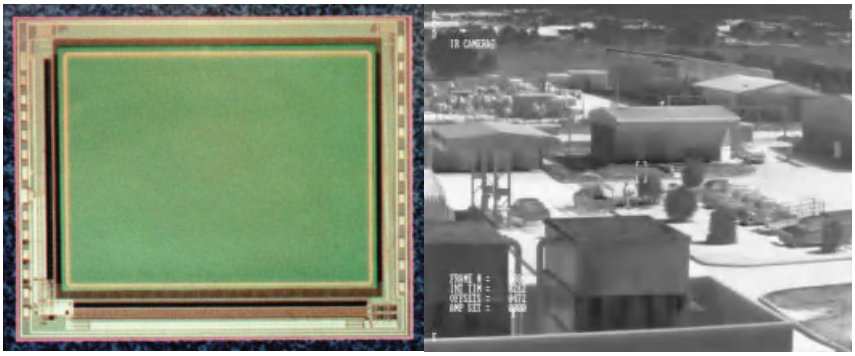

Figure 10.12 Photograph of a MW OSPREY array and a high-resolution image taken using such an array [17] (reproduced with kind permission of Springer Science + Bussiness Media).

Figure 10.12 shows a photograph of a MW OSPREY array made in LPE material and a high-resolution image taken using such an array.

Important applications in the SW (1–2.5 μm) waveband include: thermal imaging (using nightglow), spectroscopy and active imaging using lasers. SW detectors can

produce good-quality diodes in the presence of fairly high levels of misfit dislocations. For imaging and spectroscopy applications typical operating temperatures are around 200 K and thermoelectric coolers are often offered as standard products. In most SW applications the photon flux is low and it is difficult to achieve reasonable signal-to-noise performance. However, it is relatively easy to enhance the signal by providing some avalanche gain in the device. Electron avalanching in MW MCT loophole diodes has been described [39, 40]. The electron and hole ionization rates are very different in MCT and this allows almost pure exponential, noise-free avalanche gain at fairly moderate voltages. So, avalanche gain can readily be achieved for wavelengths above about 2.5 µm when the absorber region is p-type and electrons are the minority carriers. Typically, a gain of 10 is observed for around 5 V at a cut-off of 5 µm.

SW laser-gated imaging systems using avalanche gain in MCT are now being reported for use in long-range identification applications [41]. Here, the combination of sophisticated ROICs and high-quality Te-slider LPE MCT device processing is producing 320 × 256 arrays with a sensitivity down to 10 photons rms. The advantages of laser-gated imaging in conjunction with other sensors are shown in Figure 10.13 along with a typical pair of images. Figure 10.14

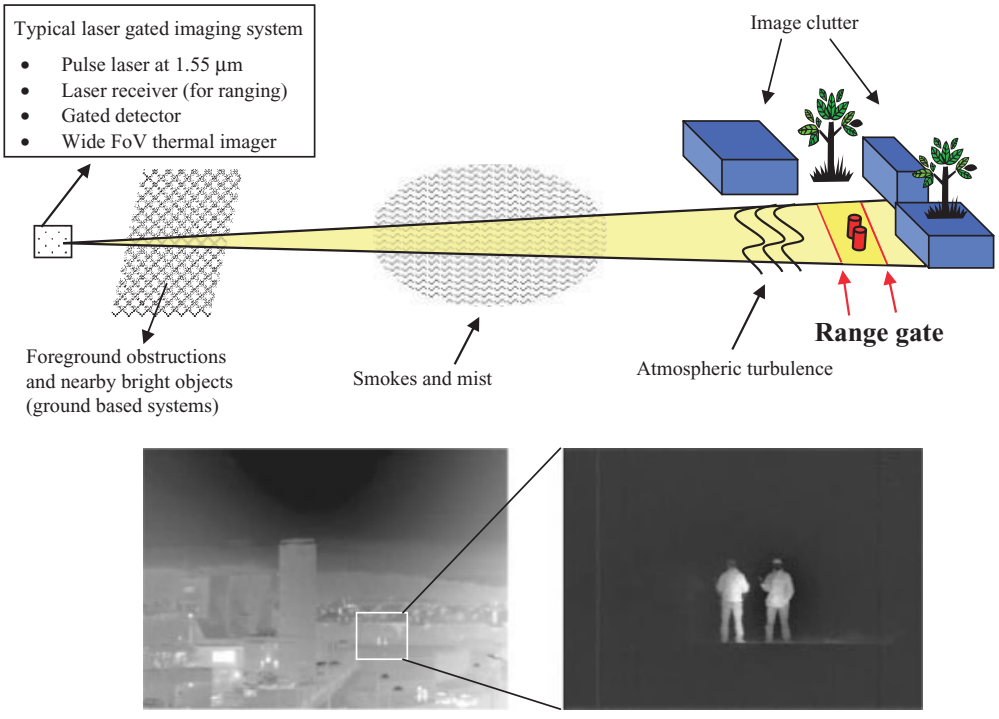

Figure 10.13 Advantages of laser-gated imaging in conjunction with other sensors along with a typical pair of images [41] (reproduced by permission of SPIE).

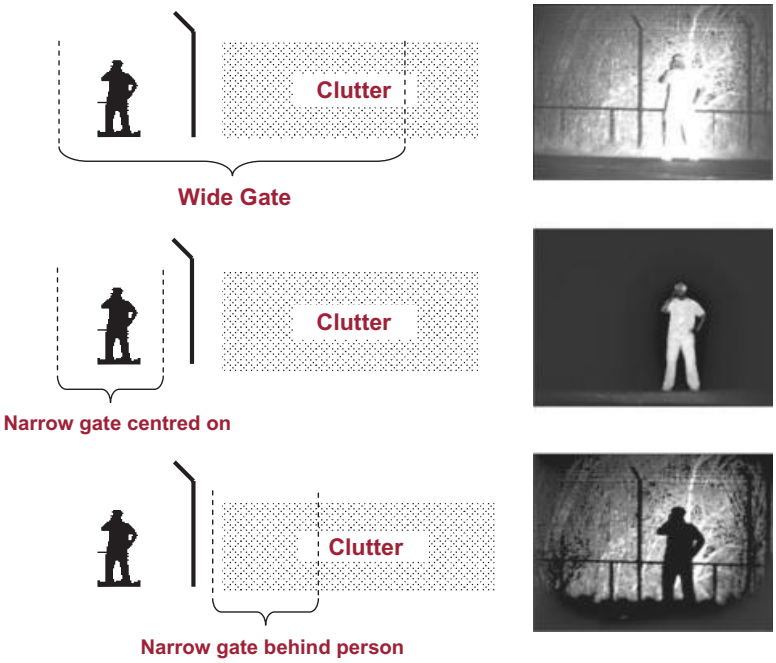

Figure 10.14 Person standing in front of a fence: illustrates how the range gate can be used to simplify the image by removing background clutter or creating a silhouette [41] (reproduced by permission of SPIE).

shows a person standing in front of a fence and illustrates how the range gate can be used to simplify the image by removing background clutter or creating a silhouette.

10.3.3 Summary

LPE from Te-rich solutions is one of the most successful technologies for the preparation of epitaxial MCT of excellent material characteristics. LPE materials are being grown routinely for PV and PC detectors with state-of-the-art performance in the entire 2–18 μm spectral region. The high throughput and high yield have enabled production of high-performance second-generation FPAs at affordable cost. The trend for developing multiple-layer heterojunction structures is toward application of vapor-phase epitaxial techniques. LPE will, however, continue to play a major role in the development of such structures because of its simplicity and maturity. This section has demonstrated the SW and MW applications of Te-rich LPE material, showing excellent image quality and novel effects in SW imaging.

References

1 Yu, T.-C., and Brebrick, R.F. (1994) *Properties of Narrow Gap Cadmium-Based Compounds*, EMIS Datareview Series No. 10 (ed. P. Capper), IEE, London, p. 55.
2 Brice, J.C. (1986) *Prog. Cryst. Growth Charact.*, **13**, 39.
3 Capper, P. (ed.) (1994) *Properties of Narrow-Gap Cadmium-Based Compounds*, INSPEC/IEE, London.
4 Capper P. (2005) *Bulk Crystal Growth of Electronic, Optical and Optoelectronic Materials* (ed. P. Capper), John Wiley & Sons, Ltd, Chichester, Chapter 7, pp. 209–240.
5 Capper, P. (1994) *Prog. Cryst. Growth Charact.*, **28**, 1.
6 Scheel, H.J. (1972) *J. Cryst. Growth*, **13/14**, 560.
7 Capper, P., and Gosney, J.J.G. (1981) UK Patent 8 115 911 May.
8 Brice, J.C., Capper, P., Jones, C.L., and Gosney, J.J.G. (1986) *Prog. Cryst. Growth Charact.*, **13**, 197.
9 Schulz-Dubois, E.O. (1972) *J. Cryst. Growth*, **12**, 81.
10 Greenspan, H.P. (1968) *The Theory of Rotating Fluids*, Cambridge University Press, London.
11 Su, C.H., Lehoczky, S.L., and Szofran, F.R. (1991) *J. Cryst. Growth*, **109**, 385.
12 Lu, Y.-C., Shiau, J.-J., Feigelson, R.S., and Route, R.K. (1990) *J. Cryst. Growth*, **102**, 813.
13 Watring, R.A., and Lehoczky, S.L. (1996) *J. Cryst. Growth*, **164**, 474.
14 Liu, W.-S., Wolf, M.F., Edwell, D., and Fiegelson, R.S. (1987) *J. Cryst. Growth*, **82**, 589.
15 Gray, R.T., Larrousse, M.F., and Wilcox, W.R. (1988) *J. Cryst. Growth*, **92**, 530.
16 Capper, P. (2007) *Liquid Phase Epitaxy of Electronic, Optical and Optoelectronic Materials* (eds P. Capper and M. Mauk), John Wiley & Sons, Ltd, Chichester, Chapter 9, pp. 259–287.
17 Baker, I.M. (2006) *Handbook of Electronic and Optoelectronic Materials* (eds S. Kasap and P. Capper), Springer, Heidelberg, pp. 855–885.
18 Reine, M.B. (2001) *Infrared Detectors and Emitters: Materials and Device* (eds P. Capper and C.T. Elliott), Kluwer Academic, Boston, Chapter 12, pp. 313–376.
19 Capper, P. (2006) *Handbook of Electronic and Optoelectronic Materials* (eds S. Kasap and P. Capper), Springer, Heidelberg, pp. 303–324.
20 Baker, I.B., Crimes, G.J., Parsons, J.E., and O'Keefe, E.S. (1994) Proc. SPIE, vol. 2269, p. 636.
21 Harman, T.C. (1980) *J. Electron. Mater.*, **9**, 945.
22 Harman, T.C. (1979) *J. Electron. Mater.*, **8**, 191.
23 Astles, M.G. (1994) *Properties of Narrow Gap Cadmium-Based Compounds*, EMIS Datareview series, No. 10 (ed. P. Capper), IEE, London, p. 13.
24 Capper, P. (1994) *Properties of Narrow Gap Cadmium-Based Compounds*, EMIS Datareview series, No. 10 (ed. P. Capper), IEE, London, p. 151.
25 Harman, T.C. (1981) *J. Electron. Mater.*, **10**, 1069.
26 Brice, J.C., Capper, P., Easton, B.C., *et al.* (1987) *Semicond. Sci. Technol.*, **2**, 710.
27 Tregilgas, J.H., Dodge, J., Colombo, L., and Liao, P.-K. (1995) MCT Workshop Ext. Abstr.
28 Tower, J.P., Tobin, S.P., Kestigian, M., *et al.* (1995) *J. Electron. Mater.*, **24**, 497.
29 Brebrick, R.F., Su, C.-H., and Liao, P.-K. (1983) *Semicond. Semimet*, **19**, 172–254.
30 Westphal, G.H., Colombo, L., and Anderson, J. (1994) Proc. SPIE, vol. 2228, p. 342.
31 Capper, P., O'Keefe, E.S., Maxey, C.D., *et al.* (1997) *J. Cryst. Growth*, **161**, 104.
32 Astles, M., Hill, H., Blackmore, G., Courtney, S., and Shaw, N. (1988) *J. Cryst. Growth*, **91**, 1.
33 Rudolph, P., Muhlberg, M., Neubert, M., Boeck, T., Mock, P., Parthier, L., Jacobs, K., and Kropp, E. (1992) *J. Cryst. Growth*, **118**, 204.
34 Capper, P., Gower, J., Maxey, C.D., O'Keefe, E.S., Harris, J.H., Bartlett, L., and Dean, S. (1998) *Growth and Processing of Electronic Materials*, IOM Communications Ltd, London.

35 List, R.S. (1993) *J. Electron. Mater.*, **22**, 1017–1025.
36 Johnson, S.M., Rhigher, D.R., Rosbeck, J.P., *et al.* (1992) *J. Vac. Sci. Technol. B*, **10**, 1499.
37 Yoshikawa, M. (1988) *J. Appl. Phys.*, **63**, 1533–1540.
38 Baker, I.M., Crimes, G.J., Ard, C.K., *et al.* (1990) 4th Int. Conf. on Advanced Infrared Detectors and Systems, IEE Conf. Pub. No. 321, p. 78.
39 Beck, J.D., Wan, C.-F., Kinch, M.A., and Robinson, J.E. (2001) Proc. SPIE, vol. 4454, p. 188.
40 Kinch, M.A., Beck, J.D., Wan, C.-F., and Campbell, J. (2004) Proc. Workshop on Phys. Chem. II-VI Materials. *J. Electron. Mater.*, **33/6**, 630–639.
41 Baker, I.M., Duncan, S.S., and Copley, J.W. (2004) Proc. SPIE, vol. 5406, p. 133.

11
The Use of a Platinum Tube as an Ampoule Support in the Bridgman Growth of Bulk CZT Crystals

Narayanasamy Vijayan, Verónica Carcelén, and Ernesto Diéguez

11.1
Introduction

In the semiconductor industry, after the high importance and applications of Si materials and the very well known III-V family compounds such as GaAs, GaN, etc., one could say that the II-VI family compounds based on CdTe are nowadays the next one in the list of strategic semiconductor materials used in many important applications. In this list, $Cd_{1-x}Zn_xTe$ mixed compounds are without any doubt the most important ones, having numerous applications. In these materials, while for a value of Zn 4% the applications are concentrated on the use of a substrate material for the epitaxial growth of (Hg,Cd)Te (MCT) in high-performance IR focal plane arrays, for Zn values in the range of 10% the applications are in the field of gamma and X-ray radiation detectors. We will concentrate our discussions on the 10% Zn concentration that will be termed CZT.

CZT bulk single crystals are used in a variety of applications, such as in medicine, in PET, SPECT, CT, instruments; in security instruments, for isotope detection; in space applications, etc. [1–4]. For these applications, bulk CZT high-quality single crystals are needed, which requires several important characteristics [5]: high resistivity, homogeneous concentration, low density of dislocations, reduced number of Te inclusions, high-quality single crystal, and last but not least a volume size of several square millimeters/centimeters. These characteristics are not easy to be completed taking into account the physical and chemical conditions of the CZT family of mixed compounds.

In fact, the growth of large high-quality CZT crystals is very difficult to obtain, and the defects that appears in a given crystal are related to the crystal growth conditions and to II-VI compound iconicity: multiple grains produced at several nucleation points, striations related to modification of the growth velocity, unsteady fluid flow due to variable temperature gradients, variable dopant concentrations, etc. For these reasons it is a pressing issue to improve the growth conditions in order to increase the amount of high-quality crystal.

As a first consideration, one must take into account the physical and chemical properties of CZT that makes it difficult to obtain large-size high-quality single

Crystal Growth Technology. Semiconductors and Dielectrics. Edited by P. Capper and P. Rudolph
Copyright © 2010 WILEY-VCH Verlag GmbH & Co. KGaA, Weinheim
ISBN: 978-3-527-32593-1

Table 11.1 General properties of CZT materials.

Property	CZT	Comments
Melting point (°C)	1120	[6]
Thermal conductivity (W/cm K)	0.01	[7]
Density (g/cm^3)	5.76	[8]
Resistivity (Ω cm)	4–9 × 10^8	[9]
Hole mobility (cm^2/V s)	56	[10]
Average atomic number	49	[11]
Dielectric constant	11	[12]
Crystal structure	Zinc blende	[13]
Bandgap (eV)	1.57	[14]

crystals and the unusual thermophysical properties that make CZT growth very different from other semiconductor crystals, as is presented in Table 11.1.

Let us comment on some of these special features that must be considered for the CZT crystal-growth process:

a) CZT has a high melt viscosity and low value of thermal conductivity which leads to a Prandtl number, Pr, approximately 0.4, which it is more than an order of magnitude greater than a typical molten semiconductor [15–17]: this value results from a liquid phase that is semiconducting rather than metallic, as is the case of the more common semiconductor melt materials such as Si and GaAs, and as a consequence, the coupling between momentum and heat transport makes the convective heat transfer in the melt significant and much more important than conduction heat transfer under typical growth conditions [15, 16]; at the same time the low thermal conductivity of the CZT solid tends to increase the temperature gradients in the solid with associated thermal stresses in the crystal [15];

b) CZT is a weak material that easily dislocates under the influence of thermal stress [16], although it must be recognized that the incorporation of Zn increases, for example, the shear modulus, which means an increasing stability of Zn-containing alloys [18];

c) The effect of the latent heat and the thermal conductivity are significant, having a large effect in the shape of the solid-liquid interface SLI, which it is more concave as the growth rate increases [16];

d) The incorporation of Zn into CdTe is essential to produce the ternary high-bandgap CZT material with high resistivity, an increased energy of defect formation, and a reduction of dislocations and subgrains, etc. [18]; nevertheless, this positive fact creates at the same time the inconvenient and deleterious effect on the CZT physical properties due to the inhomogeneity concentration of Zn in CdTe as a consequence of its segregation coefficient, which is larger than one, in the range of 1.16 and 1.35 [18]; the consequence of the fact that

CZT is an alloy with this large segregation coefficient is an inhomogeneous Zn distribution in both axial and radial directions, unless some restricted conditions are considered during or after the crystal growth process: for example the use of other elements such as Se or Mn with segregation coefficient in the vicinity of 1 and it has been demonstrated that they improve the quality and homogeneity of the given crystals [18, 19].

Considering the previous comments, the growth of large-size and high-quality CZT crystals is a difficult task, and in fact its yield is not larger than 15% generally claimed for the most important suppliers. For these reasons, any new way that will take into consideration this objective must be fully considered. In this chapter, our aim will be the growth of bulk CZT crystal by the Bridgman method with the use of a Pt tube as the growth ampoule support in order to modify the thermal and growth conditions with the final objective of high-quality large-size homogeneous CZT crystals.

The discussions will be presented in the following three sections: in the first, the importance of controlling the SLI will be briefly discussed in order to understand the importance for crystal growth and its influence in the crystal quality; secondly, other approaches with the use of ampoule support will be presented, and finally the results of the use of Pt as an ampoule support for the growth of bulk CZT crystals will be presented.

11.2
The Importance of the Solid/Liquid Interface

The SLI is an important feature in any bulk crystal that is grown from the melt, which has a strong influence an impact in the properties and the yield of a given crystal. All authors who have studied the SLI claim the importance of the controlled shape of the SLI that drastically influences the compositional homogeneity and the crystalline perfection.

In fact, the shape of the SLI is considered identical to the isotherm shape [20], which coincides with the melting point isotherm [15, 17], and is determined by the energy balance at the crystal/melt front among the latent heat, heat conduction in the solid and in the melt, which is given by the equation $K_s.G_s = K_m.G_m + \rho_s.v.L$, where K_s, K_m are the thermal conductivity; G_s, G_m are the temperature gradients, ρ is the density, and v is the crystal growth rate, subindices m and s are the melt and the solid, respectively. For this reason the control of the SLI is difficult in the case of CZT crystals due to the differences between the thermal conductivities of the melt and the solid. In general, the interface convexity is defined as the interface deformation at the symmetry axis divided by the crystal radius: it has a value or zero for planar interfaces, a shape that is used to minimize the thermal stress [21]; and it has a positive value for slightly convex SLI when seen from the melt, an interface shape that it is desirable in order to improve the grain selection [20], and at the same time to eliminate spontaneous nucleation, which can have a drastic impact on the yield process, as happens in the case of CZT.

There is a strong correlation between the interface curvature and the radial segregation along the interface [22], and in fact in concentrated alloys the curvature of the SLI depends on the local composition, as has been demonstrated on (Ga,In)Sb alloys [23]. This effect has great importance for alloys with a segregation coefficient different from unity, as happens for Zn in the case of CZT materials, and in these cases, the chemical segregation coupled with the thermosolutal convection would lead to huge deformations of the SLI, with interface curvatures that could be even larger than the sample diameter. In this way, an interesting aspect is the possibility to mark the SLI, which has been carried out in the case of conductor or semiconductor melts by the application of temporal electrical pulses during the growth process, followed by revealing the marked interface with a metallography process [22].

Another important aspect is the relation between the shape of SLI and the defects that appear as a consequence of this shape. A concave SLI will produce twins, multiple grains, undesirable defects at the walls of the ampoule followed by its propagation towards the center of the crystals [15], a feature that currently happens in CZT bulk crystal, unless precise control interface is considered; while a convex isotherm will lead to a convex SLI, often producing the best crystallinitywith a high percentage of single-crystal material, and suppresses any parasitic nucleation coming from the ampoule wall [20, 24]. Nevertheless, when the segregation phenomenon takes place in a given composition, a flat isotherm is desirable [24].

There are several ways to promote a given interface shape during Bridgman growth, and probably the best one is to design an adequate thermal environment, as has been simulated very recently and applied to the growth of CZT crystals [16, 25]. If the furnace design control is essential for promoting a given interface shape [17], other complementary approaches are also very important that significantly influence the thermal distribution, such as: a given support structure of the ampoule that contains the melt during the growth by Bridgman method, an approach that will be discussed in the next section; the use of external vibrational arrangements with electromagnetic vibrators that produce an increase of the temperature near the SLI compared with nonvibrational fluid avoiding constitutional supercooling effects, recently applied for alloys [26]; the use of pyrolitic boron nitride pBN crucibles that display steeper axial temperature gradients and promote convex SLI shapes in the growth of CZT crystals, but at the same time would create larger radial temperature gradients that could lead to higher dislocations density [15]; by contrast, for the same CZT material, the SLI in a given graphite crucible would exhibit a more concave shape with respect to the melt, and at the same time the axial thermal gradient through the crystal would increase as the growth proceeds, PBN crucibles having the advantage that they flatten the SLI shape in the case of CZT crystal growth.

For all the reasons noted above, it is extremely important to control of the shape of the SLI in the growth of CZT bulk crystals to obtain large grain size with homogeneous composition. The crystal-growth conditions are essential parameters to control, but the thermal environments are probably the most critical parameter to take into account.

11.3
Approaches for Crystal Growth Using Ampoule Support

In order to control the SLI one must taken into account the thermal environments, and in consequence the use of any kind of heater shield and/or an ampoule support in the methods of growing crystals from the melt. In fact, during recent decades, the idea of using a crucible base cooling as a heat sink to promote a nucleation point and/or to facilitate the growth process it has been deeply employed in the growth of bulk crystals from the melt and from the vapor. In consequence in both of the two most popular methods, Czochralski CZ and Bridgman BR method of growing large crystals, this approach has been widely applied. In general, several experimental solutions have been used: a metal support as a heat sink, an actively cooled stainless steel, water-cooled and air-cooled jets, radiation channels to promote favorable interface shapes, etc. In the forthcoming sections a summary of some approaches will be given that have been used as crucible base cooling either as a cold finger or as ampoule support, with the main objective of: (i) producing a nucleation point at the beginning of the growth process with a successful seeding and in consequence a more favorable SLI shape, and (ii) creating the experimental conditions during the whole process of growth in order to improve the SLI interface, going to a slightly convex SLI shape as is required from a theoretical point of view in all of the crystal-growth processes. Figure 11.1 shows the several experimental approaches that will be discussed in the next sections.

a) Cockayne *et al.* [27] proposed crucible base cooling in CZ crystal growth applied to oxide crystals (Figure 11.1a), using a gas coolant during the CZ growth in order to improve the crystal diameter for materials by transporting the heat away from the SLI, or in order to develop shallow radial temperature gradients in the molten state; the consequence of the modification of the thermal field by this way is the reason for the changes in the radial temperature gradients and the final goal of improving the SLI from initial planar to slightly convex shape. In the same way and years later, the group of Derby [28] simulated the

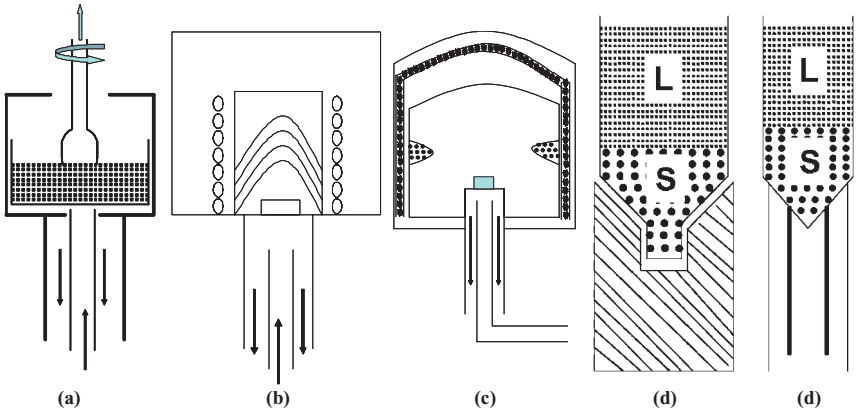

Figure 11.1 Different configurations of the ampoule support.

effect of the pedestal heat transfer on the flow in the melt, demonstrating that in a CZ melt, the heat lost through the pedestal strongly affects the flow in the melt, coming to the conclusion that more heat leaves the melt from the crucible bottom as the thermal conductivity of the pedestal increases.

b) Another approach is the well-known heat exchanger method HEM with a long history in crystal growth, although recently it has been revitalized. In this method (Figure 11.1b), the growth process is carried out in a closed chamber where the crucible containing the melt is cooled in a controlled manner by the use of a cold finger located in the bottom of the crucible [29–36]. The list of materials grown by HEM is rather large: sapphire [29, 30], BGO [31], multicrystalline Si [32], mixed fluorides [33] tungstates [35], etc. In this approach a convex freezing isotherm is produced during the crystal growth, a precise control of the temperature gradient that is necessary for the crystal growth being the most critical point and in consequence the ingot obtained normally contains large numbers of bubbles and striations along the whole ingot due to the temperature isotherms, which represents a problem when doped crystals are required.

c) In the 1980s bulk HgI_2 crystals mainly used for X- and gamma-radiation detectors were grown from the vapor phase [37, 38]. The crystal process was successfully carried out using an experimental approach where an indented ampoule forming a pedestal was used to locate a metallic support acting as a cold finger as is shown in Figure 11.1c, considering the low temperature of the process in the range of 100 and 150 °C, and taking into account the physical and chemical properties of HgI_2. The cold metallic finger acting as heat exchanger is in contact with the external part of the pedestal of the ampoule, and in this area the seed selection of the crystallization process takes place that sometimes requires temperature oscillations of the cold finger [37, 38]: the process is continued by slightly modifying both the temperature of the cold finger and the several lateral furnaces. Other authors have improved experimentally and modified this approach and/or have simulated the growth process successfully applied for bulk HgI_2 crystals [39–43].

d) In Bridgman method all the approaches have been used, they have considered either the heat extraction from the ampoule support in different ways, or the heat exchange in the SLI through different geometries of movable or static heat shields as is shown in Figure 11.1d. For the growth of GaSb crystals, Koai *et al*. [20] simulated the effect of a given ampoule support, and they claim that a more useful approach uses a concentric cylinder design in order to promote the interface convexity. In this way, several papers have been published by Derby and coworkers [25, 44] where the effect of several geometries and material support have been simulated, with a clear objective to control the shape of the SLI; when it is applied to CZT, the effect of given ampoule supports will enhance the flow of heat in the axial direction while minimizing radial heat flow, and in consequence the convex interface is promoted with a better crystal

yield compared with other designs. In summary, with this brief list of experimental approaches one can demonstrate the prime importance to take into consideration a precise control of the SLI.

11.4 Results and Discussions

As has been described in the previous section, the use of any kind of cold finger in crystal growth is not new, and the experimental results described in this section will go along the same line. In a recent paper, Kuppurao and Derby [25] where the effects of different ampoule supports have been simulated in the case of the growth of CZT bulk crystals by the Bridgman method, they analyzed the role that can be played by the use of a given support with thermal conductivity large enough compared with the material to be grown. They came to the conclusion that a given geometry of a shallow cone sitting upon a composite support made of a highly conducting core and a less conducting outer sheath promotes the axial heat transfer while inhibiting the radial thermal flow, and hence a convex SLI shape toward to the melt would be created.

Bearing in mind the above consideration, the objective of this chapter has been to have a practical approach to this idea, and to propose the use of a Pt tube as a fixed support for the ampoule that contains the melt, and in the same way to study the effect in the quality and grain size of CZT crystals grown by the Bridgman method.

The Bridgman geometry that has been used is shown in the Figure 11.2, where a schematic representation is presented. The vertical Bridgman furnace has a single zone, in the central region of which is located the ampoule for the CZT growth. The furnace is a commercial Kanthal Type R – made of Si/Mo alloy, with a length of 60 cm and an internal diameter of 40 cm. At the axial center of the furnace is located the control thermocouple of type S, taking into account that the extreme point of this thermocouple is exactly located at the same position of the Si/Mb alloy of the furnace for a better control of the furnace temperature.

In the present experimental study, a quartz ampoule was used that has an inner diameter of 23 cm, a thickness of 2 mm and a length of 30 cm with the length of the solid CZT material being 7.5 cm. The tip of the ampoule has a nearly flat shape, and it is closed on the upper part with a quartz rod. In this growth process, the ampoule is supported by a quartz tube of the same diameter and a length of 35 cm, and by a Pt tube with an external diameter of 23 cm, a thickness of 1 mm, and a length of 20 cm, which is inserted in this quartz tube. Simultaneously, the ampoule is mounted on its central part on another quartz tube of 10 cm of external diameter and a thickness of 1 mm where three thermocouples, A, B and C, are located on its interior in order to measure the temperature profile, covered with alumina wool to avoid any air convection. Another 6 thermocouples are located at the exterior part of the quartz ampoule in a circular position with a distance of 1.5 cm, in such a way that the SLI could be controlled at each moment. It is worth noting that the

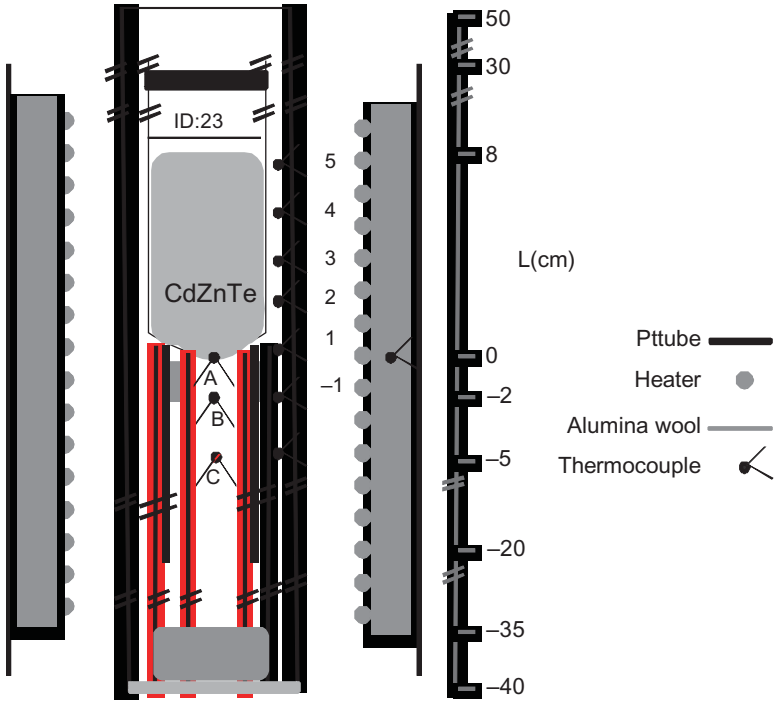

Figure 11.2 Schematic representation of the Bridgman furnace with a Pt support.

thermocouples 1–5 are in front of the melt/solid CZT at a given time, whereas the thermocouple named –1 is at 1.5 cm down the tip of the ampoule. Using this geometry, three temperature gradients could be measured at any time: the axial temperature gradient during growth by some of the 1–5 thermocouples, the radial temperature gradient by thermocouples 1 and A, and the effect of the Pt support on the axial temperature gradient measured by thermocouples A–C. Finally, if one considers that the temperature measured by any of the given 1–5 thermocouples coincide with the melting point, one can be able to know the evolution of the SLI with time can be determined, that is, the growth rate of the material.

All this process is controlled automatically as is shown in the Figure 11.3, where a photo of the real experimental is presented. At the same time, the temperatures of all the thermocouples used for measuring the temperature located in the sections described above are registered automatically on a computer, by using the experimental facilities of the system PICOLOG.

In Figure 11.4 a photo is presented that shows the experimental arrangement described above: the growth ampoule, the Pt support, and some of the thermocouples; A–C and 1–5. In this figure it can be seen that all of the lateral thermocouples located circularly around the ampoule are fixed with Pt wire.

The quartz ampoule for the growth experiment is prepared in four steps: cleaning of the ampoule, graphitization of the ampoule, starting materials introduced

Figure 11.3 View of the whole furnace assembly.

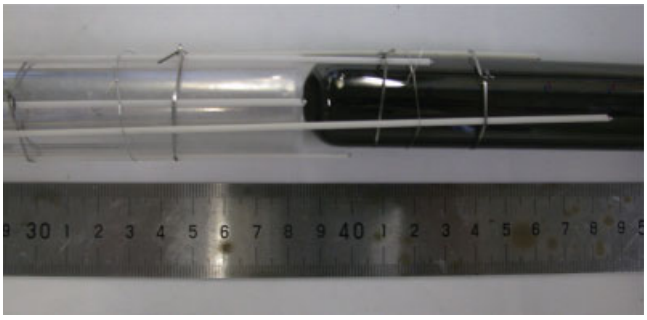

Figure 11.4 Filled ampoule tied to a Pt support.

in the ampoule, and closing of the ampoule. The cleaning process of the quartz ampoule is carried out in four steps: first, the ampoule is rinsed with trichloroethylene, acetone and methanol; them it is filled with aqua regia (HCl and nitric acid in a volume ratio of 3 : 1) and left for 24 h; then the ampoule is cleaned with distilled water and filled with hydrofluoric acid and left for 3 h; finally, the ampoule is rinsed with distilled water. In order to prevent the sticking of the melt to the quartz wall, a graphitization process must be carried out, which it is done using 500 µl acetone at 1000 °C. Later, the starting materials are introduced within the ampoule in the following order: Te, Zn, and Cd, the process being carried out in a clean atmosphere. Finally, the ampoule is held at a vacuum better than 10^{-6} torr for 24 h before being sealed. The whole process of the preparation of the growth ampoule takes three days, and it is worth noting that this process is kept constant for all the. After this process, the ampoule is introduced into the furnace with no time delay.

The complete crystal-growth process takes about 25 days in three steps: heating process, growth process and cooling process. (i) The heating process is carried out taking into consideration the melting point of the starting elements in the following way: it begins with a ramp of 50 °C/h from RT to 500 °C, remaining at this temperature for 12 h, followed by a second heating process at a rate of 50 °/C in order to reach 900 °C and being held at this temperature other 12 h; then 1000 °C is attained at a ramp of 50 °C/h and held for 12 h, and finally the maximum temperature of 1150 °C is reached in 4 h. This maximum temperature is used when the composition of $Cd_{1-x}Zn_xTe$ (x = 15%) is prepared, considering a superheating of about 15 °C. At this temperature, a process of oscillation of the furnace is carried out by oscillating the furnace from the vertical position +15 ° and −15 ° (clockwise and counter-clockwise) for about 30 min, automatically for 60 cycles. Both experimental approaches of oscillation and superheating were executed with the objective of obtaining a good mixture and breaking down of the Te clusters, respectively, as an important step for the production of large grain size in CZT bulk crystals. (ii) The growth process is done by the displacement of the ampoule at a rate of 0.4 mm/h. Afterwards, the (iii) cooling process is carried out in the following way: from the maximum temperature of 1150 to 900 °C a first cooling process is done at a rate of 5 °C/h, followed by 10 °C/h to 750 °C, and finally a rate of 25 °C/h to room temperature.

The radial and axial temperature gradients throughout the growth process have been taken using the thermocouples described above, these values being the average of two experiments in both sets with and without Pt tube, and considering that the position of the SLI interface is indicated for the thermocouple that shows the melting point temperature. As can be seen in Figure 11.5, both axial and radial temperature gradients increase during a given experiment when Pt is used as a support of the ampoule, this increase being a factor of two for the values of the radial temperature gradients, whereas in the case of the increases in the axial temperature gradient the factor is about 50%. These results must be due to the Pt

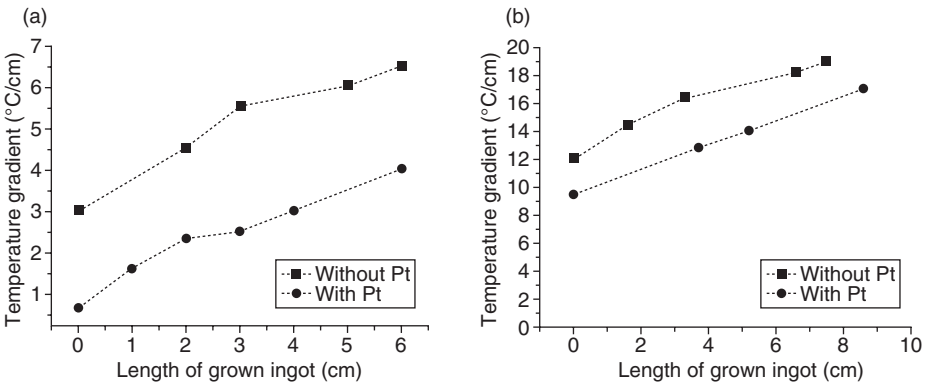

Figure 11.5 Radial (a) and axial (b) temperature gradient of the grown ingot with and without the Pt tube.

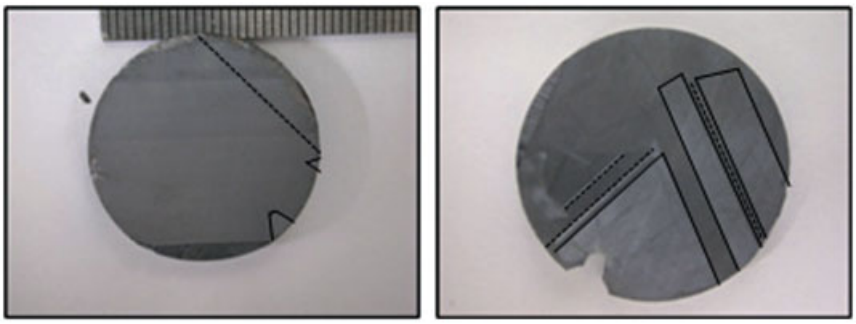

Figure 11.6 Wafers of the grown ingot with and without a Pt support.

tube, and the increasing length of the solid during the growth process considering the difference in thermal conductivity between solid and melt, taking into account that the Bridgman geometry will give a constant temperature gradient.

Otherwise, it is worth noting that in both cases the values of the radial and axial temperature gradients for the experiments using Pt tube support are larger than the experiments without Pt tube support. These results could be of great interest because it could indicate that constitutional supercooling can be avoided in the case of using a Pt tube as a support in the growth ampoule, and in consequence a flatter SLI could be produced with no roughness and in consequence better crystal quality. In fact, the analysis of the crystal quality performed on both set of samples that have been obtained with experiments carried out with and without Pt tube as a support in the growth ampoule gives interesting results. Figure 11.6 presents the results of two etched wafers in order to reveal the grains [45] that have been selected from similar positions in different ingots. In this figure it can be seen that the wafer removed from the ingot grown with a Pt tube as a support in the growth ampoule show larger grain size and nearly a single grain, while the wafer from the experiment carried out without a Pt tube shows several grains and a couple of large twins, taking into account that both experiments have been carried out on similar experimental conditions. So, the enhanced large grain size must be attributed to the use of the Pt tube.

In order to examine the crystal structural quality in both set of samples, high-resolution X-ray rocking curves were performed on the (110) polished surface with the same geometrical conditions using a Bruker D500 HR X-ray diffractometer, at is shown in Figure 11.7, where in both cases a single peak with high intensity appears. The FWHM value is 0.12° for the sample where the Pt tube was used, where a larger value of about 1° is obtained for the samples where the Pt tube was absent. While in the first case a single peak with low value of the FWHM indicates a good crystal quality, the broader peak in the second case is a consequence of poorer quality and a crystallinity deterioration when the Pt tube is absent. This last result, together with the appearance of many grains and twins clearly indicates the advantage of using a Pt tube as a support in the growth ampoule.

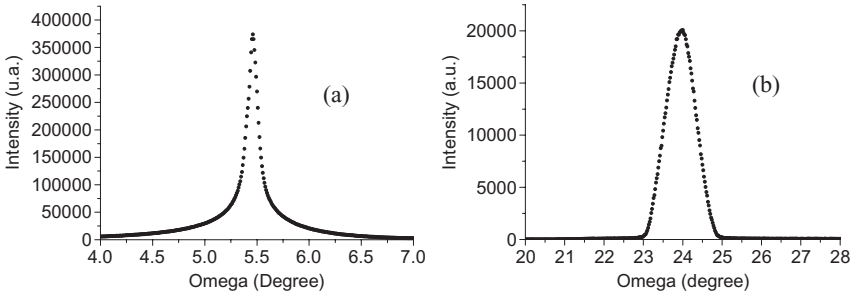

Figure 11.7 Recorded rocking curve for the ingot grown with (a) and without (b) a Pt tube.

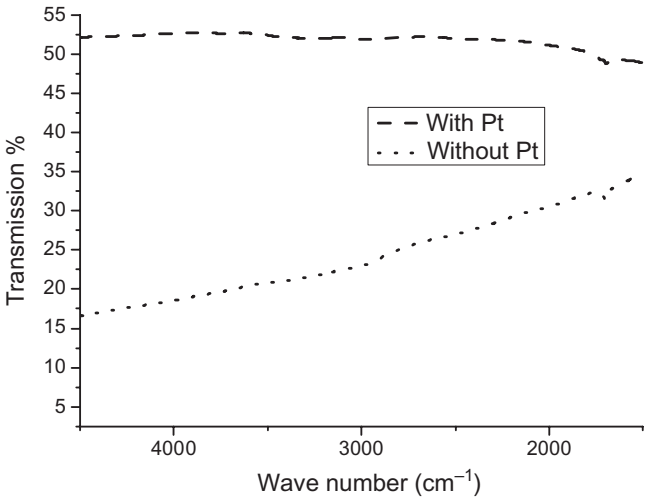

Figure 11.8 FTIR spectrum with and without a Pt support.

With the same objective of quality comparison of both samples, infrared (IR) transmittance spectrum was recorded. As can be observed in Figure 11.8, the spectrum obtained in the wave number region of 1000–5000 cm^{-1} shows a larger transmittance for the sample obtained from the experiment carried out with a Pt tube with a value larger than 65%, while the transmittance value for the sample grown without a Pt tube as an ampoule support shows a rather lower value. Once more this result supports the advantage of using the Bridgman geometry with a Pt tube, which enhances the crystalline perfection of the grown ingot.

Another important topic in the preparation of CZT samples for detector applications is the Zn concentration along the grown ingot. As its segregation coefficient is larger than one, this concentration reduces along the growth direction. Considering this, we have analyzed the Zn concentration by EDX analysis along the radial and the axial direction. In Figure 11.9, the Zn concentration along the radial direction is shown for two samples (1,2) that have been selected from similar positions at 10 and 20 cm, respectively, from the tip of the ampoule, both ingots

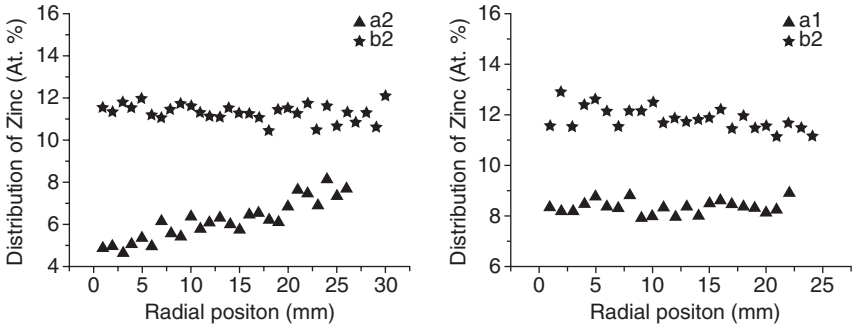

Figure 11.9 Grown samples analyzed by EDX (with and without a Pt tube).

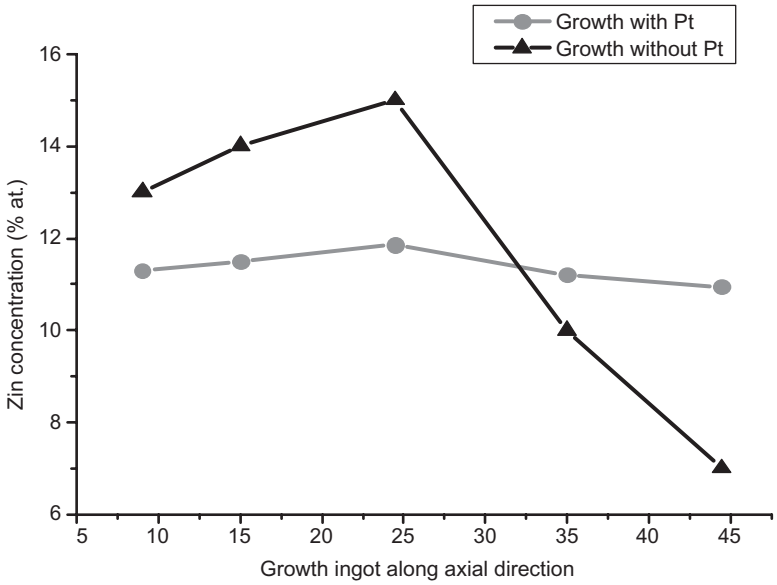

Figure 11.10 Zinc segregation along the axial direction.

being grown, respectively, without (a) and with (b) a Pt tube as a support for the growth ampoule. In the samples where the Pt support tube was used, the Zn concentration is higher and slightly more uniform that the experiment carried without Pt tube, that is, the SLI is relatively flatter and more uniform for the experiments using a Pt tube.

At the same time, the Zn concentration along the axial growth direction was analyzed in both experiments and the results are shown in the Figure 11.10, for CZT ingots of a total length of 45 mm. In the ingot that has been grown without a Pt tube, the Zn concentration follows a similar behavior, as has been published several times as a consequence of a segregation coefficient of about 1.35, with a maximum Zn concentration around 10–20% of the solidified fraction, decreasing

to the end of the ingot. By contrast, when a Pt tube is used as a support on the growth ampoule, the Zn concentration remains practically constant along the analyzed ingot.

The presence of surface defects was examined by scanning electron microscope (SEM). The sliced specimens of the crystals grown with and without Pt were subjected to etching analyses using H_2O:HNO_{3cc}:HF_{cc}:$AgNO_3$ solution and then the surface (110) was gently cleaned with soft tissue paper. The micro defects formed on the surface is mainly due to the nature of growth parameters like supersaturation, temperature, impurities and mass and heat transport processes. The etch pits were observed on the surface of the both the samples and the etch pits density (EPD) was calculated. The EPD was found to be 6×10^4 (with Pt) and 1.2×10^5 cm^{-2} (without Pt) respectively [47].

11.5 Conclusions

In summary, the use of a Pt tube as a support in the growth ampoule in CZT crystals seems to be a good alternative for getting the correct environmental conditions to enlarge the grain size, to improve the crystal quality of the samples, and to get a more uniform Zn concentration along the whole ingot. In fact, this geometrical arrangement is not unique, and other geometrical approaches can be proposed, and probably be used with more success. Not only geometrical approaches, but other support metals with larger or lower thermal properties will be of great importance. Just as one example, in Table 11.2, the thermal properties of other materials are shown, although they must be considered in comparison with Pt, quartz, mullite and alumina, which are very well known materials used in daily experimental growth processes. In this table we can appreciate the strong difference in these properties of the different materials that can be used as a cold

Table 11.2 Physical properties of different materials.

Material name	Melting point T_m (K)	Thermal conductivity W/(m K)	Emissivity (ε)	Density ρ ($g\,cm^{-3}$)	Specific heat C_p ($J\,g^{-1}\,K^{-1}$)	Thermal expansion coefficient α ($\times 10^{-6}\,K^{-1}$)	Ref.
Quartz	1510	2.8	0.6	5.71	0.4184	11	[25, 46]
Graphite	4200	25–470	0.98	1.3–1.95	0.71–0.83	6.5	[48–50]
pBN	2073	2	0.500	1.95–2.22	1.97	2.6	[51, 52]
Platinum	2042	71.6	0.97	21.45	0.13	9	[53–55]
Lanthanum	1193	13	0.282	6.15	0.195	12.1	[56–58]
Molybdenum	2896	139	0.18	10.28	0.251	4.8	[54, 56, 59]
Ceramic	2023	231	0.69–0.45	3.9	0.85	8	[60, 61]
Tungsten	3695 K	170	0.27	19.35	0.13	4.5	[54, 62–64]

finger instead of platinum. In addition, an experimental arrangement with movement of the Pt tube following the SLI will enhance without doubt the possibility of obtaining good crystalline quality of the grown ingot, an approach that it is being done in our laboratory, and future results in the growth of bulk CZT crystals will be published soon.

Acknowledgments

This work was partially supported by the following Projects: MAT2009-08582 of the Spanish "Ministerio de Educación y Ciencia"; FP7-SEC-2007-01 of the European Commission, and Contract number 14240/00/NL/SH of the European Space Agency. One of the authors, VC, is thankful to the Ministry of Education and Science, Spain for the financial support. Author NV is grateful to the Department of Science and Technology, Govt. of India for providing the BOYSCAST fellowship.

References

1 Duff, M.C., Hunter, D.B., Burger, A., Groza, M., Buliga, V., and Black, D.R. (2008) *Appl. Surf. Sci.*, **254**, 2889–2892.
2 Zeng, G.L., and Gagnon, D. (2004) *Phys. Med. Biol.*, **49**, 2257–2271.
3 Shikhaliev, P.M. (2006) *Phys. Med. Biol.*, **51**, 4267–4287.
4 Budtz-Jorgensen, C., Kuvvetli, I., Westergaard, N.J., Jonasson, P., Reglero, V., Eyles, C., and Neubert, T. (2001) *Astrophys. Space Sci.*, **276**, 281–289.
5 Pandey, A., Yeckel, A., Reed, M., Szeles, C., Hainke, M., Muller, G., and Derby, J.J. (2005) *J. Cryst. Growth*, **276**, 133–147.
6 Li, W.W., Sang, W.B., Min, J.H., Yu, F., Zhang, B., and Wang, K.S. (2002) *Semicond. Sci. Technol.*, **17**, L55–L58.
7 Carcelén, V., Vijayan, N., Rodríguez-Fernández, J., Hidalgo, P., Piqueras, J., Sochinskii, N.V., Pérez, J.M., and Diéguez, E. (2009) *J. Cryst. Growth*, **311**, 1264–1267.
8 Jung, I., Krawczynski, H., Burger, A., Guo, M., and Groza, M. (2007) *Astropart. Phys.*, **28**, 397–408.
9 Li, G.Q., Jie, W.Q., Gu, Z., Yang, G., Wang, T., and Zhang, J.J. (2004) *J. Cryst. Growth*, **265**, 159–164.
10 Suzuki, K., Seto, S., Sawada, T., and Imai, K. (2002) *IEEE Trans. Nucl. Sci.*, **49**, 1287–1291.
11 Liu, J., Mandal, K.C., and Koley, G. (2009) *Semicond. Sci. Tech.*, **24**, 045012–045016.
12 Li, Q., and Jie, W.Q. (2006) *Semicond. Sci. Tech.*, **21**, 72–75.
13 Li, G.Q., Zhang, X.L., Jie, W.Q., and Hui, C. (2006) Thermal treatment of detector-grade CdZnTe. *J. Cryst. Growth*, **295**, 31–35.
14 Xu, Y.D., Jie, W.Q., Sellin, P., Wang, T., Liu, W.H., and Zha, G.Q. (2009) Perumal veeramani and chris mills. *J. Phys. D Appl. Phys.*, **42**, 035105–035110.
15 Gasperino, D., Bliss, M., Jones, K., Lynn, K., and Derby, J.J. (2009) *J. Cryst. Growth*. doi: 10.1016/j.jcrysgro.2009.01.141
16 Kuppurao, S., Brandon, S., and Derby, J.J. (1995) *J. Cryst. Growth*, **155**, 93–102.
17 Lun, L., Yeckel, A., Reed, M., Szeles, C., Daoutidis, P., and Derby, J.J. (2006) *J. Cryst. Growth*, **290**, 35–43.
18 Triboulet, R. (2005) *Phys. Status Solidi*, **2**, 1556–1565.
19 Mycielski, A., Kowalczyk, L., Gał zka, R.R., Sobolewski, R., Wang, D., Burger, A., Sowi'nska, M., Groza, M., Siffert, P., Szadkowski, A., Witkowska, B., and Kaliszek, W. (2006) *J. Alloys Compd.*, **423**, 163–168.
20 Koai, K., Sonnenberg, K., and Wenzl, H. (1994) *J. Cryst. Growth*, **137**, 59–63.

21 Fu, T.W., and Wilcox, W.R. (1980) *J. Cryst. Growth*, **48**, 416–424.

22 Duhanian, N., Duffar, T., Marin, C., Dieguez, E., Garandet, J.P., Danten, P., and Guiffant, G. (2005) *J. Cryst. Growth*, **275**, 422–432.

23 Barat, C., Duffar, T., and Garandet, J.P. (1998) *J. Cryst. Growth*, **194**, 149–155.

24 Jones, C.L., Capper, P., Gosney, J.J., and Kenworthy, I. (1984) *J. Cryst. Growth*, **69**, 281–290.

25 Kuppurao, S., and Derby, J.J. (1997) *J. Cryst. Growth*, **172**, 350–360.

26 Fengquan, W., Shiyu, C., Deping, H., Bingbo, W., and Guangji, S. (1994) *J. Mater. Sci.*, **29**, 3997–4000.

27 Cockayne, B., Plant, J.G., and Vere, A.W. (1972) *J. Cryst. Growth*, **15**, 167–170.

28 Derby, J.J., Atherton, L.J., and Gresho, P.M. (1989) *J. Cryst. Growth*, **97**, 792–826.

29 Lu, C.W., and Chen, J.H. (2001) *J. Cryst. Growth*, **225**, 274–281.

30 Lu, C.W., and Chi, P.H. (2007) *J. Cryst. Growth*, **42**, 1259–1265.

31 Lu, C.W., Chen, J.H., and Hu, L.J. (2002) *Model. Simul. Mater. Sci.*, **10**, 147–162.

32 Ouadjaout, D., Gritli, Y., Zair, L., and Boumaour, M. (2005) *Rev. Energ. Ren.*, **8**, 49–54.

33 Ocafrain, A., Chaminade, J.P., Viraphong, O., Cavagnat, R., Couzi, M., and Pouchard, M. (1996) *J. Cryst. Growth*, **166**, 414–418.

34 Peters, R., Krankel, C., Petermann, K., and Huber, G. (2008) *J. Cryst. Growth*, **310**, 1934–1938.

35 Rahab, H., Ouadjaout, D., Manseri, A., Viraphong, O., and Chaminade, J.P. (2007) *J. Cryst. Growth*, **303**, 629–631.

36 Wang, J.H., Kim, D.H., and Huh, J.S. (1997) *J. Cryst. Growth*, **174**, 13–18.

37 Schieber, M., Schnepple, W.F., and Van Den Berg, L. (1976) *J. Cryst. Growth*, **33**, 125–135.

38 Van Den Berg, L., Schnepple, W.F., Ortale, C., and Schieber, M. (1977) *J. Cryst. Growth*, **42**, 160–165.

39 Louchev, O.A. (1994) *J. Cryst. Growth*, **142**, 124–128.

40 Manoel, E.R., Custodio, M.C.C., Guimaraes, F.E.G., Bianchi, R.F., and Hernandes, A.C. (1999) *Mater. Res.*, **2**, 75–79.

41 Dieguez, E., and Olmos, P. (1995) *Insulating Materials for Optoelectronics: New Developments*, World Scientific, Singapore.

42 Martinez Laso, L., Marin, J., Oller, J.C., and Olmos, P. (1996) *IEEE Trans. Nucl. Sci.*, **43**, 202–206.

43 Roux, A., Fedoseyev, A., and Roux, B. (1993) *J. Cryst. Growth*, **130**, 523–532.

44 Derby, J.J. (1995) *Science and Technology of Crystal Growth*, Kluwer Academic Publishers, Netherlands, pp. 97–110.

45 Carcelen, V., Vijayan, N., Dieguez, E., Zappettini, A., Zha, M., Sylla, L., Fauler, A., and Fiederle, M. (2008) *J. Optoelect. Adv. Mater.*, **10**, 3135–3140.

46 Chao, C.K., and Hung, S.Y. (2003) *J. Cryst. Growth*, **256**, 107–115.

47 Carcelen, V., Vijayan, N., and Dieguez, E., Crystal Growth and Design (Article submitted).

48 http://www.azom.com/details.asp?ArticleID=1630.

49 http://phycomp.technion.ac.il/~david/thesis/node3.html.

50 http://www.infrared-thermography.com/material-1.htm.

51 http://www.matweb.com/search/datasheettext.aspx.

52 http://www.performancematerial.com/pbn_thermal.htm.

53 http://www.unctad.org/infocomm/anglais/platinum/characteristics.htm.

54 http://www.omega.com/literature/transactions/volume1/emissivitya.html.

55 http://en.wikipedia.org/wiki/Coefficient_of_thermal_expansion.

56 http://www.chemnetbase.com/periodic_table/elements/lanthanum.htm.

57 http://www.webelements.com/lanthanum/physics.html.

58 http://books.google.com/books.

59 http://www.webelements.com/molybdenum/physics.html.

60 http://www.coleparmer.com/techinfo/techinfo.asp.

61 http://www.substech.com/dokuwiki/doku.php.

62 http://environmentalchemistry.com/yogi/periodic/W.html.

63 http://www.webelements.com/tungsten/physics.html.

64 http://www.electro-optical.com/bb_rad/emissivity/matlemisivty.htm.

Part III
Dielectrics

Crystal Growth Technology. Semiconductors and Dielectrics. Edited by P. Capper and P. Rudolph
Copyright © 2010 WILEY-VCH Verlag GmbH & Co. KGaA, Weinheim
ISBN: 978-3-527-32593-1

12
Modeling and Optimization of Oxide Crystal Growth

Svetlana E. Demina, Vladimir V. Kalaev, Alexander T. Kuliev, Kirill M. Mazaev, and Alexander I. Zhmakin

12.1
Introduction

Most oxide crystals have high melting temperatures that hamper experimental investigation of the growth process and the involved heat-transfer mechanisms *in situ* and, thus, optimization of the process. Attempts are made to exploit the *physical* simulation of crystal growth. For example, silicon oil was used to imitate the flow in the Czochralski (Cz) crucible [1, 2], including a baroclinic instability resulting in cold plumes detaching from the crystal and descending towards the crucible bottom. Gorbunov *et al.* [3] exploited a eutectic mixture InGaSn with a melting point of 285 K as the model substance and achieved the simultaneous equality of four criteria (the Grashof number, Hartmann number and two Reynolds numbers, determined by the "crystal" and the crucible rotation rates) in the physical experiment to that in industrial 200-mm Si growth. Interface shapes in Cz growth of yttrium aluminum garnet (YAG) single crystals were simulated using $NaNO_3$ [4].

Still, it is impossible to simulate issues such as the Marangoni effect, the shear stress, caused by the gas flow over the melt surface [5], the interface curvature, or growth of semitransparent crystals. Only numerical simulation can both provide insight into the intricate interaction of the different heat transfer mechanisms and aid the optimal design of the equipment and/or growth process [6–8]. The necessary stages of the model development are verification (an assessment of the correctness of the model implementation) and validation (an assessment of the adequacy of the model to the real world) [9, 10].

The chapter presents the simulations of the growth of some oxide single crystals from the melt using the numerical model coupling the global heat transfer analysis in the whole furnace with a detailed description of heat transfer in the hot zone that accounts for the specular Fresnel reflection at crystal surface; the model was implemented in the software package CGSim [11].

Crystal Growth Technology. Semiconductors and Dielectrics. Edited by P. Capper and P. Rudolph
Copyright © 2010 WILEY-VCH Verlag GmbH & Co. KGaA, Weinheim
ISBN: 978-3-527-32593-1

12.2 Radiative Heat Transfer (RHT)

In the growth of opaque semiconductors [8] when all surfaces reflect diffusively and all solids and fluids present in the growth process are either opaque or transparent, computation of gray radiation using configuration (view) factors (a "surface-to-surface" model) [12] is all one needs. In the case of semitransparent crystals such as oxides[1)] when some surfaces exhibit specular reflection and/or the crystal or the melt should be treated as a semitransparent medium one should account for all the relevant optical phenomena such as absorption, scattering, refraction, diffuse and specular reflection.

Internal radiation through the crystal depends largely on the absorption coefficient and the refractive index that determine the radiative heat transfer inside the crystal and reflection and refraction of radiation at the crystal side surface, respectively. The absorption coefficient of a melt is generally much greater than that of a crystal, allowing the former to be considered opaque (that is, however, not true for fluoride melts [14]). Therefore, radiation is crucial in heat removal from the melt through the crystal/melt interface; RTH within the crystal can even lead to instability of the crystallization front [15]. As the refractive index is large, multiple reflections and refractions at the crystal side surface occur. The side surface of single crystals is specular rather than diffusely reflective.

Oxide crystals have a small thermal conductivity in both the solid and liquid phases, thus heat transfer is determined by convection in the melt and by radiation in the crystal. The radiative heat transfer through the crystal renders the interface deeply convex toward the melt as has been well known for forty years [16], while the effect of convection is two-fold. If the rotationally driven forced convection dominates, the maximum of the thermal flux distribution along the interface on the side of the melt is at the center of the interface and convection tends to deflect the interface toward the crystal [17]. Otherwise, if buoyant convection is dominant, then the maximum of the thermal flux is shifted to a tri-junction line and the crystallization front is deflected toward the melt. An increase of the absorption coefficient of a crystal and a decrease of the absorption coefficient of a melt diminish the convexity of the crystal/melt interface toward the melt. The control of the interface shape is one of the most important tasks in crystal growth since large interface deformation results in significant thermal stress that stimulate defect formation [7, 18, 19].

An increase of the crystal radius or/and the crystal rotation rate during growth leads to a change of the flow pattern in the melt, which is accompanied by the interface inversion (the term "reversion" is also used sometimes [20]), that is, the abrupt change of the crystal/melt interface from convex to concave toward the melt when forced convection becomes dominant [21]. A study of the growth striations revealed that the spontaneous interface inversion frequently occurs at the

1) The growth of oxide crystals is the oldest industrial process: it was started over a century ago with ruby and sapphire [13].

shoulder–trunk transition and could be accompanied by the appearance of the "filamentary" defects seen as hollow ducts under the microscope [20]. The critical Reynolds number Re^c at which the interface inversion occurs decreases with the optical thickness, if the latter is relatively small [22]. The interface inversion could also be used as an intentional ("controlled") action on the growth process aimed at keeping the crystallization interface as flat as possible [20]–the thermal stresses are minimal near Re^c [21].

The influence of the crystal length is manifested mainly through the variation of the melt depth that can result in a change of melt flow pattern. It is just this aspect of the problem that was given the most attention in simulating oxide growth (see, for example [22–27]).

However, although the inversion phenomenon is hardly possible in the absence of the volume radiation transport, internal radiation plays an auxiliary role in traditional Czochralski growth characterized by significant temperature gradients in the melt, the shape of the crystal/melt interface being mainly controlled by convection. In contrast, in the low thermal gradients Czochralski (LTG Cz) growth the natural convection is weak and can not be responsible for the observed variations of the crystallization front. Flow patterns in the melt are not changed significantly with crystal length; thus, variations of the crystallization front during the growth are determined mainly by internal radiation [28], which in turn depends on the absorption coefficients of the crystal and melt, the refractive index of crystal, and the reflective properties of the crystal side surface.

Thus, semitransparency of the crystal significantly influences both the global heat transfer in the growth facility and the shape of the crystal/melt interface [26, 29]. The intensity and the distribution of the radiative heat flux from the interface can markedly change with the crystal length during the growth in crystals with a high refractive index, the effect of the total inner reflection being responsible for this variation [28]. Other effects are also observed. For example, incorporation of microbubbles at the phase boundary [30] results in the appearance of a diffusively transmitting and scattering boundary that could lead to nonmonotonic temperature variations in optical crystals [31].

Simulation of multidimensional RHT in a participating medium remains thus far difficult. Detailed comparison with experimental data [32] shows that the diffusion approximation of RHT via an additional "radiative" thermal conductivity (the Rosseland approximation [14]) used, for example, in Ref. [33] to study CaF_2 melt growth, does not describe correctly the temperature distribution in the growth system. Thus, advanced models, such as the discreet exchange factor method [34] or the characteristics method [35, 36] are needed.

Different assumptions and approximations are used in considering RHT problems in crystal growth. In an effort to study the effects of internal radiation within YAG and gadolinium gallium garnet (GGG) crystals, Xiao and Derby who simulated Czochralski growth using steady axisymmetric formulation [26, 27] assumed that the crystal is totally transparent and its side surface is covered by a vanishingly thin opaque film. This simplification frequently is claimed to be valid for real systems due to the parasitic deposition of impurities. Indeed, wall deposits are

usual in the chemical vapor deposition reactors (and often are semitransparent, increasing considerably the complexity of computations of RHT if the film thickness is comparable to the radiation wavelength), but this phenomenon is hardly a universal one in melt crystal-growth processes. An opaque crystal surface means that the refractive index of the crystal has no effect on the heat transfer. These restrictions were removed in Ref. [37], yet the crystal absorption coefficient was taken as constant and quite large since for solution of the radiant transport equation the P1-approximation was used.[2)] A similar approach was used also in [21, 23, 39] to study the effect of the absorption coefficient on the crystal/melt interface for lithium niobate and garnets. The spectral dependence of the absorption coefficient is often approximated by a simple two-band model when the medium is assumed to be either totally transparent or opaque [40].

Galazka *et al.* [41] studied the role of the internal radiation on the heat transfer during growth of YAG single crystal by the Czochralski method using the band approximation model with an effective thermal conductivity based on the detailed (with the wavelength step of 50 nm in the spectral range from 0.8 μm to 4.2 μm) measurements of the transmission characteristics of the crystal at room temperature; the experimental data was exploited to calculate the so-called Planck and Rosseland mean absorption coefficients α_P and α_R that enter into expressions for the optical thickness $\tau = L\sqrt{\alpha_P \alpha_R}$ and the "nongrayness" factor $\eta = L\sqrt{\alpha_P / \alpha_R}$.

Banerjee and Muralinder [42] simulated Czochralski growth of YAG crystals accounting for solid, liquid and gaseous phases in the furnace using axisymmetric formulation and a single domain approach, wherein the physical parameters are allowed to vary in accordance to the individual phases [42]; the S_N discrete ordinate method was exploited for the RHT computation. A few comments are due. The assumption that the gas density is constant is the well-known Boussinesque approximation that is known (as well as the extended Boussinesque approximation allowing for the temperature dependence of the transport coefficients) to be rather inaccurate when temperature variations are comparable with the average temperature [43]. The authors' note on the "possibility of the superheating of the crystal beyond its melting point" reflects, probably, a numerical artifact – the authors themselves state that "in physical terms superheated regions in a crystal will undergo melting". In contrast to supercooled liquid that is in a metastable state (with high deviation from the crystallization temperature – for example, almost 40 °C for water, up to 20 K in bismuth germanate (BGO)growth [44]), the superheated solid could not exist[3)] since there is no energetic barrier for melting. Moreover, at the temperature of the solid below, but close to the melting tempera-

2) The absorption coefficient of oxide crystals is wavelength and temperature dependent; for example, its value for sapphire at 1073 K is four times greater than at room temperature at $\lambda = 4\,\mu m$ and 75 times greater at $\lambda = 5\,\mu m$ [38].

3) Stricly speaking, the nonequilibrium state of solid with the temperature higher than the melting temperature could be attained with ultrahigh-speed heating that could be provided, for example, by an intense laser irradiation or a shock-wave loading [45].

ture, the phenomenon of *premelting* (appearance of the thin liquid layer at the solid surface) is observed for a wide class of materials including water, semiconductors, and metals [46].

The effects of the specular reflection in the crystal-growth modeling have drawn less (compared to semitransparency issues) attention so far. The first computations accounting for this phenomenon were done for BGO crystal growth in LTG Cz system using the characteristics method [36]. The shape of the crystal/melt boundary has been fixed; self-consistent computations have been reported in Ref. [28]. It was shown that incorporation of the specular reflection from the crystal inner surface, first from its conical part (and thus taking into account the large value of the refractive index for BGO crystal), allows one to reproduce the cardinal change of the interface shape with the crystal length observed in the experiments.

12.3 Numerical Model

Numerical study of bulk crystal growth requires the use of either moving computational grids or a regeneration of the grid. The latter approach is attractive since usually the characteristic time of the crystal shape changes is large compared to the hydrodynamic/thermal time and one can consider a set of stationary problems corresponding to the different stages of the growth process.

The local crystal-growth problem should be linked to the thermal environment in the furnace (global model) [7] that includes heat conduction in the solid parts of the furnace, the gas flow and the radiative heat transfer. Thus, the problem has been divided into two subproblems:

- **Global heat transfer:** Heat transfer in the whole crystal growth furnace in the domain D^{global};
- **Local (hot zone) heat transfer:** Heat transfer in the crystal, melt and the surrounding solid parts of the growth furnace D^{local}.

The global problem is usually solved in axisymmetric formulation, while either a 2D or 3D local problem is considered, depending on the nature of the melt flow. A self-consistent solution of the problem is obtained via the iteration of the solution of the heat-transfer problems in the domains $D^{\text{global}} \setminus D^{\text{local}}$ and D^{local}, coupled by the thermal conditions on the common boundary ∂D; at the first iteration the solution is sought in the domain D^{global} with some simplifying assumption on the nature of heat transfer in the hot zone. Sometimes one global iteration is sufficient if the thermal boundary conditions on ∂D are written in terms of heat fluxes [47].

The temperature distribution inside the solid block obeys the usual scalar equation of thermal conductivity; the thermal conductivity tensor should be used for anisotropic materials. The source term is zero except in the electrically conducting

elements (such as the metal crucible wall) of the furnace with RF heating where the AC electric current in the coil induces the eddy current that determines the heat power release.

Radiative heat exchange between opaque surfaces through a nonparticipating fluid can be accounted for under the assumption of gray-diffusive surface radiation. Computation of the configuration factors (view factors) with account for the shadowing effect is described in detail in [12]. The melt and gas flows are governed by the Navier–Stokes equations for the incompressible fluid and by low Mach number (hyposonic) equations. The radiation problem has been solved under the following assumptions: the melt is opaque, the crucible wall is diffusely reflective, while the crystal side surface and the free melt surface can be either diffusely or specularly reflective. Local and global subproblems are matched along the free melt surface and the crystal/melt interface.

Formulation of the radiative heat-transfer problem and the modified for this case relation that determine the crystallization front position can be found in Ref. [48] along with the solution method for axisymmetric case; the numerical method for RHT has been extended to the 3D case in Ref. [49].

12.4 Results and Discussion

The model was implemented in the CGSim software package [11]. The properties of the crystals and their melts used in computations are listed in Table 12.1.

Table 12.1 Properties of oxide crystals and their melts.

Property	Unit	Al_2O_3	$Y_3Al_5O_{12}$	$Bi_4Ge_3O_{12}$
Crystal				
Refractive index	–	1.77[a)]	1.8[b)]	2.15
Melting temperature	K	2327	2243	1323
Thermal conductivity	$W\,(m\,K)^{-1}$	5	8.0	1.2
Specific heat	$J\,(kg\,K)^{-1}$	1430	800	1000
Latent heat of fusion	$kJ\,(kg)^{-1}$	1407	455.4	156
Melt				
Density	$kg\,m^{-3}$	3030	3600	6650
Specific heat	$J\,(kg\,K)^{-1}$	1260	800	300
Thermal conductivity	$W\,(m\,K)^{-1}$	2.05	4.0	0.78
Emissivity	–	0.33	0.3	0.8
Dynamic viscosity	$kg\,m^{-1}\,s^{-1}$	0.057	0.046	0.044

a) At 532 nm.
b) The dependence of the refractive index of YAG crystal on the wavelength is rather weak in the spectral range 500–2000 nm and could be fitted by the Sellmayer relation [50].

12.4.1 Sapphire

Numerous application of sapphire crystals based on its strength, durability, scratch resistance, electrical and optical properties range from optical windows (for wrist watches, sensors and lasers as well as for aircrafts, unmanned aerial vehicles and missiles – both as viewports in forward looking infrared systems [enhanced vision systems in civil applications] and as domes) to electronics (substrates for GaN-based light emitting diodes, high electron mobility [HEMT] AlGaN transistors, silicon-on-sapphire [SoS] ultra-CMOS transistors, cell-phone antenna switch devices – the total volume is about 5 million wafers [2″ equivalent] in 2007); single-crystal sapphire fibers are used in sensor applications and for transmitting laser radiation in surgery.

Sapphire single-crystal fibers are grown by edge-defined film-fed growth (EFG)[51] or by laser-heated pedestal growth (LHPG) [52, 53]; the first method allows higher productivity by pulling a number of fibers simultaneously, while the second provides the lowest signal loss due to the absence of a crucible that can contaminate the fiber.

Several methods are used to grow bulk sapphire crystals: Czochralski, Kyropoulos (and its modification – Musatov), Bridgman, Verneuil methods, heat exchanger and gradient solidification methods, EFG (also referred to as the Stepanov method); recently a new technique based on Czochralski and Kyropoulos methods has been proposed – "sapphire growth technique with micropulling and shoulder expanding at cooled center" [38, 54].

Simulation of the Kyropoulos growth was performed for the industrial furnace used at Monocrystal Inc. (Stavropol, Russia). The global problem involves heat conduction, radiative heat transfer, laminar gas flow and turbulent flow of the sapphire melt; the local 3D domain includes the crystal, melt, the crucible and a gas region around the crystal.

Computed velocity vectors and the temperature distribution for the standard (left) and modified (right) Kyropoulos growth facility used are shown in Figure 12.1. Modification results in the melt-flow structure change from a two-vortex one to a single vortex and in significant reduction of the temperature gradients within the crystal [47, 55].

The distribution of the modulus of the temperature gradient at the intermediate growth stage along with the photo of the grown crystal are shown in Figure 12.2.

The instant temperature distribution and the melt velocity vectors at the surface before seeding for the optimal melt flow regime are shown in Figure 12.3.

12.4.2 Yttrium Aluminum Garnet

Yttrium aluminum/lutetium garnets (from the Middle English word *gernet* meaning "dark red") $Y_3Al_5O_{12}$ (YAG)/$Lu_3Al_5O_{12}$ (LuAG) as well as their solid solution $(Lu_xY_{1-x})_3$ Al_5O_{12} (LuYAG) are some of the most important materials for

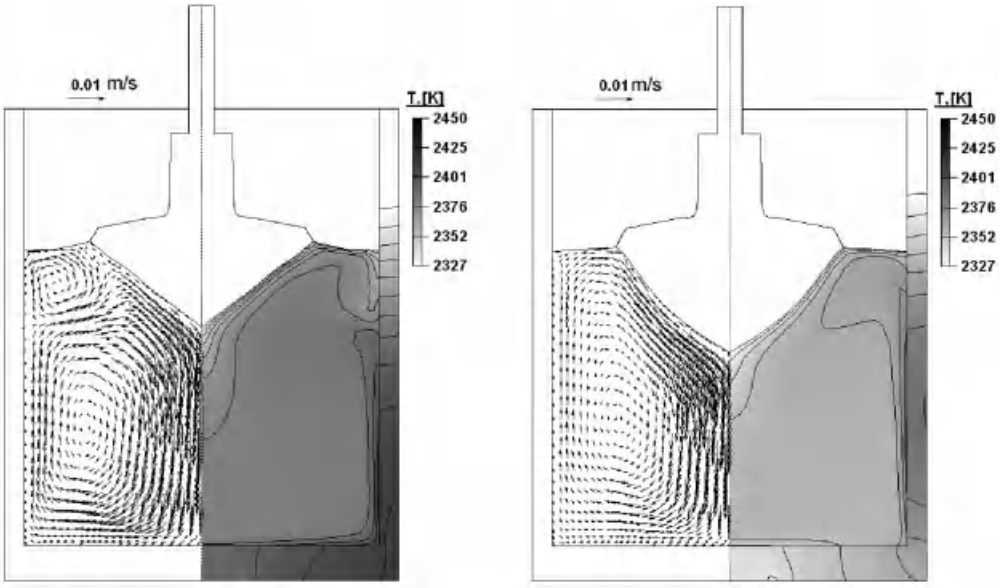

Figure 12.1 Velocity vectors and temperature distribution for the standard (left) and modified (right) Kyropoulos growth facility.

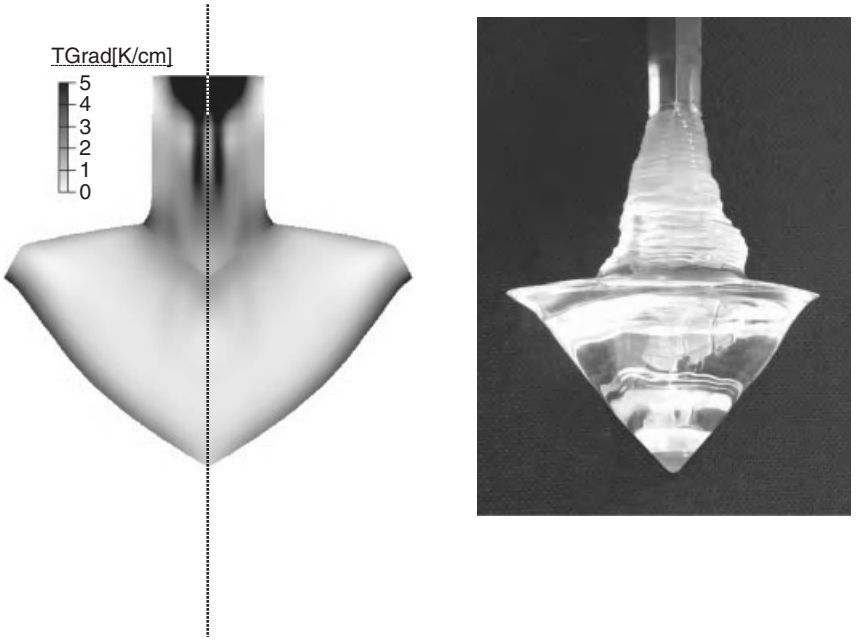

Figure 12.2 Temperature gradient (left); grown crystal (right).

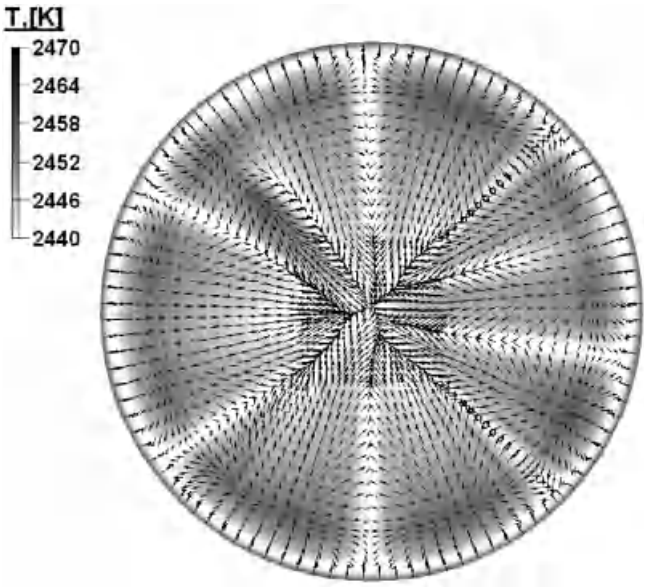

Figure 12.3 Optimal instant temperature distribution and melt velocity vectors at the surface.

quasi-three-level laser hosts [50, 56]. In spite of the emergence of the superior laser host material for the same spectral range such as yttrium orthovanadate YVO_4 (Nd:YVO_4 lasers are characterized by the lower lasing threshold [57]) and successful fabrication of the polycrystalline Nd:YAG ceramic lasers [58],[4] there is a great need for high-quality large YAG single crystals for use as laser hosts and for acousto-optoelectronic devices. Note that the laser output power is approximately proportional (assuming the same structure of the electromagnetic modes) to the volume of the host crystal. Nowadays, solid-state lasers using YAG single crystals doped by either Nd^{3+} or Yb^{3+} with CW output power in the kW range are commercially available [56].

The quality of the crystal is crucial for its operation as a laser host. Internal strain in the grown boule is the main cause of optical distortion for laser rods longer than a few tens of millimeters (the quality of the end finish is dominant for the shorter rods). YAG crystals are very brittle and cracks are frequently observed during the growth/cooling that are attributed to the microscopic voids or particle inclusions rich in Nd (solute precipitates [19]) that act as stress concentrators [61].

4) The advantage of the ceramic polycrystalline material with very low porosity and narrow grain-boundary width is its ability to reach a high neodymium concentration: incorporation of large amounts of Nd into a YAG single crystal is difficult due to the low segregation coefficient – neodymium dopants are located in the dodecahedral sites instead of yttrium and the large ionic radius of Nd^{3+} is not favorable for such substitution [59] since lattice distortion occurs [60].

Long (about 1 m) thin (0.3–1.0 mm) fiber-shaped single crystals are grown by either micropulling-down method (μ-PD) [62] or by the LHPG [63]. Bulk YAG crystals usually are grown by Czochralski method [21, 59] in argon [60, 63], nitrogen [20] or nitrogen-oxygen [50] atmosphere, the growth occurs in the [111] direction (the Bridgman growth method [64], the temperature gradient method (TGM) [65], and the EFG in a vacuum [66, 67] are also used). Frequently, a highly strained core formation in the central part of the crystal is observed due to growth with a convex interface [20, 59] and/or facet formation along the melt/crystal interface during growth (facets are parallel to [211] and [110] crystallographic planes [27, 60, 63]). This core area usually has a columnar shape; sometimes gaseous bubble inclusions are registered [68]. It is known that increasing thermal gradients or reducing the convexity of the interface decreases the facet area [69]. Facetting also occurs in the growth of single crystal YAG by the Bridgman method [64]; the low temperature gradient (LTG) method avoids the formation of facet in the center of the crystal, but three facets remain at the peripheral edge of the crystal with interface parallel to singular [211] crystallographic planes [65]. The level of strain in the crystal, especially in the shoulder region, is higher for the large cone angle (defined as the angle formed between the centerline and the crystal shoulder [27]) during necking, forcing one to prefer rather small cone angles (about 35°) in practice [60].

The surface tension coefficient is very weakly and depends on the temperature for the YAG melt [27, 63], thus the Marangoni effect can usually be neglected (this effect can be significant in other garnets, for example, it was taken into account in the recent 2D (axisymmetric) computations of the garnet melt flow in the Czochralski system [70]).

The Czochralski furnace used at Exiton Ltd. is described elsewhere [71]. The temperature distribution in the hot zone along with the velocity vectors for melt and gas (right) are shown in Figure 12.4 for crystal heights of 35 (left) and 100 mm (right). The variation of the temperature within the gas domain allows also estimation of the density variation since the static pressure in the low Mach number flows is essentially constant.

The distribution of the module of the temperature gradient in the melt for these crystal positions shown in Figure 12.5 permits one to qualitatively assess the crystal regions (in the vicinity of the triple point) that probably will display high strain. The experimental position of the crystallization front indicated in these figures shows satisfactory reproduction of growth by the numerical model.

12.4.3
Bismuth Germanate (BGO)

Bismuth germanate $Bi_4Ge_3O_{12}$ (BGO) with eulythine structure is a good scintillator material used in many fields such as high-energy physics, nuclear physics, space physics, medicine (high-energy calorimetry, low background spectroscopy, positron emission tomography, etc.).

If in Cz growth the crystallization front shape is poorly controlled, a highly curved interface will occur resulting in a higher level of strain in the crystal and

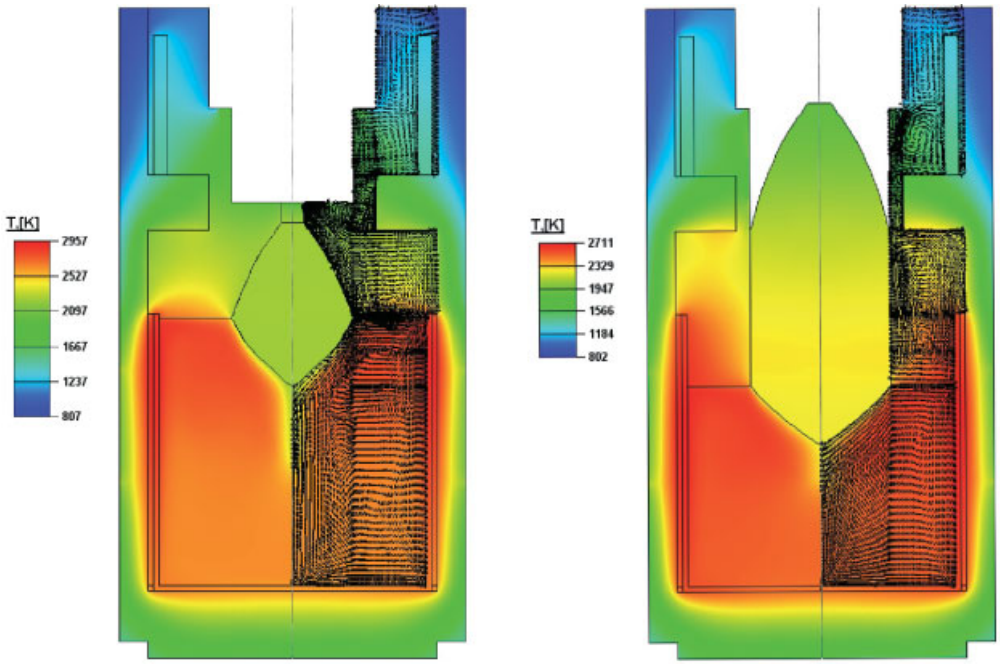

Figure 12.4 Temperature distribution in the furnace (left) and velocity vectors (right) for the crystal height 35 mm and 100 mm.

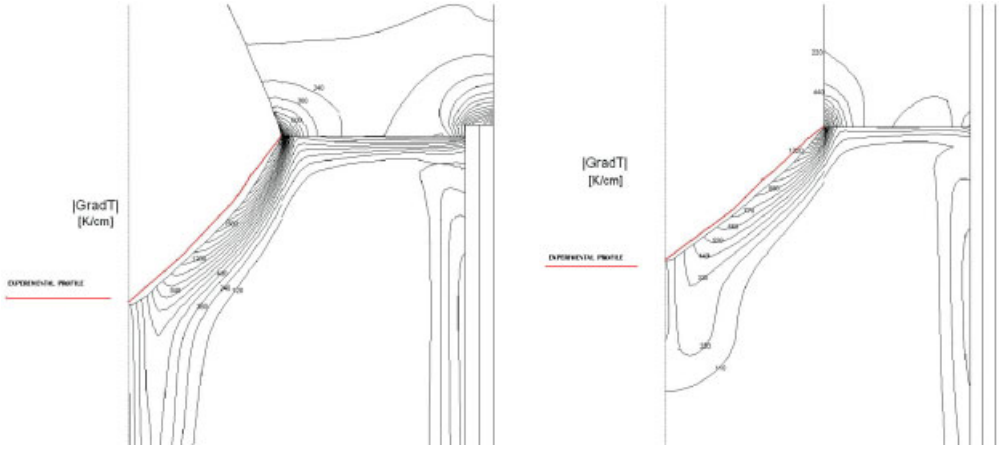

Figure 12.5 Temperature gradient distribution in the melt for the crystal height 35 mm and 100 mm.

early growth cessation (and, thus, low melt usage) due to the contact of the crystal tip with the crucible base [72].

Numerical simulations confirmed by the experimental data (the temperature distribution measured by a pyrometer, the power of the RF heater, the interface shape) showed that introduction of an additional heater (e.g., flat disk made of nickel) under the crucible significantly increases the uniformity of the temperature distribution within the melt and reduced the interface curvature. The computational results are presented for the whole furnace in Figure 12.6 and for the melt domain in Figure 12.7 for a crystal of height 80 mm.

Computations showed that the effect of the bottom heater on the flow structure and interface shape is stronger for the later stages of growth [72]. Further details can be found in the cited paper.

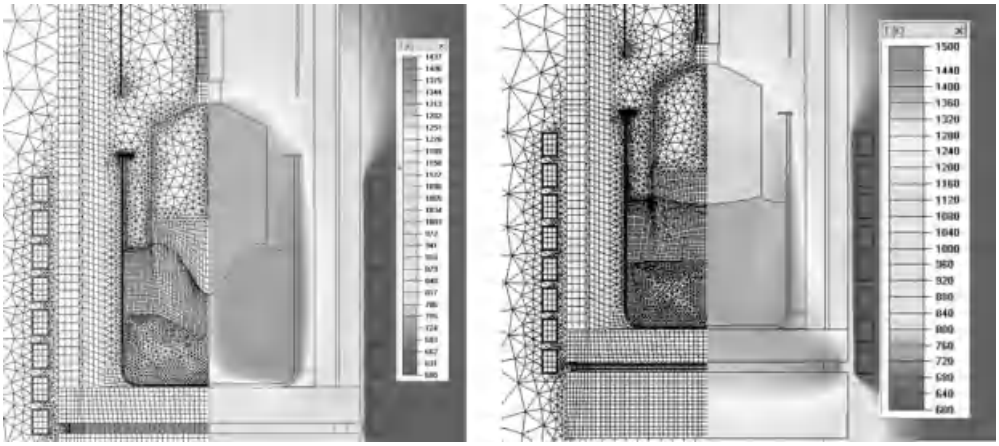

Figure 12.6 The computational grid and the temperature distribution in the furnace without (left) and with (right) an additional bottom heater.

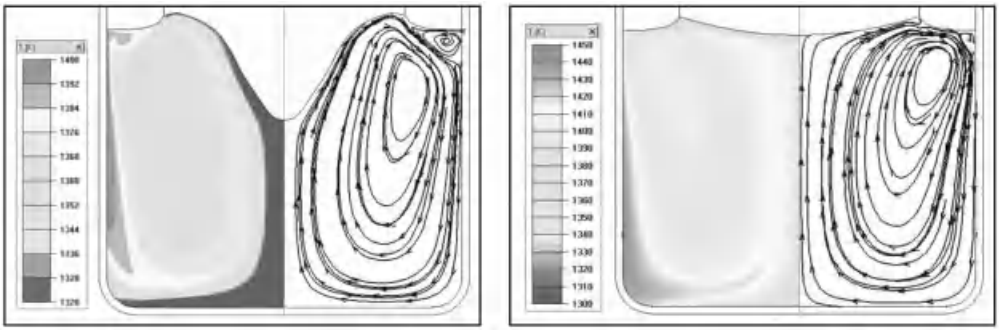

Figure 12.7 The temperature distribution within the melt and streamlines without (left) and with (right) an additional bottom heater.

The results of the simulation of growth of BGO crystals with different (sillenite) structure $Bi_{12}GeO_{20}$ that has by far the greater absorption coefficient in the near-IR spectral range have been reported in Ref. [73].

BGO crystals demonstrate the pronounced tendency towards faceting of the solidification front due to kinetic effects associated with growth in the different lattice directions. As a result, the crystal/melt interface can be composed of both rounded and faceted parts that significantly degrade the properties of crystals. Two strategies are commonly used. In the first high temperature gradients are applied to suppress facets formation and to achieve the rounded or even flat crystal/melt interface, while in the second, in contrast, very low temperature gradients are maintained so that the solidification front would be fully faceted. For the results of the simulation of the facet formation in BGO crystals and on the effect of internal radiation in the crystal on this process see Ref. [48] and references therein.

12.5 Conclusions

Numerical simulation of oxide single-crystal growth from the melt is considered. Specific features of these crystals (internal radiative heat transfer, the specular reflection from the crystal surface, the low thermal conductivity of both the crystal and the melt) are accounted for in the numerical model that has been applied to the growth simulation of selected oxide crystals. Validation of the model predictions proves that numerical simulation can be used as a reliable tool for the process and equipment optimization.

Acknowledgments

The authors are grateful to V.M. Mamedov and V.S. Yuferev for fruitful discussions.

References

1 Hintz, P., Schwabe, D., and Wilke, H. (2001) *J. Cryst. Growth*, **222**, 343.
2 Teitel, M., Schwabe, D., and Gelfgat, A. Yu. (2008) *J. Cryst. Growth*, **310**, 1343.
3 Gorbunov, L., Pedchenko, A., Feodorov, A., Tomzig, E., Virbulis, J., and von Ammon, W. (2003) *J. Cryst. Growth*, **257**, 7.
4 Schwabe, D., Sumathi, R.R., and Wilke, H. (2004) *J. Cryst. Growth*, **265**, 494–504.
5 Kalaev, V.V., Evstratov, I.Yu., and Makarov, Yu.N. (2003) *J. Cryst. Growth*, **249**, 87.
6 Dupre, F., and van den Bogaert, N. (1994) *Handbook of Crystal Growth* (ed. D.T.J. Hurle), Elsevier Science, pp. 875–1010.
7 Lan, C.W. (2004) *Chem. Eng. Sci.*, **59**, 1437.
8 Meyappan, M. (ed.) (1995) *Computational Modeling in Semiconductor Processing*, The Artech House, pp. 363.
9 Oberkampf, W.L., and Trucano, T.G. (2002) *Prog. Aerospace Sci.*, **38**, 209.
10 Roache, P.J. (1998) *Verification and Validation in Computational Science and*

Engineering, Hermosa Publishers, Albuquerque.
11 STR (2003) http://www.str-soft.com/products/CGSim/ (accessed 31 March 2009).
12 Dupret, F., Nicodéme, P., Ryckmans, Y., Wouters, P., and Crochet, M.J. (1990) *Int. J. Heat Mass Transfer*, **33**, 1849.
13 Scheel, H.J. (2003) in H.J. Scheel and T. Fukuda (eds) *Crystal Growth Technology*, John Wiley & Sons, Ltd, Chichester, pp. 3–14.
14 Barvinischi, F., Duffar, T., and Santaller, J.L. (2000) *J. Optoelectron. Adv. Mater.*, **2**, 327.
15 Yuferev, V.S., and Vasiliev, M.G. (1987) *J. Cryst. Growth*, **82**, 31.
16 Cockayne, B., Chesswas, M., and Gasson, D.B. (1969) *J. Mater. Sci.*, **4**, 450.
17 Mokruchnikov, P.W. (1999) *Cryst. Res. Technol.*, **34**, 1169.
18 Asadian, M., Seyedein, S.H., Aboutalebi, M.R., and Maroosi, A. (2009) *J. Cryst. Growth*, **311**, 342.
19 Klapper, H. (2010) *Springer Handbook of Crystal Growth* (eds G. Dhanaraj, K. Byrappa, V. Prasad, and M. Dudley), Springer, online chapt. 4, pp. 1–24.
20 Xu, T., Wu, Z., Zhen, Q., Zhou, J., Zhang, S., Xie, S., Xu, G., and Hang, C. (1993) *Chin. Phys. Lett.*, **11**, 698.
21 Kobayashi, M., Tsukado, T., and Hozawa, M. (2002) *J. Cryst. Growth*, **241**, 241.
22 Hayashi, A., Kobayashi, V., Jing, C., Tsukado, T., and Hozawa, M. (2004) *Int. J. Heat Mass Transfer*, **47**, 5501.
23 Kobayashi, M., Hagino, T., Tsukado, T., and Hozawa, M.J. (2002) *J. Cryst. Growth*, **235**, 258.
24 Kopetsch, H. (1990) *J. Cryst. Growth*, **102**, 505.
25 Schwabe, D., Sumathi, R.R., and Wilke, H. (2004) *J. Cryst. Growth*, **265**, 494.
26 Xiao, Q., and Derby, J.J. (1993) *J. Cryst. Growth*, **128**, 188.
27 Xiao, Q., and Derby, J.J. (1994) *J. Cryst. Growth*, **139**, 147.
28 Yuferev, V.S., Budenkova, O.N., Vasiliev, M.G., Rukolaine, S.A., Shlegel, V.N., Vasiliev, Ya.V., and Zhmakin, A.I. (2003) *J. Cryst. Growth*, **253**, 383.
29 Brandon, S., and Derby, J.J. (1991) *J. Cryst. Growth*, **110**, 500.
30 Binoiu, O., Duffar, T., Theodore, F., Santaller, J.L., and Nicoara, I. (2000) *J. Optoel. Adv. Mat.*, **2**, 474.
31 Linhart, J. (2002) *Cryst. Res. Technol.*, **37**, 849.
32 Molchanov, A., Hilburger, U., Friedrich, J., Finkbeiner, M., Wehrham, G., and Müller, G. (2002) *Cryst. Res. Technol.*, **37**, 77.
33 Nicoara, I., Nicolov, M., Pusztai, A., and Vizman, D. (1998) *Cryst. Res. Technol.*, **33**, 207.
34 Nunes, E.M., Naraghi, M.H.N., Zhang, H., and Prasad, V. (2002) *J. Cryst. Growth*, **236**, 596.
35 Rukolaine, S.A., Vasiliev, M.G., Yuferev, V.S., and Mamedov, V.M. (2004) *J. Quant. Spectrosc. Radiat. Transfer*, **84**, 371.
36 Rukolaine, S.A., Vasilyev, M.G., Yuferev, V.S., and Galyukov, A.O. (2002) *J. Quant. Spectrosc. Radiat. Transfer*, **73**, 205.
37 Tsukada, T., Kakinoki, K., Hozawa, M., and Imaishi, N. (1995) *Int. J. Heat Mass Transfer*, **38**, 2707.
38 Wang, G., Zhang, M., Han, J., He, X., Zuo, H., and Yang, X. (2008) *Cryst. Res. Technol.*, **43**, 531.
39 Schwabe, D., Sumathi, R.R., and Wilke, H. (2004) *J. Cryst. Growth*, **265**, 440.
40 Thomas, P.D., Derby, J.J., Atherton, L.J., Brown, R.A., and Wargo, M.J. (1989) *J. Cryst. Growth*, **96**, 133.
41 Galazka, Z., Schwabe, D., and Wilke, H. (2003) *Cryst. Res. Technol.*, **38**, 859.
42 Banerjee, J., and Muralidhar, K. (2006) *J. Cryst. Growth*, **286**, 350.
43 Zhmakin, A.I., and Makarov, Yu.N. (1985) *Sov. Phys. Dokl.*, **30**, 120.
44 Golyshev, V.D., Gonik, M.A., and Tsvetovsky, V.B. (2002) *J. Cryst. Growth*, **237–239**, 735.
45 Luo, S.N., Ahrens, T.J., Cagin, T., Strachan, A.W.A.G., and Swift, D.C. (2003) *Phys. Rev. B*, **69**, 134206.
46 Wettlaufer, J.S., and Worster, M.G. (2006) *Annu. Rev. Fluid Mech.*, **38**, 427.
47 Demina, S.E., Bystrova, E.N., Lukanina, M.A., Mamedov, V.M., Yuferev, V.S., Eskov, E.V., Nikolenko, M.V., Postolov, V.S., and Kalaev, V.V. (2007) *Opt. Mater.*, **30**, 62.
48 Kalaev, V., Makarov, Y., Yuferev, V., and Zhmakin, A. (2008) *Crystal Growth*

Technology (eds H.J. Scheel and P. Capper), Wiley-VCH Verlag GmbH, Weinheim, pp. 205–228.
49 Yuferev, V.S., and Mamedov, V.M. (2006) *High Temp. Phys.*, **44**, 565.
50 Kuwano, Y., Suda, K., Ishizawa, N., and Yamada, T. (2004) *J. Cryst. Growth*, **260**, 159.
51 LaBelle, H.E. (1980) *J. Cryst. Growth*, **50**, 8.
52 Feigelson, R.S. (1986) *J. Cryst. Growth*, **79**, 669.
53 Phomsakha, V., Chang, R.S.E., and Djeu, N. (1994) *Rev. Sci. Instrum.*, **65**, 3860.
54 Xu, C.H., Zhang, M.F., Meng, S.H., Han, J.C., Wang, G.G., and Zuo, H.B. (2007) *Cryst. Res. Technol.*, **42**, 751.
55 Demina, S.E., Bystrova, E.N., Postolov, V.S., Eskov, E.V., Nikolenko, M.V., Marshanin, D.A., Yuferev, V.S., and Kalaev, V.V. (2008) *J. Cryst. Growth*, **310**, 1443.
56 Träger, F. (ed.) (2007) *Springer Handbook of Lasers and Optics*, Springer.
57 Kaczmarek, S.M., Lukasiewicz, T., Giersz, W., Jablonski, R., Jabczy ski, J.K., Swirkowicz, M., Galazka, Z., Drozdowski, W., and Kwa ny, M. (1999) *Opto-Electron. Rev.*, **7**, 149.
58 Lu, J., Song, J., Prabhu, M., Xu, J., Ueda, K., Yagi, H., Yanagitani, T., and Kaminskii, A.A. (2000) *Jpn. J. Appl. Phys.*, **39**, L1048.
59 Lukasiewicz, T., Majchrowski, A., and Mierczyk, Z. (2001) *Opto-Electron. Rev.*, **9**, 49.
60 Golubovic, A., Nikolic, S., Gajic, R., Dohcevic-Mitrovic, Z., and Valcic, A. (2004) *Metalurgija - J. Metallurgy*, **10**, 363.
61 Eakins, D.E., Held, M., Norton, M.G., and Bahr, D.F. (2004) *J. Cryst. Growth*, **267**, 502.
62 Lebbou, K., and Perrodin, D. (2007) *Shaped Crystals* (eds T. Fukuda and V.I. Chani), Springer, Berlin Heidelberg, pp. 173–186.
63 Golubovich, A., Nikolic, S., Gajic, R., Duric, S., and Valcic, A. (2002) *J. Serb. Chem. Soc.*, **67**, 291.
64 Ma, Y., Zheng, L.L., and Larson, D.J. (2004) AIAA Paper 2004-629.
65 Li, H., Xu, J., Su, L., Jiang, B., Zhao, G., Zhou, G., and Dong, Y. (2007) *Cryst. Res. Technol.*, **42**, 107.
66 Balint, A.M., Braescu, L., Szabo, R., and Balint, S. (2006) *Opt. Mater.*, **28**, 671.
67 Braescu, L., Balint, A.M., and Balint, St. (2005) *J. Cryst. Growth*, **275**, e29.
68 Tsukada, N., Kobayashi, M., Jing, C.J., and Imaishi, N. (2005) *FDMP*, **1**, 45.
69 Lan, C.W., and Tu, C.Y. (2001) *J. Cryst. Growth*, **233**, 523.
70 Ginkin, V.P., Folomeev, V.I., Naumenko, O.M., Papin, Yu.M., and Zarikov, E.V. (2005) *J. Cryst. Growth*, **275**, e121.
71 Ignatov, A.Yu., Kalaev, V.V., Kuliev, A.T., Perfil'ev, A.A., Sinel'nikov, B.M., and Zhmakin, A.I. *J. Cryst. Growth*, submitted.
72 Mazaev, K., Kalaev, V., Galenin, E., Tkachenko, S., and Sidletkiy, O. (2009) *J. Cryst. Growth*, **311**, 3933–3937.
73 Budenkova, O.N., Vasiliev, M.G., Yuferev, V.S., Bystrova, E.N., Kalayevand, V.V., Bermudez, V., Dieguez, E., and Makarov, Yu.N. (2004) *J. Cryst. Growth*, **266**, 103.

13
Advanced Material Development for Inertial Fusion Energy (IFE)[1)]

Kathleen Schaffers, Andrew J. Bayramian, Joseph A. Menapace, Gregory T. Rogowski, Thomas F. Soules, Christopher A. Stolz, Steve B. Sutton, John B. Tassano, Peter A. Thelin, Christopher A. Ebbers, John A. Caird, Christopher P.J. Barty, Mark A. Randles, Charles Porter, Yiting Fei, and Bruce H.T. Chai

13.1
Introduction

Lawrence Livermore National Laboratory (LLNL) has developed several materials for use in high-power laser systems over the last 40 years. In particular, the world's largest laser system, the National Ignition Facility (NIF) has been completed and its 192 beamlines, with energy up to 1.8 MJ at 351 nm, will drive target experiments in the near future, (Figure 13.1) [1]. The NIF is a culmination of a long line of large glass lasers developed at LLNL over more than 3 decades to demonstrate inertial confinement fusion. Large-aperture, neodymium-doped phosphate (Nd : phosphate) glass is the gain medium for the NIF laser and a number of its predecessors. In addition, potassium dihydrogen phosphate (KDP) crystals are grown in large size for frequency conversion to the second harmonic and deuterated KDP is used for generation of the third harmonic of the Nd : phosphate glass and the

1) This document was prepared as an account of work sponsored by an agency of the United States government. Neither the United States government nor Lawrence Livermore National Security, LLC, nor any of their employees makes any warranty, expressed or implied, or assumes any legal liability or responsibility for the accuracy, completeness, or usefulness of any information, apparatus, product, or process disclosed, or represents that its use would not infringe privately owned rights. Reference herein to any specific commercial product, process, or service by trade name, trademark, manufacturer, or otherwise does not necessarily constitute or imply its endorsement, recommendation, or favoring by the United States government or Lawrence Livermore National Security, LLC. The views and opinions of the authors expressed herein do not necessarily state or reflect those of the United States government or Lawrence Livermore National Security, LLC, and shall not be used for advertising or product endorsement purposes.

This work was performed under the auspices of the U.S. Department of Energy by Lawrence Livermore National Laboratory under Contract DE-AC52-07NA27344.

Crystal Growth Technology. Semiconductors and Dielectrics. Edited by P. Capper and P. Rudolph
Copyright © 2010 WILEY-VCH Verlag GmbH & Co. KGaA, Weinheim
ISBN: 978-3-527-32593-1

Figure 13.1 The National Ignition Facility (NIF).

Pockels cell. Both the Nd : phosphate glass and the KDP have been scaled to world record sizes with high optical quality for the NIF facility.

The Mercury laser at LLNL, is a scalable, diode-pumped, solid-state laser system designed for inertial fusion energy (IFE) that uses Yb^{3+}:$Sr_5(PO_4)_3F$ (Yb : S-FAP) as the gain medium, and $YCa_4O(BO_3)_3$ (YCOB) as the frequency-conversion crystal (Figure 13.2). It has gas-cooled amplifiers designed to yield 100-J, 10-Hz and 10% efficiency in a 3-ns pulse when fully commissioned. The Mercury laser architecture can be directly scaled in aperture to achieve the energies required for an inertial fusion laser system [2]. To achieve these goals, three key technologies are used in the system: diode pumping replaces flashlamp pumping [3], high-speed helium gas cooling of the slab faces of the amplifier medium, and Yb : S-FAP crystals are used as the gain medium. Yb : S-FAP crystals have some attractive spectroscopic and material properties that make them well suited for diode pumping in moderate thermal load applications. These properties are represented in Figure 13.3 as a plot of saturation fluence versus emission lifetime. The plot indicates that the ideal material for fusion laser systems is one with a long lifetime to reduce the number and therefore the cost of diodes, and a high saturation fluence that increases energy-storage capacity, but is still substantially less than the damage threshold. If the saturation fluence is too low, it is difficult to hold off amplified spontaneous emission (ASE) and if it is too high, (a high output fluence is needed for efficient energy extraction) damage becomes an issue. Therefore, there is a preferred range of these parameters for fusion laser materials and in looking at the properties of several candidates (Table 13.1) Yb : S-FAP sits directly in the center of this preferred

Figure 13.2 The Mercury laser at Lawrence Livermore National Laboratory.

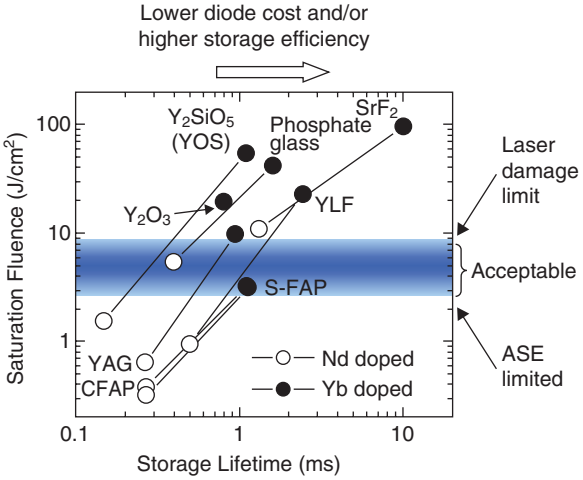

Figure 13.3 Extraction cross-section versus emission lifetime for fusion laser amplifier materials.

range with a lifetime of 1.14 ms and a saturation fluence of 3.2 J/cm^2. For this reason, Yb : S-FAP was chosen for the Mercury laser system and the development of high-quality crystals was pursued. The Mercury laser uses 14 Yb : S-FAP slabs for operation. Each slab has dimensions 4 cm × 6 cm × 0.75 cm in thickness, where the

Table 13.1 Properties of candidate fusion laser amplifier materials.

Gain medium	Emission lifetime τ_{em} (ms)	Saturation fluence F_{sat} (J/cm^2)	Nonlinear coefficient ($\times 10^{-16}$ cm^2)	Thermal conductivity (nW/m K)	Inversion intensity I_{min} (kW/cm^2)
Yb:S-FAP	1.14	3.2	4.1	2.0	0.13
Yb:YAG	0.95	9.6	6.3	10	1.53
Nd:Glass	0.4	5.4	2.8	1.2	0
Nd:SrF_2	1.3	10.6	1.5	~14	0

c-axis is oriented along the 6-cm length of the slab. A list of thermomechanical and laser properties for Yb:S-FAP is given in [4].

For the frequency conversion crystal, two materials were tested: deuterated KDP (DKDP) whose growth to 40 cm apertures has been demonstrated in the National Ignition Facility, and YCOB, a crystal with very favorable thermo-optic characteristics compared to DKDP, which can potentially be scaled to aperture sizes up to 40 cm^2. World record average power performance has been achieved from a side-cooled YCOB crystal, producing an average power of 317 W at a conversion efficiency of 50%. The previous record for average-power frequency conversion was 165 W, 5 J/pulse reported by TRW [5]. The world's largest YCOB crystals were grown by Crystal Photonics Incorporated, with a factor of 27 increase in size over previous reports [6]. Large aperture plates are harvested making it possible for a single *side-cooled* YCOB crystal to provide the equivalent of an assembly of four *face-cooled* DKDP crystals with four sapphire cooling plates; that is, one YCOB crystal can replace a complex assembly of eight optical elements. The YCOB frequency converter was activated on the Mercury laser with minimal beamline re-engineering [2]. Modeling of the thermal performance of face- and side-cooled YCOB frequency conversion crystals has also been completed. Additional experimental tests with YCOB slabs will be performed in future work.

Advanced material and laser concepts will be discussed for potential IFE designs. Glass-laser concepts and compositions are considered to be a baseline for fusion technology since Nd:phosphate glass has already proven viable in the National Ignition Facility in both size and performance. However, advanced glasses or other materials will be necessary to handle the thermal load that will be present for rep-rated laser systems that are required for fusion-energy power plants. These advanced materials include transparent ceramics that have been proven viable with fabrication into slabs of $10 \times 10 \times 2$ cm thick, by Konoshima Corporation in Takuma, Japan, and operated in quasi-continuous wave laser operation [7]. Scalability to sizes relevant to a fusion plant is still in question and has not been explored. In addition, to date, only cubic materials can be fabricated into a transparent ceramic. This is due to the random orientation of grains in the ceramic material that would cause optical scattering from refractive-index mismatch at the grain interfaces, randomizing the laser polarization and causing a significant

change in the absorption and emission cross-sections within noncubic materials. Orientation of the grains using a magnetic field has been reported for calcium hydroxy-apatite [$Ca_5(PO4)_3OH$] [8, 9], but doping with laser ions and characterization of the spectroscopy has not been reported in the literature. For fusion laser technologies, Nd:SrF_2 has been identified as a potential laser material that could be fabricated into a transparent ceramic due to its cubic structure. Large crystals of Yb:S-FAP and Nd:SrF_2 are also being considered for growth by the Bridgman technique. Very large crystals of CaF_2, 365 mm diameter by 250 mm thick, have been grown by Schott Lithotec in Jena, Germany, with a Bridgman-type technique, for the extreme ultraviolet lithography industry [10]. It is clear that much research is still required for the development of large-aperture crystalline and transparent ceramic gain media for fusion technology. These materials are very attractive for their thermal properties and ability to withstand the heat generated in a high repetition rate laser system. In addition, many of these materials have long lifetimes of >1 ms that greatly reduces the number of diodes required for pumping and the overall cost of a system, making materials research very desirable for future fusion laser systems.

13.2
Production of Nd:phosphate Laser Glass and KDP Frequency-Conversion Crystals

13.2.1
Nd:phosphate Laser Glass

High-quality, large aperture Nd:phosphate laser glass has been developed over the last 25 years [11, 12], and has been used in many generations of fusion lasers. The NIF laser, which is the largest laser in the world, uses 192 separate beamlines each of which contains 16 Nd:phosphate laser slabs approximately $44 \times 74 \times 4$ cm thick (Figure 13.4), for a total of 3072 slabs installed in the entire laser system. These slabs are very high optical quality, and are positioned at Brewster's angle to minimize Fresnel reflection losses at the slab surfaces [13] and increase the coupling efficiency of the flashlamp-pumped light [13, 14]. The neodymium ion in phosphate glass acts as a four-level laser system at room temperature with a lifetime of approximately 0.36 ms. The glass composition was specifically chosen for its properties for single-shot operation and has been proven in the NIF configuration. In the case of Hoya Corporation and Schott Glass Technologies, these compositions are represented by the designations LHG-8 and LG-770, respectively [15].

Since the development of the continuous melting process in 1989, significant numbers of laser slabs were produced for the NIF laser, making this a well-established technology. This is a process whereby homogeneously mixed molten laser glass is extruded onto a moving belt in a continuous strip, followed by annealing in a multizone oven to reduce internal stresses for crack-free fabrication [12, 16], (Figure 13.5). There are six main process zones in the continuous melting process to form the glass; (i) raw material mixing and feeding, (ii) melting, (iii)

Figure 13.4 Nd:phosphate glass laser slab used in the NIF.

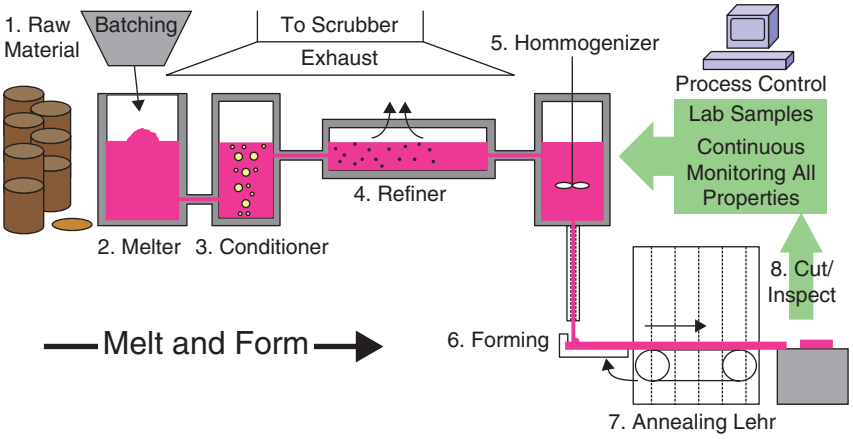

Figure 13.5 Continuous melt system developed for the fabrication of Nd:phosphate laser glass.

conditioning, (iv) refining, (v) homogenization and (vi) continuous strip forming. In the raw material mixing stage, high-purity starting materials are critical and there is a need to maintain the purity levels in tons of material for the formation of high-quality laser glass. The raw materials for the phosphate laser glass are then melted in the range of 1000–1200 °C in a refractory vessel. Once melted, the molten glass is conditioned to remove any hydroxyl groups or water that is left. This is accomplished by bubbling an oxidizing gas, typically chlorine-containing gases, through a melt contained in a platinum (Pt)-lined vessel. From this point forward, each of the succeeding vessels is lined in Pt to reduce dissolution of the container wall material into the molten glass. Pt can be dissolved into the melt and results in particulates in the finished glass that are an issue for laser damage; however,

the rate of dissolution is significantly lower than with other container materials [17]. The oxidizing gasses bubbled through the melt to remove water, are also very effective in dissolving the Pt particulates to a level acceptable for high-power operation without any significant laser damage. After conditioning, the melt is put through the refining, homogenization, and forming process steps. The purpose of these process steps is to remove bubbles and obtain high homogeneity to limit compositional variations and striations in the formed glass. Annealing of the glass directly after forming cools it slowly to avoid generating unwanted stresses in the continuous strip. At the end of the coarse annealing step, the glass is cut into individual pieces for further processing into laser slabs. All of the slabs that are produced are thoroughly characterized before being placed into the NIF laser for operation.

13.2.2
KDP Frequency-Conversion Crystals

The NIF laser at LLNL also employs KDP (potassium dihydrogen phosphate) and DKDP for frequency-conversion crystals to the second and third harmonic, respectively, as well as the Pockels cell. These crystals have been developed over the last 40 years to the sizes required for a $40 \times 40\,cm^2$ laser beam aperture [18–20]. The growth rate of such large crystals by traditional techniques is approximately 0.5–1 mm/day which is typical for low-temperature solution growth techniques. Slow growth leads to growth cycles exceeding 1–2 years which is prohibitive for the number of crystals required for a project the size of NIF. The difficulties in providing reliable equipment, the high risk of failure, and defect formation during such long periods results in low yield and high cost for the final crystals. These reasons stimulated the development of new techniques to accelerate the growth without sacrificing the optical quality of large crystals. Based on this need, a rapid growth technique was developed by Zaitseva, *et al.*, at LLNL approximately 25 years ago, where the rate of growth is increased to 10–20 mm/day, decreasing the overall growth time to approximately 2–3 months [21]. "Process improvements at LLNL over the last 10 years have doubled the potential yield of optics from each rapid-growth KDP crystal. The current rapid growth process produces optics that are up to 66 cm wide, 50 cm tall, and weighing 380 kilograms (Figure 13.6). NIF requires 192 optics produced from traditionally grown DKDP and 480 optics rapidly grown from KDP. The complete set of NIF KDP optics required approximately 75 production crystals which weighed nearly 100 tons" [22].

13.3
Yb:S-FAP Crystals

The growth of apatite crystals has been studied since the late 1960s by J. Hopkins at Westinghouse, who reported on the $Ca_5(PO_4)_3F$ (C-FAP) material [23]. Many of the initial proof-of-principal laser measurements on Yb:S-FAP crystals were performed on material provided by Bruce Chai at CREOL in Orlando, Florida, who

Figure 13.6 A KDP crystal grown at LLNL.

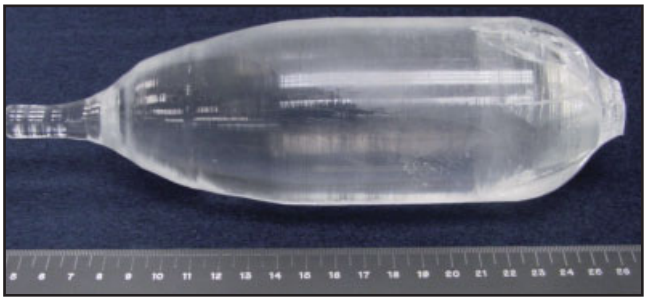

Figure 13.7 A 7.0-cm diameter Yb:S-FAP crystal.

grew the first small, high-quality boules in 1992 [24]. Based on these measurements, a program was pursued at LLNL and Northrop-Grumman/Synoptics to produce high-quality Yb : S-FAP crystals with apertures suitable for the Mercury laser (4×6 cm).

Currently, the growth of large, high optical quality, 7.0-cm diameter crystals is the focus for the Mercury laser (Figure 13.7). The growth of these crystals poses a challenge due to a number of crystal-growth issues that have been discussed elsewhere and will not be repeated here [4]. Only the defects that remain a challenge for yield will be addressed. A significant effort has been put into under-

standing the nature of the defect chemistry in Yb : S-FAP crystals and to develop a growth process to yield crystals from which slabs can be routinely fabricated.

13.3.1 Crystal Growth

Yb:S-FAP melts are prepared for growth by combining the appropriate ratios of $SrHPO_4$ (Optical Grade, General Electric Corp.), $SrCO_3$ (Optical Grade, General Electric Corp.), and Yb_2O_3 (99.99%, All-Chemie Corp.) powders. The $SrHPO_4$, $SrCO_3$, and Yb_2O_3 are mixed well and decompose, giving off water and carbon dioxide; leaving the composition $Sr_3(PO_4)_2$: Yb in the crucible (13.1). This composition is then allowed to set for approximately 18 h to fully decompose the orthophosphate and the carbonate. SrF_2 (99.99%, GFI, Advanced Technologies) is then added to the decomposed melt to form the appropriate melt stoichiometry for growth (13.2). By first predecomposing the $SrHPO_4$ and $SrCO_3$, the SrF_2 is prevented from oxidizing that would contaminate the melt and remove fluorine from the composition. The full melt is allowed to equilibrate for approximately five hours before seeding the crystal.

$$3[2SrHPO_4 + SrCO_3 + xYb_2O_3 \rightarrow Sr_3(PO_4)_2 : Yb + H_2O\,(g) + CO_2\,(g)] \quad (13.1)$$

$$3Sr_3(PO_4)_2 : Yb + SrF_2 \rightarrow 2Yb : Sr_5(PO_4)_3F \quad (13.2)$$

The oxide form of ytterbium, or Yb_2O_3, is the dopant that aides in providing a charge compensation mechanism where a Yb^{3+}–O^{2-} ion pair exchanges for a Sr^{2+}–F^- pair [25]. This specific charge-compensation mechanism sets the energy-level structure for this material, resulting in the laser line at 1047 nm. There is a distribution coefficient (C_s/C_l) of approximately 0.12 for the amount of Yb^{3+} that is incorporated into the S-FAP crystal lattice from the melt. In addition, an excess of 33 mol% of SrF_2 is added to the melt to compensate for vaporization and compositional variations that cause cloudiness in crystals grown from stoichiometric melts [4]. An introductory phase diagram, completed by NIST, is based on differential thermal analysis (DTA) experimental data as well as models (Figure 13.8). This phase diagram helps to explain the need for excess SrF_2 during growth to prevent vaporization that would cause the melt composition to move toward the $Sr_3(PO_4)_2$-rich end of the diagram, where impurity phases can precipitate out into the crystal during growth and phase separation can occur on cooling.

Crystals are grown using the Czochralski method in a standard oxide-type furnace configuration with a 6 × 6 inch iridium crucible and controlled induction heating. The melting temperature at which growth occurs is approximately 1786 °C [4]. Seeds are oriented along the [001] direction to maximize the laser slab yield and minimize the diameter required. Rotation rates of approximately 10–15 rpm have been effective for boule diameters up to 7.0 cm and a pull rate of 0.33–0.5 millimeters per hour is used to reduce defect formation. Diameter control is maintained by a computer-based, closed-loop power control system that is based on weighing the crystal and calculating a growth rate per unit time. A

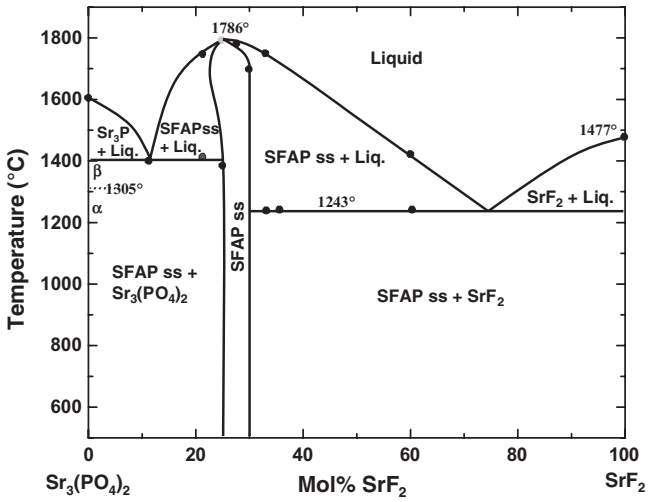

Figure 13.8 Introductory phase diagram developed for Yb:S-FAP crystal growth.

motor-generator power isolation unit is used to damp out power fluctuations to within ±0.5 V on the 480 V input to the RF power supplies, and chillers are used to control the variations that occur in water temperatures to ±0.5 °C. With these controls in place, outside perturbations to the crystal-growth process are minimized.

Crystals of 7 cm diameter by approximately 12 cm in length are producing full-size slabs, however, the yield is affected by grain boundaries, bubble core and internal stress leading to cracking, which are being addressed at this time. A description of each of these defects can be found in a previous article [4]. Slabs are harvested from either side of the bubble core where yield is determined by the bubble-core diameter.

13.3.2 Modeling

A modeling program has been developed to look at the growth process and develop a set of parameters that will address the remaining defects to improve the yield of high-quality boules for laser slab production. A model of the furnace was first produced by a group at the State University of New York at Stony Brook. With this model, predictions of thermal gradients and stresses in the crystal during the growth process [26] made it possible to reduce the number of growths required for successful mitigation of defects.

Modeling of cooling profiles has lead to a three-stage cool down that extends the cooling of crystals at the lower temperatures (powers) to mitigate cracking (Figure 13.9). The low-angle grain boundaries have been reduced by approximately sixty per cent by controlling the flow of nitrogen from the bottom of the furnace over the crucible and crystal. It is believed that the nitrogen carries the heat from the crucible up to the crystal decreasing the axial gradient within the crystal and pre-

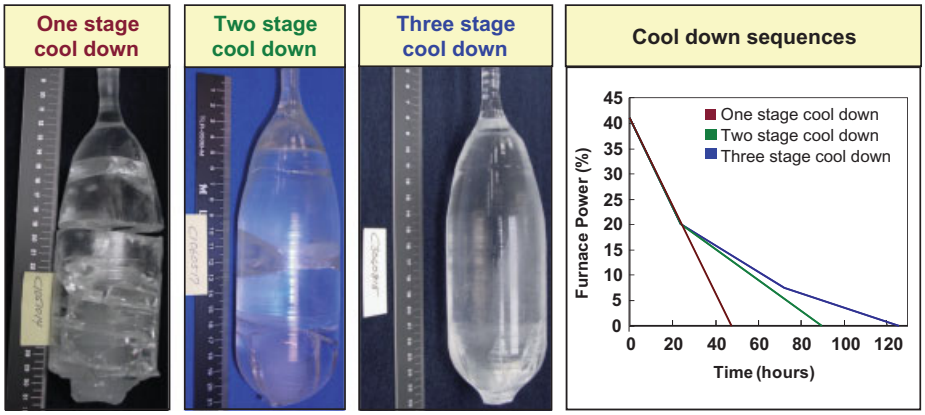

Figure 13.9 Mitigation of cracking in Yb:S-FAP crystals based on modeling of the cool-down phase of the growth.

venting the stresses that cause grain boundaries to form during the cooling of the immediately formed crystal, just above the melt interface. Reduction of the bubble core could lead to a further reduction of the grain boundaries, as seen in 3.5-cm diameter growth where the grain boundaries were eliminated simultaneously when the bubble core was eliminated [4].

The parameters required for reducing the bubble core are in direct conflict with those that reduce grain boundaries and cracking. This is the current focus of a modeling effort started at LLNL based on the CrysVUN program written at the *Fraunhofer-Institut für Integrierte Systeme und Bauelementetechnologie Abteilung Kristallzüchtung* [27]. Based on this program, furnace configurations, thermal gradients, and crystal interface characteristics can be studied. With these parameters, the discovery of the optimal phase space for mitigation of bubble core, grain boundaries, and cracking can be predicted and then confirmed with growth experiments. This work is ongoing and has currently reduced the number of experiments by approximately a third to a half.

13.3.3 Slab Fabrication

A maximum yield of two Yb:S-FAP slabs can be harvested from a 7-cm diameter crystal. There are a number of fabrication steps required to produce a full-size slab for the Mercury laser as shown in Figure 13.10. After the crystals are grown and cut at the top and bottom for inspection down the *c*-axis length, reference flats are placed on the sides of the crystal to further examine the quality perpendicular to the *c*-axis. A suitable crystal is shaped into a rectangular block for cutting into two separate pieces; slabs are harvested from either side of the bubble core near the outside of the boule. The crystal block is cut in half using water-jet cutting that has been found to be the gentlest method and produces the least amount of cracking at this stage of fabrication. Each separate half is then ground from the inside

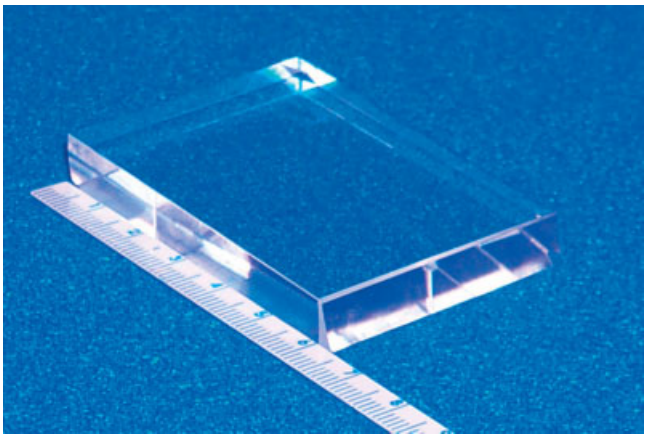

Figure 13.10 An Yb:S-FAP laser slab.

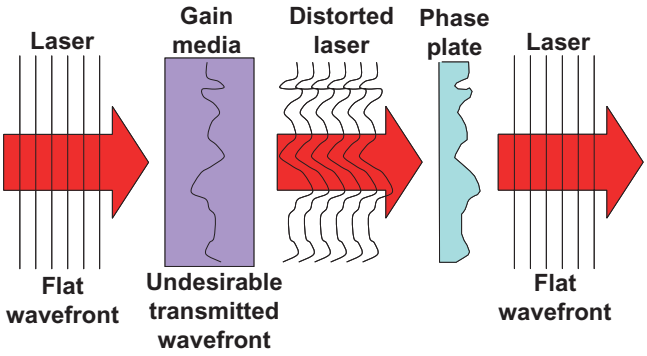

Figure 13.11 Sketch of how the magneto-rheological finishing (MRF) technique works.

and outside of the half-block to the appropriate dimensions of a slab. A laser-quality conventional polish is put onto one side of the slab and magneto-rheological finishing (MRF) [28, 29] is performed on the other side to compensate for any distortions in the transmitted wavefront of the slab. Distortions in the laser beam can result in damage of the slab or damage of the optics downstream from the gain medium during laser operation. A pictorial of the power of the MRF technique is shown in Figure 13.11, where the incoming laser light interacts with a gain medium having bulk anomalies to produce a distorted wavefront. If the opposite distortion is put into an optic surface, represented by the phase plate, it will compensate for the laser beam distortions to give a flat or near-flat wavefront. In the case of Yb:S-FAP slab fabrication, MRF is used to write the opposite distortion pattern directly onto one face of the laser slab eliminating the need for an additional optic. These distortions in Yb:S-FAP can result from residual grain boundaries or imperfections in the bulk material. Although current MRF technol-

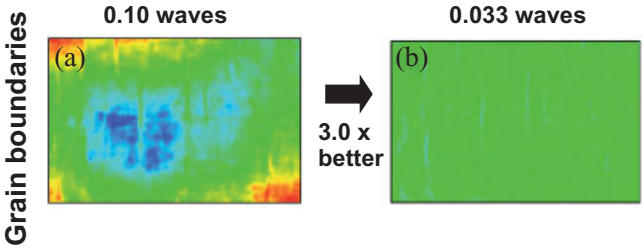

Figure 13.12 Improved transmitted wavefront of a Yb:S-FAP slab; (a) before MRF and (b) after MRF.

ogy cannot completely compensate for grain boundaries due to the small scale of the feature, it reduces much of the distortion surrounding the grain boundaries to significantly improve the transmitted wavefront. An example of a typical slab before and after MRF is shown in Figure 13.12, where the transmitted wavefront was reduced by 3× relative to the unmodified slab. MRF also has the advantage of not inducing any subsurface damage and can be used to remove subsurface damage from the surface of optics, thereby increasing the laser damage threshold [30, 31]. Current state-of-the-art in MRF technology allows for the compensation of submillimeter features that may greatly improve the grain-boundary distortions not removed by the original technology that only compensated for features greater than 3 mm. Future work will yield slabs with greatly improved transmitted wavefront and surface damage threshold.

13.4 YCOB Crystals

$YCa_4O(BO_3)_3$ (YCOB) belongs to a relatively new class of frequency-conversion materials with the designation $RCa_4O(BO_3)_3$ where R = La, Nd, Sm, Gd, and Y that was first reported in 1989 [6, 32]. This monoclinic class of materials melts congruently [33, 34], and therefore large-sized single crystals can be grown by the conventional Czochralski pulling method. Both the YCOB and GdCOB crystals show good optical quality, high damage threshold, fairly large nonlinear coefficients, and adequate birefringence for efficient frequency conversion. In particular, YCOB has three times the thermal conductivity and three times the nonlinearity of the well-known and accepted materials KDP and DKDP [35, 36]. These properties are attractive for high-energy, rep-rated lasers which are being developed for IFE systems where heat dissipation requires thinner crystals to avoid thermal cracking. Thermal insensitivity to 2ω operation and an equivalent 3ω bandwidth to DKDP also make it suitable for frequency conversion of 1-μm lasers. With an equivalent hardness to quartz crystals, hard antireflective (AR) coatings can be applied that decreases damage at high energies. These properties make YCOB attractive for high-power laser systems and therefore growth of high-quality crystals is being

pursued for frequency conversion. Crystals of YCOB have been grown and scaled by Crystal Photonics for the Mercury laser project.

13.4.1 YCOB Crystal Growth and Fabrication

A full description of the growth process can be found in [6]. YCOB melts are prepared by combining the appropriate ratios of Y_2O_3, $CaCO_3$, and B_2O_3 powders with 99.99% purity. These components are mixed together to form a stoichiometric composition with the exception of small additional amounts of B_2O_3 to adjust for vaporization during growth. The $CaCO_3$ is decomposed to give low water content CaO and CO_2 before it is mixed with the Y_2O_3 and B_2O_3 to maintain strict control of the melt composition. Adjusting for losses during the growth process and for the hygroscopic nature of several of the starting components is a critical step to producing high optical quality YCOB crystals as the field of growth stability is narrow [6].

Crystals are grown by using the Czochralski process with a computer-automated diameter-control program and a 50-kW induction power supply. Crystals are grown from an iridium crucible to accommodate the growth temperature of 1510 °C and with an iridium ring placed on the top of the crucible to add stability to the growth. Typical growth is done at rotation rates of 3–10 rpm and pull rates of 0.5–1.0 mm/h depending on diameter, to produce high-quality boules. A nitrogen atmosphere is used to prevent oxidation of the iridium crucible. Crystals are typically grown along the *b*-axis direction of the structure and boules of approximately 8 cm diameter by 12 cm in length have been produced. Crack-free boules are high quality (Figure 13.13), with slight vales of inclusions near the bottom of the crystal and along one side.

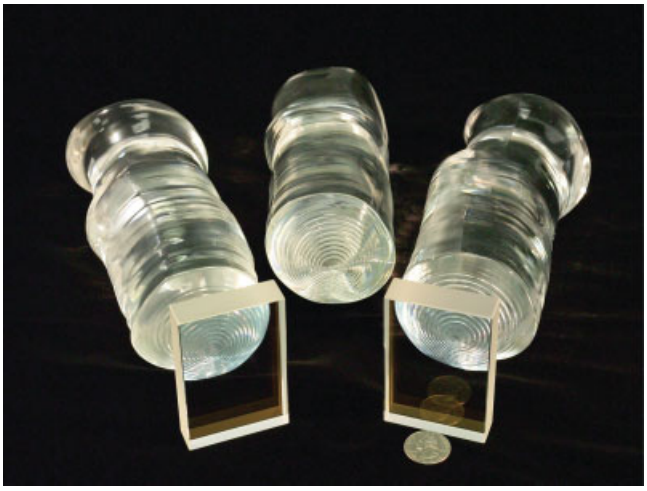

Figure 13.13 High-quality YCOB boules grown at Crystal Photonics Incorporated and two slabs of YCOB (8 × 5 × 1 cm) required for the Mercury laser frequency conversion.

Cracking and fiber-like inclusions can occur in boules [6], but have been mitigated to the extent that they are not the yield-determining factor for harvesting slabs. The growth spiral at the top of the crystals can be more limiting to the yield of slabs that would be harvested from any one boule. This spiral is attributed to asymmetric growth of the crystal facets that cause the boule to tip during cone section of the growth when enough weight is put onto one side of the crystal relative to the other. Normally, the spiral will straighten out in the full diameter growth stage, limiting the length of material available for harvesting slabs. Varying the growth rate and rotation rate during this section of the boule has greatly reduced the magnitude of the spiral resulting in much straighter boules. YCOB slabs of 8 cm long by 5 cm wide and 1 cm in thickness are harvested from the boules produced. The slab orientation has the *b*-axis along the 8-cm length. The orientation of slabs from the boules is determined by the phase-matching angle to yield the highest efficiency. Slabs are cut from the boules with a standard diamond saw and polished using conventional polishing technology. Typically, two slabs can be harvested from each boule.

13.5
Advanced Material Concepts for Power-Plant Designs

Advanced glasses and compositions are considered to be a baseline for fusion technology as Nd:phosphate glass has already been proven viable in the National Ignition Facility in both size and performance. Advanced glasses or possibly other materials will be necessary to handle the thermal load that will be present for reprated laser systems required for fusion energy power plants. Specifically the advanced glass APG-1, reported in 1996 by Schott Glass Technologies [37], is the baseline material; however, other glasses such as APG-2 [38] are being considered for their improved mechanical properties and longer lifetime to reduce diode pump costs.

Yb : S-FAP is being produced by the Czochralski method for the Mercury laser, however, more advanced material concepts are also being explored to produce gain media of the size required for a fusion power plant. Other materials of interest include scaling of Yb : S-FAP crystals and transparent ceramic gain media. Each of these material types is being considered for its mechanical, spectroscopic and laser properties, as well as the ability to scale to the appropriate aperture and produce high-quality material. Modeling of laser designs required for each type of material will be essential to determining its viability as a fusion laser gain media.

Scaling of Yb : S-FAP crystals up to fusion scale aperture sizes of 10–40 cm^2, depending on the laser design, will be considered based on its "ideal" laser and spectroscopic properties already discussed for fusion laser systems. Both the Czochralski and Bridgman techniques are being looked at for scaling Yb:S-FAP crystal size; current scaling has yielded 12.0 cm diameter Czochralski grown crystals and the largest slab to date (Figure 13.14a,b, respectively). However, it is believed that the Czochralski method will not be able to produce the diameter required for a full-size laser slab due to the inability to remove heat efficiently during growth,

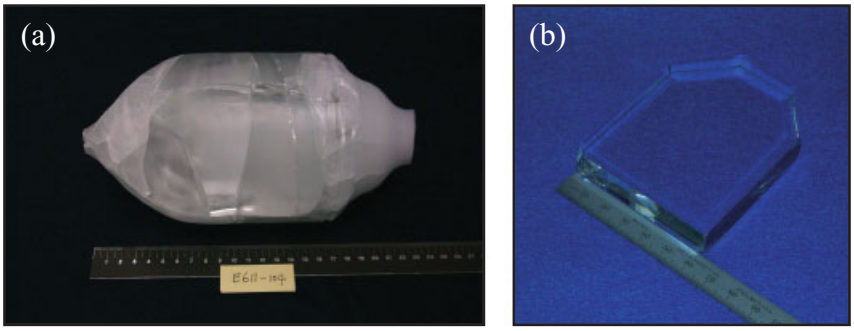

Figure 13.14 (a) First attempts at growing a 12.0-cm diameter Yb:S-FAP boule and (b) world's largest Yb:S-FAP slab to date (approximately 6 × 8 × 1.4 cm).

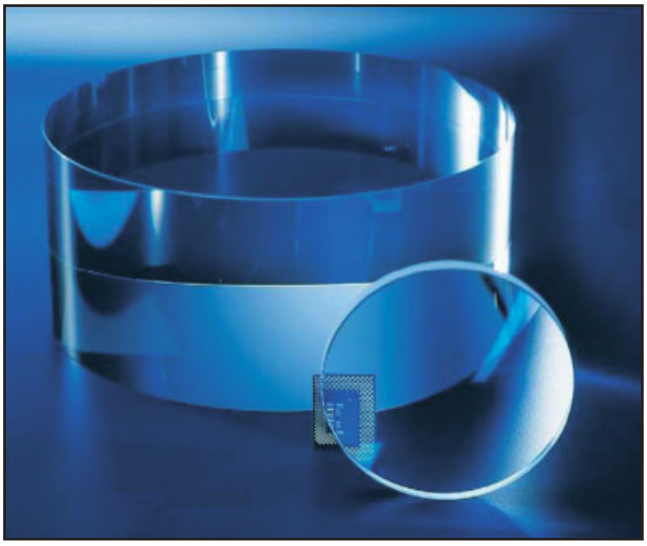

Figure 13.15 A 385-mm diameter × 250 mm long CaF_2 crystal grown at Schott Lithotec.

which will result in cracking. An alternative Bridgman growth technique is being considered for scaling the size of the crystals. This technique has been successfully used by Schott Lithotec to produce up to 385 mm diameter × 250 mm high calcium fluoride (CaF_2) crystals for EUV lithography [39] (Figure 13.15). An intense program of connecting modeling, furnace design, and growth parameters was used to produce a full-size CaF_2 crystal on the first growth run. Subsequent runs quickly improved the quality, and production was then pursued. Yb:S-FAP has similar growth challenges to the CaF_2 material such as ease of cracking along one

crystalline axis and difficulties with oxygen impurity control. The potential of producing large aperture Yb:S-FAP crystals by a similar method has been looked at and appears very promising.

In addition to traditional crystalline gain media, transparent ceramic technology presents a relatively new and exciting materials area for scaling and unique, engineered architectures [7, 40, 41]. This technology looks very promising for large apertures for high-power lasers and has the ability to be formed into specific shapes including, slabs, shells, and tubes. It presents the ability to set up multiple functionalities in one monolithic piece, such as directly attaching an edge cladding to the gain medium without any bonding or possibility for bond reflections. Requirements for a laser material are rather stringent including very low porosity of $<10^{-5}$–10^{-6} to obtain good transmission as well as no change in refractive index across the grain boundaries that currently limits this technology to cubic materials and requires a very high degree of phase purity. In addition, transparent ceramic YAG materials have been shown to have a high resistance to thermal cracking and lower residual stress than the single-crystal counterparts. A higher dopant concentration and more uniform distribution of dopant has been shown for Nd:YAG manufactured parts. Current technological advances by Konoshima Chemical Co., Ltd. have yielded the world's largest slabs of Nd:YAG with Sm : YAG edge cladding cosintered around the outside, of dimension $10 \times 10 \times 2$ cm (Figure 13.16).

Transparent ceramic technology has progressed a great deal since its inception around 15 years ago. A significant understanding of the process steps has been achieved; however, there are still some unknowns for the development of materials for high-power laser systems. The importance of the purity of the starting materials required as the size is scaled must be fully understood as it is a key variable to

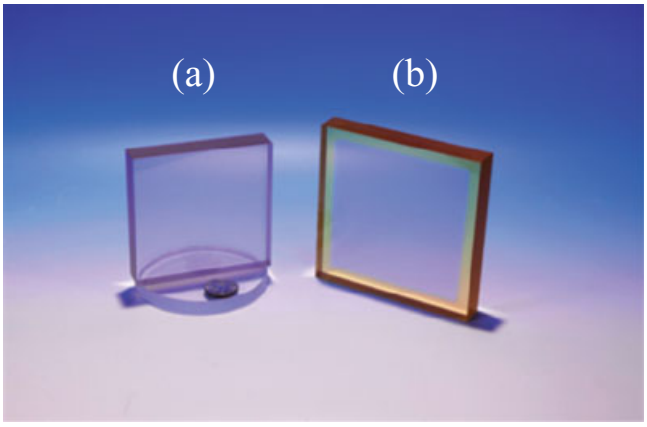

Figure 13.16 Konoshima Chemical Company, Ltd. has produced; (a) a $10 \times 10 \times 2$ cm Nd:YAG transparent ceramic slab and (b) a slab with Sm:YAG co-sintered around the edges (b) for an ASE absorber.

achieving high-quality optics. The effect of the migration of the dopant to the grain boundaries in highly doped materials must also be understood if these materials are to be adopted for IFE. New fabrication technology may have to be developed as the size increases to accommodate heating and purity/doping effects. Another step that is not well understood for scaling is the need for developing a complex polishing process to accommodate the possibility of different polishing rates of randomly oriented grains within the transparent ceramic matrix. There is a significant understanding of transparent ceramic technology for up to the $10 \times 10 \times 2\,cm^3$ dimensional size, but this technology has not yet been pushed to the required sizes for a fusion laser design and there are many unknown aspects to be understood in the scaling process. However, the transparent ceramic technology shows great promise and will be pursued for the large-scale optics needed for high-power laser systems.

13.6 Summary

Materials will play a critical role in the development of laser technology for fusion power plants. In particular the development of the appropriate gain material and frequency-conversion material will be important for the high repetition rate required for such a system. The NIF is a proven laser that utilizes both large-aperture Nd:phosphate glass amplifier slabs and KDP/DKDP for frequency conversion. Yb:S-FAP and YCOB are materials that have been developed for the Mercury laser that has proven the feasibility of a number of key technologies required for future fusion technologies. The current baseline for a future, reprated, fusion laser is an advanced glass with improved mechanical properties and longer lifetime to prevent damage. However, other technologies including scaling of Yb:S-FAP crystals by the Bridgman technique and cubic transparent ceramic materials are being pursued.

References

1 Moses, E. (2008) *Energ. Convers. Manage.*, **49**, 1795.
2 Orth, C.D., Payne, S.A., and Krupke, W.F. (1996) *Nucl. Fusion*, **36** (**1**), 75.
3 Bayramian, A.J., Beach, R.J., Behrendt, W., Bibeau, C., Ebbers, C.A., Freitas, B.L., Kanz, V.K., Payne, S.A., Schaffers, K.I., Skulina, K., Smith, L.K., and Tassano, J.B. *International Fusion Science and Applications 2001* (eds K.A. Tanaka, D.D. Meyerhofer, and J. Meyer-ter-Vehn), (2001 Conference), p. 459.
4 Schaffers, K.I., Tassano, J.B., Bayramian, A.B., and Morris, R.C. (2003) *J. Cryst. Growth*, **253**, 297.
5 Pierre, R.J.S., Mordaunt, D., Injeyan, H., Berg, J.G., Hilyard, R.C., Weber, M.E., Wickham, M.G., and Harpole, G. (1998) Diode array pumped kilowatt laser. SPIE Confernce on High-Power Lasers, vol. 3264, pp. 2–8.
6 Fei, Y.T., Chai, B.H.T., Ebbers, C.A., Liao, Z.M., Schaffers, K.I., and Thelin, P. (2006) *J. Cryst. Growth*, **290**, 301.

7 Soules, T. (2006) Transparent ceramics spark laser advances. Sci. Technol. Rev., LLNL publication, April issue, p. 10–17.
8 Akiyama, J., Sato, Y., and Taira, T. (2009) *Advanced Solid State Photonics Conference* (eds C. Ebbers and T. Taira), Optical Society of America, MF1, 2009 Conference presentation.
9 Chen, W., Kinemuchi, Y., Tamura, T., Miwa, K., and Watari, K. (2007) *Mater. Lett.*, **61**, 6.
10 Wehrhan, G. (2005) "Recent development in CaF_2-production" presentation. Third International Workshop on Crystal Growth Technology, Beatenberg, Switzerland, Sept. 10–18, 2005.
11 Campbell, J.H. (1996) Recent advances in phosphate laser glasses for high power applications. SPIE International Symposium on Optical Science, Engineering, and Instrumentation, Information Bridge: DOE Scientific and Technical Information.
12 Hayden, J.S., Campbell, J.H., and Payne, S.A. (2007) Proc. of SPIE, 654508, vol. 6545, p. 1.
13 Emmett, J.L., Krupke, W.F., and Trenholme, J.B. (1982) The future development of high-power solid-state laser systems. Lawrence Livermore National Laboratory Report UCRL-53344, p. 1.
14 Erlandson, A.C., Rotter, M.D., Frank, D.N., and McCracken, R.W. (1994) Design and performance of the beamlet amplifiers. ICF Quarterly Report, Lawrence Livermore, National Laboratory Report UCRL-LR-105821-95-1, p. 18.
15 Campbell, J.H., and Suratwala, T.I. (2000) *J. Non-Cryst. Solids*, **263 & 264**, 381.
16 Campbell, J.H., Suratwala, T.I., Thorseness, C.B., Hayden, J.S., Thorne, A.J., Cimino, J.M., Marker, A.J., III, Takeuchi, K., Smolley, M., and Ficini-Dorn, G.F. (2000) *J. Non-Cryst. Solids*, **263 & 264**, 342.
17 Campbell, J.H., Wallerstein, E.P., Hayden, J.S., Sapak, D.L., Warrington, D.E., Marker, A.J., III, Toratoni, H., Meissner, H., Nakajima, S., and Izumitani, T. (1989) Elimination of Platinum Inclusions in Phosphate Laser Glasses, Information Bridge: DOE Scientific and Technical Information.
18 Zaitseva, N., and Carman, L. (2001) *Prog. Cryst. Growth Charact.*, **43**, 1–118.
19 Zaitseva, N.P., De Yoreo, J.J., Dehaven, M.R., Vital, R.L., Carman, L.M., and Spears, H.R. (1996) Rapid growth of large-scale (40–55 cm) KDP crystals. Lawrence Livermore National Laboratory Report UCRL-JC-126805, p. 1.
20 Zaitseva, N.P., De Yoreo, J.J., Dehaven, M.R., Vital, R.L., Montgomery, K.E., Richardson, M., and Atherton, L.J. (1997) *J. Cryst. Growth*, **180**, 255.
21 Li, G., Xue, L., Su, G., Li, Z., Zhuang, X., and He, Y. (2005) *Cryst. Res. Technol.*, **40** (**9**), 867.
22 Lawrence Livermore National Laboratory (2009) NIF&Photon Science website: lasers.llnl.gov/programs/nif/how_nif_works/optics.php (accessed 2009), section on Crystal Growth.
23 Hopkins, R.H., and Kramer, W.E. (1969) *J. Electrochem. Soc. Solid State Sci.*, **116** (**5**), 637.
24 Marshall, C.D., Smith, L.K., Sutton, S., Emanuel, M.A., Schaffers, K.I., Mills, S., Payne, S.A., Krupke, W.F., and Chai, B.H.T. (1996) *OSA Trenbs in Optics and Photonics on Advanced Solid State Lasers*, vol. **1** (eds S.A. Payne and C.R. Pollock), Optical Society of America, Washington, DC, (January 1996 Conference), p. 208.
25 DeLoach, L.D., Payne, S.A., Kway, W.L., Tassano, J.B., Dixit, S.N., and Krupke, W.F. (1994) *J. Lumin.*, **62**, 85.
26 Fang, H.S., Qiu, S.R., Zheng, L.L., Schaffers, K.I., Tassano, J.B., Caird, J.A., and Zhang, H. (2008) *J. Cryst. Growth*, **310**, 3825.
27 Friedrich, J. (2007) CrysVun Flyer: Modeling of Crystal Growth, Frauhofer Institute of Integrated Systems and Device Technology.
28 Schaffers, K. (2005) "Growth of large laser crystals for high power lasers" talk UCRL-PRES-215275. Third International Workshop on Crystal Growth Technology, Beatenberg, Switzerland, Sept. 10–18, 2005.
29 Bagnoud, V., Guardalben, M.J., Puth, J., Zuegel, J.D., Mooney, T., and Dumas, P. (2005) *Appl. Optics*, **44** (**2**), 282.
30 Menapace, J.A., Davis, P.J., Steele, W.A., Wong, L.L., Suratwala, T.I., and Miller,

P.E. (2005) Laser induced damage in optical materials. SPIE Proc., 599103, vol. 5991, pp. 1–11.

31 Menapace, J.A., Davis, P.J., Steele, W.A., Wong, L.L., Suratwala, T.I., and Miller, P.E. (2005) Laser induced damage in optical materials. SPIE Proc., 599102, vol. 5991, pp. 1–13.

32 Pajaczkowska, A., Klos, A., Hilczer, B., Menguy, N., and Novosselov, A. (2001) *Cryst. Growth Des.*, **1** (**5**), 363.

33 Aka, G., Kahn-Harari, A., Vivien, D., Benitez, J.M., Salin, F., and Godard, J. (1996) *Eur. J. Sol. State Inor. Chem.*, **33**, 727.

34 Iwai, M., Kobayashi, T., Furaya, H., Mori, Y., and Sasaki, T. (1997) *Jpn. J. Appl. Phys.*, **36**, L277.

35 Luo, J., Fan, S.J., Xie, H.Q., Xiao, K.C., Qian, S.X., Zhong, Z.W., Qian, G.X., Sun, R.Y., and Xu, J.Y. (2001) *Cryst. Res. Technol.*, **36** (**11**), 1215.

36 Schaffers, K. (2008) "Advanced material development for fusion energy" talk LLNL-PRES-404026. Fourth International Workshop on Crystal Growth Technology, Beatenberg, Switzerland, May 18–25, 2008.

37 Payne, S.A., Marshall, C.D., Bayramian, A., Wilke, G.D., and Hayden, J.S. (1995) *Appl. Phys.*, **B61**, 257.

38 Schott Glass Technologies (2009) website: www.us.schott.com/advanced_optics/english/download/catalogs.html?highlighted_text=APG-2 data sheet; APG-2 Phosphate Laser Glass – Product Datasheet. Data sheet on APG-2 glass, provided on the Schott Glass Technologies website: www.us.schott.com/advanced_optics/english/download/phosphate_laser_glass_apg2_dec_2009_us_final.pdf.

39 Engel, A., Mörsen, E., Jordanov, A., and Knapp, K. (2001) Proceedings of SPIE, vol. 4449, p. 1.

40 Lu, J., Takaichi, K., Uematsu, T., Shirakawa, A., Musha, M., Ueda, K., Yagi, H., Yaagitani, T., and Kaminskii, A.A. (2002) *Appl. Phys. Lett.*, **81** (**23**), 4324.

41 Ding, J., Yang, Q., Tang, Z., Xu, J., and Su, L. (2007) *J. Opt. Soc. Am. B*, **24** (**3**), 681.

14
Magneto-Optic Garnet Sensor Films: Preparation, Characterization, Application

Peter Görnert, Andreas Lorenz, Morris Lindner, and Hendryk Richert

14.1
Introduction

In contemporary magneto-optics [1] both the Kerr effect and Faraday effect are applied. The Kerr effect in metals and alloys – such as Fe, Ni, Co, FePt, CoPt, MnBi, PtMnSb – with thicknesses <100 nm is used widely for magneto-optic discs. The Faraday effect of ferrimagnetic Bi-substituted rare earth iron garnet films (Bi-REIG) [2–5] with thicknesses of 1–5 μm is utilized for sensors to visualize magnetic fields. Nonreciprocal optical elements of the same material with thicknesses >300 μm are established as commercial isolators in optical systems and for developments of waveguide applications [6]. Both sensor and isolator applications as well as conditions of preparation and characterization of Bi-REIG films have been already reviewed in a recent book [7]. A survey of answers and problems of contemporary magneto-optic imaging is given in [8]. For all these applications, sensor films with a high Faraday rotation and low optical absorption are necessary. Additionally, magneto-optic sensors should possess high sensitivity and a large dynamic range. All these demands can be fulfilled with conventional $(RE_{3-x}Bi_x)(Fe_{5-y-z}Ga_yAl_z)O_{12}$ liquid phase epitaxy (LPE) films grown in $PbO–B_2O_3–Bi_2O_3$-based solvents [9].

Here, we report on Bi-substituted iron garnet films and discuss current results concerning preparation, characterization, and application of Bi-TmDyLuIG-LPE layers deposited on high-quality gadolinium gallium garnet (GGG) or lattice-matched Ca-, Mg-, Zr-substituted GGG substrates. The applications are focused on high-quality magneto-optic sensor films for studying the spatial distribution of magnetic fields in real time. Such films are applied already in commercial systems.

14.2
Bi-Substituted Garnets

Faraday rotation in $Y_3Fe_5O_{12}$ (YIG) is mainly determined by the spin-orbit coupling coefficient of 3d electron ζ_{3d}, which is much larger than that of the 2p electron ζ_{2p}.

Crystal Growth Technology. Semiconductors and Dielectrics. Edited by P. Capper and P. Rudolph
Copyright © 2010 WILEY-VCH Verlag GmbH & Co. KGaA, Weinheim
ISBN: 978-3-527-32593-1

However, Faraday rotation in Bi^{3+}-substituted $Y_3Fe_5O_{12}$ is determined by ζ_{2p}, which is increased from the original ζ_{2p} by the hybridization of 6p bismuth orbitals. Thus, for Bi^{3+}-substituted $Y_3Fe_5O_{12}$, ζ_{2p} is modified as $\zeta^*_{2p} \sim \zeta_{2p} + \gamma^2\zeta_{6p}$, where γ is the covalency factor and ζ_{6p} is the spin-orbit coupling coefficient of 6p electrons in bismuth: $\zeta_{6p} = 17\,000\,cm^{-1}$ [7]. Therefore, the Bi content should be as large as possible and hence the highest Faraday rotation – which is negative for Bi ions in iron garnets and increases linearly with Bi concentration – is obtained in $Bi_3Fe_5O_{12}$ (BIG) [10]. Due to the large lattice parameter $a_{BIG} = 1.263\,nm$, however, this compound cannot be grown by LPE, which is a "near-equilibrium method". Here, the maximum Bi content is roughly 2.2 f.u. To prepare pure BIG nonequilibrium methods are used like sputtering [11, 12], pulsed laser deposition (PLD) [13–17], and similar methods [18–20]. Recently, Heinrich *et al.* [21] reported on PLD deposition of BIG on different orientations of GGG and SiO_2 substrates. In the case of BIG on GGG a 3D island growth appeared and the preferential growth direction of BIG could be assigned towards <110>. The deposition of BIG on SiO_2 was only possible with a YIG buffer layer and an annealing procedure. The Faraday rotation of BIG on GGG and SiO_2 substrates is reported to be comparable. Indeed, no investigations have been carried out concerning the responsivity of such samples. Because of the 3D island growth of BIG on GGG and the polycrystalline structure of BIG on SiO_2 it is expected that the coercivity is fairly large, so that the responsivity is low compared with LPE grown garnets. Recently, Dubinko *et al.* [22] studied the coercivity of LPE grown (111)-oriented $(Bi,Sm,Lu,Ca)_3(Fe,Sc,Ga,Al)_5O_{12}$ on GGG and found that the coercivity initially increases, passes through a maximum, and then decreases. The maximum coercivity occurs when the period of local stress is equal to the domain wall width. The periodically localized stress is due to a misfit dislocation [23] network whose period is determined by the relative misfit.

In addition, experiments were carried out to prepare Bi-YIG nanoparticles via mechanochemical processing and subsequent heat treatment [24]. The mean crystallite size of the single-phase powder was about 45 nm and the specific saturation magnetization was 22 A m^2/kg, compared with 26 A m^2/kg of bulk Bi-YIG [25]. These powders were dispersed in an organic binder and the magnetic inks were deposited on precoated aluminum glass substrates by spin coating [24, 26–28]. Maximal Faraday rotations are in the order of $-0.15°$ for a fairly inhomogeneous film due to agglomerated nanoparticles. Therefore, this preparation technology is inexpensive and versatile – however, the physical parameters of the garnet films are moderate.

High-quality liquid phase epitaxy (LPE) garnet films are grown on plane and perfect single-crystalline garnet substrates with maximal diameters of 4 inch (≈100 mm) and sometimes 6 inch at present.

Indeed, it depends on the foreseen application which preparation techniques of Bi-REIG films – LPE, PLD, sputtering, other physical methods, or polymeric bond nanoparticles – will be used. However, whenever highest sensitivities are required LPE films are applied. Hence, here we focus our attention on LPE films.

14.3
LPE Deposition and Topological Film Properties

The standard garnet LPE dipping technique with $PbO–Bi_2O_3–B_2O_3$-based flux melts [7, 9, 29] in 170–310 cm^3 Pt crucibles is used for the deposition of Bi-REIG films with a thickness of 1–5 micrometer on 1-inch high-quality <111> and <100> $Gd_3Ga_5O_{12}$ (GGG) or lattice-matched $(Gd_{3-x}Ca_x)(Ga_{2-x-2y}Mg_yZr_{x+y})Ga_3O_{12}$ (CMZGGG) [30] substrates with lattice constants 1.2385 nm ($x = y = 0$), 1.2400 nm ($x = y = 0.050$), 1.2422 nm ($x = y = 0.125$), and 1.2499 nm ($x = y = 0.325$). The Czochralski crystals were grown in IKZ Berlin and the substrates were prepared at CrysTec GmbH Berlin. Our 1-inch substrates have an orientation accuracy of ±0.5 ° and the surfaces are mechanochemically polished with an average roughness <0.5 nm.

The typical deposition parameters of LPE films are

- temperature distribution: almost isothermal at 700–900 °C;
- undercooling: 5–100 K;
- substrate rotation rate: 40–100 rpm (alternating);
- deposition time: 4–100 min;
- growth rate: 0.01–1.1 µm/min.

To obtain a correlation between defect density of substrates and LPE films, the substrates have been etched for 10 min in dehydrated H_3PO_4 at 170 °C. After drying in deionized water the defects were inspected with a polarization microscope. It could be seen that the main defects are due to polishing and handling of the substrates. Relatively large "pit densities" on LPE films – as shown in Figure 14.1 – are caused by compression stress due to the relative misfit $\Delta a/a_s = (a_s - a_f)/a_s$

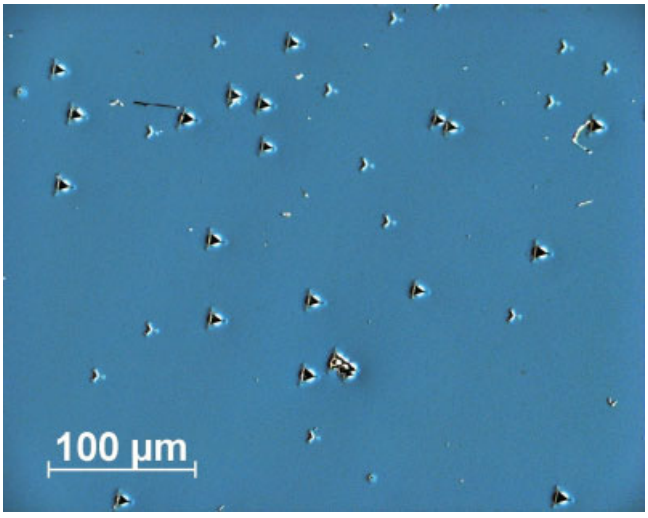

Figure 14.1 Typical "pits" on [111]-oriented Bi-DyIG film due to compressive stress.

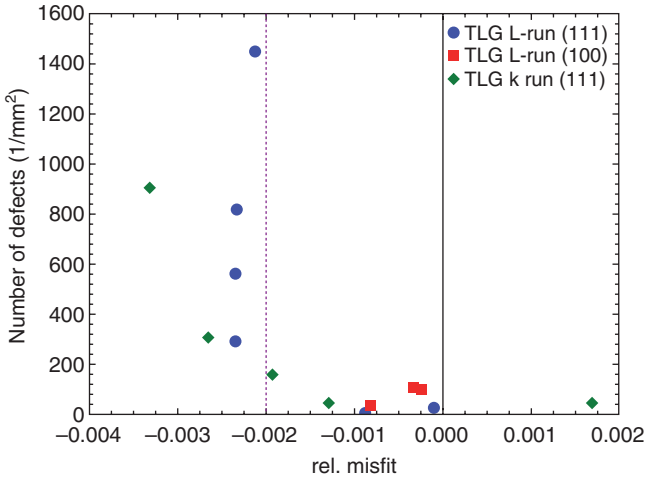

Figure 14.2 "Pit density" in Bi-TmIG films vs. relative misfit $\Delta a/a_s = (a_s - a_f)/a_s$.

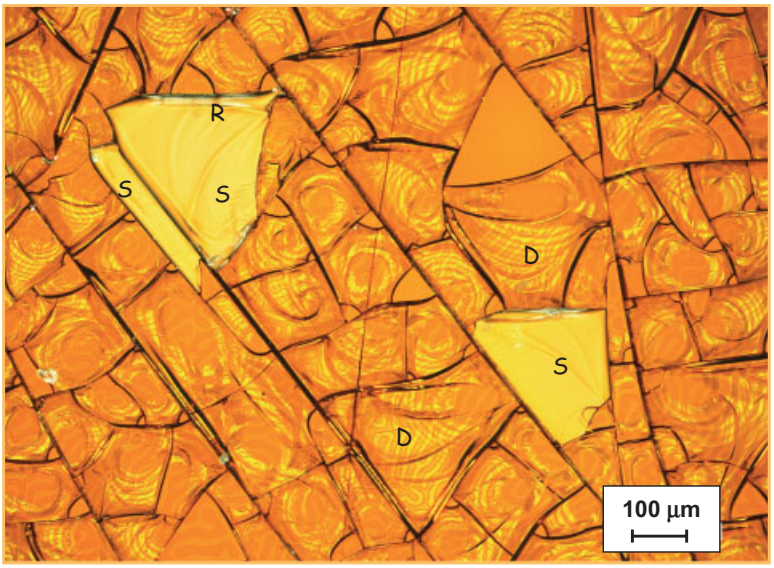

Figure 14.3 Magnetic domains D and cracks R in a film with large tensile stress. In regions S the film flaked off from the substrate.

between substrate s and film f. We think that substrate defects etched by lead and bismuth oxide vapor before dipping [31] do not play a large role.

Figure 14.2 presents the number of defects of Bi-TmIG films as a function of the relative misfit. A relative misfit $\Delta a/a_s$ larger than –0.002 leads to a drastic increase of the "pit density". This effect almost quantitatively agrees with the

strong increase of the partial strain relief of $(YEu)_3(FeGa)_5O_{12}$ films illustrated in figure 11.23 of Ref. [7].

Miller and Caruso [32] found that no stress relief will occur below a relative misfit of -1.5×10^{-3} at the growth temperature. Strain relief is caused by misfit-dislocation formation [23] and its climb to the film surface. Morphological instabilities connected with the development of {110} growth faces – sometimes called "facetting" – occur when the relative lattice misfit $\Delta a/a_s$ of comprehensively strained layers exceeds –0.0034 [7].

In the case of large tensile stress, however, cracks occur up to the substrate surface. Sometimes regions appear where the film flakes off from the substrate, as shown in Figure 14.3.

14.4 Magnetic and Magneto-Optic Film Properties

14.4.1 Magnetic Properties

Principally, two types of garnet films are grown

a) **Films with inplane magnetization:** Easy axis parallel to film surface, where the effective anisotropy $K_{eff} < 0$
b) **Films with out-of-plane magnetization:** Easy axis perpendicular to film surface, where the effective anisotropy $K_{eff} > 0$.

The effective anisotropy

$$K_{eff} = K_v + \frac{K_{su}}{d} = K_u^g + 2B_1 e - \frac{\mu_0 M_s^2}{2} + \frac{K_{su}}{d} \tag{14.1}$$

consists of two parts given by the film volume K_v and by the surface K_{su} of films with thickness d. In our case of film thicknesses between 1 and 5 µm, the surface contribution K_{su} may be neglected. K_u^g is the uniaxial growth-induced anisotropy [33] due to ordering between bismuth and the rare earth [7, 25] (this anisotropy is truly uniaxial only for the <111> and <100> directions [34]), $2B_1e$ is the magnetoelastic anisotropy with strain e, and $\mu_o M_s^2/2$ is the magnetostatic anisotropy. Since in our good films the relative misfit is less than 0.2%, the magnetoelastic anisotropy is in general small compared with the growth induced and magnetostatic anisotropy. The growth-induced anisotropy K_u^g can be adjusted in such a way that $K_u^g - \mu_0 M_s^2/2 \approx 0$ so that the sensor films are highly sensitive for changes of magnetic fields. The condition K_{eff} or better $K_{eff}/M_s \approx 0$ can also be obtained by applying an external magnetic field. It should be noted, however, that under such conditions the magnetoelastic anisotropy – although small – can play a role and small changes of strain influence the magnetic domain structure.

Bulk cubic magnetocrystalline anisotropy K_1 neither favors nor hinders perpendicular magnetization. Cubic anisotropy K_1 of inplane {111} films results in

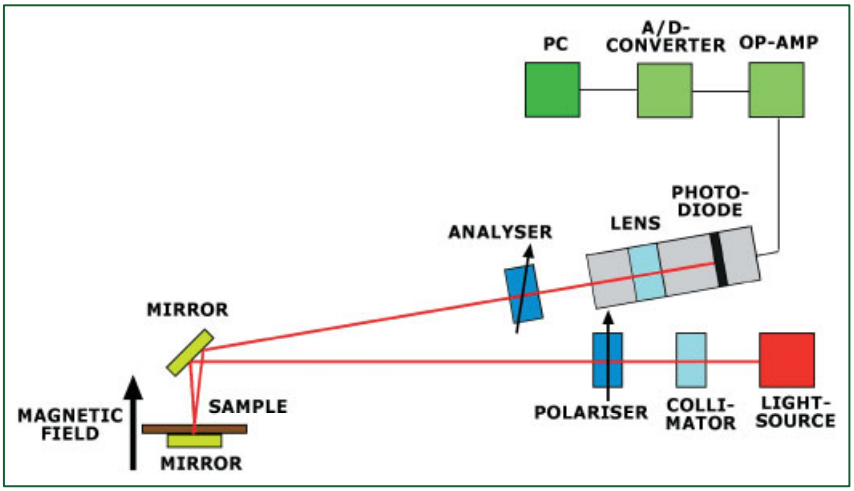

Figure 14.4 Faraday setup – schematic; OP: operation amplifier.

slightly oblique orientations of the magnetization in "zero field" connected with the occurrence of special magnetic domains [35]. For inplane {100} films, however, there is no K_1 contribution in "zero field" and the magnetization is completely in the plane [34].

14.4.2 Magneto-Optic Properties

The Faraday rotation is measured with the setup shown in Figure 14.4.

Figure 14.5 shows a typical Faraday hysteresis of a (111) Bi-TmLuIG film with magnetic domains in the remanent state pinned by defects, which hinders the motion of domain walls. This hysteresis is due to remagnetization processes caused by domain-wall displacement and, possibly, by a "two-layer structure" consisting of a layer with "easy plane" anisotropy close to the surface and uniaxial anisotropy in the thinner layer adjacent to the substrate [36, 37]. The following linear part characterizes, as usual, remagnetization by rotation of the inplane magnetization vector.

As can be seen in Figure 14.5 the pinning of domains results in a relatively large coercivity of roughly 2.5 kA/m connected with the fairly low responsivity of sensor films – although a movement of domain walls can be observed. Obviously, H_c and the formation of pits are due to both misfit stress and substrate surface quality.

Figure 14.6 presents the almost rectangular Faraday hysteresis of a (111) out-of-plane Bi-TmLuIG film.

Whereas the Bi-TmLuIG inplane films show mostly a more or less pronounced hysteresis (see Figure 14.5) the (111) Bi-DyLuIG inplane films possess an excellent

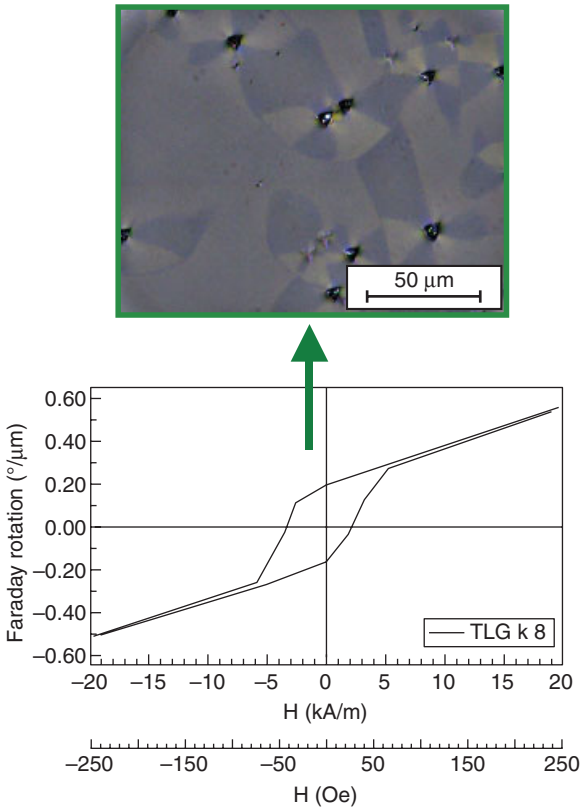

Figure 14.5 Faraday hysteresis of a (111) Bi-TmLuIG film and corresponding magnetic domains pinned by defects in the remanent state. The magnetic field *H* is perpendicular to the film surface.

linear characteristic as demonstrated in Figure 14.7 for wavelengths in the range 505–625 nm.

The coercivities of our good films are of the order of 0.02 kA/m and the saturation fields are about 20 kA/m (25 mT), which can be seen from the magnetization curve in Figure 14.8 measured with a SQUID magnetometer.

Figure 14.9 shows that the absorption coefficient α increases markedly below a wavelength of 520 nm. The position of the absorption edge corresponds to the typical opacity of iron garnet films. The absorption spectra are determined by transmission and reflection measurements using UV-VIS spectroscopy.

The figure of merit FOM = $2\theta_{SAT}/\alpha$ is maximal in the range of 510 to 560 nm, as illustrated in Figure 14.10. Our values of specific Faraday rotation, absorption coefficient, and FOM agree well with those published by Keszei *et al.* [38].

For applications, however, the photoresponse PR defined as the ratio I_{det}/I_0 of intensity I_{det} reaching the detector and input intensity I_0 is important. PR for inplane films is given as [39]

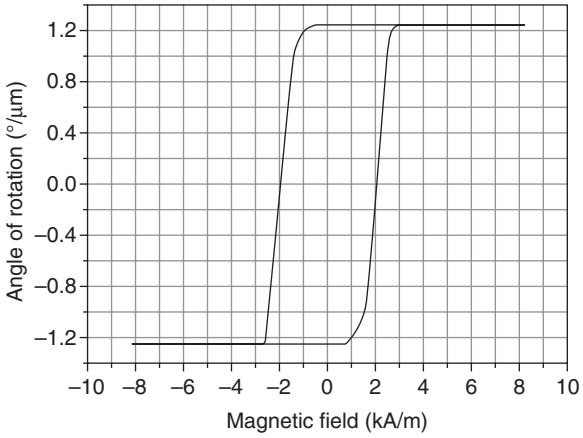

Figure 14.6 Faraday hysteresis of (111) out-of-plane Bi-TmLuIG film. The magnetic field is perpendicular to the film surface.

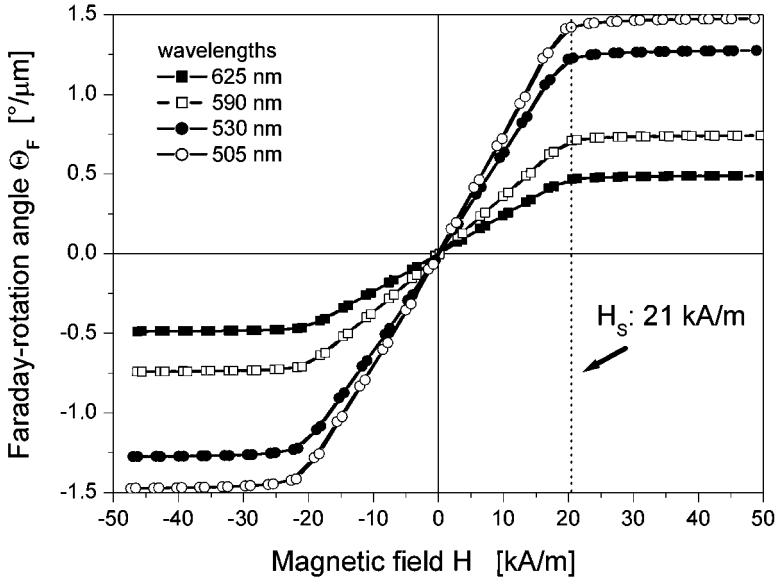

Figure 14.7 Specific Faraday rotation angle Θ_F as a function of magnetic field H perpendicular to the surface of an (111) inplane Bi-DyLuIG film measured at wavelengths from 505 to 625 nm; film thickness $d = 4.4\,\mu m$.

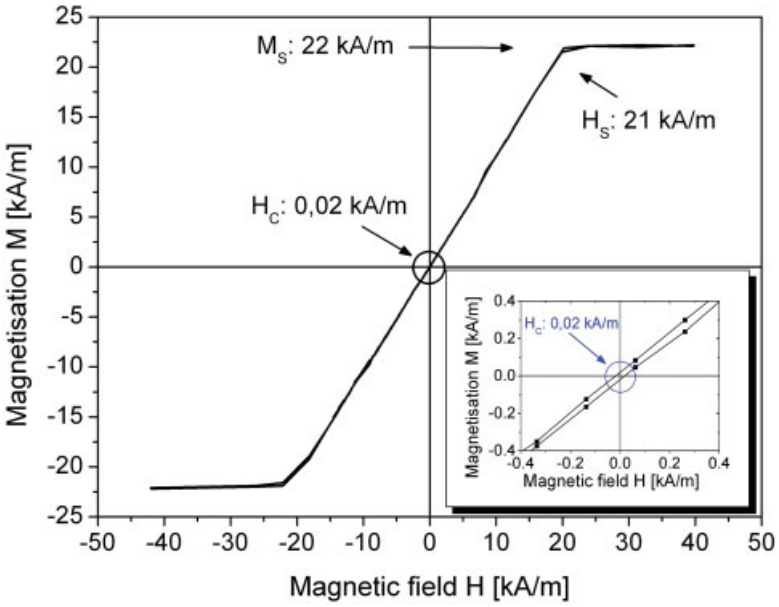

Figure 14.8 Magnetization *M* vs. magnetic field *H* perpendicular to the surface of an (111) inplane Bi-DyLuIG film (SQUID magnetometry).

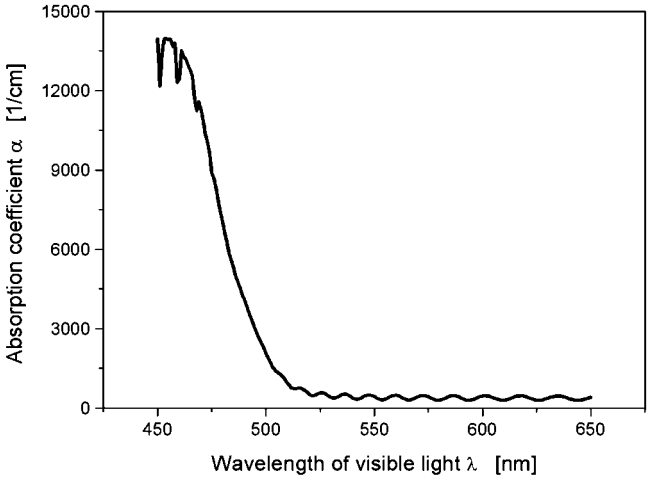

Figure 14.9 Absorption coefficient α vs wavelength λ of a (111) Bi-DyLuIG film (without substrate).

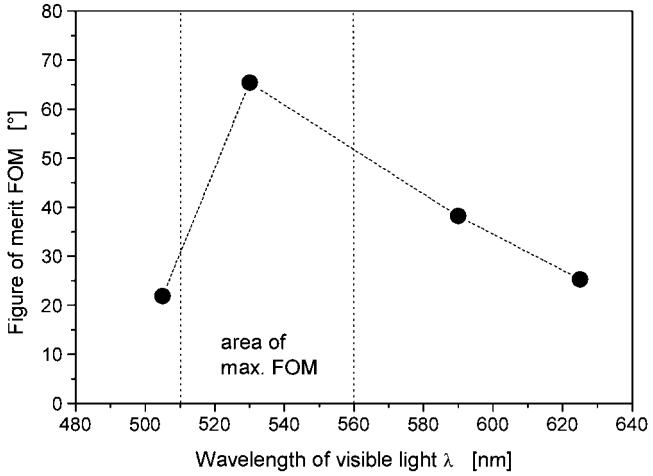

Figure 14.10 Figure of merit FOM in dependence on wavelength λ of a Bi-DyLuIG film.

$$\mathrm{PR} = \frac{I_{\mathrm{det}}}{I_0} = \exp(-L\alpha)\cosh^2\Psi\left[\cos^2(\beta-\Theta)+\tanh^2\Psi\sin^2(\beta-\Theta)\right] \tag{14.2}$$

with L as total propagation length of light inside the film, which is for mirror-type sensors twice the film thickness d; α as absorption coefficient; Ψ as the ellipticity angle [40] given by the difference of the absorption coefficients for right- and left-handed circularly polarized light; β as angle between polarizer and analyzer; and Θ as the Faraday rotation angle. For wavelengths $\lambda > 520\,\mathrm{nm}$ the absorption (compare Figure 14.9) is relatively small and with it the ellipticity may be neglected. When we choose an angle $\beta = 45°$, where the sensitivity is maximal, we get therefore approximately

$$\mathrm{PR} = \frac{I_{\mathrm{det}}}{I_0} \approx \exp(-L\alpha)\left[\cos^2(45°-\Theta)\right] \tag{14.3}$$

where the Faraday rotation angle Θ is, of course, a function of the applied magnetic field $B_\perp$ perpendicular to the film surface. Figure 14.11 shows the corresponding PR curves for the films of Figure 14.7. For very small absorption coefficients $\alpha \approx 0$ and $B = 0$ the photoresponse PR = 0.5.

The sensitivity S of the system described above can be defined for small fields as the change of photoresponse in dependence on the perpendicular induction $B_\perp$ [39]

$$S = \left.\frac{\mathrm{d(PR)}}{\mathrm{d}B_\perp}\right|_{B_\perp=0} \tag{14.4}$$

Figure 14.12 illustrates the sensitivities S and the swing Q_S for the films characterized in Figures 14.7 and 14.11 as a function of the wavelength, where Q_S is defined as the difference between the maximal and minimal photoresponse. Obviously,

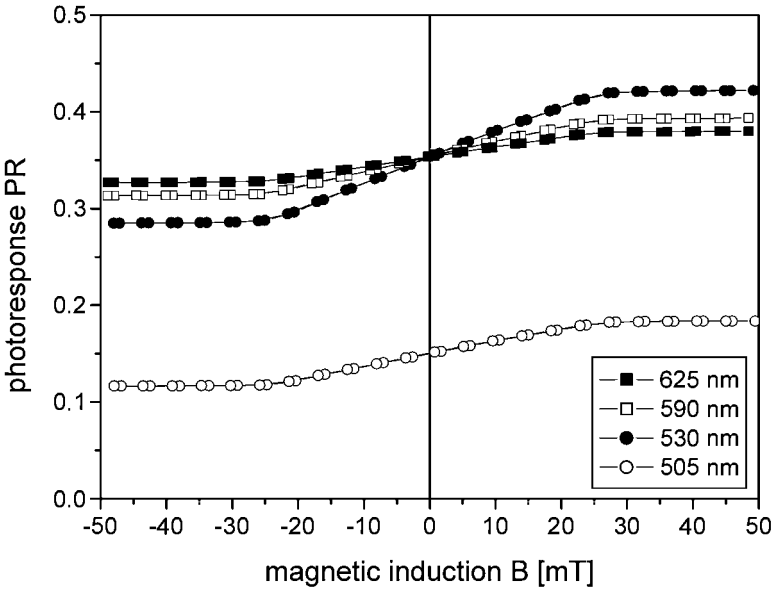

Figure 14.11 Photoresponse PR according to Equation 14.3 for the films of Figure 14.7 as a function of the magnetic induction *B* perpendicular to the film surface.

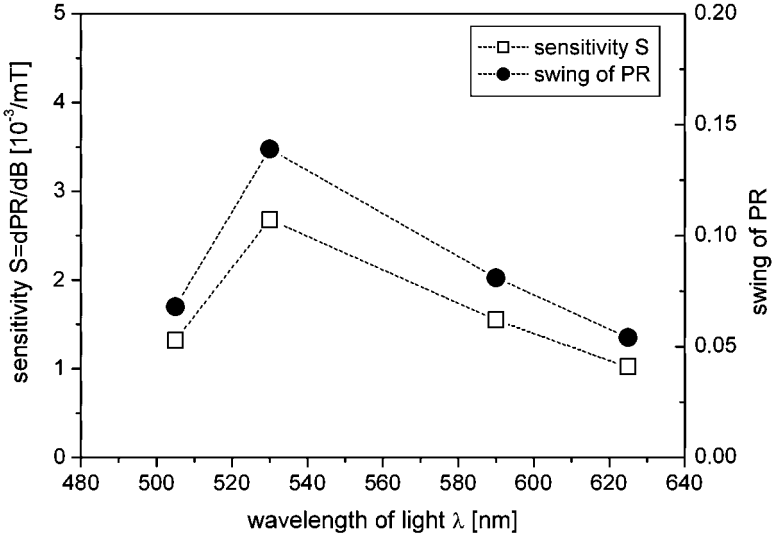

Figure 14.12 Sensitivity *S* and swing of photoresponse PR in dependence on the light wavelength.

Table 14.1 Comparison of specific Faraday rotation angle Θ_F, film thickness d, and saturation field H_S of Bi-DyLuIG films produced under "reproducible" conditions.

Garnet film	Θ_F (°/μm)	d (μm)	H_S (kA/m)
DLG g10	0.52	4.4	33.5
DLG g11	0.53	4.5	32.0
DLG g12	0.53	4.4	33.5
DLG g13	0.54	4.5	33.5
Average	0.53 ± 0.01	4.5 ± 0.1	33.1 ± 0.8

the figure of merit, sensitivity, and swing behave very similarly in dependence on the light wavelength. Figure 14.12 reveals that the maximal sensitivity S is 3.5×10^{-3}/mT at $\lambda = 530$ nm. Although this is a good value for (111) inplane films the sensitivity can be enlarged to 13×10^{-3}/mT at the same light wavelength for a (112) $(YBiPr)_3(FeGa)_5O_{12}$ film, where the easy plane is inclined by an angle of 35° with respect to the film plane [41]. It should be noted, however, that for the calculation of this sensitivity the absorption has been neglected. In other words α has been set equal to zero in Equation 14.3.

The magneto-optic sensitivity can be improved by applying an external induction $B_\perp$ for inplane films and $B||$ for out-of-plane films [42].

14.4.3 Reproducibility

One crucial requirement for magneto-optic applications of garnet films is a high reproducibility of film properties like chemical film composition, film thickness, Faraday rotation, sensitivity, and dynamic range. For the production of such films technological conditions such as high quality of substrates and reproducible growth conditions are indispensable. However, the real growth conditions are never completely the same. Above all, the ratios of the $PbO–B_2O_3–Bi_2O_3$-based solvent change with time due to evaporation losses. Nevertheless, it is possible to develop a reproducible LPE technology to adjust optimized sensor properties of Bi-REIG in a wide technology window. Table 14.1 shows typical data of magneto-optic films produced under "reproducible" growth conditions.

It can be seen that the standard deviations of film thickness d, specific Faraday rotation angle Θ_F, and saturation field H_S are fairly low.

14.5 Applications

The high sensitivity and the excellent homogeneity of MO sensor films allow a number of technical applications based on qualitative and quantitative imaging of

magnetic fields with high spatial resolution to be met. The resolution of conventional magneto-optics with inplane films is limited essentially by Abbe's fundamental theory, the minimal width of domain walls, which is typically 200 nm [31], and the active film thickness [43]. In very specials cases there is the possibility to improve the resolution using out-of-plane films and diffraction spectra [37].

Both the construction of magneto-optic sensors and some examples of technical application have been already demonstrated in former book articles [7, 44]. Thus, only some recent developments are presented here.

14.5.1
Images of Magnetic Field Distributions

Figure 14.13 shows a fairly simple equipment made by Matesy GmbH [45]–called MagView–for visualization of a two-dimensional cross-section of inhomogeneously magnetic fields. The MagView consists of an usual magneto-optic sensor film with in- or out-of-plane magnetization, a light source for illumination, a polarizer and an analyzer. Other commercial magneto-optic systems made by Matesy GmbH to check magnetic cards and tapes have been shown already [7].

Figure 14.14 presents the magnetic information of (a) a 1.4-MB 3.5-inch floppy disc and (b) a 127-MB hard disc taken by an ordinary polarizing microscope and an inplane sensor film. The smallest stripe distance is about 2 μm. High-density hard discs (HDD), however, cannot be read in this way due to limitation of the lateral resolution discussed above.

Figure 14.15 shows the magneto-optic visualization of the magnetically printed INNOVENT logo in polymer-bonded NdFeB compound (size $5 \times 10\,\mathrm{mm}^2$). It

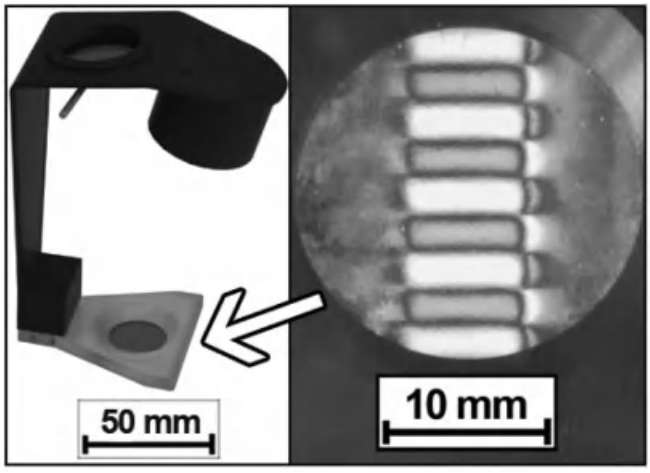

Figure 14.13 MagView for visualization of magnetic field structures (left-hand side) and magnetic field structure of an encoder (right-hand side).

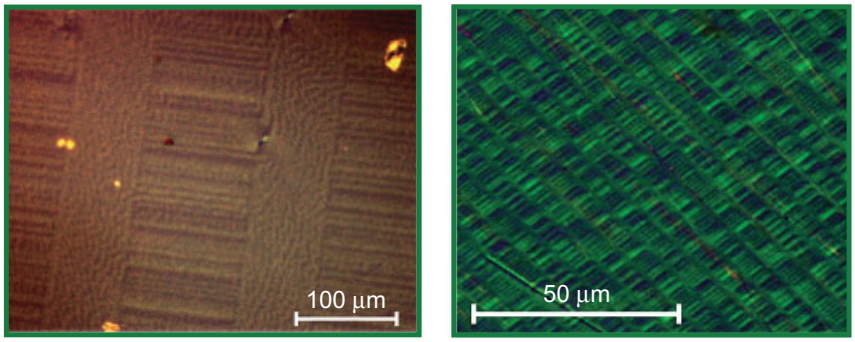

Figure 14.14 Visualization of the magnetic information of (a) a 1.4-MB floppy disc 3.5″ and (b) a 127-MB hard disc.

Figure 14.15 Magneto-optical visualization of the magnetically printed INNOVENT logo in polymer-bonded NdFeB compound (size $5 \times 10\,mm^2$).

should be stressed that this logo is not visible with the naked eye. Therefore, this technology can be used for product and trademark protection.

An eddy current test system for nondestructive evaluation of defects in magnetic and "nonmagnetic" materials [46] has been constructed (Figure 14.16) by the

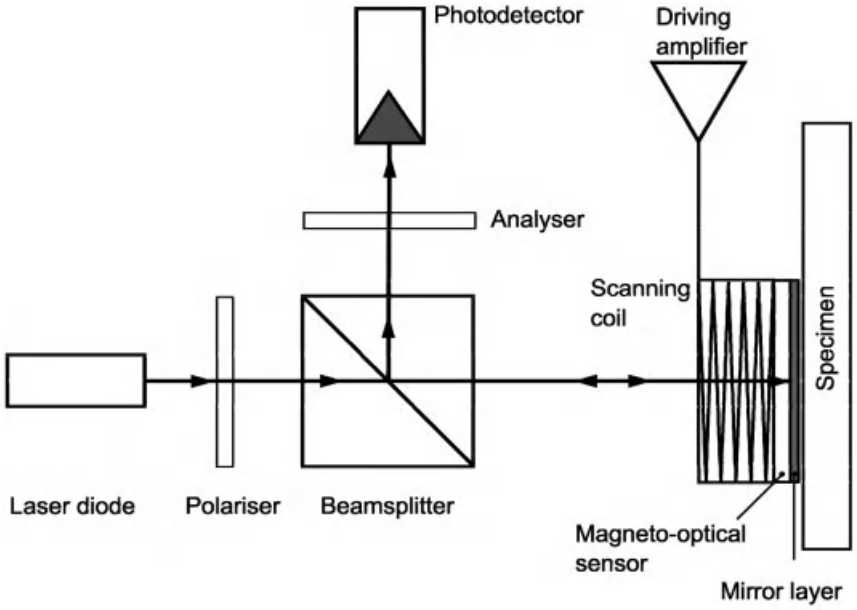

Figure 14.16 Schematical setup of the magneto-optic eddy-current sensor system.

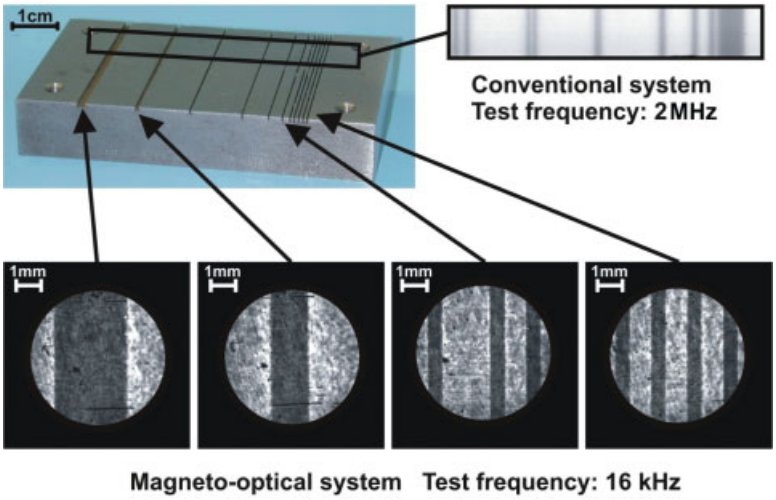

Figure 14.17 Comparison of the resolution of a conventionally inductive and a magneto-optic system using a ST 37 test specimen (courtesy of R. Zielke, Uni Dortmund).

University of Dortmund [47, 48]. Here, the detection coil of an usually inductive system is replaced by a sensitive magneto-optic sensor, which allows considerable improvement in the lateral resolution of the eddy-current system, what is shown in Figure 14.17 by the comparison of a conventionally inductive and the new

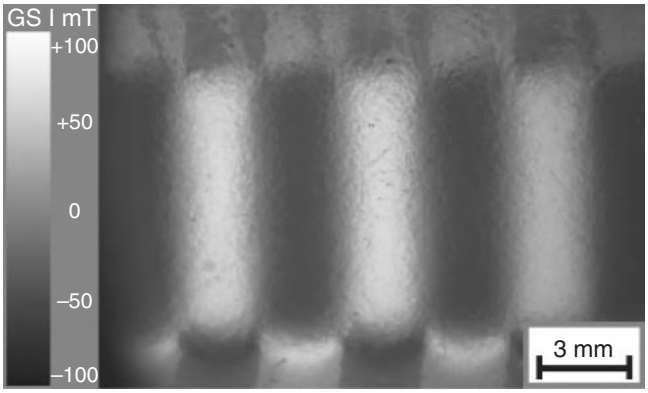

Figure 14.18 Quantitative magnetic image of a linear encoder, which is directly visualized by means of magneto-optic sensor technique. The image was recorded with a CCD-camera at an 80° position of polarizers using monochromatic light. The 8-bit gray scale to quantify the magnetic field is shown on the left-hand side of the image.

magneto-optic system. The skin depth of the magneto-optic system at 16 kHz is larger by a factor of 11 compared with those of the high-resolution inductive system at 2 MHz.

14.5.2
Quantitative Determination of Magnetic Fields

Magneto-optic sensors with inplane magnetization and linear characteristic can be used to measure the local magnetic field distribution quantitatively [49]. For exact calibration of a system a known field must be applied before measurement. After that each field value corresponds to a pseudocolor or gray value, as shown in Figure 14.18 for a linear encoder. This image was recorded with a CCD camera at an 80° position of polarizers using monochromatic light.

Using a magneto-optic sensor with dynamic range from 0.05 to 50 kA/m, 16-bit converter, low-noise diode and current-limited stable light source the minimally detectable change of magnetic fields has been estimated to be 10 A/m.

14.6
Conclusions

LPE is the best deposition method for the preparation of highly sensitive garnet films with large Faraday rotation, low absorption, and fairly different characteristic hysteresis curves. Misfit stress results in misfit dislocations, morphological instabilities, cracks, enlarged coercivities, and the well-known optical birefringence. The most sensitive magneto-optic films are characterized by low misfit, low effective anisotropy $K_{\text{eff}} \approx 0$, low defect density, and suitable crystallographic orientation.

Such films are used for commercial applications as sensors with high lateral resolution to visualize and measure the spatial distribution of magnetic fields.

Acknowledgments

The authors thank Prof. Dr. H. Dötsch (Osnabrück) for critically reading the manuscript and for helpful discussions.

References

1 Zvezdin, A.K., and Kotov, V.A. (1997) *Modern Magnetooptics and Magnetooptical Materials*, Taylor & Francis Group, New York.

2 Kidoh, H., Morimoto, A., and Shimuzi, T. (1991) *Appl. Phys. Lett.*, **59**, 237.

3 Buhrer, C.F. (1969) *J. Appl. Phys.*, **40**, 4500.

4 Hansen, P., Witter, K., and Tolksdorf, W. (1983) *Phys. Rev. B*, **27**, 6608.

5 Fratello, V.J., and Wolfe, R. (2000) *Handbook of Thin Film Devices*, vol. **4** (ed. M.H. Francombe), Academic Press, London, Ch 3, pp. 93–141.

6 Dötsch, H. (2000) Herstellung und Charakterisierung magnetischer Granatschichten, Abschlußbericht Teilprojekt A2, Modulatoren und Laser in Granat-Wellenleitern Teilprojekt D11, Universität Osnabrück.

7 Hibiya, T., and Görnert, P. (2007) *Liquid Phase Epitaxy of Electronic, Optical and Optoelectronic Materials* (eds. P. Capper and M. Mauk), John Wiley & Sons, Ltd, Chichester, p. 305.

8 Johansen, T.H., and Shantsev, D.V. (2004) *Magneto-Optical Imaging*, Kluwer Academic Publishers, Dordrecht.

9 Aichele, T., Lorenz, A., Hergt, R., and Görnert, P. (2003) *Cryst. Res. Technol.*, **38**, 575.

10 Okuda, T., Koshizuka, N., Hayashi, K., Taniguchi, H., Satoh, K., and Yamamoto, H. (1988) *IEEE Trans. J. Magn. Jpn.*, **3**, 483.

11 Kim, Y.H., Kim, J.S., Kim, S.I., Levy, M., and Kore, J. (2003) *Phys. Soc.*, **43**, 400.

12 Boudier, T., Payet-Gervy, B., Bianc-Mignon, M.F., Rousseau, J.J., Le Berre, M., and Joiten, H. (2004) *J. Magn. Magn. Mater.*, **284**, 77.

13 Okuda, T., Katayama, T., Kobayashi, H., Kobayashi, N., Satoh, K., and Yamamoto, H. (1990) *J. Appl. Phys.*, **67**, 4944.

14 Chern, M.Y., and Liaw, J.S. (1997) *Jpn. J. Appl. Phys.*, **36**, 1049.

15 Adachi, N., Denysenkov, V.P., Khartsev, S.I., Grishin, A.M., and Okuda, T. (2000) *J. Appl. Phys.*, **88**, 2734.

16 Lux, R., Heinrich, A., Leitenmeier, S., Körner, T., Herbort, M., and Stritzker, B. (2006) *J. Appl. Phys.*, **100**, 113511.

17 Kahl, S., Khartsev, S.I., Grishin, A.M., Kawano, K., Kong, G., Chakalov, R.A., and Abell, J.S. (2002) *J. Appl. Phys.*, **91**, 9556.

18 Okada, M., Katayama, S., and Tominaga, K. (1991) *J. Appl. Phys.*, **69**, 3566.

19 Thavendrarajah, A., Pardavi-Horvath, M., Wigen, P.E., and Gomi, M. (1989) *IEEE Trans. Magn.*, **25**, 4015.

20 Mino, S., Matsuoka, M., Tate, A., Shibukawa, A., and Ono, K. (1992) *Jpn. J. Appl. Phys*, **31**, 1786.

21 Heinrich, A., Leitenmeier, S., Körner, T., Lux, R., Herbort, M., and Stritzker, E. (2006) *J. Magn. Soc. Jpn.*, **30**, 584.

22 Dubinko, S.V., Nedviga, A.S., Vishnevskii, V.G., Shaposhnikov, A.N., Yagupov, V.S., Nesteruk, A.G., and Prokopov, A.R. (2005) *Tech. Phys. Lett.*, **31**, 979.

23 Fratello, V.J., Licht, S.J., Brandle, C.D., O'Bryan, H.M., and Baiocchi, F.A. (1994) *J. Cryst. Growth*, **142**, 93.

24 Hasanpour, A., Mozaffari, M., Amighian, J., Richert, H., Lorenz, A., Lindner, M., Görnert, P., and Heegn, H. (2007) *J. Magn. Magn. Mater.*, **317**, 41.

25 Hansen, P., and Krumme, J.-P. (1984) *Thin Solid Films*, **114**, 69.

26 Kuroda, C.S., Kim, T.Y., Hirano, T., Yoshida, K., Namikawa, T., and Yamazaki, Y. (1999) *Electrochim. Acta*, **44**, 3921.

27 Kuroda, C.S., Taniyama, T., Kitamoto, Y., and Yamazaki, Y. (2002) *J. Magn. Magn. Mater.*, **241**, 201.

28 Lee, J.W., Oh, J.H., Lee, J.C., and Choi, S.C. (2004) *J. Magn. Magn. Mater.*, **272–276**, 2230.

29 Görnert, P., Aichele, T., Lorenz, A., Hergt, R., and Taubert, J. (2004) *Phys. Status Solidi A*, **201**, 1398.

30 Mateika, D. (1984) *Current Topics in Materials Science*, vol. **11** (ed. E. Kaldis), North-Holland, Amsterdam, pp. 151–239.

31 Hagedorn, O. (2002) Herstellung und Charakterisierung Magnetischer Granatfilme für die magnetooptische Sensorik, Dissertation Universität Osnabrück, März.

32 Miller, D.C., and Caruso, R. (1974) *J. Cryst. Growth*, **27**, 274.

33 Görnert, P., and Voigt, F. (1984) *Current Topics in Materials Science*, vol. **11** (ed. E. Kaldis), North-Holland, Amsterdam, pp. 1–149.

34 Fratello, V.J., Mnushkina, I., and Licht, S.L. (2004) *Magneto-Optical Imaging* (eds T.H. Johansen and D.V. Shantsev), Kluwer Academic Publishers, Netherlands, p. 311.

35 Shamonin, M., Beuker, T., Rosen, P., Klank, M., Hagedorn, O., and Dötsch, H. (2000) *NDT&E Int.*, **33**, 547.

36 Vértesy, G., and Keszei, B. (2003) *J. Magn. Magn. Mater.*, **254–255**, 550.

37 Sohatsky, V., and Kovalenko, V. (2004) *Magneto-Optical Imaging* (eds T.H. Johansen and D.V. Shantsev), Kluwer Academic Publishers, Netherlands, p. 293.

38 Keszei, B., Vértesy, Z., and Vértesy, G. (2001) *Cryst. Res. Technol.*, **36**, 953.

39 Dötsch, H., Klank, M., Hagedorn, O., Holthaus, C., Shamonim, M., and Trifonov, A. (2004) *Magneto-Optical Imaging* (eds T.H. Johansen and D.V. Shantsev), Kluwer Academic Publishers, Netherlands, p. 301.

40 Hansen, P., Rosenkranz, M., and Witter, K. (1982) *Phys. Rev. B*, **25**, 4396.

41 Klank, M., Hagedorn, O., Shamonin, M., and Dötsch, H. (2002) *J. Appl. Phys.*, **92**, 6484.

42 Dötsch, H., Holthaus, C., Trifonov, A., Klank, M., Hagedorn, O., Shamonin, M., and Schützmann, J. (2005) *Mater. Res. Soc. Symp. Proc.*, **834**, 217.

43 Dreyer, S. (2007) Entwicklung eines quantitativen Verfahrens zur Streufeld- und Magnetisierungsbestimmung magnetischer Strukturen, Dissertation Universität Göttingen, Mai.

44 Krafft, C., Zhang, J., Marr, K., Dottelis, J.B., and Mayergoyz, I. (2004) *Magneto-Optical Imaging* (eds T.H. Johansen and D.V. Shantsev), Kluwer Academic Publishers, Netherlands, p. 273.

45 Matesy GmbH: www.matesy.de.

46 Fitzpatrick, G.L., Thome, D.K., Skaugset, R.L., Shih, E.Y.C., and Shih, W.C.L. (1993) *Mater. Eval.*, **51**, 1402.

47 Radtke, U., Zielke, R., Rademacher, H.-G., Crostack, H.-A., and Hergt, R. (2001) *Opt. Laser. Eng.*, **36**, 251.

48 Zielke, R., Rademacher, H.-G., Crostack, H.-A., Lorenz, A., and Görnert, P. (2007) *DGZfP-Jahrestagung in Fürth*, DGZfP, Berichtsband 104-CD. ISBN: 978-3-931381-98-1.

49 Jooss, C., Brinkmeier, E., Born, V., Westhäuser, W., and Guth, K. (2004) *Magneto-Optical Imaging* (eds T.H. Johansen and D.V. Shantsev), Kluwer Academic Publishers, Netherlands, p. 29.

15
Growth Technology and Laser Properties of Yb-Doped Sesquioxides

Rigo Peters, Klaus Petermann, and Günter Huber

15.1
Introduction

The cubic rare-earth doped sesquioxides are known for their excellent thermal properties and the possibility for high doping concentrations of laser-active rare-earth ions. For high-power solid-state lasers ytterbium is the most attractive laser ion due to its favorable spectroscopic properties, that is, high absorption and emission cross-sections and long fluorescence lifetime. The combination of the low Stokes shift of the ytterbium ion with the thin-disk laser geometry [1], which is one of the most sophisticated laser designs for power scaling [2], allows for an excellent beam quality and high optical efficiency. A schematic of the thin-disk laser is shown in Figure 15.1. Thus, for laser output powers in the multi-kW range Yb-doped sesquioxides could be superior to the standard thin-disk laser material Yb:YAG. There is also a great potential for mode-locked laser operation of Yb-doped sesquioxides [3–5] due to the relatively broad emission bands.

However, the very high melting temperatures of about 2500 °C hindered the production of crystalline material with sufficient optical quality in the past [6]. Recent advances in crystal-growth technology of sesquioxides using the heat-exchanger-method (HEM) and high-purity rhenium crucibles allow for the production of high-quality bulk material [7]. Now, single-crystalline blocks with a volume of more than 10 cm^3 have been prepared from the grown boules, limited only by the crucible size. In contrast to former samples these high-purity crystals exhibit no concentration quenching of the fluorescence yield for doping levels up to 10 at.%.

15.2
Structure and Physical Properties

The sesquioxides Sc_2O_3, Y_2O_3, and Lu_2O_3 as well as their solid solutions belong to the cubic Bixbyite structure with the space group Ia3 (T_h^7) [8]. Two different sites exist in the unit cell, which are sites with C_2 symmetry (24) and sites with C_{3i}

Crystal Growth Technology. Semiconductors and Dielectrics. Edited by P. Capper and P. Rudolph
Copyright © 2010 WILEY-VCH Verlag GmbH & Co. KGaA, Weinheim
ISBN: 978-3-527-32593-1

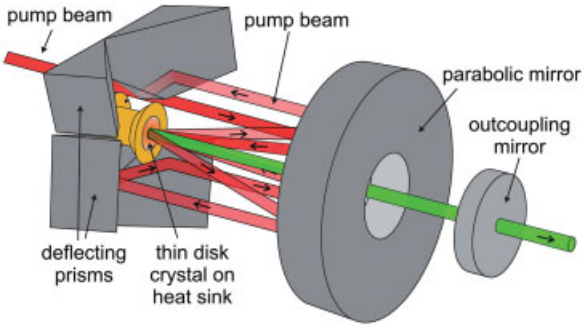

Figure 15.1 Schematic of a thin-disk laser.

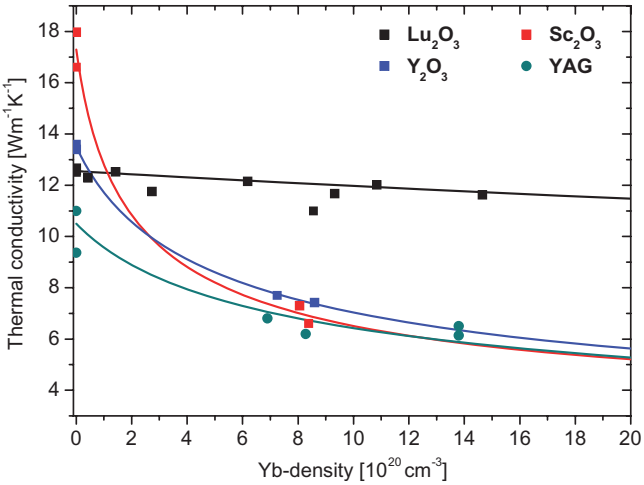

Figure 15.2 Heat conductivity of different Yb-doped sesquioxides in comparison to Yb:YAG.

symmetry (8). Both sites may be substituted by Yb, whereas the optical properties are mainly determined by Yb in the C_2 sites.

One of the most desirable properties of host crystals for high-power solid-state lasers is a high thermal conductivity. From this point of view the sesquioxides Sc_2O_3, Y_2O_3, and Lu_2O_3 appear to be suitable due to their high heat conductivity in undoped crystals. However, as in all host materials the heat conductivity drops significantly when doped with Yb, as demonstrated in Figure 15.2. Due to the different atomic weights of the Yb dopant and the host cation this effect is strongest in Sc_2O_3 and weakest in Lu_2O_3. Thus, especially for high doping levels the thermal conductivity of Lu_2O_3 is much larger than that of Yb-doped YAG.

In Table 15.1 some physical properties as well as a few spectroscopic and laser relevant data at room temperature are collected.

Table 15.1 Physical and spectroscopic properties at 300 K of Sc_2O_3, Y_2O_3 and Lu_2O_3 in comparison to YAG.

	Sc_2O_3	Y_2O_3	Lu_2O_3	YAG
Melting point (°C)	2430	2430	2500	1930
Therm.-cond. (undoped) (W/m·K)	16.5	13.6	12.5	11.0
Therm. cond. (3 at.% Yb-doped) (W/m K)	6.4	7.4	10.8	7.1
Density of cation sites (10^{22} cm^{-3})	3.3	2.7	2.9	1.38
Fluorescence lifetime (μs)	800	850	820	1040
Pumping wavelength (nm)	975.1	976.7	976.0	968.8
Absorption bandwidth FWHM (nm)	1.5	2.1	2.2	2.5
σ_{abs} (10^{-21} cm^2)	45	24	30	8

15.3 Crystal Growth

Due to their high melting temperatures, high demands on the growth of the sesquioxides Sc_2O_3, Y_2O_3, and Lu_2O_3 have to be fulfilled. In particular, the crucible as well as the insulation material must have a high thermal, chemical and mechanical stability.

To avoid these problems crucible-free growth techniques can be used, where the melt is not in contact with any other material except the growth atmosphere. Another possibility is to reduce the needed temperatures by using growth techniques from solutions. Both, solution growth as well as crucible-free methods like Verneuil, floating-zone or laser-heated pedestal growth have been investigated in the past, but due to inclusions or high stress the crystal quality was limited [9–12].

Using crucibles the crystal quality as well as the achievable crystal size can be improved, which is attributed to a better control of the process parameters. However, to apply these techniques the crucible and the thermal insulation have to withstand the high growth temperatures. If this precondition is fulfilled, well-established growth methods like the Czochralski, Nacken–Kyropoulos, and the micropulling down technique as well as the Bridgman or the heat-exchanger method (HEM) can be used.

15.3.1 Growth Methods with Crucibles

The first attempts to grow high melting sesquioxides from small Re crucibles by the Czochralski-method (Cz) have been performed at the Institute of Laser-Physics, University of Hamburg in the late 1990s [13]. The achieved crystal dimensions were 5–15 mm diameter with some mm in length. After a few millimeters of growth, the crystals lost contact with the melt. This behavior could not be overcome by reducing the heating power because of crystallization of the entire melt. These

problems can be explained by the high absorption and low emissivity of the sesquioxides of 0.6 to 0.8 at the melting temperature [14]. Since the energy transport at high temperatures is dominated by radiation, the high absorption of the crystal leads to an increase of the temperature at the interface and thus the crystallization stops.

The problems can be partly avoided by using the Nacken–Kyropoulos technique. This method is similar to the Cz method in the beginning. After a short Czochralski-growth period the pulling process is stopped and the crystal remains in contact with the melt, while the system is slowly cooled down. So, the already grown crystal acts as a seed. Unfortunately, this method cannot prevent parasitic nucleation at the melt surface and the crucible wall, which leads to the formation of several crystallites. Furthermore, there is no room to compensate for volume changes of the material during crystallization and cooling down. Thus, after the surface of the melt has solidified, strong thermal stress appears and very often the crystal is cracked. Nevertheless, the size and quality of the sesquioxide crystals grown by this method were substantially better than those grown by the Czochralski technique [15].

In contrast to the Nacken–Kyropoulos method, crystals with rather low thermal stress can be produced by the Bridgman technique, since there are no problems with volume changes during solidification of the melt. However, parasitic crystallization is a serious problem with this growth technique. The Bridgman method has been successfully used to grow large sesquioxide boules with single crystals up to a volume of a few cm^3 [16].

15.3.2 Heat-Exchanger Method

Like the Bridgman technique the HEM technique uses a seed crystal that is placed at the bottom of the crucible [17, 18]. In contrast to the Bridgman technique with a fixed axial temperature gradient the seed crystal is cooled by a gas flow through a nozzle at the bottom of the crucible. Thus, with the HEM technique the heat is extracted selectively at the seed, leading to nearly hemispherical isothermal lines [19].

In Figure 15.3 the HEM growth process is shown schematically. After melting the raw material the gas flow is increased slowly at a constant heating power. The crystal grows without coming into contact with the melt. After reaching the maximum gas flow, the heating power is reduced and the melt crystallizes completely. Due to the relatively late contact with the crucible wall, less stress is induced in the crystal in comparison with the Bridgman technique.

In industrial production this technique is used to fabricate high-quality sapphire with diameters up to 35 cm and weights up to 65 kg [20] as well as polycrystalline silicon, with crystal weights up to 200 kg [21].

15.3.2.1 Crucible

Due to the high melting points of the sesquioxides only a few materials fulfill the demands for crucibles. In addition to rhenium with a melting temperature of

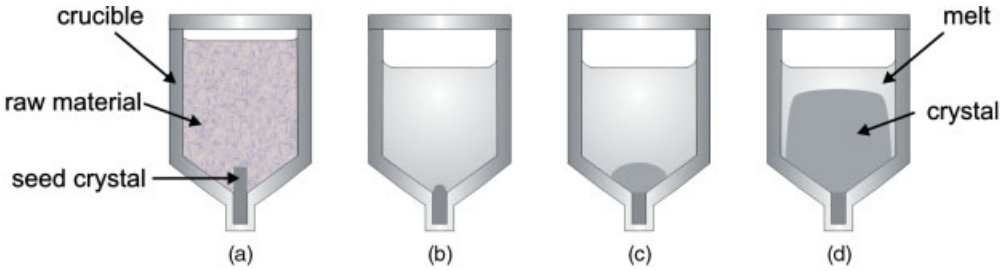

Figure 15.3 Schematic of the HEM growth process: (a) with raw material filled crucible; (b) melting of the raw material with partially melting of the seed; (c) increasing of the gas flow and crystallization of the melt starting from the seed; (d) at maximum gas flow nearly completely crystallized melt.

T_m = 3186 °C only tungsten (T_m = 3422 °C), osmium (T_m = 3033 °C), tantalum (T_m = 3020 °C), and carbon (T_{sbl} = 4000 °C) have melting points that are high enough for the high-temperature crystal growth. Osmium and tantalum cannot be used practically due to toxicity or high chemical reactivity with oxidic melts. Also, crucibles made from glasslike carbon are strongly corroded by the oxidic melts of the sesquioxides. Growth attempts with tungsten crucibles resulted in all cases in a dark-green coloration of the crystals, which can be attributed to a high solubility of tungsten in the melt. In contrast to these materials rhenium is practically inert to the melt, although it shows a high sensitivity to oxygen in the atmosphere. Due to the resistance against hydrochloric and phosphoric acids, rhenium crucibles can be cleaned relatively easy from melt leftovers.

15.3.2.2 **Atmosphere**

Due to the high oxygen sensitivity of rhenium a reducing growth atmosphere has to be used. In the past a combination of nitrogen with a small amount of hydrogen (5–15%) has been found to be well suited [22]. The hydrogen acts as a scavenger for the oxygen released from the insulation and the melt and thus prevents the rhenium from oxidation.

To investigate the influence of the growth atmosphere on the grown crystals phase diagrams have been calculated using the program Factsage. For an atmosphere consisting of 85% N_2 and 15% H_2 the resulting phase diagram is shown in Figure 15.4 for Lu_2O_3 as an example. The actual oxygen partial pressure is given at the y-axis for residual oxygen concentrations between 10 ppm and 1000 ppm. Due to the chemical reaction between oxygen and hydrogen at low temperatures the oxygen in the atmosphere is bound as water vapor. With increasing temperature the water vapor dissociates and the oxygen partial pressure increases. If the oxygen pressure is above a certain value different rhenates like ReO_2, ReO_3, and Re_2O_7 can be formed, which has to be prevented. On the other hand, for very low oxygen contents the sesquioxides can be reduced even to the metal phase. However, there is a relatively large range of oxygen partial pressures, where the growth of Lu_2O_3 is possible.

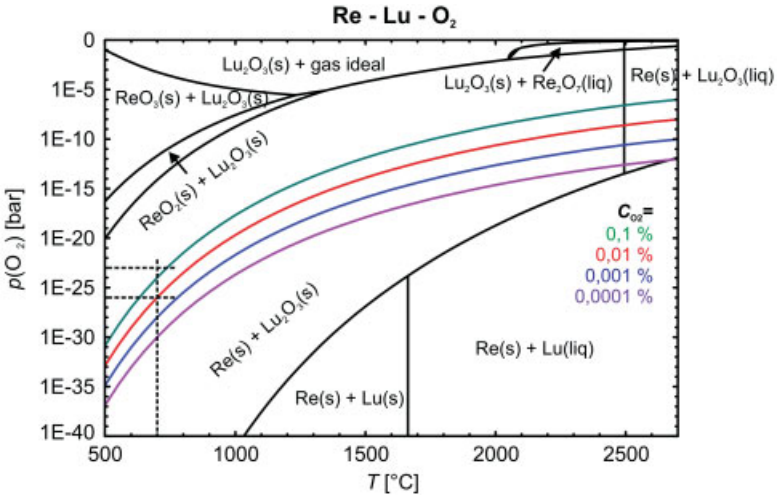

Figure 15.4 Predominance diagram of Re, Lu, and O_2 under an atmosphere of 85% N_2 and 15% H_2.

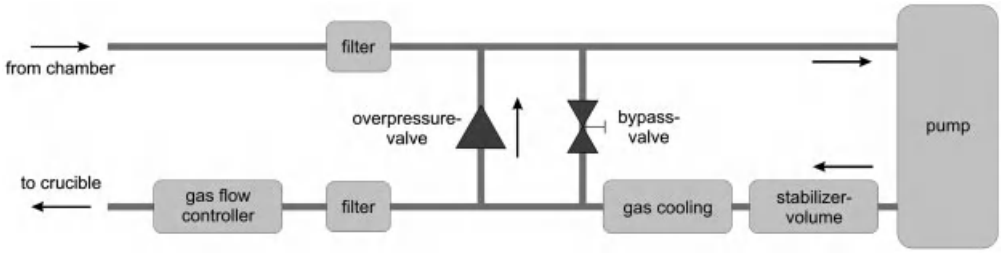

Figure 15.5 Schematic of the gas-cooling circuit.

The oxygen partial pressure in the growth chamber is measured with a potentiometric zirconia cell, working at a cell temperature of 700 °C. Thus, using the calculated phase diagrams and the measured oxygen content in the atmosphere the oxygen partial pressure can be estimated for any temperature up to the melting point (colored curves in Figure 15.4). For the used H_2/N_2 mixture the typical $p(O_2)$ was measured to be between 1×10^{-26} and 1×10^{-23} bar, corresponding to a residual oxygen concentration between 200 ppm and 6000 ppm.

15.3.2.3 **Setup**

The crystal-growth facility is a modified Czochralski setup with an implemented pump circuit as shown in Figure 15.5. The chamber gas is pumped by an oil-free membrane-pump through a nozzle onto the bottom of the crucible. Between the pump and the flow controller a buffer volume is placed to stabilize the gas flow. To reduce the gas temperature a gas cooling stage is also implemented. Further-

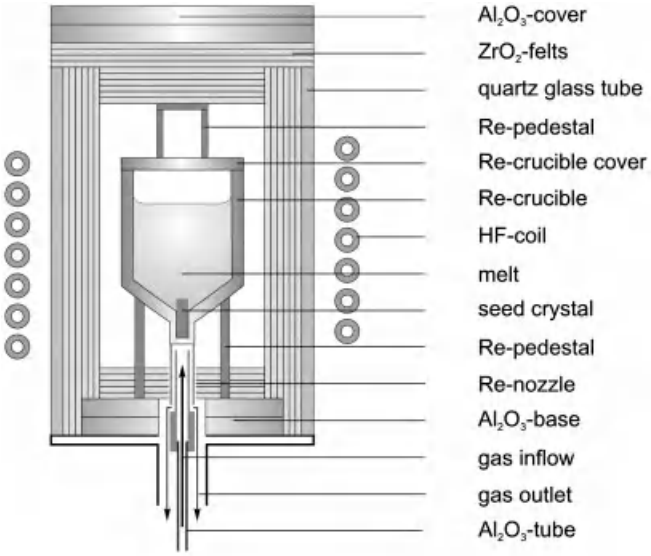

Figure 15.6 Schematic of the HEM setup.

more, particle filters are used to prevent damage of the pump. The gas flow is adjusted by a flow controller with a dynamical range of 0 to 50 l/min.

To reduce heat losses by thermal radiation efficient insulation is required, which is able to withstand the high growth temperatures. A combination of yttria-stabilized fiber-type ZrO_2 felts and ceramic Al_2O_3 disks has been found to be the optimum insulation [23]. To prevent melting or sintering of the felts, which are stable up to 2480 °C, the direct contact with the crucible has to be prevented.

The experimental setup is shown in Figure 15.6. The inductively heated 40-mm diameter crucible is placed on a pedestal, made of rhenium-rods. On top of the Re lid a spacer is located on which several layers of ZrO_2 felts and finally some ceramic Al_2O_3 disks are placed. Additional layers of felts provide the thermal insulation on the sides and the bottom of the set-up. Special attention has to be paid to the accurate fitting of the insulation around the gas nozzle to prevent a gas flow along the conical crucible bottom, leading to flattening of the isotherms, and thus enhancement of parasitic crystallization from the crucible edges. With the described setup a nearly isothermal temperature distribution can be achieved. A further advantage of the completely closed insulation is the strongly reduced heating power, in contrast to the Czochralski technique.

15.3.2.4 **Growth Procedure**

The high-purity raw materials are mixed according to their stoichiometric composition and placed in the crucible. Under a H_2/N_2 atmosphere the crucible is heated to about 1500 °C within a few hours to slowly release oxygen from the insulation materials. By the same step shrinking of the zirconia felts at higher temperatures

can be reduced. After two hours the temperature is increased to 2500 °C to melt the raw materials. Due to the low density of the starting powders, this procedure has to be repeated 3–4 times to fill about 75% of the crucible volume. After final heating to about 2600 °C the melt is held at this temperature for 2 h for homogenization. Next, the gas flow is increased over 20 h to a maximum value of 15–20 l/min. After reaching the maximum flowrate, the heating power is reduced with a slope of ~30 °C/h for a complete crystallization of the melt. Finally, the grown boule is cooled to room temperature over 72 h. As a last step the boule is drilled out of the crucible with a diamond core drill.

15.3.2.5 **Results**

With optimized parameters colorless crystalline boules with dimensions up to 40 mm in diameter and 35 mm in height could be drilled out of the rhenium crucible (see Figure 15.7). From these boules monocrystalline regions up to 30 cm^3 can be obtained, which are suitable for the preparation of a large number of laser disks.

To investigate the internal stress, Yb:Lu_2O_3 and Yb:Y_2O_3 samples with 0.5 mm thickness have been polished on two sides and placed between crossed polarizers. Under a microscope only weak birefringence has been found for Yb:Lu_2O_3, which could be expected for the contact-free growth by the HEM technique. In contrast to Lu_2O_3, Yb:Y_2O_3 shows relatively strong birefringence, as can be seen in Figure 15.8. This behavior was observed in all Y_2O_3 samples and may be due to different phase transitions during cooling to room temperature, leading also to significantly higher scattering losses in the range of 0.2 dB/cm [24].

In Figure 15.9a,b microscope images of the seed region of an Yb:Lu_2O_3 crystal are shown. At the lower part of Figure 15.9a the seed can be seen with only few inclusions and weak scattering. Above a sharp boundary an increased density of dark spots occurs. The small defects are Re inclusions, which are generated by a

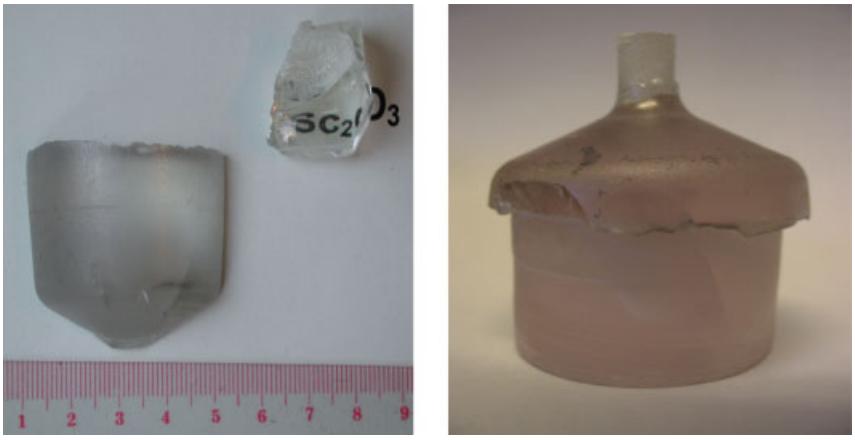

Figure 15.7 Photographs of different Sc_2O_3 (left) andY_2O_3 samples (right). The diameters of the grown boules are between 35 mm and 40 mm.

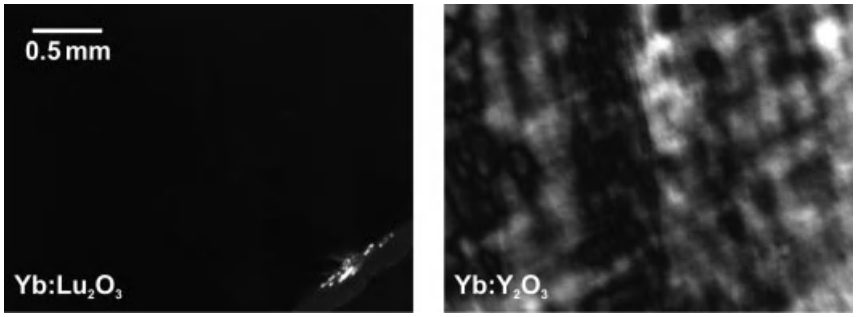

Figure 15.8 Microscope images under crossed polarizers of 0.5-mm thick Yb(5at.%):Lu_2O_3 and Yb(5at.%):Y_2O_3 crystals.

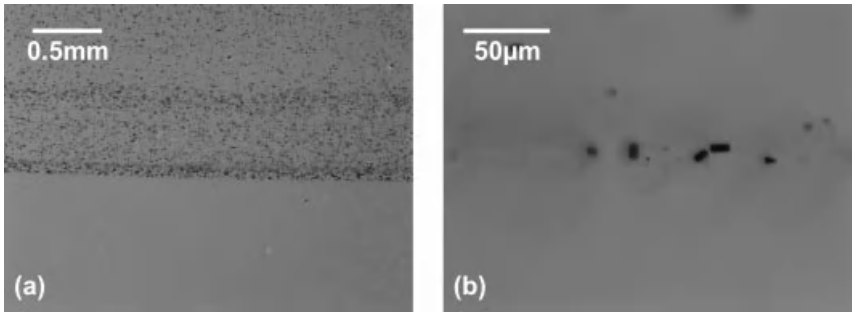

Figure 15.9 Microscope images of Yb:Lu_2O_3 with Re particles at the seed/crystal interface.

Re transport from the crucible to the melt as a result of the chemical reaction with oxygen in the growth atmosphere, mainly released from the ZrO_2 insulation. The typical particle size is in the range of 5 µm to 20 µm. Due to their higher density these particles sink to the bottom of the crucible and accumulate on the top of the seed. With increasing cooling-gas flow and thus the grown volume, the density of these defects decreases because of the decreasing O_2 content in the insulation and the growth atmosphere. Thus, the composition of the growth atmosphere is the most crucial parameter for the optimization of the crystal quality.

For further investigation of the seeding and growth process, microprobe analyses of a variety of Yb:Lu_2O_3 samples have been performed. It was found that the distribution coefficient of Yb is close to unity, that is, it varied between 0.96 and 1.09. In Figure 15.10 the Yb concentration in the seed region of a 5 at.% Yb-doped Lu_2O_3 crystal is shown. The local resolution was 40 µm over a length of 13 mm. One can see a homogeneous distribution of the Yb ions with a sharp rise from 2 at.% (seed concentration) to 5 at.% of the grown crystal within the 40-µm step width. Surprisingly no interdiffusion occurred at the seed/crystal boundary despite the extremely high growth temperature.

In Table 15.2 some results of growth runs at various oxygen concentrations in the growth atmosphere are collected. It can be seen that with decreasing oxygen

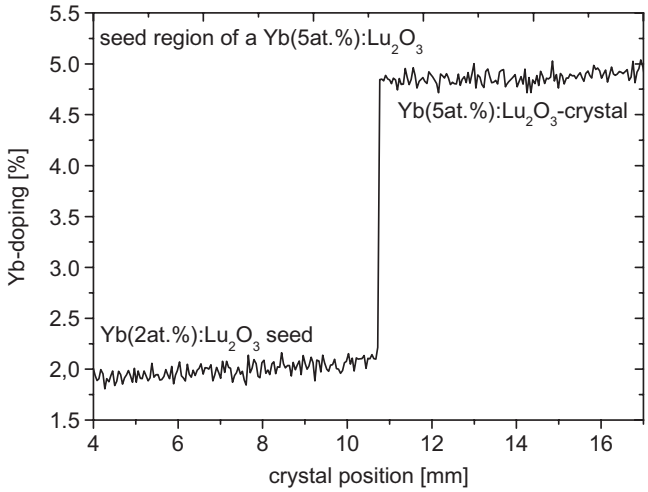

Figure 15.10 Microprobe analysis of the seed region of an Yb : Lu_2O_3 crystal.

Table 15.2 Influence of oxygen content on color-center formation, Re inclusions and crucible corrosion by oxidation of rhenium.

p (O_2) (mbar)	c (O_2) (%)	Color centers	Re inclusions	Crucible corrosion at contact with insulation
$>1 \times 10^{-20}$	>0.6	Clear	Many	Strong
$>1 \times 10^{-21}$	>0.2	Clear	Medium	Medium
$<1 \times 10^{-21}$	<0.2	Bottom	Few	Few
1×10^{-23}	0.02	Complete	No	Few

content the color center concentration increases strongly, whereas the concentration of Re inclusions decreases. At the same time, the surface corrosion of the crucible, where it is in contact with the ZrO_2 felt of the thermal insulation, decreases considerably. So, the optimal growth condition seems to be at an oxygen pressure below 10^{-21} mbar, although the color centers have to be removed in a separate annealing process. Of course, the annealing can also be performed during cooling, after exchange of the growth atmosphere.

15.4 Spectroscopic Characterization

Depending on the growth atmosphere the grown crystal boules are often colored, that is they are red, blue or black. Because all sesquioxides are grown under

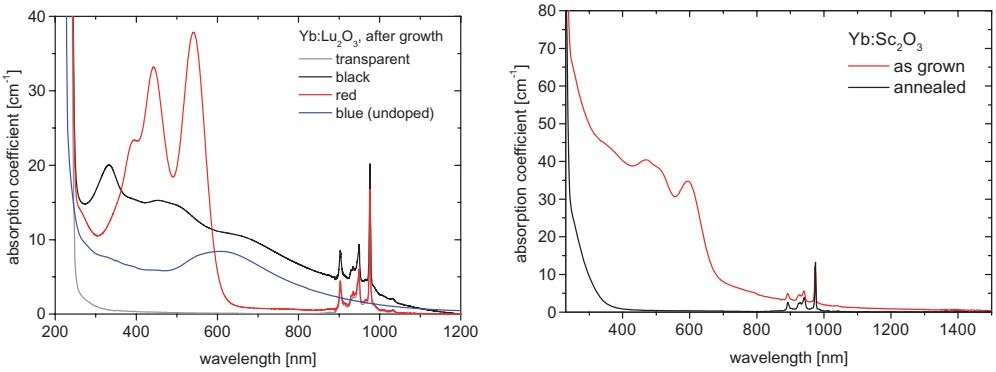

Figure 15.11 Absorption coefficients of as grown Yb : Lu_2O_3 and Ybz : Sc_2O_3 crystals showing different types of color centers.

strongly reducing conditions, a large amount of oxygen is removed from the melt by the hydrogen in the growth atmosphere and thus a large number of oxygen vacancies remains in the grown crystal. These vacancies may trap electrons and form color centers, so-called F centers.

The absorption spectra of the color centers in Yb : Lu_2O_3 and Yb : Sc_2O_3 are shown in Figure 15.11. Besides the well-known Yb absorption between 900 nm and 1100 nm strong absorption bands are present in both crystals extending from the UV to the NIR spectral range and causing the red, blue, and black coloration. The crystallographic structure of the color centers has not yet been determined. However, all these centers can be removed by annealing the crystals at temperatures above 800 °C in air, resulting in colorless samples.

The formation of color centers at the growth temperature is probably the reason for the unsuccessful crystal growth by the Czochralski technique. Due to the absorption of the thermal radiation of the melt by the color centers the growing crystal is heated up, resulting in a distortion of the radial and axial temperature gradients. Okano *et al.* observed also poor growth behavior of $LiTaO_3$, similar to that of the high melting point sesquioxides, when color centers were present in the growing crystal [25].

Figures 15.12a and b show the absorption and emission cross-sections of Yb-doped Lu_2O_3 in comparison with Yb : YAG. In contrast to Yb : YAG where the absorption cross-sections around 940 nm and 969 nm are similar, σ_{abs} is about 4 times larger in Yb : Lu_2O_3 for the zero-phonon line (ZPL) at around 976 nm than for the 950-nm absorption band. In fact, this allows a strong reduction of the disk thickness for the same doping concentration, leading to a better heat removal from the disk; but on the other hand, with a FWHM of 2.1 nm the absorption bandwidth is considerably narrower than for the 950-nm band, which increases the demands on the bandwidth for the pump diodes and makes the laser more sensitive to shifts of the pump wavelength. Nevertheless, laser diodes fulfilling these demands are now commercially available at output powers in the kW range.

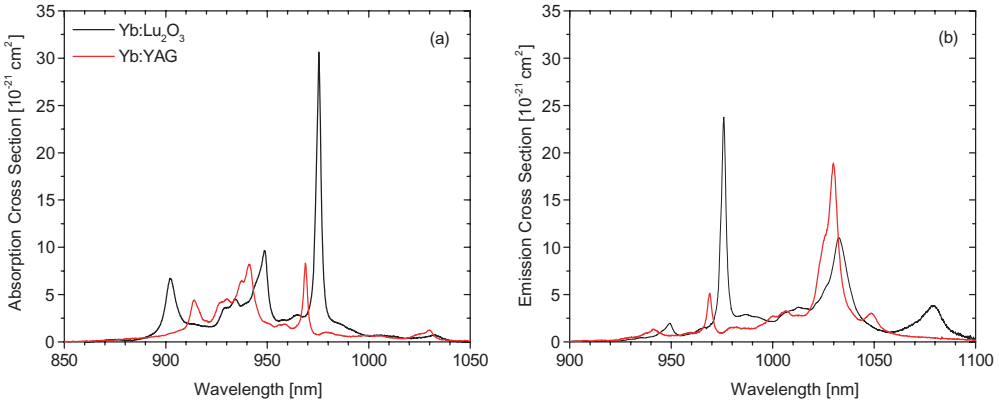

Figure 15.12 Absorption (a) and emission cross-sections (b) of Yb:Lu_2O_3 in comparison to Yb:YAG.

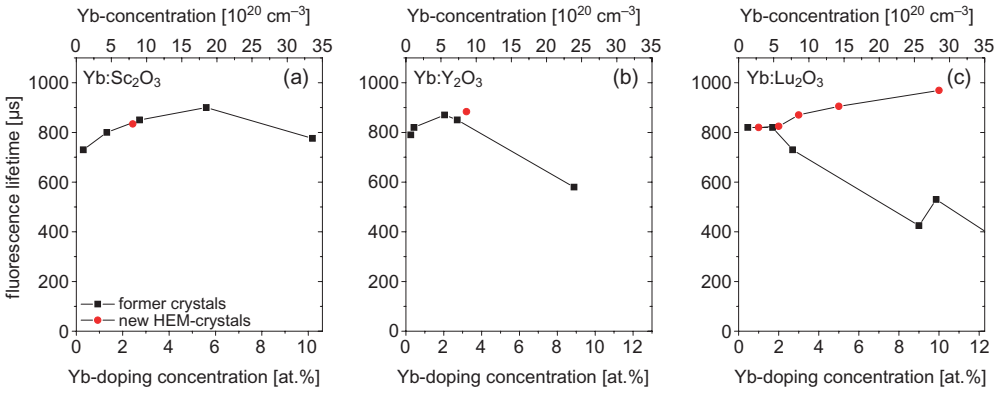

Figure 15.13 Fluorescence lifetime of Yb:Sc_2O_3 (a), Yb:Y_2O_3 (b), and Yb:Lu_2O_3 (c) versus Yb concentration demonstrating the improvement with high-purity crystals (red data points).

As can be seen in Figure 15.12b the emission cross-section of the main laser transition around 1034 nm is somewhat lower but slightly broader than for Yb:YAG. This results in a broader gain profile and enables the generation of shorter pulses with Yb:Lu_2O_3 (220 fs) than for Yb:YAG (340 fs), when the laser operates in a mode-locked regime [26, 27].

Because energy transfer from excited Yb ions to impurities leads to a decrease in quantum efficiency, the fluorescence lifetime can be used as an indicator of the crystal quality. Thus, in order to compare the purity of the new-generation crystals with that of samples grown in former experiments, detailed fluorescence lifetime measurements have been performed. Using the pinhole method [28] to prevent radiation trapping, values between 820 µs and 905 µs have been determined in high-purity Yb:Lu_2O_3 crystals (see Figure 15.13). For Y_2O_3 and Sc_2O_3 the lifetime data are also given in Figure 15.13. In contrast to previous growth experiments no

concentration quenching, that is no decrease in quantum efficiency was observed up to the highest doping concentration of 10 at.%, corresponding to an Yb density of $2.9 \times 10^{21}\,\mathrm{cm}^{-3}$.

15.5 Laser Experiments

For the laser experiments one side of each disk was highly reflective (HR) coated from 900 nm to 1150 nm, covering the pumping wavelength and the emission band. This side was soldered to a water-cooled copper heat sink with a thin layer of indium-tin solder providing a low thermal impedance between the laser medium and the cooling system. The opposite side of each crystal was antireflective (AR) coated for the same spectral range. The fiber-coupled diode pump laser (JENOPTIC LaserDiode GmbH, Germany) delivered 50 W output power at 976 nm with a spectral width of 2.5 nm; the fiber diameter was 600 µm with NA = 0.22. Efficient absorption of the pump radiation was achieved with a pumping module that provided 24 passes of the pump beam through the crystals. The pump beam diameter on the crystal was 1.2 mm. A plane-concave resonator of 70 mm length was used to investigate the characteristics of the laser emission; the radius of curvature of the concave output mirror was 100 mm. To achieve optimum absorption at the maximum of the Yb zero-phonon line, the diode temperature was varied between 8 °C and 21 °C, depending on the pump power.

Figure 15.14 presents the output power versus pump power (measured at the fiber end) for the most efficient crystals used in the laser experiments. The 0.15-mm thick 5 at.%-doped Yb:Lu_2O_3 crystal delivered at an optimum outcoupling transmission of $T_{oc} = 1.6\%$ a maximum output power of 36.3 W at a pump power of 49.8 W (see Figure 15.14 left). The maximum slope efficiency η_s and opt.–opt. efficiency η_{opt} was 80% and 73%, respectively [29]. It was observed that even for $T_{oc} = 0.4\%$ the slope efficiency is well above 75%, which is an indicator of very low crystal losses. As is known from previous experiments, the laser wavelength

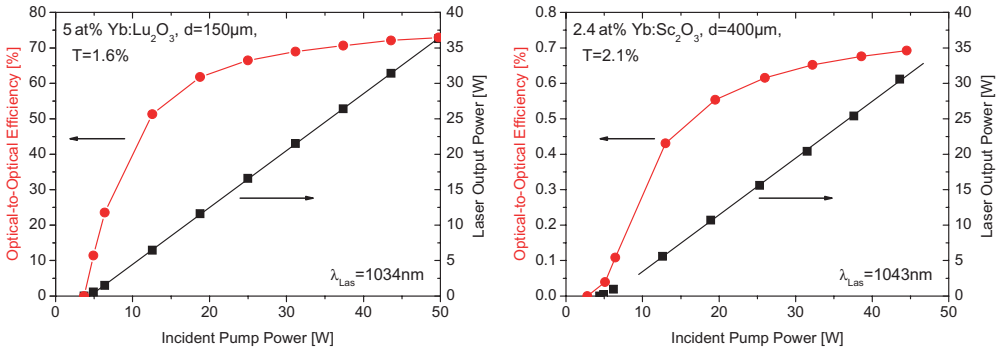

Figure 15.14 Thin-disk laser results with HEM-grown Yb:Lu_2O_3 (left) and Yb:Sc_2O_3 crystals (right).

changes from 1080 nm to 1034 nm at outcoupling rates exceeding a few per cent. No differences between crystals of different growths runs have been observed. Furthermore, up to the maximum disk thickness of 0.45 mm no decrease in slope efficiency, caused by an increased thermal loading of the disk was noted. This fact is due to the high thermal conductivity of $Yb:Lu_2O_3$ and is proof of an efficient heat removal even from thicker disks.

Also, for $Yb:Sc_2O_3$ highly efficient thin-disk laser operation has been achieved (see Figure 15.14 right) with output data very similar to those of $Yb:Lu_2O_3$. Here, the maximum slope efficiency was 82% at an optical-to-optical efficiency of more than 75% [30].

15.6 Summary and Outlook

Due to the achievable crystal size, as well as the relatively low stress, the HEM technique has been proven to be an adequate growth method to produce high-quality sesquioxide crystals. Crystalline boules up to 40 cm^3 volume with single-crystalline regions of nearly 30 cm^3 have been grown from rhenium crucibles under a reducing atmosphere. No rhenium inclusions were found, if the residual oxygen or water concentration was below a few thousand ppm. The purity of the crystals was monitored by lifetime measurements of the Yb fluorescence. No concentration quenching, that is, no decrease of the quantum efficiency due to impurities was observed up to a doping concentration of 10 at.%. Furthermore, thin-disk laser experiments have been performed. At a pumping power of 50 W about 36 W of output power could be obtained with $Yb:Lu_2O_3$ as well as with $Yb:Sc_2O_3$, corresponding to a slope efficiency of 80% (73% optical efficiency). Again, these results are strong indicators of the very high optical quality of the grown sesquioxide crystals.

Till now the boule dimensions are quite small in comparison with those of sapphire grown by the HEM technique. In principle, there are no limitations for the Re crucible size and thus larger crystals may be grown in the future. Furthermore, the seeding process has to be improved in order to produce single-crystalline boules.

Currently, the growth runs are performed with a closed atmosphere, that is the oxygen partial pressure is not exactly known. New experiments with a flowing atmosphere of fixed composition are in progress and will improve the reproducibility of the grown boules.

Acknowledgment

The authors would like to thank Dr. Detlef Klimm from the Leibniz-Institut für Kristall-züchtung (IKZ), Berlin for many helpful discussions and the calculation of the Ellingham diagrams.

References

1 Giesen, A., *et al.* (1994) Scalable concept for diode-pumped high-power solid-state lasers. *Appl. Phys. B*, **58**, 365.
2 Giesen, A., and Speiser, J. (2007) Fifteen years of work on thin-disk lasers: results and scaling laws. *IEEE J. Select. Top. Quant. Electron.*, **13**, 598.
3 Griebner, U., *et al.* (2004) Passively mode-locked Yb:Lu_2O_3 laser. *Opt. Exp.*, **12**, 3125.
4 Tokurakawa, M., *et al.* (2009) Ultra-short pulses from diode-pumped Yb3+-doped crystal and ceramic lasers with high average power, Advanced Solid-State Photonics (ASSP), Denver, paper MC3.
5 Marchese, S.V., *et al.* (2007) Efficient femtosecond high power Yb:Lu_2O_3 thin disk laser. *Opt. Exp.*, **15**, 16966.
6 Larionov, M., *et al.* (2001) Thin disk laser operation and spectroscopic characterization of Yb-doped sesquioxides and potassium tungstate. Proceedings of Advanced Solid-State Lasers and Photonics Conference, p. 625.
7 Peters, R., *et al.* (2007) Broadly tunable high-power Yb:Lu_2O_3 thin disk laser with 80% slope efficiency. *Opt. Exp.*, **15**, 7075.
8 Pauling, L., and Shappell, M.D. (1930) The crystal structure of Bixbyite and the C-modification of the sesquioxides. *Z. Krist.*, **75**, 128.
9 Barta, C., Petru, F., and Hajek, B. (1957) Über die Darstellung des Einkristalls von Scandiumoxyd. *Die Naturwissenschaften*, **45 (2)**, 36.
10 Lefever, R.A. (1962) Flame fusion growth of C-type rare-earth oxides. *Rev. Sci. Instrum.*, **33 (12)**, 1470.
11 Kitazawa, K., Nagashima, K., Mizutani, T., Fueki, K., and Mukaibo, T. (1977) A new thermal imaging system utilizing a Xe arc lamp and an ellipsoidal mirror for crystallization of refractory oxides. *J. Cryst. Growth*, **39 (2)**, 211.
12 Huber, G., Payne, S.A., Chase, L.L., and Krupke, W.F. (1988) Optical spectroscopy of Cr^{3+} in ScF_3 and Sc_2O_3. *J. Lumin.*, **39 (5)**, 259.
13 Fornasiero, L., Mix, E., Petermann, K., and Huber, G. (1999) New oxide crystals for solid state lasers. *Cryst. Res. Technol.*, **34**, 255.
14 McMahon, W.R., and Wilder, D.R. (1968) Hemispherical spectral emittance of selected rare earth oxides. *J. Am. Ceram. Soc.*, **51 (4)**, 187–192.
15 Petermann, K., Huber, G., Fornasiero, L., Kuch, S., Mix, E., Peters, V., and Basun, S.A. (2000) Rare-earth-doped sesquioxides. *J. Lumin.*, **87**, 973.
16 Petermann, K., Fornasiero, L., Mix, E., and Peters, V. (2002) High melting sesquioxides: crystal growth, spectroscopy, and laser experiments. *Opt. Mater.*, **19**, 67.
17 Schmid, F., and Viechnicki, D. (1970) Growth of sapphire disks from the melt by a gradient furnace technique. *J. Am. Ceram. Soc.*, **53 (9)**, 528.
18 Schmid, F. (1973) New approach to high temperature crystal growth from the melt. *Solid State Technol.*, **16**, 45.
19 Lu, C.W., and Chen, J.C. (2001) Numerical computation of sapphire crystal growth using heat exchanger method. *J. Cryst. Growth*, **225**, 274.
20 Khattak, C.P., and Peters (2001) Growth of the world's largest sapphire crystal. *J. Cryst. Growth*, **225**, 572.
21 Crystal Systems (2008) www.crystalsystems.com.
22 Peter, V., Bolz, A., Petermann, K., and Huber, G. (2002) Growth of high-melting sesquioxides by the heat exchanger method. *J. Cryst. Growth*, **237–239**, 879.
23 Peters, R., Kränkel, C., Petermann, K., and Huber, G. (2008) Crystal growth by the heat exchanger method, spectroscopic characterisation, and laser operation of high purity Yb^{3+}-doped Lu_2O_3. *J. Cryst. Growth*, **310 (7–9)**, 1934–1938.
24 Schenk, K., Peters, R., Petermann, K., and Huber, G. (2009) Investigation of the scattering properties of Yb:Y_2O_3 and its effect on laser parameters, CLEO/Europe-EQEC 2009, paper CA.P.20 TUE.
25 Okano, Y., Tsuji, Y., Yoon, D.H., Hoshikawa, K., and Fukuda, T. (1994) Internal radiative heat transfer in

Czochralski growth of $LiTaO_3$ single crystal. *J. Cryst. Growth*, **141**, 383–388.

26 Griebner, U., Petrov, V., Petermann, K., and Peters, V. (2004) Passively mode-locked Yb:Lu_2O_3 laser. *Opt. Exp.*, **12**, 3125–3130.

27 Hönninger, C., Paschotta, R., Graf, M., Morier-Genoud, F., Zhang, G., Moser, M., Biswal, S., Nees, J., Braun, A., Mourou, G.A., Johannsen, I., Giesen, A., Seeber, W., and Keller, U. (1999) Ultrafast ytterbium-doped bulk lasers and laser amplifiers. *Appl. Phys. B*, **69**, 3–17.

28 Kühn, H., Fredrich-Thornton, S.T., Kränkel, C., Peters, R., and Petermann, K. (2007) Model for the calculation of radiation trapping and description of the pinhole method. *Opt. Lett.*, **32**, 1908–1910.

29 Peters, R., Kränkel, C., Petermann, K., and Huber, G. (2007) Broadly tunable high-power Yb:Lu_2O_3 thin disk laser with 80% slope efficiency. *Opt. Exp.*, **15** (**11**), 7075–7082.

30 Peters, R., Kränkel, C., Petermann, K., and Huber, G. (2008) High power laser operation of sesquioxides Yb:Lu_2O_3 and Yb:Sc_2O_3. Conference on Lasers and Electro-Optics (San Jose, California, USA), p. paper CTuKK4.

16
Continuous Growth of Alkali-Halides: Physics and Technology

Oleg Sidletskiy

16.1
Modern Requirements to Large Alkali-Halide Crystals

The size of growing crystals is an important factor in the fabrication cost of crystals and devices made from them. For some applications crystal elements are needed in dimensions up to hundreds of millimeters, with high transparency and homogeneity of properties through the crystal volume. In these cases obtaining large crystals is not only the method of fabrication cost minimization, but a functional need. Analysis of growth techniques shows that large-size crystals may be grown with good efficiency by Czochralski, Kyropoulos, Bridgman–Stockbarger methods, and their modifications. Continuous growth techniques developed for large-size alkali halide crystals (AHC) is an example of successful optimization of a conventional growth method aimed to pull large-size crystals.

AHC are widely used as optical and scintillation materials. Optical materials, such as KCl, KBr, CsI, possess good transmittance in the IR range and are used as IR optical components. The requirements on crystal absorption are very tough (absorption coefficient in the IR band must not exceed $10^{-4}\,cm^{-1}$). Scintillators are another basic field of AHC application. They are used in medical imaging, medium-energy physics, industrial and security applications [1–3]. Scintillators for medium-energy physics have dimensions up to 300 mm, SPECT detectors for whole-body screening reach 600 mm in size and more. One can see the need for large-size detectors in both optical and scintillation applications. These requirements increase from decade to decade. Currently, the annual need for alkali-halide crystals is several tens of tons, a half of this quantity are large-size crystals. Therefore, crystal size increase claims requires uniformity of functional characteristics along the growing crystals. Variation of transmission, light yield, and energy resolution in many cases must not exceed 2–3%.

These conditions may be satisfied only by constant distributions of activator and admixtures along the crystal. Most alkali-halide scintillators contain activators (Na^+, Tl^+) with segregation coefficients well below unity. For instance, k(Tl) equals 0.18 in CsI and 0.2 in NaI [4]. The activator concentration greatly influences the scintillation properties of crystals. For example, light yield and energy resolution

Crystal Growth Technology. Semiconductors and Dielectrics. Edited by P. Capper and P. Rudolph
Copyright © 2010 WILEY-VCH Verlag GmbH & Co. KGaA, Weinheim
ISBN: 978-3-527-32593-1

of NaI(Tl) is optimal at 500–2000 ppm Tl content. Reasonable radiation hardness is observed at Tl concentrations below 2000 ppm [5]. Sometimes, the presence of several activators is necessary to obtain the required properties, and the concentration of every activator must be constant along the crystal [6].

From the physical viewpoint a crystal growing is a nonequilibrium process impacted by a number of external and internal factors. Only quasi-stationary conditions may be achieved during growth. Temperature change and crystal pulling could be the driving forces for crystallization, but simultaneously they disturb the system equilibrium. The main task of technology is to create growth conditions such that the system may be returned to equilibrium after disturbances without a decrease of crystal quality.

The following physical principles may be formulated for growth of large-size crystals with uniform characteristics along the crystals, low cost, and large industrial yield:

- steady conditions at crystal/melt interface (CMI) during growth (stable heat balance, constant crystallization mass rate, fixed CMI shape, good melt homogeneity);
- stable concentration of activator(s) in the growing crystal.

For crystal-growth technology this means:

- fixed CMI position in respect to heaters, crucible, and other furnace parts;
- stable melt composition during the growth, and good melt mixing;
- easy and reliable automated control method for growth of crystals with weights of several hundred kilo.

16.2 Conditions of Steady-State Crystallization in Conventional Melt-Growth Methods and in Their Modifications

16.2.1 Conventional Methods

Let us consider conventional growth methods in the context of the requirements mentioned above. The Bridgman–Stockbarger method and its modifications do not require difficult growth algorithms. The CMI in this method can be fixed with respect to the heaters, implying relatively stable crystallization conditions. However, the Bridgman method has several fundamental drawbacks. These are adhesion of growing crystals to the crucible and problems of their separation after crystal growth. Difference in thermal expansion coefficient of crystal and ampoule often leads to cracking. In accordance with Pfann [7], it is impossible to avoid nonuniform activator distribution C_S along the crystal if its segregation coefficient does not equal unity. Melt homogeneity in Bridgman is not good because of poor convection. For this reason, the additional procedures of melt stirring by accelerated

crucible rotation technique (ACRT [8]), vibration stirring [9], electromagnetic field [10], etc., were developed.

In the Czochralski and Kyropoulos methods some drawbacks of the Bridgman method can be avoided. There is no contact of the crucible with the crystal. Rotation of crystal and/or crucible and intensive thermal convection in the melt provide better melt homogeneity. However, the melt level in the crucible moves down during crystal growth and the crystal is subjected to heating by hot crucible walls. Consequently, thermal gradients decrease, and the growth process may become unstable. The activator distribution in a crystal, as in the Bridgman–Stockbarger method, depends on the size of the crystallized melt. A relatively stable activator content in crystals in the conventional Czochralski method may be obtained only for small crystals, related to the melt weight.

Therefore, conventional growth methods are not good enough for reproducible growth of large crystals. Problems of a fixed CMI position and stable activator concentration were solved rather easily by raw-material feeding at a rate equal to the mass crystallization rate [11]. Sustaining of steady-state conditions appears to be a more difficult task. Additionally, a stable thermal field configuration and a constant balance of heat inflow and heat removal at CMI must be maintained. Heat-balance changes increase with crystal size, even for a stable melt level in crucible, and the easiest way to regulate this is a heater-power correction.

16.2.2
Melt-Feeding Methods

The aforementioned principles may be successfully implemented in the known growth methods. Some AHC producers tried to modify the Bridgman–Stockbarger method. For instance, in [12] melt feeding is provided from the outer vessel situated above the growth chamber. Only a small amount of melt must be situated in growth in the crucible at a certain moment to avoid turbulent flow. The authors claim that this method is applicable to grow alkali-halide crystals of 30 inches diameter and 20 inches height. However, this method is not applied in industrial-scale growth. In a modification of horizontal Bridgman [13], the melt is fed to the crystallization zone from another crucible and the growing crystal is pulled in the horizontal direction by a special appliance. As the result, in both examples the CMI is fixed with respect to heaters, and the melt composition can be controlled. However, the last example implies limitations on crystal thickness, because strong thermal convection in large melt volumes does not provide temperature homogeneity along the CMI.

Examples of melt feeding by raw material in Czochralski and Kyropoulos growth are more numerous. Great success was achieved in the growth of large semiconductor crystals (see, for example, [14, 15]). There are many modifications of the so-called double-crucible Czochralski method developed for oxide and semiconductor crystals, such as InGaAs [16], $LiNbO_3$ [17], $LiTaO_3$ [18], $YAlO_3$ [19], Lu_2SiO_5 [20]. According to these methods, raw material is fed to the lateral part of the crucible, or to the outer crucible. Crystallization on a seed is provided in the

smaller inner crucible, which is situated, as a rule, inside the larger crucible. Raw material is supplied from the lateral to the inner crucible at a rate equal to crystallization mass rate. Small temperature fluctuations and a constant melt level inside the inner crucible promote crystallization stability. The common feature of these methods is that the melt volume in the inner crucible should be rather large to damp temperature fluctuations called by melt inflow from the lateral crucible.

16.2.3
Growth-Process Control

Melt feeding in the Czochralski–Kyropoulos method and formation of steady conditions at the CMI appears to be the most attractive way to create a technique for large crystal growth. Large crystals take a substantial time to grow. This is why development of an automated control system is an important issue.

Crystal shape and diameter in conventional Czochralski and Kyropoulos methods are usually controlled by weight or optical sensors. In weighing control a crystal diameter is calculated from changes in the crystal or melt weight. Optical methods are based on pyrometric control of the meniscus shape at the crystal/melt boundary. Sometimes, hybrid control systems utilizing both optical and weight sensors demonstrate better performance [21]. However, for AHC continuous growth, if crystal weight is several hundreds kg and direct meniscus sighting is difficult due to clouds of evaporating melt, the melt-level regulation is the most reliable and easiest method [22]. The melt-level control by an electrocontact sensor provides 10-μm precision and depends on neither the crystal transverse shape, nor crystal weight, nor melt weight, nor growth atmosphere permeability [23]. The first successive attempts of melt-level probe utilization were made in the 1980s [11, 24]. The main potential drawback of this method (the same as for weighing and optical control methods) is that changes of melt volume on CMI shape transformations or melt evaporation can be interpreted as a crystal-diameter change. Equation 16.1 for crystal diameter d at growth with melt feeding is the follows: [24] ($\dot{m}$ – feeding mass rate, V_P – puling rate, D – crucible diameter, h – melt column height, ρ_S and ρ_l – densities of crystal and melt, respectively, α – thermal expansion coefficient of melt, $\dot{T}$ – averaged melt temperature, γ – evaporation rate, W_S – undermelt crystal volume).

$$d \approx d_S\left\{1+\frac{1}{2\dot{m}}\left[\left(\frac{\pi D^2}{4}h - W_S\right)\rho_l\alpha\dot{T} - (\rho_S-\rho_l)\dot{W}_S - \frac{\pi}{4}(D^2\rho_l - d_S^2\rho_S)\dot{h} - \frac{\pi}{4}(D^2-d_S^2)\gamma\right]\right\} \tag{16.1}$$

One can see that if W_S increases during crystal growth the real crystal diameter d will be smaller than at steady state (d_S). This means that a measured crystal diameter will be smaller than in reality. The same phenomenon is observed from melt volatility (large γ). Thus, the growth process will tend to steady-state conditions ($d \rightarrow d_S$) with an increase of Ws, $\dot{m}$, γ, the d_S/D ratio, and smaller melt volume (larger W_S) in the crucible. However, it is obvious that W_S, γ, $\dot{m}$, d_S/D parameters may not be increased infinitely.

16.3 Macrodefect Formation in AHC

The limits of acceptable fluctuations of growth characteristics may be determined directly by forced variation of these parameters and observation of their impact on the grown crystal quality. Absence of macrodefects (inclusions) in a crystal evidences steady-state conditions and stable CMI shape. In turn, formation of macrodefects in crystals leading to a decrease of transmission and other crystal characteristics indicates disturbance of steady-state conditions. It was established that macrodefects in AHC include inclusions of foreign phases and gaseous bubbles dissolved in the melt [25].

The concentration of gases and admixtures dissolved in the melt is determined by the Henry law (16.2): C_0 – equilibrium concentration of gas (admixture); P – partial pressure.

$$C_0 = KP \tag{16.2}$$

Gas-bubble formation in melts and their capture by CMI occurs on temperature decrease when their concentration in the melt becomes higher than the equilibrium one. The time τ_δ of diffusional accumulation of an admixture (16.3) depends on the diffusion layer thickness δ_0 and the diffusion coefficient D:

$$\tau_\delta = \frac{\delta_0^2}{D} \tag{16.3}$$

If the growth rate is too high, or, τ_δ is smaller than the time of melt temperature correction by the control system, the melt supersaturates with gaseous bubbles and admixtures at CMI, and they are captured into the crystal. This time is about 15 min for KCl [26].

The dependence of light scattering intensity in crystals on growth rate is well illustrated by KCl example [26]. Light scattering (that is, the quantity of macrodefects) increases linearly with pulling rate. Thus, we may achieve the needed light scattering value and, theoretically, achieve conditions without scattering by choosing the correct growth rate. It has been demonstrated [26, 27] that the growth rate 2–4 mm/h for CsI and NaI, and 2–6 mm/h for KCl crystals are optimal for continuous growth method and conditions of Equation 16.1.

Changes in crystallization rate may cause CMI-shape transformations and macrodefect formation in certain regions of a crystal. These transformations can be performed by simultaneous increasing of feeding and pulling rates during continuous growth (Figure 16.1) leading to a melt-level rise in the crucible. A diameter-control system based on the electrocontact probe stabilizes melt level by heater-power regulation. However, the time of crystal-diameter stabilization after a disturbance is significantly larger than the melt-level stabilization time. This means that the CMI-shape transformation (W_S value) continues for a long time period after melt-level stabilization [24].

Consequences of CMI-shape transformation on thermal-balance disturbance were observed in CsI(Na) on forced change of the control (bottom) heater

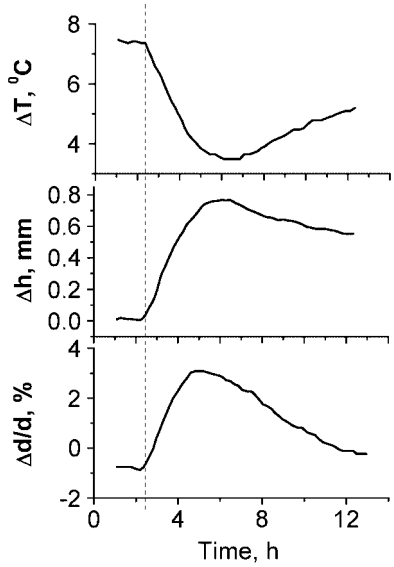

Figure 16.1 Trends of heater temperature, melt level, and crystal diameter after forced increase of pulling rate from 2 to 5 mm and corresponding increase of feeding rate during KCl growth. The moment of increase is shown by the dashed line.

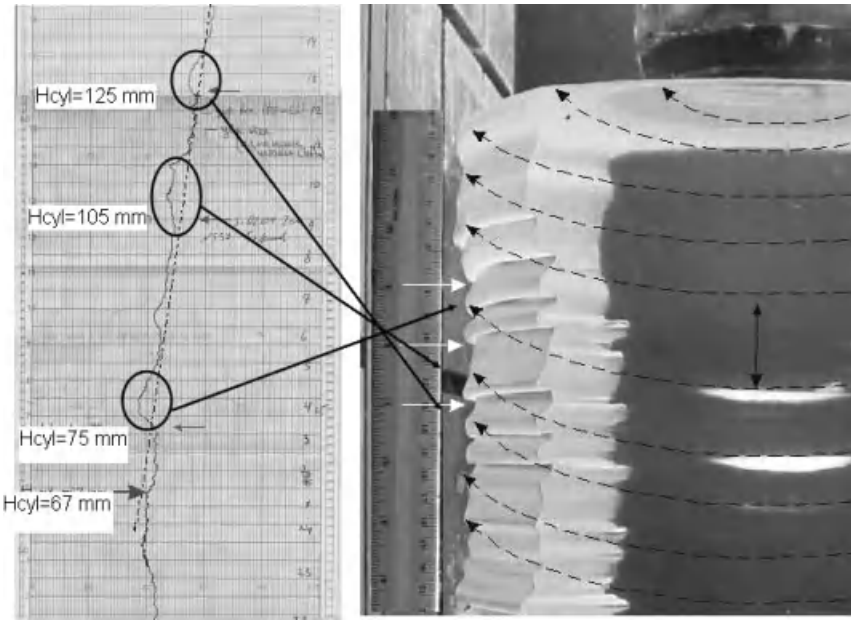

Figure 16.2 Visualization of macrodefects initiated by forced decrease of control heater power in a longitudinal cut of an as-grown 320-mm diameter CsI(Na) crystal [28].

temperature (Figure 16.2) [28]. Macrodefects appear in the center part of crystal as the heater power (melt temperature) decreases. This indicates that temperature fluctuations lead to sharp changes in the crystallization rate in the CMI central part and influence its convexity.

Efficient prevention of undesirable CMI shape transformations may be provided by adjustment of temperature, but not by changes of feeding/pulling rate. The evaluations (16.4) show that the time of crystallization-rate stabilization after melt temperature change τ_T for KCl is by 2 orders of magnitude smaller than after a pulling and feeding rate change τ_V [26] (C_P – heat capacity of melt, L – latent crystallization heat, G – temperature gradient at CMI). Theoretically, this ratio may be changed by a large increase in G. However, this means is not acceptable, because the growing crystal will be subjected to severe thermal overstress causing cracking.

$$\frac{\tau_V}{\tau_T} \sim \frac{L}{GC_P} = 40 - 400 \tag{16.4}$$

Melt-temperature fluctuations can also cause periodical fluctuations of crystallization rate. It is known [21] that the melt-convection pattern at Czochralski growing depends on thermal and forced convection. The first causes ascending fluxes along the crucible walls and descending fluxes in the crucible center. The forced convection initiated by crystal and/or crucible rotation creates fluxes of melt in the opposite direction. A certain balance between these two factors must be sustained to maintain a stable temperature near CMI. For instance, measured temperature fluctuations in KCl melt due to thermal convection and forced convection reach 6–7 °C (Figure 16.3). It was noted that the observed inclusions in crystals (striations) appear with the same time periodicity as these fluctuations [26]. Choosing optimal crystal and crucible rotation rates and directions provides a decrease of fluctuation amplitude by several fold. Melt-temperature fluctuations ±1–2 °C usually do not lead to formation of inclusions. In practice, for large AHC

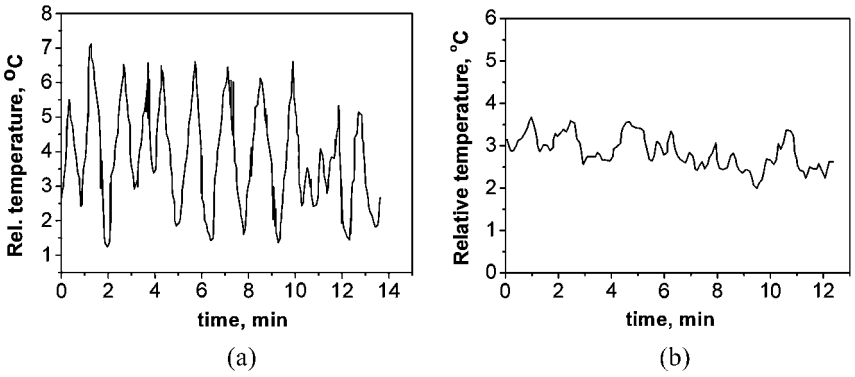

Figure 16.3 KCl melt temperature fluctuations without forced convection (a) and in optimized regime of crucible rotation (b). The crucible diameter is 500 mm [26].

this condition may be achieved at crystal and crucible rotation rates in the range 1–5 rpm.

16.4
Dynamics of Thermal Conditions during Continuous Growth

Equation 16.4 illustrates why diameter control during continuous AHC growth is provided by correction of the bottom-heater power. The second heater on the periphery of the crucible is installed for melting of a feeding material [29]. The process of bottom heater control during real growth with feeding is the following (Figure 16.4). At the beginning (cone growth and start of cylinder growth) the heater temperature (power) must be decreased to initiate crystallization. The bottom heater temperature increase ("stage of inhibition of crystallization") starts at about 100 mm length when the crystal emerges from the crucible and heat transfer from its surface sharply intensifies. Finally, the heater power stabilizes when the crystal height reaches a certain value (200–400 mm). The given heater power trend is observed for setups with cylindrical crucible shape [11, 22]. For setups with conical crucible shape [22, 30], the heater power may increase just after seeding due to other heat-removal effects from the crystal.

Numerical modelling of heat and mass transfer in the furnace is able to predict growth stages with sharp changes of thermal conditions and maximal probability of macrodefect formation [31]. The dynamics of heat transfer during 300-mm diameter CsI(Na) growth in a growth setup with a cylindrical-shaped crucible [11] was calculated using the CGSim program package [32]. Boundary conditions for simulation (temperature across the crystal and other furnace elements) was determined by a IR pyrometer and thermocouples. A numerical model was proposed to make a conjugated analysis of heat exchange, melt and gas flows in the growth

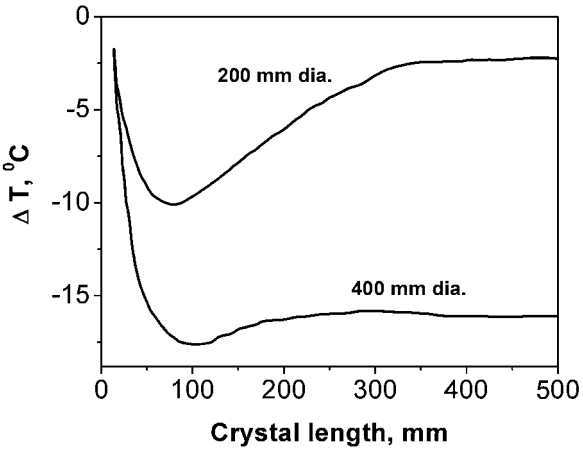

Figure 16.4 Dynamics of control-heater temperature during growth of KCl single crystals.

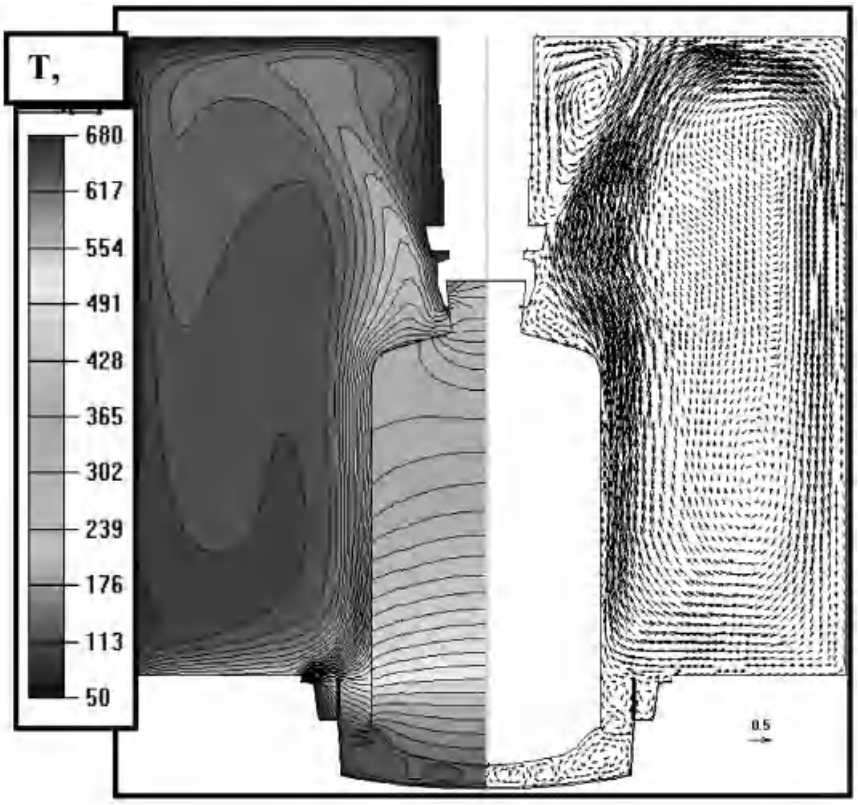

Figure 16.5 Temperature distribution, and melt and gas convection in a ROST-type setup at CsI(Na) growth of 300 mm diameter [32].

setup with account being taken of radiative heat transport in the semitransparent crystal and melt.

Simulation illustrates a temperature distribution in the crystal (Figure 16.5) together with nonlinear changes of temperature gradient (Figure 16.6). The thermal gradient slope at a crystal cylindrical part height H_{cyl} = 50 mm (that is, overall crystal length about 100 mm) shows a significant heat-transfer increase if the crystal emerges from the crucible. This growth stage is dangerous from the point of CMI transformations and macrodefect formation (see Figure 16.6). A growth-rate decrease at this stage or adequate correction of heater power prevents macrodefect formation.

Returning to Figure 16.4, one can see that at the same stage (at a crystal height about 100 mm) the heater-temperature trend changes its sign from negative to positive, evidencing a CMI shape change; herein, CMI stabilizes faster for larger crystal diameters (400 mm). This phenomenon is in agreement with Equation 16.1, which shows that diameter deviation from a steady value can be decreased at a minimal possible difference $(D^2\rho_l - d_S^2\rho_S)$ between the crucible and crystal diameters. However, at small $(D^2\rho_l - d_S^2\rho_S)$ values the lateral heater primarily used

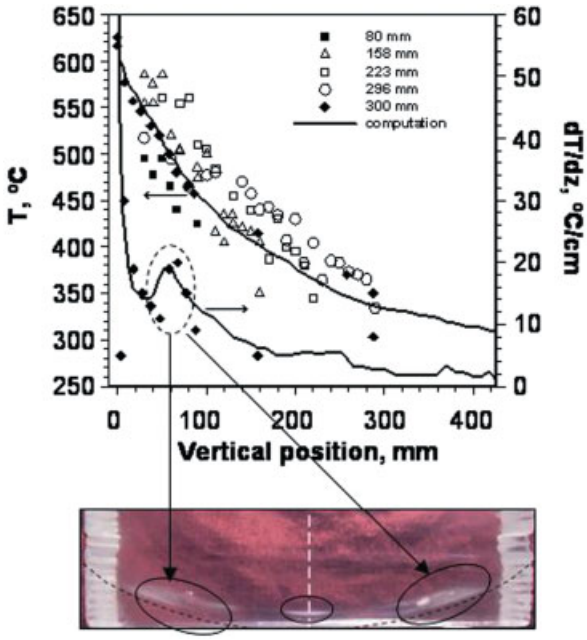

Figure 16.6 The distribution of temperature and axial temperature gradient along the side crystal surface at CsI(Na) growth of 300 mm diameter [32] (the symbols show the measurements, the solid heavy lines stand for the computation). Below – macrodefects in as-grown crystal for H_{cyl} about 50 mm.

for raw-material melting also substantially influences the CMI shape. Consequently, its power must also be regulated during growth.

At the same time, power-correction frequency and its amplitude must be limited in order to avoid superposition of sequent regulation events. The optimal frequency of correction impulses was determined by forced variation of the heater power for CsI(Na) growth of 300 mm in diameter [33]. The temperature trend after variation of power on the main and lateral heaters was measured at the crystal surface near CMI (Figure 16.7). The time of system response increases with crystal size. The temperature stabilization time is 5–10 min at the beginning of growth, and 10–15 min for a crystal length of 120 mm. The time of temperature stabilization after the bottom heater regulation is less than for a lateral heater at the start of growth. Lateral heater correction becomes more efficient with increase of crystal size.

16.5 Advanced Growth-Control Algorithms

Summarizing the analyzed data, the requirements for the growth furnace and control system for continuous AHC growth should be the following:

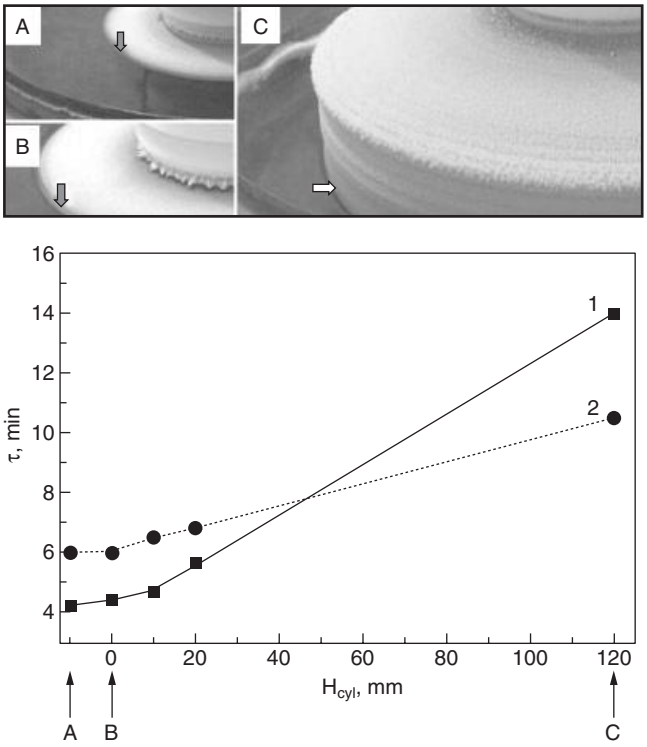

Figure 16.7 Time of crystal-temperature stabilization after forced variation of the bottom (curve 1) and lateral (curve 2) heaters during growth of 300-mm diameter CsI(Na) [33]. Places of temperature measurement at different growth stages are shown by the arrows.

- The system is more reliable if two independent heaters are installed. The bottom heater regulates crystal diameter by feedback scheme from the melt-level probe, and the lateral heater is used for raw-material melting, respectively.
- Melt volume in the crucible should not be too large, in accordance with Equation 16.1, and not too small in order to avoid disturbance of the steady-state conditions at the CMI caused by fed melt inflow.
- The interval of acceptable growth rates is 2–6 mm/h.
- The amplitude of temperature fluctuations at the CMI must not exceed 1–2 °C.
- The time range between consecutive temperature regulations depends on crystal size and should be not less than 10 min at the start of growth and not less than 20 min in the end of growth.

Growth-control algorithms for large-size AHC were developed in two directions. Their peculiarities were described in detail in [22, 30]. In the first method, the crystal pulling and melt feeding are continuous in accordance with mass

balance. Crystal diameter is controlled by heater power by a feedback scheme [23, 24, 29]. The main problem of this method is feeding-rate uniformity, because melt-level changes due to nonuniform feeding are attributed by the system to a crystal-diameter change, and an incorrect temperature correction is made. It appeared that good feeding uniformity is provided only for granulated starting material with uniform particle size due to peculiarities of the raw-material feeding apparatus [22].

The problem of feeding nonuniformity is eliminated in the algorithm with discrete feeding and pulling suggested in [34]. A growing crystal is pulled with a certain frequency. The crystal control system calculates the crystal diameter by the melt-level decrease and adjusts the main-heater temperature. Feeding with raw material starts after pulling, and it stops when the melt rises to the initial level. The temperature is adjusted once per cycle.

Discrete pulling and feeding are connected with periodical changes of crystal and melt temperature disturbing the steady-state conditions. The measured amplitude of temperature fluctuations for 300-mm diameter CsI(Na) growth reaches 3 °C. Temperature changes on crystal pulling and melt feeding can be decreased by a synthesis of the described methods ("method with background feeding") [35]. Feeding by small portions (background feeding) is provided during the crystal pulling along with basic feeding in the periods without crystal pulling (Figure 16.8). the amplitude of the single pulling is decreased by several fold. The temperature is adjusted by the system both during pulling and during the basic feeding. The thermal fluctuation amplitude on feeding for large crystals of 450–500 mm diameter decreases to 1–2 °C.

Continuous growth with the d_S/D ratio up to 0.9 allows larger crystals to be obtained without increase of crucible size. However, the vicinity of the lateral

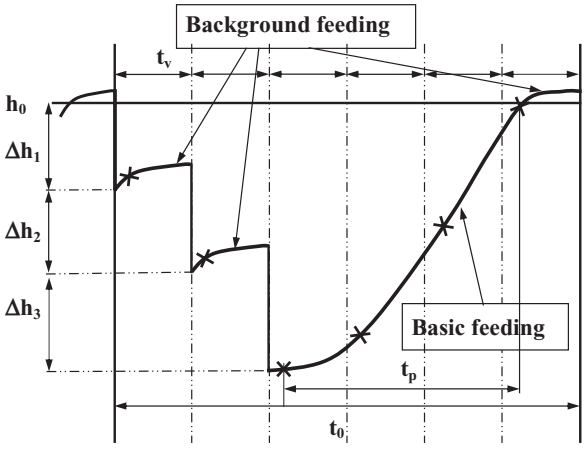

Figure 16.8 Melt-level changes during growth control by the algorithm with background feeding [35].

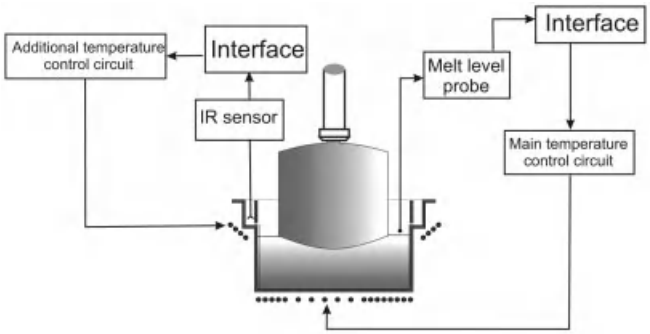

Figure 16.9 Two-circuit method of growth-process control [36].

heater to the crystal side surface may call for a significant increase of the crystal-undermelt section without visible changes of crystal diameter above the melt surface [27]. This problem may be solved by prompt regulation of the lateral heater power implemented in the control algorithm with simultaneous correction of both bottom and lateral heaters (Figure 16.9) [36]. The method is based on tight correlation of crystal diameter with temperature in the lateral crucible. It was shown that a constant crystal diameter is maintained at constant temperature in the lateral crucible [27]. The second circuit in two-circuit control comprises a lateral heater the power of which is adjusted by a feedback scheme from an infrared sensor measuring the temperature in the outer (lateral) crucible.

16.6 Summary

The alkali-halide market calls for more and better performance large-size single crystals for optical and scintillation applications. The most advanced continuous-growth technology with the family of techniques on the basis of the raw-material feeding approach satisfies the main application specification. The core advantage of these technologies is the ability to sustain the steady conditions at the crystal/melt interface during growth (heat balance, constant crystallization mass rate, fixed CMI shape, good melt homogeneity). This allows uniform activator distribution along the crystal and functional parameters to be sustained. At the same time, new developments in the process algorithms and control-system upgrades improved the process: provide fixed CMI position and shape, stable melt composition during the growth, temperature fluctuations at CMI below 1–2 °C, good melt mixing, as well as precise diameter control for crystals with weight of several hundreds of kg. This demonstrates large-size continuous crystal-growth improvement and the ability to optimize a proper industrial process.

The present chapter discusses possibilities of sustaining the given principles in different methods of growth from melt, in particular, advantages and drawbacks of the modified Czochralski-Kyropoulos method used for large-size AHC. Also, a review of recent works concerning peculiarities of heat- and mass-transfer at AHC growth, and optimization of automated growth control algorithms is presented.

Acknowledgements

The author acknowledges Prof. A. Gektin, Prof. V. Goriletsky, as well as V. Vasyliev and M. Tymoshenko (Institute for Scintillation Materials NAS of Ukraine) for useful discussions about continuous-growth method features and critical remarks concerning this chapter.

References

1 Lecoq, P., Annenkov, A., Gektin, A., Korzhik, M., and Pedrini, C. (2006) *Inorganic Scintillators and Detecting Systems. Physical Principles and Crystal Engineering*, Springer-Verlag, Berlin, Heidelberg, 251 pp.
2 The Belle Collaborations (1995) Technical Design Report. KEK Report 95-1, April 95.
3 The BaBar Collaborations (1995) BaBar Technical Design Report SLAC-R-95-457.
4 Goriletsky, V.I., and Smirnov, N.N. (2000) *J. Cryst. Growth*, **218**, 125–131.
5 Trefilova, L.N., Kudin, A.M., Kovaleva, L.V., Zaslavsky, B.G., Zosim, D.I., and Bondarenko, S.K. (2002) *Nucl. Instrum. Methods*, **A486**, 474–481.
6 Vinograd, E., Goriletsky, V., Kovaleva, L., Korsunova, S., Kudin, A., Mitichkin, A., Panova, A., Protsenko, V., Shakhova, K., Shpilinskaya, L. (1999) USA Patent No. 5,876,630.
7 Pfann, W.G. (1962) *Science*, **135**, 1101–1109.
8 Scheel, H.J. (1972) *J. Cryst. Growth*, **13/14**, 560.
9 Fedyushkin, A., Bourago, N., Polezhaev, V., and Zharikov, E. (2005) *J. Cryst. Growth*, **275**, e1557.
10 Rudolph, P. (2008) *J. Cryst. Growth*, **310**, 1298.
11 Eidelman, L.G., Goriletsky, V.I., Nemenov, V.A., Protsenko, V.G., and Radkevich, A.V. (1985) *Cryst. Res. Technol.*, **20**, 167.
12 Pandelisev, K. (1993) USA Patent No. 5,178,719.
13 Pandelisev, K. (1999) USA Patent No. 5,993,540.
14 Witter, D., Bawa, M. (1985) USA Patent No. 4,547,258.
15 Takano, K., Fusegawa, I., Yamagishi, H. (1994) USA Patent No. 5,361,721.
16 Nakajima, K., and Kusunoki, T. (1996) *J. Cryst. Growth*, **169**, 217.
17 Katsurayama, M., Anzai, Y., Sugiyama, A., Koike, M., and Kato, Y. (2001) *J. Cryst. Growth*, **229**, 193.
18 Kan, S., Sakamoto, M., Okano, Y., Hoshikawa, K., and Fukuda, T. (1992) *J. Cryst. Growth*, **119**, 215.
19 Furukawa, Y., Kitamura, K., Suzuki, E., and Niwa, K. (1999) *J. Cryst. Growth*, **197**, 889.
20 Matsumura, H., Watanabe, Sh., Nakamura, O., and Ito, T. (2007) *J. Cryst. Growth*, **308**, 348.
21 Bruni, F.J. (2008) Interface stability and its impacts on control dynamics, in *Crystal Growth Technology. From Fundamentals and Simulation to Large-Scale Production* (eds H.J. Scheel and P. Capper), Wiley-VCH Verlag GmbH, Weinheim, pp. 267–282.
22 Gektin, A., Goriletskiy, V., and Zaslavskiy, B. (2008) Continuous

growth of large halide scintillation crystals, in *Crystal Growth Technology. From Fundamentals and Simulation to Large-Scale Production* (eds H.J. Scheel and P. Capper), Wiley-VCH Verlag GmbH, Weinheim, pp. 351–379.

23 Apilat, V.Y., Oleinik, G.M., and Eidelman, L.G. (1966) *Prib. I Techn. Exper.* (in Russian), **3**, 216–218.

24 Goriletsky, V.I., Nemenov, V.A., Protsenko, V.G., Radkevich, A.V., and Eidelman, L.G. (1981) *J. Cryst. Growth*, **52**, 509.

25 Kudin, A., Mitichkin, A., Zaslavsky, B., Zaslavsky, A., and Kudin, K. (2006) Evolution of gas inclusions in NaI(Tl) crystals grown in Ar and CO_2 atmosphere (in Russian). Abstracts of the XII National Conference on Crystal Growth, Moscow, p. 275.

26 Goriletsky, V.I., Nemenov, V.A., Leybovich, V.S., Radkevich, A.V., and Eidelman, L.G. (1985) *Neorganich. Mater.* (in Russian), **21**, 115–118.

27 Goriletsky, V.I., Grinyov, B.V., Sidletskiy, O.Ts., and Tymoshenko, N.N. (2005) Proc. of the VI International conference Crystal Growth and Heat-mass Transfer (ICSC-2005), Obninsk, Russia, pp. 882–889.

28 Goriletsky, V.I., Tymoshenko, M.M., Vasyliev, V.V., and Ilyashenko, T.O. (2008) *Funct. Mater.*, **14**, 550–555.

29 Eidelman, L.G., Goriletsky, V.I., Protsenko, V.G., Radkevich, A.V., and Trofimenko, V.V. (1993) *J. Cryst. Growth*, **128**, 1059.

30 Gektin, A.V., and Zaslavsky, B.G. (2003) *Crystal Growth Technology* (eds H. Scheel and T. Fukuda), John Wiley & Sons, Ltd, Chichester, pp. 511–528.

31 Vasilyev, V.V., Goriletsky, V.I., Sidletskiy, O.Ts., Bystrova, E.N., and Kalaev, V.V. (2007) *Opt. Mater.*, **30**, 109–112.

32 http://www.semitech.us/products/cz_growth_simulator/ (accessed 09 April 2009).

33 Goriletsky, V.I., Vasilyev, V.V., Sidletskiy, O.Ts., Tymoshenko, M.M., and Sumin, V.I. (2007) *Funct. Mater.*, **14**, 541.

34 Radkevich, A., Eidelman, L., Lvovich, A., Protsenko, V., Goriletsky, V., Nemenov, V. (1993) USSR Patent No. 1116763 (A1).

35 Grinyov, B., Suzdal, V., Goriletsky, V., Gerasimcuk, L., Strelnikov, M., Yepifanov, Yu. (2007) Ukraine Patent No. 81196.

36 Goriletsky, V., Grinyov, B., Suzdal, V., Yepifanov, Yu., Sumin, V., Kuznetsov, V., Tymoshenko, N., Kisil, A. (2006) Ukraine Patent No. 71835.

17
Trends in Scintillation Crystals

Alexander V. Gektin

17.1
Introduction

The scintillation method of radiation detection has been in progress since the invention of the very first scintillators. The first material that was in wide use then was a man-made crystal of NaI(Tl) discovered in 1949 [1]. This landmark achievement provided an impetus for active insertion of the scintillation technologies into diverse applications. Before analyzing the state-of-the-art trends, a few historic digressions are in order. At first, in the mid-past century, there were predominant problems of detection of radiation *de facto* as well as those associated with locating the radiation sources. For this reason, the requirements for scintillators were limited by the ultimate registration needs, the so-called counting-mode detectors being in high demand. A gradual development of the electronics shifted the accent toward the radiation spectroscopy and verification of radionuclide types and their activities. In view of the above, the main attention was concentrated on R&D of the spectroscopy-grade scintillators. In the past few years, or even the last decade, a new trend has become clearly established, namely, the visualization of radiation fields and images.

In this way, besides high energy resolution the detection systems now have special requirements, such as a high spatial resolution. The optimum combination of these requirements depends on the application areas and the specifics of the detector. *In high-energy physics* applications, scintillators are an integral part of the electromagnetic and hadron calorimeters that register the results of the interactions of particle beams [2]. Any calorimeter is a granulated hodoscopic system (as a rule, a ball or barrel calorimeter) consisting of many individual large-size (tens of centimeters) crystal elements. Here, the spatial pattern is reconstructed due to the recovery of signal trains registered by each individual element of the hodoscope. Predominant of late in the astrophysics area have been gamma- and X-ray telescopes that visualize the image of radiation sources in the intergalactic space. Large-size scintillators are also in wide use here on account of the range of registered energies being broad enough. In radiation medicine diagnostics one of the issues of modern PETs (positron emission tomography) and

Crystal Growth Technology. Semiconductors and Dielectrics. Edited by P. Capper and P. Rudolph
Copyright © 2010 WILEY-VCH Verlag GmbH & Co. KGaA, Weinheim
ISBN: 978-3-527-32593-1

SPECTs (single-photon emission computer tomography) [3] is achieving high enough resolution to enables inspection of even small details of the human body. In this case, the resolution is as high as 1–4 cm, and it is implemented either by dedicated algorithms (the Anger-type algorithm for a gamma camera), or by using matrix detectors in which the signal is read out by each scintillator with subsequent computer reconstruction of the spatial pattern. The best spatial resolution pattern has been achieved to date in visualization of X-rays. Prominent here are two mainstream directions: 1) the scintillation film visualization with subsequent CCD cameras readout or α:Si + CsI(Tl) screens and 2) the scintillation arrays or matrix X-ray CT (computer tomography) [4]. X-ray image visualization is commonly used in medicine, security applications, industrial defectoscopy, and so on [5]. In these systems the resolution can be as high as millimeters or even tenths or hundredths of millimeters.

The above examples indicate that the tendency in advancement for the high spatial resolution technologies has come to embrace all of the leading scintillator areas of applications. The general technical solution in all cases is the transition from large-size crystals to various kinds of detector arrays and matrices that consist of many individual scintillation elements. The evolution of this kind made the researchers concentrate their efforts in two principal directions. First, development of novel materials that would be suitable for use in pixels and manufacture of matrix detectors, secondly, on development of suitable new crystalline forms (films, ceramics) of detectors with a high spatial resolution.

17.2 Novel Scintillation Materials

Long ago, the widening of the scintillation applications area ran the idea of the ideal scintillator creation into the ground. The past decade saw the "specialization" of scintillation materials according to their efficiency for various applications. In this respect, it is important to emphasize that not only do the recently discovered materials (first two rows in Table 17.1) have a high efficiency of radiation detection, but they also prove suitable for radiation image visualization systems. Above all, this concerns LSO, GSO and LYSO crystals for medical PET systems [6].

The beginning of the twenty-first century was marked by the appearance of a new family of scintillators, lanthanum halogenides doped with ions Ce^{3+} ions [7, 8]. These materials have a considerably higher absolute light yield, with respect to the conventional alkali-halide scintillators (NaI(Tl), CsI(Tl), CsI(Na)), and, as a result, an energy resolution across the range 2.9–3.3% (^{137}Cs source). These discoveries formed the basis for the development of devices with a high spectroscopic efficiency. The underlying physics of this kind of efficiency and the specifics of processes occurring during the scintillation spike are described in Ref. [9]. The most important here is the fact that, in contrast to the conventional halides and oxide (BGO, CWO, LSO etc.) scintillators, the time span of industrial-grade development has been reduced from 10–12 years to 2–4 years. The physical and technological features of the single-crystal growth today are described in detail in Refs. [9–11].

Table 17.1 List of the main scintillators available for imaging systems.

Scintillator	Density g/cm^3	Attenuation length at 511 keV, mm	Photoelectric effect %	Light yield Phot/MeV	Decay ns	Emission max mm
NaI:Tl	3.67	29.1	17	41 000	230	410
$Bi_4Ge_3O_{12}$ (BGO)	7.1	10.4	40	9 000	300	480
Lu_2SiO_5: Ce(LSO)	7.4	11.4	32	26 000	40	420
$Lu_{2(1-x)}Y_{2x}SiO_5$: Ce (LYSO) $x = 0.1$	7.1	12		30 000	40	420
$LuAlO_3$: Ce (LuAP)	8.3	10.5	30	11 000	10 160	385
$Lu_xY_{2x}AlO_3$: Ce (LuYAP) $x = 0.2$	7.3	13.5	27	13 000	20 200	380
$LaCl_3$: Ce	3.86	28 0	14.7	46 000	25 (65%)	350
$LaBr_3$: Ce	5.07	223	13.1	70 000	16 (97%)	380
LuI_3: Ce	5.6	182	28	90 000	6–40 (72%)	472 535

A distinctive feature of the past several years is the rise in development of a new direction in the scintillation technique. This deals with advanced spectroscopy portals (ASP) that are used for detection and control over relocation of the radioactive materials. The key role in this is the capability of discrimination between defense isotopes and civilian ones. The need for detection of low-activity sources and the capability of ASP to identify radionuclides on the basis of spectroscopic properties of a scintillator has provoked a new spiral of R&D on high-efficiency scintillators. That is to say that, earlier the main driving forces for scintillator development were high-energy physics and nuclear medicine, and now they have security systems added to them. The key requirements for scintillator in this case are the ultimately high light yield, good energy resolution, and, which is most important, the feasibility of production of large-sized single crystals at a reasonable cost.

The detection of weak radiation fluxes allows the use of slow scintillators, that is, materials with decay times in the microsecond range. This led the researchers to the renaissance of Eu^{2+}-containing scintillators. Table 17.2 cites examples of the most advanced research in these materials. One can see that the absolute light yield has been achieved, and in many instances exceeded, the level of 100 000 photons/MeV, which was quite recently the theoretical limit of the scintillator efficiency. There have been many innovations of the SrI_2:Eu type, which are 40-year-old discoveries in physics [12]. It is important to note that, in both the past and up to today, the industrial-grade technologies for these scintillators are absent. A surge in R&D in this direction may well be expected soon. Obviously, in the meantime, the APS development trends will inevitably lead to new generations of

Table 17.2 New scintillation materials based on Eu^{2+} crystals.

Scintillator	ρ g/cm^3	Z_{eff}	Lum, nm	$\sim E_g$ eV	LYtheor Ph/MeV	β LY Ph/MeV	γ LY Ph/MeV	R % 662 keV
SrI_2 (Eu)	4.549	49.4	435	3.7	111 000	110 000	120 000	2.8
$SrBr_2$ (Eu)	4.216	36.1	410	4.0	100 000	25 000	20 000	7
BaI_2 (Eu)	5.150	54.1	422	3.9	103 000	40 000	35 000	8
$BaBr_2$ (Eu)	4.781	45.5	406	4.1	98 000	22 000	16 000	11
CaI_2 (Eu)	4.000	48.0	467	3.5	114 000	110 000	110 000	5.2
$LaBr_3$ (Ce)	5.080	44.1	360	4.5	89 000	60 000	60 000	2.6

the portals that will provide, along with selective spectroscopy, for visualization of the source location. This is to say that the general trend in the growth of the role of radiation image visualization and R&D carried out in concomitant engineering are sure to bring passive surveillance systems into play.

17.3 Scintillation Detectors for Image Visualization and Growth Techniques for Scintillation Crystals

Historically, the first ideas for digital visualization using scintillation detectors were brought forward by successful R&D on active inspection (airport) scanners and those used in the medical X-ray CT. Each of the directions has outlived several generations of the scanners. In the former case, the design was based on detector arrays that were as predominant then as they are now. In the medical applications there was a noticeable transition from arrays to matrix detectors [3, 4]. The latter tendency concerns increasing X-ray radiation energy and the need for ever thicker detectors, for the transverse dimensions of pixel to become smaller and smaller. This development brings about a change in manufacturing technologies and a transition from single-crystal arrays to ceramic scintillators [4].

Another independent field of matrix detectors in medical diagnostics is the use of PET scanners. In contrast to X-ray CT, PET uses the registration of annihilation gamma-quanta (511 keV) and calls for a relatively large volume of the matrix; the typical pixel sizes are in the range of 3 to 5 mm. In this way, as far as the manufacture of matrix detectors is concerned, the classical technologies of crystal cutting are very relevant, indeed. Companies such as GE Healthcare, Siemens Medical Solutions, and Philips Medical Systems employ LSO, LYSO, GSO crystals in their scanners that actively replace the earlier predominantly utilized BGO crystals. One of the main requirements for such scintillators (along with the high density, Z-value, and light yield) is for the decay time to be small, in the range of 20–30 ns decay times. Yet, the desire for a higher resolution capability as a trade-off for the time-of-flight technology will make the requirements for decay time more strin-

Table 17.3 Typical materials and parameters for scintillation element separation in arrays and matrices.

Separator	Thickness	Reflectivity
MgO powder	1 mm	100%
Tetratex	0.15 mm	98%
Reflector paint	0.05 mm	95%
Epoxy paint	0.1 mm	94%
Metals	0.05 mm	>70%
VM2000 foil	0.05	96%

gent. Therefore, Ce^{3+}-activated oxides (Table 17.1) will become dominant in the future to ensure short scintillation decay times.

One of the outstanding merits of the oxide scintillators is their nonhygroscopicity. We know of attempts at employing the crystals NaI(Tl), CsI(Tl), $LaCl_3$:Ce, $LaBr_3$:Ce as pixels for matrix detectors, however, none of them culminated in the development of a commercially available scanner sue to their hygroscopic nature.

The major parameters of the matrix detector are its pixel or element size and crosstalk between adjustment channels (usually ~2.4%). However, there are a number of other extremely important parameters that look at the state-of-the-art for arrays and matrix assembly. The tendency to minimize the pixel size currently leads to the following minimal commercially available elements: 1.0 mm for NaI(Tl), 0.3 mm for CsI(Tl), CdWO4, BGO, and 0.8 mm for LSO and LYSO [13]. The latter relates to the separator (septa) type and such thickness (see Table 17.3) that prevents light leakage from neighboring pixels. Note that one of the most important functional requirements for the assembly is its homogeneity, which affects the signal spread from channel to matrix channel. To achieve the perfect assembly, it is necessary that the parameters of the crystal be uniform and that 1) the lateral surfaces of the element be treated in such a way that would make for homogeneous light collection in all elements of the matrix (array) and that 2) the dimensions of the elements and entire assembly be maintained with precision. The distance from the center of one element to the center of an adjacent one should exactly correspond to the PD (photodiode) array geometry. Thus, mechanical cutting and assembly become the key factors of the technology as a whole.

One of the alternatives to crystal cutting is an attempt to grow a crystal with an assigned transverse cross-section. Small-diameter, long-length crystals (fibers) are of considerable interest for potential scintillation arrays and matrix technology development. The physical basics of this approach were first proposed by Stepanov in 1936 [14] (see, Figure 17.1a, classical Stepanov (CS) method). Later, this method was modified many times over and many of its subspecies are known to be in use to date (see, Figure 17.1b–d), such as the edge-defined film-fed growth (EFG), the growth from an element of shape (GES), and the inverted Stepanov (IS) growth. The latter is closest to the method that was transformed into the so-called micro-pulling method (μ-PD) [15, 16] in the past few years. Schemes for crystal fiber

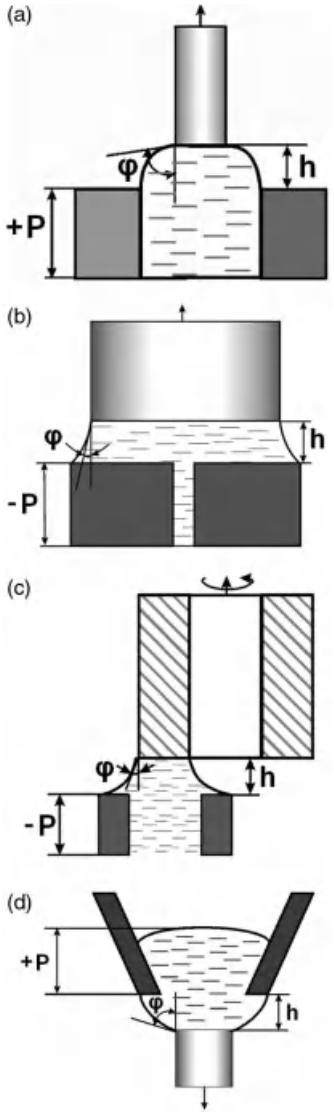

Figure 17.1 (a) classical Stepanov (CS) method; (b) edge-defined film-fed growth (EFG); (c) growth from an element of shape (GES); (d) inverted Stepanov (IS) growth.

growth are found in Figure 17.2. There are a few modifications that allow for preparing elongated single crystals with a diameter in the range of 0.05–1.0 mm. In general, the μ-PD technique involves growing single crystals through a micronozzle (die) by pulling them in a downward direction [15, 16]. The growth apparatus includes a heated platinum crucible, an annealing furnace and a seed holder with a lowering mechanism. The axial gradient in the vicinity of the crystal/melt interface can reach 200–300 C/mm, which is the cause of the ultrafast crystalliza-

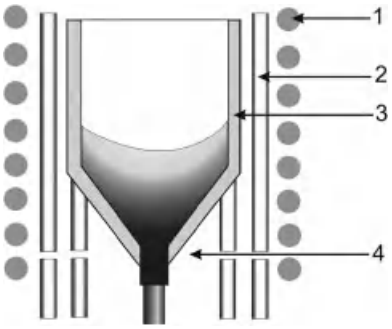

Figure 17.2 Scheme for the micropulling down method (μ-PD). 1 – RF-heater, 2 – Ceramic holder, 3 – Crucible, 4 – Fiber.

tion. (In this case, crystals can be grown of an assigned cross-section at high growth rates, that is, the feasibility is there for a high-productivity manufacturing process). As a first step, the oriented polycrystalline seed material is grown down, but at later stages the preferential crystallographic orientation is developed by the necking process. Despite many attempts at modeling the formation process of the stable growth stage and the minimization of oscillations of the melt meniscus mold (and the subsequent instability and irregularity of the cross-section of the crystal) [15], the growth of the perfect inorganic fiber scintillator still remains a highly state-of-the-art process.

Yet another challenge has to do with the functional inhomogeneity of the fiber. Nearly all of the scintillators in use today are activated (doped) crystals. The inhomogeneous distributions of the activator are associated with the dependence of the segregation coefficient of dopant on the fiber crystallization rate (17.1) [17]. As a result, the activator distribution is not uniform enough through the fiber. The core of a pixel has a lower scintillation efficiency relative to the peripheral regions.

$$k_{\text{eff}} = k\left[k + (1-k)\mathrm{e}^{\left(-\frac{V\delta}{D}\right)}\right]^{-1} \tag{17.1}$$

where $k = C_S/C_L$, (C_S and C_L – activator concentration in crystals and melt, D is the diffusion coefficient, V is the growth rate, and δ is the distance of the freezing interface.

However, a few different scintillation materials have been successfully grown by the micro-pulling-down (μ-PD) technique in the last several years [18, 19], but the crystal perfection is still far from meeting the high-level requirements for medical applications.

17.4
High Spatial Resolution Scintillation Detectors

The history of registration and visualization of X-ray imaging began with the discovery by Roentgen. For more than half a century screen-film technology was

used to produce images and for visual control. Late in the twentieth century, the shortcomings of this film technology became an obstacle to the progress of science. Since 1995 a trend has become well formulated in the development of digital systems for radiography. Today, the high acquisition costs of the equipment are the main obstacles to digital radiography technology being used widely. Yet, this technology has a number of advantages over the preceding technologies. This is to indicate an improved quality of imaging, an increased productivity and a better health treatment. From this viewpoint, the change of the generations has taken place very rapidly. According to some estimates, in 2008 the market of the digital X-ray diagnostic hardware was on the order of 80 thousand new systems across the world (estimated revenue of 28 billion USD).

Most widely used is flat panel technology that employs an indirect process of X-ray conversion similar to screen-film radiography. Those systems use a scintillation material, for example, CsI(Tl) or Gd_2O_2S:Tb, which absorbs the X-ray energy and converts it into light. The energy of the light is converted into a photonic signal using a matrix of thin-film diodes (TFD) and registered for the readout by an analog-to-digital converter (ADC) (thin-film transistor [TFT]) or by CCD-reader.

Another approach includes matrices of light diodes based on amorphous hydrogenated silicon. Originally, the α-Si:H photodiodes were developed as high-efficiency photovoltaic transducers for solar-energy production [20], however, their subsequent upgrading has turned them into a viable replacement for CCDs. Major features of matrices based on α-Si:H are their high radiation resistance, relative low production costs and a possibility of forming large-area matrices, up to $43 \times 43\,cm^2$. An important factor is that the CsI(Tl) layer can be deposited immediately on those matrices by vacuum deposition that excludes the need, in the intermediate devices, for light photon transmission from the scintillation layer to the photodetector. The matrix has primary signal processing units connected to it, including a line-addressing system, preamplifiers, multiplexers, and ADCs. The implementation is made of an integration device used for imaging, and uses the digital signal at the output [21].

The matrix detector consists of a scintillation screen connected directly to a complex of silicon photodiodes. The unique feature of the scintillation matrix based on CsI(Tl) or Gd_2O_2S is its fast data reading, up to 30 frames per second, which provides for useful applications of these detectors in X-ray radiography and fluoroscopy.

A fundamental problem of scintillation and storage film screens is the limitation of the spatial resolution owing to the light spread inside the film proper. This phenomenon is evident from Figure 17.3. As a result, the outgoing light has a washed-out profile instead of the ideal signal distribution (Figure 17.3 bottom) which results in decreasing spatial resolution. This problem is enhanced as the X-ray energy is raised. In this event thicker films would be in order to retain the high registration efficiency. As a result, we have an enhancement of the light output spread of the scintillation flash point. The conventional polycrystalline films are considered to be Lambert sources that radiate uniformly in all directions off the track of interactions with a particle or a quantum. The size of the light spot

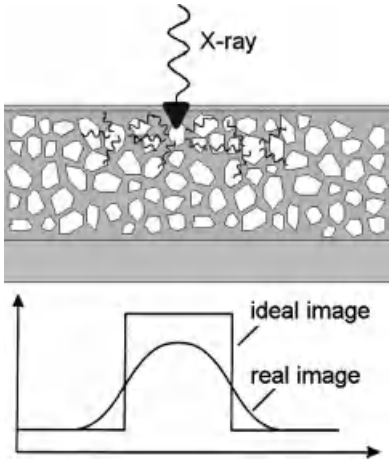

Figure 17.3 Light scattering and output signal shape for polycrystalline scintillation film.

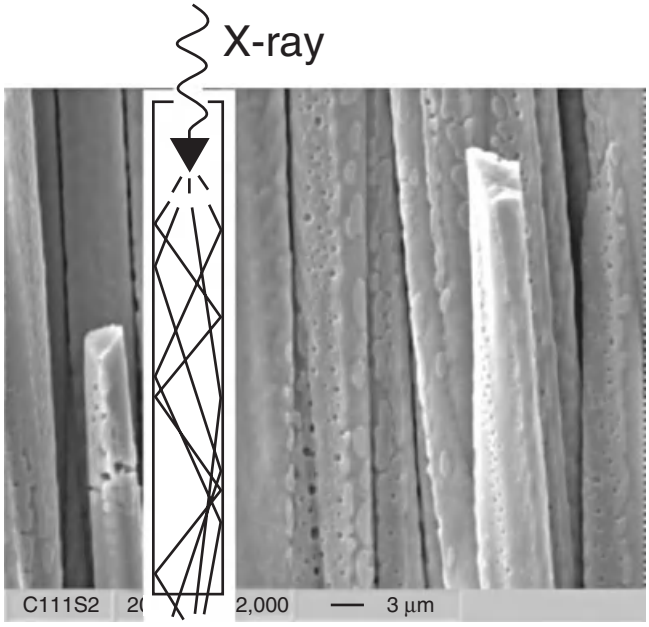

Figure 17.4 Light collection along the bar of columnar-structured scintillation film.

on the output surface in this case is equated to roughly double the layer thickness, which determines exactly its spatial resolution.

The key idea about overcoming the above problem is to use films with a columnar structure (Figure 17.4). The implication in this case is such that each of the film columns acts simultaneously as scintillator and light guide concentrating all

the light on the column exit endface. Obviously, the lengthening of the column length allows for registration of quanta with greater energies without incurring substantial losses to the light output and spatial resolution on the endfaces.

This approach is based on a remarkable feature of CsI(Tl), as reported in refs. [22–24], which is the formation of columnar layer morphology during vacuum deposition. The refractive index of CsI is 1.78 corresponding to the critical angle for total reflection being about 34° at the scintillator emission wavelength (560 nm). As a result, different from the isotropic phosphorus, the columnar morphology of CsI(Tl) layers provides for directivity in light propagation and promotes decreasing light diffusion in the lateral direction, the acceptable solution still being there.

The vacuum deposition method is used to produce CsI(Tl) layers of various thicknesses (from several micrometers to more than several hundred micrometers) which had the columnar morphology. The layer morphology is evident, as a rule, from SEM images. The samples are transverse chippings of the film on the substrate that are covered with a thin layer of carbon to preclude distortions in the electron microscopy image due to the charge accumulation. Typical images of the transverse chippings of those samples are given in Figure 17.5.

By analyzing the images of the transverse cross-sections of the layers, the following conclusions can be made:

- The characteristic thickness of columnar aggregates can be as low as 10 micrometers, which predetermines the subsequent spatial resolution;
- The surfaces of columnar aggregates are very smooth that stimulates the total internal reflection;
- It is not always possible to obtain a layer consisting of a set of uniform columns with a smooth surface; the self-organized layer growth in this morphology calls for the observance of a certain deposition mode.

The formation of columnar morphology during the vacuum deposition of CsI(Tl) layers is often proposed to be interpreted within the structural zone model (SZM) [24, 27, 28]. We shall now consider the peculiar features of the realization of SZM, as observable during the vacuum deposition of CsI(Tl).

The first study on the variation of the morphology of thick condensates of metals and some oxides during the deposition onto a substrate that has a temperature gradient on its surface was given in Ref. [27]. It was clear that three characteristic zones were formed in the direction of the gradient in which the layer-formation mechanism differed and depended on a given temperature. Zone evolution depends on Ts/Tm, where Ts is the substrate temperature, and Tm is the condensate melting temperature as is shown in Figure 17.6. Zone I is located in the region Ts/Tm < 0.3; for Zone III Ts/Tm > 0.5. Between those zones is a transitional Zone II, in which due to acceleration of the surface diffusion of adatoms the competition begins for aggregate growth with the most favorable orientation. Some of the grains grow out due to absorption of their neighbors that are in less favorable positions energetically, although due to the insufficient diffusion this absorption occurs incompletely. As a result, a peculiar substructure is formed that contains

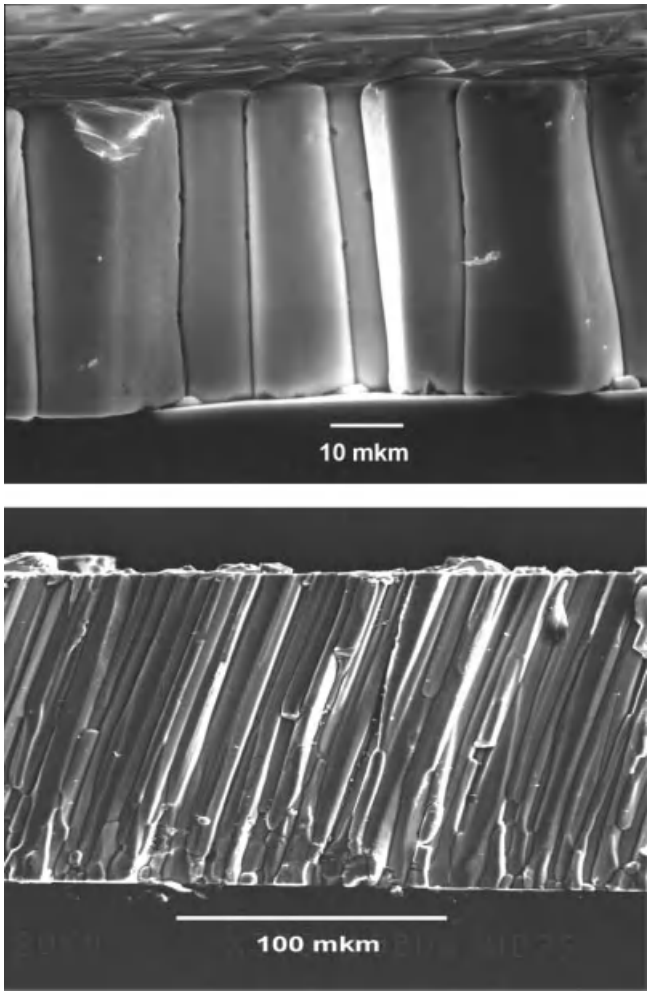

Figure 17.5 SEM view of columnar structure CsI(Tl) film. LiF substrate (upper photo) and glass substrate (bottom). Condensation temperature 300 °C [25, 26].

regions of growing grains. This process can be completed during the growth in Zone II, where volume diffusion plays a major role and the competition for growth leads to the formation of aggregates with a more favorable orientation, which are aligned as columns with a smooth surface.

The SZM was developed for thick layers of metals and oxides. Also, the columnar growth was made for semiconductor compounds as well [29, 30], where, depending on the substance, a shift of boundaries was observable between the zones over the temperature scale. For the CsI(Tl) layers, deposited at different temperatures and onto different substrates, the self-organized growth was observable, and as a rule, with distinct homogeneous columns. Violations of the homogeneity appear as a

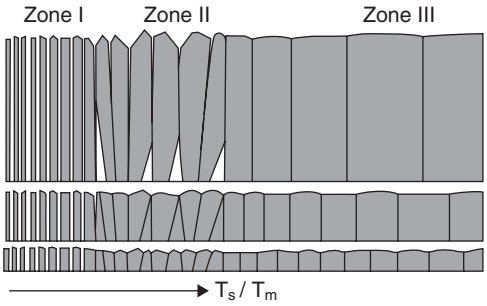

Figure 17.6 Zone model scheme [28].

result of deviations from the deposition-mode stability both in temperature and in condensation rate. In this way, the stability of the deposition mode is a major factor determining the homogeneity of growth of the columnar aggregates in the film. An increase in the rate of condensation up to 50–100 Å/s limits the mobility of molecules incident on the substrate and causes the condensation conditions to shift to Zone II, even if the substrate temperature is 300 °C. Time and again [22, 31], attempts have failed to achieve self-organized growth of the homogeneous columns of CsI(Tl) with smooth walls after the vacuum deposition. In those cases, the researchers had to resort to an additional operation of the surface profiling in order to form the sites of nucleation and growth of the aggregates.

If we use as substrate the matrix of α-Si (Figure 17.7), then we have a scintillator-photodiode sandwich, that is, the preimage of a detector that is ready to visualize X-ray images. Exactly, these kinds of technical solutions are realized in systems by companies such as Philips, Trixel, and so on.

Note that the technologies of α:Si + CsI(Tl) have many nuances and proprietary know-how that allow for perfection of the scintillator structure. As an example, Figure 17.8 presents an external view of a matrix with the regular pixel structure produced by a dedicated thermal treatment of the crystalline film. A separate effort is associated with deposition of the special protective film [32] on the hygroscopic CsI(Tl) layer.

On the whole, one can safely say that the epitaxial (film) methods of X-ray scintillator manufacture with a high spatial resolution have matured to the level of the industrial-grade frame of reference. Moreover, with the scintillation detector problem now resolved, the way has been paved to the full transition to digital techniques in radiography.

17.5 Conclusions

The diversity should be emphasized in the trends of development of the modern scintillation techniques and scintillation materials. The development and diversi-

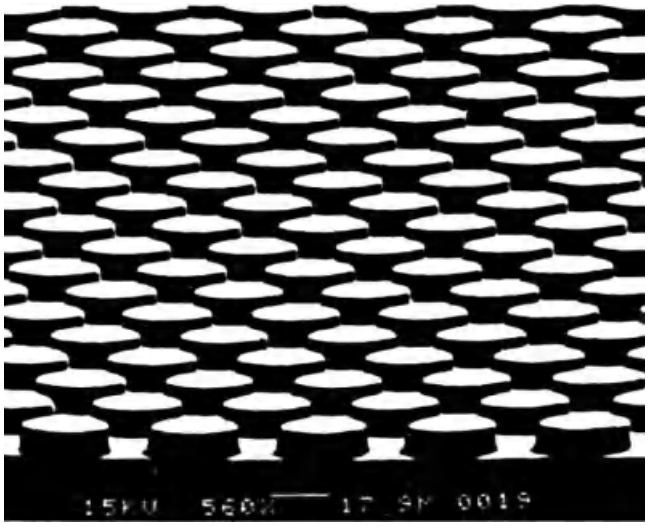

Figure 17.7 Regular Si substrate for columnar film growth [31].

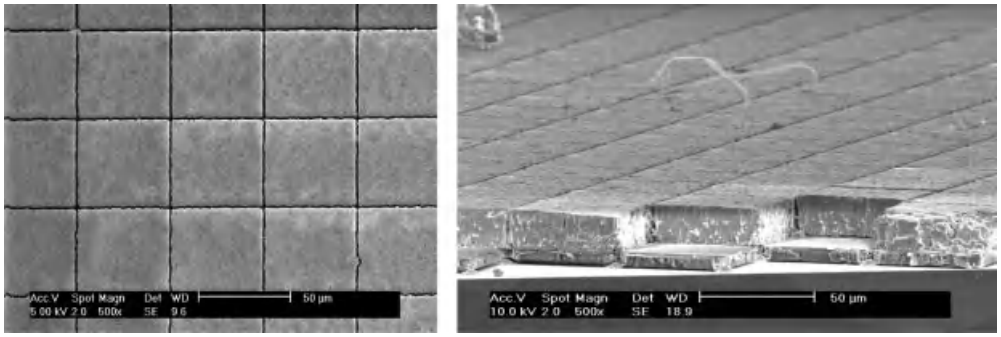

Figure 17.8 SEM images of the pixel structure CsI(Tl) scintillator [32].

fication of the dedicated radiation registration devices and areas of their applications bring out the necessity of finding novel technical solutions. Each of the cases faces R&D on new scintillation crystals, development of the techniques of synthesis for raw materials and crystal growth, engineering and technologies of such detectors that would be based on the novel solutions, and, finally, correct design and manufacture of the new devices. The progress in radiation registration technologies triggers a string of state-of-the-art research and development, testing, and manufacture. In this respect, the above trends and instances of the scintillation materials and detectors used for visualization of radiation imaging can serve as a typical example of such tendencies over the past decade.

References

1 Hofstadter, R. (1949) *Phys. Rev.*, **N5 (75)**, 796–910.
2 Novotny R. (2006) The Electromagnetic Calorimeter of the Future PANDA Detector, in "*Calorimetry in High Energy Physics. Series: AID Conference Proceedings*", vol. 867, ed by Magill Stephen, Yoshida Rik., p. 315.
3 Moses W.W., Gayshan V., Gektin A. (2006) The Evolution of SPECT – From Anget to Today and Beyond., in "*Radiation Detectors for Medical Applications. NATO Security through Science Series – B*", Springer, p. 37.
4 Deych R., Dolazza E. (2005) New Trends in X-ray CT Imaging., in "*Radiation Detectors for Medical Applications. NATO Security through Science Series – B*", Springer, p. 15.
5 http://www.varian.com/media/xray/, http://www.canon.com/technology/canon_tech/explanation/x_ray.html, http://smithsdetectionpid.com/.
6 Melcher, C.L. (2005) *Nucl. Instrum. Methods*, **A537**, 6–14.
7 van Loef, E.V.D., Dorenbos, P., van Eijk, C.W.E., *et al.* (2001) *Appl. Phys. Lett*, **79**, 1573.
8 Owens, A., Bos, A.J.J., Brandenburg, S., *et al.* (2007) *Nucl. Instrum. Methods*, **A574**, 158–162.
9 Lecoq, P., Annenkov, A., Gektin, A., Korzhik, M., and Pedrini, C. (2006) *Inorganic Scintillators for Detector Systems*, Springer, p. 251.
10 Weber, M.J. (2004) *Nucl. Instrum. Methods*, **A527**, 9–14.
11 Nikl, M. (2006) *Meas. Sci. Technol.*, **17**, R37–R54.
12 Hofstadter, R. (1968) Europium activated strontium iodide scintillators, US Patent 3,373,279, USA.
13 Krus, D.J., Novak, W.P., and Perna, L. (1999) SPIE Int. Symposium on Optical Science, Engineering and Instrumentation, July 18–23, 1999, Hard X-Ray, Gamma Ray and Neutron Dettector Physics, SPIE, vol. 3768.
14 Stepanov, A.V. (1959) *J. Tech. Phys.* (in Russian), **29.3**, 381–393.
15 Fukuda, T., and Chani, V.I. (2007) *Growth by Micro-Pulling-down Techique*, Springer, p. 341.
16 Shimamura, K., and Fukuda, T. (2003) *Handbook of Advanced Ceramics*, vol. 1, Elsevier, p. 339.
17 Chani, V.I., Yoshikawa, A., Fukuda, T., *et al.* (1999) *J. Cryst. Growth*, **204**, 155–162.
18 Chani, V., Lebbou, K., Hautefeuille, B., Tillement, O., and Fourmigue, J.-M. (2006) *Cryst. Res. Technol.*, **41**, 972.
19 Santo, A.M.E., Ranieri, I.M., Brito, G.E.S., Epelbaum, B.M., Morato, S.P., Vieira, N.D., and Baldochi, S.L. (2005) *J. Cryst. Growth*, **275**, 528–533.
20 Madan, A., McGill, J., Czubatyj, W., *et al.* (1980) *Appl. Phys. Lett.*, **37**, 826.
21 Moy, J.-P. (2000) *Nucl. Instrum. Methods*, **442**, 26–37.
22 Jing, T., Cho, G., Drewery, J., *et al.* (1992) *IEEE Trans. Nucl. Sci.*, **39**, 1195–1198.
23 Wieczorek, H., Fringis, G., Quadfield, P., *et al.* (1995) Proc. Int. Conf. SCINT'95, Delft (Netherlands), pp. 547–554.
24 Nagarkar, V.V., Gupta, T.K., Miller, S.R., *et al.* (1998) *IEEE Trans. Nucl. Sci.*, **45**, 492–496.
25 Fedorov, A., Lebedinsky, A., and Zelenskaya, O. (2006) *Nucl. Instrum. Methods A* (in Russian), **564**, 328–331.
26 Lebedinsky, A., Fedorov, A., Ananenko, A., and Mateychenko, P. (2006) *Acta Cryst.* (in Russian), **A62**, S159.
27 Movchan, B.A., and Demchishin, A.V. (1969) *Fiz. Met.* (in Russian), **28**, 653–660.
28 Petrov, I., Barna, P.B., Hultman, L., *et al.* (2003) *J. Vac. Sci. Technol. A*, **21**, S117–S128.
29 Ristic, J., Sanchez-Garcia, M.A., Calleja, E., *et al.* (2002) *Phys. Status Solidi A*, **192**, 60–66.
30 Muthukumar, S., Sheng, H., Zhong, J., *et al.* (2003) *IEEE Trans. Nanotech.*, **2**, 50–54.
31 Jing, T., Goodman, C.A., Drewery, J., *et al.* (1994) *IEEE Trans. Nucl. Sci.*, **41**, 903–909.
32 Kim, B.-J., Cho, G., Cha, B.K., *et al.* (2006) SCINT 2005, Proc. of 8th Int. Conf. on Inorganic Scintillators and Their Application, Ed. A. Gektin, B. Grinyov, Kharkov, Ukraine, pp. 307–309.

Part IV
Crystal Machining

Crystal Growth Technology. Semiconductors and Dielectrics. Edited by P. Capper and P. Rudolph
Copyright © 2010 WILEY-VCH Verlag GmbH & Co. KGaA, Weinheim
ISBN: 978-3-527-32593-1

18
Crystal Machining Using Atmospheric Pressure Plasma

Yasuhisa Sano, Kazuya Yamamura, and Kazuto Yamauchi

18.1
Introduction

In plasma-processing technologies, plasma is usually generated at a low pressure; however, Professor Yuzo Mori's group has used atmospheric-pressure plasma since 1986. In atmospheric-pressure plasma, the density of radicals is very high; thus, a high processing rate is expected. Also, the mean free path of gas molecules is very short (about 0.1 μm), therefore the ion energy in the plasma is very low, which results in a damage-free processed surface, which is particularly important, especially for semiconductor crystals. Because the region of plasma with a short mean free path is localized in an area with high electric field intensity, this results in a maskless process. When a plasma is generated at atmospheric pressure including a halogenide gas or oxygen, only the surface facing the localized plasma is chemically etched or oxidized. In this chapter, two crystal-machining techniques using atmospheric-pressure plasma are described. One is plasma chemical vaporization machining (PCVM). A general description of the process and recent topics such as beveling and thinning silicon carbide (SiC) wafers are described. The other technique is numerically controlled sacrificial oxidation. Its basic concepts and application to uniformizing silicon on insulator (SOI) substrates are described.

18.2
Plasma Chemical Vaporization Machining (PCVM)

18.2.1
General Description of PCVM

PCVM is plasma etching using atmospheric pressure plasma (Figure 18.1a) [1–7]. It has a high removal rate and no damaged layer is formed on the processed surface because of the low ion energy. Also, the removal area is limited to near the localized plasma region. In the case of etching using low-pressure plasma, a

Crystal Growth Technology. Semiconductors and Dielectrics. Edited by P. Capper and P. Rudolph
Copyright © 2010 WILEY-VCH Verlag GmbH & Co. KGaA, Weinheim
ISBN: 978-3-527-32593-1

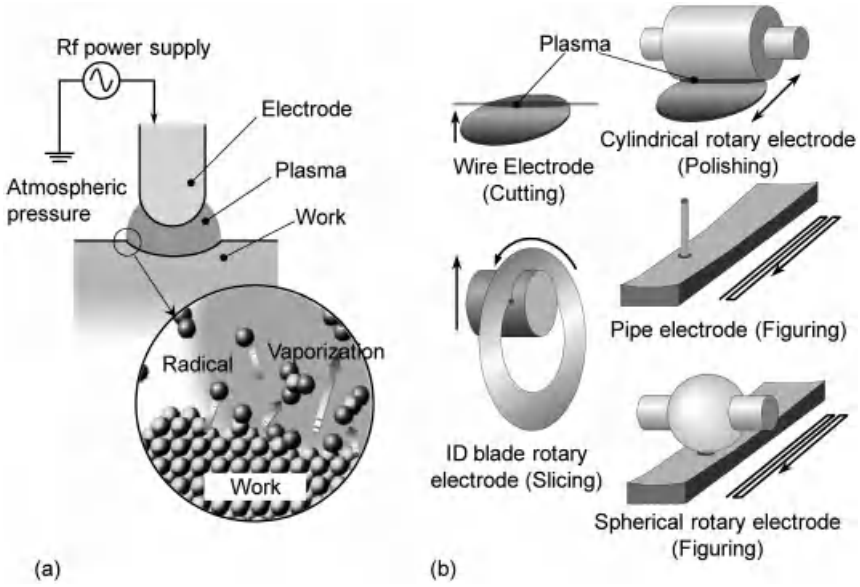

Figure 18.1 Schematic of PCVM: (a) machining mechanism and (b) various types of electrode used with PCVM. (Reproduced from Scheel and Capper: Crystal Growth Technology, 476, Copyright 2008 Wiley-VCH Verlag GmbH & Co. KGaA with permission (b).)

mask pattern must be prepared to create a structure on the surface. However, in PCVM, mask patterns are not needed. There are a number of applications of PCVM using various electrodes (Figure 18.1b) including cutting using a wire electrode, slicing using a disk or inner-diameter blade electrode, polishing using a cylinder electrode, and figuring using a pipe or spherical electrode.

18.2.2 Machining of SiC by PCVM

SiC has attractive properties such as a wide bandgap, high thermal conductivity, a high breakdown electric field, and high thermal stability. It is a suitable substrate for low power consumption power devices and high-temperature applications. However, because of its hardness and chemical stability, there are few efficient machining methods. Figure 18.2 shows an example of a procedure for fabricating an SiC power device. An SiC wafer is formed by crystal growth, slicing, lapping, beveling, and polishing. Then, the device wafer is fabricated by the processes shown in the figure. After processing the device, it is thinned, diced, and packaged. Mechanical machining processes are used in slicing, lapping, polishing, thinning, and dicing. We are currently considering the replacement of these mechanical machining processes with chemical processes such as PCVM [8, 9] and catalyst-referred etching [10, 11]. Basic studies on beveling [12] and thinning [13] processes by PCVM have been carried out, as discussed in more detail below.

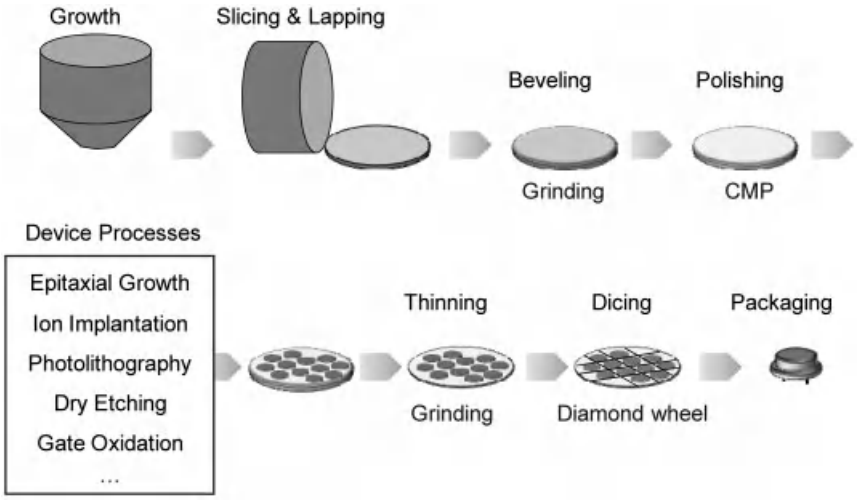

Figure 18.2 Example of procedure for fabricating SiC power device.

18.2.3 Beveling of SiC Wafer

18.2.3.1 Background

Beveling is essential for preventing the chipping of particles from the edge of a wafer during surface polishing. It is desirable that the beveled surface has no microcracks and that no particles are detached from the surface. Therefore, we consider that PCVM is a highly suitable beveling method for SiC wafers because it is a chemical process and leaves no microcracks on the processed surface.

18.2.3.2 Apparatus and Experimental Method

Figure 18.3 shows a schematic of the PCVM beveling apparatus. It was designed in order that a ring-shaped atmospheric-pressure plasma is generated by supplying RF power between the SiC wafer and the outer electrode. This enables high-efficiency etching of the entire circumferential surface. An SiC wafer was fixed in position using a vacuum chuck. The chamber was evacuated to replace the initial air with reactive gases. The ratio of the reactive gases was controlled using mass-flow controllers ($He:SF_6 = 99:1$), and gas was supplied up to a pressure of 1 atm. The reactive-gas mixture flows from the lower side to the upper side of the electrode through the plasma region. Then, the plasma breaks down upon the supply of a 13.56-MHz RF power source. The gap between the circumferential surface and the outer electrode is 500 μm. The shape of the outer electrode corresponds to the orientation flat of the wafer, resulting in gap uniformity. In addition, a dielectric membrane is formed on the outer electrode surface to prevent the generation of arc-discharge plasma with thermoelectronic emission and secondary electron emission and to maintain the low temperature and stability of the plasma.

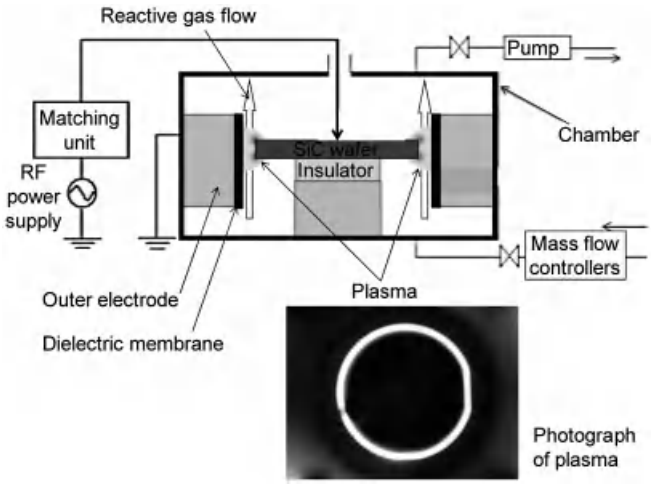

Figure 18.3 Schematic of PCVM beveling apparatus. (Reprinted from Kato *et al.*, Mater. Sci. Forum 600–603, 844, Copyright 2009 Trans Tech Publications.).

The sample used was a 2-inch 4H-SiC (0001) on-axis wafer (n-type, 0.01–0.05 Ω cm). The (0001) Si face of the wafer was the lapping surface, and the C face (back side) was the sliced surface. The wafer was machined for 20 min with an rf power of 160 W.

18.2.3.3 **Results and Discussion**

Figure 18.4 shows cross-sectional images of both unprocessed and processed edges of the wafer viewed using a scanning electron microscope (SEM). It is clear that the sharp edge was rounded after machining. This appears to be mainly caused by the high radical density near the edge because of the high concentration of the electric field there. Figure 18.4 also shows top and bottom views of the edges of both Si and C faces obtained using a Nomarski differential interference microscope. Both a steep and cracked edge (Si face) and a bumpy edge (C face) were well beveled and smoothed without the formation of any microcracks. Figure 18.5a shows detailed cross-sectional profiles of both the unprocessed and processed edges of the wafer measured using a confocal laser scanning microscope, which can provide cross-sectional profiles without breaking the wafer. There is no significant difference in shape between the edges of the Si and C faces. The side face and the corner of the wafer were processed to depths of about 30 and 75 μm, indicated by A and B in Figure 18.5a, respectively. The wafer was processed more around the edge than at other parts because of the local generation of plasma. The edge of the wafer was selectively etched because the density of fluorine radicals was highest there, since the electric field intensity was highest (Figure 18.5b). This means that the beveling of SiC wafers by PCVM will enable the manufacture of wafers with smooth edges by removing the damage at both the edges and circumferential surface. The shape of a wafer edge is standardized in accordance with

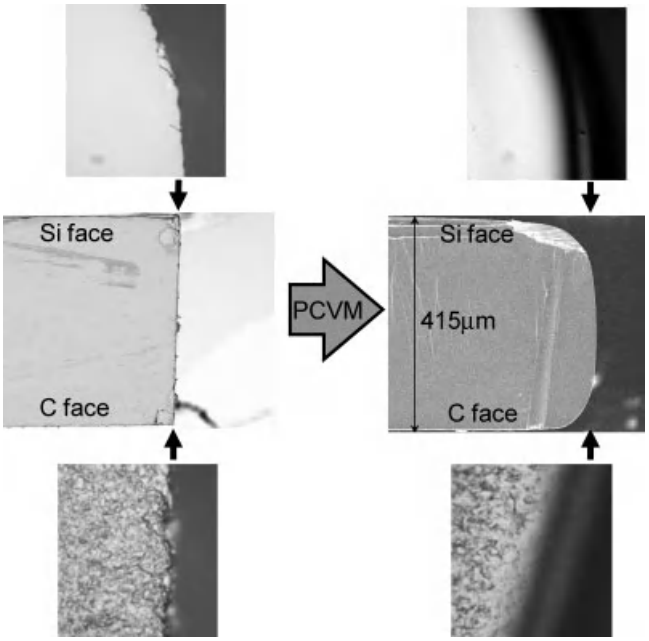

Figure 18.4 Cross-sectional SEM images of edges of SiC wafer and top and bottom views of edges of Si and C faces. (Reprinted from Kato *et al.*, Mater. Sci. Forum 600–603, 845, Copyright 2009 Trans Tech Publications.)

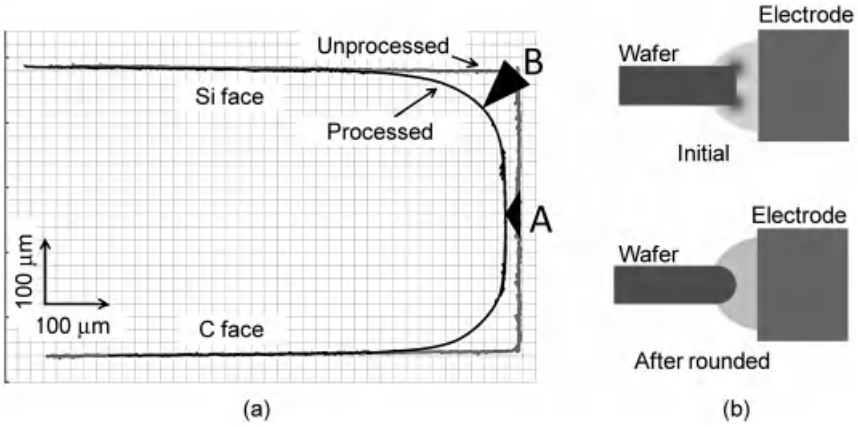

Figure 18.5 (a) Detailed cross-sectional profiles of unprocessed and processed edges of wafer measured using a confocal laser scanning microscope and (b) schematic of electric-field intensity. (Reprinted from Kato *et al.*, Mater. Sci. Forum 600–603, 846, Copyright 2009 Trans Tech Publications (a).)

the SEMI standard. In the beveling of SiC wafers by PCVM, the edge shape depends on experimental conditions such as the process pressure and reactive-gas composition. Therefore, it appears that arbitrarily shaped edges can be fabricated by optimization of the electrode shape and various experimental conditions.

18.2.3.4 Summary of Beveling of SiC Wafer

The beveling of a SiC wafer by PCVM was carried out. As a result, the entire circumference of the wafer was beveled uniformly to a smooth and round edge. PCVM is a chemical etching process; thus, no microcracks were formed at the beveled edges, which are inevitably formed in conventional grinding methods. It appears that PCVM can be used as an effective method of beveling the edge of SiC wafers.

18.2.4 Thinning of SiC Wafer

18.2.4.1 Background

A thinning process is required after device processing to reduce the on-resistance in vertical devices such as power metal-oxide semiconductor field-effect transistors (MOSFETs). Although it is easy to thin a Si wafer by conventional mechanical machining processes such as grinding and polishing, it is difficult to thin an SiC wafer with a high yield rate by these processes because its high hardness and brittleness cause cracking and chipping during thinning. Thus, thinning an SiC wafer by PCVM was attempted. PCVM has no external force that causes cracking and chipping because it is a noncontact machining method.

18.2.4.2 Sample Preparation and Experimental Conditions

A strip specimen of size 20 mm × 5 mm was cut off from a 2-inch 4H-SiC (0001) 8-degree-off-angle wafer using a diamond grinding wheel. Usually devices are fabricated on the Si face; thus, thinning is performed from the C face, which is on the reverse of the device side. The specimen was thinned from an initial thickness of 400 μm to 100 μm by rough mechanical polishing then was used as the PCVM specimen. A PCVM polishing apparatus with a cylindrical rotary electrode of 200 mm diameter and 250 mm length was used. The specimen was set parallel to the central axis of the electrode in order that the entire area of the specimen was completely immersed in the plasma. The reactive gas was 1% SF_6 balanced by helium, and the supplied power was 1000 W.

18.2.4.3 Results and Discussion

Figure 18.6a shows the relationship between the thickness of the sample and processing time. The thickness decreases almost linearly with increasing processing time. The removal rate obtained from the slope is approximately 1.5 μm/min. After 40 min, the sample was successfully thinned to 40 μm without any cracking or chipping. Figure 18.6b shows a photograph of samples with thicknesses of 400, 100, and 40 μm. It is shown that the initially colored sample became nearly trans-

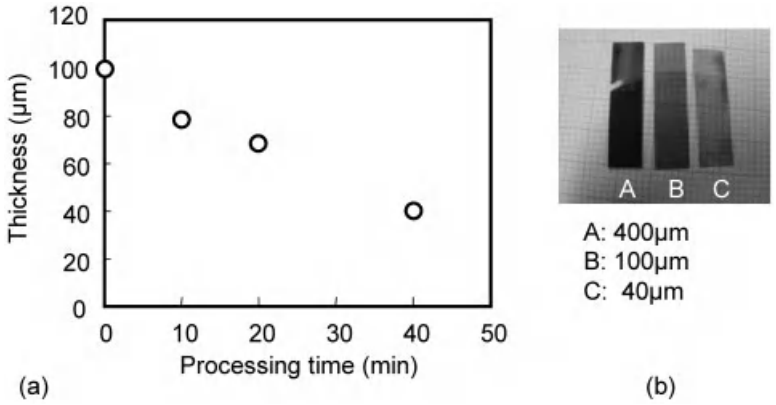

Figure 18.6 Relationship between thickness and processing time.

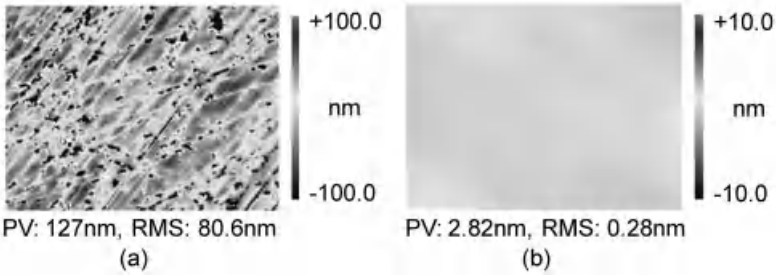

Figure 18.7 Surface roughness (a) before and (b) after PCVM.

parent upon thinning to 40 μm. It is possible, in principle, to thin the sample further because no external force is applied to the sample in PCVM.

Figure 18.7a,b show the surface roughness of the sample before and after PCVM, respectively, measured using a microscope interferometer (Zygo, NewView200). Although the initial surface was very rough (PV [peak-to-valley]: more than 1 μm, RMS [root-mean-square]: 80 nm) because it was finished by mechanical rough polishing, the surface after thinning to 40 μm by PCVM became much smoother (PV: 3 nm, RMS: 0.3 nm). This shows that thinning and smoothing can be simultaneously performed by PCVM. In this experiment, because the sample was cut from the 2-inch SiC wafer using a diamond wheel, the cut surface was also observed both before and after PCVM (Figures 18.8a and b), respectively) using an SEM. It was found that not only did the very rough cut surface become smooth but also the edge of the sample was beveled and rounded. This is because the plasma also faced the side faces of the sample. In a mechanical thinning process the edge of the wafer becomes sharp and chipping of the edge may occur, whereas in the PCVM thinning process the edge becomes rounded automatically and there is no possibility of chipping of the edge.

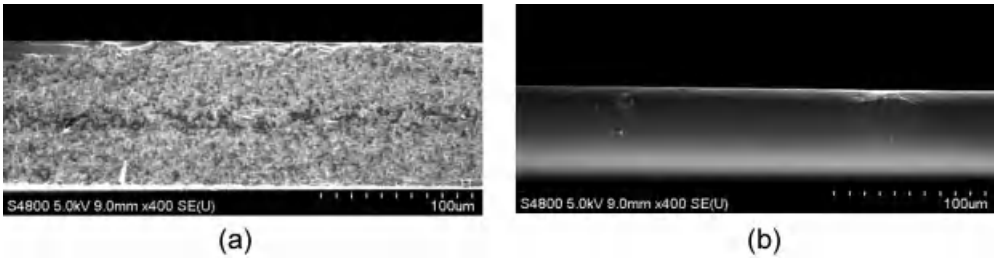

Figure 18.8 SEM images of cut surfaces (a) before and (b) after PCVM.

18.2.4.4 **Summary of Thinning of SiC Wafer**

The thinning of 4H-SiC (0001) wafers by PCVM was investigated. The C face of a strip specimen was successfully thinned to 40 μm without any cracking or chipping, which are unavoidable in mechanical machining methods. Furthermore, the surface roughness was improved after thinning and the edge of the sample was beveled and rounded. Therefore, it appears that PCVM can be used as an effective method for thinning SiC wafers.

18.3
Numerically Controlled Sacrificial Oxidation [14]

18.3.1
Basic Concepts

Numerically controlled sacrificial oxidation consists of two steps, numerically controlled oxidation followed by hydrofluoric acid treatment. An atmospheric-pressure plasma is used for the oxidation. When plasma is generated at atmospheric pressure in the presence of oxygen gas, only the area that faces the localized plasma is oxidized, which results in the formation of an oxidation layer with an arbitrary thickness distribution by controlling the dwell time at each location of the sample. Therefore, numerically controlled oxidation can be realized by controlling the dwell time of plasma exposure on each part of the surface. After oxidation, the intended surface is revealed when the sample is dipped into HF solution (Figure 18.9). The HF cleaning process is generally used as a final cleaning process in silicon wafer production. Thus, additional HF treatment is considered not to be necessary by combining the final cleaning process and the removal of the oxidation layer formed by this technique.

The following are the advantages of this method compared with direct dry etching processes. First, the surface is protected from contamination during the plasma process because the finished surface is generated as an interface. Secondly, there is no need for fluoride gases such as CF_4 or SF_6, which are used in dry etching processes and are well-known greenhouse gases. In this method, the gases used are oxygen and an inert gas, which are not only more environmentally friendly, but also cost effective. Thirdly, the reaction product is not a gas but a solid oxide

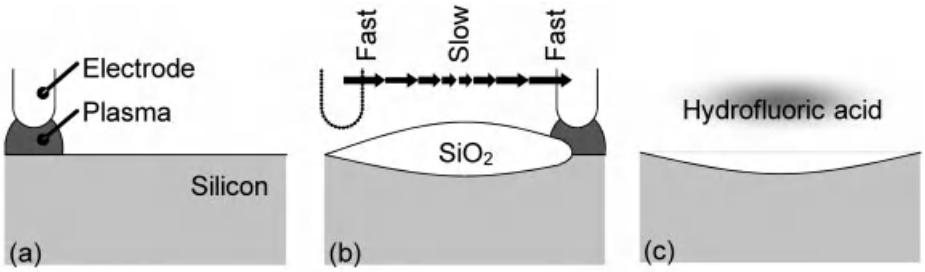

Figure 18.9 Procedure of numerically controlled sacrificial oxidation using atmospheric-pressure plasma. (a) Initial state, (b) numerically controlled oxidation by scanning speed control, and (c) dipping into hydrofluoric acid. (Reproduced from Sano *et al.*, 2008 IEEE international SOI conference proceedings, 166, Copyright 2008 IEEE with permission.)

film; thus, there is no need for special waste gas treatment equipment. It is also easy to control the gas composition during the process. Although in this method, HF treatment is required after the oxidation, this is not disadvantageous because HF cleaning must be performed even after dry etching to remove contamination. Thus, this method has the potential of achieving more environmentally friendly and ultraclean precision machining.

18.3.2 Basic Experiments

18.3.2.1 Experimental Apparatus

For experiments, we used a numerically controlled PCVM apparatus, which is described elsewhere [15]. This apparatus has a spherical electrode (ϕ200 mm) for the generation of localized atmospheric-pressure rf plasma and a speed-controllable X-Y table. The oxidation characteristics of silicon were examined. A p-type 8-inch bulk silicon wafer was used as a specimen. The crystal orientation was (100) and the resistivity was 10–20 Ω cm. Gas with composition $He:O_2 = 98:2$ was used to fill the chamber to atmospheric pressure after evacuating air from the chamber. The gap between the electrode and the specimen was 0.5 mm, and the supplied rf power was 750 W. The thickness of the oxide layer was measured by spectroscopic ellipsometry (SPORA, GESP-5).

18.3.2.2 Oxidation Mark

Figure 18.10a shows the distribution of the thickness of the oxide layer after 1 min of oxidation. The distribution has a convex shape and is nearly axisymmetric. This is caused by the distribution of the gap between the spherical electrode and the specimen. The gap at the center of the plasma is 0.5 mm, whereas that in the plasma-boundary region is approximately 1.6 mm. Thus, the electric-field strength and the density of oxygen radicals are maximum at the center of the plasma, which results in such a distribution. We call this distribution the "oxidation mark". Figure 18.10b shows the relationship between the oxide thickness at the thickest

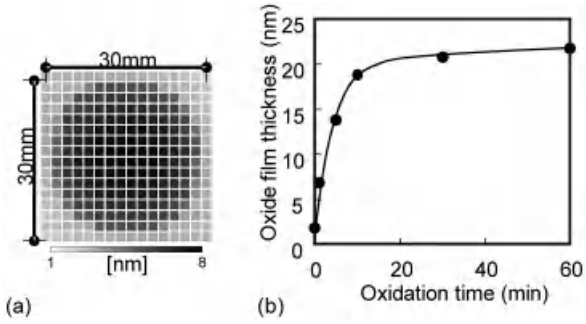

Figure 18.10 Basic oxidation characteristics. (a) Thickness distribution of oxide layer after 1 min oxidation (oxidation mark) and (b) relationship between oxide thickness and oxidation time. (Reproduced from Sano *et al.*, 2008 IEEE international SOI conference proceedings, 166, Copyright 2008 IEEE with permission.)

part of the oxide layer and the oxidation time. The thickness increases rapidly in the first few minutes, but the rate of increase is low after 10 min. The former indicates reaction-controlled growth and the latter indicates diffusion-controlled growth. To obtain good controllability, numerically controlled oxidation should be performed during the linearly increasing period of the reaction-controlled growth.

18.3.2.3 **Oxidation Rate**

To ensure that the oxide thickness can be efficiently controlled by the dwell time, the relationship between oxide thickness and table speed was examined. After the plasma was broken down, a silicon wafer was moved in one direction at a constant speed of V. This produced a band-like oxidation area, as shown in Figure 18.11a. The thickness profile was measured by spectroscopic ellipsometry and evaluated by its width and maximum thickness. Figure 18.11b shows the relationship between the oxide thickness and dwell time. The dwell time has an inverse relationship with table speed. The figure shows that the oxide thickness was proportional to the dwell time. It seems that reaction-controlled growth is more dominant than diffusion-controlled growth in such a thin oxide region. Figure 18.11c shows the relationship between the width of the oxide area and the dwell time. It is shown that the width did not change with dwell time. This means that the size of the plasma did not change with table speed. From these results, it is shown that numerically controlled oxidation is feasible by controlling the scanning speed.

18.3.2.4 **Surface Roughness**

The roughness of the surface after sacrificial oxidation followed by HF treatment was evaluated. The reduction in thickness was approximately 3 nm. Surface roughness was measured by atomic force microscopy (AFM). The surface roughness of the as-received silicon wafer was also measured for comparison. Figures 18.12a and b show AFM images of the surface of the as-received silicon wafer and

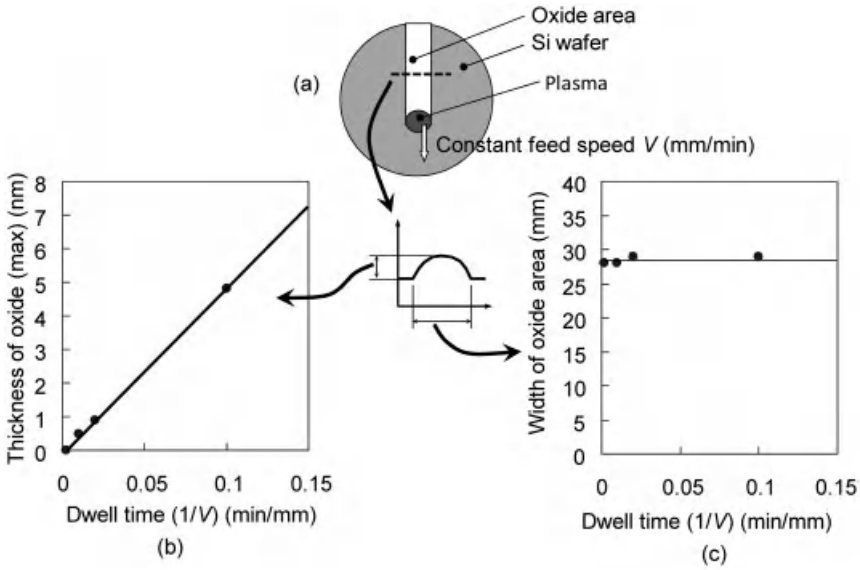

Figure 18.11 Thickness profiles of oxide at various scanning speeds. (a) Schematic of experiment, (b) relationship between thickness of oxide and scanning speed, and (c) relationship between width of oxide and scanning speed. (Reprinted from Sano *et al.*, J. Cryst. Growth 310, 2175, Copyright (2008), with permission from Elsevier.)

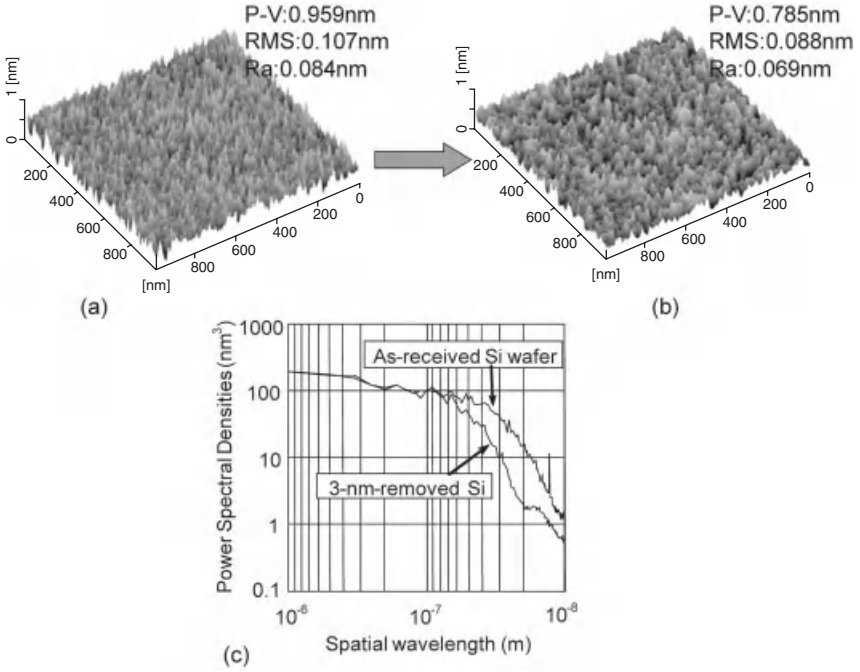

Figure 18.12 AFM images of surface of silicon wafer. (a) As-received silicon wafer, (b) processed wafer, and (c) power spectral densities of (a) and (b). (Reprinted from Sano *et al.*, J. Cryst. Growth 310, 2175, Copyright (2008), with permission from Elsevier.)

processed wafer, respectively. It is clear that all values of roughness, such as PV, RMS and centerline average roughness (Ra) were improved. It seems that the roughness, particularly that of the high-frequency component, decreased. Figure 18.12c shows the power spectral densities of both surfaces shown in Figures 18.12a and b. It is clear that the surface roughness was improved, particularly for a spatial wavelength of up to 50 nm. The reason for the improved roughness is qualitatively considered to be that the oxidation reaction proceeds not only in the vertical direction into the substrate but also in the lateral direction. Therefore, the nanometer-scale convex regions are considered to become smaller and finally to disappear as the oxidation progresses.

18.3.2.5 Summary of the Basic Experiments

The basic experiments of numerically controlled sacrificial oxidation were conducted using a silicon substrate. As a result, it was found that the thickness of the oxide produced was proportional to the dwell time of the plasma for the oxide thicknesses of less than 5 nm. It was also found that the surface roughness was improved, particularly for a spatial wavelength of 10–50 nm.

18.3.3 Improving Thickness Uniformity of SOI

18.3.3.1 Background

Semiconductor substrates such as silicon and related materials are required to be increasingly precise and of increasingly high quality. A silicon-on-insulator (SOI) wafer is one such substrate with a layered silicon-insulator-silicon structure. MOSFETs fabricated on the top thin silicon layer of an SOI wafer operate faster and at a lower power than those fabricated on a bulk silicon wafer. SOI MOSFETs have been installed in high-end CPUs for high-performance computers and in low-power LSIs for wristwatches. The scaling down of MOSFETs, which improves performance, results in thinner SOI wafers being required. An SOI layer of less than 20 nm is required for the dynamic random-access memory (DRAM) half-pitch node of 40 nm [16]. In addition, the deviation of the thickness is required to be within ±5% because of the need for threshold voltage uniformity. To fabricate such an ultrathin and highly uniform SOI wafer, conventional polishing methods cannot be applied. Thermal expansion and mechanical vibration render precise thickness control impossible. In addition, a crystallographically deformed layer is introduced into the machined surface because plastic deformation or brittle fracture is utilized in machining mechanisms. The thinning of an SOI layer by numerically controlled PCVM (NC-PCVM) was reported. Using NC-PCVM, a commercially available 8-inch SOI wafer was thinned. Although the SOI layer thickness of 97.5 ±4.7 nm was successfully reduced to 7.5 nm and the deviation was improved to 1.5 nm by NC-PCVM [17], greater accuracy is desired. Thus, numerically controlled sacrificial oxidation was attempted as a more precise finishing technique to improve the thickness variation of an SOI.

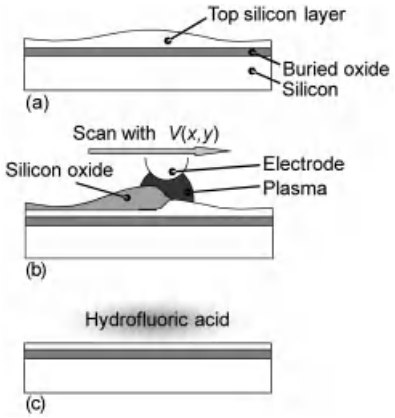

Figure 18.13 Procedure for finishing SOI by numerically controlled sacrificial oxidation. (a) Initial state, (b) numerically controlled oxidation by controlling the scanning speed of the plasma, and (c) dipping into HF solution after oxidation. (Reprinted from Sano *et al.*, J. Cryst. Growth 310, 2176, Copyright (2008), with permission from Elsevier.)

18.3.3.2 **Procedure for Uniformizing**

Figure 18.13 shows the procedure for finishing the SOI by numerically controlled sacrificial oxidation. Figure 18.13a shows the initial state. The thickness distribution of the silicon layer of the initial SOI wafer is measured by spectroscopic ellipsometry or reflection spectroscopy. The scanning speed at each point $V(x,y)$ is calculated as the inverse of the dwell time, which is computed so that silicon of the redundant thickness at each point can be completely oxidized. Then, numerically controlled oxidation is performed by controlling the scanning speed of the plasma using the calculated $V(x,y)$ (Figure 18.13b). After oxidation, the uniform silicon layer is revealed when the wafer is dipped into HF solution (Figure 18.13c).

18.3.3.3 **Uniformizing of 300 mm SOI** [18]

A commercially available p-type ϕ300-mm SOI wafer was used. The thickness of the top silicon layer was 60 nm, the thickness of the buried oxide layer was 145 nm, the crystal orientation was (100), and the resistivity was 8–12 Ω cm. Figure 18.14a shows the thickness distribution of the silicon layer of the as-received wafer measured by reflection spectroscopy. The spatial resolution used in the measurement was 1 mm, and the data for the outer 10 mm edge were excluded (that is, measurement was over a circular area with a diameter of 280 mm). Figure 18.14b shows the thickness distribution of the wafer processed by numerically controlled sacrificial oxidation. A raster scan method with a pitch of 1 mm was used to control the X-Y table motion. Figure 18.14c,d show histograms based on the distributions shown in Figures 18.14a and b, respectively. P–V indicates the range of the thickness, and σ is the standard deviation of the thickness. The range was improved from 2.4 to 0.9 nm, and the standard deviation was also improved from 0.334 to 0.136 nm.

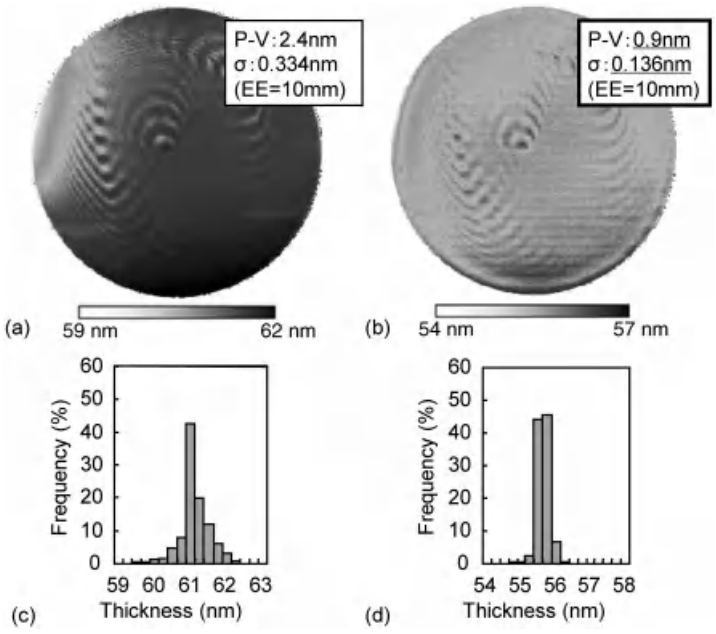

Figure 18.14 Thickness distributions of top silicon layer of SOI wafer. (a) As-received ϕ300-mm SOI wafer, (b) processed ϕ300-mm SOI wafer, (c) histogram based on (a), and (d) histogram based on (b). (Reproduced from Sano *et al.*, 2008 IEEE international SOI conference proceedings, 166, Copyright 2008 IEEE with permission.)

It is clear that the initial thickness distribution was corrected with high accuracy. The main cause of the residual thickness fluctuation was considered to be that the size of the plasma was much larger than the spatial wavelength of the thickness fluctuation of the as-received wafer. Thus, a more uniform SOI is expected to be formed when a smaller plasma is applied using a smaller electrode.

18.3.3.4 Summary of Improving Thickness Uniformity of SOI

Numerically controlled sacrificial oxidation using localized atmospheric-pressure plasma was applied to the ultraprecision finishing of an SOI wafer. As a result of applying this finishing technique to a commercially available ϕ300-mm SOI wafer, the range was improved from 2.4 to 0.9 nm, and the standard deviation was also improved from 0.334 to 0.136 nm. It was shown that numerically controlled sacrificial oxidation is very effective for finishing an ultraprecision SOI wafer.

18.4 Conclusions

Using atmospheric-pressure plasma, a high processing rate, a damage-free processed surface, and a maskless process can be achieved because of its high radical

density and short mean free path. Two crystal-machining techniques using atmospheric-pressure plasma, PCVM and numerically controlled sacrificial oxidation have been described.

As recent topics of PCVM, the beveling and thinning of a SiC wafer, were investigated. As a result of beveling a 2-inch 4H-SiC (0001) wafer, the entire circumference of the SiC wafer was beveled uniformly to a smooth and round edge with no microcracks. In addition, the C face of a strip 4H-SiC (0001) substrate was successfully thinned to 40 μm without any cracking or chipping. Furthermore, surface roughness was improved after thinning. It appears that PCVM can be used as an effective method of beveling and thinning SiC wafers.

Numerically controlled sacrificial oxidation is a recently developed ultraprecision machining technique using atmospheric-pressure plasma. As a result of basic experiments using a silicon substrate, it was found that the thickness of the oxide produced was proportional to the dwell time of the plasma for the oxide thicknesses of less than 5 nm. It was also found that the surface roughness was improved. By applying numerically controlled sacrificial oxidation to improving the thickness uniformity of a commercially available ϕ300-mm SOI wafer, the range of thickness was improved from 2.4 to 0.9 nm. It was shown that this technique is very effective for finishing an ultraprecision SOI wafer. Although the application range of this technique is limited to a finishing with a small amount of removal at this time, it will be expected to be broadened to such areas as figuring, polishing, and patterning by concurrent use of a heating technique which enables larger removal.

References

1 Mori, Y., Yamamura, K., and Sano, Y. (2003) *Crystal Growth Technology* (eds H.J. Scheel and T. Fukuda), John Wiley & Sons, Ltd, Chichester, Chapter 26, pp. 587–606.

2 Sano, Y., Yamamura, K., Mimura, H., Yamauchi, K., and Mori, Y. (2008) *Crystal Growth Technology* (eds H.J. Scheel and P. Capper), Wiley-VCH Verlag GmbH, Weinheim, Chapter 19, pp. 475–495.

3 Mori, Y., Yamamura, K., Yamauchi, K., Yoshii, K., Kataoka, T., Endo, K., Inagaki, K., and Kakiuchi, H. (1993) *Nanotechnology*, **4**, 225–229.

4 Mori, Y., Yamauchi, K., Yamamura, K., and Sano, Y. (2000) *Rev. Sci. Instrum.*, **71**, 4627–4632.

5 Mori, Y., and Yamauchi, K. (1996) Jpn. Patent No. 2521127.

6 Mori, Y., and Yamauchi, K. (1990) U.S. Patent No. 4960495.

7 Mori, Y., and Yamauchi, K. (1993) Eur. Patent No. 0300224.

8 Sano, Y., Watanabe, M., Yamamura, K., Yamauchi, K., Ishida, T., Arima, K., Kubota, A., and Mori, Y. (2006) *Jpn. J. Appl. Phys.*, **45**, 8277–8280.

9 Sano, Y., Watanabe, M., Kato, T., Yamamura, K., Mimura, H., and Yamauchi, K. (2009) *Mater. Sci. Forum*, **600–603**, 847–850.

10 Hara, H., Sano, Y., Mimura, H., Arima, K., Kubota, A., Yagi, K., Murata, J., and Yamauchi, K. (2006) *J. Electron. Mater.*, **35**, L11–L14.

11 Arima, K., Hara, H., Murata, J., Ishida, T., Okamoto, R., Yagi, K., Sano, Y., Mimura, H., and Yamauchi, K. (2007) *Appl. Phys. Lett.*, **90**, 202106.

12 Kato, T., Sano, Y., Hara, H., Mimura, H., Yamamura, K., and Yamauchi, K. (2009) *Mater. Sci. Forum*, **600–603**, 843–846.

13 Kato, T., Sano, Y., Hori, T., Yamamura, K., Mimura, H., Katsuyama, Y., and Yamauchi, K. (2008) The 4th Asian Conference on Crystal Growth and Crystal Technology, p. 189.
14 Sano, Y., Masuda, T., Mimura, H., and Yamauchi, K. (2008) *J. Cryst. Growth*, **310**, 2173–2177.
15 Mori, Y., Yamamura, K., and Sano, Y. (2004) *Rev. Sci. Instrum.*, **75**, 942–946.
16 International Technology Roadmap for Semiconductors (ITRS) (2007) International Technology Roadmap for Semiconductors 2007 Edition, Front End Processes, http://www.itrs.net/Links/2007ITRS/2007_Chapters/2007_FEP.pdf.
17 Sano, Y., Yamamura, K., Mimura, H., Yamauchi, K., and Mori, Y. (2007) *Rev. Sci. Instrum.*, **78**, 086102.
18 Sano, Y., Masuda, T., Kamisaka, S., Mimura, H., Matsuyama, S., and Yamauchi, K. (2008) 2008 IEEE International SOI Conference Proceedings, pp. 165–166.

Index

Note: References in **bold** indicates a table and references in *italics* indicates a figure or photograph.

a
accelerated crucible rotation technique (ACRT) 41, 178–182
active inspection (airport) scanners 302
advanced spectroscopy portals (ASP) 301
Al–In–Ga–P–As–Sb, possible ternary alloys from 157
AlAsSb
– growth from AlGaAsSb **164**, 164
– growth from AlInAsSb 165, **165**
AlGaAs, growth from AlGaAsSb 163, 164, **164**
AlGaAsSb melt, growth from 163, 164
AlGaInSb melt, growth from 167, 168
AlGaN HVPE 26
– computed aluminum nitride (AlN) molar fraction vs. Al content in *33*, 33
– distribution of AlCl and $AlCl_3$ molar fractions *32*, 32
– quasi-thermodynamic model 27, 29, 30
– results and discussions 31–35
– theoretical analysis 27
AlGaN quantum wells, deep-UV emission of 123
AlGaP, growth from AlGaPSb 166, 167, **167**
AlGaPSb melt, growth from 166, 167
AlGaSb, growth from AlGaInSb **168**, 168
AlInAs, growth from AlInAsSb **165**, 165
AlInAsSb melt, growth from 164, 165
AlInP, growth from AlInPSb **166**, 166
AlInPSb melt, growth from 165, 166
alkali halide crystals (AHC)
– advanced growth-control algorithms 292–295
– continuous growth of 283–297
– conventional melt-growth methods 284, 285
– dynamics of thermal conditions during continuous growth 290–292
– growth-process control 286
– macrodefect formation in 287–290
– melt-feeding methods of growth 285, 286
– melt-level changes during growth control by the algorithm with background feeding *294*, 294
– modern requirements 283, 284
– principles for growth of large-size 284
– size of crystals 283
– steady-state crystallization conditions 284–286
– two-circuit method of growth-process control 295, *295*
AlPAs 172
– growth from AlPAsSb 170, 171, **171**
AlPAsSb melt, growth from 170, 171
alumina crucibles 154, 156, 167
aluminum chloride (AlCl) *32*
aluminum nitride (AlN)
– computed growth rate vs NH_3 flow rate 31, 32
– concentration of residual oxygen for sublimation growth 121
– cooling of devices on 121
– description of 25
– distribution of supersaturation and evolution of 128, *129*
– growth of bulk crystals 131
– growth rate 38
– hydride vapor phase epitaxy (HVPE) 26
– local interface flux on surface of 128
– manufacture of 121–135

Crystal Growth Technology. Semiconductors and Dielectrics. Edited by P. Capper and P. Rudolph
Copyright © 2010 WILEY-VCH Verlag GmbH & Co. KGaA, Weinheim
ISBN: 978-3-527-32593-1

– modeling of sublimation growth 126–129
– modeling of vapor-phase growth of bulk crystals 25–39
– pressure inside the crucible and crystal growth rate 128, *128*
– quasi-thermodynamic model of HVPE 27, 29, 30
– raising growth rates to grow bulk crystals 34
– resistivity 131, 132
– results and discussions 131, 132
– results and discussions of HVPE 31–35
– SiC seeds use in crucibles and initial growth of 129, 131
– sublimation growth of 125, 126
– substrate production 25
– theoretical analysis of HVPE 27
– transversal slice of bulk crystal *132*
aluminum trichloride ($AlCl_3$) *27*, 27, 30, 31, *32*, 32, 33, 35, 38
amorphous hydrogenated silicon 306
amplified spontaneous emission (ASE) 230
ampoule support
– – configurations of 199–201
– CZT bulk crystals grown using 199–201
angular vibrational technique (AVT) 41, 42
ANSYS 110
anti-Schlichting flow 46
antimonide-based quaternary melts, low-temperature growth of ternary III-V semiconductor crystals from 151–174
APG-1 243
APG-2 243
arsenic 75
atmospheric pressure plasma, crystal machining using 315–329
atomic force microscopy (AFM) 324
averaged vibrational flow (AVF) 48
axial Lorentz force intensity 111, *112*
axial low-frequency vibration
– interaction between Marangoni convection and 52
– surface flow 51, 52, *52*
axial vibrational control (AVC) 52, 53
– advantages of 59
– in crystal growth 42–48
axial vibrational control (AVC)-assisted Bridgman method 54–58
– crystals grown by 56
– effects of vibration 57, 58
– flow pattern *55*, 55
– insertion of axial vibration 55, *55*
– vibration parameters 57
axial vibrational control (AVC)-assisted Czochralski method 49–54
– effect of crystal penetration on bulk flow pattern in *51*, 51
– flow pattern in *49*, 49
– mechanism of change of flow direction under the crystal in 51, *51*
axial vibrational control (AVC)-assisted floating zone method 58, 59

b

B_2O_3 242
– GaAs crystals grown without encapsulant of 75–99
$BaBr_2$ (Eu) **302**
BaI_2 (Eu) **302**
basal plane dislocations (BPD) 138
– conversion during SiC epitaxy 141–144
– conversion mechanism to TEDs 143, 144
– conversion rates into TEDs 142
– ratio to etch pit density 142, *143*
bending angles 145, 147
beveling, of SiC 317–320
beveling, of silicon carbide (SiC) 328, 329
Bi-DyLuIG films 254, 255
– absorption coefficient vs. wavelength of 255, *257*
– comparison of specific Faraday rotation angle, film thickness and saturation field **260**
– figure of merit in dependence on wavelength of 255, *258*
– magnetization vs. magnetic field perpendicular to the surface of inplane 255, *257*
– magneto-optic sensitivity 260
– photoresponse as function of magnetic induction perpendicular to the film surface 258, *259*
– sensitivity and swing of photoresponse in dependence on the light wavelength 258, *259*
– specific Faraday rotation angle *256*
Bi-substituted garnets 249, 250
Bi-substituted rare earth iron garnet films (Bi-REIG) 249
Bi-TmIG films, "pit density" number as function of the relative misfit *252*, 252
Bi-TmLuIG films, Faraday hysteresis of 254, *255*, 256
Bi-YIG 250
$Bi_3Fe_5O_{12}$ (BIG) 250
$Bi_4Ge_3O_{12}$(BGO) 222–225, **301**

bismuth germanate (BGO) 222–225, **301**
– computational grid and temperature distribution in the furnace 224, *224*
– temperature distribution within the melt *224*, 224
boron 75
– influence on intrinsic point defects of GaAs crystals 94
Bridgman furnace
– vertical 201
– view of *203*
– with a Pt support 201, *202*
Bridgman growth, of mercury cadmium telluride (MCT) 177, 178
Bridgman–Stockbarger method 284
Bridgman technique *47*, 270
– axial vibrational control (AVC) and 54–58
buoyancy convection 103
Burgers vector 139, **139**

c

c-type dislocations 138, **139**, 139, 147
$CaCO_3$ 242
cadmium zinc telluride (CZT) bulk crystals
– cooling process 204
– crystal growth using ampoule support 199–201
– crystal structural quality 205
– FTIR spectrum with and without a Pt support *206*, 206
– furnace assembly 202, *203*
– grown samples analyzed by EDX with and without a Pt tube 206, 207, *207*
– growth process 204
– heating process 204
– physical and chemical properties 195, 196, **196**
– Prandtl number 196
– radial and axial temperature gradients with and without the Pt tube 204, *204*
– recorded rocking curve for the ingot grown with and without a Pt tube 205, *206*
– results and discussions 201–208
– solid/liquid interface 197, 198
– use of a platinum tube as ampoule support in Bridgman growth of 195–210
– uses of 195
– wafers of the grown ingot with and without a Pt support 205, *205*
– zinc concentration 206, 208
– zinc segregation along the axial direction *207*, 207, 208
CaF_2 233, *244*, 244
CaI_2 (Eu) **302**
calcium fluoride 233, *244*, 244
calcium hydroxyl-apatite [$Ca_5(PO4)_3OH$] 233, 234
carbon
– concentration variation and growth of GaAs 79, *80*
– impurity in MC-Si 71
– injection into Si-C-O-Ar crystallizer 13, *14*
cathodoluminescence (CL) spectra, of gallium arsenide (GaAs) 85, *86*
CdTe, incorporation of Zn into 196
CdZnTe, *see* cadmium zinc telluride (CZT) bulk crystals
Ce (LuYAP) **301**
Ce (LYSO) **301**
ceramics, physical properties **208**
CFX 102, 110
ChemApp 5
ChemSage 3, 5, 6, 19, 22
ChemSheet 6
coercivities 250, 254, 255, 264
cold finger 199–201, 208
combined heater magnet technology 101–120
continuous melting process, for production of Nd:phosphate laser glass 233, *234*
convection-driven forces 102–104
convective flows 41
convective meridional flows 103
COREMA 132
crucibles
– base cooling in CZ crystal growth applied to oxide crystals 199, 200
– for synthesis of ternary III-V semiconductor crystals 154, *155*
– mass exchange between ambient and 127
– preparation for aluminum nitride (AlN) growth 129, 130
– selection of material for 125
– used for GaInP growth from GaInPSb melt *157*, 157
CrysMAS 110
crystal growth
– axial vibrational control in 42–48
– from quaternary melts 152
– in Si-C-O-Ar 6–15
– modeling and optimization of oxide crystal growth 213–227
– of carbon-doped GaAs 15–22
– thermodynamic modeling 3–24
– time scales 41
– using vibrational influence 41–64
– without B_2O_3 encapsulant 77–80

crystal machining, using atmospheric pressure plasma 315–329
crystallization, global model *15*, 15
crystals, impurities in 71–74
CsI(Na) crystal
– distribution of temperature and axial temperature gradient 291, *292*
– temperature distribution and melt and gas convection in a ROST-type setup *291*, 291
– visualization of macrodefects initiated by force decrease of control heater power in 287–289, *288*
CsI(Tl) 300, 303, 306–308, 310
– SEM images of the pixel structure 310, *311*
– SEM view of columnar structure 308, *309*
Czochralski technique 70, 76, 77, 102, 199, 219, 222, 269, 270, 277, 285
– axial vibrational control (AVC) and 49–54
– growth of silicon single crystals 7
– growth of YAG single crystal 215
– of silicon crystals under TMF 105, 216
– use of axial-vibrational control in *47*
– Yb:S-FAP crystal growth 237
– YCOB crystal growth 241–243
– *see also* liquid-encapsulated Czochralski (LEC)

d

defect selective etching (DSE) 139, 140, *141*
detached Bridgman technique *47*
deuterated KDP (DKDP) 232
diode pumping 230
dipping techniques *185*, 185, **186**, 186
directional solidification method 67, 68, *69*
dislocation density, of liquid phase epitaxy MCT 187
dislocation elimination by inverse pyramids (DEEP) 145
dislocations 184
– classification of 138
– inclusions, precipitates and 80–83
– interactions during epitaxial growth of SiC and GaN 137–150
– propagation direction of different types of *141*, 141
double-crucible Czochralski method 285

e

eddy current sensor system 262, *263*
edge-defined film-fed growth (EFG) 303, *304*
– of sapphire 219
– of silicon 10–15
edge-defined film-fed growth (EFG) reactor, schematic cross-section 11, *11*
edge dislocations 138
EL2 16, 84, 85
elastic energy 143
electrochemical solution growth (ESG) 124
epitaxial lateral overgrowth (ELO) 145
epoxy paint **303**
equilibrium conditions, state variables 4, 5
etch pits 142
– density 115
– density distribution 82

f

facet angle 145, 147
FactSage 3, 6, 8, 271
FAP, properties of **232**
Faraday effect, of ferrimagnetic Bi-substituted rare earth iron garnet films (Bi-REIG) 249
Faraday hysteresis 254, *255*
– of out-of-plane Bi-TmLuIG film 254, *255*
Faraday rotation
– apparatus for measurement of 254, *254*
– in $Y_3Fe_5O_{12}$ (YIG) 249, 250
flat panel technology 306
floating zone technique *47*
– axial vibrational control (AVC) and 58, 59
floppy discs, visualization of the magnetic information of 261, *262*
flow formation, governing of 60
free-standing nitride substrates 123
freezing temperatures 20, *21*, 22
fusion laser amplifier materials, properties of **232**

g

GaAs, *see* gallium arsenide (GaAs)
GaAsSb, growth from GaInAsSb **159**, 161
GaInAs 152
– growth from GaInAsSb 154, 156, 158–161, *160*
– room-temperature transmission spectra of *160*
GaInAsSb 152, 154
– growth from 158–161
GaInP *153*
– grown from an indium-rich Ga-In-P solution 153
– growth from GaInPSb **162**
– growth of 161–163
– polycrystalline crystal embedded inside a GaInPSb solidified mass *162*
– room-temperature absorption spectra *163*

GaInPSb melt, growth from 161–163
gallium arsenide (GaAs) 101
– apparatus for uncovered VCz crystal growth method *77*
– boundary criteria between regions of stationary laminar, oscillating and nonstationary convection 103, *104*
– chemical potentials of the sublattice species 20
– crystal growth of carbon-doped 15–22
– crystal growth without B_2O_3 encapsulant 77–80
– diameter control of VCz crystals grown from uncovered melts 78, 79, *79*
– DSL-revealed interface morphologies of as-grown *116*
– electrical resistivity and freezing temperatures 20
– freezing temperatures *21*, 22
– gas phase 16
– grown without B_2O_3 encapsulant 75–99
– growth features of SI and SC **80**
– growth results of LEC of 112–114
– heater-magnet modules for LEC growth of *107*, 107
– history of growth without B_2O_3 encapsulant 76, 77
– homogeneity range 20, *21*
– images of as-grown crystals by TMF-LEC within the HMM arrangement *113*, 113
– inclusions, precipitates and dislocations 80–83
– liquid phases 16
– microscopic striation analysis from TMF-LEC *117*
– numerical modeling of growth within LEC chamber 109–111
– positions of the localized states in the bandgap 19, **20**
– residual impurities and special defect studies 83, 84
– results of growth of carbon-doped GaAs 17–19
– room-temperature electrical resistivity *21*, 21, 22
– scatter intensities *81*, 81
– semi-insulating 84–89, 118
– stability analysis 103
– stability region 17
– sublattice model (SUBS) 19–22
– temperature oscillations 109, *110*
gallium monochloride (GaCl) 27, 28
gallium nitride (GaN) 121
– basal plane dislocations (BPD) 145
– classification, nomenclature and characterization of dislocations in 138–141
– commercialization of 138
– computed growth rate vs V/III ratio at different dilutions
– dislocation density 137
– dislocation reduction 145–147
– dislocations 138
– growth of 26, 124
– growth rate 38
– growth rate vs NH_3 flow rate *31*, 31, 32
– HVPE 26
– HVPE, results and discussions 31–35
– nomenclature for some dislocations in **139**
– quasi-thermodynamic model 27
– raising growth rates to grow bulk crystals 34
– reduction of dislocations during homoepitaxy of 144–147
GaN, *see* gallium nitride (GaN)
GaP 152
– room-temperature absorption spectra *163*
GaPAs
– growth from GaPAsSb **169**, *170*
– growth of 169, 170
– room-temperature absorption spectra *163*
GaPAsSb melt, growth from 169, 170
garnet films, high-quality liquid phase epitaxy 250
garnets
– Bi-substituted 249, 250
– *see also* magneto-optic garnet sensor films
GaSb 200
germanium (Ge) 102
– DSL-revealed interface morphologies of as-grown 115, *116*
– growth by VGF in a TMF 118
– growth results of VGF under TMF 114–117
– images of as-grown body and shoulders of *115*, 115
– microscopic striation analysis from TMF-LEC *117*
– radial distribution of carrier concentration and carrier mobility in as-grown VGF 117, *117*
– VGF growth of 108
Gibbs free energy 5, **8**, 8
– calculation for selected reactions 8, 9
– minimization for complex systems 9, 10

global heat transfer 217
graphite 17
– physical properties **208**
group III nitrides
– growth of bulk crystals 123–125
– substrates for 121–123
growth from an element of shape (GES) 304, *304*

h

hard discs, visualization of the magnetic information of 261, *262*
heat-exchanger method (HEM) 200, 270–276
– atmosphere 271, 272
– crucibles 270, 271
– schematic of *271*, *273*
heater-magnet modules (HMM) 106, 107
– controller systems 106
– design 107–109
– for LEC growth of GaAs crystals 107, *107*
Hertz–Knudsen equations 29, 126
HF treatment 322, 323
HgI_2 crystals 200
HgTe-CdTe
– liquidus and solidus lines 175, *176*
– pseudobinary phase diagram *176*, 180
– temperature-phase diagram *176*, 180
high melting point 171
high nitrogen pressure solution growth (HNPSG) 124
high spatial resolution scintillation detectors 306–311
high-temperature chemical vapor deposition (HTCVD) 26, 27
– reactor scale modeling of SiC 38, *38*
high vapor pressure 171
high-*x*-material 179–182
– FTIR map of a short-wavelength slice 180, *181*
hot-wall Czochralski (HWC) chamber 76, 77
HSC chemistry 3
HVPE, *see* hydride vapor phase epitaxy (HVPE)
hydride vapor phase epitaxy (HVPE) 26, 27–35
– of AlGaN 27, 28
– of AlN 26–28
– of GaN 26, 27
– quasi-thermodynamic model of AlN and AlGaN 29, 30, 38
– results and discussions of GaN, AlN and AlGaN 31–35

i

III-V compound semiconductors 151
impurities, in MC-Si 71–74
inclusions, precipitates and dislocations 80–83
inertial fusion energy (IFE) 229–248
infrared laser scattering tomography (LST) 81
InGaN, epitaxy on foreign substrates 122
InGaSn 213
InN bulk crystals 123
InP 152
InPAs, growth from InPAsSb 168, 169, **169**
InPAsSb melt, growth from 168, 169
internal radiation 214
inverted Stepanov (IS) growth *304*, 304
iron 72, 73
– distribution in a solidified silicon ingot *73*, 73

k

KCl
– dynamics of control-heater temperature during growth of 290, *290*
– melt temperature fluctuations 289, *289*
– trends of heater temperature, melt level and crystal diameter during growth of 287, *288*
KDP, *see* potassium dihydrogen phosphate (KDP)
Kerr effect 249
KRIST*MAG* project 92, 102, 106, 107, 118
"Kronos" equipment 108, *108*
Kyropoulos growth 219, *220*
Kyropoulos technique *47*, 285

l

$LaBr_3$: Ce **301**, **302**
$LaCl_3$: Ce **301**
lanthanum halogenides 300
lanthanum, physical properties **208**
laser-gated imaging *190*, 190
laser-heated pedestal growth (LHPG), of sapphire 219
lattice mismatch 122, 123
light scattering 287
line energy 143, *146*
linear encoder 264, *264*
liquid-encapsulated Czochralski (LEC) 16, 75, 76, 101, 102, 104
– dummy measurements with the HMM 111, 112, *112*
– GaAs 84, 85, 107, 112–114, 118

– predominance area diagrams *18*
– *see also* Czochralski technique
liquid phase epitaxy (LPE) *47*, 125, 264
– deposition and topological film properties 251–253
– of mercury cadmium telluride (MCT) 184–191
liquid phase epitaxy (LPE) films
– flaked off from the substrate surface *252*, 253
– pit densities *251*, 251
– typical deposition parameters 251
lithium (Li), use in growth of GaN 124
local (hot zone) heat transfer 217
loophole technology *189*
Lorentz force 92
– axisymmetric toroidal pattern 105
Lorentz force density 102
– vertical component from dummy measurements 111, 112
low-bandgap materials, availability of 171
low-frequency vibrations
– influence on a liquid 46
– influence on crystal growth 43, 44
$Lu_{2(1-x)}Y_{2x}SiO_5$ **301**
Lu_2O_3 267, 268
– crystal growth 269–276
– physical and spectroscopic properties **269**
Lu_2SiO_5: Ce(LSO) **301**
$LuAlO_3$: Ce (LuAP) **301**
LuI_3: Ce **301**
lutetium (Lu), phase diagram *272*
$Lu_xY_{2x}AlO_3$ **301**
LW arrays 184

m

macrodefects, formation in alkali halide crystals 287–290
magnetic fields 91–94
– quantitative determination 264
magnetic induction 104
– of steady and nonsteady fields 105
magneto-optic garnet sensor films 249–266
– applications of 260–264
– comparison of the resolution of an inductive and magneto-optic system using ST 37 test specimen *263*, 263, 264
– effective anisotropy 253
– films with inplane magnetization 253
– films with out-of-place magnetization 253
– images of magnetic field distributions 261–264
– LPE deposition and topological film properties 251–253
– LPE method for production of 264
– magnetic properties 253, 254
– magneto-optic properties 254–260
– quantitative determination of magnetic fields 264
– reproducibility of film properties 260
magneto-rheological finishing (MRF) *240*, 240, 241
magnetoelastic anisotropy 253
MagView 261, *261*
Marangoni convection 52
mathematical modeling 46, 47
matrix detector 306
MC-Si, *see* multicrystalline silicon (MC-Si)
MCT, *see* mercury cadmium telluride (MCT)
melt-convection pattern 289
mercury cadmium telluride (MCT)
– Bridgman/ACRT growth apparatus *179*
– Bridgman/ACRT growth of 177–183
– development history 175
– dislocation density of LPE 187
– growth from Hg-rich solution 185
– growth from Te-rich solution 185, 186
– growth of 185–191
– growth technology using ACRT and LPE 175–193
– liquid phase epitaxy (LPE) of 184–191
– pressure-temperature diagram *176*
– processing 178
– processing using LPE material and loophole technology *189*
Mercury laser 230, 231, *231*, 236, 246
metal-oxide semiconductor field-effect transistors (MOSFETs) 320, 326
metals, thickness and reflectivity for scintillation element separation in arrays and matrices **303**
MgO powder **303**
micro-pulling method 304, 305, *305*
micropipes 137
modeling, of vapor-phase growth of SiC and aluminum nitride (AlN) bulk crystals 25–39
molybdenum, physical properties **208**
MOSFETs, *see* metal-oxide semiconductor field-effect transistors (MOSFETs)
multicrystalline silicon (MC-Si) 67
– crystallization process 68–71
– flow velocity of the melt and temperature distributions during solidification of *70*, 70
– heater power, fraction solidified and solidification rates 68, 69, *69*
– impurities in 71–74

– phase diagram between silicon and carbon 71, *72*
– removal of heavy metals from 72, 73
– solidification furnace 68, *69*
multidimensional radiative heat transfer (RHT), simulation of 215
MW detectors 184
MW OSPREY array *189*

n

Nacken–Kyropoulos technique 270
NaI(Tl) 299, **301**
National Ignition Facility (NIF) 229, *230*
National Ignition Facility (NIF) laser 233, 246
NdFeB compound, magneto-optical visualization of the magnetically printed logo in polymer-bonded 261, 262, *262*
Nd:phosphate glass 229, 232
– production of 233–235
– properties of **232**
– used in the NIF *234*
Nd:SrF_2 **232**, 233
Nd:YAG transparent ceramic slab 245, *245*
– with Sm:YAG co-sintered around the edges *245*, 245
near-IR material 179
nitrogen, solubility in Ga melt 123, 124
novel scintillation materials 300–302
numerical modeling, of growth of semiconductor crystals 109–111
numerically controlled sacrificial oxidation 322–328, *323*
– basic concepts 322, 323
– basic experiments 323–326
– experimental apparatus 323
– oxidation mark 323, 324
– oxidation rate 324
– summary of the basic experiments 326
– surface roughness 324–326

o

optical materials 283
oscillatory crystallization 43
osmium 271
oxidation mark 323, 324
oxidation rate 324
oxide crystal growth
– history of 214
– modeling and optimization of 213–227
– numerical modeling 217, 218
– results and discussions 218–225
oxide crystal melts
– density **218**
– dynamic viscosity **218**
– emissivity **218**
– specific heat **218**
– thermal conductivity **218**
oxide crystals
– absorption coefficient 216
– heat transfer 214
– latent heat of fusion **218**
– melting temperature **218**
– properties of **218**
– refractive index **218**
– specific heat **218**
– thermal conductivity **218**
oxide scintillators 303
oxygen
– effect on aluminum nitride (AlN) crystal growth 130
– phase diagram *272*

p

pBN, physical properties **208**
PCVM, *see* plasma chemical vaporization machining (PCVM)
PETs (positron emission tomography) 299, 302
photovoltaics 184
– silicon crystal growth for 67–74
physical vapor transport (PVT) technology 25, 26
PICOLOG 202
plasma 315
plasma chemical vaporization machining (PCVM) 315–322, 326
– apparatus 323
– applications of *316*, 316
– beveling apparatus and experimental method 317, 318, *318*
– general description 315, 316
– machining of SiC by 316
– numerically controlled 326
– results and discussions 318–320
platinum, physical properties **208**
polycrystalline Nd:YAG ceramic lasers 221
polycrystalline scintillation film, light scattering and output signal shape 306, *307*
potassium dihydrogen phosphate (KDP) 229, 235, *236*
power-plants, advanced material concepts for design of 243–246
Prandtl numbers 58

precipitates, inclusions, dislocations and 80–83
predominance area diagrams 17
premelting 217
pressure, ambient and critical 127
pressure-controlled solution growth (PCSG) 124
propane (C_3H8) 28, 35, 36
pseudo-bulk nitride substrates 123
pulsed laser deposition (PLD) 250

q
quartz **208**
quasi-thermodynamic model 27
– of aluminum nitride (AlN) and AlGaN HVPE 29, 30
quaternary melts
– advantages of 152–154
– crystal growth from 152
– preparation 154–156, *155*

r
radiative heat transfer (RHT) 214–217
– between opaque surfaces 218
range gate 191, *191*
reflector paint **303**
residual impurity concentration 83, 84
resistivity 131, 132
– and carrier mobility 85, *87*
rhenium (Re) 271
– phase diagram *272*
rotation of the melt crucible 103
rotation rate and convection force, stability analysis 103

s
sacrificial oxidation, numerically controlled 322–328
sapphire 122, 219, **220**
saturation fluence, plot versus emission lifetime for fusion amplifier materials 230, *231*
SC GaAs, *see* semiconducting (SC) gallium arsenide (GaAs)
Sc_2O_3 267, 268
– crystal growth 269–276
– physical and spectroscopic properties **269**
– samples *274*
scanners 302
Schlichting flow 45, 46
scintillation film, light collection along the bar of columnar-structured 307, *308*
scintillation materials 300–302
– based on Eu^{2+} crystals **302**
scintillator crystals 283, 299–312
– available for imaging systems **301**
– growth techniques for 302–305
– history of 299
– typical materials and parameters for element separation in arrays and matrices **303**
scintillator detectors
– for image visualization 302–305
– high spatial resolution 306–311
screw dislocations 138
sealed silica crucible *157*
semi-conducting (SC) gallium arsenide (GaAs)
– boron in 89–91
– vacancy concentrations *89*, 89
semiconducting crystals, growth by combined heater magnet technology 101–120
semi-insulating (SI) gallium arsenide (GaAs) 118
– characteristics 88
– electrical and optical properties 84–89
sesquioxides
– structure and physical properties 267–269
– Yb-doped 267–282
Si-C-O-Ar
– crystal growth in 6–15
– Gibbs free energy minimization 9, 10
– selection of species **7**, 7
– test calculation and consistency check 7, 8
SI GaAs, *see* semi-insulating (SI) gallium arsenide (GaAs)
SiC, *see* silicon carbide (SiC)
silane (SiH_4) 28, 36
silica (quartz) crucibles 154
silicon
– axial vibrational control (AVC)-assisted floating zone method 59
– conditions for production in a high-temperature reactor 10
– crystal growth for photovoltaics 67–74
– directional solidification method of crystal growth 67, 68
– dominance in semiconductor wafers 137
– evaporation into an Ar-filled reactor 12, *13*
– partial pressures of different species of 10, *11*
– reaction between oxygen and 14
– regular Si substrate for columnar film growth 310, *311*

– thermodynamic-technological model of the edge-defined film-fed growth of 10–15
– *see also* multicrystalline silicon (MC-Si)
silicon carbide (SiC) 13, 125
– 4H-SiC sample, typical etch patterns 140, *140*
– beveling of 317–320
– classification, nomenclature and characterization of dislocations in 138–141
– conversion of basal plane dislocations during epitaxy 141–144
– description of 25
– dislocation density 137
– fabricating 316, *317*
– growth rate and thickness uniformity versus SiH_4 flow rate 37, *37*
– growth rate as a function of the C_3H_8 flow rate 35, *36*
– growth rate as a function of the $SiCl_4$ flow rate 35, *36*
– high-temperature chemical vapor deposition (HTCVD) 26
– machining by PCVM 316
– modeling of gas-phase nucleation in SiC CVD and HTCVD 30, 31
– modeling of vapor-phase growth of bulk crystals 25–39
– nomenclature for some dislocations in **139**
– seeds 129–131
– semiconductor-on-insulator structures 122
– substrate production 25
– substrates 122
– thickness profiles *325*
silicon carbide (SiC) HTCVD 35–38
silicon carbide (SiC) HTCVD reactor
– flow patterns and temperature distribution *35*
– schematic view and flow patterns 36, *37*
silicon carbide (SiC) wafer
– AFM images of *325*
– beveling of 320
– cross-sectional SEM images of edges of 318, *319*
– electric-field intensity 318, *319*
– profiles of unprocessed and processed edges of 318, *319*
– relationship between thickness and processing time 320, *321*
– SEM images of the cut surfaces before and after PCVM 321, *322*
– surface roughness before and after PCVM *321*, 321
– thinning of 320–322
silicon oil 213
silicon-on-insulator (SOI)
– thickness distribution of top silicon layer of *328*
– thickness uniformity 326–328
– uniformizing of 300 mm 327
silicon tetrachloride ($SiCl_4$) 35
SimuSage 6
single-photon emission computer tomography (SPECTs) 300
SiO_2 15
– *see also* quartz; silica (quartz) crucibles
sliding boat technology 186, **186**, *187*, 187, *188*
slow scintillators 301
sodium (Na), use in growth of bulk group III nitride crystals 124
software 3
solid/liquid interface 197, 198
– concave 198
– convex 198, 200, 201
– correlation between interface and radial segregation 198
– thermal distribution 198
special defect studies 83, 84
$SrBr_2$ (Eu) **302**
$SrCO_3$ 237
SrF_2 237
$SrHPO_4$ 237
SrI_2 (Eu) **302**
state variables, for the description of equilibrium conditions **4**, 4, 5
Stepanov technique *47*, 303, *304*
strain relief 253
stress relief 253
structural zone model 308, *310*, 310
substrates
– for group III nitride devices 121–123
– foreign 122
surface roughness 324–326
SW detectors 189, 190

t
tantalum 271
temperature gradient 219, *220*
templates 123
ternary III-V semiconductor crystals, synthesis and bulk crystal growth 154–171
Tetratex **303**
thermal conductivity 268

Thermo-Calc 3
thermodynamic modeling 3–24
– basics 4–6
– *ChemSage* 5, 6
– crystal growth in the Si–C–O–Ar system 6–15
– crystal growth of carbon-doped GaAs 15–22
thermodynamics, definition 4
thin-disk laser *268*
threading dislocations 138
threading edge dislocations (TED) 138, *139*, 142
threading screw dislocations (TSD) 138
tipping technology 186, **186**
TMF-vapor-pressure controlled Czochralski gallium arsenide (GaAs) crystals, striation patterns 93
transmission electron microscopy (TEM) 140
transparent ceramic technology 245, 246
traveling magnetic field (TMF) 104–106
– generation in heater-magnet modules 106, 107
– growth results 112–117
– research 105
traveling magnetic field (TMF)-vapor-pressure controlled Czochralski 91–94
– and mean dislocation densities 93
– design *92*
– effects on residual impurity concentrations 94
– gallium arsenide (GaAs) crystals, striation patterns *93*
– magnetic-heater *92*
– melt flows and 94
tungsten crucibles 271
tungsten, physical properties **208**

v

vacuum deposition method 306–308
vapor-pressure controlled Czochralski (VCz) gallium arsenide (GaAs)
– absorption coefficient 87, *88*
– CL spectra of *91*
variables, equilibrium conditions **4**, 4, 5
vertical Bridgman (VB) 101
vertical gradient freeze (VGF) 75, 101
– CL spectra of Si-doped boron-contaminated gallium arsenide (GaAs) 90, *90*
– dummy measurements with the HMM 111, 112, *112*
– VCz GaAs crystals 114–117
vibrations
– history of studies of influence on crystal growth 43, 44
– influence on crystal growth 41–64
– kinds of 42
Virtual Reactor™ 127
VM2000 foil **303**
vortices 45, 46, 49, 51, 52, 58, 70, 103, 109, 114, 118

w

wavelength uniformity plots *181–183*

x

X-ray CT 302
X-ray topography (XRT) 140

y

Y_2O_3 242, 267, 268
– crystal growth 269–276
– physical and spectroscopic properties **269**
– samples *274*
$Y_3Fe_5O_{12}$ (YIG) 249, 250
YAG, *see* yttrium aluminum garnet (YAG)
Yb-doped sesquioxides
– crystal growth 269–276
– growth methods with crucibles 269, 270
– growth procedure 273, 274
– growth runs at various oxygen concentrations 275, 276, **276**
– growth technology and laser properties of 267–282
– heat conductivity *268*, 268
– heat-exchanger method of crystal growth 270–276
– heat-exchanger method setup 273, *273*
– laser experiments 279, 280
– modified Czochralski setup *272*, 272, 273
– results 274–276
– spectroscopic characterization 276–279
– structure and physical properties 267–269
Yb_2O_3 237
$Yb:Lu_2O_3$ 274, 280
– absorption and emission cross-sections of 277, 278, *278*
– absorption coefficient 277, *277*
– fluorescence lifetime 278, *278*
– microprobe analysis of the seed region of 275, *276*
– microscopic images *275*
– thin-disk laser results with HEM-grown *279*, 279

Yb:S-FAP crystals 230, 231, 233, 235–241, *236*, 243–246
– first attempts at growing a 12.0-cm diameter boule *244*
– growth of 237, 238
– improved transmitted wavefront of slab before MRF and after MRF *241*, 241
– introductory phase diagram 237, *238*
– laser slab 239, *240*
– magneto-rheological finishing (MRF) *240*, 240
– modeling program 238, 239
– scaling of 243
– slab fabrication 239–241
– world's largest slab 243, *244*
Yb:S-, properties of **232**
Yb:Sc_2O_3 280
– absorption coefficient 277, *277*
– fluorescence lifetime 278, *278*
– thin-disk laser results with HEM-grown 279, *279*
Yb:Y_2O_3 274
– fluorescence lifetime 278, *278*
– microscopic images *275*
Yb:YAG
– absorption and emission cross-sections of 277, 278, *278*
– properties of **232**
$YCa_4O(BO_3)_3$ (YCOB) 232, 241–243, 246
– crystal growth and fabrication 242, 243
– high-quality boules 242, *242*
YIG 249, 250
ytterbium 267
yttrium aluminum garnet (YAG) 213, 219, 220
– role of internal radiation on heat transfer during growth of 216
– simulation of Czochralski growth of 216
– temperature distribution in the furnace *222*, *223*
– temperature gradient distribution 222, *223*
– uses of 221
– velocity vectors 222, *223*
yttrium orthovanadate (YVO_4) 221
yttrium-scandium-gallium garnet, Er concentration fluctuations in crystals grown with and without vibrational influences *50*, 50